Resonant Tunnelling in Semiconductor Heterostructures

by

Mark Levence Leadbeater *B.A.*

Thesis submitted to the University of Nottingham for the degree of Doctor of Philosophy, May 1990.

MISSING PAGES ARE UNAVAILABLE

Abstract

This thesis examines the electrical transport properties of a series of n-type GaAs/(AlGa)As double barrier resonant tunnelling devices with well widths between 50 Å and 2400 Å. The current-voltage characteristics show peak-to-valley ratios as high as 25:1 and as many as seventy resonances, with clear evidence of quantum interference effects at room temperature. The application of a high magnetic field parallel to the current flow produces magneto-oscillations in the transport properties which allow the sheet charge density in the accumulation layer to be determined. The energy level in the well over a wide range of bias is obtained from analysis of thermal activation of resonant tunnelling. The contributions of elastic scattering and LO phonon emission to the valley current are investigated spectroscopically with a magnetic field and two phonon modes of the (AlGa)As barrier are observed.

The buildup of space charge in the quantum well at resonance leads to intrinsic bistability in the current and differential capacitance of an asymmetric structure. Magnetoquantum oscillations due to a degenerate electron gas in the well are used to measure this charge buildup and demonstrate that the tunnelling process is truly sequential. The bistability is dramatically enhanced at high magnetic fields when the lowest energy Landau level of the well can accommodate a high electron density. In a strongly asymmetric sample, a new kind of bistability is observed where the off-resonant current exceeds the resonant current due to enhancement of charge buildup by intersubband scattering. The modulation of the scattering rate by a magnetic field produces periodic oscillations in the width of the bistability.

In a magnetic field applied perpendicular to the current, the resonances are broadened as a consequence of the conservation of canonical momentum. The transition from electric to magnetic quantisation in wide wells is investigated and tunnelling into interfacial Landau levels is observed. The angular dependence of the resonances is used to probe conduction band anisotropy. In a tilted field, a completely new type of magneto-oscillations is observed.

Contents

Acknowledgements

I would like to express my thanks to:

Professor C. A. Bates for allowing me to use the facilities of the Physics Department.

My supervisor, Professor Laurence Eaves, for his enthusiasm, inventiveness and physical insight.

All my colleagues and friends at Nottingham, in particular Elmo Alves, Tim Foster, Mark Fromhold, Dave Hayes, Duncan Maude, Chris Payling, Richard Taylor and Chris White.

Drs. M. Henini and O. H. Hughes for growing the exceptionally high quality samples investigated in this thesis.

Drs. F. W. Sheard and G. A. Toombs of Nottingham University and Dr. P. E. Simmonds from the University of Wollongong for invaluable discussions.

SNCI-CNRS, Grenoble for permitting me to use the high magnetic field facility.

Profesor J. C. Portal and Mr. A. Celeste of INSA, Toulouse and SNCI-CNRS, Grenoble, for making possible the high magnetic field experiments described in this thesis.

Drs. G. Hill and M. A. Pate of Sheffield University and Drs. M. Davies, M. Heath and Mr. J. Middleton at Nottingham for processing of the devices.

Mr. J. L. Dennis for the provision of liquid helium.

The Science and Engineering Research Council for a studentship and funds to attend a conference.

My family for their continual support and encouragement.

Publications

The following publications are related to the work described in this thesis:

'Magnetic Field Studies of Negative Differential Conductivity in Double Barrier Resonant Tunnelling Structures Based on n-InP/(InGa)As.'
M. L. Leadbeater, L. Eaves, P. E. Simmonds, P. A. Claxton, G. Hill and M. A. Pate, *Proc. 5th Int. Conf. Hot Carriers in Semiconductors, Boston, 1987,* published in *Solid-State Electron.* **31**, 707 (1988).

'Magnetic Field Studies of Resonant Tunnelling Double Barrier Structures.'
G. A. Toombs, E. S. Alves, L. Eaves, T. J. Foster, M. Henini, O. H. Hughes, M. L. Leadbeater, C. A. Payling, F. W. Sheard, P. A. Claxton, G. Hill, M. A. Pate and J. C. Portal, *Proc. 14th Int. Symp. GaAs and Related Compounds, Crete, 1987,* published in *IOP Conference Series* **91**, 581 (1988).

'Sequential Tunnelling Due to Intersubband Scattering in Double-Barrier Resonant Tunneling Devices.'
L. Eaves, G. A. Toombs, F. W. Sheard, C. A. Payling, M. L. Leadbeater, E. S. Alves, T. J. Foster, P. E. Simmonds, M. Henini and O. H. Hughes, *Appl. Phys. Lett.* **52**, 212 (1988).

'Investigations of Double Barrier Resonant Tunnelling Devices Based on (AlGa)As/GaAs.'
O. H. Hughes, M. Henini, E. S. Alves, L. Eaves, M. L. Leadbeater, T. J. Foster, A. Celeste and J. C. Portal, *Proc. 15th Conf. Physics and Chemistry of Semiconductor Interfaces, 1988, Monterrey,* published in *J. Vac. Sci. Technol. B* **6**, 1161 (1988).

'Magnetic Field Studies of Resonant and Non-resonant Tunnelling in n-(AlGa)As/GaAs Double Barrier Structures.'
L. Eaves, E. S. Alves, T. J. Foster, M. Henini, O. H. Hughes, M. L. Leadbeater, F. W. Sheard, G. A. Toombs, K. S. Chan, A. Celeste, J. C. Portal, G. Hill and M. A. Pate, in *Physics and Technology of Submicron Structures*, H. Heinrich, G. Bauer and F. Kuchar (Eds.), Springer-Verlag, Berlin (1988).

'Charge Build-up and Intrinsic Bistability in Resonant Tunnelling Devices.'
E. S. Alves, L. Eaves, M. Henini, O. H. Hughes, M. L. Leadbeater, F. W. Sheard and G. A. Toombs, *Proc. International Conference on Electronic Materials, Tokyo, June 13–15, 1988*, published by the Materials Research Society (1989).

'Observation of Intrinsic Bistability in Resonant Tunnelling Devices.'
E. S. Alves, L. Eaves, M. Henini, O. H. Hughes, M. L. Leadbeater, F. W. Sheard and G. A. Toombs, *Electron. Lett.* **24**, 1190 (1988).

'Charge Build-up and Intrinsic Bistability in an Asymmetric Resonant-Tunnelling Structure.'
M. L. Leadbeater, E. S. Alves, L. Eaves, M. Henini, O. H. Hughes, F. W. Sheard and G. A. Toombs, *Semicond. Sci. Technol.* **3**, 1060 (1988).

'Current Bistability in Double-Barrier Resonant-Tunneling Devices.'
T. J. Foster, M. L. Leadbeater, L. Eaves, M. Henini, O. H. Hughes, C. A. Payling, F. W. Sheard, P. E. Simmonds and G. A. Toombs, *Phys. Rev. B* **39**, 6205 (1989).

'Magnetic Field and Capacitance Studies of Intrinsic Bistability in Double-Barrier Structures.'
M. L. Leadbeater, E. S. Alves, L. Eaves, M. Henini, O. H. Hughes, F. W. Sheard, G. A. Toombs, G. Hill and M. A. Pate, *Proc. 4th Int. Conf. Superlattices, Microstructures and Microdevices, Trieste, Italy, 1988*, published in *Superlatt. Microstruct.* **6**, 59 (1989).

'Hybrid Magneto-Electric States in Resonant Tunnelling Structures.'
E. S. Alves, M. L. Leadbeater, L. Eaves, M. Henini, O. H. Hughes, A. Celeste, J. C. Portal, G. Hill and M. A. Pate, *Proc. 4th Int. Conf. Superlattices, Microstructures and Microdevices, Trieste, Italy, 1988*, published in *Superlatt. Microstruct.* **5**, 527 (1989).

'Resonant and Non-Resonant Processes in Double Barrier Structures.'
M. L. Leadbeater, E. S. Alves, L. Eaves, M. Henini, O. H. Hughes, A. Celeste and J. C. Portal, *Proc. 4th Int. Conf. Superlattices, Microstructures and Microdevices, Trieste, Italy, 1988*, published in *Superlatt. Microstruct.* **6**, 63 (1989).

'Magnetic Field Investigations of n-(AlIn)As/(InGa)As Resonant Tunnelling Devices Grown by MOCVD.'
C. A. Payling, C. R. H. White, L. Eaves, E. S. Alves, M. L. Leadbeater, J. C. Portal, P. D. Hodson, D. J. Robbins, R. H. Wallis, J. I. Davies and A. C. Marshall, *Proc. 4th Int. Conf. Superlattices, Microstructures and Microdevices, Trieste, Italy, 1988*, published in *Superlatt. Microstruct.* **6**, 193 (1989).

'Resonant Tunnelling Devices in a Quantising Magnetic Field.'
L. Eaves, E. S. Alves, M. Henini, O. H. Hughes, M. L. Leadbeater, C. A. Payling, F. W. Sheard, G. A. Toombs, A. Celeste, J. C. Portal, G. Hill and M. A. Pate, *Proc. Int. Conf. High Magnetic Fields in Semiconductor Physics II*, Wurzburg, 1988, published in *Springer series in Solid-State Sciences* **87**, 324 (1989).

'Etudes sous Champ Magnétique de l'Effet Tunnel Résonnant et Non Résonnant dans les Structures à Double Barrière n-(AlGa)As/GaAs.'
A. Celeste, J. C. Portal, L. Eaves, E. S. Alves, T. J. Foster, M. Henini, O. H. Hughes, M. L. Leadbeater, F. W. Sheard, G. A. Toombs, K. S. Chan, J. C. Portal, G. Hill and M. A. Pate, *Revue Phys. Appl.* **24**, 343 (1989).

'Investigations of Asymmetric Double Barrier Resonant Tunneling Structures Based on (AlGa)As/GaAs.'
O. H. Hughes, M. Henini, E. S. Alves, L. Eaves, M. L. Leadbeater, F. W. Sheard, G. A. Toombs, G. Hill, M. A. Pate, J. C. Portal and A. Celeste, *Proc. 5th Int. Conf. on MBE, Sapporo, 1988*, published in *J. Cryst. Growth* **95**, 352 (1989).

'Magnetic Field Studies of Elastic Scattering and Optic-Phonon Emission in Resonant-Tunneling Devices.'
M. L. Leadbeater, E. S. Alves, L. Eaves, M. Henini, O. H. Hughes, A. Celeste, J. C. Portal, G. Hill and M. A. Pate, *Phys. Rev. B* **39**, 3438 (1989).

'Hot-Electron Magnetospectroscopy in Resonant Tunneling Devices: A Probe of Conduction-Band Anisotropy.'
O. H. Hughes, M. Henini, E. S. Alves, M. L. Leadbeater, L. Eaves, M. Davies and M. Heath, *Proc. 16th Conf. Physics and Chemistry of Semiconductor Interfaces, Bozeman, Montana, 1989*, published in *J. Vac. Sci. Technol. B* **7**, 1041 (1989).

'Ballistic Transport in Resonant Tunnelling Devices With Wide Quantum Wells.'
M. Henini, M. L. Leadbeater, E. S. Alves, L. Eaves and O. H. Hughes, *J. Phys: Condensed Matter* **1**, 3025 (1989).

'High Magnetic Field Studies of Intrinsic Bistability, Electron Thermalization and Ballistic Transport in Resonant Tunneling Devices.'
M. L. Leadbeater, E. S. Alves, L. Eaves, M. Henini, O. H. Hughes, F. W. Sheard and G. A. Toombs, in *Nanostructure Physics and Fabrication*, M. A. Reed and W. P. Kirk (Eds.), Academic Press, Boston (1989).

'Resonant Tunnelling Studies of Magnetoelectric Quantisation in Wide Quantum Wells.'
M. L. Leadbeater, E. S. Alves, L. Eaves, M. Henini, O. H. Hughes, A. Celeste, J. C. Portal, G. Hill and M. A. Pate, *J. Phys: Condensed Matter* **1**, 4865 (1989).

'Inverted Bistability in the Current-Voltage Characteristics of a Resonant Tunneling Device.'
M. L. Leadbeater, L. Eaves, M. Henini, O. H. Hughes, G. Hill and M. A. Pate, *Proc. 6th Int. Conf. Hot Carriers in Semiconductors, Scottsdale, 1989,* published in *Solid-State Electron.* **32**, 1467 (1989).

'Electrical and Spectroscopic Studies of Space-Charge Buildup, Energy Relaxation and Magnetically Enhanced Bistability in Resonant-Tunneling Structures.'
L. Eaves, M. L. Leadbeater, D. G. Hayes, E. S. Alves, F. W. Sheard, G. A. Toombs, P. E. Simmonds, M. S. Skolnick, M. Henini and O. H. Hughes, *Proc. 6th Int. Conf. Hot Carriers in Semiconductors, Scottsdale, 1989,* published in *Solid-State Electron.* **32**, 1101 (1989).

'Quantum Interference and Space Charge Effects in Double Barrier Structures Incorporating Wide Quantum Wells.'
E. S. Alves, M. L. Leadbeater, L. Eaves, M. Henini and O. H. Hughes, *Proc. 6th Int. Conf. Hot Carriers in Semiconductors, Scottsdale, 1989,* published in *Solid-State Electron.* **32**, 1627 (1989).

'The Effect of the X Conduction Band Minima on Resonant Tunnelling and Charge Build-Up in Double Barrier Structures Based on n-GaAs/(AlGa)As.'
T. J. Foster, M. L. Leadbeater, D. K. Maude, E. S. Alves, L. Eaves, M. Henini, O. H. Hughes, A. Celeste, J. C. Portal, D. Lancefield and A. R. Adams, *Proc. 6th Int. Conf. Hot Carriers in Semiconductors, Scottsdale, 1989,* published in *Solid-State Electron.* **32**, 1731 (1989).

'Observation of Space-Charge Build-Up and Thermalisation in an Asymmetric Double-Barrier Resonant Tunnelling Structure.'
M. L. Leadbeater, E. S. Alves, F. W. Sheard, L. Eaves, M. Henini, O. H. Hughes and G. A. Toombs, *J. Phys: Condensed Matter* **1**, 10605 (1989).

'Optical Investigation of Charge Accumulation and Bistability in an Asymmetric Double Barrier Resonant Tunneling Heterostructure.'
D. G. Hayes, M. S. Skolnick, P. E. Simmonds, L. Eaves, D. P. Halliday, M. L. Leadbeater, M. Henini and O. H. Hughes, *Proc. 4th Int. Conf. Modulated Semiconductor Structures, Ann Arbor, U.S.A.,* to be published in *Surf. Sci.* (1989).

'The Effect of Conduction Band Anisotropy on Hybrid Magneto-Electric States in Resonant Tunneling Devices.'
M. Henini, M. L. Leadbeater, E. S. Alves, L. Eaves, O. H. Hughes, G. Hill and M. A. Pate, *Proc. 4th Int. Conf. Modulated Semiconductor Structures, Ann Arbor, U.S.A.,* to be published in *Surf. Sci.* (1989).

'Electronic Processes in Double Barrier Resonant Tunneling Structures Studied by Photoluminescence Spectroscopy in Zero and Finite Magnetic Field.'
M. S. Skolnick, D. G. Hayes, P. E. Simmonds, A. W. Higgs, G. W. Smith, H. J. Hutchinson, L. Eaves, M. Henini, O. H. Hughes, M. L. Leadbeater and D. P. Halliday, *Phys. Rev. B*, to be published (1990).

'Inverted Bistability: A New Type of Intrinsic Effect in Asymmetric Double Barrier Structures.'
M. L. Leadbeater, L. Eaves, M. Henini and O. H. Hughes, *Proc. 16th Int. Symp. GaAs and Related Compounds, Karuizawa, Japan, 1989, IOP Conf. Series*, to be published (1990).

'A New Bistability Effect in the Current-Voltage Characteristics of a Resonant Tunneling Device.'
M. L. Leadbeater, L. Eaves, M. Henini and O. H. Hughes, *Appl. Phys. Lett.*, to be published (1990).

CHAPTER 1

Resonant Tunnelling

1.1 Introduction

In 1970 Esaki and Tsu [1] proposed the artificial creation of a new type of electronic materials consisting of alternating potential barriers and wells by successive deposition of different semiconductor layers. Advances in growth technology over the last twenty years have made possible the routine fabrication of such semiconductor structures with one or more dimensions comparable to the de Broglie wavelength of the conduction electrons. The properties of these 'low-dimensional' devices are governed by the quantum-mechanical interference effects associated with the wave nature of the electrons and reveal a wide variety of macroscopic quantum effects. The best examples have been in the III-V semiconductors and alloys where there are a number of latticed-matched compounds with large band offsets, *e.g.* GaAs/(AlGa)As, (InGa)As/InP and (InGa)As/(AlIn)As — see Figure 1.1. Interfaces of extremely high quality can be obtained. The application of band-gap engineering through the techniques of epitaxial growth results in nearly limitless opportunities for creating structures for physical exploration as well as for electronic and optical applications. Some indication of the wide range of investigations is given in references [2] and [3]. Most experimental and theoretical work to date has focussed on the transport properties in the plane of the confined structures, for example in modulation-doped heterojunctions, but there has recently been a resurgence of interest in transport perpendicular to the interfaces which has been brought about by the improvements in growth quality.

One of the simplest devices is the double barrier resonant tunnelling device (DBS) [4] which is the subject of this thesis. This basically consists of a narrow (20-2000 Å) layer of a low-band-gap material, such as GaAs, sandwiched between two thin layers of a material with a higher band gap, in this case the alloy (AlGa)As, as schematically depicted in Figure 1.2. Electrons in the central well region are confined by the potential barriers and so their momentum in the direction perpendicular to the plane is quantised, producing a sequence

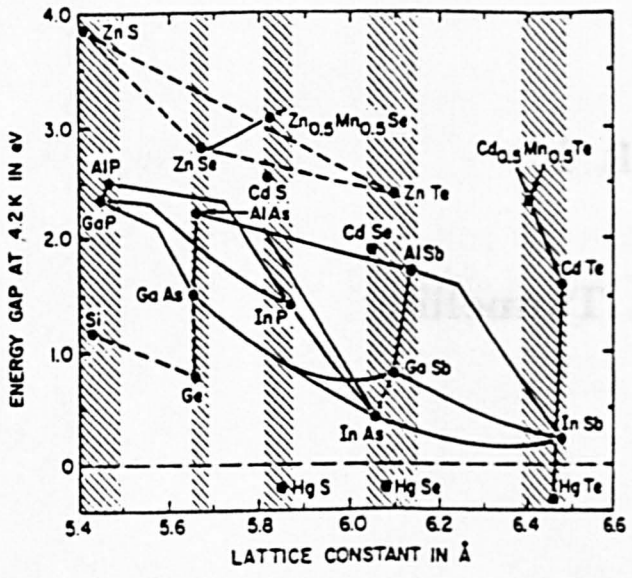

Figure 1.1: Energy gaps at 4 K versus lattice constant (reference [5]).

of quasi-two-dimensional subbands. Because the barriers have finite thickness, electrons can leave the well by tunnelling and the states have a finite lifetime τ, which means that the energy levels have a finite width, $\delta\epsilon \sim \hbar/\tau$ [6].

When an electron from the contact region is incident on the barriers, they act like partially reflecting mirrors — hence the common analogy to the Fabry-Pérot étalon in optics. If the energy and lateral momentum of an incident electron coincide with those of a quasi-bound state in the well, it tunnels through both barriers without attenuation — even though its kinetic energy may be considerably below the height of the potential barriers [7, 8, 9]. A plot of transmission coefficient against incident energy is reproduced in Figure 1.2.

In an actual device, we can vary the energy of the incident electrons relative to the energy levels of the well by applying a bias across the structure, as shown in Figure 1.3. The electrons are supplied by heavily-doped regions on either side of the double barrier structure. With no applied bias, the energy level in the well lies above the occupied states in the contact. But if the energy level is brought down below the Fermi level in the left-hand contact (conventionally called the emitter), a large resonant current flows. The magnitude of this current is governed by the number of electrons which can tunnel into the quasi-bound state of the well with the conservation of energy and transverse momentum, and the transmission coefficients of the emitter (left-hand) and collector (right-hand) barriers. The peak in the current corresponds to the maximum number of incident electrons having the same energy as the well state which occurs when the energy level is aligned with the conduction band edge in the contact. At higher biases, there are no electrons which can tunnel whilst conserving transverse momentum and so the current drops sharply, creating a region of negative differential resistivity (NDR) *i.e.* an increase in bias produces a decrease in the current. This is a basic consequence of the conservation conditions and the reduced dimensionality of the states in the quantum well

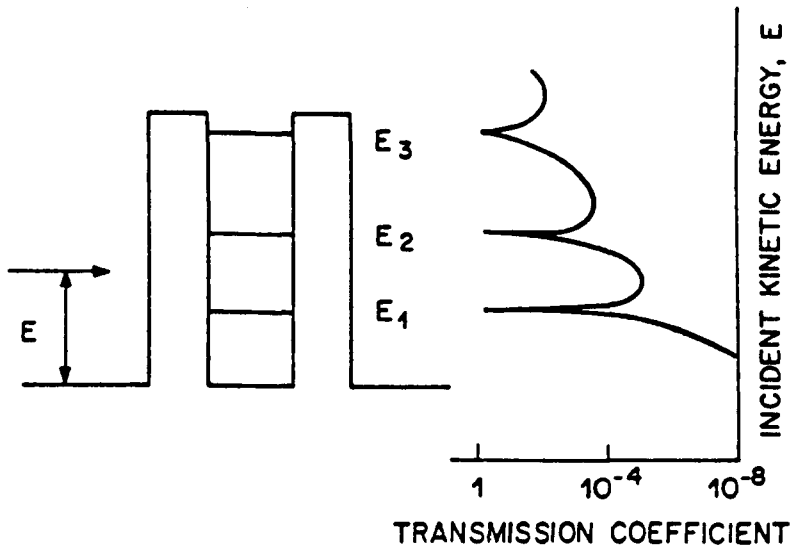

Figure 1.2: Schematic illustration of a double barrier structure. The transmission coefficient is unity when the kinetic energy of the incident electron coincides with a quasi-bound state of the well.

[10]. When biased beyond the resonant peak, the main contribution to the current is from scattering-assisted transitions (*e.g.* LO phonon emission) which are discussed in Section 3.4. If the bias is further increased, the next state of the quantum well is eventually brought into resonance producing another peak in the current (Section 3.6).

The first investigation of resonant tunnelling in double barrier heterostructures was made by Chang, Esaki and Tsu in 1974 [11] who observed weak features in the low temperature characteristics of a GaAs/(AlGa)As device, which are reproduced in Figure 1.4. The recent renewal of interest in resonant tunnelling, and vertical transport as a whole, is partly attributable to the experiments of Sollner *et al.* [12, 13, 14] who used the negative differential resistance of a double barrier device to produce a high-frequency oscillator which was capable of mixing and detection at frequencies up to 2.5 THz, showing the transport processes to be extremely fast.

A simple figure of merit for a DBS is the peak-to-valley ratio which is given by the current at the peak of the resonance divided by the minimum current which occurs at a slightly higher applied bias. Remarkable progress has recently been made in the characteristics of double barrier devices. The first observation of NDR at room temperature came in 1985 [15, 16], since when typical values in the GaAs/(AlGa)As system have climbed to nearly 4:1 at room temperature and around 25:1 at low temperatures [17, 18, 19]. The most promising material system at present is (InGa)As/AlAs [20] where peak-to-valley ratios of 30:1 at room temperature and 60:1 at low temperature have been reported recently [21]. Resonant tunnelling has also been observed in many other materials systems, for example: Ga(AsP)/GaAs [22], InP/(InGa)As [23, 24, 25], p-type GaAs/(AlGa)As [26], AlSb/InAs [27], HgTe/(HgCd)Te [28], Si/Ge_xSi_{1-x} [29, 30] and even in amorphous materials — a-Si/Si_3N_4 [31], and semiconductor/metal layers [32]. In this thesis we concentrate on the GaAs/(AlGa)As

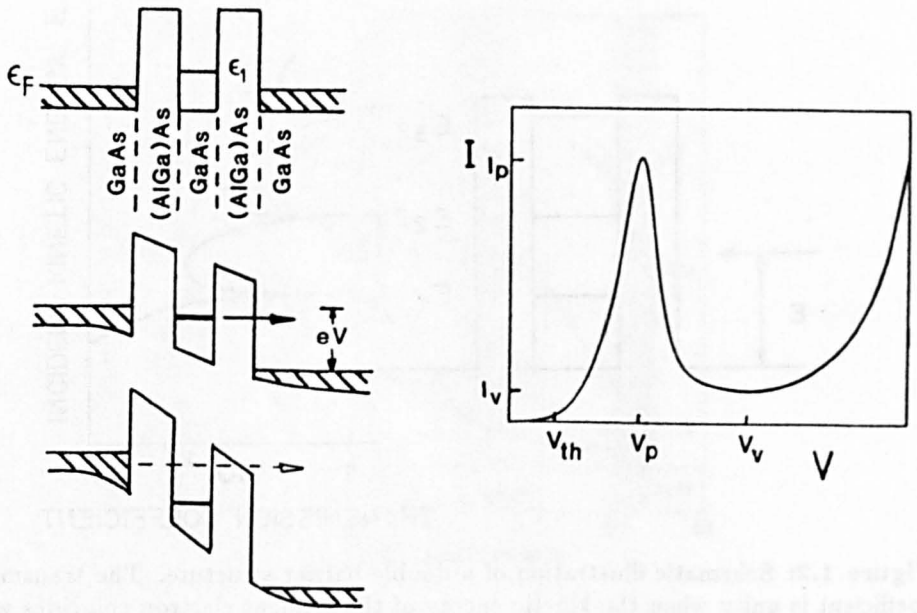

Figure 1.3: Schematic conduction band profiles showing the origin of negative differential resistance in a double barrier structure. When the quasi-bound state of the well is below the Fermi energy, a large resonant current flows but when the bias is increased so that ϵ_1 goes below the conduction band edge, the current falls.

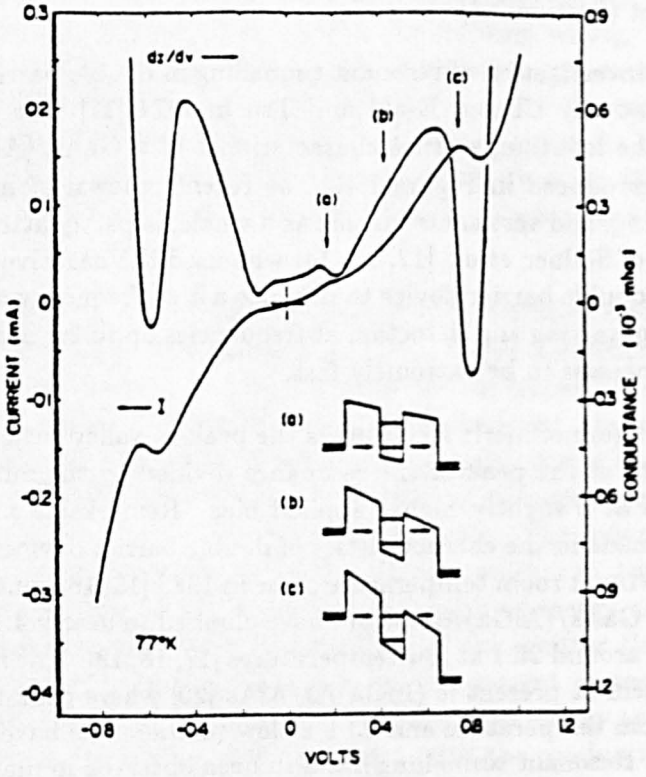

Figure 1.4: Current and conductance characteristics at 77 K of the GaAs/(AlGa)As resonant tunnelling device investigated by Chang, Esaki and Tsu [11].

system.

Numerous applications of resonant tunnelling in high-speed electronic devices have been proposed. As previously mentioned, Sollner *et al.* have pioneered the use of double barrier diodes as high-frequency oscillators [12, 33] with latest reported results of a fundamental frequency of 420 GHz [34], much higher than achieved in Esaki diodes. Whitaker *et al.* have used a double barrier structure to demonstrate switching with a rise time of 2 ps, which is apparently the fastest switching event yet observed for an electronic device [35]. Sollner *et al.* have also used double barrier devices as resistive multipliers [36]. For a review of the high-frequency applications of double barrier diodes see reference [37]. In addition, a number of three-terminal devices have been proposed and demonstrated: for example double barrier structures have been incorporated into the emitter of a hot electron transistor [38] and a heterojunction bipolar transistor [39], and into the source or gate of a field effect transistor [40, 41] as well as forming the basis of several new devices [42, 43, 44, 45, 46]. Hence it is clear that there is a great deal of interest in the possible technological applications of resonant tunnelling and this provides added impetus for research into the basic physical properties of these devices.

Resonant tunnelling devices are also of widespread interest from the point of view of solid-state physics since they constitute a relatively well characterised system where the dynamics of quasi-two-dimensional electrons can be readily investigated and compared to theoretical models. Although the basic ideas of resonant tunnelling can be appreciated from one-dimensional quantum mechanics, real devices are complicated by the need to consider elastic scattering processes (for example due to interface roughness or ionized impurities), space charge buildup, the time development of resonant phenomena, electrostatic interactions between carriers, phonon emission and absorption, the potential distribution in the contact regions, the effects of finite temperature and externally applied magnetic fields — among others. To date, quantitative agreement between theoretical models and the measured $I(V)$ characteristics of any actual double barrier device is lacking.

A number of these physical processes are investigated in this thesis, with particular regard to the effect of high magnetic fields on the tunnelling process. A brief outline is as follows:

In the remainder of this chapter, the fundamental properties of GaAs and (AlGa)As relevant to this thesis are presented followed by a brief outline of some of the basic concepts in the theory of resonant tunnelling.

In Chapter 2 the experimental techniques used to obtain the results are described and details of the samples are given.

Chapter 3 describes several aspects of both resonant and non-resonant tunnelling in double barrier structures. Section 3.3 uses magnetoquantum oscillations in the tunnel current and differential capacitance to characterise the 2DEG in the emitter accumulation layer, Section 3.4 presents an investigation of the contributions of elastic scattering and LO phonon scattering to the valley current using high magnetic fields, the temperature dependence of the $I(V)$ characteristics is analysed in Section 3.5

and Section 3.6 discusses ballistic transport and quantum interference effects in wide quantum wells.

Chapter 4 presents a detailed study of bistability in double barrier devices, showing first how charge buildup in the quantum well or high-frequency oscillations in the measuring circuit can lead to hysteresis in the current-voltage characteristics and then using an asymmetric structure to enhance charge buildup and observe a genuinely intrinsic bistability. Fourier analysis of magnetoquantum oscillations in a magnetic field applied parallel to the current demonstrates that carriers undergo energy relaxation in the well and therefore the tunnelling process is sequential. Two new effects are noted, the enhancement of charge buildup in high magnetic fields and the observation of a region of inverted bistability in a very asymmetric structure where the off-resonant current actually exceeds the resonant current.

Chapter 5 investigates the effect of a magnetic field applied perpendicular to the current. In samples with relatively narrow quantum wells ($<$ 200 Å), a broadening of the resonance consistent with the conservation of canonical momentum is observed and in wider wells, tunnelling into hybrid magnetoelectric energy levels is seen. Rotation of the magnetic field direction is used to probe the anisotropy of the conduction band and to investigate energy levels in a tilted field.

1.2 Basic Properties of Gallium Arsenide

A very comprehensive review of the properties of gallium arsenide has been given by Blakemore [47] and this has been extended to the alloy (AlGa)As by Adachi [48]. Further data is available in Landolt-Börnstein [49]. Here we present some of the most basic properties required for this thesis.

1.2.1 Lattice

In GaAs each gallium atom is bonded to four arsenic atoms in a tetrahedral arrangement, and vice versa. The bonds are predominantly covalent but with about 30% ionic character [47]. The bond length is 2.45 Å. Gallium arsenide crystallises in the zinc blende structure consisting of two interpenetrating face centred cubic sub-lattices of Ga and As atoms displaced by (1/4, 1/4, 1/4). In the alloy (AlGa)As, the aluminium atoms are taken to be randomly distributed throughout the gallium sites. The conventional cubic unit cell of GaAs has a lattice constant of 5.65 Å. The lattice constant in AlAs differs by only 0.008 Å, so the whole range of alloy compositions are almost perfectly lattice-matched allowing the production of high quality interfaces. In reciprocal space, the first Brillouin zone is a truncated octahedron as shown in Figure 1.5.

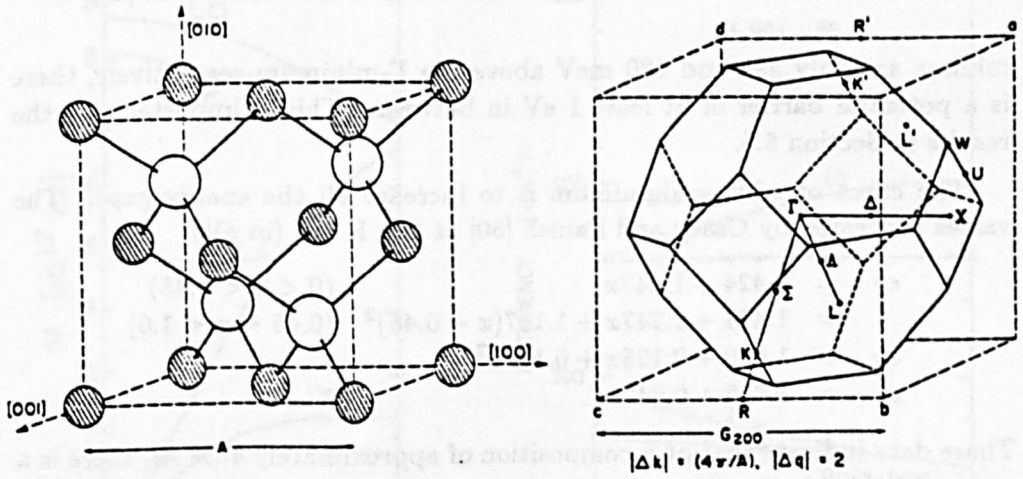

Figure 1.5: (a) Conventional unit cell for GaAs (b) First Brillouin zone for the GaAs lattice (from J. S. Blakemore [47]).

1.2.2 Band Structure

The band structure of GaAs in the main symmetry directions is shown in Figure 1.6 (taken from reference [47]). Unlike germanium or silicon, GaAs is a direct-gap semiconductor with a room temperature band gap of 1.42 eV. This increases at lower temperatures according to the numerical formula

$$\epsilon_G(T) = 1.519 - 5.405 \times 10^{-4} T^2/(T + 204) \text{ eV}$$

Since we deal solely with n-type material, this thesis is only concerned with the conduction band properties. The subsidiary minima near L and X are not usually occupied except at very high electric fields (when electron transfer into the upper valleys produces the Gunn effect). Note that although the L and X

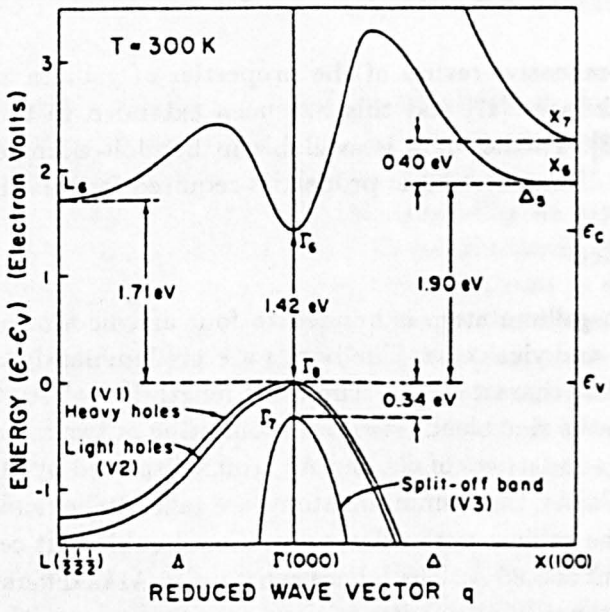

Figure 1.6: Variation of energy with reduced wavevector $q = 2\pi/A$ for the lowest set of conduction band minima and the uppermost levels of the valence band [47].

minima are only 290 and 480 meV above the Γ-minimum respectively, there is a potential barrier of at least 1 eV in between. This is important for the results in Section 5.5.

The effect of adding aluminium is to increase all the energy gaps. The values suggested by Casey and Panish [50] at 300 K are (in eV)

$$\begin{aligned}
\epsilon_\Gamma &= 1.424 + 1.247x && (0 < x < 0.45) \\
&= 1.424 + 1.247x + 1.147(x - 0.45)^2 && (0.45 < x < 1.0) \\
\epsilon_X &= 1.900 + 0.125x + 0.143x^2 \\
\epsilon_L &= 1.708 + 0.642x
\end{aligned}$$

These data indicate that at a composition of approximately 43% Al, there is a cross over to an indirect gap. The samples considered here all have composition 40% aluminium and have a direct band gap. The application of hydrostatic pressure moves the X-minima down relative to Γ; the effects of this on resonant tunnelling in these samples is reported in references [19] and [51].

1.2.3 Effective Mass

Near the bottom of the Γ-minimum, the conduction band is practically isotropic and the 'inertial' effective mass is usually taken to be a scalar, $m^* = \hbar^2(\partial^2\epsilon/\partial k^2)^{-1}$. At the conduction band edge this is $\sim 0.067m_e$. For energies more than a few meV above the band edge it is necessary to take into account the nonparabolicity of the band structure and m^*, as defined above, is given by $m^*(\epsilon) = m_0^*(1 + \alpha\epsilon)$ where ϵ is measured from the band edge and $\alpha = 3.26\ (\text{eV})^{-1}$. At very high energies, $\epsilon > 100$ meV, there is also appreciable anisotropy in the band structure; this is investigated in Section 5.5.

The effective mass in the alloy is approximately linearly dependent on the aluminium concentration, at $T = 4$ K, $m^*(x) = 0.067 + 0.083x$ [52].

1.2.4 Phonons

The phonon dispersion relations for GaAs are shown in Figure 1.7. The electrons couple most strongly to the longitudinal optic modes, for low q values. At temperatures above 100 K, phonon absorption is the dominant mobility-limiting scattering mechanism in GaAs. In resonant tunnelling the emission of LO phonons makes an important contribution to the valley current and to intersubband scattering processes — see Section 3.4. The polar mode LO phonon emission rate is typically $\sim 5 \times 10^{12}$ s^{-1} [53] in bulk material. When the electron energy is less than the LO phonon energy (36 meV), acoustic phonon scattering (deformation potential and piezoelectric) becomes important. This is much less rapid ($\sim$ 100 ps), but is the only way a hot carrier distribution can completely relax to the lattice temperature (Section 4.7.2). The polar mode electron-LO phonon interaction has a $1/q^2$ dependence [54] and so is less important for the large momentum transfers associated with Γ-X or Γ-L transfer. A recent review of electron-phonon interactions in GaAs/(AlGa)As heterostructures has been given by Ferreira and Bastard [55].

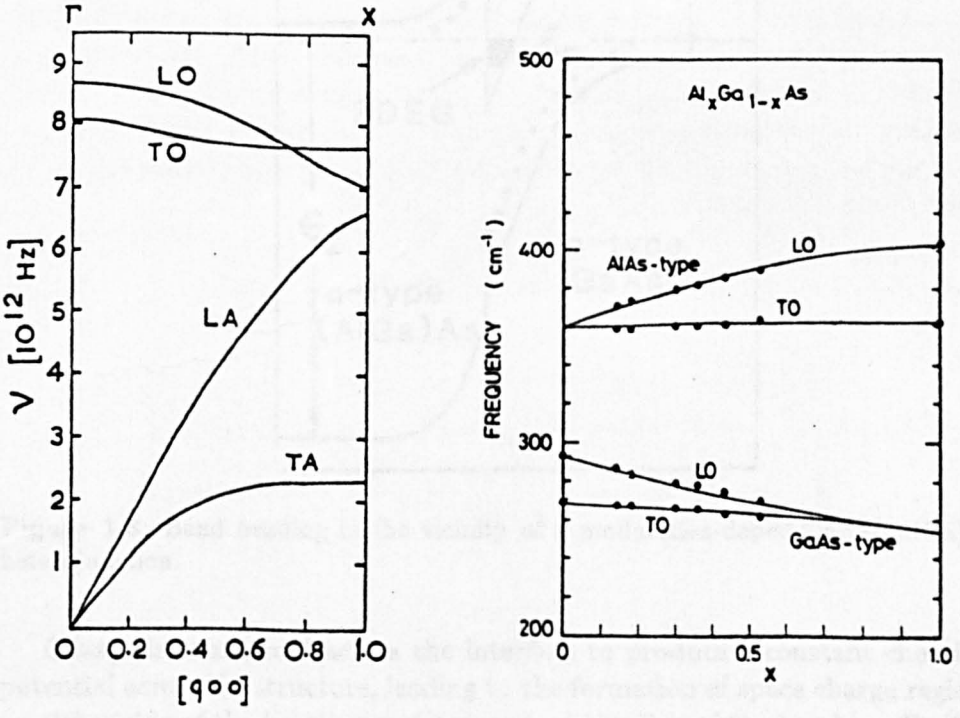

Figure 1.7: (a) Phonon frequency vs wavevector for GaAs along the ⟨100⟩ direction, (b) optical phonon energy as a function of composition for (AlGa)As [57].

In (AlGa)As there are two optical phonon modes [56, 57], one associated with Ga-As and one with Al-As, although the frequencies are not identical to those of the binary crystals (36 meV for GaAs and 49 meV for AlAs). This two-mode behaviour is common in III-V alloys. It is usually found that electrons couple more strongly to the higher-frequency mode [58], which in this case is the AlAs-like mode. However in low-dimensional structures this is complicated by the possibility of interface or confined phonon modes [59].

1.2.5 Impurities

The presence of impurities in a semiconductor can alter the conductivity by orders of magnitude by introducing energy levels into the band gap between the valence and conduction band. Silicon added to GaAs goes preferentially to gallium sites to form a donor impurity. Its extra valence electron is only loosely bound (~6 meV) and so is easily excited into the conduction band where it is free to carry current. For high donor densities, the wavefunctions of the impurity electrons overlap to form an impurity band. When this merges with the conduction band the conduction becomes metallic. In GaAs this Mott metal-insulator transition takes place for a doping level $\sim 10^{16}$ cm^{-3}. In the samples considered in this thesis, silicon doping is used to provide metallic contact regions which supply electrons to the double barrier region. At low temperatures and high magnetic fields we see some evidence for electrons freezing-out onto the donors in the lightly-doped region of the device, see Section 4.7.4, but under most conditions the conduction in the contacts is taken to be metallic — in the sense that the voltage drop across the doped region is negligible compared to that across the double barrier. The (AlGa)As layers are both undoped.

1.3 The GaAs/(AlGa)As Heterojunction

At the interface between two semiconductor layers there is a change in the band gap, hence there are discontinuities in the conduction and valence band edges [60]. The relative magnitudes of these band offsets has proved difficult to calculate. The presently accepted experimental value in GaAs/(AlGa)As is that approximately 62% of the band gap discontinuity appears in the conduction band [61], this gives a conduction band offset of 8.3 meV/% Al. GaAs/(AlGa)As is a 'type I' heterojunction where the higher band gap material has a higher energy conduction band and a lower energy valence band than the low gap material. We shall make the general assumption that the interface is abrupt on the atomic scale and that it is possible to describe both layers by their bulk band structure right up to the interface.

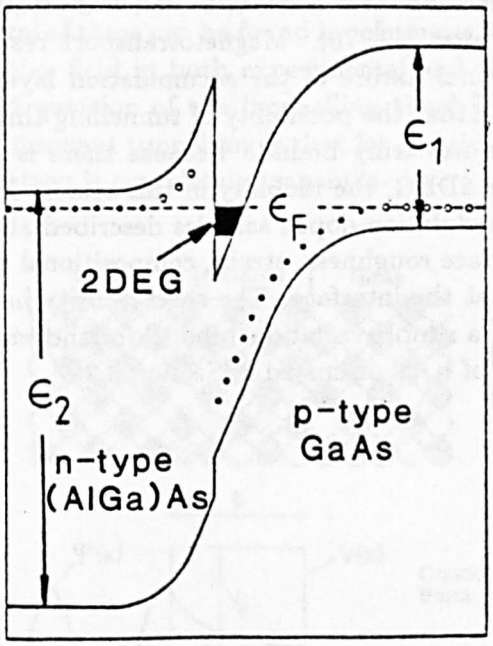

Figure 1.8: Band bending in the vicinity of a modulation-doped GaAs/(AlGa)As heterojunction.

Charge is transferred across the interface to produce a constant chemical potential across the structure, leading to the formation of space charge regions on either side of the junction and consequent bending of the band profile [60]. The most widely studied semiconductor heterostructure is the modulation-doped GaAs/(AlGa)As single heterojunction [62] where the GaAs layer is not intentionally doped and the (AlGa)As is n-type (the doping is usually set back from the interface by ~ 100 Å to improve the mobility). In this case, electrons are transferred from the higher band gap material to the low gap material, leaving behind a region of positive space charge due to ionized donors and creating an inversion (or accumulation) layer of electrons in the GaAs. This is shown schematically in Figure 1.8. The approximately triangular potential well in the inversion layer confines the electrons near the interface and produces one or more bound states. The electrons are free to move in the plane of the interface and so a series of subbands form, each with a density of states

$m^*/\pi\hbar^2$ [63]. At low temperatures, electrons only occupy one subband (for sheet electron densities less than $\sim 6 \times 10^{11}$ cm^{-2}) and so the electron gas is an almost ideal two-dimensional system, referred to as a 2DEG. Because the electrons are spatially separated from the charged donor ions, this structure has produced by far the highest electron mobilities reported (currently in excess of 10,000,000 cm^2/Vs [64]) and allowed the observation of new phenomena such as the Fractional Quantum Hall Effect [65], the quantisation of the resistance of a narrow channel [66, 67] and the oscillatory magnetoresistance of a lateral superlattice [68].

The situation in the resonant tunnelling devices studied here is slightly different in that the (AlGa)As region is undoped and hence there is no 2DEG formation at zero bias. However, the application of a bias voltage produces an accumulation layer adjacent to the barrier and a bound state forms in this potential. The presence of a 2DEG has been well-established for single barrier tunnelling structures [69, 70]. Magnetotransport results which demonstrate the two-dimensional nature of the accumulation layer state are reported in Section 3.3. Note that the possibility of tunnelling through the barrier means that the state is not truly bound. Because there is some n-type doping in the region of the 2DEG, the mobility in this system is not expected to be as high as in the modulation-doped samples described above. The 2DEG is also affected by interface roughness, strain, compositional grading of the interface and any defects at the interface. The sheet density in the 2DEG depends on the applied bias, a simple variational model for the wavefunction [71] and the bias dependence of n_s is discussed in Section 3.2.

1.4 Tunnelling

Tunnelling is a pure quantum-mechanical effect which allows particles to traverse potential barriers — despite not having enough kinetic energy to do so. Classically, a particle with kinetic energy ϵ which is incident on a potential barrier of height ϕ is *always* reflected if $\epsilon < \phi$ and *always* transmitted for $\epsilon > \phi$. In quantum mechanics, an incident particle with kinetic energy less than the barrier height has a finite probability of tunnelling through the barrier — and one with kinetic energy above the barrier also has a finite probability of being reflected. This was appreciated relatively early on in the history of quantum mechanics [72, 73] and has attracted much study ever since. Tunnelling is of fundamental importance in many fields of physics — for example α-decay in nuclear physics, field emission from solids, interband tunnelling in p-n junctions, the Josephson effect and, more recently, scanning tunnelling microscopy (reviews covering several of these can be found in references [74] and [75]). Tunnelling remains an active field in both experimental and theoretical physics, *e.g.* the much-debated question of the 'tunnelling time' [76, 77, 78, 79, 80]. The special feature of resonant tunnelling is that for certain energies below the barrier height, the electron is completely transmitted.

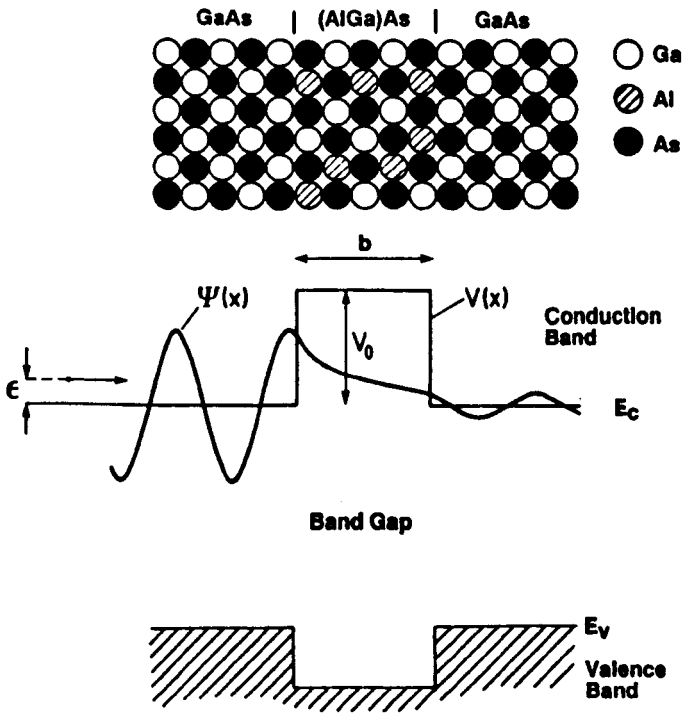

Figure 1.9: Schematic diagram of a rectangular single barrier.

If a thin layer of (AlGa)As is grown between two GaAs layers, there are no allowed states below the conduction band of the (AlGa)As region and this therefore constitutes a barrier to electrons incident from the GaAs. This is illustrated in Figure 1.9 which shows an electron of kinetic energy ϵ and effective mass m^* incident on a barrier of height V_0 and width b. The tunnelling probability is a straight-forward exercise in one-dimensional quantum mechanics

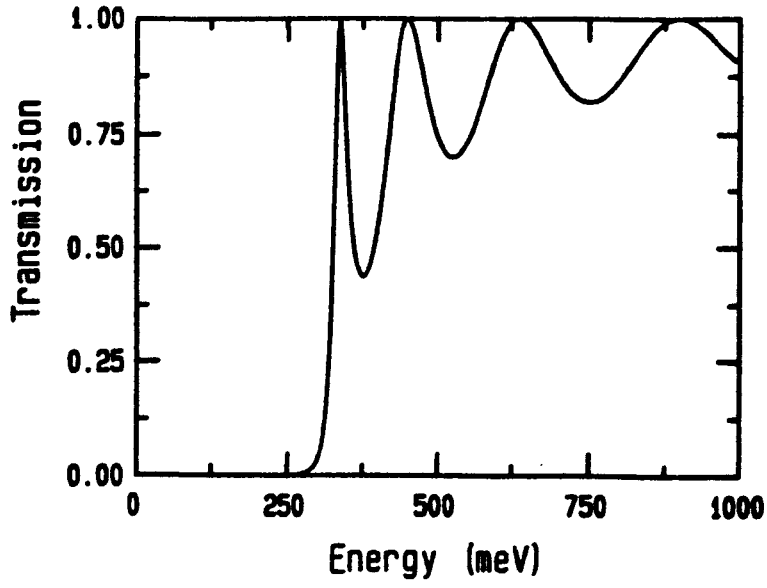

Figure 1.10: Transmission coefficient of a 300 meV barrier of width 100 Å plotted against the incident energy showing the peak in the transmission whenever a half-integral number of de Broglie wavelengths fit within the width of the barrier.

and is obtained by solving the Schrödinger equation

$$\frac{\hbar^2}{2m^*}\frac{\partial^2\psi}{\partial x^2} + (\epsilon - V(x))\psi = 0 \tag{1.1}$$

in each of the three regions and matching ψ and $\partial\psi/\partial x$ at each interface. This gives

$$T(\epsilon) = \left[1 + \frac{V_0^2}{4\epsilon(V_0 - \epsilon)}\sinh^2(\kappa b)\right]^{-1} \tag{1.2}$$

where $\hbar^2\kappa^2/2m^* = V_0 - \epsilon$. For $\kappa b \gg 1$ this can be approximated to

$$T(\epsilon) \simeq \frac{16\epsilon(V_0 - \epsilon)}{V_0^2}\exp(-2\kappa b) \tag{1.3}$$

For energies above the top of the barrier, we replace $\sinh \kappa b$ with $\sin kb$ where $\hbar^2k^2/2m^* = \epsilon - V_0$. At energies where $k = n\pi/b$ for $n = 1, 2, 3, \ldots$, ($\epsilon = \phi_0 + \hbar^2\pi^2n^2/2m^*b^2$), there is unity transmission [81]. This corresponds to fitting a half-integral number of de Broglie wavelengths within the width of the barrier. A plot of the transmission coefficient of a 100 Å thick (AlGa)As barrier against incident energy is shown in Figure 1.10. This variation in the transmission coefficient of a single barrier is reflected in the amplitudes of the resonant tunnelling peaks in the current-voltage characteristics of double barrier devices with wide quantum wells at very high biases where the electron energy is higher than the collector barrier (see Section 3.6).

This simple treatment neglects several important points: (i) there is an applied bias across the structure and so the wavefunctions which should be matched are Airy functions rather than plane waves, (ii) the effective mass is different in the barrier layer and to conserve flux we should match $1/m^*\ \partial\psi/\partial x$ not $\partial\psi/\partial x$ at each interface (iii) the effective mass depends on energy, in the

GaAs it increases for energies above the band edge and in the (AlGa)As barrier it decreases as the energy goes below the band edge [82] (iv) a real system is three-dimensional, so to obtain the tunnel current we should integrate over the transverse momenta and the energy in the tunnelling direction up to the Fermi energy (v) there may be contributions from other conduction band minima [83] (vi) there are contributions from scattering-assisted tunnelling process, such as phonon absorption/emission or tunnelling via impurity levels in the barrier [75] (vii) there are also corrections due to the image potential — this is discussed very fully by Guéret *et al.* [84]. Most of these points are equally relevant to resonant tunnelling processes.

1.5 Resonant Tunnelling

There has been much discussion about the fundamental mechanism which produces negative differential resistance (NDR) in double barrier devices. Tsu and Esaki considered the effect as a coherent process similar to the Fabry-Pérot étalon in optics [9]. Luryi [10] proposed that the NDR arises from a sequential process in which electrons first tunnel from the emitter electrode into the quantum well and subsequently tunnel from the well to the collector. Between these two steps the electron phase memory may be completely lost and hence it was suggested that a resonant enhancement of the transmission coefficient was not necessary.

Luryi claimed that these two mechanisms could be distinguished experimentally because they would have different time dependencies and coherent tunnelling would be more sensitive to the symmetry of the barriers [10, 44, 46]. However he gave no expressions for the tunnel current or the time delay associated with sequential tunnelling, nor did he specifically consider the effect of the phase randomising scattering on the characteristics. It has since been shown that both mechanisms predict the same DC resonant current, at least in the absence of scattering processes [85, 86]. This is because the tunnel current depends on the square of the magnitude of the transmission coefficient integrated over a finite range of energy and so, unless the the incident electrons are limited to energies in a range narrower than the width of the resonant peak, it is the average transmission coefficient rather than the peak value which determines the resonant tunnel current.

A brief outline of the two points of view is given below, a more detailed description of both mechanisms has recently been given by Toombs and Sheard [87]. The original motivation for Luryi's proposal was that the time delay he calculated [10] to be associated with the coherent tunnelling process was incompatible with the high-frequency results of Sollner *et al.* [12]. However other authors [86, 88, 89, 90, 91, 92] have obtained a time delay consistent with high-frequency oscillation. Luryi's suggestion has had the useful effects of highlighting the role of scattering processes in resonant tunnelling and in stimulating theoretical interest in this field.

1.5.1 Coherent Tunnelling

In this model resonant transmission is regarded as a wave-like property of the electrons and the barriers as two partially reflecting mirrors. The incident electron undergoes multiple reflection in the well with some transmission and reflection at each interface. When the wavelength (or a half-integral multiple) matches the width of the cavity, the amplitude of the resonant mode builds up and the electron waves leaking out in both directions cancel the reflected wave and enhance the transmitted ones. For symmetrical barriers this leads to unity transmission. There is a time delay associated with the resonant buildup of the wavefunction in the well.

The transmission coefficient can be calculated in a similar manner to that outlined above for a single barrier. This is frequently generalised to the so-called transfer matrix method which can be used for any number of barriers

[9, 93]. We consider an electron with kinetic energy ϵ_x associated with motion in the tunnelling direction which is incident on two barriers which have transmission coefficients T_L and T_R and enclose a quantum well of width w which has a bound state of energy ϵ_1 — as depicted in Figure 1.3. Off resonance the transmission coefficient is simply that of two single barriers in series;

$$T(\epsilon_x) \sim T_L(\epsilon_x)\, T_R(\epsilon_x) \tag{1.4}$$

Near resonance the transmission coefficient is approximately Lorentzian [94, 95]

$$T(\epsilon_x) = T(\epsilon_1) \frac{(\Gamma/2)^2}{(\Gamma/2)^2 + (\epsilon_x - \epsilon_1)^2} \tag{1.5}$$

where the peak transmission coefficient is

$$T(\epsilon_1) = \frac{4T_L T_R}{(T_L + T_R)^2} \tag{1.6}$$

which is equal to unity for symmetric barriers. The width of the resonance is given semiclassically by [96]

$$\Gamma = \frac{\hbar v_w (T_L + T_R)}{2w} \tag{1.7}$$

with the electron velocity in the well $v_w = \sqrt{2\epsilon_1/m^*}$. The width of the resonant peak is related to the lifetime of the quasi-bound state in the well by $\tau = \hbar/\Gamma$ [97]. For a typical structure with well and barriers of thickness 50 Å and barrier height 300 meV this gives a lifetime of 5 ps. The transmission coefficient as a function of bias for a double barrier structure with 50 Å wide barriers and a 60 Å wide well is plotted in Figure 1.11 for an incident energy of 20 meV. Note that the application of a voltage across the barriers means that they are no longer symmetrical and the peak transmission is less than unity. It can also be seen that the resonance with the upper energy level in the well is much broader, reflecting the reduced lifetime of the quasi-bound state due to the increased transparency of the barriers at high energies. The voltage drop in the contacts is taken into account by assuming a constant screening length of 100 Å.

The tunnel current is given by integrating the transmission coefficient over the energy distribution of the incoming electrons. If we consider a three-dimensional electron gas in the emitter and only take biases greater than the Fermi energy, for $T = 0$ K this gives

$$\begin{aligned} J &= \frac{e}{4\pi^3} \int f(\epsilon) v_x T(\epsilon_x)\, dk_x\, dk_\parallel^2 \\ &= \frac{em^*}{2\pi^2\hbar^3} \int_0^{\epsilon_F} (\epsilon_F - \epsilon_1 + eV_e) T(\epsilon_x)\, d\epsilon_x \end{aligned} \tag{1.8}$$

where V_e is the voltage drop between the emitter and the quantum well and $v_x = \hbar\, k_x/m^*$ for a parabolic band [9]. Off-resonance we can assume that $T(\epsilon)$ is constant over the range of integration so the valley current is

$$J_v = \frac{em^* \epsilon_F^2 T_L T_R}{4\pi^2\hbar^3} \tag{1.9}$$

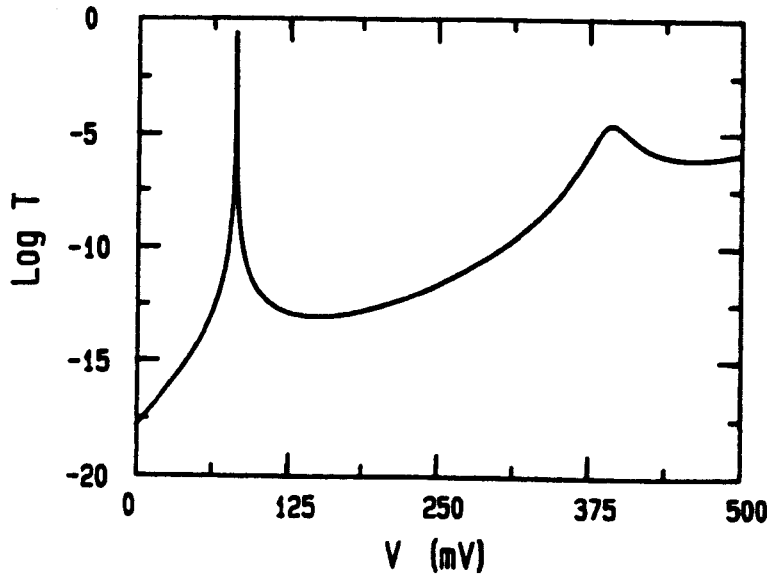

Figure 1.11: Transmission coefficient of a 50 Å, 60 Å, 50 Å double barrier device as a function of applied bias for an incident energy of 20 meV.

When the resonant level lies between the conduction band edge and the Fermi energy in the emitter we assume that the transmission coefficient is narrow compared to the Fermi energy so that we obtain a resonant current of

$$J_r = \frac{em^* v_w}{2\pi\hbar^2 w}(\epsilon_F - \epsilon_1 + eV_e)\frac{T_L T_R}{T_L + T_R} \tag{1.10}$$

At the peak of the resonance, $eV_e = \epsilon_1$, and so the coherent theory predicts a peak-to-valley current ratio of

$$\frac{J_p}{J_v} = \frac{h v_w}{w\epsilon_F(T_L + T_R)} \tag{1.11}$$

For a typical device this is of the order of 1000, which is more than an order of magnitude higher than the best reported values [21]. This discrepancy is mostly due to the neglect of scattering processes which contribute to the valley current [98]. Note that this calculation shows that the peak current is not sensitive to the symmetry of the device which has often been claimed [94, 10], there is simply a monotonic increase with increasing transmission coefficient of the second barrier.

1.5.2 Sequential Tunnelling

The origin of NDR in the sequential picture of Luryi [10, 46] is the bias dependence of the number of electrons in the emitter which can tunnel into the confined state of the well with conservation of energy and lateral momentum. Assuming that there is a narrow energy level in the well, these states lie on the disc in k-space corresponding to the intersection of the plane $k_x = k_0 = \sqrt{2m^*(\epsilon_1 - eV_e)}/\hbar$ and the Fermi sphere (where V_e is the voltage drop across the first barrier). This is illustrated in Figure 1.12. As the bias increases, this disc moves down towards the equatorial plane of the Fermi

sphere and increases in area — therefore the resonant current increases. For $k_0 = 0$, the number of tunnelling electrons per unit area equals $m^*\epsilon_F/\pi\hbar^2$. At higher biases, there are no electrons which can tunnel into the well state with conservation of lateral momentum and therefore the current drops — producing a region of NDR. This mechanism is in fact contained explicitly in the

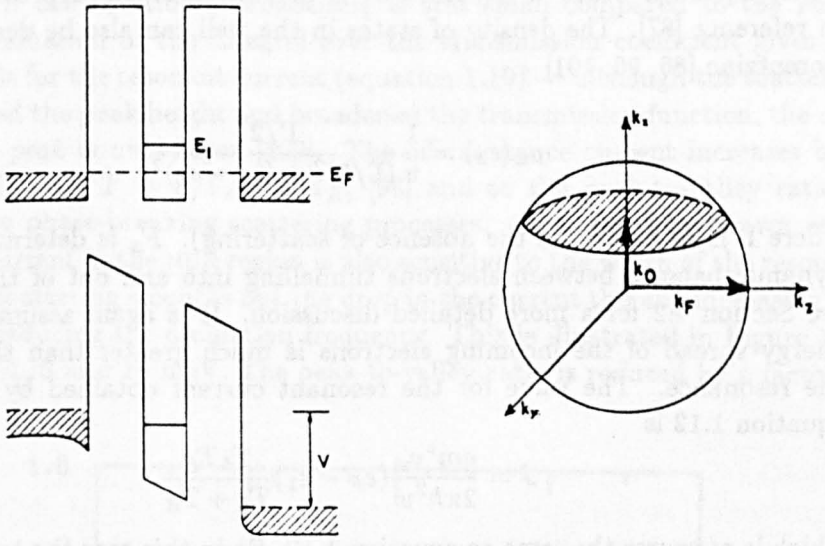

Figure 1.12: Illustration of the operation of a double barrier resonant tunnelling device (taken from reference [10]). The upper conduction band diagram shows the situation at equilibrium and the lower one displays the band diagram for an applied bias V when the energy of certain electrons in the emitter matches the unoccupied levels of the lowest subband ϵ_1 of the quantum well. Assuming conservation of transverse momentum during tunnelling, only those emitter electrons whose momentum lies on the disc k_x=k_0 can tunnel resonantly, where the energy separation between ϵ_1 and the conduction band edge is given by $\hbar^2 k_0^2/2m^*$. Resonant tunnelling occurs for the range of bias for which the shaded disc lies between the pole and the equator of the Fermi sphere. At higher V (when $k_0^2 < 0$) resonant tunnelling cannot occur.

expressions for the tunnelling current first obtained by Tsu and Esaki in the coherent model [9] — see equation 1.8. Moreover, the assumption of a quasi-bound state in the well with a sharply-peaked density of states is equivalent to the sharp peak in the transmission coefficient. Luryi claimed that there should be a different time dependence to this process but the state in the well still has a finite lifetime as discussed above.

The current in the sequential model in the absence of scattering (*i.e.* the width of the quasi-bound state is solely determined by the tunnelling probabilities through the barriers) has been calculated within the transfer Hamiltonian approach by Payne [85] and by Weil and Vinter [86] — see also reference [99]. It is not clear whether tunnelling without phase-randomization can be considered to be sequential [100], but the method can be extended to cover the effects of scattering [86, 98]. The current is given by the probability of tunnelling through a single barrier

$$J = e\frac{2\pi}{\hbar}\int \rho_L(\epsilon_x)\rho_w(\epsilon_x)|M|^2[F_L(\epsilon_x) - F_w(\epsilon_x)]\, d\epsilon_x \qquad (1.12)$$

where ρ is the density of states, F is the Fermi function integrated over the transverse momenta, and the matrix element is given by

$$|M|^2 = \frac{\hbar^2 v_L v_w T_L(\epsilon_x)}{4 L_x w} \tag{1.13}$$

where L_x is the width of the emitter. A derivation of this expression is given in reference [87]. The density of states in the well can also be described by a Lorentzian [86, 96, 101]

$$\rho_w(\epsilon_x) = \frac{1}{\pi} \frac{\Gamma/2}{(\Gamma/2)^2 + (\epsilon_x - \epsilon_1)^2} \tag{1.14}$$

where Γ is as before (in the absence of scattering). F_w is determined by the dynamic balance between electrons tunnelling into and out of the well [99], see Section 4.2 for a more detailed discussion. It is again assumed that the energy spread of the incoming electrons is much greater than the width of the resonance. The value for the resonant current obtained by integrating equation 1.12 is

$$J = \frac{e m^* v_w}{2\pi\hbar^2 w} (\epsilon_F - \epsilon_1) \frac{T_L T_R}{T_L + T_R} \tag{1.15}$$

which is of course the same as equation 1.10. So in this case the two processes give identical values of resonant current, with the Lorentzian transmission coefficient of the coherent model simply being replaced by the Lorentzian density of states in the well. For a monoenergetic incident beam [86], *i.e.* T does not change significantly within the width of the distribution, the peak current is

$$J_p = eN v_x \frac{4 T_L T_R}{(T_L + T_R)^2} \tag{1.16}$$

where N is the number density of incident electrons. It is clear that the distinction is not between whether the current is calculated using a transfer Hamiltonian method or a transfer matrix method but to what extent scattering processes affect the resonant current, *i.e.* the distinction between coherent and *incoherent* tunnelling.

1.5.3 Scattering Processes

Büttiker has calculated the transmission coefficient of a double barrier structure in the presence of a phase-randomizing reservoir connected to the well by applying the Breit-Wigner formulae [96] (see also reference [102]). The double barrier structure is viewed as a target at which carriers are either reflected or allowed to traverse and there is a coherent contribution to the current from carriers which suffer only collisions with the barriers and an incoherent contribution from carriers which undergo a phase-breaking scattering event. The effect of scattering is to broaden the transmission coefficient and reduce the peak value, similarly the density of states in the well becomes broader. The width of the resonance is given by

$$\Gamma = \Gamma_e + \Gamma_i = \frac{\hbar v_w}{2w} (T_L + T_R + \xi) \tag{1.17}$$

where ξ is the probability that the electron suffers a phase-breaking collision in one traversal of the well. The transmission coefficient near resonance is then

$$T = \frac{4T_L T_R}{(T_L + T_R)^2} \frac{\Gamma_e \Gamma/4}{(\Gamma/2)^2 + (\epsilon_x - \epsilon_1)^2} \tag{1.18}$$

which shows that the peak transmission is reduced by a factor of Γ_e/Γ [103]. However, if the additional broadening is still small compared to the Fermi energy, evaluation of the integral over the transmission coefficient gives the same result for the resonant current (equation 1.10) — although the scattering has reduced the peak height and broadened the transmission function, the *area under the peak is unchanged* [102]. The off-resonance current increases by a factor Γ/Γ_e, *i.e.* $T = \Gamma/\Gamma_e \times T_L T_R$, [96] and so the peak-to-valley ratio *is* reduced by phase-breaking scattering processes. As stressed by Brown *et al.* [92], the current in the NDR region is also sensitive to the width of the resonant function; scattering smooths out the drop in the current thereby increasing the NDR and reducing the oscillation frequency. This is illustrated in Figure 1.13 for Γ_i =0, 1, 5 and 10 meV. The peak-to-valley ratio is reduced by a factor of 100.

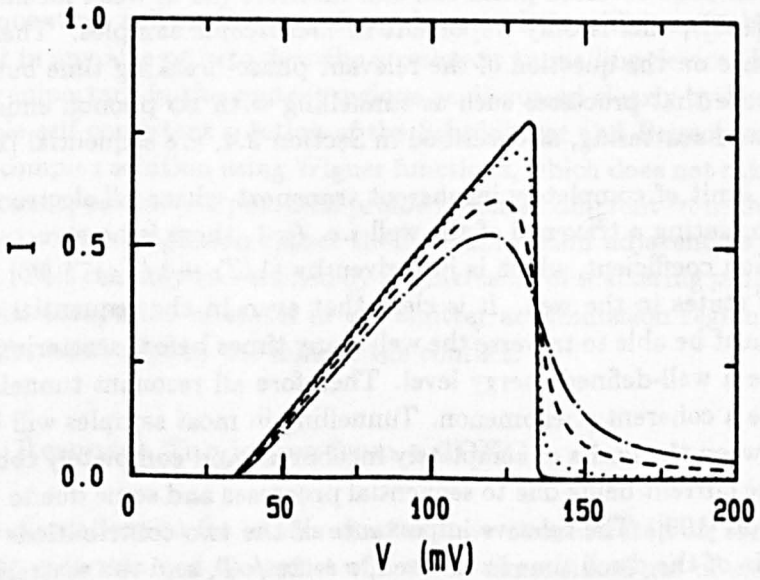

Figure 1.13: Calculated current-voltage characteristics of a double barrier diode for increasing amounts of inelastic scattering, Γ_i =0, 1, 5 and 10 meV. The elastic width of the resonance is approximately $\Gamma_e \sim 0.1$ meV.

Gupta and Ridley [104] suggest that the reduction in peak-to-valley ratio with increasing scattering is different for 'coherent' and 'incoherent' models. However they also calculate that there is a difference in the current density of four orders of magnitude even when there is no scattering — in contrast to all other published calculations [85, 86, 87, 102]. If there is a monoenergetic incident beam of electrons, both the peak current and the peak-to-valley ratio decrease rapidly with increasing scattering [96].

The question of precisely what kind of scattering event is sufficient to prevent buildup of the wavefunction is confused, with different authors providing

contradictory answers. It is often assumed that only *inelastic* collisions contribute to the loss of coherent transmission [102]. Weil and Vinter state that an intrasubband scattering event which merely changes the momentum in the plane of the well does not affect the longitudinal motion and so the transport remains coherent [86]. Büttiker [96] argues that only scattering events which produce an *irreversible* change in phase contribute to the sequential current, *i.e.* an elastic scattering event *does not* affect the coherence of the wavefunction since there is still a definite phase relationship with the incident carriers. The alternative view has been put forward by Luryi [105] and by Leggett [106]. The illustration chosen by both authors is that of a scattering event which changes only the electron spin; partial waves of opposite spin do not cancel each other — yet the interaction could be perfectly elastic. A similar argument can be made for two states at the same energy but with different directions of momentum in the plane of the barriers. Therefore it is generally clear that *any* scattering process, including electron-electron interactions, breaks the phase relationship and so the relevant phase-relaxation time is *at least as short* as the momentum relaxation time deduced from mobility measurements. Although elastic collisions do not destroy the phase memory, so electrons on time-reversed paths can still interfere (as in weak localisation for example [107]), this is only important in *mesoscopic* samples. There is still much debate on the question of the relevant phase-breaking time but it is beyond dispute that processes such as tunnelling with LO phonon emission and intersubband scattering, as described in Section 3.4, are sequential [108].

In the limit of completely incoherent transport where *all* electrons scatter before completing a traversal of the well *i.e.* ξ=1, there is no structure in the transmission coefficient, which is just given by $(1/T_L + 1/T_R)^{-1}$ [96] or in the density of states in the well. It is clear that even in the sequential case, the electron must be able to traverse the well many times before scattering in order to produce a well-defined energy level. Therefore all resonant tunnelling is in some sense a coherent phenomenon. Tunnelling in most samples will be somewhere between the limits of completely incoherent and completely coherent — some of the current being due to sequential processes and some due to resonant transmission [109]. The relative importance of the two contributions depends on the ratio of the dwell time in the well, $\tau \sim 2w/vT$, and the scattering time, τ_s. Although, as discussed above, there is some disagreement on which is the relevant scattering time, Capasso *et al.* [44] have calculated the ratio between the two contributions by using scattering rates deduced from the mobility in heterojunctions and find that coherent tunnelling dominates at low temperatures for barrier widths less than $\sim$ 70 Å , but is unlikely to be important for room temperature operation. The measurements reported in this thesis (Chapter 4) clearly demonstrate sequential tunnelling at low temperatures in samples with thick barriers ($\sim$ 100 Å). Scattering processes in resonant tunnelling are further discussed in Sections 3.4, 3.5, 3.6, 4.6 and 4.7.2.

1.5.4 Space Charge

The importance of space charge effects in the tunnelling process is examined in detail in Chapter 4. Here we will just note that the preceding discussions neglected the effects of space charge accumulation at the emitter barrier and

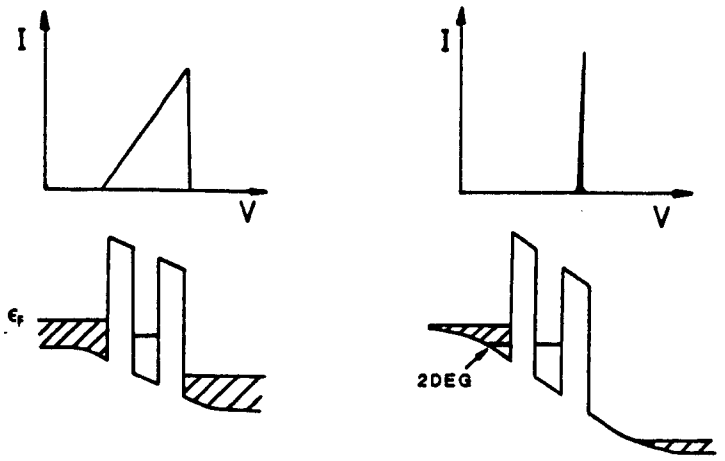

Figure 1.14: Schematic diagram illustrating the difference between resonant tunnelling through a double barrier structure from a three-dimensional and a two-dimensional emitter state. For a 3D emitter, resonance occurs over a *range* of applied biases but if the emitter has a two-dimensional bound state there is only a *single* bias at which resonant tunnelling can occur.

in the quantum well on the tunnelling characteristics. This must be taken into account in any attempts to describe a resonant tunnelling device. Scattering is equally important in the contact regions as discussed clearly by Frensley [110]. A simple self-consistent solution of the Schrödinger and Poisson equations, or even a complex solution using Wigner functions, which does not take scattering into account, produces a potential profile radically different from that expected to exist — with depletion rather than accumulation adjacent to the emitter barrier. This can only be rectified by the inclusion of scattering processes which allow the occupation of states in the emitter accumulation region at energies below the band edge in the bulk of the contact.

1.5.5 Resonant Tunnelling from a 2DEG

All the discussions so far in this chapter have concentrated on samples where the emitter is assumed to consist of a three-dimensional gas of electrons with a Fermi energy much greater than the energy width of the resonant level. However, as described in Section 3.2, the samples studied in this thesis have lightly-doped regions adjacent to the barriers and a quasi-two-dimensional electron gas forms in the emitter under bias. Therefore it is not possible to use the expressions for peak and valley currents derived in the preceding sections. Neither is it necessarily appropriate to just consider the expressions derived for a monoenergetic beam of incident electrons since the quasi-bound state of the 2DEG has a finite width due to scattering and to the probability of tunnelling into the well. For a two-dimensional emitter, the occupied states lie on a Fermi disc in k-space and so the picture of a plane moving down through the Fermi sphere with a range of voltages at which resonant tunneling can take place is replaced by only a single applied bias at which the two energy levels are coincident. Therefore the resonance from a 2DEG is much narrower (neglecting charge buildup) than from a three-dimensional emitter. This is sketched in Figure 1.14.

In a coherent theory, aligning the states in the emitter and the well by applying a bias would cause a splitting of the energy levels. However a coherent theory is not very satisfactory since prior to tunnelling from the accumulation layer, the electron must scatter into the 2DEG from bulk levels in the contact — and therefore the current is always sequential to a certain extent. However, the transfer Hamiltonian methods used to calculate the sequential current assume that the wavefunction in the emitter is not much affected by the finite thickness of the emitter barrier — which will not be an adequate description for thin barriers or high electric fields. The simplest approximation is to treat the 2DEG as a monoenergetic state and approximate the transmission coefficient by that of an incident plane wave at the same energy. The attempt rate is then just given by $v_a/2\lambda_a$ where v_a is the electron velocity and λ_a is the width of the accumulation layer potential. This approach has been used by Lassnig and Boxleitner [111], who term it the *quasifree* approximation, to discuss the dwell time of an electron in a quantum well. In this case the resonant and off-resonant currents are [96]

$$J_{res} = en_a\nu_a \frac{4T_LT_R}{(T_L+T_R)^2}\frac{\Gamma_e}{\Gamma}\frac{(\Gamma/2)^2}{(\Gamma/2)^2+(\epsilon_0-\epsilon_1)^2} \tag{1.19}$$

$$J_v = en_a\nu_a \frac{\Gamma}{\Gamma_e}T_LT_R \tag{1.20}$$

$$\frac{J_p}{J_v} = \frac{\Gamma_e^2}{\Gamma^2}\frac{1}{(T_L+T_R)^2} = \left(\frac{\hbar\nu_w}{\Gamma}\right)^2 \tag{1.21}$$

where n_a is the sheet density in the emitter accumulation layer, ϵ_0 is the energy of the 2DEG state, ν_a is the semiclassical attempt rate in the accumulation layer (using the Fang-Howard wavefunction this is $\epsilon_0/10\hbar$ — see Section 3.2) and ν_w is the attempt rate in the well and equals $\sqrt{2\epsilon_1/m^*}/2w$. A slightly more realistic model is to take a spread of energies in the emitter of width γ and then calculate the transmission coefficient by evaluating the integral over this range. The width of the state in the emitter 2DEG is likely to be similar to that in the well since there will be only slight differences in the scattering rates. Increasing γ also reduces the peak-to-valley ratio, but less strongly than increasing Γ.

It is clear that when tunnelling from a quasi-2DEG in which the width of the energy distribution is comparable to the width of the energy level in the well, the current *is* sensitive to the shape of resonant peak *i.e.* to whether the tunnelling is predominantly coherent or sequential. The simulation presented in Section 3.2 for a sample with barriers approximately 100 Å thick shows that the scattering rate is nearly four orders of magnitude greater than the tunneling rate from the well. This reduces the peak-to-valley ratio from $\sim 10^{10}$ to ~ 100 which is rather more reasonable. The electron on average still makes 20-30 traversals of the well before scattering and so the state is well-defined. Very little theoretical work has been done on resonant tunnelling from a 2DEG which is surprising in view of the trend towards lighter doping in the contacts. A full theoretical treatment would have to consider scattering processes in both the emitter and the quantum well. The ideas discussed above whilst lacking any rigorous justification do at least provide a qualitative picture.

CHAPTER 2

Experimental Techniques and Sample Details

This chapter briefly describes the experimental equipment and techniques which were used in the investigations presented in this thesis. The composition and details of the preparation of the samples studied are also included.

2.1 Experimental Techniques

2.1.1 Magnetic Field Facilities

The high magnetic fields used for the magnetotransport measurements described in this thesis were provided either by superconducting magnets at Nottingham or by a water-cooled resistive magnet at the Service National des Champs Intenses, Grenoble, France.

The Nottingham magnets were supplied by Cryogenic Consultants Ltd. The maximum available field is 11.4 or 12 Tesla in a 32.5 mm bore. The field is homogeneous to within 0.5% in a cylinder of length 1 cm and diameter 1 cm. The coil is immersed in a bath of liquid helium contained in a superinsulated cryostat. A continuous flow variable temperature insert allows the sample temperature to be maintained to within ± 0.2 % in the range between 1.6 and 300 K. For normal operation, liquid helium from the magnet bath is drawn into the sample space through a heat-exchanger with an integral heating element. A Cryogenics Consultants model ASC2 temperature controller monitors the temperature of the exiting gas with a rhodium-iron thermometer and automatically provides the heater power required to maintain the set temperature. To attain temperatures below 4.2 K, the vapour pressure of a reservoir of liquid helium in the insert is reduced by pumping. The variable temperature insert reduces the the usable magnet bore to 20 mm. The field is swept using a Cryogenics Consultants PS120A power supply. A typical sweep containing 1500 data points takes approximately ten minutes. For the data

reported here, there was found to be no significant difference in the results for up and down field sweeps.

The high magnetic field used in Grenoble is provided by three concentric water-cooled Bitter coils powered by four independent supplies, each of which is capable of generating 7500 A. The total power output is 10 MW and the maximum field 20 Tesla in a 50 mm bore, homogeneous to within 0.2% in a volume of 1 cm^{-3}. Details of the magnet system are given by Picoche *et al.* [112]. All the magnetotransport measurements made in Grenoble were taken with the sample at 4.2 K.

2.1.2 Electrical Measurements

Current measurements

The bulk of the measurements in this thesis involve monitoring the current through the device whilst sweeping the voltage across the device at constant magnetic field or sweeping the magnetic field for a fixed bias. Voltage is the natural variable for a resonant tunnelling device since it is (usually) single-valued whereas the current is double-valued over most of the range of the resonance. All the current-voltage measurements were performed using Keithley digital multimeters (Model 195A or 196) and voltage sources (Model 230). The voltage source has remote sensing which allow for voltage drops in the current leads. However this introduces an impedance of 205000 Ω in parallel with the device which must be compensated for when measuring samples of very high impedance.

The meters are controlled by a data collection program written by E. S. Alves on a Hewlett-Packard 300-series microcomputer. This enables rapid numerical processing of the data using a wide range of techniques including numerical differentiation, automatic peak-finding and Shubnikov-de Haas analysis, line fitting and Fourier transforms. The latter routine was supplied by Professor C. Hamaguchi. Before Fourier transformation equally-spaced data points are produced by linear interpolation.

Temperature measurements

The temperature of the sample is monitored using a rhodium-iron thermometer mounted close to the sample. For the measurements described in Section 3.5, rather than using the temperature controller the sample was left to slowly warm up from liquid nitrogen temperatures in a dewar. This process required at least one day ensuring a slow and uniform heating.

Angular dependence

Some of the measurements reported in Sections 3.3, 5.5 and 5.6 require the angle of the magnetic field to be varied. This is achieved by mounting the sample on a rotatable table whose alignment is controlled by means of a micrometer. The table can be rotated through about 120°. The sample can either be rotated about the growth axis, which is kept perpendicular to the magnetic field direction — allowing investigation of the anisotropy of the band structure (Section 5.5), or it can be rotated about an axis perpendicular to both the field and the growth axis so J changes from parallel to the magnetic

field to perpendicular to it (Sections 3.3 and 5.6). The angle could be set with an accuracy of about 2°. All angles must be set by turning the micrometer in the same direction to avoid backlash.

Capacitance measurements

The differential capacitance and conductance were measured using a Hewlett-Packard 4275A multi-frequency LCR meter. This essentially consists of an internal oscillator to generate the test signal and two phase-sensitive detectors to measure the in-phase and 90° components of the impedance. The meter can measure the impedance at 10 set frequencies between 10 kHz and 10 MHz. The quoted accuracy in the range of the measurements considered here is 0.2%. The test signal was set at 3 mV. The DC bias was supplied externally by a Keithley voltage source. The external bias is supplied to the sample through a series resistor of between 80 and 8000 Ω depending on the frequency and the range. The LCR meter also provides an additional parallel impedance and both these factors must be adjusted for to enable comparison of the current-voltage and the capacitance measurements. Although the quoted measurement range is from 0.01 fF to 200 μF, it is impossible to take measurements of the capacitance for samples with a resistance of much less than 1 kΩ and therefore the results are restricted to high-impedance samples and low voltages. For the magnetic field sweeps, the field was stepped using an HP59501B power supply controller to allow sufficient time (~1 s) for the LCR meter to make a measurement at a constant field.

The LCR meter was connected to the sample using 2 m of coaxial cable. This introduces a phase delay in the propagation signal proportional to the test frequency. At high frequencies this produces a significant reduction, ~ 70%, in the measured parameters. The LCR meter automatically adjusts for a cable length of only 1 m. Large errors are introduced if the results are not compensated for this difference in length. The loss is approximately 37% at 10 MHz for a 1 m cable and is proportional to the square of the frequency. To adjust the value quoted by the LCR meter it is necessary to multiply the output by $(1-x)/(1-2x)$ where $x = 0.37(f(\mathrm{MHz})/10)^2$.

The LCR meter analyses the device impedance in terms of a simple two component equivalent circuit consisting of a resistor and capacitor either in series or in parallel. The measurements reported here were all taken in the 'parallel' mode where the quoted conductance G and differential capacitance C are related to the total impedance Z and the phase angle θ by

$$G = (Z(1+\tan^2\theta)^{1/2})^{-1} \tag{2.1}$$

$$C = \frac{\tan\theta}{2\pi f Z(1+\tan^2\theta)^{1/2}} \tag{2.2}$$

However, the equivalent circuit of a resonant tunnelling device does not correspond to this simple representation since it contains two parallel *RC* elements in series, as well as some (negative) inductance — see Section 4.5.3 and reference [113]. Therefore it is often difficult to relate the values obtained by the LCR meter to actual device parameters. This can also lead to anomalies where structure in the conductance produces an apparent variation in the capacitance, as discussed in more detail in Section 4.5.3.

2.2 Samples

2.2.1 Growth

All the samples investigated in this thesis were grown by molecular beam epitaxy (MBE) on $<100>$-oriented n^+GaAs substrates. For a description of the growth process see reference [114]. The substrate is heated and rotated in a high vacuum chamber and atomic or molecular beams of the growth material impinge on the surface. These beams are produced by effusion or Knudsen cells which have computer-controlled shutters to turn the beams on and off as required, producing atomic control over the layer structures. The growth process is monitored *in situ* using RHEED oscillations. The growth rate is typically 150 Å per minute so a typical sample with 3 μm thick epitaxial growth would take 3 hours to produce. The doping is provided by a cell containing silicon whose temperature governs the level of doping.

The samples were grown in Nottingham by Dr. Mohammed Henini using a Varian Gen II reactor. Up to the time of the samples considered in this thesis, this reactor was dedicated to the production of silicon-doped GaAs and (AlGa)As and has produced extremely high quality material. For intrinsic GaAs a background impurity concentration of 7×10^{13} cm^{-3} has been achieved with a peak mobility in excess of 250,000 cm^2/Vs. In modulation-doped heterojunctions mobilities of up to 3,000,000 cm^2/Vs have been recorded. Therefore this machine is particularly well-suited to the production of resonant tunnelling samples where high interface quality is required and scattering from ionized impurities has been shown to degrade device performance [115]. The samples produced show peak-to-valley current ratios of 3.5:1 at room temperature and 25:1 at liquid helium temperatures — comparable to the best reported values in this material system [18]. The high quality of the material has enabled us to investigate a number of new effects discussed in Section 3.6 and Chapter 5. The samples were grown at a substrate temperature of 650 °C to provide good quality interfaces between GaAs and (AlGa)As. Most of the samples show some evidence of asymmetry in the doping profile due to silicon diffusion in the growth direction but no evidence was found for space-charge within the barrier region which had proved to be a problem in single-barrier heterostructures [116].

2.2.2 Fabrication

The layers were processed by Dr. G. Hill and Dr. M. A. Pate of the University of Sheffield and by Dr. M. Davies, Dr. M. Heath and Mr. J. Middleton of this department. Standard photolithographic techniques were used to define mesas of diameters between 5 and 200 μm which were then etched to a depth of $\sim$3 μm. Ohmic contacts were formed to the substrate and the top of the mesas by evaporation of AuGe. The samples were mounted in standard TO5 headers.

2.2.3 Layer structure

A series of symmetrical samples with quantum well widths of between 50 Å and 2400 Å and barriers of width 56 Å were investigated — the most com-

plete range reported to date. These samples (*NU104 – NU219*) have the same series of layers in the contacts and differ only in the width of the well, allowing comparison to be made between them. In addition, two structures with unequal barrier widths were grown in order to investigate the effects of space charge buildup in the quantum well. The thicker barrier retains charge in the well leading to intrinsic bistability in the current-voltage characteristics (Section 4.4). *NU183* has barriers of width 83 Å and 111 Å and *NU221* is even more asymmetric with barriers of width 60 Å and 141 Å. Both samples have a well of width $\simeq$ 60 Å. A schematic cross-section of a typical mesa structure is shown in Figure 2.1. For samples *NU104–NU219*, the direction of the applied bias is defined to be 'forward' when the substrate is positively biased, *i.e.* the electric field is parallel to the growth direction and electrons are injected from the top contact and traverse the double barrier region to reach the substrate. For the asymmetric samples, this definition is reversed because the principle purpose of these samples was to investigate the bistability which occurs when the collector barrier is thicker than the emitter barrier. Therefore in these two samples, forward bias corresponds to the substrate negative and electrons are injected into the well from the substrate through the thinner barrier and subsequently tunnel to the top contact via the thicker barrier. Throughout this thesis the direction of bias for these two samples is stated at each diagram to minimize the confusion. Chapters 3 and 5 deal predominantly with these devices in reverse bias where they act as conventional double barrier structures and Chapter 4 investigates the effects of charge buildup which occurs in forward bias.

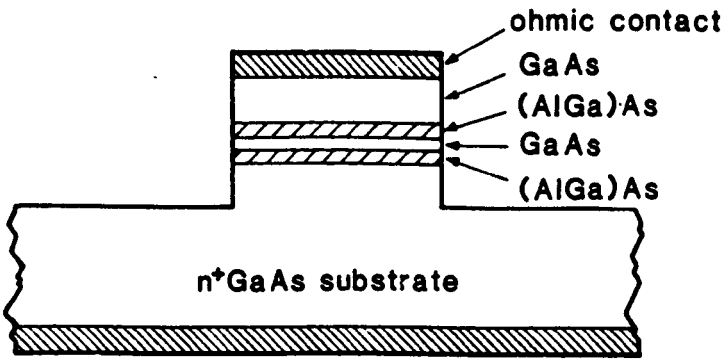

Figure 2.1: Schematic cross-section of a typical mesa device.

The detailed layer structures, in order of growth from the n^+ substrate, are given in Table 2.1. The doping levels quoted are all n-type and are in units of cm^{-3}. A schematic diagram illustrating the various layers is included in Figure 2.2. The heavily-doped region adjacent to the substrate provides a buffer layer between the substrate and the active region of the device. Then the doping level is stepped down towards the double barrier region as the reduction in impurity concentration has been shown to produce improved device characteristics [18]. The narrow undoped spacer layers reduce the diffusion of dopants into the barriers. The double barrier region itself is undoped in all samples. The aluminium concentration in the barriers was chosen to be 40%

which is almost the highest concentration at which the barriers remain direct gap, so avoiding any complications involved in tunnelling via the subsidiary conduction band minima [115]. On the other side of the double barriers, the doping is stepped back up to 2×10^{18} cm^{-3} to facilitate contacting to the devices. The low doping in the regions adjacent to the barriers has the important consequence that, when a bias is applied, a quasi-two-dimensional electron gas forms in the accumulation layer potential adjacent to the emitter barrier. Therefore, for all the structures studied in this thesis, resonant tunnelling occurs from a two-dimensional emitter state rather than the more commonly considered situation of a heavily-doped contact region where the emitter states are three-dimensional. The implications of this are discussed in Section 3.2.

Table 2.1: Compositions of the samples studied in this thesis. The doping levels are n-type in units of 10^{18} cm^{-3} and the dopant is silicon. The central five layers of each sample are undoped and the aluminium concentration in the barriers is 40%.

Sample	Layer Structure										
	d_1	d_2	d_3	s	b_1	w	b_2	s	d_4	d_5	d_6
NU104	2 μm	500 Å	—	25 Å	56 Å	50 Å	56 Å	25 Å	—	500 Å	0.5 μm
	2×10^{18}	2×10^{16}	—						—	2×10^{16}	2×10^{18}
NU153	2 μm	500 Å	—	25 Å	56 Å	117 Å	56 Å	25 Å	—	500 Å	0.5 μm
	2×10^{18}	2×10^{16}	—						—	2×10^{16}	2×10^{18}
NU154	2 μm	500 Å	—	25 Å	56 Å	217 Å	56 Å	25 Å	—	500 Å	0.5 μm
	2×10^{18}	2×10^{16}	—						—	2×10^{16}	2×10^{18}
NU167	2 μm	500 Å	—	25 Å	56 Å	600 Å	56 Å	25 Å	—	500 Å	0.5 μm
	2×10^{18}	2×10^{16}	—						—	2×10^{16}	2×10^{18}
NU207	2 μm	500 Å	—	25 Å	56 Å	1204 Å	56 Å	25 Å	—	500 Å	0.5 μm
	2×10^{18}	2×10^{16}	—						—	2×10^{16}	2×10^{18}
NU288	2 μm	500 Å	—	25 Å	56 Å	1800 Å	56 Å	25 Å	—	500 Å	0.5 μm
	2×10^{18}	2×10^{16}	—						—	2×10^{16}	2×10^{18}
NU219	2 μm	500 Å	—	34 Å	56 Å	2400 Å	56 Å	34 Å	—	500 Å	0.5 μm
	2×10^{18}	2×10^{16}	—						—	2×10^{16}	2×10^{18}
NU183	2 μm	500 Å	500 Å	34 Å	83 Å	58 Å	111 Å	34 Å	500 Å	500 Å	0.5 μm
	2×10^{18}	1×10^{17}	1×10^{16}						1×10^{16}	1×10^{17}	2×10^{18}
NU221	2 μm	500 Å	500 Å	34 Å	57 Å	59 Å	141 Å	34 Å	500 Å	500 Å	0.5 μm
	2×10^{18}	1×10^{17}	1×10^{16}						1×10^{16}	1×10^{17}	2×10^{18}

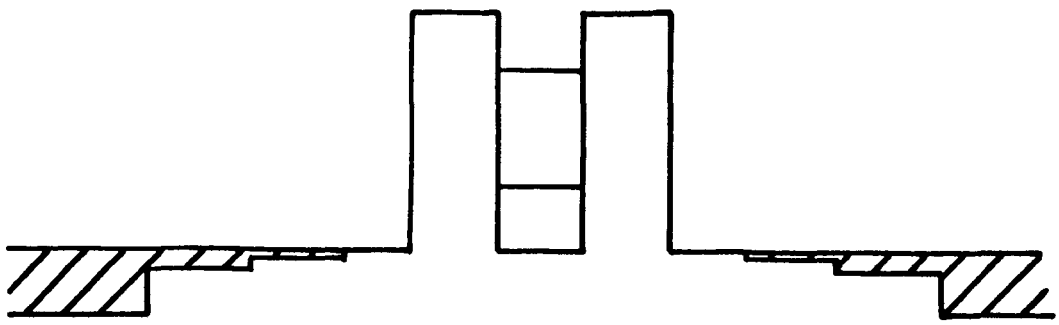

Figure 2.2: Schematic conduction-band profile through a double barrier device.

CHAPTER 3

Resonant and Non-Resonant Processes in Double Barrier Structures

3.1 Introduction

This chapter discusses several topics in resonant tunnelling which illustrate how the basic theory presented in Chapter 1 must be extended to include a wide variety of external influences on the resonant tunnelling process. In particular, the role of scattering processes is highlighted in several of the sections. The other main theme of the chapter is the characterisation of double barrier devices using a range of techniques: current-voltage measurements, differential capacitance characteristics, temperature-dependence and the application of high magnetic fields $\boldsymbol{B} \parallel \boldsymbol{J}$.

It is vital for any quantitative discussion of the physical processes occurring in a resonant tunnelling device to have a good estimate of the energy of the bound state in the quantum well relative to the conduction band edge in the emitter contact over a wide range of biases. Section 3.2 presents a simple analysis of the voltage distribution within a typical resonant tunnelling device, based on the Fang-Howard variational wavefunction, which enables us to obtain this information. The model is extended to cover the resonant current and peak voltage as well as the differential capacitance.

The application of a magnetic field, $\boldsymbol{B} \parallel \boldsymbol{J}$, leads to clear magnetoquantum oscillations in the transport properties of a resonant tunnelling device. These are caused by Landau levels in the two-dimensional electron gas of the emitter contact passing through the Fermi level as the field is swept. The mechanism producing these magneto-oscillations is distinguished from that responsible for the Shubnikov-de Haas oscillations in the conductivity of a 2DEG when the transport is in the plane of the 2DEG. The periodicity of the observed magnetoquantum oscillations in the current and the differential capacitance is directly related to the electron sheet density in the emitter 2DEG, so facilitating the calculations of Section 3.2.

The contributions of the various scattering processes to the valley current are discussed in Section 3.4. A magnetic field $B \parallel J$ allows us to spectroscopically investigate the scattering processes in a double barrier structure and, for the first time, to identify tunnelling with the emission of both GaAs-like and AlAs-like LO phonons of the alloy barrier. In samples with more than one energy level in the quantum well, intersubband scattering processes play a major role. The energy level separation can be determined from the periodicity of the magnetoquantum oscillations which arise from a modulation of the intersubband scattering rate due to the formation of Landau levels in the quantum well. In a device with a 200 Å wide quantum well, up to four different series of magneto-oscillations are observed when the device is biased so that electrons are injected into the fifth subband of the quantum well.

In Section 3.5, the temperature-dependence of the $I(V)$ characteristics is considered. At biases below the low temperature threshold for resonant tunnelling, electrons may be thermally excited to the resonant energy level giving rise to a thermally activated resonant tunnelling process (TARTs). Analysis of the variation of this current with temperature allows the energy of the bound state in the well to be determined relative to the emitter Fermi energy over a wide range of applied bias voltages. The peak resonant current is found to decrease at high temperatures due to a fall in the occupancy of the 2DEG in the emitter. In contrast, the valley current rises rapidly with temperature due to both an increase in scattering processes, *e.g.* phonon absorption, and to thermionic emission of electrons over the potential barriers. At room temperature the valley current is dominated by the latter process.

Finally, Section 3.6 tries to answer the question 'How wide can you make a resonant tunnelling device?' By investigating a series of double barrier structures made from the highest-quality MBE material with well widths ranging from 50 Å to 2400 Å, we find that, even at room temperature, a *significant fraction* of electrons make at least two traversals of a 1200 Å wide well *without* undergoing scattering. This demonstrates that quantum interference is not exclusively a low temperature phenomenon. In the widest wells, as many as seventy resonances are seen in the conductance, much the best reported to date. At high biases, a novel beating effect in the amplitude of the resonances is observed and is related to a quantum interference effect within the width of the collector barrier.

3.2 Device Model

This section presents a simple analytical model of the device which allows an estimate of the voltage distribution through the structure to be made. This enables us to estimate the voltage positions of the resonances and the peak currents.

3.2.1 Voltage Distribution

Figure 3.1 shows a schematic diagram of the voltage drops within a typical double barrier device. The total applied bias is V. The voltage distribution across the device can be divided up into several parts depending on the process

under discussion. The voltage drop between the emitter contact and the centre of the well is labelled V_e and that from the centre of the well to the collector contact V_c, these two terms are used when the device is modelled as two parallel plate capacitors in series as in Chapter 4. The voltage dropped across the emitter barrier and the first half of the well is referred to as V_1 and is used in the discussion of off-resonant transitions between the emitter and the quantum well in Section 3.4. The voltage across the quantum well itself is V_w and is referred to in Section 3.6. In this section we consider the voltage drop in three separate sections: that across the emitter accumulation layer is V_a, that across the double barrier region is V_{db} and across the depletion region in the collector contact it is V_d. We consider each region in turn.

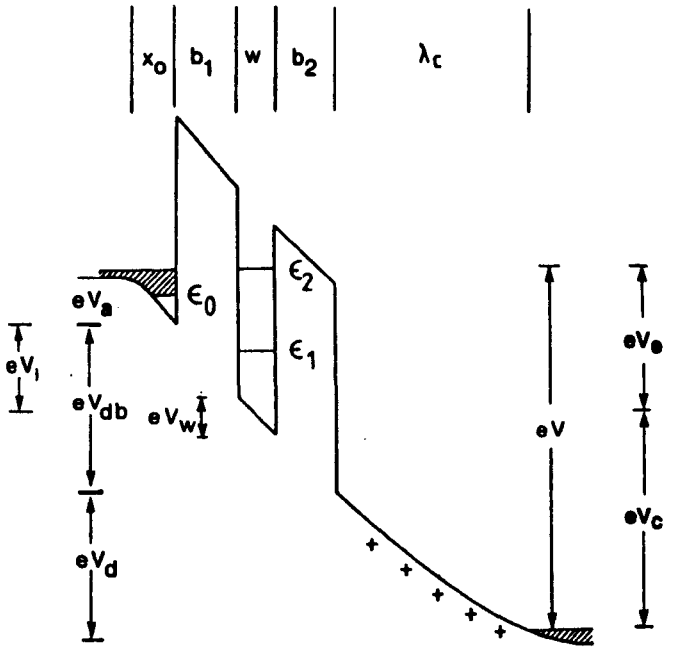

Figure 3.1: Schematic diagram of the conduction-band profile through a resonant tunnelling device, showing the voltages referred to in the text.

Emitter

When a bias is applied across a double barrier device, electrons accumulate adjacent to the emitter barrier. The low doping level in this region for the GaAs/(AlGa)As samples considered here (see Table 2.1) leads to the formation of a quasi-two-dimensional bound state (2DEG) in this accumulation potential. This has been well-established in single-barrier devices [69, 70] and is confirmed by the angular dependence of the magneto-oscillations in the tunnel current (see reference [108] and Section 3.3). Self-consistent calculations of the accumulation layer potential have also indicated that a bound state forms at relatively low accumulation density [117, 118].

Electrons are continually removed from this 2DEG by tunnelling through the barrier, these are replaced by electrons from the bulk 3D emitter contact. An incident electron from the left-hand electrode can either tunnel directly through the barrier, be reflected back into the bulk contact or scatter into an unoccupied state of the 2DEG. Electrons in the 2D bound state can either tunnel into the well or scatter back into a continuum state. The occupancy of

the 2DEG states is therefore determined by the balance between the scattering rate and the tunnelling rate. When the device is off-resonance and the voltage drop across the emitter barrier is low, we can consider all the states in the 2DEG below the bulk Fermi energy to be filled. However, when there is a large bias on the device, or it is biased at a resonance, the tunnelling rate may be sufficiently large to produce a non-thermal energy distribution in the emitter.

We describe the quasi-bound state of the emitter 2DEG using the variational wavefunction of Fang and Howard [71, 119]. This approach was intended to approximately describe the bound state in a silicon MOSFET, and hence is not necessarily suitable in the present case where the electrons are not truly bound and there is background concentration of bulk 3D-like electrons. A more realistic approach would take into account the penetration of the electron wavefunction into the barrier (see Bastard [120]) and the screening effects of the 3D electrons (see Baraff and Appelbaum [117]). However, since the bulk concentration is relatively low and, at least off-resonance, the probability of finding the electron in the barrier is also low, we neglect both these effects in the interests of computational ease. The variational wavefunction is given by

$$\begin{aligned} \psi &= -2\left(\frac{a}{2}\right)^{\frac{1}{2}} x \exp\left(\tfrac{ax}{2}\right) \quad \text{for } x < 0 \\ &= 0 \qquad\qquad\qquad\qquad\quad \text{for } x > 0 \end{aligned} \tag{3.1}$$

The origin is taken at the barrier interface. The variational parameter is a, which is determined by minimizing the total energy ϵ. This is given by

$$\epsilon = -e\langle psi|V(x)|\psi\rangle + \langle psi| - \hbar^2\nabla^2/2m^*|\psi\rangle \tag{3.2}$$

where $V(x)$ is the conduction-band profile determined by solving Poisson's equation *i.e.*

$$\frac{d^2V}{dx^2} = \frac{en_a|\psi|^2}{\varepsilon_r\varepsilon_0} \tag{3.3}$$

The electron sheet density is n_a and ε_r is the relative permittivity. This neglects any contributions to the potential from the bulk electrons in the emitter contact or from fixed space charges. The conduction band edge in the emitter at a large distance from the interface is taken as the zero of potential. The band-bending due to the electrons in the 2DEG is

$$V(x) = \frac{en_a e^{ax}}{2\varepsilon_r\varepsilon_0 a}\left(a^2x^2 - 4ax + 6\right) \tag{3.4}$$

The expectation value of the electrostatic potential energy is found by evaluating the first term on the right-hand side of equation 3.2 and the expectation value of the kinetic energy is

$$\langle K.E.\rangle = \frac{\hbar^2a^2}{8m^*} \tag{3.5}$$

Adding the two terms together and then setting the derivative with respect to a equal to zero yields

$$a = \left(\frac{33e^2m^*n_a}{8\varepsilon_r\varepsilon_0\hbar^2}\right)^{\frac{1}{3}} \tag{3.6}$$

and

$$\epsilon = -\frac{15e^2 n_a}{16\epsilon_r\epsilon_0 a} + \frac{\hbar^2 a^2}{8m^*}$$

$$= -\frac{9}{88}\frac{\hbar^2 a^2}{m^*} \tag{3.7}$$

The average distance of an electron in the 2DEG from the emitter barrier interface is

$$-x_0 = \langle\psi|x|\psi\rangle = -\frac{3}{a} \tag{3.8}$$

and the potential energy at the interface ($x = 0$) is

$$-eV_a = -e\left(\frac{72e\hbar^2 n_a^2}{11m^*\epsilon_r^2\epsilon_0^2}\right)^{\frac{1}{3}} = -\frac{e^2 n_a x_0}{\epsilon_r\epsilon_0} \tag{3.9}$$

The binding energy of the 2DEG is

$$\begin{aligned}\epsilon_0 &= \langle\epsilon\rangle - eV_a \\ &= \frac{5}{8}\frac{\hbar^2 a^2}{m^*} = \frac{5}{32}\left(\frac{33\hbar e^2 n_a}{\epsilon_r\epsilon_0\sqrt{m^*}}\right)^{2/3} \\ &\simeq 2.109 \times 10^{-12}\, n_a^{2/3}\end{aligned} \tag{3.10}$$

where ϵ_0 is in eV and n_a in m^{-2}. This set of results gives all the parameters of the 2DEG relevant to this work. We again stress that this model takes no account of the penetration of the wavefunction into the barrier or screening due to bulk electrons, therefore it will probably overestimate the binding energy. Note also that it is not self-consistent in that $\epsilon_0 + \epsilon_F \neq eV_a$.

Double barrier region

When there is no charge in the quantum well, the potential across the double barrier region is just

$$V_{db} = eE(b_1 + w + b_2) \tag{3.11}$$

where the electric field E is given by

$$E = \frac{en_a}{\epsilon_r\epsilon_0} \tag{3.12}$$

To calculate the voltage due to charge in the quantum well, the wavefunction of the lowest subband is taken to be

$$\psi_1(x') = \sqrt{\frac{2}{w}}\sin\left(\frac{\pi x'}{w}\right) \tag{3.13}$$

where n_w is the sheet charge density in the well. Note that the penetration of the wavefunction into the barriers is again neglected and the origin here is taken at the left hand side of the well (*i.e.* $x' = x + b_1$). The voltage drop across the well due to this charge distribution is then obtained from Poisson's equation

$$\frac{d^2V}{dx^2} = \frac{en_w|\psi_1|^2}{\epsilon_r\epsilon_0} \tag{3.14}$$

hence

$$V(x') = \frac{en_w}{\varepsilon_r \varepsilon_0 w}\left(\frac{x'^2}{2} + \left(\frac{w}{2\pi}\right)^2\left[\cos\left(\frac{2\pi x'}{w}\right) - 1\right]\right) \tag{3.15}$$

which gives a total voltage drop

$$V_w = \frac{en_w}{\varepsilon_r \varepsilon_0}\frac{w}{2} \tag{3.16}$$

i.e. the electrons in the well can be effectively described as a sheet of charge situated at the centre of the well. Therefore the voltage across the double barrier region is

$$V_{db} = \frac{en_a}{\varepsilon_r \varepsilon_0}(b_1 + w + b_2) + \frac{en_w}{\varepsilon_r \varepsilon_0}(\frac{w}{2} + b_2) \tag{3.17}$$

Depletion region

The voltage drop in the depletion region is complicated by the fact that there are up to three different doping levels in the various layers which make up the collector contact. We shall take the simplest possible treatments of each layer. For sample *NU183* there are two relatively lightly doped layers, $N_1 = 10^{16}$ cm^{-3}, $d_1 = 500$ Å and $N_2 = 10^{17}$ cm^{-3}, $d_2 = 500$ Å, and then a heavily doped region, $N_3 = 2 \times 10^{18}$ cm^{-3} — see Table 2.1. When the total charge density in the emitter and the well, $n_s = n_a + n_w$, is less than $N_1 d_1$, the first layer is considered to be completely depleted for a length $\lambda_c = n_s/N_1$ and the voltage is

$$V_d = \frac{en_s^2}{2\varepsilon_r \varepsilon_0 N_1} \tag{3.18}$$

When the total sheet charge density exceeds $N_1 d_1$, the depletion in the second layer is treated in exactly the same way since the doping level here is also relatively low *i.e.* for $N_1 d_1 < n_s < N_1 d_1 + N_2 d_2$ we have

$$V_d = \frac{e}{\varepsilon_r \varepsilon_0}\left(n_s - \frac{N_1 d_1}{2}\right) d_1 + \frac{e(n_s - N_1 d_1)^2}{2\varepsilon_r \varepsilon_0 N_2} \tag{3.19}$$

If $n_s > N_1 d_1 + N_2 d_2$ we must consider the depletion in the heavily doped region with $N_3 = 2 \times 10^{18}$ cm^{-2}. This is simply treated using the Thomas-Fermi screening theory with

$$\lambda_{TF} = \left(\frac{\varepsilon_r \varepsilon_0 \hbar^2 \pi^{\frac{4}{3}}}{3^{\frac{1}{3}} e^2 m^* N_3^{\frac{1}{3}}}\right)^{\frac{1}{2}} \tag{3.20}$$

and we have

$$V_d = \frac{e}{\varepsilon_r \varepsilon_0}\left[\left(n_s - \frac{N_1 d_1}{2}\right) d_1 + \left(n_s - N_1 d_1 - \frac{N_2 d_2}{2}\right) d_2 + (n_s - N_1 d_1 - N_2 d_2)\lambda_{TF}\right] \tag{3.21}$$

Equations 3.10, 3.17 and 3.21 allow us to calculate the total bias for any value of sheet charge density in the well and in the emitter. The magnetic field measurements described in Section 3.3 give n_s as a function of applied voltage.

These results agree fairly well with the model presented here. This experimental determination of n_s means that we only need to use equations 3.10 and 3.17 and the voltage dropped in the collector region is given by the difference between the sum of these two terms and the applied voltage, this removes any uncertainty caused by the approximate treatment of the depletion voltages. A more accurate method would involve the self-consistent solution of the Schrödinger and Poisson equations, however the complexity involved is unlikely to lead to a worthwhile improvement over this simplest of calculations.

The other voltage drops marked in Figure 3.1 are: the voltage drop across the emitter barrier and the first half of the well $V_1 = eE(b_1 + w/2)$, the voltage drop across the quantum well $V_w = eEw$, the voltage drop to the centre of the quantum well $V_e = V_a + V_1$ and that between the centre of the well and the collector contact $V_c = V_{db} - V_1 + V_d$.

3.2.2 Current

As discussed in Section 1.5.5, tunnelling from a two-dimensional state is most easily described using the *quasi-free* approximation of Lassnig and Boxleitner [111] where the transmission coefficient of the 2D bound state is replaced by that for an incident plane wave of the same energy, $T(\epsilon_0)$. The transmission coefficient in the presence of phase-breaking scattering processes is given in Section 1.5.3. The energy width of the well state is $\Gamma = \Gamma_e + \Gamma_i$ where $\tau_e = \hbar/\Gamma_e$ is the dwell time of an electron in the well in the absence of scattering and $\tau_i = \hbar/\Gamma_i$ is the scattering time. The current is given by

$$J = e\, n_s \nu T(\epsilon_0) \tag{3.22}$$

The classical attempt rate ν is defined by

$$\nu = \frac{v}{2x_c} \tag{3.23}$$

where x_c is the distance between the classical turning points and $m^*v^2/2$ is $< \psi | - \hbar^2\nabla^2/2m^* | \psi >$. The average kinetic energy within the Fang-Howard approximation is obtained from equation 3.5, hence

$$v = \frac{\hbar a}{2m^*} \tag{3.24}$$

At the classical turning points the kinetic energy is zero, *i.e.* $-\hbar^2\nabla^2\psi/2m^* = 0$ which gives

$$x_c = \frac{4}{a} \tag{3.25}$$

In order to account for the finite energy width of the quasi-bound state in the emitter 2DEG we can replace $T(\epsilon_0)$ with the *average* transmission coefficient over an energy range of width $\gamma \sim \hbar/\tau$ where τ is the lifetime of the emitter state. The resonant current density in this approximation is

$$\begin{aligned} J_r &= e\frac{\hbar a^2}{16m^*} n_a T(\epsilon_0) \frac{\Gamma_e}{\gamma\Gamma} \int_{\epsilon_0-\gamma/2}^{\epsilon_0+\gamma/2} \frac{(\Gamma/2)^2}{(\Gamma/2)^2 + (\epsilon - \epsilon_r)^2}\, d\epsilon \\ &= \frac{e n_a \epsilon_0 \overline{T}}{10\hbar} \end{aligned} \tag{3.26}$$

and the nonresonant current is simply

$$J_o = \frac{en_a\epsilon_0}{10\hbar}\frac{\Gamma}{\Gamma_e}T_L T_R \tag{3.27}$$

The transmission coefficients of the barriers are calculated using a transfer matrix algorithm written by E. S. Alves.

Example

Figure 3.2 shows the logarithm of the calculated current for a 200 μm diameter mesa of sample *NU183* which has a 58 Å wide well, a 111 Å wide emitter barrier and an 83 Å wide collector barrier. The solid curve is the current when the emitter bound state is assumed to have an energy spread of 10^{-5} meV, which is less than the elastic width of the resonance, 10^{-4} meV. Although the voltage at the resonant peak is in good agreement with measured data (see Figure 3.37), the valley current is three orders of magnitude too low and the resonance width is a fraction of that observed. The narrowness of the resonant peak reflects the fact that we have neglected scattering. In a real sample, scattering processes broaden both states substantially. Since we cannot distinguish between the broadening due to scattering in the well and that due to the width of the emitter state, we take them to be equal *i.e.* $\gamma = \Gamma_i$. The simulated $I(V)$ characteristics

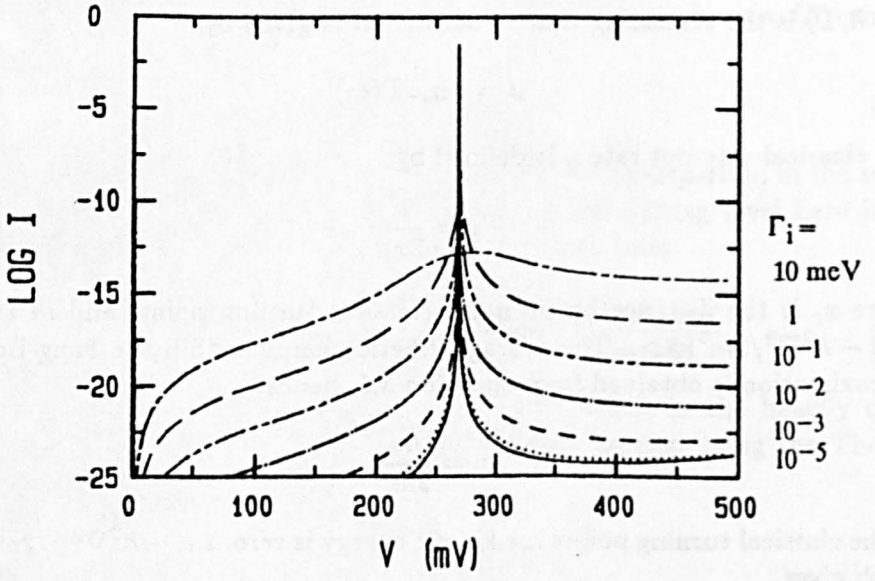

Figure 3.2: Natural logarithm of the current plotted against applied bias for a resonant tunnelling device with a 2DEG in the emitter showing the effect of increasing level broadening from $\Gamma_i = 10^{-5}$ meV to $\Gamma_i = 10$ meV. The barrier and well widths are for sample *NU183* and the elastic width of the resonance is 10^{-4} meV. The width of the accumulation layer state is taken to be the same as that of the state in the well.

for various values of Γ are shown as the dotted curves in Figure 3.2. In order to reproduce the experimentally observed resonance width we need to take $\Gamma \sim 4$ meV, corresponding to a scattering time of 160 fs — which is reasonable if electron-electron scattering is assumed to contribute to the broadening and is in good agreement with the values deduced in Section 3.6 for wide well samples. In this sample, the current is almost completely sequential. The

transit time across the well is only ~8 fs and therefore an electron can make an average of twenty transits before scattering — so the energy level is still well-defined. Note that the peak-to-valley ratio is in much better agreement with experiment when scattering is taken into account; for a scattering time ~160 fs the peak-to-valley ratio is 27:1 compared to 10^{10} with no scattering. The experimental value is 25:1.

This simple calculation gives a good idea of the importance of scattering processes in resonant tunnelling, particularly where the energy range of the incident energy distribution is narrow. However many factors have not been taken into account — for example the energy and bias dependence of the scattering rates and the interaction between the tunnelling rate and the lifetime of the quasi-bound state in the emitter.

Thermalisation

The attempt rate for a number density close to resonance is approximately 5×10^{12} s^{-1}. If the transmission coefficient were unity at resonance, the scattering time would have to be much less than 200 fs to maintain a degenerate 2DEG in the emitter. Whilst this is sufficient time for LO phonon emission and electron-electron scattering it would not allow enough time for acoustic phonon emission (~ 0.1 ns) which is necessary if incoming electrons from the bulk emitter contact are to thermalise completely in the 2DEG. However the bias applied across the structure and the unequal barrier widths mean that peak transmission is less than unity. For this resonance, the peak transmission coefficient under bias is < 0.001. This corresponds to a dwell time in the emitter accumulation layer of ~1 ns, therefore in this sample there is a degenerate 2DEG in the emitter even when biased on resonance.

3.2.3 Capacitance

The total voltage drop across the device when there is no charge buildup in the quantum well can be written as

$$V = \frac{\epsilon_F}{e} + \frac{\epsilon_0}{e} + \frac{en_a(b_1 + w + b_2)}{\varepsilon_r \varepsilon_0} + V_d \tag{3.28}$$

From this we can derive an expression for the differential capacitance C,

$$\frac{1}{C} = \frac{dV}{dQ} = \frac{1}{e^2}\frac{d\epsilon_F}{dn_a} + \frac{1}{e^2}\frac{d\epsilon_0}{dn_a} + \frac{1}{\varepsilon_r \varepsilon_0}(b_1 + w + b_2 + \lambda_c) \tag{3.29}$$

where λ_c is equal to the depletion length in the collector contact, which varies with applied voltage. From equation 3.10, we have

$$\frac{1}{e^2}\frac{d\epsilon_0}{dn_a} = \frac{165}{288}\frac{x_0}{\varepsilon_r \varepsilon_0} = \frac{\gamma x_0}{\varepsilon_r \varepsilon_0} \tag{3.30}$$

The last two terms on the right hand side of equation 3.29 simply correspond to the geometrical capacitance of a parallel plate capacitor $C = \varepsilon/d$ with width

$$d = \gamma x_0 + b_1 + w + b_2 + \lambda_c \tag{3.31}$$

where $\gamma \sim 0.58$. Therefore we can consider the device to consist of two sheets of charge, one at a distance γx_0 from the emitter barrier and one λ_c from the collector barrier.

The first term on the right-hand side of equation 3.29 is the 'quantum capacitance' [121, 122], $C_Q = e^2 D(\epsilon_F)$ where $D(\epsilon_F)$ is the density of states at the Fermi energy. This is a consequence of the Pauli Exclusion principle, which requires electrons added to the emitter to be at the Fermi energy rather than the bound state energy, thereby increasing the energy of the system [45]. This is equivalent to adding a capacitance in series with the geometrical capacitance,

$$\frac{1}{C} = \frac{d}{\epsilon_r \epsilon_0} + \frac{1}{C_Q} \tag{3.32}$$

For a two-dimensional electron gas in the emitter, the density of states at the Fermi energy is $D(\epsilon_F) = m^*/\pi\hbar^2$, so the quantum capacitance is just

$$C_Q = \frac{e^2 m^*}{\pi\hbar^2} \tag{3.33}$$

The quantum capacitance is $\sim$ 1500 pF for a 200 μm diameter mesa. This is much larger than the geometrical capacitance of a typical resonant tunnelling device, which is $<$ 50 pF. Therefore, C_Q only reduces the measured capacitance by about 2% of the geometrical value. C_Q would only be important (*i.e.* small) for devices with extremely low effective masses. However, in the presence of a quantising magnetic field $\boldsymbol{B} \parallel \boldsymbol{J}$, Landau levels are formed and the density of states is given by $D(\epsilon) = 2eB/h \; \delta(\epsilon - (n + 1/2)\hbar\omega_c)$ (see Section 3.3). Hence the density of states at the Fermi level varies greatly as the magnetic field is swept and this contributes to the magnetoquantum oscillations in the capacitance of the device, as described in Section 3.3.

We can use the above expressions for C, in conjunction with the equations for x_0 and λ_c in Section 3.2.1, to simulate the capacitance-voltage characteristics of a typical device. This is shown in Figure 3.3 for sample *NU183*. The rapid decrease in C as the bias is increased is caused by the depletion of the lightly-doped region in the collector. As can be seen by comparison with Figure 4.21, there is general agreement with the measured curve — apart from the region where the device is biased on resonance. This is discussed in detail in Section 4.5.

When there is a buildup of charge in the quantum well, we follow the approach of Luryi [45] to derive the quantum capacitance. Consider the situation sketched in Figure 3.4 where there is a negative charge $\sigma_1 = -en_a$ on the emitter plate which is separated by a distance $d_1 = \gamma x_0 + b_1 + w/2$ from the central plate which has a negative charge $\sigma_w = -en_w$ and there is a positive charge σ_2 on the collector plate which is a distance $d_2 = w/2 + b_2 + \lambda_c$ from the centre of the well. For overall neutrality we obviously have $\sigma_1 + \sigma_w + \sigma_2 = 0$, this can be written in the form

$$\sigma_1 = -\sigma_2 \sin^2\phi \tag{3.34}$$

$$\sigma_w = -\sigma_2 \cos^2\phi \tag{3.35}$$

where ϕ is a variational parameter to be obtained by minimizing the total energy of the system, ϵ. There are two contributions to this, the energy stored in the electric fields

$$\epsilon_E = \sum_{i=1,2} \epsilon_r \epsilon_0 E_i^2 d_i/2 \tag{3.36}$$

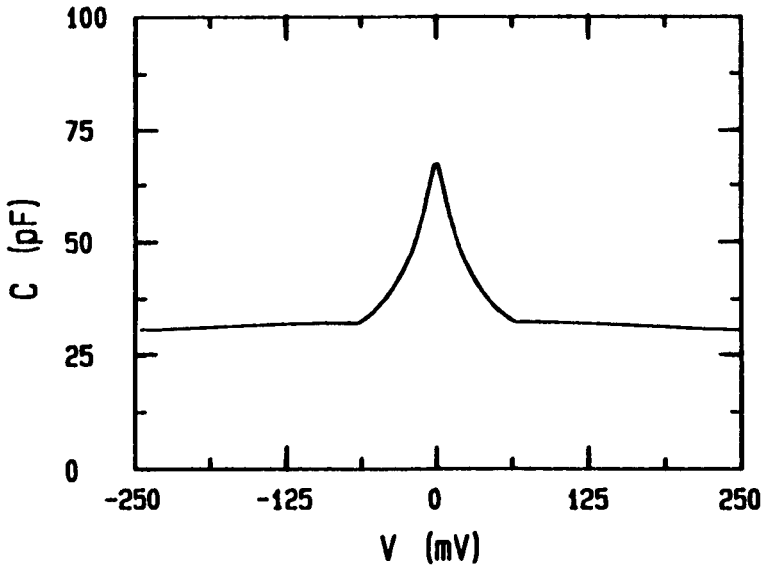

Figure 3.3: Calculated capacitance of a double barrier device, *NU183*, near zero bias. The rapid fall in C is due to depletion of the lightly-doped contacts.

and the Fermi-degeneracy energy

$$\epsilon_D = \sum \int_0^{\epsilon_F} D(\epsilon)\epsilon \, d\epsilon = \frac{\pi\hbar^2}{2m^*e^2}(\sigma_1^2 + \sigma_w^2) \tag{3.37}$$

We assume that the density of states in the well is simply that of a two-dimensional electron gas. We can therefore write

$$\epsilon = \frac{\sigma_2^2 d_1 \sin^4\phi}{2\varepsilon_r\varepsilon_0}\frac{\sigma_2^2 d_2}{2\varepsilon_r\varepsilon_0} + \frac{\pi\hbar^2\sigma_2^2}{2m^*e^2}(\sin^4\phi + \cos^4\phi) \tag{3.38}$$

Minimizing this with respect to ϕ gives

$$\tan^2\phi = \frac{\frac{\pi\hbar^2}{m^*e^2}}{\frac{\pi\hbar^2}{m^*e^2} + \frac{d_1}{\varepsilon_r\varepsilon_0}} \tag{3.39}$$

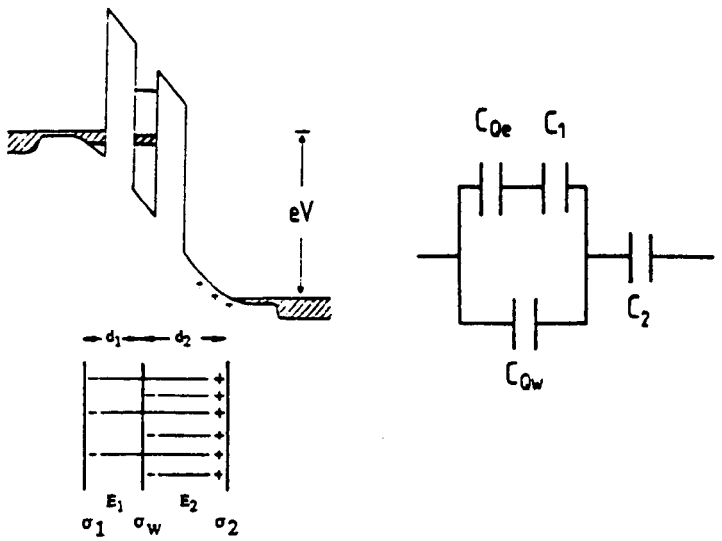

Figure 3.4: Diagram of the space-charge distribution in a double barrier device and the equivalent circuit showing the 'quantum capacitance'.

This distribution of charge is equivalent to the circuit shown in Figure 3.4. The quantum capacitance of the well state should therefore be considered to be in parallel with the quantum capacitance of the emitter and the geometrical capacitance of the emitter barrier. When the device is off-resonance, the density of states in the well is very low and the quantum capacitance of the well can be neglected. It is however important in explaining the magnetocapacitance oscillations observed in samples *NU183* and *NU221* where there is a substantial buildup of charge in the well at resonance, these results are discussed in detail in Sections 4.7.2 and 4.8. As described in Section 4.5.3, the equivalent circuit must be extended to allow for the leakage of electrons through the barriers and the time delays involved in the tunnelling process [113].

3.3 Resonant Tunnelling in a High Magnetic Field

3.3.1 Introduction

This section describes the use of a high magnetic field $B \parallel J$ to investigate and characterise resonant tunnelling devices. The electrons in the well and in the emitter are effectively confined in one direction (x) by the electrostatic potential, this leads to the quantisation of energy in this dimension. The addition of a magnetic field parallel to the tunnelling direction quantises the motion in the plane of the well; therefore the electron states are *totally* quantised in high magnetic fields. This produces a very strong modulation of the density of states, which is reflected in magnetoquantum oscillations in the tunnel current and in the differential capacitance. The origin of these oscillations is briefly described and then results are presented which show how the periodicity of the magnetoquantum oscillations is used to determine the electron density in the emitter accumulation layer, and hence the electric field within the device.

We stress that the origin of the magneto-oscillations in the transport properties is not the same for vertical transport as in parallel transport, where the well-known Shubnikov-de Haas oscillations in the conductivity are directly related to the modulation of the density of states at the Fermi energy due to the formation of Landau levels. For tunnelling structures, the origin of the magnetoquantum oscillations is rather more subtle and is explained in terms of self-consistent adjustments in the charge density and the bound state energy of the two-dimensional electron gas in the emitter. In vertical transport, the current is governed primarily by the probability of tunnelling through the barrier. This is not directly related to the density of states at the Fermi level since (for a two-dimensional emitter state) all the electrons have the same tunnelling probability depending only on the bound state energy and the voltage drop across the barrier.

When the device is biased on resonance, the magnetic field has different effects depending on the dimensionality of the emitter. For a parabolic conduction band, the field has little effect on a resonance between a 2D emitter state and a state in the well, since all Landau levels coincide at the same bias. When there is a range of longitudinal momenta in the emitter, the magnetic field has a bigger effect and, at biases near to threshold, the tunnel current can be completely quenched.

3.3.2 The Effect of a Magnetic Field on a Two-Dimensional Electron Gas

When a bias is applied to a resonant tunnelling device, an accumulation layer forms in the emitter contact adjacent to the barrier. If the doping in this region is sufficiently low (as is the case in nearly all samples considered in this thesis) a quasi-bound state forms in this accumulation potential, as described in Section 3.2. Therefore, the electrons in both the emitter and the well effectively form two-dimensional systems. Note that since tunnelling *i.e.* transport perpendicular to the plane of the 2DEG, can occur, neither state is truly bound, however we shall take this to be a good approximate description — at least

when the device is off-resonance. In the absence of a magnetic field this quantisation can be represented by the one-dimensional Schrödinger equation

$$\left[\frac{p_x^2}{2m^*} + eV(x)\right]\psi_i(x) = \epsilon_i\psi_i(x) \tag{3.40}$$

where $i = 0, 1, 2, \ldots$, p_x is the momentum, ϵ_i is the energy of the ith bound state, and $V(x)$ is the confining potential; given by the two barriers for states in the well and in the accumulation layer by the self-consistent potential as calculated from the Fang-Howard wavefunction. In the other two directions the electron motion is unconfined so the total energy is $\epsilon = \epsilon_i + \hbar^2(k_y^2+k_z^2)/2m^*$.

If a magnetic field $\boldsymbol{B}$ is now applied parallel to x, we must consider the canonical momentum $\boldsymbol{p} = m^*\boldsymbol{v} - e\boldsymbol{A}$ where $\boldsymbol{A}$ is the vector potential, which we take as $\boldsymbol{A} = (0, Bz, 0)$. The Hamiltonian is now [123]

$$\begin{aligned}
\mathcal{H} &= \frac{(\boldsymbol{p}+e\boldsymbol{A})^2}{2m^*} + eV(x) \\
&= \frac{p_x^2}{2m^*} + eV(x) + \frac{p_z^2}{2m^*} + \frac{p_y^2 + 2eBzp_y + e^2B^2z^2}{2m^*} \\
&= \frac{p_x^2}{2m^*} + eV(x) + \frac{p_z^2}{2m^*} + m^*\omega_c^2(z - Z_{k_y})^2/2
\end{aligned} \tag{3.41}$$

where $\omega_c = eB/m^*$ and Z_{k_y}, the origin of the simple harmonic oscillator potential, is given by $Z_{k_y} = \hbar k_y/m^*\omega_c = l_B^2 k_y$ (the magnetic length, $l_B^2 = \hbar/eB$). The eigenstates of this Hamiltonian are

$$\Psi = \psi_i(x)e^{ik_y y}\phi_n(z) \tag{3.42}$$

where $\phi_n(z)$ is the simple harmonic oscillator wavefunction. The energies are given by

$$\epsilon_{i,n} = \epsilon_i + (n + \frac{1}{2}\hbar\omega_c) \tag{3.43}$$

where n is an integer. Note that the energy is *completely* quantised so, in the absence of scattering, the density of states consists of a series of δ-functions separated by $\hbar\omega_c$ for each electrostatic subband. This is shown schematically in Figure 3.5. In any real system, scattering produces a broadening of these levels. When the magnetic field is applied in this direction, the Hamiltonian is separable and there is no effect on the bound state energy; this is in contrast to the geometry with the magnetic field in the plane of the 2DEG where the energy levels are strongly affected – see Chapter 5.

We can derive the degeneracy of each Landau level by noting that for the origin of the simple harmonic oscillator potential to lie within the sample,

$$0 < \frac{\hbar k_y}{eB} < L_x$$

i.e.

$$0 < k_y < \frac{L_x}{l_B^2} \tag{3.44}$$

Therefore the number of states that can be accommodated in a single Landau level (neglecting spin splitting) is

$$g = \frac{L_x}{l_B^2}\rho(k_y) = \frac{2L_yL_x}{2\pi l_B^2} = \frac{2eB}{h}\,.\,\text{Area} \tag{3.45}$$

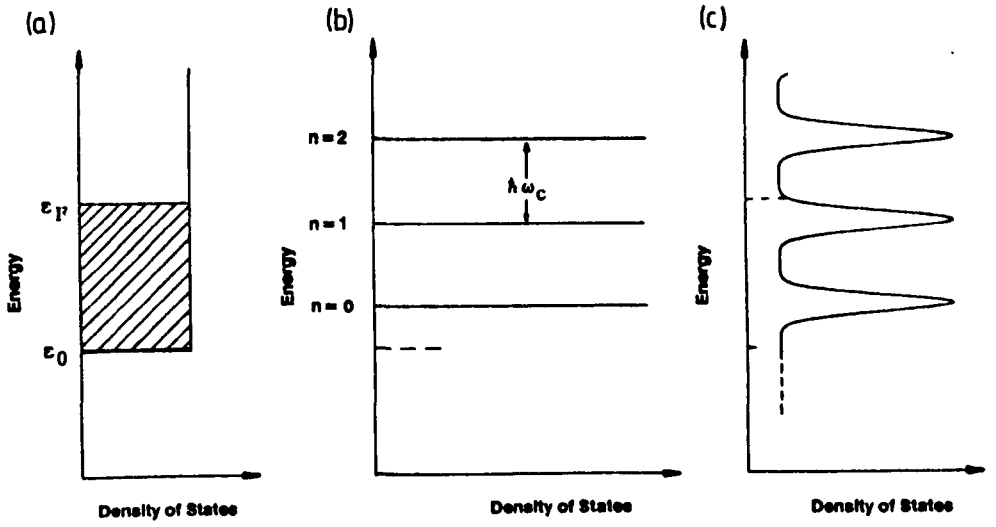

Figure 3.5: Density of states in a 2DEG with a magnetic field applied perpendicular to the plane: (a) with no scattering the Landau levels are delta functions, (b) scattering broadens the resonances and there is a non-zero background density of states.

The Shubnikov-de Haas Effect

For transport parallel to the layer structure, the electrical conductivity of a degenerate electron gas is proportional to the scattering rate and the number of electrons within an energy k_BT of the Fermi energy [124]. In a two-dimensional system both of these quantities depend on the density of states at the Fermi energy. When the magnetic field is swept, the degeneracy of the Landau levels increases and a given number density can be accommodated in fewer Landau levels. Therefore the Fermi energy makes transitions between Landau levels. When the Fermi energy lies between Landau levels, the density of states is low and so is the conductivity, conversely when the Fermi level lies within a Landau level the conductivity is high. This is the well-known Shubnikov-de Haas effect [123]. The minima in conductance occur when an integral number of Landau levels are completely filled *i.e.* $n_s = N(2eB/h)$ where N is an integer, so the oscillations are periodic in $1/B$ with a frequency B_f given by

$$B_f = [\Delta(1/B)]^{-1} = \frac{h}{2e} n_s \tag{3.46}$$

The conditions for observing clear oscillations are $\omega_c\tau \ll 1$ and $k_BT/\hbar\omega_c \ll 1$. In addition there must be a well-defined Fermi energy so $\epsilon_F \gg k_BT$.

If there is no electrostatic confinement in the x direction, there is still one degree of freedom. Although the density of states of a three-dimensional system also has singularities, it does not go to zero between Landau levels and the effects of a magnetic field are less pronounced — with typically only a few percent modulation in the resistance as the field is swept. In a two-dimensional system the effects are much more dramatic and the longitudinal resistance can change by several orders of magnitude [125].

Analysis of the amplitudes of the Shubnikov-de Haas oscillations can be

used to determine the scattering times in heterojunctions (for example see reference [126]), which in turn can be related to the Landau level broadening. Measurements of the density of states in GaAs/(AlGa)As heterostructures — from specific heat [127], magnetisation [128], electrochemical potential [129], capacitance [121, 122, 130] and activated transport [121] — have indicated that there is a quite large background density of states between Landau levels. This density of states is schematically shown in Figure 3.5(b). The non-zero background density of states is related to the presence of localised states at energies between Landau levels. This background has been measured as anything between 5 and 30% of the density of states within a Landau level. This schematic picture of the density of states in a magnetic field will be assumed to be broadly similar to that for the tunnelling structures under investigation here, although the scattering processes are rather different. In the samples we have studied, the ionized impurities are not spatially separated from the electron gas and so the scattering will probably be stronger, leading to broader Landau levels and a higher background density of states.

3.3.3 Magnetoquantum Oscillations in Vertical Transport

As described above, the effect of a magnetic field on the transport properties of a 2DEG for transport parallel to the layers has been widely investigated and is generally understood. The situation for vertical transport through a tunnel barrier is much less clear. Early measurements by Hickmott *et al.* [69] showed appreciable magnetoquantum oscillations in the tunnel current, but much smaller than those observed in parallel transport. Both systems consist of a two-dimensional electron gas at a GaAs/(AlGa)As heterojunction — but there the similarity ends.

For the modulation-doped heterojunction, the number density in the 2DEG is fixed and the Fermi energy oscillates as a function of magnetic field. The current is controlled by scattering processes and depends on the density of states at the Fermi energy. In a tunnelling structure, neither n_s nor ϵ_F are fixed. The total bias dropped across the device, *i.e.* the difference between the Fermi level in the emitter 2DEG and that in the collector contact, is held constant. The current is limited by the tunnelling probability through the barrier and scattering processes are much less important. This means that the magnetoquantum oscillations have an altogether different origin. Although the periodicity is found to be the same, the amplitudes and temperature dependences derived for parallel transport do not describe the situation in a tunnelling device. Note that we still require a well-defined Fermi level in order to observe Landau level effects, which means that the electron distribution must be cold, *i.e.* $k_B T_e \ll \hbar\omega_c$. In parallel transport, this is easily achieved since the electron temperature will be close to the lattice temperature if the measuring current is low. In a tunnel structure, it is somewhat harder to be certain of this since electrons are continually being removed from the accumulation layer by the tunnelling process, which could lead to a non-degenerate electron distribution. Therefore we require the energy relaxation time to be much less than the tunnelling rate *i.e.* electrons arriving in the 2DEG region from the bulk emitter contact thermalise *before* tunnelling through the barrier. This condition will be met when the tunnelling probability is low, but at

high biases, or when the device is on resonance, there could be a non-thermal distribution which would damp the magneto-oscillations.

Tunnel current

The tunnelling current through a single barrier, or a double barrier when biased off-resonance, depends on the energy of the tunnelling electron relative to the top of the barrier and the bias dropped across the barrier, the WKB approximation gives [81]

$$T(\epsilon) \sim \exp\left(-2/\hbar \int_0^b \sqrt{2m^*(eV(x) - \epsilon_x)}\, dx\right) \tag{3.47}$$

So if the number density in the accumulation layer or the bound state energy changes, the current changes. The magnetic-field dependence of the accumulation layer has been discussed by Baraff and Appelbaum [117]; they find that the magnetic field affects nearly all the parameters governing the tunnel current. In particular, the bound state energy and the screening length due to the electrons in the 3D states above the conduction band edge are strong functions of field. Self-consistent analyses of the tunnel current have been performed by Böckenhoff *et al.* [131] and Chan *et al.* [132]. They both assume that the density of states is approximately the same as that in parallel transport *i.e.* a constant background with Gaussian-broadened Landau level peaks. The accumulation layer state is approximated by the Fang-Howard wavefunction as described in Section 3.2. Within this approximation, the binding energy is proportional to the number density, $\epsilon_0 \propto n_s^{2/3}$, and the stand-off distance from the emitter barrier, x_0, is proportional to $n_s^{-1/3}$. Note that the situation in the resonant tunnelling devices differs from that considered by both authors in that there is a substantial voltage drop in the depletion region of the collector. This increases nonlinearly with n_s, so providing an additional mechanism for modulation of the current. Also, our resonant tunnelling samples have a degenerate 3D electron gas in addition to the 2DEG which was not the case in the single barrier structures considered in the theoretical analyses. This means that the accumulation layer potential can also be modulated due to oscillations in the screening length of the bulk electrons as described by Appelbaum and Baraff [117].

If we first consider the case where the Fermi level lies in the region of low density of states between Landau levels, an increase in B increases the degeneracy of the lower-lying Landau levels so the sheet density in the accumulation layer rises. This affects the accumulation layer potential, raising ϵ_0 and reducing the Fermi energy. This leads to an increase in the tunnel current because both the voltage drop across the barrier and the incident energy are higher. Conversely, when ϵ_F lies within a Landau level, an increase in the field raises the Landau level energy, forcing electrons out of the well and increasing the Fermi energy. Therefore both the potential drop across the barriers and the tunnelling energy are reduced so the current is lower. Hence the tunnel current undergoes a sawtooth-like oscillation as the field is swept. This is illustrated in the plots in Figure 3.6 (based on those in Chan *et al.* [132]). This is a very simple description of a very complex system and all of the parameters are inter-related, necessitating a self-consistent approach. The sharp rises in current correspond to the Fermi level lying between Landau levels. At the

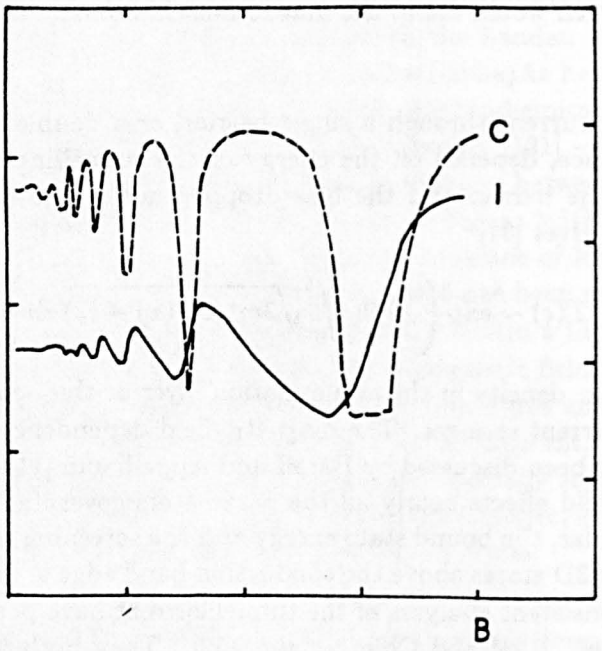

Figure 3.6: Plots of the tunnel current and differential capacitance for a single-barrier tunnelling device in a parallel magnetic field, based on calculations by Chan *et al.* [132].

centre of each region there is an integral number of occupied Landau levels. Therefore the periodicity of the magneto-oscillations is the same as in parallel transport *i.e.*

$$B_f = \frac{h}{2e} n_s$$

Capacitance

Several authors have used magnetocapacitance studies of a single heterojunction to measure the density of states of the 2DEG [133, 122, 121], this is possible because there is a direct relationship between the capacitance and the density of states — the 'quantum capacitance', C_Q, discussed in Section 3.2.3. In a tunnelling system, the situation is again more complex both because the number density is no longer fixed and because the other parameters affecting the capacitance vary as a function of the magnetic field. The expression derived in Section 3.2 is

$$\frac{1}{C} = \frac{\gamma x_0 + 2b + w + \lambda_c}{\epsilon_0 \epsilon_r} + \frac{1}{e^2 \mathcal{D}(\epsilon_F)} \tag{3.48}$$

where x_0 is the average distance of an electron in the 2DEG from the interface, $\gamma \sim 0.6$ and λ_c is the depletion length in the collector.

When the Fermi level lies in the region of low density of states between two Landau levels the quantum capacitance is low, and when it is within a Landau level it is high — which is the origin of the magneto-oscillations described by Kaplit and Zimel [133]. However, n_s is increasing when the Fermi level is between Landau levels, this makes x_0 decrease and λ_c increase. Since x_0 varies sublinearly with n_s and λ_c superlinearly this produces a net increase in the

width of the capacitor, so lowering the capacitance in this region. The decrease in n_s when ϵ_F is within a Landau level leads to a decrease in the effective width and an increase in C. Therefore, the quantum capacitance and the electrostatic capacitance vary in the same way with magnetic field producing sharp drops in the capacitance whenever ϵ_F lies in the gap between Landau levels. Because the capacitance no longer simply reflects $\mathcal{D}(\epsilon_F)$ we cannot easily measure the density of states from the magnetocapacitance. Chan *et al.* [132] have modelled the capacitance of a single barrier and find that the inclusion of the variation in n_s leads to broader minima in C than in a model where the charge density is held constant. As will be shown below, the form of the experimental magnetocapacitance closely resembles the model results of Chan *et al.* shown in Figure 3.6.

3.3.4 Experimental Results

Figure 3.7 shows typical magneto-oscillation traces ($\boldsymbol{B} \parallel \boldsymbol{J}$) for sample *NU104* (56 Å barriers, 50 Å well) at 4 K for a bias of 240 mV. Strong magnetoquantum oscillations are seen in both I and C, and these are periodic in $1/B$ as expected. These oscillations are associated with the degenerate 2DEG in the emitter contact. It is immediately apparent that, although the general form of both curves is similar to that predicted by the self-consistent calculations of Chan *et al.* the phase relationship between them is not that predicted. The reason for this discrepancy is not known. However, both measurements give the same periodicity, B_f. The oscillations have larger amplitudes than those observed by Payling *et al.* for tunnelling from a three-dimensional emitter electron distribution [134], which is consistent with Landau level effects being more pronounced in low-dimensional systems.

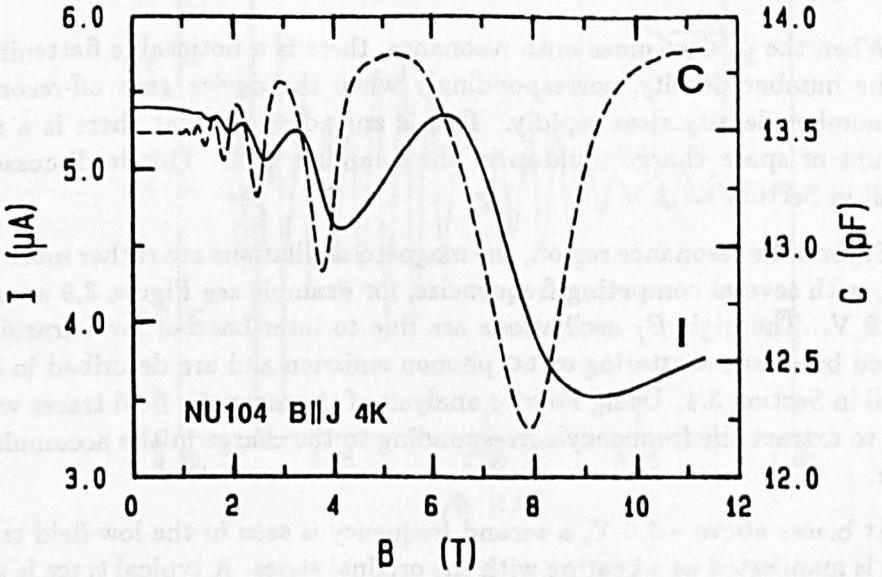

Figure 3.7: $I(B)$ and $C(B)$ for sample *NU104* with a constant applied bias of 240 mV at 4 K and with the magnetic field applied parallel to the current. The capacitance trace was taken at 1 MHz with a modulation of 3 mV.

The periodicity of the magneto-oscillations is used to obtain the number

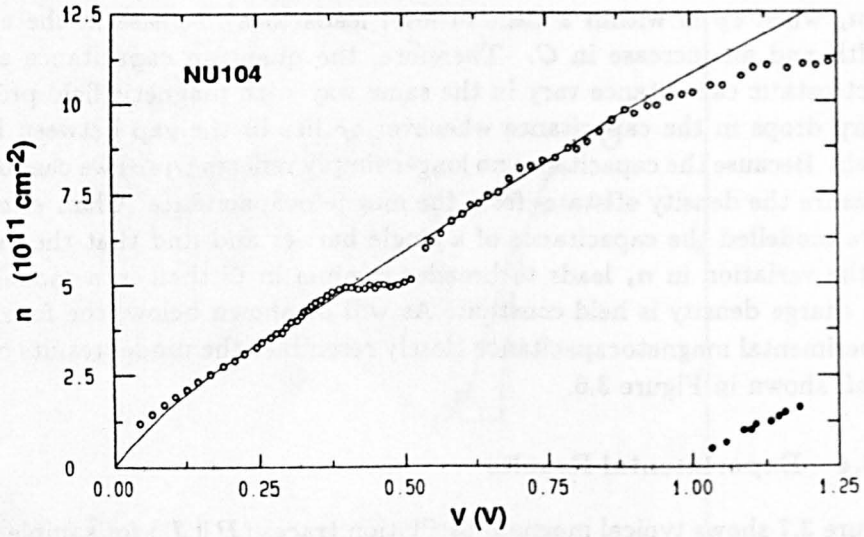

Figure 3.8: Electron sheet density in the emitter 2DEG, n_a, deduced from the periodicity of the magnetoquantum oscillations in $\boldsymbol{B} \parallel \boldsymbol{J}$. The solid line shows the values calculated from the expressions in Section 3.2.

density in the accumulation layer n_a from equation 3.46. These values are plotted against applied bias in Figure 3.8. The sheet density builds up steadily with bias and the device is simply acting like a parallel plate capacitor. There is a decrease in the slope with increasing bias which is related to the increasing depletion length in the collector contact (equation 3.42). The model of the accumulation and depletion layers described in Section 3.2 can be used to provide a good fit to the measured number density, using a doping level of 1.5×10^{16} cm^{-3} in the contact, which is slightly less than the nominal doping (Table 2.1).

When the device comes onto resonance, there is a noticeable flattening off in the number density, correspondingly when the device goes off-resonance the number density rises rapidly. This is an indication that there is a small amount of space charge buildup in the quantum well. This is discussed in detail in Section 4.7.2.

Beyond the resonance region, the magneto-oscillations are rather more complex, with several competing frequencies, for example see Figure 3.9 at a bias of 0.9 V. The high B_f oscillations are due to inter-Landau level transitions caused by elastic scattering or LO phonon emission and are described in more detail in Section 3.4. Using Fourier analysis of the magnetic field traces we are able to extract the frequency corresponding to the charge in the accumulation layer.

At biases above ~1.0 V, a second frequency is seen in the low-field traces. This is manifested as a beating with the original series. A typical trace is given in Figure 3.10 which is a plot of the second derivative d^2I/dB^2 against $1/B$ — clearly revealing the beating. The appearance of this series with a lower value of B_f is accompanied by a decrease in the slope of the higher B_f series with bias. This is explained by attributing the new set of oscillations to the Landau levels of a second subband in the accumulation layer potential, see Figure 3.10. This has previously been observed in single barrier (AlIn)As/(InGa)As heterostruc-

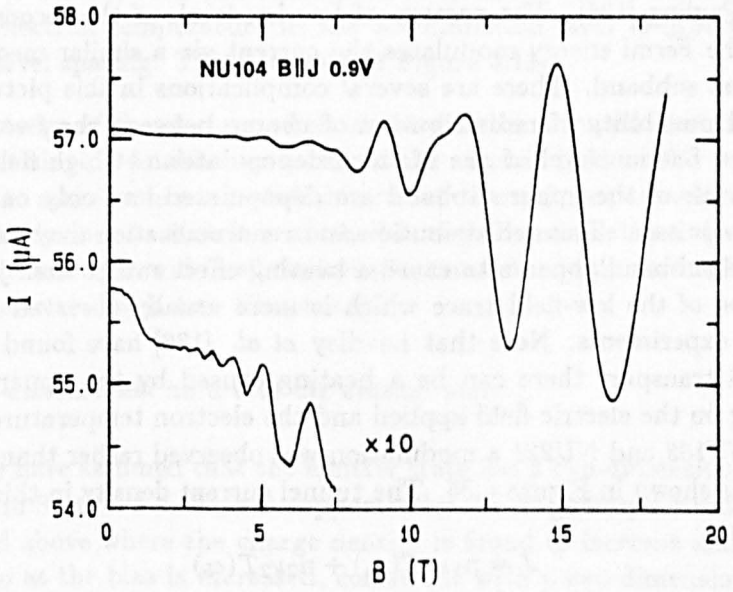

Figure 3.9: Magnetoquantum oscillations in the tunnel current in $\boldsymbol{B} \parallel \boldsymbol{J}$ for sample *NU104* (50 Å well) at 4 K. The applied bias is 0.9 V. The high frequency oscillations above 5 T are due to inter-Landau level transitions as described in the text. The expanded plot at low field shows the distinct series of magneto-oscillations due to Landau levels passing through the Fermi energy of the emitter.

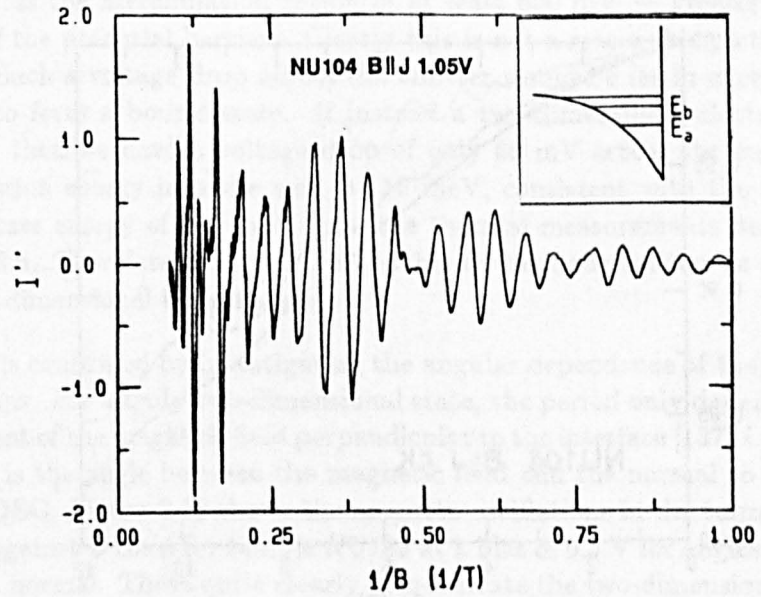

Figure 3.10: d^2I/dB^2 against $1/B$ at an applied bias of 1.05 V, showing the beating in the magnetoquantum oscillations due to the occupation of a second subband in the emitter 2DEG. The inset shows a schematic diagram of the emitter.

tures by Payling [135]. The passage of Landau levels of the second subband through the Fermi energy modulates the current via a similar mechanism as for the first subband. There are several complications in this picture due to the added possibility of redistribution of charge between the two subbands whenever a Landau level of one of them depopulates. At high fields, all the Landau levels of the upper subband are depopulated and only one series of oscillations is seen. This redistribution and renormalisation may explain why the second subband appears to cause a beating effect rather than just a slow modulation of the low-field trace which is more usually observed in parallel transport experiments. Note that Leadley *et al.* [136] have found that even in parallel transport there can be a beating caused by the upper subband, depending on the electric field applied and the electron temperature. Also, in samples *NU183* and *NU221* a modulation was observed rather than a beating effect — as shown in Figure 4.35. The tunnel current density in this situation is given by

$$J = n_1\nu_1 T(\epsilon_a) + n_2\nu_2 T(\epsilon_b) \tag{3.49}$$

where ϵ_a and ϵ_b are the energy levels in the accumulation layer, ν is the classical attempt rate and T is the transmission probability. Since the upper subband has a higher confinement energy, the tunnelling probability from this level is much greater than from the lower level. Therefore it is possible that most of the current is due to tunnelling from the upper subband even though most of the electrons reside in the lower level. For example, at 1.1 V we estimate that the lower energy level is 40 meV above the conduction band edge and the upper level 56 meV. This leads to an order of magnitude difference in the tunnelling probabilities and so most of the current flows via the upper subband.

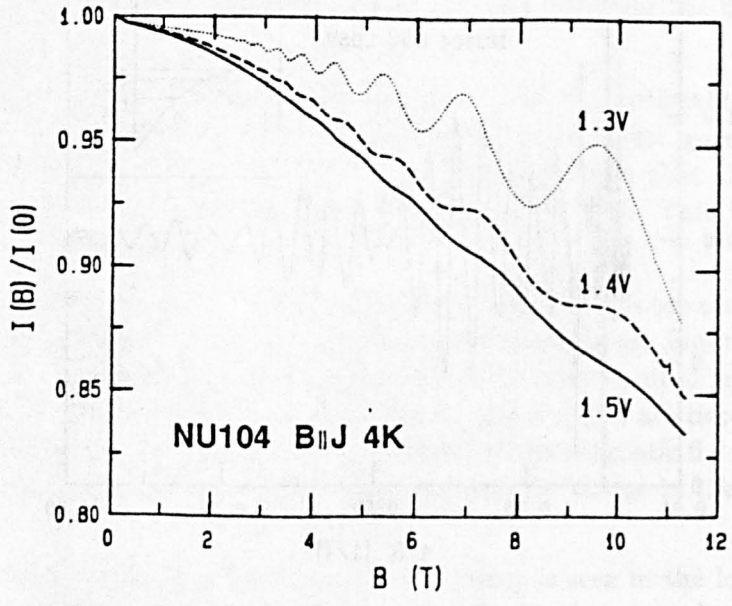

Figure 3.11: $I(B)$ plots for *NU104* at $V = 1.3$ V, 1.4 V and 1.5 V showing the effect of electron heating on the magnetoquantum oscillations.

At biases >1.2 V, the current density is very large and no oscillations are seen from the second subband. This may indicate that the tunnelling probability via the upper level is now so high that the dwell time in the accumulation layer is insufficient to allow thermalisation of the second subband. At higher

voltages (>1.4 V), even the oscillations from the lower subband are removed *i.e.* the electron temperature in the accumulation layer is greater than the Landau level spacing. This is shown in Figure 3.11.

Knowledge of the electron sheet density in the accumulation layer is most important since it enables us to know the electric field in the region of the well and to make rather more reliable calculations of the potential distribution within the device. As such it is a valuable tool when investigating other effects such as tunnelling in wide well devices (Section 3.6) and the formation of hybrid magnetoelectric levels (see Chapter 5).

The two-dimensional nature of the emitter state

So far we have assumed that the emitter state has a two-dimensional nature as outlined in Section 3.2. This is supported by the magnetoquantum oscillations described above where the charge density is found to increase almost linearly from zero as the bias is increased, consistent with a two-dimensional electron gas in the emitter as modelled using the Fang-Howard wavefunction. If the emitter were somehow three-dimensional in character, it is hard to see how the observed magneto-oscillations could arise with a clearly voltage-dependent periodicity. Note that magneto-oscillations observed in structures with heavily-doped emitter regions show a constant periodicity with bias which can be identified as being due to a three-dimensional electron gas [134]. One possibility is that the whole of the 500 Å wide doping layer is accumulated uniformly. At resonance the measured magneto-oscillation frequency would correspond to a three-dimensional density $\sim 2 \times 10^{17}$ cm^{-2}. This would produce a voltage drop across the accumulation region of at least 600 mV — greater than the height of the potential barriers. Clearly this is not a reasonable picture of the device. Such a voltage drop across the emitter would be far in excess of that needed to form a bound state. If instead a two-dimensional electron gas is assumed then we have a voltage drop of only 60 mV across the emitter and the injection energy into the well is 115 meV, consistent with the estimated bound state energy of 107 meV from the thermal measurements described in Section 3.5. Therefore it is quite reasonable to treat the emitter as consisting of a two-dimensional bound state.

This is confirmed by investigating the angular dependence of the magneto-oscillations. For a truly two-dimensional state, the period only depends on the component of the magnetic field perpendicular to the interface [137] *i.e.* $B\cos\phi$ where ϕ is the angle between the magnetic field and the normal to the plane of the 2DEG. Figure 3.12 shows the magneto-oscillations in the tunnel current plotted against $B\cos\phi$ for sample *NU183* at a bias of 0.3 V for angles up to 40° from the normal. These quite clearly demonstrate the two-dimensional nature of the emitter state.

3.3.5 The Effect of a Magnetic Field on Resonant Tunnelling

The influence of a magnetic field $\boldsymbol{B} \parallel \boldsymbol{J}$ on the resonant tunnelling current depends on the nature of the emitter

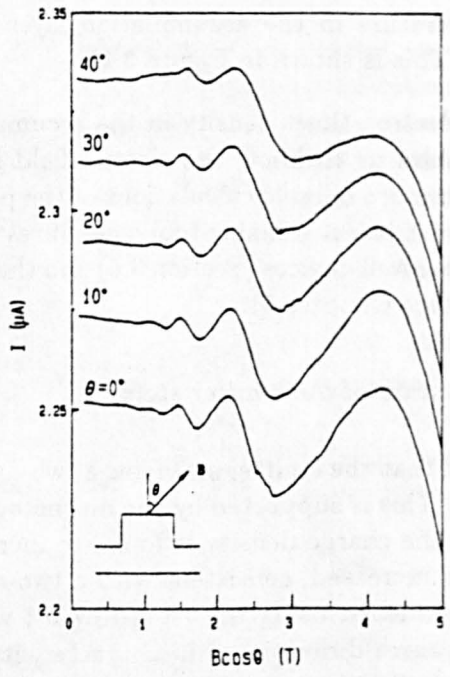

Figure 3.12: Angular dependence of the magnetoquantum oscillations in sample *NU183* at an applied bias of 0.3 V. This demonstrates the two-dimensional nature of the emitter state.

Two-dimensional emitter state

For a two-dimensional emitter state, resonant tunnelling occurs when the energy of the quasi-bound state in the emitter is aligned with that of a state in the well. The application of a magnetic field leads to the formation of Landau levels with spacing $\hbar\omega_c = \hbar eB/m^*$. The conservation of $\boldsymbol{k}_\perp$ at zero field corresponds to the conservation of Landau level index in a finite magnetic field. If the effective mass is the same in both the emitter and the well, the Landau level spacing is identical and the magnetic field has no effect on the resonance condition. Where there is significant non-parabolicity, or where the well is of a different composition to the emitter [138], the Landau levels do not all coincide at the same voltage, which would produce structure in the tunnel current. However no experiments have been performed to date in such a system with a two-dimensional electron gas in the emitter. For the samples considered here, the energy level in the well is usually less than 50 meV further above the conduction band edge than the emitter state. Therefore the difference in effective mass is at most 3%, which is not large enough for the energy difference between Landau levels to be significant compared to their width (~1 meV). Therefore the effect of a parallel magnetic field on the position of the resonance is not measurable in these samples.

The above argument neglects the role of space charge in the quantum well at resonance. As will be seen in Section 4.7.2, the presence of a degenerate electron distribution in the well produces marked magnetoquantum effects.

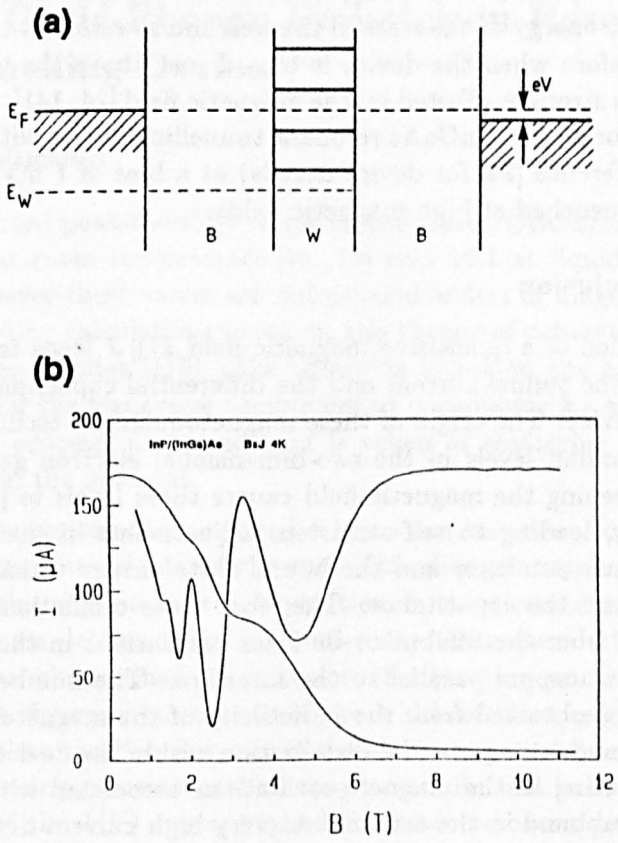

Figure 3.13: (a) Schematic diagram of the energy levels in a resonant tunnelling device in a magnetic field $\boldsymbol{B} \| \boldsymbol{J}$ showing the Fermi levels of the 3D electron gases in the emitter and collector for an applied bias V. The Landau levels in the well are indicated by solid horizontal lines. (b) The quenching of the tunnel current by a parallel magnetic field at a bias of 1 mV in an InP/InGaAs resonant tunnelling device [24].

Three-dimensional emitter

When the emitter region is heavily doped right up to the barrier, the application of a magnetic field leads to a series of oscillations in the tunnel current. This was first observed by Mendez [139]. Consider Figure 3.13 where the energy level in the well is at an energy $\hbar^2 k_0^2/2m^* = \epsilon_1 - eV_e$ above the conduction band edge in the emitter, ϵ_1 is the bound state energy and V_e is the voltage drop across the emitter barrier and accumulation layer. Electrons in the emitter with $k_x = k_0$ can tunnel into the well. The lateral energy of these electrons is quantised by the magnetic field *i.e.* $\epsilon_F - \hbar^2 k_0^2/2m^* = (n + 1/2)\hbar\omega_c$. Thus sweeping the magnetic field causes oscillations in the tunnel current with a frequency

$$B_f = \frac{m^*}{e\hbar}(eV_e + \epsilon_F - \epsilon_1) \tag{3.50}$$

The variation in B_f with total applied bias gives V_e as a function of the total voltage drop which allows an estimate of the sheet charge density in the well to be made, see Goldman *et al.* [140] and Eaves *et al.* [108].

When $\epsilon_0 + 1/2\ \hbar\omega_c > \epsilon_F + eV_e$, there are no occupied states in the emitter with the same energy as the state in the well and so resonant tunnelling cannot occur. Therefore when the device is biased just above the threshold voltage the current is strongly affected by the magnetic field [24, 141]. This is shown in Figure 3.13 for an InP/InGaAs resonant tunnelling device with a well of width 40 Å (see reference [24] for device details) at a bias of 1 mV. The current is completely quenched at high magnetic fields.

3.3.6 Conclusion

The application of a quantising magnetic field $\boldsymbol{B} \parallel \boldsymbol{J}$ leads to pronounced oscillations in the tunnel current and the differential capacitance of a resonant tunnelling device. The origin of these magnetoquantum oscillations is the formation of Landau levels in the two-dimensional electron gas of the emitter contact. Sweeping the magnetic field causes these levels to pass through the Fermi energy, leading to self-consistent adjustments in the number density in the accumulation layer and the bound state energy which in turn modify the current and the capacitance. Therefore these oscillations are fundamentally distinct from the Shubnikov-de Haas oscillations in the conductivity of a 2DEG for transport parallel to the interface. The number density in the emitter can be obtained from the periodicity of the magneto-oscillations, enabling us to model the potential distribution within the device. At high biases there is a beating in the magneto-oscillations associated with the formation of a second subband in the emitter. At very high current densities, the magnetoquantum oscillations are destroyed due to the electron gas in the emitter becoming non-degenerate. The absence of any theoretical treatment of the form of these oscillations means that useful information relating to the electron temperature and scattering processes in two-dimensional systems cannot be extracted from these data. Given the extensive theoretical efforts devoted to transport parallel to the interfaces and the growing experimental interest in tunnelling measurements, it is perhaps surprising that theoretical work on tunnelling processes in high magnetic fields is not forthcoming.

When the device is biased on resonance from a 2D emitter state, the magnetic field has little effect on the position of the resonant peak, in the absence of space charge in the well (the situation is very different in the presence of significant charge buildup as shown in Section 4.7.3). The only influence is on the scattering rates which effect the width and strength of the resonances in devices with wide quantum wells (Section 3.6). Where there is a three-dimensional electron distribution in the emitter, the magnetic field quenches the resonant current near the threshold bias and leads to a new series of magneto-oscillations.

3.4 Magnetic Field Studies of Elastic Scattering and Optic-Phonon Emission in Resonant Tunnelling Devices

3.4.1 Introduction

The best reported peak-to-valley ratios in the GaAs/(AlGa)As system are in excess of 3:1 at room temperature [18, 19] and 20:1 at liquid nitrogen temperature. However these values are still several orders of magnitude less than those predicted by calculations based on the theory of coherent tunnelling — for example see Mendez [115]. The theory is based on the assumption that both energy and the transverse component of wavevector $\boldsymbol{k}_\perp$ are conserved in the tunnelling process, *i.e.* no account is taken of scattering processes or of imperfections in the material.

In the valley region, the measured current can be several orders of magnitude higher than the calculated current. This discrepancy is due to the fact that real samples contain ionized impurities, fluctuations in composition and in layer thickness, lattice vibrations and more than one electron. Weil and Vinter [86] have shown that the inclusion of scattering processes in the well does not affect the resonant current if the width of the energy level remains much smaller than the Fermi energy in the emitter contact (see Section 1.5.3). However, scattering processes make a major contribution to the current in the valley region of the $I(V)$ curve, beyond the main resonant peak. Tunnelling assisted by the emission of LO phonons was first identified in a triple barrier structure by Bando *et al.* [142] and by Goldman, Tsui and Cunningham [143] in double barrier structures. The contribution to the valley current from imperfections in the lattice has been calculated by Pötz and Li [144] and that from inelastic scattering by emission or absorption of LO phonons by Wingreen *et al.* [145] and by Cai *et al.* [146], among others.

At high temperatures there is also a large thermionic contribution to the valley current, associated with energetic electrons in the high-energy tail of the emitter energy distribution (see Section 3.5), however this will not be important at the low temperatures considered here ($T < 77$ K).

Here we study the nature of the scattering processes which contribute to the valley current by applying a high magnetic field perpendicular to the plane of the tunnel barriers (*i.e.* $\boldsymbol{B} \parallel \boldsymbol{J}$). The density of electron states is quantised into discrete Landau levels allowing us to investigate the scattering processes spectroscopically and to distinguish between the contributions to the valley current arising from elastic scattering and from inelastic processes involving the emission of longitudinal optic phonons by the tunnelling electrons [147, 148, 149].

3.4.2 Scattering Processes in Resonant Tunnelling Devices

If an electron traverses the barriers without scattering, the k-vector component, $\boldsymbol{k}_\perp$, perpendicular to the tunnelling direction is conserved. Scattering processes break the conservation conditions assumed in the coherent theory of tunnelling. For example, if a double barrier device is biased so that the energy

level in the well lies below the conduction band edge in the emitter contact, the purely resonant current will be zero [10]. This is because the incident electrons have too much momentum in the tunnelling direction to match the resonant state in the well. However a scattering process which transfers this excess momentum into the transverse direction could allow the electron to scatter into the resonant state of the well, thus producing a higher valley current.

Pötz and Li [144] have calculated the effect of interface defects and layer width fluctuations on resonant tunnelling in a Green's function model of a linear chain. They find that fluctuations in the layer widths of less than one monolayer have only a small influence on the device characteristics whereas a rather small amount of defects at the heterointerfaces (*e.g.* lattice mismatch and dangling bonds) can produce significant reduction in the device current.

The contributions of scattering processes to the valley current are most easily analysed with a sequential tunnelling approach based on Fermi's Golden rule, as described by Chevoir and Vinter [98], which is a natural extension of the method used by Sheard and Toombs [99], who did not specifically include scattering processes in their treatment. The tunnelling is treated as a two-stage process; scattering-assisted capture of an electron by the bound state of the well followed by transmission out of the well through the collector barrier. Figure 3.14 shows a schematic conduction band profile of a resonant tunnelling device illustrating the condition for LO phonon assisted tunnelling.

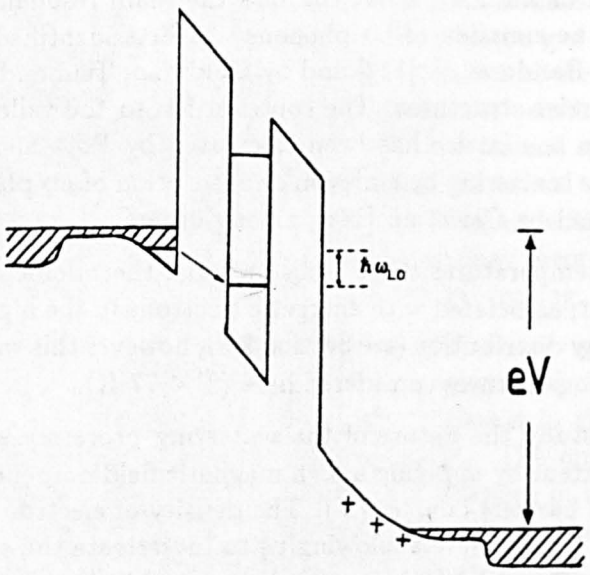

Figure 3.14: Schematic conduction-band profile of a resonant tunnelling device under bias showing the condition for tunnelling assisted by the emission of an LO phonon.

The scattering process considered is from an occupied bulk emitter state $\psi_1(k_x, \boldsymbol{k}_\perp)$ at energy $\epsilon = \hbar^2(k_x^2 + k_\perp^2)/2m^*$ to an unoccupied state in the well $\psi_2(0, \boldsymbol{p}_\perp)$ with energy $\epsilon' = \Delta\epsilon + \hbar^2 p_\perp^2/2m^*$, where $\Delta\epsilon = \epsilon_1 - eV_e$ is the energy of the well state relative to the conduction band edge in the emitter contact and V_e is the voltage drop from the emitter to the centre of the well. For the emission (or absorption) of an LO phonon of wave-vector $\boldsymbol{q} = (q_x, \boldsymbol{Q})$ and energy $\hbar\omega_{LO}$ the scattering rate can be calculated from the Fröhlich Hamiltonian describing

electron-phonon interactions [54].

$$W^{\pm}_{\boldsymbol{k},\boldsymbol{p}} = \frac{2\pi\, e^2 \hbar\omega_{LO}\, N^{\pm}_{LO}}{2\Omega\hbar}\left(\frac{1}{\varepsilon_\infty} - \frac{1}{\varepsilon_0}\right)\frac{|<1|e^{i\boldsymbol{q}\cdot\boldsymbol{r}}|2>|^2}{|\boldsymbol{q}|^2}\,\delta_{\epsilon'-\epsilon\pm\hbar\omega_{LO}} \tag{3.51}$$

where $N^{-}_{LO} = N^{+}_{LO} - 1$ is the Bose-Einstein factor, ε_0 and ε_∞ are the low and high frequency limits of the dielectric constant [98] and Ω is the volume of a unit cell. If we neglect the occupancy of the well, the current from these processes is simply given by

$$J_{LO} = \sum_{\boldsymbol{k},\boldsymbol{p}} f_{\boldsymbol{k}} W^{\pm}_{\boldsymbol{k},\boldsymbol{p}} \tag{3.52}$$

where f is the occupancy of the emitter states. Conservation of momentum requires that $\boldsymbol{q} = \boldsymbol{k} - \boldsymbol{p}$ and that of energy $\hbar^2 p_\perp^2/2m^* = \Delta\epsilon + \hbar^2 k_\perp^2/2m^* \pm \hbar\omega_{LO}$. The numerical evaluation of this term by Chevoir and Vinter for a typical GaAs/(AlGa)As double barrier structure gives a valley current four orders of magnitude higher than that for purely coherent tunnelling [98]. As in the result of Wingreen *et al.* who also obtain a small shoulder in $I(V)$ corresponding to the LO phonon process, the peak-to-valley ratio is still unrealistically high. Electrons couple much more strongly to the polar optic modes than the transverse modes, so the contribution from other phonon modes is likely to be much less important. Chevoir and Vinter also consider the contributions of acoustic phonon scattering (introduced via the deformation potential) and alloy disorder in a similar manner. The latter has considerable importance at low temperatures when acoustic phonon scattering is small. This suggests that the performance of devices with simple binary barriers should be markedly superior as has been demonstrated in the pseudomorphic AlAs/InAs system [21]. The current due to all the scattering processes decreases at higher voltage and the coherent tunnelling current again dominates.

The influence of ionized impurity scattering has been experimentally investigated by Wolak *et al.* [150] and by Söderström *et al.* [151] who grew samples where the well region was deliberately doped with impurities. They find that, although the peak-to-valley ratio is reduced, the effect is unlikely to be significant at the low levels of impurities found in a nominally undoped sample. It should be pointed out that the devices investigated by both groups of authors show rather poor peak-to-valley ratios, even when the well region is undoped (peak-to-valley ratios <6:1 at 77 K). The same conclusion may not be reached for higher quality samples.

In devices where there is a buildup of space charge in the quantum well on resonance (see Section 4.2), electron-electron scattering may become significant. However, this does not change the overall energy and momentum of the electron gas, and an individual electron could only lose its excess momentum in the tunnelling direction by giving it to another electron — reducing the probability of that electron tunnelling. Therefore it is not clear whether these processes produce an important effect on the $I(V)$ characteristics. This situation has not as yet received theoretical consideration.

3.4.3 Current-Voltage Characteristics

Three different double barrier structures will be considered in this section: *NU104* which has a well of width 50 Å and barrier width 56 Å, *NU153* well-

width 117 Å, barriers 56 Å, and *NU183* with a well-width of 58 Å, an emitter barrier 111 Å thick and a collector barrier of 83 Å. The full details are given in Table 2.1. All three samples have lightly-doped (1 or 2 × 10^{16} cm^{-3}) buffer layers adjacent to the double barrier structure. As described in Section 1.5, this means that tunnelling takes place from a quasi-two-dimensional electron gas adjacent to the enitter barrier. In order to measure stable $I(V)$ curves for samples *NU104* and *NU153* it was necessary to connect a small resistor in parallel with the device to suppress current oscillations (Section 4.3).

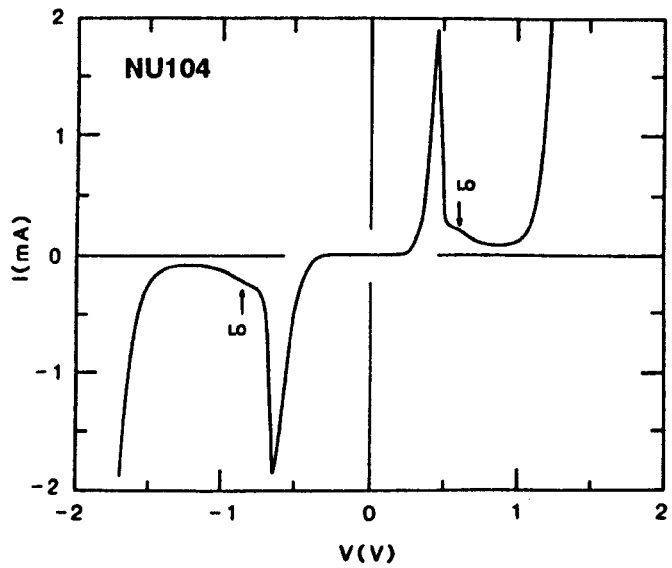

Figure 3.15: Current-voltage characteristics at 77 K of a 10 μm diameter mesa fabricated from *NU104* (50 Å well).

The current-voltage characteristics of these devices are shown in Figures 3.15, 3.16 and 3.17(lower traces) at a temperature of 4 K (77 K for *NU104*). Only the bias region corresponding to the first resonance is shown. The characteristics of *NU183* are for *reverse* bias. In *NU183* there are in fact two resonances and in *NU153* there are three. These samples all show exceedingly good peak-to-valley ratios at low temperatures; the 4 K values are *NU104* 25:1, *NU153* 16:1 and *NU183* 26:1. This indicates good material quality. In all three curves there is a replica peak, or a shoulder, beyond the main resonant peak. This is due to the LO phonon assisted tunnelling process. This subsidiary peak is typically less than 5% of the height of the main peak. This is consistent with the rather low electron-phonon coupling constant in GaAs. More strongly polar materials such as II-VI compounds might be expected to show larger effects but, to date, no results have been reported.

In zero magnetic field, the threshold for elastic transitions occurs when the quasi-bound state of the well, ϵ_1, moves below the Fermi energy in the emitter contact, and elastic scattering transitions can occur for all biases above this — *i.e.* there is a contribution to the current in the region just before resonance as well as in the valley region. The inelastic LO phonon scattering can only occur for biases where the energy difference between the Fermi energy in the emitter and the state in the well is greater than the LO phonon energy (36 meV). At

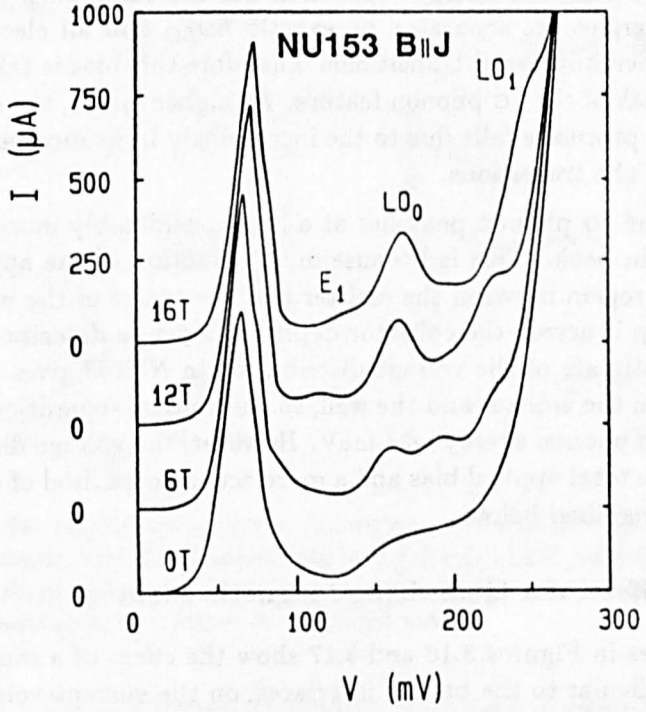

Figure 3.16: The current-voltage characteristics at 4 K and various magnetic fields $\boldsymbol{B} \parallel \boldsymbol{J}$ of a 100 μm diameter mesa of *NU153* (117 Å well). The curves show only the region of the first resonance.

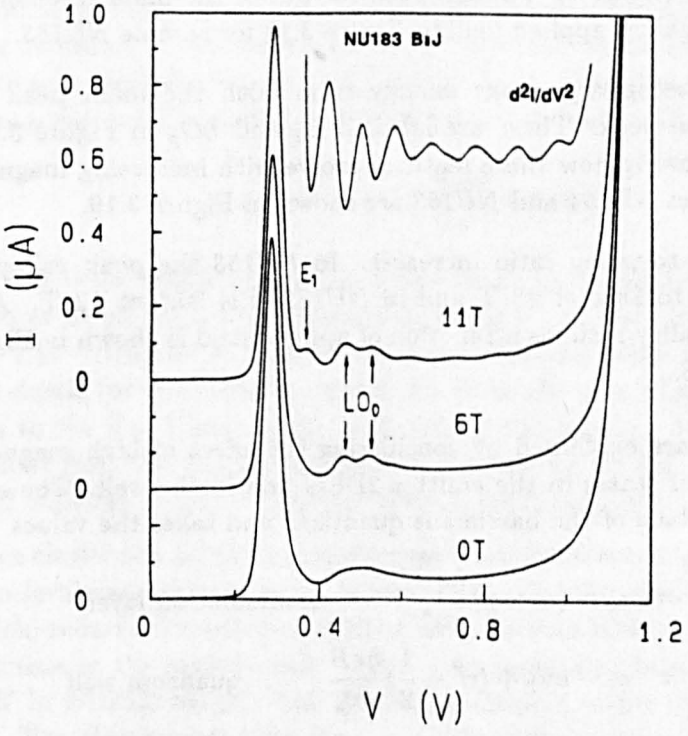

Figure 3.17: The current-voltage characteristics of the first resonance in reverse bias at 4 K and various magnetic fields $\boldsymbol{B} \parallel \boldsymbol{J}$ for a 200 μm mesa fabricated from *NU183*. The inset shows d^2I/dV^2 for the 11 T curve, emphasising the magneto-oscillatory structure.

a slightly higher bias, the energy separation has increased such that the two bound state energies are separated by exactly $\hbar\omega_{LO}$ and all electrons in the emitter can undergo inelastic transitions. Therefore this bias is taken to correspond to the peak of the LO phonon feature. At higher biases, the contribution from scattering processes falls due to the increasingly large momentum change associated with the transitions.

Note that the LO phonon peak lies at a bias considerably more than $\hbar\omega_{LO}$ beyond the main peak. This is because only a fraction of the applied bias is dropped in the region between the emitter and the centre of the well. Most of the voltage drop is across the collector depletion layer as described in Section 3.2. A rough estimate of the voltage distribution in *NU153* gives only 30% of the bias between the emitter and the well, so the voltage separation of 110 mV corresponds to a phonon energy ~34 meV. However, the voltage distribution is a function of the total applied bias and a more accurate method of determining $\hbar\omega_{LO}$ will be described below.

3.4.4 The Effect of a Quantizing Magnetic Field

The upper traces in Figures 3.16 and 3.17 show the effect of a magnetic field, applied perpendicular to the barrier interfaces, on the current-voltage characteristics. The following features are noteworthy:

1. The magnetic field enhances the main LO phonon-related peak. It has a peak-to-valley ratio of 2.6:1 at 18 T for sample *NU153*. The ratio of the height of the LO phonon peak to that of the main resonant peak is plotted against applied field in Figure 3.18 for sample *NU153*.

2. Weaker, secondary peaks emerge from both the main peak and the LO phonon peak. These are labelled E_1 and LO_p in Figure 3.16. Fan-charts showing how these features evolve with increasing magnetic field for samples *NU104* and *NU153* are shown in Figure 3.19.

3. The peak-to-valley ratio increases. In *NU153* the peak/valley ratio is increased to 25:1 at 18 T and in *NU183* it is 30:1 at 12 T. A plot of peak-to-valley ratio as a function of applied field is shown in Figure 3.20 for *NU153*.

These features are explained by considering the effect of high magnetic field on the density of states in the emitter 2DEG and in the well. The energy of motion in the plane of the barriers is quantized and takes the values

$$\epsilon = \epsilon_0 + (n + \frac{1}{2})\frac{\hbar eB}{m_e^*} \qquad \text{accumulation layer}$$

$$\epsilon = \epsilon_1 - eV_1 + (n' + \frac{1}{2})\frac{\hbar eB}{m_w^*} \qquad \text{quantum well}$$

where n and n' are the Landau-level quantum numbers, ϵ_0 and ϵ_1 are the lowest quasi-bound state energies in the emitter and the well respectively, V_1 is the voltage dropped across the emitter barrier and the first half of the quantum well and m_e^* and m_w^* are the effective masses. The conservation of $k_\perp$ at $B = 0$ corresponds to conservation of Landau-level index at finite field

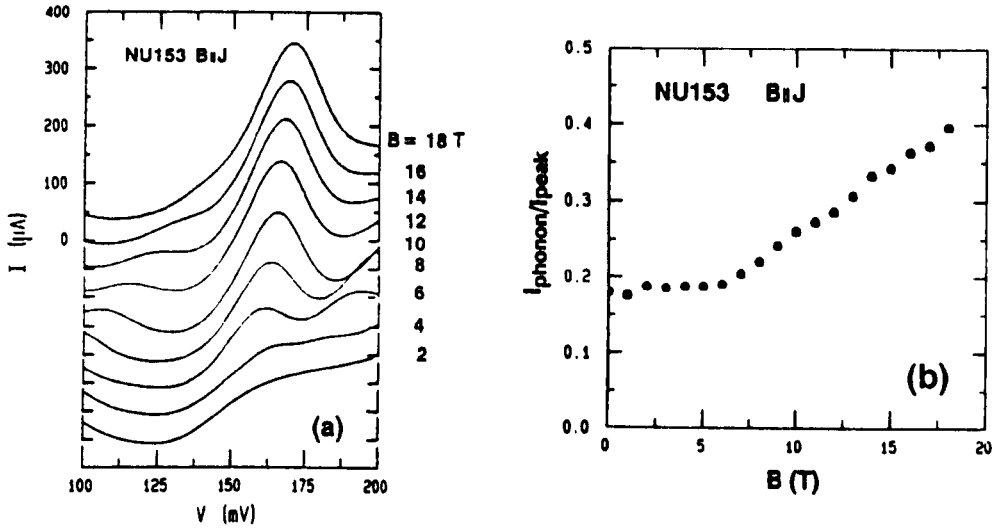

Figure 3.18: (a) Expanded plot of the valley current in the region of the LO phonon peak for sample *NU153* in magnetic fields $\boldsymbol{B} \parallel \boldsymbol{J}$ up to 12 T, showing the enhancement of the LO phonon peak. (b) Ratio of the current at the LO phonon peak to that at the main resonant peak as a function of applied field.

i.e. $p = n' - n = 0$. Resonant tunnelling occurs at the applied voltage for which $\epsilon_0 = \epsilon_1 - eV_1$ independent of the magnetic field — as long as the effective masses in the emitter and the well are the same (Section 3.3). There is a shift in the peak position of less than 5 mV at 18 T in *NU153*. This would correspond to a difference in effective mass of less than 2%. Note that for most of the voltage and field range considered here, there is only one occupied Landau level in the emitter contact. The possible elastic and inelastic transitions in a magnetic field are schematically illustrated in Figure 3.21. Transitions for which $\boldsymbol{k}_\perp$ is not conserved are governed only by energy conservation. Therefore,

$$\epsilon_0 = \epsilon_1 - eV_1 + p\,\frac{\hbar eB}{m^*} + i\,\hbar\omega_{LO} \tag{3.53}$$

where $i = 0$ for elastic scattering and $i = 1$ for LO phonon emission. We have no evidence for multiphonon emission ($i > 1$). The peak marked E_1 in Figure 3.17 extrapolates back to the main resonant peak as $B \to 0$ and is due to elastic (or quasi-elastic) scattering from the $n = 0$ Landau level in the emitter to the $n = 1$ level in the well. The peaks labelled LO_p correspond to transitions from the nth landau level in the emitter to the $(n + p)$th level in the well with the emission of an LO phonon [142, 143, 147].

Since elastic and LO phonon scattering transitions are only allowed at when Landau levels are aligned or separated by $\hbar\omega_{LO}$, the application of a magnetic field reduces the valley current at intermediate biases. This accounts for the increase in the peak-to-valley ratio with increasing field. At a voltage of 200 mV in *NU153*, roughly half the valley current is due to LO phonon processes. The elastic scattering peak is much weaker, which may indicate the relative strengths of acoustic and LO phonon coupling. The part of the valley current unaffected by a magnetic field may contain several components: coherent tunnelling, tunnelling via impurity states in the well region and any leakage currents. These measurements do not provide any information on

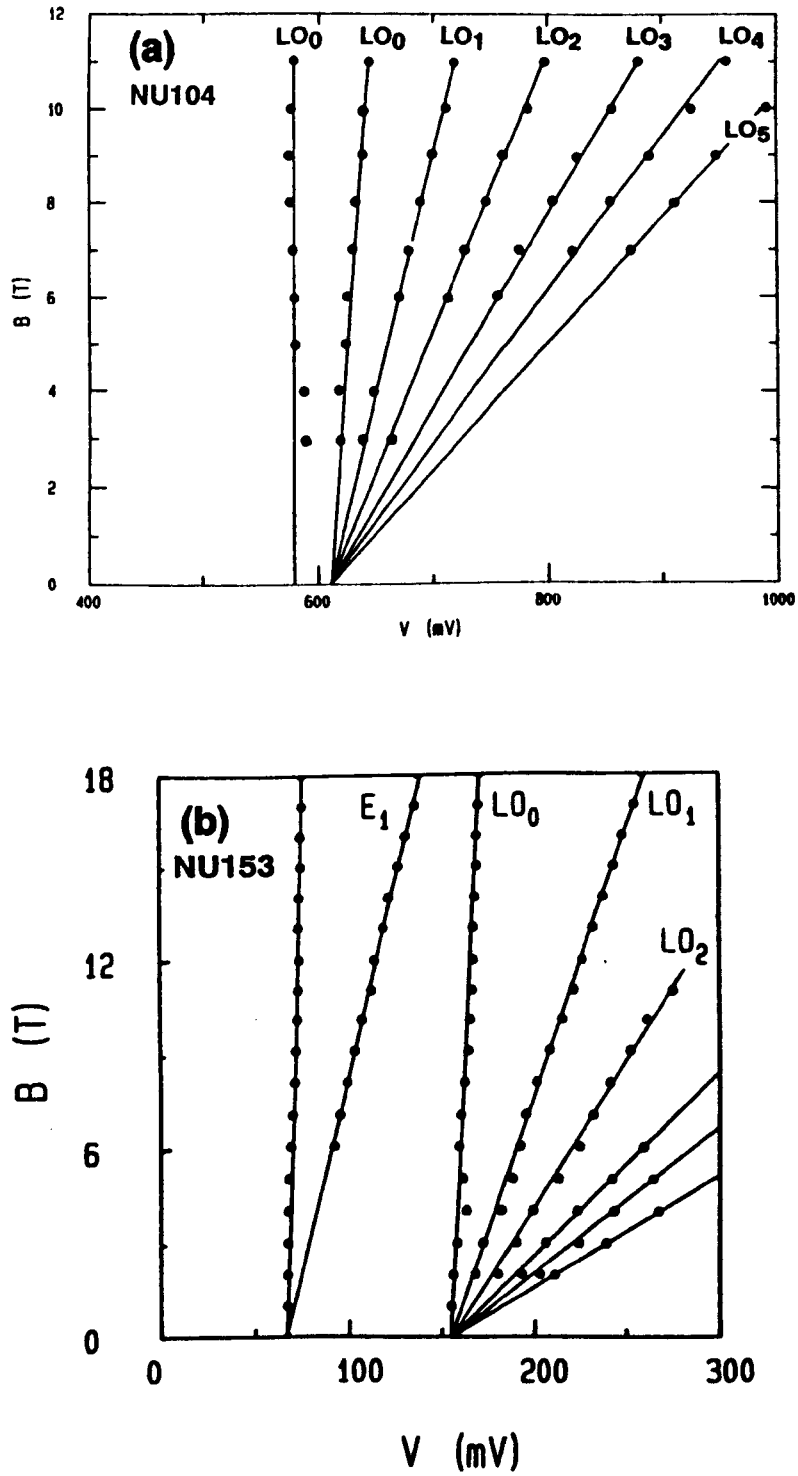

Figure 3.19: Fan chart showing the magnetic-field dependence $\boldsymbol{B} \parallel \boldsymbol{J}$ of the peaks in $I(V)$ for (a) *NU104* and (b) *NU153*. The elastic and inelastic (LO phonon) scattering processes giving rise to the oscillations are discussed in the text.

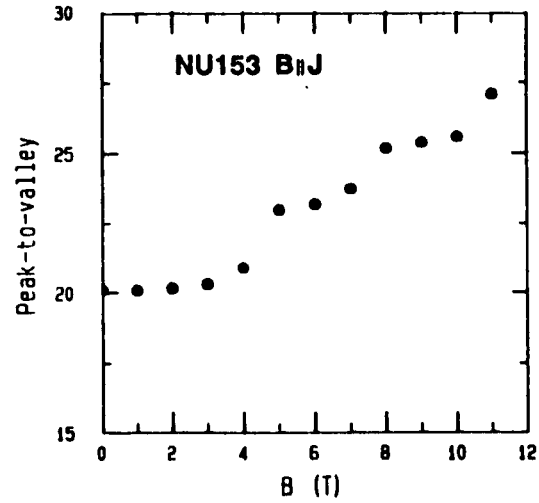

Figure 3.20: Peak-to-valley ratio of *NU153* as a function of magnetic field $\boldsymbol{B} \parallel \boldsymbol{J}$.

whether the tunnelling process is predominantly coherent or sequential since scattering processes which do not involve a change in Landau-level index are not revealed.

The characteristics of the asymmetric double barrier device, *NU183*, (Figure 3.17) in reverse bias, show that at a finite magnetic field, the LO phonon peak is clearly resolved into two separate components, which do not shift in voltage as B increases [148, 149]. They must arise from optical-phonon emission with no change in Landau-level quantum number. We attribute the two components to the two LO phonon modes of (AlGa)As; one corresponding to GaAs-like and one to AlAs-like lattice vibrations. This two-mode behaviour is well-known in ternary compounds [56]. Similar behaviour is observed in *NU104*, as can be seen from the fan-chart in Figure 3.19(a) where the lowest two lines remain parallel throughout the field range. This is the first observation of two-mode behaviour in resonant tunnelling devices — although a wide range of such phenomena have been investigated in single-barrier tunnelling. A recent study of (InGa)As/(AlIn)As double barrier structures by Celeste *et al.* has produced similar results [152].

Fairly accurate estimates of the LO phonon energies involved in the transitions may be obtained by noting that the voltage between the main resonant peak and E_1, or between peaks LO_p and LO_{p+1}, corresponds to a change in the energy separation of the emitter and well states of $\hbar\omega_c = \hbar eB/m^*$. Therefore we may use these voltage differences to calibrate the voltage distribution across the device and obtain values for $\hbar\omega_{LO}$. Although there is some uncertainty involved in this, and the bias drop across the emitter is not linearly related to the total applied bias, the values obtained are in good agreement with the standard parameters for GaAs and (AlGa)As. For *NU153* we obtain $\hbar\omega_{LO} = 35$ meV which corresponds to the LO phonon energy in GaAs. For *NU104* we obtain $\hbar\omega_{LO_1} = 34.5$ meV and $\hbar\omega_{LO_2} = 48.5$ meV and for *NU183*, $\hbar\omega_{LO_1} = 35.5$ meV and $\hbar\omega_{LO_2} = 48$ meV. These values are in good agreement with the energies of the GaAs-like and AlAs-like modes of $Al_{0.4}Ga_{0.6}As$ as given by Kim and Spitzer [57].

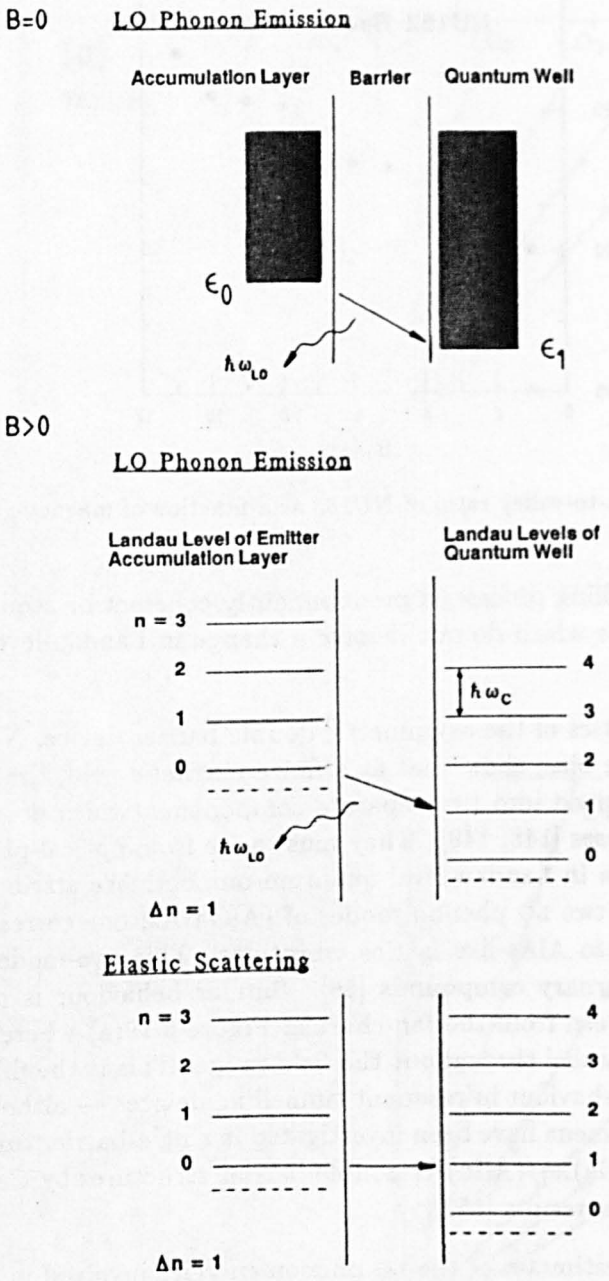

Figure 3.21: Elastic and inelastic tunnelling transitions from the two-dimensional electron gas in the emitter to the quasi-bound state ϵ_1 of the quantum well. At zero magnetic field there is no structure in the density of states and inelastic transitions can take place for any bias at which the well state lies more than the optic phonon energy below the Fermi level in the emitter (top diagram). In a finite field scattering can only occur when a Landau level in the well is aligned with one in the emitter (for elastic transitions — bottom diagram) or at an energy separation of $\hbar\omega_{LO}$ (for LO phonon emission — centre).

Goldman *et al.* [143] assigned the LO phonon feature they observed to the AlAs mode. When there are two modes it is usually expected that the electrons will couple more strongly to the higher energy mode since this is more polar [58]. However, it might also be expected that since the GaAs-mode is present throughout the structure, whereas the AlAs-mode is confined to the barrier region, the electrons would couple more strongly to this mode. A possible explanation of the observation of two phonon modes in *NU104* and *NU183* but only one in *NU153* is that these two structures have narrower quantum wells so that the wavefunction of the quasi-bound state penetrates further into the (AlGa)As barriers. Tunnelling electrons might then be expected to couple more effectively to the AlAs-mode.

3.4.5 $I(B)$ Measurements

As can be seen in Figure 3.10, the elastic and inelastic series of transitions can also be seen in measurements of $I(B)$ at constant applied bias. A series of rapid magneto-oscillations are observed whose frequency is given by $\epsilon_0 - \epsilon_1 + eV_1 - i\,\hbar\omega_{LO} = \hbar e B_f/m^*$, *i.e.* these oscillations are a measure of the energy difference between the energy of an injected electron and the bound state of the quantum well. As the bias increases, the energy of injection increases and so does the frequency of the magneto-oscillations — as plotted in Figure 3.22 for sample *NU104*. The low frequency oscillations (•) are due

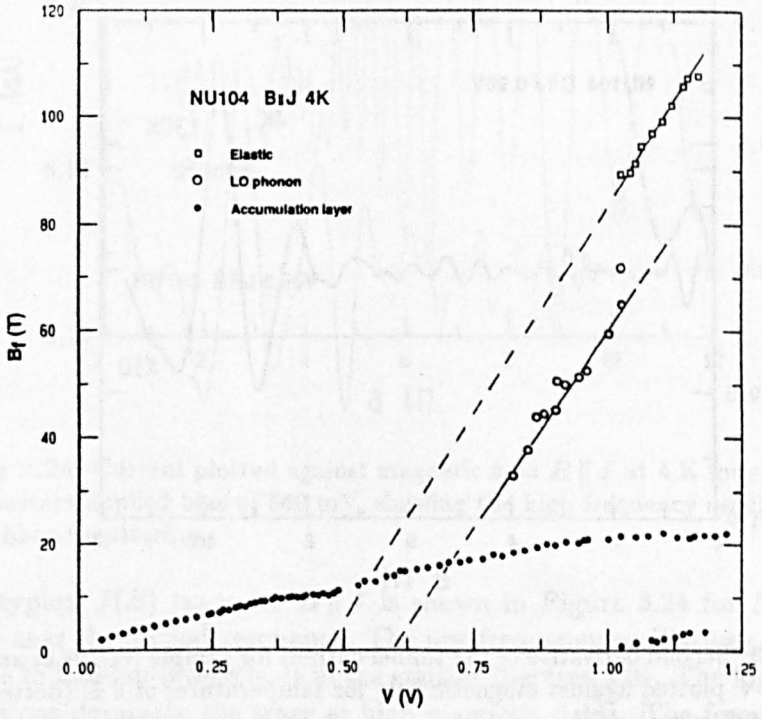

Figure 3.22: Frequency of the magneto-oscillations in the tunnel current in a magnetic field $B \parallel J$ for sample *NU104* as a function of applied bias: accumulation layer •, elastic inter-Landau level transitions □ and LO phonon transitions o.

to Landau levels passing through the Fermi level in the emitter 2DEG as described in Section 3.3, and two series of high frequency oscillations are seen,

one corresponding to the elastic transitions (□) and the other, with a rather lower frequency, to transitions involving the emission of an LO phonon (o). The frequencies of these sets of oscillations extrapolate back to the main resonant peak and the LO phonon replica respectively. We observe oscillations with frequencies of up to 110 T corresponding to an energy difference between the emitter and the well of 190 meV. At this point (1.15 V), the total voltage dropped across the device has increased by more than 700 mV from the resonant peak, again illustrating the point that only about one third of the applied bias is dropped cross the emitter and the first part of the quantum well. At biases below 1 V, the LO phonon series dominates but for higher voltages only the elastic series is observed, this may reflect the $1/q^2$-dependence of polar optic mode scattering.

Figure 3.23 shows magneto-oscillation traces for *NU104* at a bias of 0.96 V at temperatures of 4 K and 130 K. This shows that the LO phonon series is still strong at relatively high temperatures whereas the series of oscillations associated with the 2DEG in the accumulation layer is much more strongly attenuated. This is because the inter-Landau level series only require the energy difference between the injection energy and the quantum well state to be well-defined whereas the accumulation layer series requires a definite Fermi energy in the emitter contact. Although increasing temperature may well broaden the level widths it smears out the Fermi energy much more rapidly and destroys the accumulation layer series.

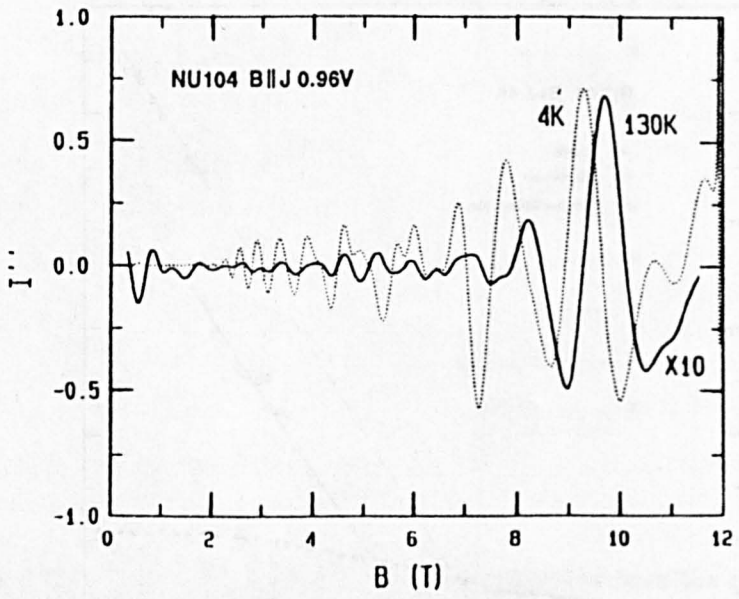

Figure 3.23: Second derivative of the tunnel current for sample *NU104* at an applied bias of 0.96 V plotted against magnetic field for temperatures of 4 K (dotted curve) and 130 K (full curve).

3.4.6 Intersubband Scattering

When a resonant tunnelling device with more than one quasi-bound state in the well is biased so that electrons are injected into an upper subband of the quantum well, the electrons undergo intersubband scattering into a lower sub-

band (possibly with the emission of an LO phonon). This process is modulated in a magnetic field due to the formation of Landau levels, and leads to a series of magnetoquantum oscillations in the tunnel current, as demonstrated by Eaves *et al.* [108]. These oscillations are similar to those discussed above for sample *NU104* when the device was biased beyond the resonant peak. This process is a clear demonstration of a sequential tunnelling process. Intersubband scattering can lead to substantial charge buildup in the quantum well since the probability of tunnelling out of the lower bound state is generally several orders of magnitude less than from the upper level. This has been shown to lead to bistable behaviour in the current-voltage characteristics (see Section 4.8).

The period of the oscillations is given by

$$\epsilon_2 - \epsilon_1 \, (-\hbar\omega_{LO}) = \hbar e B_f / m^* \tag{3.54}$$

for scattering elastically (or with LO phonon emission). Note that in cases where there is substantial buildup of space charge in the well on resonance electron-electron scattering may become important.

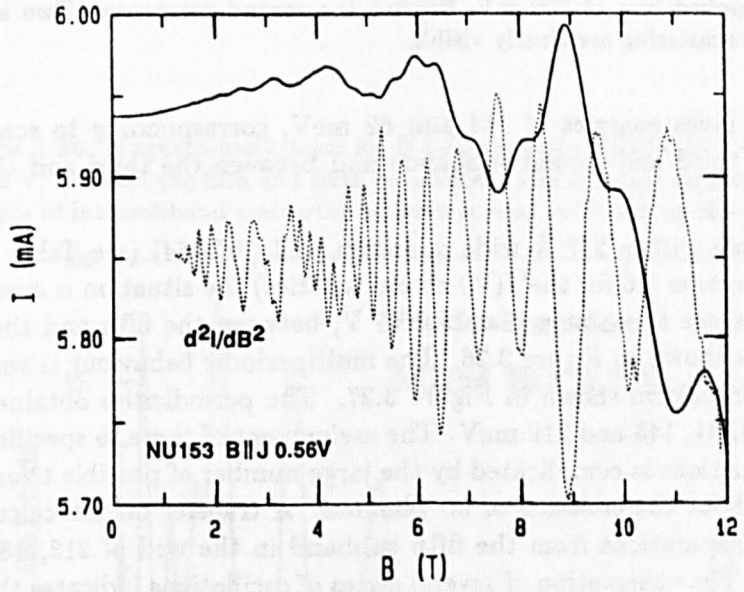

Figure 3.24: Current plotted against magnetic field $\boldsymbol{B} \parallel \boldsymbol{J}$ at 4 K for sample *NU153* at a constant applied bias of 560 mV, showing the high-frequency oscillations due to intersubband scattering.

A typical $I(B)$ trace for $\boldsymbol{B} \parallel \boldsymbol{J}$ is shown in Figure 3.24 for *NU153* when biased near the second resonance. The low frequency oscillations at low fields are due to Landau-level effects in the emitter (Section 3.3). The high frequency oscillations dominate the trace at high magnetic fields. The frequency of this trace corresponds to an energy separation of 122 meV.

When the bias is increased to beyond the second resonance, two series of intersubband transitions become possible. This situation is illustrated in Figure 3.25 at an applied bias of 0.7 V. There are clearly two series of oscillations one has a period approximately twice that of the other. By using Fourier analysis of the magnetic field traces we can determine the periodicities of both

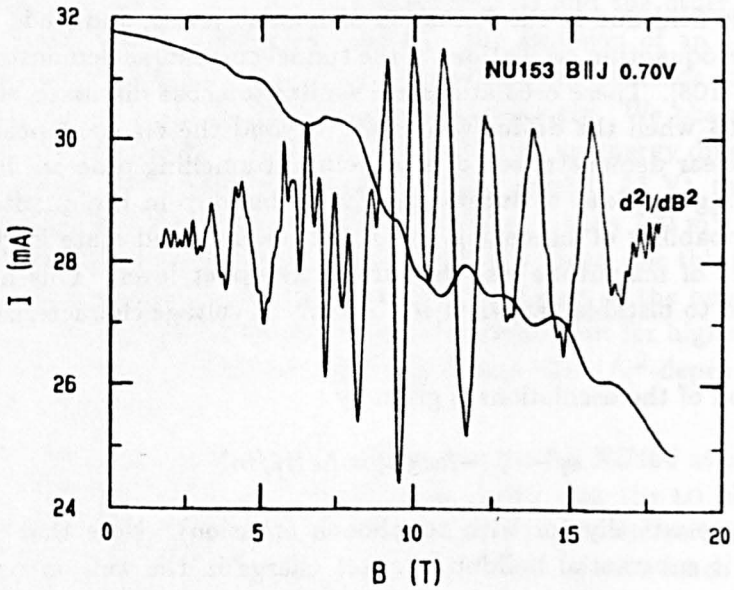

Figure 3.25: Magnetoquantum oscillations in the tunnel current for *NU153* (117 Å well) at an applied bias of 700 mV, beyond the second resonance. Two series of inter-subband scattering are clearly visible.

series. This gives energies of 184 and 82 meV, corresponding to scattering between the third and second subbands and between the third and the first subband.

In a sample with a 217 Å wide quantum well (*NU154*) (see Table 2.1 for details and Section 3.6 for the $I(V)$ characteristics) the situation is even more complex. A trace taken at a bias of 0.75 V, between the fifth and the sixth resonances, is shown in Figure 3.26. The multiperiodic behaviour is shown in the Fourier transform shown in Figure 3.27. The periodicities obtained give energies of 66, 84, 143 and 219 meV. The assignment of these to specific inter-subband transitions is complicated by the large number of possible transitions with and without the emission of LO phonons. A transfer matrix calculation gives energy separations from the fifth subband in the well of 213, 180, 140 and 80 meV. The observation of several series of oscillations indicates that the scattering rate is not strongly dependent on the momentum change involved, this might imply that the process does not involve LO phonon emission since this falls off as $1/q^2$ (3.51).

In very wide well samples, there are so many subbands available to scatter into that the formation of Landau levels does not significantly affect the scattering probability and so the tunnel current does not show a strong high-B_f series. This is shown by Figure 3.28 for a 600 Å wide quantum well sample (*NU167* — see Section 3.6) at a bias corresponding to the 22^{nd} resonance.

3.4.7 Conclusions

We have demonstrated that scattering processes make a very important contribution to the valley current in resonant tunnelling devices. By applying a magnetic field $\boldsymbol{B} \parallel \boldsymbol{J}$ we can determine the energies of the LO phonon modes which couple to the tunnelling electrons. In samples with more than one energy

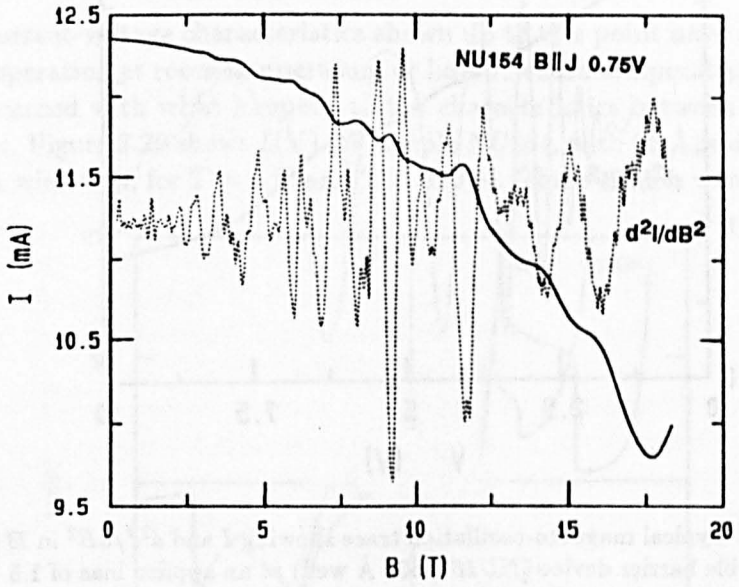

Figure 3.26: Magneto-oscillations for $B \parallel J$ in sample *NU154* (217 Å well) at a bias of 0.75 V, between the fifth and sixth resonances. The complex structure is due to the presence of intersubband scattering between several subbands in the quantum well.

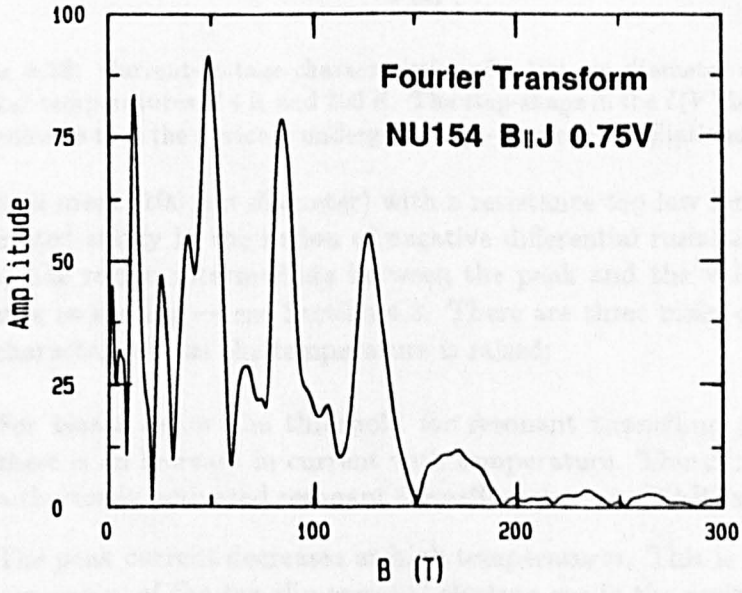

Figure 3.27: Fourier transform in $1/B$-space of the magneto-oscillation trace in Figure 3.26 revealing the multi-periodic behaviour.

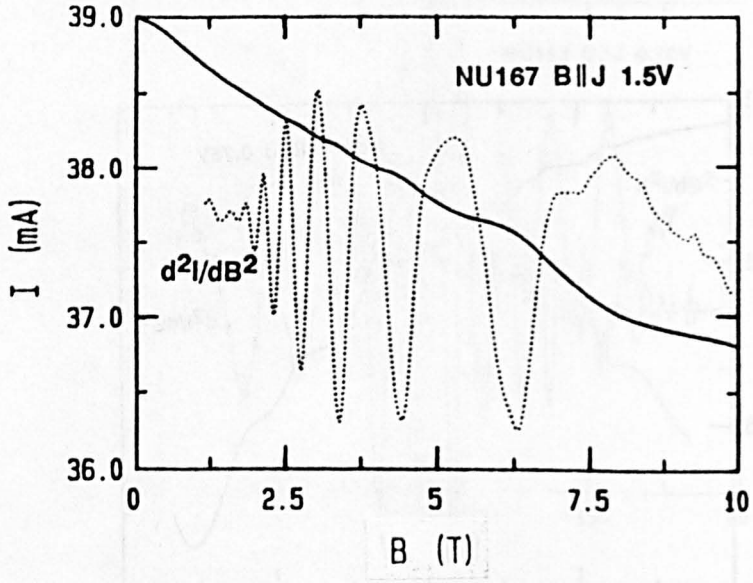

Figure 3.28: Typical magneto-oscillation trace showing I and d^2I/dB^2 in $\boldsymbol{B} \parallel \boldsymbol{J}$ for a wide well double barrier device (*NU167*, 600 Å well) at an applied bias of 1.5 V. Only low-frequency oscillations associated with Landau-level effects in the emitter 2DEG are observed. No clear periodicity due to intersubband scattering is apparent.

level, intersubband energy separations can be calculated from the frequency of magnetoquantum oscillations caused by the modulation of the intersubband scattering rates by the formation of Landau levels.

3.5 Thermal Effects in Resonant Tunnelling

3.5.1 Introduction

The current-voltage characteristics shown up to this point have all been of devices operating at room temperature or liquid helium temperature; this section is concerned with what happens to the characteristics between these two extremes. Figure 3.29 shows $I(V)$ for sample *NU104*, with 56 Å wide barriers and a 50 Å wide well, for $T = 4$ K and $T = 290$ K. These results were taken with a

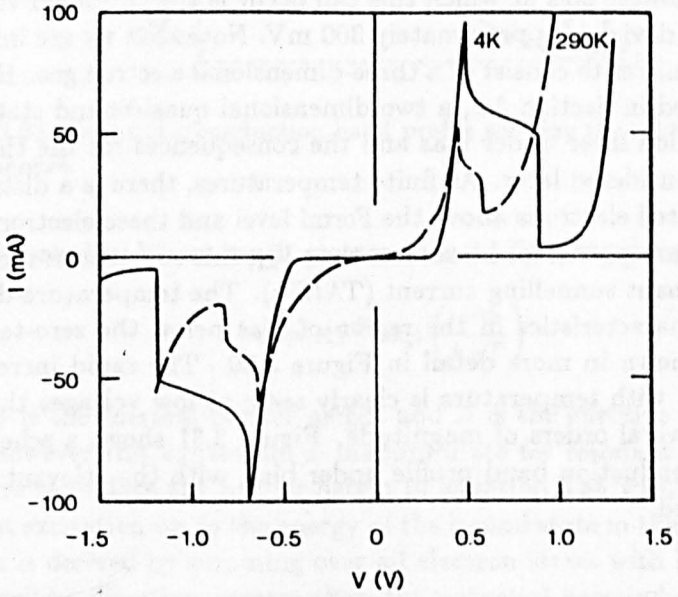

Figure 3.29: Current-voltage characteristics of a 100 μm diameter mesa of sample *NU104* at temperatures of 4 K and 290 K. The step-shape in the $I(V)$ beyond the main peak indicates that the device is undergoing high-frequency oscillations — Section 4.3.

large area mesa (100 μm diameter) with a resistance too low for the device to be operated stably in the region of negative differential resistance, hence the plateau-like region intermediate between the peak and the valley where the current is oscillating — see Section 4.3. There are three main changes in the $I(V)$ characteristics as the temperature is raised:

- For biases below the threshold for resonant tunnelling ($V < 0.3$ V), there is an increase in current with temperature. This current is due to a thermally activated resonant tunnelling process (TARTs) [19].
- The peak current decreases at high temperatures. This is related to the occupancy of the two-dimensional electron gas in the emitter.
- At biases beyond the resonance, there is a rapid increase in the off-resonant current. The origin of this is thermionic emission of electrons in the high-energy tail of the emitter energy distribution over the top of the barriers.

The net result of these changes is that the peak-to-valley ratio drops dramatically from 25:1 at 4 K to only 3.5:1 at room temperature. Therefore it is

obviously important to have an understanding of the physical processes which govern the temperature-dependence of the resonant and non-resonant currents. We consider each region of bias in turn.

3.5.2 Thermally Activated Resonant Tunnelling

At zero temperature, resonant tunnelling can only occur when the quasi-bound state in the quantum well lies at an energy below the Fermi level of the emitter contact. The lowest bias at which this can occur is the threshold voltage, V_{th}, which for this device is approximately 300 mV. Note that we are initially considering the emitter to consist of a three-dimensional electron gas. However, as has been stated in Section 3.2, a two-dimensional quasi-bound state forms in the accumulation layer under bias and the consequences for the thermal current will be considered later. At finite temperatures, there is a distribution of thermally excited electrons above the Fermi level and these electrons can tunnel via the quantum well for biases less than V_{th}, this constitutes the thermally activated resonant tunnelling current (TARTs). The temperature-dependence of the $I(V)$ characteristics in the region of bias below the zero-temperature threshold is shown in more detail in Figure 3.30. The rapid increase in the tunnel current with temperature is clearly seen; at low voltages this increase amounts to several orders of magnitude. Figure 3.31 shows a schematic diagram of the conduction band profile under bias, with the relevant activation energies marked.

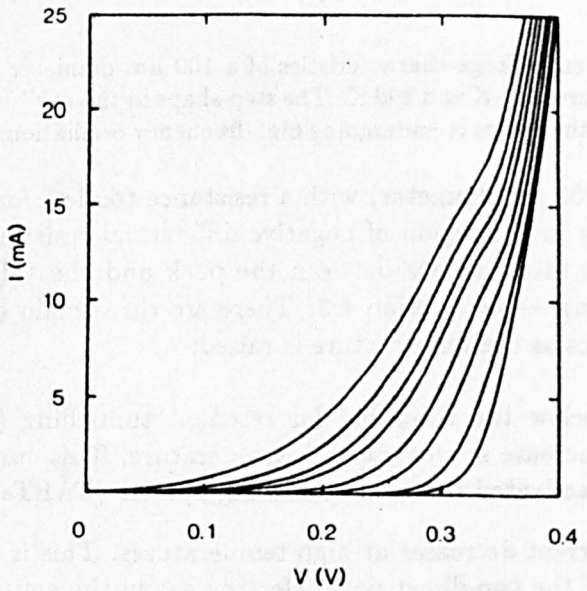

Figure 3.30: Thermally activated current for *NU104* at the following temperatures, in order of increasing current: 4, 45, 80, 110, 150, 180, 210 and 290 K.

Theory

In single barrier structures and Schottky barriers, the expressions for the 'over the barrier' thermionic current are well-known, for example see Sze, [153, Chap-

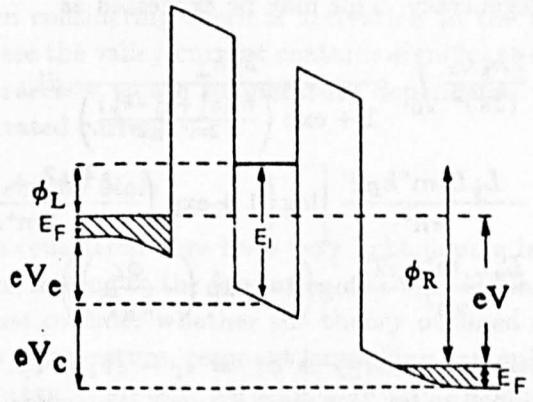

Figure 3.31: Schematic conduction band profile showing the relevant thermal activation energies.

ter 5]. For applied biases much greater than k_BT/e this gives

$$J = AT^2 \exp\left(\frac{-\phi}{k_BT}\right) \tag{3.55}$$

Where ϕ is the thermal barrier height and A is the effective Richardson constant. However this expression is inappropriate for resonant tunnelling, even if we were to replace the barrier height in equation 3.55 with a lower value to represent excitation up to the energy of the bound state in the well. The above equation is derived by summing over all electron states with kinetic energy in the tunnelling direction greater than the potential barrier height. This does not apply for resonant tunnelling where we need the number of electrons with a specific k-vector in the tunnelling direction since these are the only ones which can correctly match to the energy level in the well. Electrons with higher or lower energy will be unable to tunnel at finite temperature just as at low temperatures. Therefore we must derive a different expression for the thermally activated resonant current.

The theory of thermally activated resonant tunnelling has been developed by F. W. Sheard [154] from the sequential theory of resonant tunnelling presented for $T = 0$ K in reference [99]. If we consider the schematic band diagram in Figure 3.31, then only electrons with $k_x = k_0$ where $\hbar^2k_0^2/2m^* = \epsilon_1 - eV_e$ can tunnel resonantly (V_e is the voltage drop across the first half of the double barrier structure and ϵ_1 is the bound state energy in the well). The total number of electrons with this value of k_x is given by summing over the Fermi distribution, *i.e.*

$$F(V_e) = \sum_{k_\perp} f_{k_0,k_\perp} = \int_0^\infty \rho(k_\perp) f_{k_0,k_\perp} 2\pi k_\perp \, dk_\perp \tag{3.56}$$

where f is the Fermi function, the transverse wavevector $k_\perp$ is given by

$$\hbar^2k_\perp^2/2m^* = \epsilon - \hbar^2k_0^2/2m^*$$

and $\rho(k_\perp)$ is the density of states in $k_\perp$, which is $2L_yL_z/(2\pi)^2$. The factor of

two is for spin degeneracy. This may be expressed as

$$\begin{aligned} F(V_e) &= \frac{2L_yL_z}{(2\pi)^2}\int_0^\infty \frac{2\pi k_\perp}{1+\exp\left(\frac{\hbar^2(k_\perp^2+k_0^2-k_F^2)}{2m^*k_BT}\right)}\,dk_\perp \\ &= -\frac{L_yL_zm^*k_BT}{\pi\hbar^2}\left[\log\left(1+\exp\left(-\frac{\hbar^2(k_\perp^2+k_0^2-k_F^2)}{2m^*k_BT}\right)\right)\right]_0^\infty \\ &= \frac{L_yL_zm^*k_BT}{\pi\hbar^2}\log\left(1+\exp\left(-\frac{\phi_L}{k_BT}\right)\right) \end{aligned} \tag{3.57}$$

The effective activation energy is $\phi_L = \epsilon_1 - eV_e - \epsilon_F$. For the thermally activated case $\phi_L > 0$ so for $T = 0$, $F(V_e) = 0$. The current into the well state from this number of states in the emitter is simply given by

$$j_1 = e\sum_{k_\perp} f_{k_0,k_\perp}W_{k_0} \tag{3.58}$$

If we replace $\sum W_{k_0}$ by $1/\tau_1$ [87], the current density due to electrons flowing from the emitter to the collector is given by

$$J_L = \frac{eF(V_e)}{\tau_1}\frac{1/\tau_2}{1/\tau_1+1/\tau_2} \tag{3.59}$$

where τ_2 is the time for charge in the well to decay to unoccupied states in the collector. There is a similar expression for electrons thermally activated from the collector making transitions to the emitter, except that ϕ_L is replaced by $\phi_R = (\epsilon_1+eV_c-\epsilon_F)/ek_BT = \phi_L+eV$. Hence the total current may be written as

$$J = \frac{eL_yL_zm^*k_BT}{\pi\hbar^2(\tau_1+\tau_2)}\log\left(\frac{1+\exp\left(-\frac{\phi_L}{k_BT}\right)}{1+\exp\left(-\frac{\phi_R}{k_BT}\right)}\right) \tag{3.60}$$

When $\phi \gg k_BT$ we can approximate this by

$$J = J_0T\left(\exp\left(-\frac{\phi_L}{k_BT}\right)-\exp\left(-\frac{\phi_R}{k_BT}\right)\right) \tag{3.61}$$

If there is a sufficiently large applied bias ($eV \gg k_BT$), the current from the right hand side is negligible and we can further simplify this to

$$\log\left(\frac{J}{T}\right) = \log(J_0) - \frac{\phi_L}{k_BT} \tag{3.62}$$

A plot of $\log(J/T)$ against $1/T$ is a straight line of gradient $-\phi_L/k_B$. Therefore we can determine the energy of the state in the well relative to the Fermi level in the emitter contact over a wide range of bias voltages.

This theory neglects the variation of ϵ_F with temperature which is likely to be significant for the low doping levels considered here. At low biases one cannot neglect the collector current, and at high temperatures one cannot take $\phi \gg k_BT$, this leads to a deviation from the straight line dependence. Therefore in many cases it will be necessary to fit the temperature dependence of the current to equation 3.60 rather than equation 3.62. We have also assumed that all the current is due the tunnelling process and so any leakage

currents must be subtracted from the data before fitting. This is a particular problem when considering thermal activation in the region beyond the first resonance where the valley current contains significant contributions from phonon-assisted processes whose temperature dependence may mask that of the thermally activated current.

Two-dimensional emitter state

Given the samples considered here have very light doping in the regions adjacent to the barriers, leading to the formation of a two-dimensional bound state under bias, we must consider whether the theory outlined above is at all appropriate. At zero temperature, resonant tunnelling can only take place when the bound state energy in the emitter is aligned with a bound state of the well. The transverse momentum does not affect the tunnelling probability. When the temperature is increased, the spread of the Fermi function to higher energy only leads to a smoothing out of the distribution of transverse momentum so, in the absence of scattering processes, there is no change in the tunnel current.

However, the 2DEG state is only weakly bound and there are a large number of travelling wave states at relatively low energies above the bound state energy. At low temperatures, the conduction band edge in the bulk of the emitter contact is very close to the Fermi energy. Therefore we can take the binding energy of the 2DEG state to be approximately equal to the Fermi energy of the 2DEG, ϵ_F. Electrons in the 2DEG with energy above this Fermi energy are able to scatter into three-dimensional states. As the temperature is increased, more and more electrons populate the bulk three-dimensional energy levels. Since the density of states is higher in three dimensions and the tunnelling rate is much greater for states above the conduction band edge, we can effectively take all electrons with kinetic energy greater than the Fermi energy to be in bulk states. For $k_BT > \epsilon_F$ the occupation of these states will be virtually the same as in the completely three-dimensional case *i.e.* we can only consider the emitter to have a truly two-dimensional character at $T = 0$. This means that the theory presented above is a good description for either a 2D or 3D emitter provided the temperature is high enough. For many of the samples considered here, the Fermi energy at the first resonance is less than 10 meV and so we can use this theory for $T > 100$ K. For lower temperatures there will be an additional temperature dependence relating to the occupancy of the bulk states due to scattering from the 2D-like states. Note however that these low Fermi energies also mean that it is incorrect to neglect the temperature dependence of the chemical potential which produces a temperature dependence of the slope of equation 3.62.

Results

Figure 3.32 shows a set of plots of $\log(I/T)$ against $1/T$ for sample *NU104* at biases between 10 mV and 240 mV. For temperatures up to $\sim$ 200 K, there is a good straight line dependence as predicted from equation 3.62. The activation energies deduced from these plots are shown by the open circles in Figure 3.33. The activation energy decreases approximately linearly with bias in both forward and reverse bias directions with a common intercept close to 86 meV at zero bias. The different rate of change of ϕ in forward and reverse bias can be explained by slightly differing doping levels on either side of the

double barrier structure. Note that the intercepts on the voltage axis at 300 and -400 mV correspond closely with the threshold in the current at 4 K. These plots show that the theory presented above is in reasonably good agreement with the experimental data.

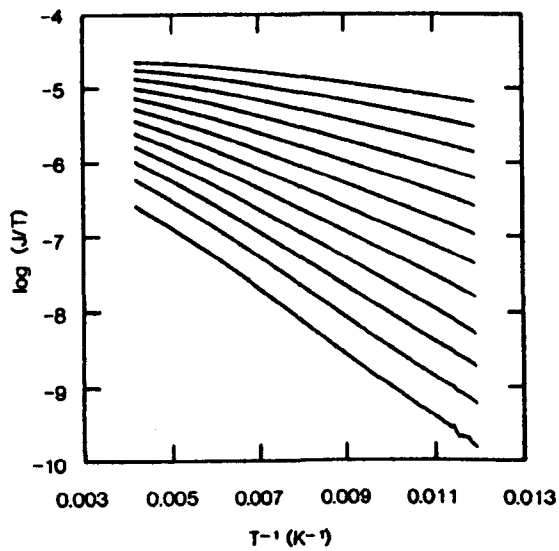

Figure 3.32: Plots of $\log(I/T)$ against $1/T$ for biases between 20 mV (bottom) and 240 mV (top), showing the approximately linear relationship over nearly two orders of magnitude.

Guéret *et al.* [155] recently claimed that the thermal activation data could be fitted to the form $J \propto \exp(-\phi/k_B T)$, however this was fitted over a much narrower temperature range than that shown here. It is possible that a better fit to their data could be obtained by using the complete expression in equation 3.60. Reed *et al.* [156] have also examined the low bias thermal activation, here again it would be necessary to include all the terms in equation 3.60.

At low biases the activation energy from the $\log(I/T)$ vs $1/T$ plots changes very slowly with bias. This is because we have assumed that $eV \gg k_B T$, which is not true for $V < 30$ mV. Therefore in the low bias range it is necessary to fit to the complete formula of equation 3.60. This is done using a simple least squares algorithm to find the best fit values for ϕ and I_0. This involves minimizing the derivative of the sum of the squares of the errors with respect to small changes in ϕ and I_0 in a self-consistent fashion, as outlined below:

1. Obtain approximate values for ϕ and I_0 from the straight line fit.
2. Evaluate
$$\sigma = \sum_i \left(\frac{I_i}{T_i} - I_0 \log \left(\frac{1 + \exp\left(\frac{-\phi}{k_B T_i}\right)}{1 + \exp\left(\frac{-(\phi + eV)}{k_B T_i}\right)} \right) \right)^2$$
3. Change ϕ slightly, $\phi \rightarrow \phi \pm \delta\phi$, and evaluate $\sigma_\pm$
4. Generate new value of activation energy ϕ' from
$$\phi' = \phi - \frac{(\sigma_+ - \sigma_-)\delta\phi}{2(\sigma_+ - 2\sigma + \sigma_-)}$$

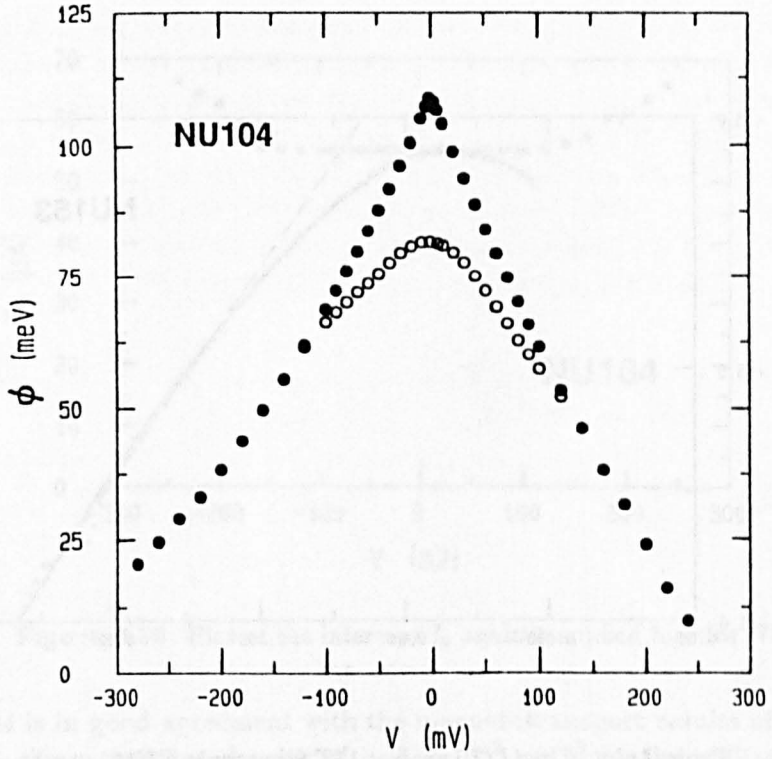

Figure 3.33: Activation energies: o deduced from straight line plots of $\log(I/T)$ vs $1/T$ and • deduced from fits to the complete equation 3.60.

5. Repeat stages 2–4 until $\phi' \sim \phi$.

6. Use a similar procedure to find a new value of I_0.

7. Repeat stages 2–6 until both values converge.

This is a somewhat long-winded method compared to a simple straight line fit. Note that the non-resonant current was assumed to be equal to that at 4 K and this was subtracted from all the current values before fitting, and, to avoid undue weight being given to the high-temperature portion of the curve, points were interpolated at equal intervals in $1/T$.

A typical $I(T)$ trace for sample *NU153* is shown in Figure 3.34 for an applied voltage of 10 mV. The full fit is clearly a much better representation of the data at high temperatures than the simple straight line treatment. The filled circles in Figure 3.33 show the activation energies obtained for *NU104* using this method, and Figure 3.35 shows the equivalent plot for *NU153*. At low biases the energies obtained are well-above those from the straight line fits. The intercept at $V = 0$ corresponds to the energy of the quantum well state relative to the Fermi energy in the emitter contact. This is $\sim$ 107 meV for *NU104* (50 Å well) and $\sim$ 14 meV for *NU153* (117 Å well). The value for *NU104* is rather higher than that expected for a 50 Å wide well (from a transfer matrix calculation) and that for *NU153* is lower than expected from the nominal growth parameters. However, it should be remembered that we have no characterisation of these widths and it may well be that the actual devices differ significantly from the nominal parameters. The energy level for

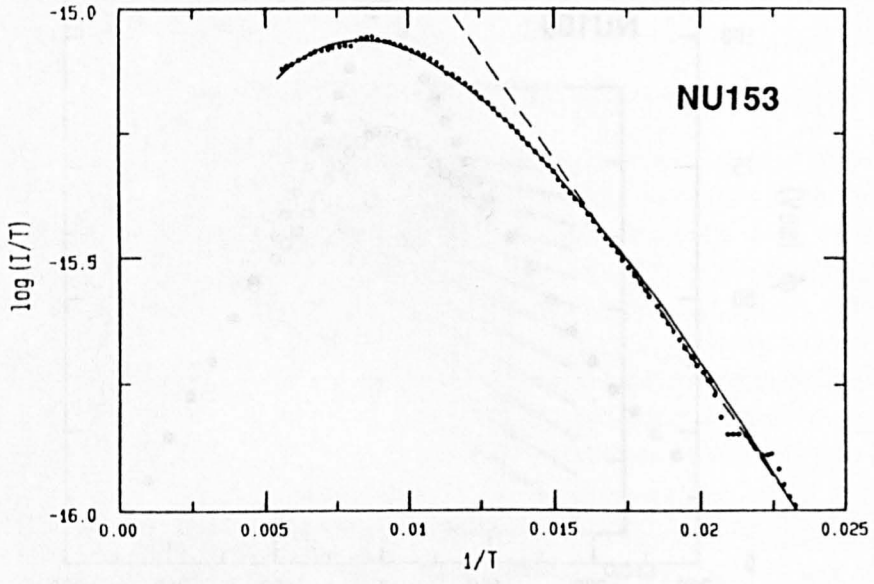

Figure 3.34: Typical plot of $\log(I/T)$ against $1/T$ for sample *NU153* at a bias voltage of 10 mV. The dotted line is the straight line fit and the solid line is the full fit, which shows much improved agreement at high temperatures.

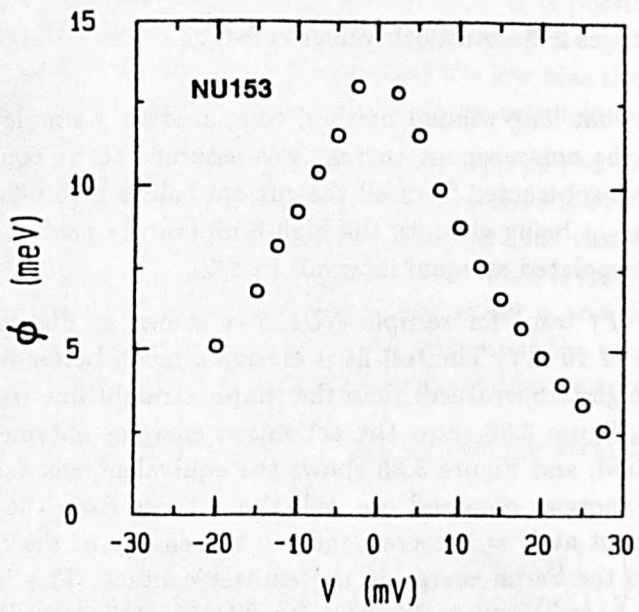

Figure 3.35: Thermal activation energies for sample *NU153*.

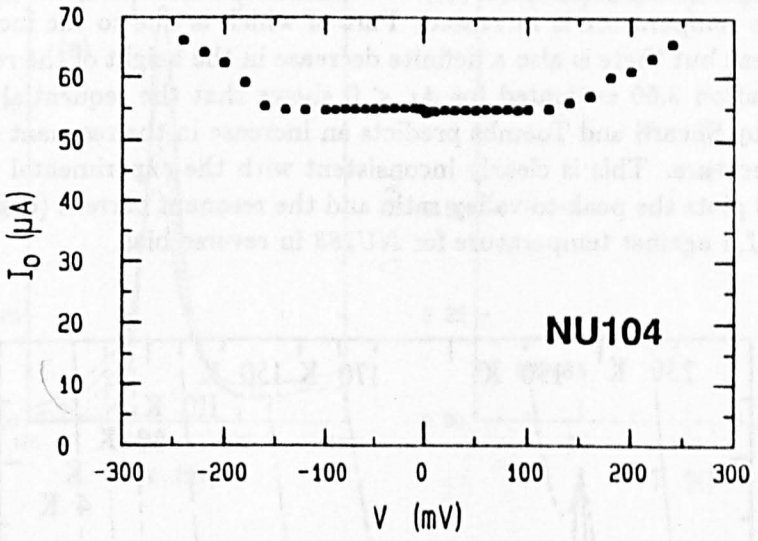

Figure 3.36: Plot of the intercept I_0 against applied bias for *NU104*.

NU104 is in good agreement with the magnetotransport results of Section 3.3 which give a number density of $\sim 5 \times 10^{11}$ cm^{-2} in the emitter 2DEG at the threshold voltage which corresponds to electrons being injected into the well with energies $\sim$ 115 meV — close to the measured activation energy, and higher than the nominal value. The pressure-dependence of the resonance also supports a narrower well-width [157]. This shows that thermal activation studies are a useful method of characterising double barrier structures.

Figure 3.36 shows a plot of the intercepts I_0 against applied bias for *NU104*. This remains fairly constant for biases below 150 mV in *NU104* and 20 mV in *NU153*, and then increases rapidly with bias. According to equation 3.60, the intercept is given by $I_0 = eAm^* k_B/\pi\hbar(\tau_1 + \tau_2)$, where A is the area of the mesa. At low bias the measured value is $\sim 3 \times 10^{-5}$ A for *NU104* and $\sim 1.4 \times 10^{-6}$ A for *NU153* (both for 100 μm diameter mesas). These values correspond to $\tau_1 + \tau_2 \sim 1$ ns and ~ 20 ns for *NU104* and *NU153* respectively. These are approximately of the order of magnitude expected for barriers of this width, but detailed agreement is lacking. The increase in I_0 at higher biases may indicate that it is no longer possible to treat the emitter as a three-dimensional electron gas even at high temperatures because the binding energy of the 2DEG is not small compared to $k_B T$. No account is taken of the variation of the transmission coefficients of the barriers with temperature or bias. As the bias increases, the transmission coefficient of the collector barrier increases and this causes some increase in I_0. As the temperature increases the effective mass and the conduction band offset decrease. This also increases the transmission coefficients. Therefore this could also produce some error in both the intercept and the activation energy obtained.

3.5.3 The Effect of Temperature on the Resonant Current

Figure 3.37 shows a series of $I(V)$ characteristics for sample *NU183* (56 Å well, 83 and 111 Å barriers) in reverse bias at various temperatures. As for

sample *NU104* (see Figure 3.29), there is a rapid decrease in the peak-to-valley ratio as the temperature is increased. Part of which is due to the increasing valley current but there is also a definite decrease in the height of the resonant peak. Equation 3.60 evaluated for $\phi_L < 0$ shows that the sequential theory developed by Sheard and Toombs predicts an increase in the resonant current with temperature. This is clearly inconsistent with the experimental results. Figure 3.38 plots the peak-to-valley ratio and the resonant current (defined by $\Delta I = I_p - I_v$) against temperature for *NU183* in reverse bias.

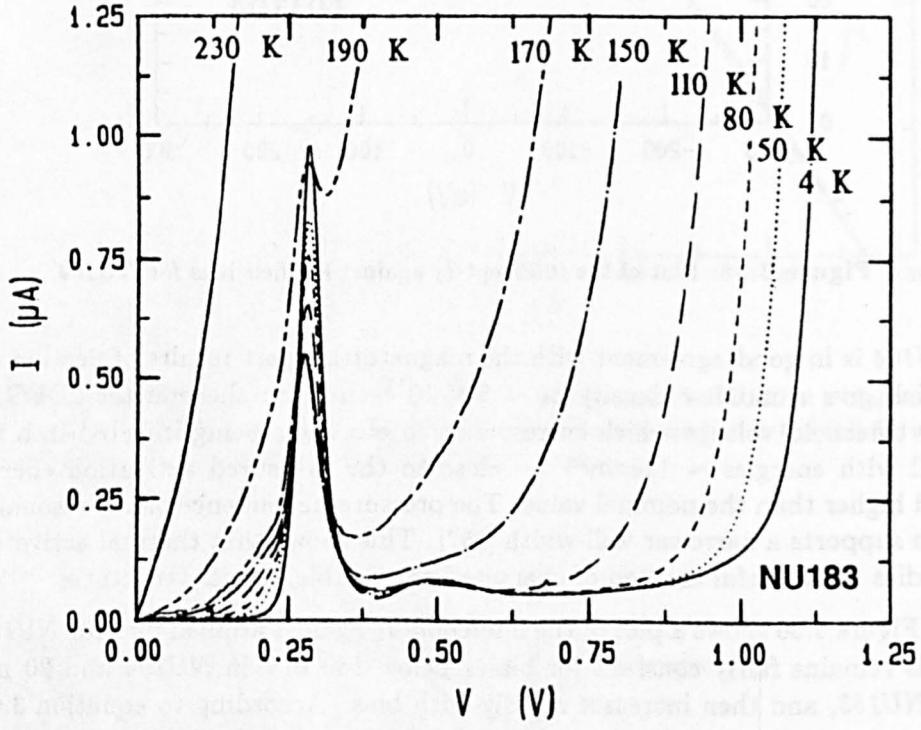

Figure 3.37: $I(V)$ characteristics of sample *NU183* in the region of the first resonance in reverse bias as a function of temperature.

The explanation for these results lies in the fact that resonant tunnelling takes place from a quasi-two-dimensional state in the emitter contact. In the preceding section it was argued that the increase in the thermally activated current at biases below resonance could be explained by the thermal population of bulk three-dimensional states in the emitter. This will also explain the decrease in resonant current, since if the electrons are in three-dimensional states above the band edge they are not occupying the two-dimensional bound state, *i.e.* the resonant current simply drops in proportion to the occupancy of the 2DEG. For *NU183* at the first resonance, the bound state of the emitter lies about 6 meV below the conduction band edge, so by a temperature of $\sim$ 125 K we would expect approximately half the electrons to have been thermally excited into the above-band edge states. At this temperature, the resonant current is just slightly more than half its low temperature value. Therefore this explanation is in rough agreement with the results. It is interesting to note that the total area under the current-voltage curve is almost unchanged as the temperature increases — as the peak current drops, the TART current

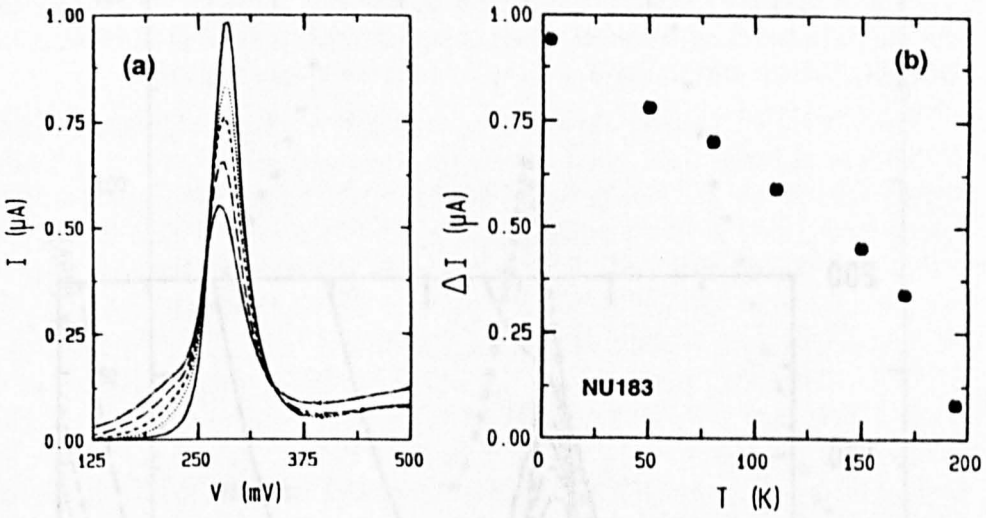

Figure 3.38: (a) $I(V)$ characteristics of *NU183* at the first resonant peak in reverse bias at the following temperatures, in order of decreasing peak height: 4 K (solid line), 50 K, 80 K, 110 K and 150 K, showing the decrease of the resonant current. (b) Resonant current (peak–valley) plotted against temperature.

rises. It would also be expected that resonances where the Fermi energy is higher would be less strongly affected by increasing temperature. This can be seen in Figure 3.39 which shows the characteristics of *NU183* in the region of the second resonance in reverse bias. At this resonance, the resonant current does not fall to half the 4 K value until a temperature of $\sim$ 160 K is reached, consistent with the bound state lying further below the conduction band edge.

3.5.4 The Off-Resonant Current

Off-resonance we can treat the device as a simple single barrier structure and the activation energy corresponds to the barrier height. The variation of current with temperature should now be fitted to the form given in equation 3.55 *i.e.* a plot of $\log(I/T^2)$ against $1/T$ should give a straight line. The experimental results fit the expected form reasonably well, although it should be borne in mind that there is not a great deal of difference in the quality of the fit to $\log(I/T)$. The activation energies obtained from the $\log(I/T^2)$ curves are plotted against bias in Figure 3.40. Although the bias is greater, the activation energy is higher in the valley region than those obtained from the TARTs analysis at biases below threshold. This is good evidence for the thermally activated resonant tunnelling process. Note that the activation energy decreases rapidly above 1.2 V. At this point the current, even at room temperature, is dominated by the tunnelling process and so the thermal activation analysis is no longer applicable.

Figure 3.41 shows a plot of $\log(I/T)$ against $1/T$ for *NU183* at a bias of 0.9 V in reverse bias, below the threshold of the second resonance. The low temperature part of the curve fits to thermally activated resonant tunnelling via the upper bound state of the quantum well with an activation energy of 60 meV. For temperatures above 160 K there is a much steeper slope

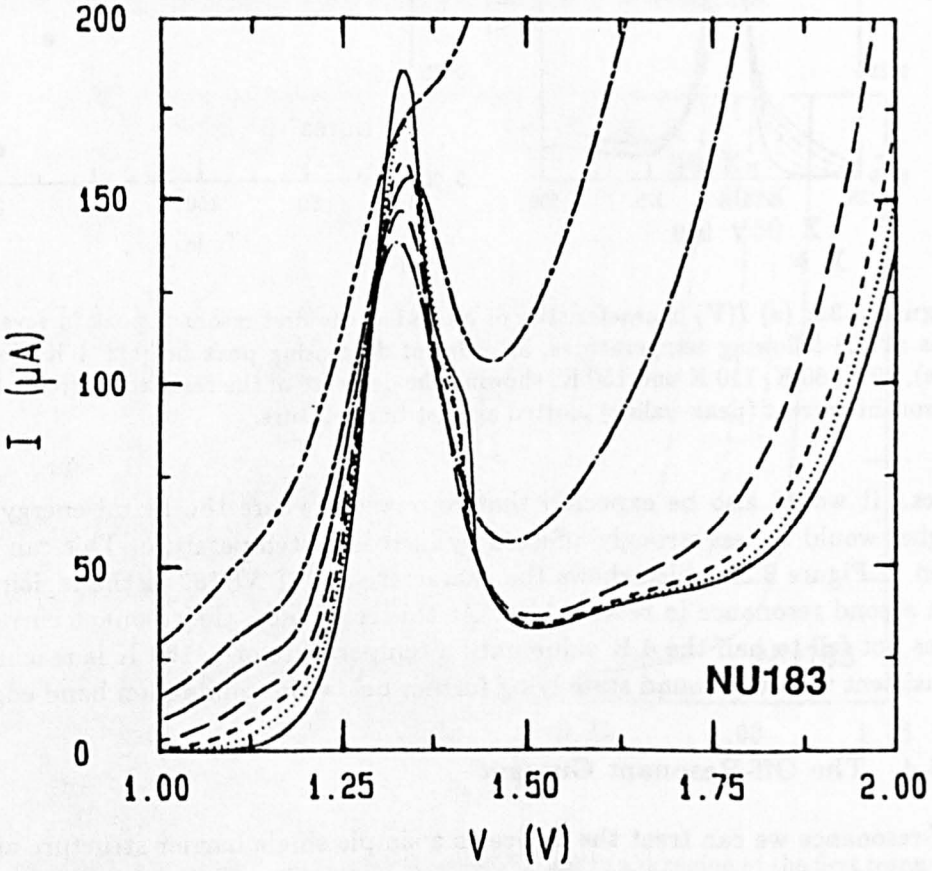

Figure 3.39: Current-voltage characteristics of *NU183* in the region of the second resonance in forward bias at temperatures between 4 K and 190 K. The curves are for the same temperatures as Figure 3.37. The 230 K trace is not shown and that at 190 K (dash/double-dash) is multiplied by 0.5.

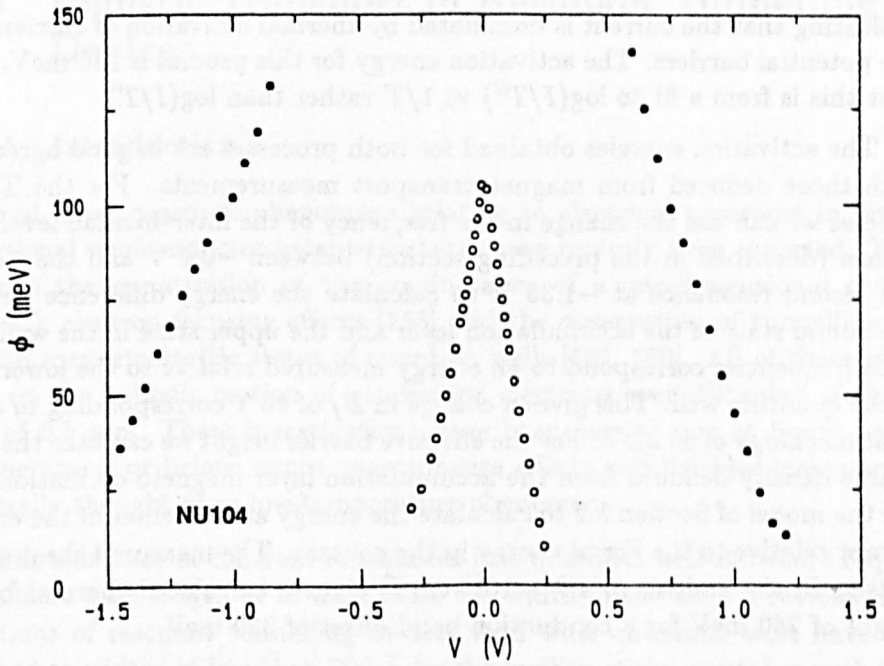

Figure 3.40: Activation energies for *NU104* over the whole bias range. The open circles o correspond to the thermally activated current at biases below the threshold voltage and the activation energies are obtained from plots of $\log(I/T)$ vs. $1/T$. The filled circles • correspond to thermal activation over the barrier at biases beyond the resonance, in which case the activation energy is deduced from a plot of $\log(I/T^2)$ against $1/T$.

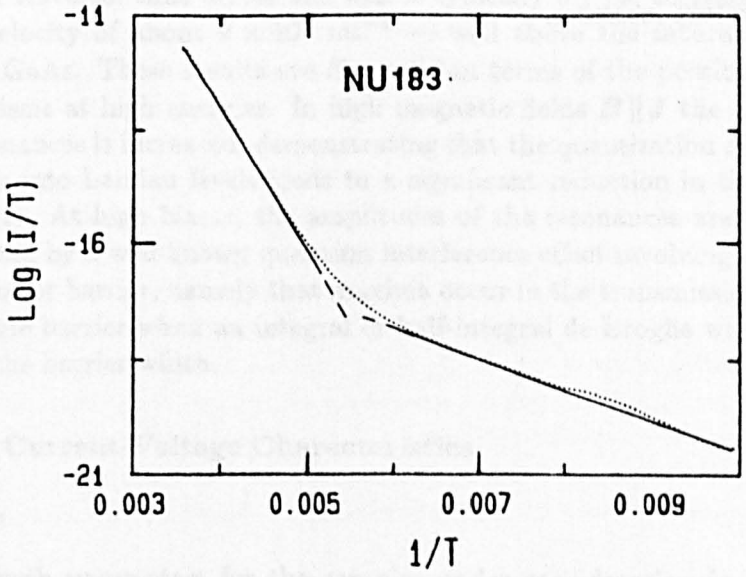

Figure 3.41: Plot of $\log(I/T)$ against $1/T$ for *NU183* at a bias of 0.9 V in reverse bias, below the threshold of the second resonance. The low temperature points show thermal activation to the energy of the resonant state and the high temperature ones activation over the barriers.

indicating that the current is dominated by thermal activation of carriers over the potential barriers. The activation energy for this process is 245 meV. Note that this is from a fit to $\log(I/T^2)$ vs $1/T$ rather than $\log(I/T)$.

The activation energies obtained for both processes are in good agreement with those deduced from magnetotransport measurements. For the TARTs process we can use the change in the frequency of the inter-Landau level transitions (described in the preceding section) between -0.9 V and the peak of the second resonance at -1.35 V to calculate the energy difference between the bound state of the accumulation layer and the upper state in the well since both frequencies correspond to an energy measured relative to the lower state in the quantum well. This gives a change in B_f of 40 T corresponding to an activation energy of 66 meV. For the effective barrier height we can take the sheet charge density deduced from the accumulation layer magneto-oscillations and use the model of Section 3.2 to calculate the energy at the center of the emitter barrier relative to the Fermi energy in the contact. The measured sheet charge density in the emitter of 4.7×10^{11} cm^{-2} gives a calculated thermal barrier height of 240 meV for a conduction band offset of 320 meV.

3.5.5 Conclusion

In this section we have shown how the effects of temperature on the current-voltage characteristics of double barrier devices can be simply explained in terms of thermal activation of electrons to either the resonant level when biased below resonance, or the top of the barrier when biased beyond resonance. The formation of a two-dimensional electron gas in the emitter under bias should be taken into account by a detailed theory of this effect. The decreasing occupancy of this 2DEG leads to a reduction in the peak resonant current as the temperature increases.

3.6 Ballistic Transport in Resonant Tunnelling Devices

3.6.1 Introduction

Several novel quantum phenomena relating to electrical transport in low-dimensional semiconductor heterostructures have recently been reported. These include the quantisation of the conductance of a one-dimensional channel [66, 67], electron focusing effects [158] and the observation of tunnelling into hybrid magnetoelectric states of quantum wells [159, 160]. All of these effects rely on the ballistic motion of conduction electrons over distances of the order of 0.1 μm. These investigations have been carried out at liquid helium temperatures or below; hence quantum-size effects and ballistic transport are generally thought of as low-temperature phenomena.

The existence of coherent resonances in a quantum well structure requires a ballistic path length of *at least* twice the width of the well. Previous investigations of resonant tunnelling devices with wide quantum wells have been limited to widths of less than 700 Å by the quality of the crystal growth techniques [161, 162, 163, 164]. These results have shown only very weak tunnelling features at room temperature. In this section we present an investigation of a series of resonant tunnelling devices with quantum well widths from 50 Å to 2400 Å. For well widths up to 1800 Å clear quantum resonances are seen in the conductance, and for widths up to 1200 Å resonances are observed at room temperature [165]. This implies a coherence length in the intrinsic GaAs in excess of 0.1 μm. Even when the electrons reach the collector barrier with kinetic energy of 1 eV or more, clear tunnelling effects are observed. The electron traversal time across the well is typically 0.1 ps, corresponding to a mean velocity of about 9×10^5 ms^{-1} — well above the saturation velocity of bulk GaAs. These results are discussed in terms of the possible scattering mechanisms at high energies. In high magnetic fields $\boldsymbol{B} \parallel \boldsymbol{J}$ the amplitude of the resonances is increased, demonstrating that the quantisation of the density of states into Landau levels leads to a significant reduction in the scattering rate [161]. At high biases, the amplitudes of the resonances are found to be modulated by a well-known quantum interference effect involving the width of the collector barrier; namely that maxima occur in the transmission coefficient of a single barrier when an integral or half-integral de Broglie wavelengths fit within the barrier width.

3.6.2 Current-Voltage Characteristics

Samples

The growth parameters for the samples under consideration in this section are given in Table 2.1. They form a complete series of well widths: *NU104* has a 50 Å wide quantum well, *NU153* 117 Å, *NU154* 217 Å, *NU167* 600 Å, *NU207* 1200 Å, *NU288* 1800 Å and *NU219* with a well-width of 2400 Å. All the samples have the same sequence of doping levels in the contacts, making direct comparisons between them possible. The growth conditions were also identical. Mesas of diameter 10 μm were measured for *NU104*, since larger mesa

diameters gave very high currents and a broad region of current oscillations which obscure the valley current (Section 4.3), 100 μm mesas were used for *NU153 - NU207*, and 200 μm diameter mesas for *NU288* and *NU219*, which had lower current densities. The current-voltage characteristics of *NU153* in the region of the first resonance are discussed in more detail in Section 3.4 in relation to the LO phonon-assisted scattering processes, and those of *NU104* are discussed in Section 3.5.2 with respect to their temperature-dependence. They are also included here to facilitate comparison. This series of samples allows us to investigate how a range of tunnelling properties depend on the width of the quantum well. To the best of our knowledge, no other investigation has covered such a wide range of well widths.

Low temperature characteristics

Figure 3.42 shows the current-voltage characteristics of all eight samples at 4 K. The derivative plots (dI/dV or d^2I/dV^2) are also shown for the wide well samples in order to emphasize the resonant structure. The narrow-well sample (50 Å) shows only one resonance, the 117 Å wide quantum well shows three, the 217 Å well 7, the 600 Å shows 28, the 1200 Å 70 and the 1800 Å well shows a total of 60 resonances. The widest well sample (2400 Å) does not show any clear resonant tunnelling structure even at 4 K. The 1200 Å wide well shows at least 23 regions of negative differential resistance (NDR). The splitting of the minima in dI/dV observed for *NU167* in the voltage range between 200 and 900 mV is characteristic of the onset of high-frequency oscillations in the tunnel current when the sample is biased in the region of NDR (see Section 4.3). The regions of bistability observed in *NU153* and *NU154* are due to the buildup of space charge in the well, which is increased by intersubband scattering processes. These curves are considered in more detail in Section 4.9.

As discussed earlier in this chapter, there is a two-dimensional bound state in the accumulation layer of the emitter contact and resonant tunnelling only occurs when the energy of this state is aligned with that of a quasi-bound state in the well. This produces sharper resonances than with three-dimensional emitter states because, in three dimensions, the device is on resonance for the range of biases corresponding to the energy level in the well lying between the emitter Fermi energy and conduction band edge *i.e.* even for an infinitely narrow state in the well, the three-dimensional resonance has an energy-width of ϵ_F (the Fermi energy in the contact) whereas the two-dimensional case reflects the width of the energy level. This neglects the influence of space charge buildup in the quantum well at resonance which can substantially broaden the resonance for a two-dimensional or three-dimensional emitter state — see Section 4.2. Therefore, the low doping level in the emitter contact is a distinct advantage when trying to investigate the closely-spaced energy levels of a wide quantum well.

Room temperature characteristics

When the samples are warmed to room temperature there is a reduction in the peak-to-valley ratio and in the number of observed resonances. The detailed effects in samples *NU104* and *NU153* have been discussed in Section 3.5.2. Figure 3.43 shows the current-voltage characteristics of *NU167* and *NU207* (600 Å and 1200 Å) at room temperature. In *NU167* a total of 18 resonances

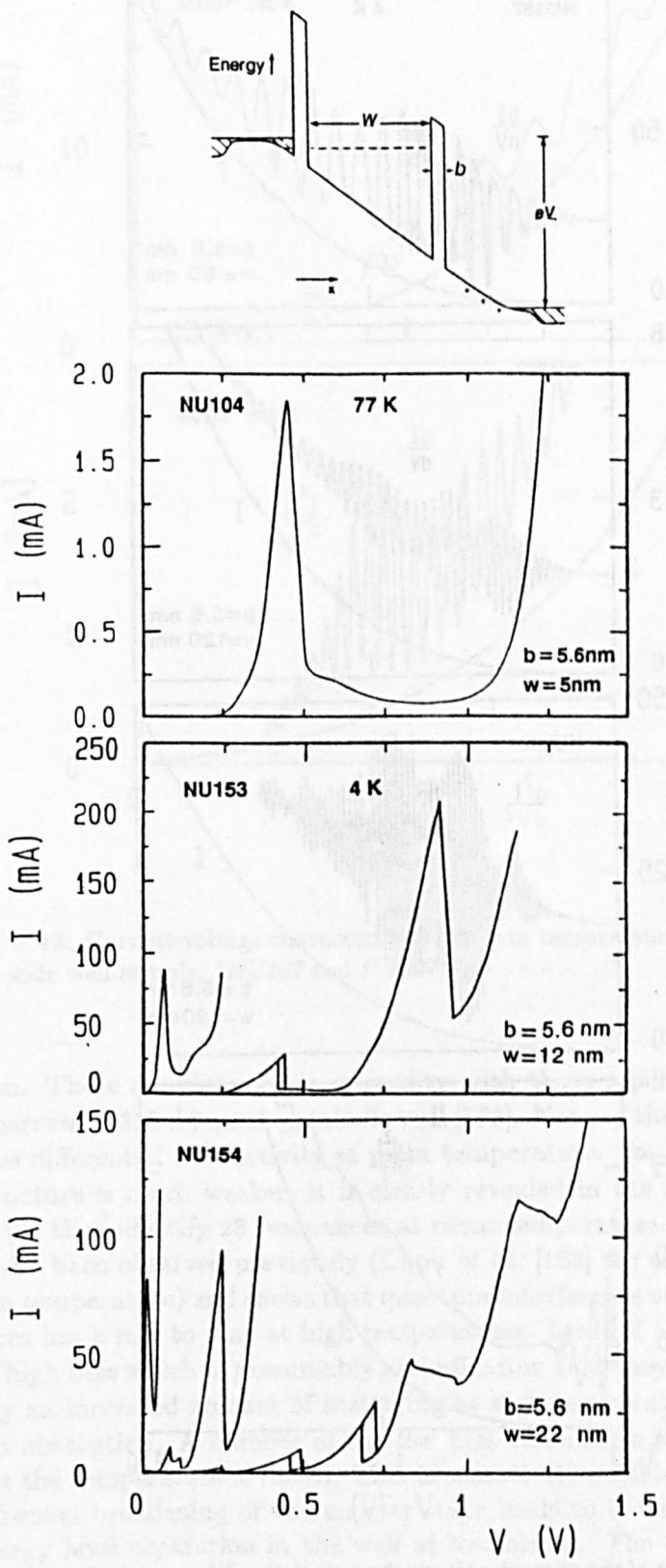
Energy
W
b
eV
x
NU104
77 K
b = 5.6nm
w = 5nm
NU153
4 K
b = 5.6 nm
w = 12 nm
NU154
b=5.6 nm
w=22 nm
I (mA)
V (V)
0.0
0.5
1.0
1.5
2.0
50
100
150
200
250
0
0.5
1
1.5

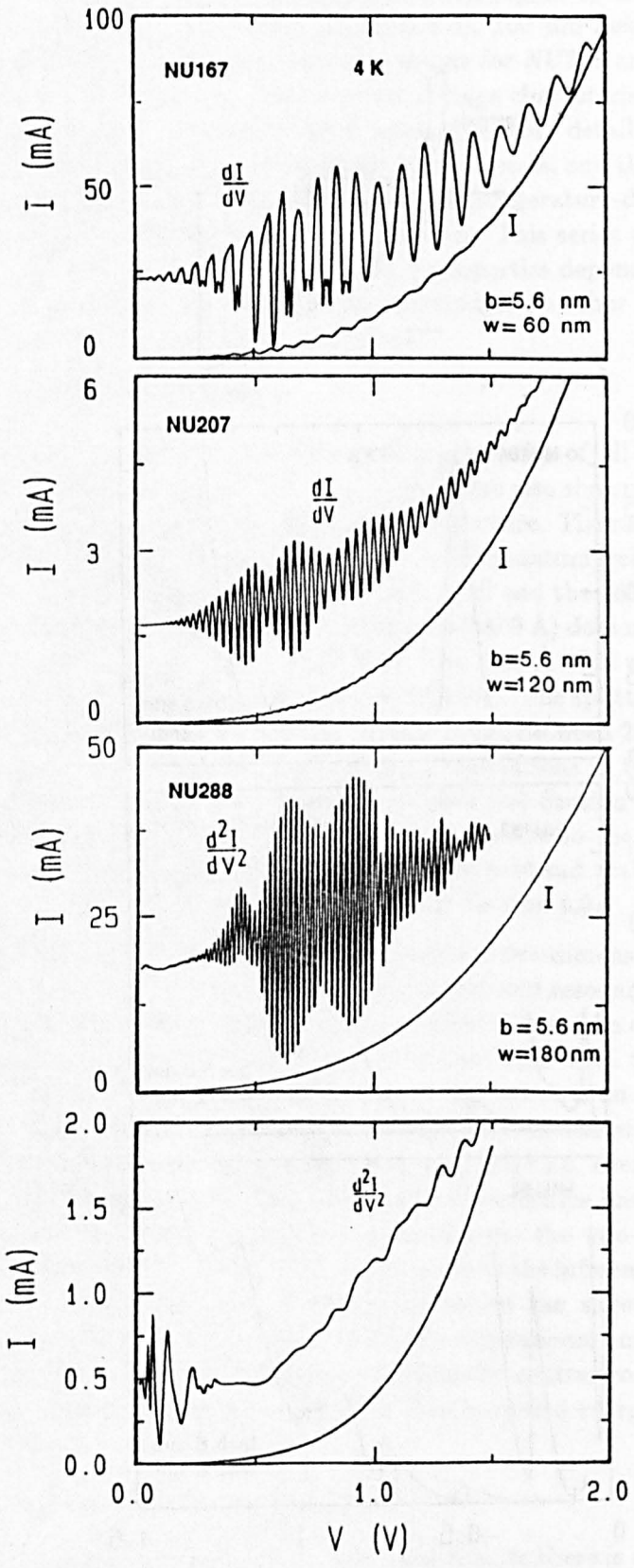

Figure 3.42: Plots of the current-voltage characteristics $I(V)$ and derivatives (dI/dV or d^2I/dV^2) at 4 K for the series of resonant tunnelling structures *NU104* to *NU219* with well width increasing from 50 Å to 2400 Å. The well thickness for each sample is marked in the figure. The inset shows a schematic conduction band profile.

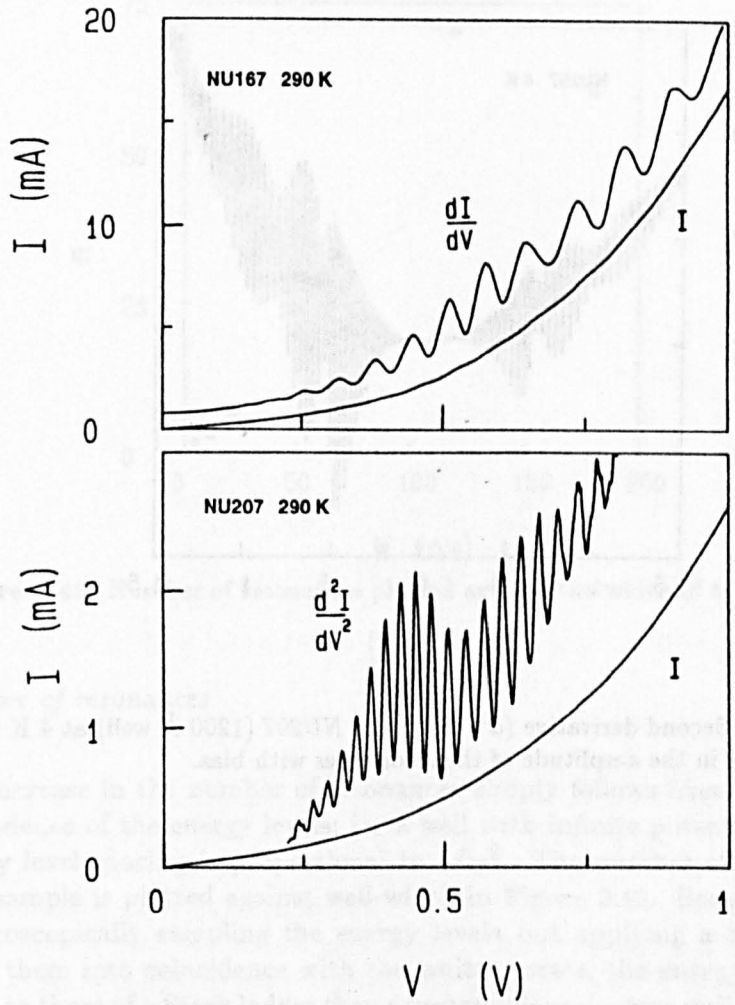

Figure 3.43: Current-voltage characteristics at room temperature of the 600 Å and 1200 Å wide well samples (*NU167* and *NU207*).

are seen. These are comparable in quality with those reported recently in a much narrower (315 Å) quasi-parabolic well [163]. None of the resonances show negative differential conductivity at room temperature. For *NU207*, although the structure is much weaker, it is clearly revealed in the second derivative trace. We then identify 28 resonances at room temperature. This is far more than have been observed previously (Chou *et al.* [163] see only 11 resonances at room temperature) and shows that quantum interference over relatively long distances has a role to play at high temperatures. Most of the resonances are lost at high bias which is presumably an indication that they are being broadened by an increased amount of scattering at high temperatures, for example phonon absorption. A number of the low bias resonances also become indistinct as the temperature is raised. This is tentatively explained by suggesting that thermal broadening of the emitter state leads to it being broader than the energy level separation in the well at low biases. The 1800 Å wide well (*NU288*) does not show resonance effects at room temperature, this demonstrates that the ballistic path length is much lower at room temperature, as expected.

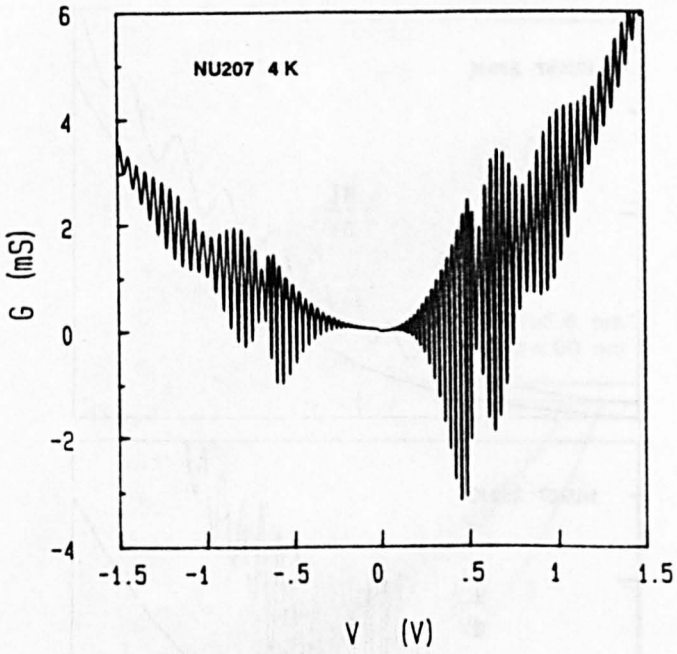

Figure 3.44: Second derivative (d^2I/dV^2) for *NU207* (1200 Å well) at 4 K showing the asymmetry in the amplitude of the resonances with bias.

Asymmetry

For all the devices, resonances are also observed in the opposite bias direction, here forward bias corresponds to the substrate being positively biased. The resonances in reverse bias (substrate biased negative) have a smaller amplitude, see for example Figure 3.44 which plots the second derivative d^2I/dV^2 in both bias directions for sample *NU207*. The asymmetry with respect to bias may be related to the quality of the barrier interfaces. It is well known that the quality of the interface is better for (AlGa)As grown on GaAs than *vice versa*. When the substrate is positively biased, the electron wavefunction in the well has a small amplitude near the collector barrier — classically this corresponds to the electron spending little time near this interface and longer near the emitter barrier. In this bias sense, the well/collector interface is GaAs on (AlGa)As and so likely to be of a lower quality than the emitter barrier/well interface, (AlGa)As on GaAs. In reverse bias the opposite will hold *i.e.* the electron will spends more time in the vicinity of the lower quality interface. This could lead to a higher probability of scattering from interface defects and consequently a reduction in the amplitude of the resonances. It should also be borne in mind that there will also be a slight asymmetry in the doping levels on either side of the double barrier structure due to silicon diffusion in the growth direction. At a given magnitude of bias, there is a lower electron density in the accumulation layer in reverse bias and so the voltage drop across the barriers is less and the transmission coefficients of the barriers are similarly lower. This will also contribute to the asymmetry in the magnitude of oscillations in d^2I/dV^2.

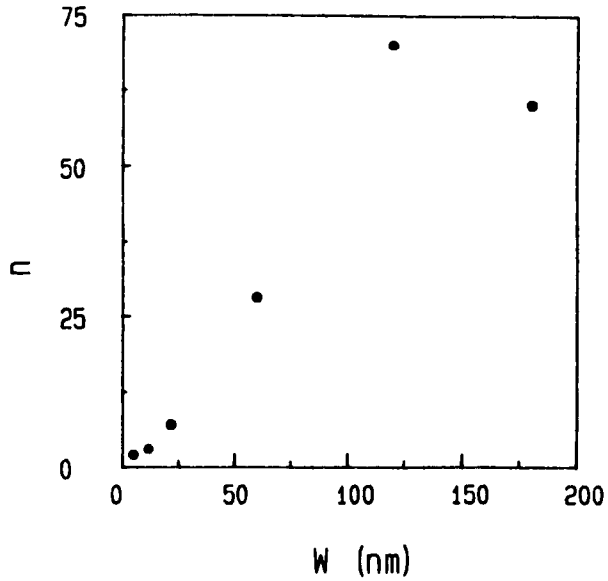

Figure 3.45: Number of resonances plotted against the width of the quantum well

Number of resonances

The increase in the number of resonances simply follows from the well-width dependence of the energy levels; for a well with infinite potential barriers the energy level spacing is proportional to $1/w^2$. The number of resonances for each sample is plotted against well-width in Figure 3.45. Because we are not spectroscopically sampling the energy levels but applying a bias voltage to bring them into coincidence with the emitter state, the energy levels will be closer to those of a Stark ladder than a rectangular quantum well, as can be seen in the schematic band diagram in Figure 3.42. The fact that the two widest samples (*NU288* and *NU219*) show fewer resonances is probably caused by the washing out of quantum interference effects by scattering as will be discussed below. The number of resonances observed in these samples is several times larger than the best reported by other groups, for example Potter *et al.* [164] only observe 22 resonances, and the widest well in which resonances have been observed is nearly twice the width of those in previous reports. In addition, the 1200 Å well shows many more regions of NDR than previously seen. This indicates that the MBE-grown material is of the highest available quality.

Peak-to-valley ratio

The peak-to-valley ratio of the 50 Å well is as high as 25:1, but increasing the width of the well dramatically reduces this, as shown by the plot of peak-to-valley ratio against width of well in Figure 3.46. For samples with more than one resonance, the maximum value obtained is plotted. The 1800 Å wide well shows no negative differential resistance *i.e.* the peak-to-valley ratio is something of a misnomer in this case. The decrease in peak-to-valley ratio indicates that the well states are becoming increasingly broad and begin to overlap.

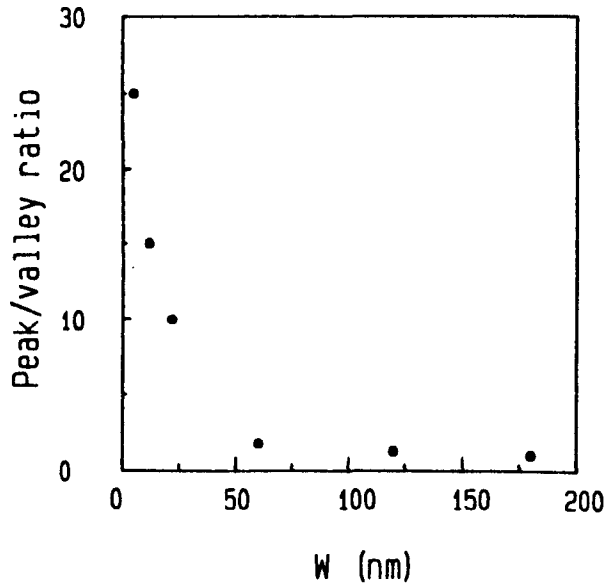

Figure 3.46: Peak-to-valley ratio plotted against the width of the quantum well.

Current density

It can be seen from Figure 3.42 that the current density drops as the wells get wider. This is merely a reflection of the fact that the voltage is dropped over a much shorter distance in the narrower samples and so a larger proportion of the applied bias is dropped across the barriers — producing a higher transmission coefficient. The magnetic field studies described in Section 3.3 allow us to calculate the distribution of potential within the samples. This shows that in *NU207* more than half the applied voltage is dropped across the well region but only 2% across the emitter barrier, whereas in *NU104* 15% of the bias is across the emitter barrier. This also influences the voltage spacing of the peaks.

Voltage spacing

In Figure 3.47 we have assigned indices n to the resonant peaks and plot n against the applied bias for each sample. As the width of the well increases, the spacing of the peaks decreases, reflecting the energy-spacing of the quantum well states. At high biases the $n(V)$ plots become approximately linear. A detailed analysis of these curves is complicated because it is necessary to model the non-parabolicity of the GaAs conduction band at high energies. In principle, the voltage positions of the peaks could be used to probe the high-energy band structure, as first suggested by Levi *et al.* [161]. In order to do this systematically it is necessary to know the potential distribution within the device exactly. We can obtain the voltage across the well from measurements of the magneto-oscillations in $\boldsymbol{B} \parallel \boldsymbol{J}$ as described in Section 3.3 and use the Fang-Howard wavefunction to approximate the quasi-bound state in the 2DEG. However, attempts to fit the positions of the peaks using either a transfer matrix method or the WKB approximation have proved relatively unsuccessful. A possible cause of this is the presence of electronic space charge in the well. Although the barriers in this sample are relatively thin and over most of the bias range the electrons are injected into the well with high energies,

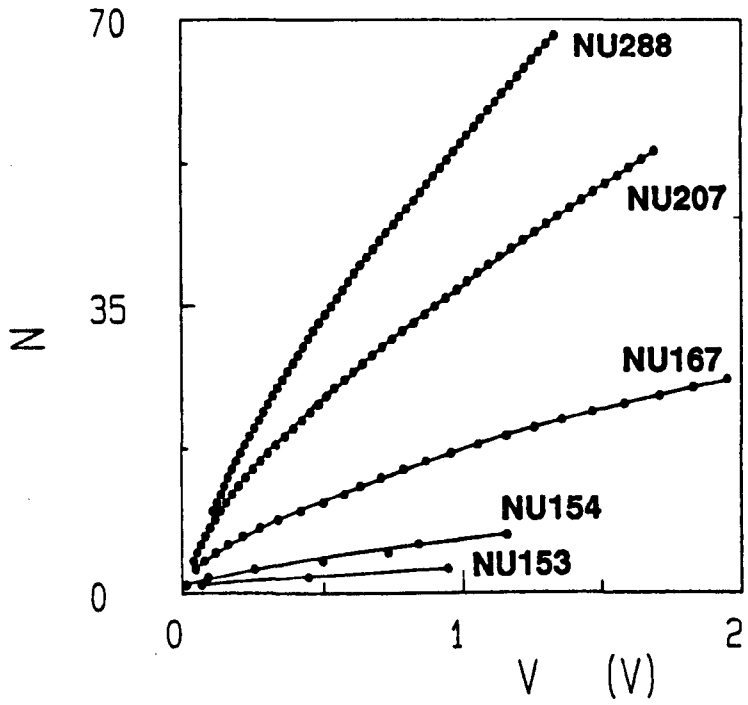

Figure 3.47: Plots of peak number against peak voltage for the series of resonant tunnelling structures described in the text.

the possibility of rapid intersubband scattering means that there could be a substantial population of electrons in the lowest subbands of the quantum well even at high biases. The amount of charge buildup is impossible to quantify in this case and hence it is not possible to translate the voltage-spacing of the resonant peaks into an energy spacing of the quantum well states.

It is interesting to note that for sample *NU207* (w = 1200 Å), the mean peak separation is $\Delta V = 39$ mV over the voltage range from 0.5 to 1.5 V. The corresponding energy $e\Delta V$ is approximately equal to the LO phonon energy in GaAs. Recently, Böckenhoff *et al.* [166] observed oscillations with similar values of ΔV for a tunnelling structure where the quantum well width was 1000 Å. The collector barrier in their device was formed by a δ-doping spike of silicon donors. They suggested that the oscillatory structure they observed was related to the 'Hickmott' oscillations which occur in the $I(V)$ characteristics of single barrier heterostructures of the type n^-GaAs/(AlGa)As/n^+GaAs [167]. It is now fairly well-established that the Hickmott oscillations arise from a process involving space charge effects and the LO phonon energy relaxation of hot carriers [168]. Böckenhoff *et al.* suggested that in their devices the LO phonon emission process could be resonantly enhanced by the standing wave states of the well. However, the magnetic field dependence of the resonances for $\boldsymbol{B}$ applied parallel to the plane of the barriers appears to be consistent with the evolution of the standing wave states in the well into hybrid magneto-electric states (see Chapter 5). Our own results do not reveal any strong evidence of resonant coupling between the standing wave state of the well and the LO phonon mode. Although LO phonons can give rise to important

effects in resonant tunnelling [148], we attribute the resonances reported here to purely electronic standing wave states of the quantum well. Note that the mean peak separation for *NU288* is 25 meV which is less than the LO phonon energy.

3.6.3 Above-barrier resonances

The analysis of the voltage distribution within the devices referred to above indicates that for biases above ~ 0.8 V in *NU154* and ~ 0.4 V in *NU288* (and at intermediate values for the other samples). The electrons reach the collector barrier with energies greater than the conduction band offset (which is taken to be ~ 320 meV [48]) and therefore they can leave the well without tunnelling. However there is still a finite reflection coefficient due to the potential discontinuity and hence interference effects are still possible [7, 169, 161, 170]. It is quite remarkable that these virtual levels can give rise to many regions of negative differential resistance (9 in *NU207*). Note that the increasing transmission coefficient leads to a significant lifetime broadening of the energy levels — so that, even in a perfect structure with no scattering, the resonance amplitudes will eventually die away. However a calculation of the transmission coefficient of these structures based on the transfer matrix approach [93] shows that, although the theoretical peak-to-valley ratio decreases by several orders of magnitude at high bias, it is still $\sim$10:1 for *NU207* at a bias of 1.5 V. Clearly then, scattering processes are still determining the width of the energy levels.

The highest voltage V_m at which resonances can be observed in *NU167* is 2.1 V. At this bias the electron sheet density in the accumulation layer of the emitter contact is $n_a = 9.5 \times 10^{11}$ cm^{-2}, producing an electric field in the well of $E = 1.4 \times 10^7$ Vm^{-1}. The corresponding voltage drop across the well is $V_w = 0.84$ V. For *NU207* the corresponding values of V_m, n_a and V_w are 2.4 V, 7×10^{11} cm^{-2} and 1.2 V respectively. Thus resonances in dI/dV are still observed when electrons reach the collector barrier with kinetic energies greater then 1 eV. The existence of well-defined quantum resonances implies a coherent standing-wave state in the well. Semi-classically, if *all* the electrons scatter before completing one traversal of the well, the tunnelling is totally incoherent *i.e.* the tunnel probability is just the sum of those of the two barriers independently [96]. In such a case there is no structure in dI/dV. Therefore, the observation of resonances shows that a *significant fraction* of the electrons which contribute to the tunnel current *must* have made more than one traversal of the well before undergoing a scattering process. At these energies, electrons can emit an LO phonon and scatter into a lower-energy state of the Γ-conduction band minimum or else scatter into the X and L minima with the emission of a zone-boundary phonon (as in the Gunn effect). To our knowledge the effect of the very high electric field on the phonon emission rate in a quantum well has not been calculated. However, we can expect the typical electron lifetime τ_s to be $\simeq 200$ fs [53] for Γ-Γ scattering and $\simeq 60$ fs for $\Gamma - L$ and $\Gamma - X$ scattering [171].

The traversal time

If the electron is injected into the well with kinetic energy ϵ_1 (see the schematic diagram in Figure 3.42), the classical traversal time from the emitter to the

collector barrier τ_t is given by

$$\tau_t = \int_0^w \frac{dx}{v_g} = \frac{\hbar}{eE}\left[k(\epsilon_1 + eEw) - k(\epsilon_1)\right] \tag{3.63}$$

where v_g is the group velocity. We can estimate τ_t from the values of E and ϵ_1 (deduced from the measured value of n_a and the Fang-Howard variational wavefunction — Section 3.2) and the non-parabolic dispersion relation for conduction electrons in GaAs [47]. This gives $\tau_t = 70$ fs for two traversals of the well in *NU167* at an applied bias of 870 mV. At this voltage, the device exhibits clear negative differential resistance — even though the electrons arrive at the collector with a kinetic energy of 450 meV, which is well above the L minima and the $\Gamma - \Gamma$-height of the collector barrier. This value of τ_t is shorter than the mean time for $\Gamma - \Gamma$ scattering, but somewhat longer than that for scattering into the subsidiary minima. Note also that τ_t is comparable to the period of vibration of the LO phonon mode. The time scale of other scattering processes is less well-known. Electron-electron scattering is certainly faster than this in degenerate systems, but may not be significant when there is no charge buildup in the quantum well. The loss of the higher bias resonances as the temperature is raised shows that scattering rates increase with temperature, the high temperature scattering is likely to be dominated by phonon absorption. Note that the mean traversal velocity is 9×10^5 ms^{-1}, well above the saturation velocity in bulk GaAs.

An accurate estimate of the fraction $\Delta n/n$ of electrons that successfully complete a traversal of the well ballistically would require a detailed knowledge of the energy width of the quasi-bound states in the well. The energy width is determined by monolayer fluctuations in the well thickness, scattering processes and the transmission rate through the collector barrier. However, a lower limit for $\Delta n/n$ may be estimated from the peak-to-valley ratio I_p/I_v, since we expect that

$$\frac{\Delta n}{n} > \frac{I_p - I_v}{I_p} \tag{3.64}$$

For the 600 Å well $I_p/I_v = 1.75$ at $V = 500$ mV and 4 K, giving $\delta n/n > 0.4$. For the 1200 Å well (*NU207*), the corresponding figure is $\Delta n/n > 0.2$ at 420 mV. If we set $\Delta n/n \sim \exp(-\tau_t/\tau_s)$, we find $\tau_s \sim 140$ fs for both devices when the voltage drop across the well is approximately 200 mV. This value for the scattering time is comparable to those quoted above (and with the calculations in Section 3.2 for a sample with a narrower well) although this is a very rough calculation. It is interesting to note that if the residual doping in the GaAs is $\sim 5 \times 10^{14}$ cm^{-2}, the average separation of donor ions is ~1250 Å which gives a mean time between scattering events of 140 fs for an electron velocity of 9×10^5 ms^{-1}. This suggests that the mean free path is limited by the background impurity level.

3.6.4 'Over-the-Barrier' Resonances

The finite thickness of the collector barrier gives rise to another interesting quantum-mechanical effect. For a rectangular barrier, it is well-known that the reflection coefficient falls to zero when an integral or half-integral number of de Broglie wavelengths fit within its width [81] — see Section 1.4. In our

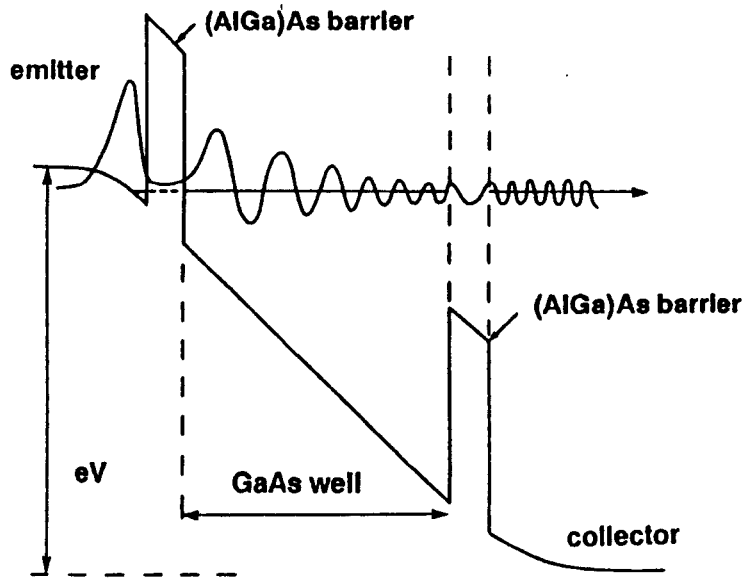

Figure 3.48: Schematic conduction-band profile illustrating the condition for minimum reflection at the collector barrier.

device, the potential drop across the collector barrier means that the reflection coefficient is a minimum rather than zero when this condition is satisfied. For a varying potential the condition for minimum reflection may be expressed as

$$\int_0^b k(x)\,dx = n\pi \tag{3.65}$$

where the integral is over the width of the collector barrier, $n = 1, 2, 3, \ldots$, and $k(x)$, the electron wavevector, is given by the kinetic energy and the (energy-dependent) effective mass in the collector barrier region, $\hbar^2 k^2/2m^*(\epsilon) = \epsilon - \phi$ (ϕ is the conduction band offset). This condition is illustrated in Figure 3.48 for the case where one complete de Broglie wavelength fits into the width of the collector barrier. Since the above-barrier resonant states arise from a standing-wave interference between de Broglie waves incident on and reflected from the collector barrier/well interface, when this reflection is a minimum there is also a minimum in the amplitude of the resonances in $I(V)$. This is shown in Figure 3.49 which plots the transmission coefficient against bias for an incident electron energy of 10 meV and a double barrier structure with 85 Å barriers and a 1200 Å well (see reference [172]). The inset shows the probability density across the well at several applied biases showing that when there is a resonance in the collector barrier region the amplitude of the standing wave states in the well is reduced. The transfer matrix calculation was performed by E. S. Alves.

This explains the oscillations in the amplitude of the conductance at high bias visible in *NU167*, *NU207* and *NU288*. Three minima are clearly identifiable. This explanation has been verified by measurements on a sample with a thicker collector barrier (85 Å) and all other layers the same as in *NU207*. The current-voltage characteristics are plotted in Figure 3.50. This device

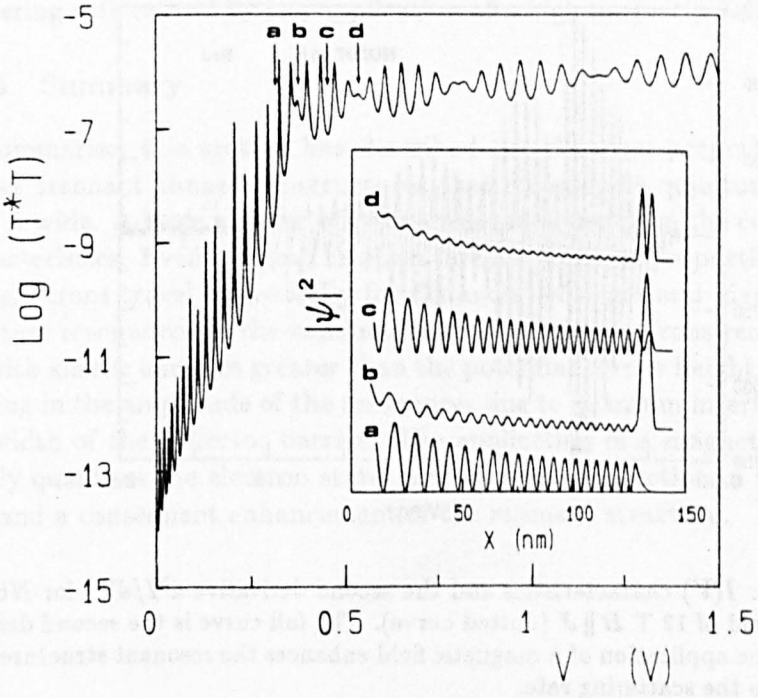

Figure 3.49: Transmission coefficient plotted against bias voltage for an electron wave incident on a double barrier structure with a kinetic energy of 10 meV. The calculation is for a 85 Å-1200 Å-85 Å structure with 320 meV potential barriers and GaAs and (AlGa)As electron effective masses of 0.067 m_e and 0.1 m_e. The inset plots the probability densities, $\Psi^*\Psi$, against position for four different voltages (indicated by arrows in the main figure), indicating the reduced amplitude of the standing wave state of the well when there is a resonance in the collector barrier.

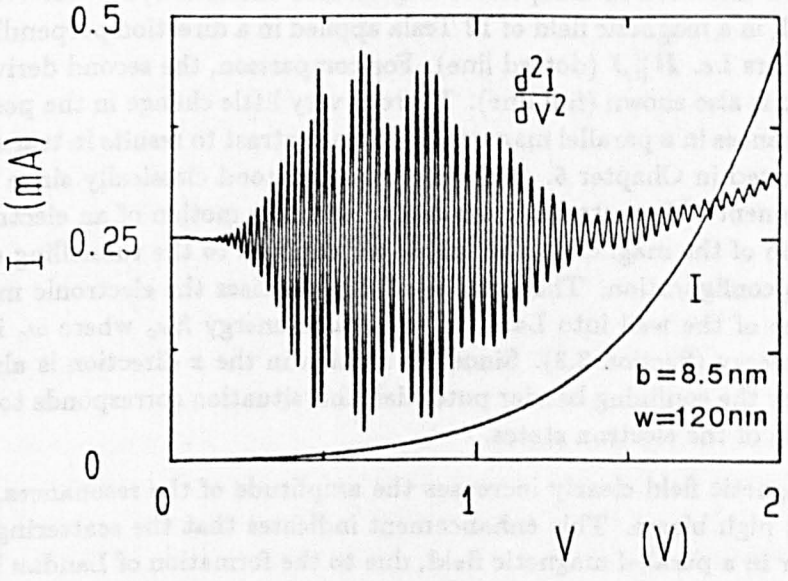

Figure 3.50: Current-voltage characteristics of a double barrier device with a well width of 1200 Å and barriers of width 85 Å. The wider barrier leads to a greater number of 'beats' in the amplitude of the high bias resonances. See Alves *et al.* [172] for details of the device.

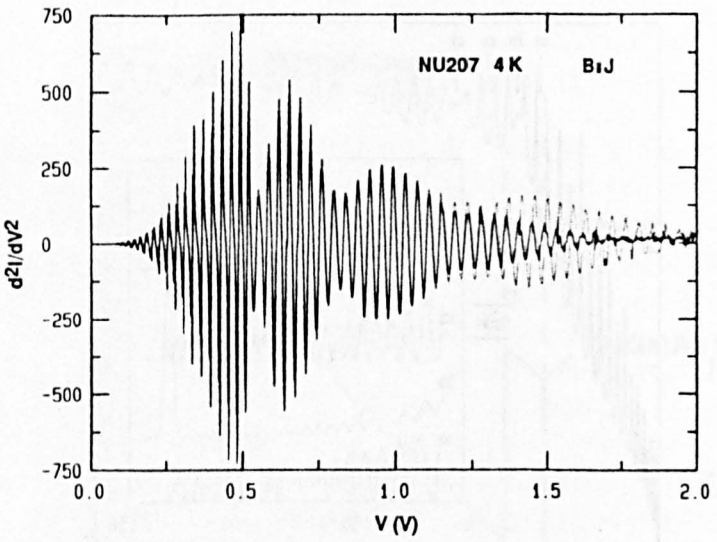

Figure 3.51: $I(V)$ characteristics and the second derivative d^2I/dV^2 for *NU207* in a magnetic field of 12 T $\boldsymbol{B} \parallel \boldsymbol{J}$ (dotted curve). The full curve is the second derivative for $B = 0$. The application of a magnetic field enhances the resonant structure due to a reduction in the scattering rate.

shows six clear minima in the oscillation amplitude [172], in agreement with the width-dependence expected from equation 3.65.

3.6.5 The Effect of a Magnetic Field

The effects of a magnetic field applied in the plane of the barriers — the formation of hybrid magneto-electric states and tunnelling into interfacial Landau levels — are discussed in Chapter 5. Figure 3.51 shows d^2I/dV^2 for *NU207*, 1200 Å well, in a magnetic field of 12 Tesla applied in a direction perpendicular to the barriers *i.e.* $\boldsymbol{B} \parallel \boldsymbol{J}$ (dotted line). For comparison, the second derivative in zero field is also shown (full line). There is very little change in the position of the resonances in a parallel magnetic field, in contrast to results in transverse fields presented in Chapter 5. This can be understood classically since there is no component of Lorentz force associated with the motion of an electron in the direction of the magnetic field, which corresponds to the tunnelling direction in this configuration. The magnetic field quantises the electronic motion in the plane of the well into Landau levels with energy $\hbar\omega_c$ where ω_c is the cyclotron energy (Section 3.3). Since the motion in the x direction is already quantised by the confining barrier potential, this situation corresponds to *total* quantisation of the electron states.

The magnetic field clearly increases the amplitude of the resonances, particularly at high biases. This enhancement indicates that the scattering rate τ_s^{-1} is lower in a parallel magnetic field, due to the formation of Landau levels which restrict the number of states the electrons can scatter into. This has a marked effect at high biases where the resonances are particularly broad. This is in agreement with the results of Levi *et al.* [161]. In the samples studied here, the electrons are injected from a two-dimensional state so the spread of tunnelling energies is comparable to the energy width of the levels in the well

and therefore the tunnel current is particularly sensitive to the reduction in scattering rate caused by the application of a high magnetic field.

3.6.6 Summary

To summarise, this section has described the electrical properties of double barrier resonant tunnelling structures that incorporate quantum wells up to 2400 Å wide. A large number of resonances are observed in the current-voltage characteristics. Even at room temperature a significant proportion of conduction electrons travel ballistically for distances $\sim$0.4 μm and give rise to clear quantum resonances in the conductance. When the electrons reach the collector with kinetic energies greater than the potential barrier height, we observe a beating in the amplitude of the resonances due to quantum interference within the width of the collector barrier. The application of a magnetic field $\boldsymbol{B} \parallel \boldsymbol{J}$ totally quantises the electron states and leads to a reduction in the scattering rate and a consequent enhancement of the resonant structure.

CHAPTER 4

Charge Buildup and Bistability

4.1 Introduction

One of the most controversial topics in resonant tunnelling over recent years has been the origin of the bistable behaviour observed in the current-voltage characteristics of some resonant tunnelling devices [173, 174, 175]. The resolution of this controversy will be the main theme of this chapter. Goldman *et al.* [173] interpreted the bistability as an intrinsic feature of the device arising from the electrostatic effects of a buildup of negative space charge in the quantum well when biased on resonance. The theoretical basis for this effect is described in Section 4.2, together with a brief review of the experimental verification of charge buildup. Although the physical mechanism that could lead to an intrinsic bistability phenomenon was clearly understood [99], there was disagreement as to whether the effect observed was a manifestation of this mechanism or simply a property of the measuring circuit. Sollner [174] pointed out that bistability is a common feature of devices which exhibit negative differential conductance, due to high-frequency current oscillations in the external circuit. The origin of these oscillations is outlined in Section 4.3, which presents a simple simulation of the device and the measuring circuit [141] which reproduces bistable behaviour similar to that reported by Goldman *et el.*, and describes how the device may be stabilized against these oscillations [176, 148].

Although space charge buildup had been experimentally observed by magnetotransport and photoluminescence studies [140, 177, 178], it was not until asymmetric double barrier structures [179] were designed and investigated that the observation of an unambiguously intrinsic bistability was made [180, 181]. Results are presented in Section 4.4 for an asymmetric device showing two regions of intrinsic bistability (*NU183*). The characteristics of the device are shown to be independent of the external measuring circuit, demonstrating that the effect is genuinely intrinsic to the device. Section 4.5 describes the first investigation of charge buildup using the differential capacitance of the device

[182, 183, 184]. These measurements are interpreted in terms of a simple equivalent circuit taking into account the distribution of electronic space charge within the device. An estimate the charge buildup in the well is obtained, thereby demonstrating the usefulness of this technique.

The effect of increasing the temperature is discussed in Section 4.6 which shows that the variation in the voltage at the resonant peak can be related to the reduction in the amount of charge stored in the well due to thermal excitation of carriers over the confining barriers. The width of the bistable region as a function of temperature is discussed in terms of the broadening of the energy state by scattering processes.

The charge density in the well is obtained directly from a Fourier analysis of the magnetoquantum oscillations in the capacitance when a magnetic field is applied perpendicular to the plane of the barriers [185]. These results are presented in Section 4.7. There is good agreement with the capacitance data of Section 4.5. The observation of magnetoquantum oscillations due to a charge distribution in the well means that the electron temperature characteristic of this distribution is low ($k_B T_e \ll \epsilon_F$) and hence the electrons must undergo energy relaxation in the quantum well. Estimates of the charge storage time in the well are much greater than the acoustic phonon scattering time, providing confirmation that the tunnelling process in this sample is sequential rather than coherent.

The effects of high magnetic fields, both in the plane of the barriers and perpendicular to it, on the current and capacitance-voltage characteristics are investigated in Section 4.7. The application of a magnetic field $\boldsymbol{B} \parallel \boldsymbol{J}$ leads to a remarkable enhancement of the voltage width of the bistable region [186, 187] and a three-fold increase in the peak current. This behaviour is explained by the high degeneracy of Landau levels in the quantum limit. When $\boldsymbol{B}$ is perpendicular to the current, there is also an increase in the peak current but, in contrast to the parallel configuration, the bistability is quenched at high fields.

Having clearly demonstrated intrinsic bistability, we then turn to a more asymmetric sample (*NU221*) where a completely new kind of bistable behaviour is observed, as described in Section 4.8. There is a region of 'inverted' bistability where the off-resonant current exceeds the resonant current, leading to a 'butterfly'-shaped hysteresis loop in $I(V)$ [188, 189, 190]. The width of this loop is periodically modulated in a magnetic field $\boldsymbol{B} \parallel \boldsymbol{J}$ due to the formation of Landau levels. Magnetic field and capacitance techniques are used to investigate charge buildup in this device and reveal the importance of non-resonant scattering processes.

4.2 Electrostatic Feedback and Intrinsic Bistability

It has long been recognized that when a double barrier resonant tunnelling device is biased on resonance, there is a buildup of carriers within the quantum well [94, 95, 191, 192, 193] and that this can have important implications for device behaviour. The presence of electrons in the well for some time modifies the potential distribution within the device in accordance with Gauss's law, bringing a feedback operation into effect which must be taken into account when calculating the characteristics of a device by using a self-consistent algorithm [192, 191]. Space charge in the well affects both the static current-voltage characteristics and the time evolution of the resonance [94, 194], and hence also the high-frequency response [113, 195]. Goldman *et al.* [173] proposed that a large buildup of charge would lead to hysteresis in the current-voltage characteristics since the device could be in either of two states with the same applied bias: on resonance with a high charge density in the well or off-resonance with no charge in the well (but correspondingly more in the emitter accumulation layer). These states give different currents, producing hysteresis. This was also predicted by Berkowitz and Lux [196] from a self-consistent quantum model of a resonant tunnelling device.

Both the coherent and the sequential theories of tunnelling have been used to model the effect. In the coherent approach, the space charge is simply related to the increased amplitude of the wavefunction in the well when on resonance, see Price [197]. From the point of view of sequential tunnelling, the charge buildup may be obtained from the dynamic balance between electrons tunnelling into and out of the well, this has been clearly described by Payne [194] and by Sheard and Toombs [99]. The results obtained from the alternative approaches are essentially in agreement. The sequential theory is simpler to handle and is more appropriate to the samples considered here since scattering processes in the well are of great importance, as will be described later in this chapter.

4.2.1 Theory of Charge Buildup

This section follows the approach adopted by Sheard and Toombs [99] to derive expressions for the charge buildup and the bistability it produces. We begin by considering a device where the emitter is heavily doped so that the electron gas in the contacts has a three-dimensional character. The effect of space charge buildup on the voltage distribution across a resonant tunnelling device is schematically illustrated in Figure 4.1. The application of a voltage across the device causes the formation of space charge regions on either side of the double barrier structure, with electrons accumulating adjacent to the emitter barrier and a depletion region forming in the collector contact. For simplicity these space charge regions are considered to be plane sheets of charge offset from the interfaces by a screening length λ which is taken to be the same on both sides of the double barrier structure. A reasonable value to use is the Thomas-Fermi screening length which is approximately 100 Å for a doping level of 10^{18} cm^{-3}. In general, the screening lengths are unequal and vary as a function of the applied voltage.

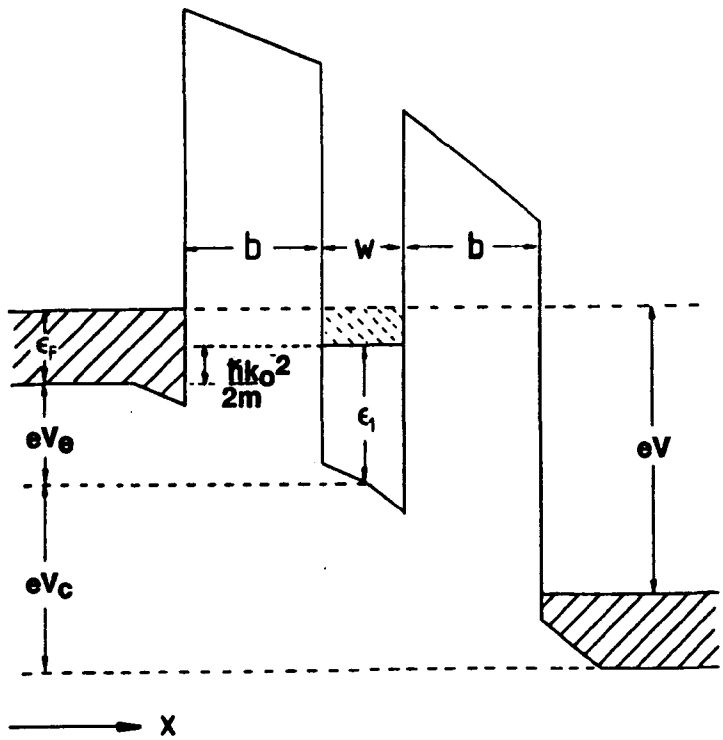

Figure 4.1: Schematic diagram showing the conduction band profile for a resonant tunnelling device with space charge buildup in the quantum well.

The device is considered to consist of two parallel plate capacitors in series, with negative charge $-Q_e$ on the emitter, positive charge Q_c on the collector side and a net negative charge $-Q_w$ on the common central plate representing the well. Obviously for overall neutrality of the device we have $Q_c = Q_w + Q_e$. The voltage drop across the first half of the device (accumulation layer, emitter barrier and the first half of the well) is $V_e = Q_e/C$ and that across the remainder (second half of te well, collector barrier and the depletion region) is $V_c = (Q_e + Q_w)/C$, where the capacitance of one half of the device is given by

$$\frac{1}{C} = \frac{\lambda + b + w/2}{\varepsilon_0 \varepsilon_r} \tag{4.1}$$

The total bias is then simply $V = V_e + V_c = 2Q_e/C + Q_w/C$. The presence of charge in the well means that the voltage is distributed unequally between the two barriers. To illustrate the electrostatic feedback effect, consider the simplified band diagrams in Figure 4.2. When the device is biased so that the bound state of the well is below the Fermi energy in the emitter contact, electrons are able to tunnel into the well. The number of electrons which tunnel is determined by the energy difference between the bound state and the Fermi level [10]. If a charge $-q$ is transferred from the emitter into the well, as is shown in Figure 4.2(b), the voltage drop across the collector is unchanged, but that across the emitter decreases by q/C. To maintain the applied bias, a charge of $-q/2$ must flow from the collector to the emitter via the external circuit (Figure 4.2(c)). Although the external voltage is the same, the well state is now $q/2C$ higher with respect to the emitter Fermi energy, this leads to a

readjustment of Q_w and further changes in the bias distribution. Therefore, the charge in the well is determined by the position of the energy level relative to the Fermi level in the emitter contact — which in turn depends on the amount of charge in the well *i.e.* there is an electrostatic feedback mechanism in operation.

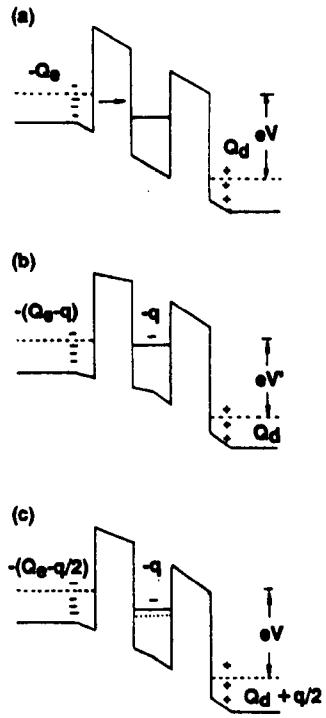

Figure 4.2: Schematic diagrams illustrating the electrostatic feedback mechanism: (a) If the structure is biased so that the energy level in the well is below the Fermi level in the emitter contact, electrons can tunnel into the well. (b) Transferring a charge $-q$ from the emitter into the well changes the voltage drop across the emitter barrier (c) Charge $-q/2$ must flow in the external circuit to maintain the applied bias. The energy level in the well has changed by $q/2C$ with respect to the emitter Fermi level.

The device comes onto resonance (at $T = 0$ K) when the energy level in the well coincides with the Fermi energy in the emitter contact, for the device illustrated here this corresponds to a threshold voltage of $eV_{th} = 2(\epsilon_1 - \epsilon_F)$. This is shown as point a in the schematic current-voltage characteristics of Figure 4.3. As the bias is increased, the current increases to a maximum, $a \rightarrow b$. When the well energy level goes below the emitter conduction band edge, the device comes off resonance and the current falls ($b \rightarrow c$). If no account is taken of the space charge in the well this occurs at a bias of $2\epsilon_1/e$ giving a resonance width of $2\epsilon_F/e$, and no bistability.

In the sequential model, the steady-state charge density in the well at a given bias is determined by the balance between the currents flowing into and out of the well [194, 99]. We consider the case illustrated in Figure 4.1 and label states in the emitter by $\boldsymbol{k} = (k_x, \boldsymbol{k}_\perp)$, those in the well by $\boldsymbol{q} = (0, \boldsymbol{q})$ and those in the collector by $\boldsymbol{p} = (p_x, \boldsymbol{p}_\perp)$. Following Sheard and Toombs [99] the

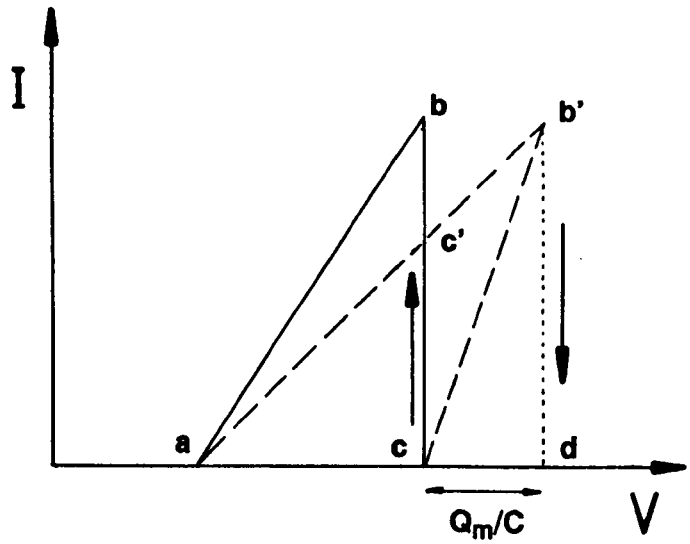

Figure 4.3: Schematic current-voltage characteristics of a double-barrier device with no space charge buildup (full line) and with charge buildup taken into account (dashed line).

current-balance condition may be expressed as

$$\sum_{k,q}(f_k - f_q)W_{kq} - \sum_{q,p}(f_q - f_p)W_{qp} = 0 \tag{4.2}$$

where f is the occupancy given by the Fermi-Dirac distribution; at low temperatures this is sharply cut-off at $k = k_F$. W_{kq} ($= W_{qk}$) is the transition rate from the emitter to the well. This is a function of k_z and the bias across the emitter barrier V_e. Conservation of momentum in the plane perpendicular to the barriers gives $k_\perp = q$ and $p_\perp = q$. Note that electrons can scatter in the well, so momentum is only considered to be conserved during the actual tunnelling transitions. If the resonance is taken to be very narrow, tunnelling can only occur when

$$\frac{\hbar^2(k_z^2 + k_\perp^2)}{2m^*} = \epsilon_1 - eV_e + \frac{\hbar^2 q^2}{2m^*} \tag{4.3}$$

i.e. for $\hbar^2 k_z^2/2m^* = \hbar^2 k_0^2/2m^* = \epsilon_1 - eV_e$, and for the collector $\hbar^2 p_z^2/2m^* = \hbar^2 p_0^2/2m^* = \epsilon_1 + eV_c$. So equation 4.2 may be written as

$$\sum_{k,q} W_{kq}(f_{k_z,k_\perp} - f_q)\delta_{k_\perp q}\delta_{k_z k_0} - \sum_{q,p} W_{qp}(f_q - f_p)W_{qp}\delta_{p_\perp q}\delta_{p_z p_0}$$

$$= 0 \tag{4.4}$$

We consider biases where there are no occupied collector states at the same energy as the well state *i.e.* $f_p = 0$. Sheard and Toombs [99, 87] have used a Transfer Hamiltonian approach to show that the transition elements are given by $\sum_{k_z} W_{k_z q} = \nu T_e$ where ν is the classical attempt rate ($= \sqrt{2\epsilon_1/m^*}/2w$) and T_e is the transmission coefficient of the emitter barrier for an incident kinetic energy of $\hbar^2 k_0^2/2m^*$. The equivalent expression for the collector is νT_c.

The transition rates are related to the decay time of electrons in the well to unoccupied states in the emitter or collector, $\nu T_e = \tau_e^{-1}$ and $\nu T_c = \tau_c^{-1}$. The values of T_e and T_c depend on the incident energy and on the bias dropped across each barrier (and therefore on the charge in the well). $\sum_q f_q$ is simply the number of carriers stored in the well Q_w/e. Finally $\sum_{k_\perp} f_{k_x,k_\perp}$ is the number of states in the emitter with $k_x = k_0$ which is

$$F(V_e) = \begin{cases} (k_F^2 - k_0^2)/2\pi & \text{if } 0 < k_0 < k_F \\ 0 & \text{otherwise} \end{cases} \tag{4.5}$$

Therefore equation 4.2.1 may be simplified to

$$\nu T_e(eF(V_e) - Q_w) - \nu T_c Q_w = 0 \tag{4.6}$$

This gives a charge in the well of

$$Q_w = Q_m \frac{k_F^2 - k_0^2}{k_F^2} \theta(k_0^2 - k_F^2)\theta(k_0^2) \tag{4.7}$$

where Q_m, the maximum charge density in the well, is

$$Q_m = \frac{ek_F^2}{2\pi} \frac{T_e}{T_e + T_c} \tag{4.8}$$

This result is identical to that obtained by Price [197] from the theory of coherent tunnelling.

Each point on section $a \rightarrow b$ of the schematic $I(V)$ in Figure 4.3 is shifted to higher bias by Q_w/C. The peak of the resonance (b') is at a voltage of $2\epsilon_0/e + Q_m/C$. If the bias is increased to beyond this point, the energy level in the well goes below the emitter conduction band edge and the device is no longer on resonance. The charge is ejected from the well and the current falls ($b' \rightarrow d$). To maintain the applied bias, the charge in the emitter accumulation layer increases by $Q_m/2$ and at point d the well state is at an energy $Q_m/2C$ below the conduction band edge. If the bias is decreased from this point, the device stays in the low-current, off-resonant state until the emitter charge has been reduced to bring the bound state of the well back into alignment with the conduction band edge of the emitter. This occurs at a bias of $2\epsilon_0/e$ (point c), at which point the current steps back up onto the resonant portion of the curve ($c \rightarrow e$). The current can take two values over the voltage range between points c and d. The voltage width of this bistable region is [99]

$$\Delta V = \frac{Q_m}{C} = \frac{ek_F^2}{2\pi} \frac{T_e}{T_e + T_c} \frac{\lambda + b + w/2}{\epsilon_0 \epsilon_r} \tag{4.9}$$

Sheard and Toombs have calculated that this is quite appreciable (~ 30 mV) for devices similar to those of Goldman *et al.* [173]. However, the effect can be eliminated if the resonance has a broad energy width.

In the region between c and d, the current is actually *triple-valued* as pointed out by Sheard and Toombs [99] and re-stated by Coon *et al.* [198, 199]. The third state corresponds to maintaining a constant charge in the accumulation layer of the emitter contact (so keeping the well state aligned with the emitter conduction band edge) but reducing the charge in the well, thereby reducing

the total bias ($b' \rightarrow c$ in Figure 4.3). Although Coon *et al.* claim that this third solution is stable because it has positive differential resistance this is not so at the turning points and hence it is difficult to see how this region of the curve could be accessed experimentally. This has not been reported to date, therefore we will continue to refer to the effect as intrinsic *bistability*.

4.2.2 Evidence for Intrinsic Bistability

Goldman's data

The first claim to have observed intrinsic bistability was made by Goldman *et al.* [173] who presented the $I(V)$ characteristics reproduced in Figure 4.4. Their sample was a symmetric GaAs/(AlGa)As double barrier structure with 80 Å thick barriers. Two regions of bistability were observed, whereas the theory of Sheard and Toombs predicts only one. Goldman *et al.* explained this by postulating that one peak was due to electrons tunnelling into the well from three-dimensional states in the emitter contact and that the other, at higher bias, was due to electrons in a two-dimensional bound state which formed in the emitter under bias. However, they offered no proof of the existence of such a state and did not explain why it gave rise to a lower current but a wider region of bistability than the resonance with the three-dimensional emitter states.

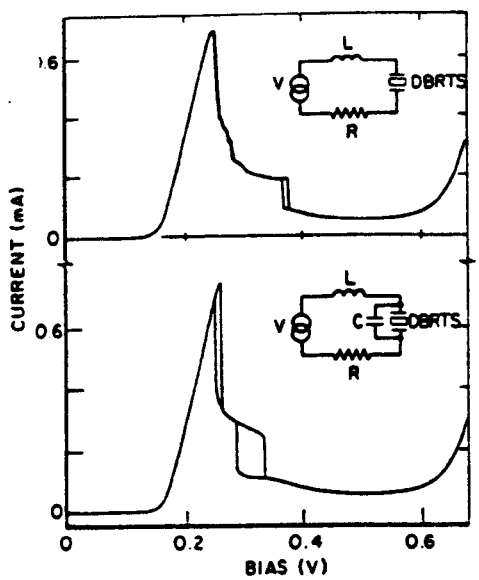

Figure 4.4: Current-voltage characteristics reported by Goldman *et al.* [173] showing two regions of bistability.

A more serious objection was raised by Sollner [174] who pointed out that the $I(V)$ curve was dependent on the parameters of the external circuit, in particular the width of the bistable region was shown to change when a capacitor was connected in parallel with the device. The double-stepped decrease in the current is characteristic of measurements taken when the device is undergoing high-frequency oscillations as shown in the following section.

Evidence for charge buildup

Despite these doubts over the observation of bistability, the buildup of space charge in the quantum well at resonance was clearly established by both high magnetic field [140, 177] and by photoluminescence [178] investigations. Magnetotransport measurements of charge buildup will be described in more detail in Section 4.7. Basically, these investigations make use of the fact that when charge builds up in the well the voltage drop across the emitter increases less rapidly as a function of the total applied bias than it does when the device is biased off-resonance, due to the screening effect of the electrons in the well.

When the emitter is heavily-doped (three-dimensional) magnetoquantum oscillations occur whenever a Landau level of the well passes above the emitter Fermi energy as described by Mendez *et al.* [139]. The period of these oscillations is related to the position of the energy level in the well relative to the Fermi energy in the emitter, and hence the bias-dependence of the energy level and of the space charge density in the well are obtained. For the devices investigated by Goldman *et al.* [140] and by Payling *et al.* [177], the charge in the well was estimated to be $\sim 10^{11}$ cm^{-2} in agreement with the theoretical calculations of Sheard and Toombs [99]. Samples with a two-dimensional emitter state have been investigated by several authors [108, 182, 200, 201, 202]. Here the charge buildup is revealed by a region of bias where the number density in the emitter remains constant allowing a value to be deduced for the charge density in the well. These results will be the subject of Section 4.7.

Young *et al.* [178, 203] measured the photoluminescence intensity from a resonant tunnelling device due to the recombination of photo-created holes and tunnelling electrons. They found that there was a large increase in intensity when the device was biased on resonance. Although their calibration of the electron density from the integrated PL intensity has been challenged by Frensley *et al.* [204, 205], these results provide clear evidence of charge buildup. Photoluminescence has proved to be a most fruitful technique for investigating space charge effects in these devices [206, 207].

4.2.3 Conclusion

The buildup of charge in the well on resonance and the consequent hysteresis in the current-voltage characteristics are well-founded theoretically and charge buildup has been experimentally verified by several groups. However, the claims of Goldman *et al.* [173] to have observed a bistability intrinsic to the device must be regarded as unproven due to the possible external origins of bistability, these are the subject of the next section.

4.3 Extrinsic Bistability

One of the main reasons for the renewed interest in resonant tunnelling devices in recent years has been the experiments of Sollner and colleagues [12, 33] who have demonstrated detection and mixing of submillimetre radiation by resonant tunnelling devices at frequencies of up to 4 THz, as well as the production of oscillators with fundamental frequencies in excess of 400 GHz [34]. Oscillations in the voltage and current in a resonant tunnelling device occur when the device is biased in the region of negative differential resistivity. These oscillations have aroused considerable interest in the production of high-speed devices. Both fundamental research and possible practical applications depend on the correct understanding of the conditions leading to oscillation and the ability to stabilize the device against such oscillations. It is well-known from studies of the Esaki diode, whose current-voltage characteristics are broadly similar to those of resonant tunnelling devices, that the onset of oscillation often appears as an inflection or step in the DC current. Therefore, negative differential resistance can lead to step-like structure in the $I(V)$ characteristics, obscuring useful information contained in the 'true' DC curve, for example the phonon emission assisted transitions described in Section 3.4. In response to Goldman *et al.'s* [173] suggestion that hysteresis in $I(V)$ is an intrinsic phenomenon caused by space charge, discussed in the preceding section, Sollner [174] pointed out that the occurrence of high-frequency oscillations could produce a bistable behaviour governed by the nature of the measuring circuit and not just by the properties of the tunnelling device itself. Although the need to measure the stable $I(V)$ curve has been recognized for some time [208, 22], the controversy over intrinsic bistability has led to a large number of recent studies of the effect of current oscillations on the DC characteristics [141, 176, 209, 210, 211, 212].

This section describes the circuit oscillations and the theoretical conditions for stable operation of the device. A simple simulation of the device is used to show how oscillations can produce hysteresis in the time-averaged $I(V)$ curve. The results are compared to the measured $I(V)$ and current oscillations of an actual device. The effect of external circuit parameters on the bistability is discussed and finally a stable $I(V)$ curve is obtained.

4.3.1 Stability

The simplest model for a circuit containing a resonant tunnelling device is a negative resistance element $-r$ in parallel with a capacitor C connected to a voltage source E via leads of resistance R and inductance L. The capacitor may represent the internal capacitance of the device or an external component. This simple circuit is shown in Figure 4.5 where J is the total current in the external circuit, I is the current flowing through the device and V is the voltage drop across the device. The impedance of this circuit is

$$Z = R - \frac{r}{1+\omega^2 C^2 r^2} + i\left(\omega L - \frac{\omega C r^2}{1+\omega^2 C^2 r^2}\right) \tag{4.10}$$

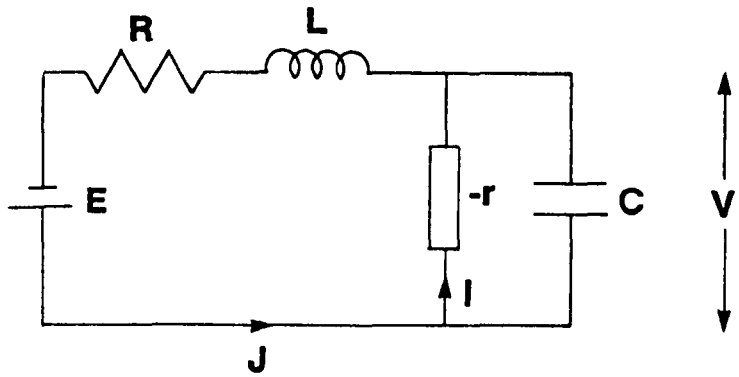

Figure 4.5: Simple equivalent circuit for a double barrier device.

The reactance is zero at a frequency of

$$f_0 = \frac{1}{2\pi}\left(\frac{1}{LC} - \frac{1}{(rC)^2}\right) \tag{4.11}$$

and the circuit has negative differential resistance for frequencies below

$$f_R = \frac{1}{2\pi rC}\sqrt{\frac{r}{R} - 1} \tag{4.12}$$

If $f_0 < f_R$ the circuit will oscillate.

For a more general device, the resistance is a function of the voltage drop across the device and is given by the current-voltage characteristics $I(V)$, therefore we replace $-r$ in the above circuit by $r = dV/dI$. The stability of the circuit can be considered by inspecting the differential equations governing the total current J and the device voltage V

$$V = E - RJ - L\dot{J} \tag{4.13}$$

$$J = C\dot{V} + I(V) \tag{4.14}$$

There are fixed points at $V_0 = E - RJ_0$; $J_0 = I(V_0)$ which simply correspond to the intersections of the load line with the current-voltage characteristics, as shown in the schematic diagram in Figure 4.6. The stability in the neighbourhood of the fixed point can be investigated by considering a small deviation given by $(V_0, J_0) \rightarrow (V_0 + v, J_0 + j)$. The time development of this deviation is given by

$$L\dot{j} = -Rj - v \tag{4.15}$$

$$C\dot{v} = j - v/R \tag{4.16}$$

The general solution for these equations is

$$v(t) = Ae^{\lambda_1 t} + Be^{\lambda_2 t} \tag{4.17}$$

where

$$\lambda_{1,2} = \tag{4.18}$$

$$-\frac{1}{2}\left(\left(\frac{R}{L} + \frac{1}{rC}\right) \pm \sqrt{\left(\frac{R}{L} + \frac{1}{rC}\right)^2 - \frac{4}{LC}\left(1 + \frac{R}{r}\right)}\right)$$

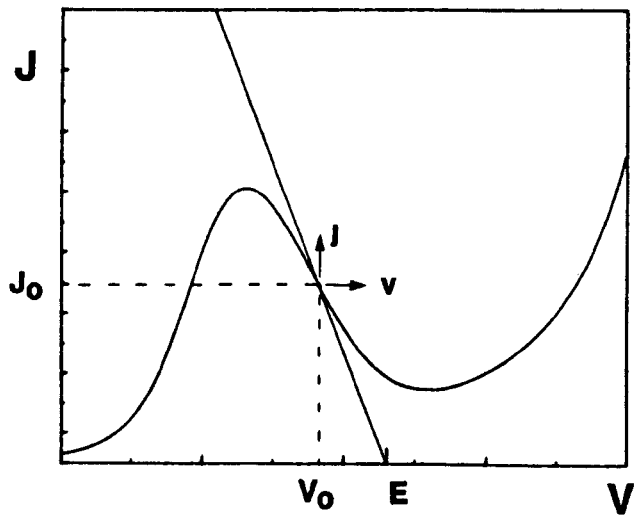

Figure 4.6: Schematic diagram showing the fixed points given by the intersection of the load line with $I(V)$.

which can be parameterised as

$$\lambda_{1,2} = -\frac{R}{2L}\left(\left(1+\frac{\beta}{\alpha}\right) \pm \sqrt{\left(1+\frac{\beta}{\alpha}\right)^2 - \frac{4\beta}{\alpha}}\right) \tag{4.20}$$

with

$$\alpha = \frac{R^2}{LC} \text{ and } \beta = \frac{R}{r} \tag{4.21}$$

If the real parts of λ_1 and λ_2 are negative, any disturbance dies away and the system is stable. On the other hand, if $Re(\lambda_1), Re(\lambda_2) > 0$ the disturbance grows and the system is unstable. The case in between, with $Re(\lambda_1) < 0$ and $Re(\lambda_2) > 0$ corresponds to a saddle point in phase space and is considered in Section 4.3.5. If there is also an imaginary component, *i.e.* $\lambda = \gamma + i\omega$, then $v(t) = A(e^{\gamma t} + e^{i\omega t})$, in which case v and $\jmath$ oscillate about the fixed point, either with decreasing amplitude ($\gamma < 0$) or increasing amplitude ($\gamma > 0$). The latter usually results in the formation of a limit cycle and steady oscillatory behaviour. The five possible situations are illustrated in the plot of Figure 4.7. The condition for stability is $\beta \geq -\alpha$, *i.e.*

$$\frac{1}{|r|} \geq \frac{R}{LC} \tag{4.22}$$

and that for λ to have no imaginary part is

$$\alpha - 2\sqrt{\alpha} \leq \beta \leq \alpha + 2\sqrt{\alpha} \tag{4.23}$$

As the voltage across the device is increased, the value of r, and hence that of β, change as shown in Figure 4.8. When $r > 0$, the circuit is always stable, so as the voltage is swept up the resonant peak there are no current oscillations at equilibrium. Whether or not there are transient oscillations before the device settles to equilibrium depends on which section of Figure 4.7 point (α, β) is in. For a typical device one might expect that the high resistance section at low

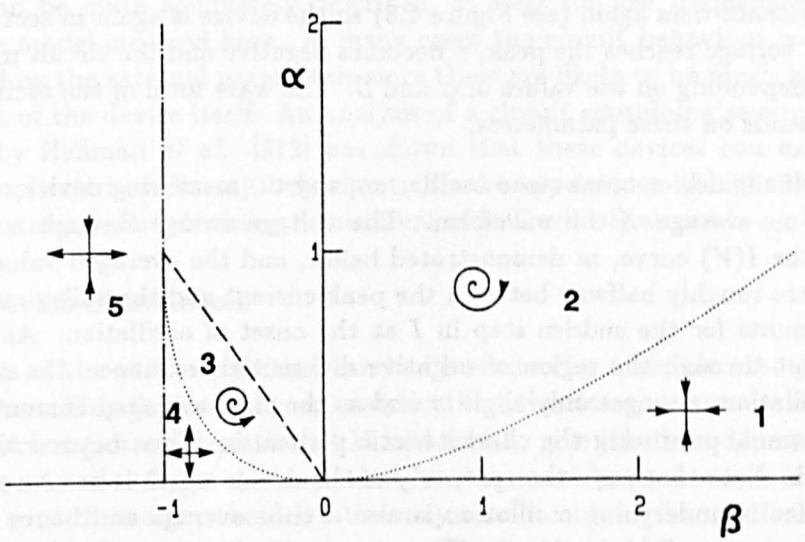

Figure 4.7: Diagram showing the stability or otherwise of a double barrier device as a function of $\beta = R/r$ and $\alpha = R^2/LC$.

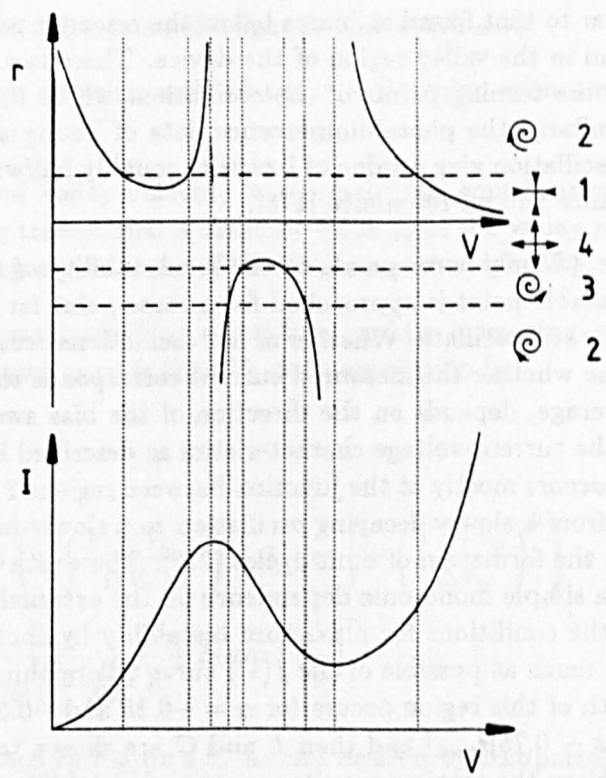

Figure 4.8: Schematic diagram showing the variation in the differential resistance of a typical double barrier device and the different oscillatory behaviour that can be obtained as the bias voltage is swept.

bias would be in section 2 (*i.e.* damped oscillation), the low resistance section as the device comes on to resonance in section 3 (no oscillation at all) and then, as the voltage climbs up to the peak of the resonance, the differential resistance rises again (see Figure 4.8) so the device is again in section 2. Once the voltage reaches the peak, r becomes negative and the circuit may oscillate — depending on the values of α and β. The wave form of the oscillations also depends on these parameters.

If the device breaks into oscillation, any DC measuring device simply takes a time-average of the waveform. The voltage swings through a wide range of the $I(V)$ curve, as demonstrated below, and the averaged value lies somewhere roughly halfway between the peak current and the valley current. This accounts for the sudden step in I at the onset of oscillation. As the bias is swept through the region of negative differential resistance, the range of the oscillations changes only slightly and so the time-averaged current is roughly constant, producing the characteristic plateau in I just beyond the resonant peak. Note that any other property of the device which is measured while the device is undergoing oscillation is also a time average and hence an average over a range of bias voltages. For example, Payling *et al.* [177] reported magnetotransport measurements on a bistable part of the $I(V)$ curve and obtained different values of magnetic field period on the two sections of the curve. Off resonance they observed a single period corresponding to the accumulation layer charge, and on the oscillating part of the curve they observed two series: one similar to that found at biases below the resonant peak and one similar to that found in the valley region of the device. These two regions of bias correspond to the turning points of the oscillations where the device spends most time. Similarly, the photoluminescence data of Young *et al.* in the region of current oscillation give a value of intensity roughly halfway between the values on resonance and off-resonance [178].

Figure 4.7 only corresponds to the *local* stability of the circuit. If an apparently stable point is approached from some point far from equilibrium the circuit may still oscillate. Whether or not oscillations occur at a particular voltage, and so whether the measured current corresponds to the true DC value or a time-average, depends on the direction of the bias sweep, leading to bistability in the current-voltage characteristics as described by Sollner [174]. This situation occurs mostly at the junction between regions 2 and 3, where there is a change from a slowly decaying oscillation to a slowly increasing one. This is related to the formation of limit cycles [212]. The width of the bistability will not have a simple monotonic dependence on the external parameters. We can estimate the conditions for maximum bistability by choosing the parameters so that as much as possible of the $I(V)$ curve falls within region 3. The maximum width of this region occurs for $\alpha = -0.25$ and $-0.25 > \beta > -0.75$, so if R is set as $\sim 0.75|r_{min}|$ and then L and C are chosen to make $\alpha = 0.25$ this should achieve the maximum voltage range of bistability. Although increasing the value of the capacitance will eventually lead to stability (if $\alpha \geq 1$ then the circuit is always stable) as claimed by Goldman *et al.* [173], it can also lead to an increase in the width of the bistable region which is exactly the effect Goldman *et al.* observed.

More complex equivalent circuits have been proposed to provide a more

physically realistic model of a resonant tunnelling device [195, 213, 113] including elements such as a negative inductance to account for the time delay in charging the quantum well. However the main features of the circuit behaviour can be quite adequately described, at least for low frequencies, by the simple model outlined here. In many cases the circuit behaviour will be dominated by the external parameters since these are likely to be much higher than those of the device itself. An analysis of a circuit containing several LC elements by Hellman *et al.* [212] has shown that these devices can exhibit rather complicated oscillatory behaviour with the appearance of higher order limit cycles and period doubling reminiscent of a 'Devil's Staircase'.

4.3.2 Device Simulation

The results of the previous section can be illustrated by a simple model of a resonant tunnelling device using an analytical function to represent the device $I(V)$ characteristics and equations 4.13 and 4.14 to give the time dependence of the current and voltage. An analytical function was chosen because it simplifies the procedure since the derivative may also be obtained analytically — which speeds up the numerical processing. The basic principles can be illustrated using any simple function that shows negative differential resistance, for example a simple cubic. In order to accurately reproduce the current-voltage curve of a real device the function used contained several terms:

- The main peak: a Gaussian of height I_r and width ΔV_r.
- The LO phonon emission assisted peak: a Gaussian with amplitude I_p and width ΔV_p.
- The background valley current, to represent the contribution from $k_\perp$ non-conserving transitions: a constant value I_e in the valley region with a smoothed step at the onset of the resonance of width ΔV_e.
- The non-resonant tunnelling current: a rapidly increasing exponential function for biases greater than V_0, with amplitude I_0.

$$I(V) = I_r \exp\left(-\left(\frac{V-V_r}{\Delta V_r}\right)^2\right) + I_p \exp\left(-\left(\frac{V-V_p}{\Delta V_p}\right)^2\right) + \frac{I_e}{1+\exp\left(-\frac{V-V_r}{\Delta V_e}\right)} + I_0 \exp\left(\frac{V}{V_0}\right)^3 \tag{4.24}$$

This function is plotted in Figure 4.9. As can be seen by comparing this with Figure 3.15 for sample *NU104*, a good approximation to the device characteristics is obtained.

Combining equations 4.13 and 4.14 gives

$$LC\ddot{V} + \left(RC + \frac{L}{r}\right)\dot{V} + V + RI(V) - E = 0 \tag{4.25}$$

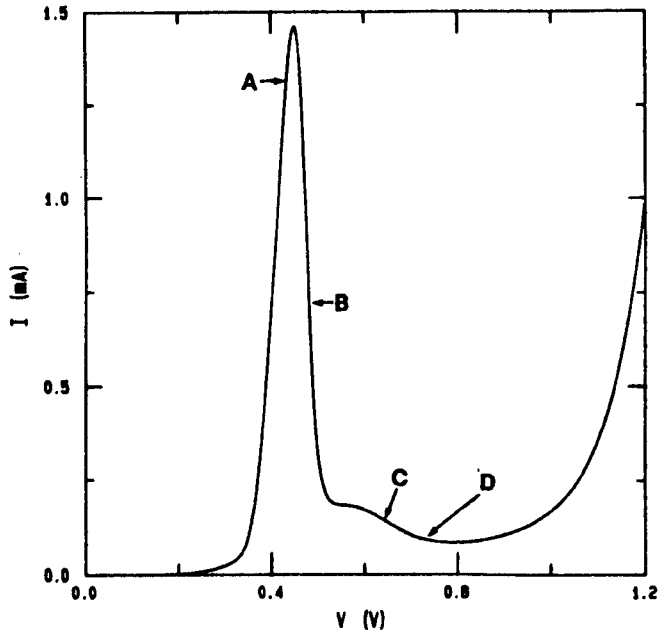

Figure 4.9: Plot of the analytical function used to simulate a typical resonant tunnelling characteristic.

where we have used $dI/dt = dI/dV \times dV/dt = \dot{V}/r$. This can be used to generate values of V and J at successive time intervals δt given the initial conditions $V_{i=0}$ and $V_{i=1}$.

$$\begin{aligned} V_{n+1}\left(1+\frac{\delta t}{2}\left(\frac{R}{L}+\frac{1}{rC}\right)\right) & \\ = V_n\left(2-\frac{\delta t^2}{LC}\right)+V_{n-1}\left(\frac{\delta t}{2}\left(\frac{R}{L}+\frac{1}{rC}\right)-1\right) & \\ +\frac{\delta t^2}{LC}(E-RI(V_n)) & \qquad (4.26) \end{aligned}$$

$$J_n = I(V_n)+C\left(\frac{V_{n+1}-V_{n-1}}{2\delta t}\right) \qquad (4.27)$$

This is incorporated in a simple computer program and used to simulate the time-development of the oscillations [214]. Figure 4.10 shows typical plots of V and J against time at several different bias voltages, illustrating the behaviour discussed in the last section. At A, the differential resistance is positive and low and so the system is stable. At point B, r is low and negative producing oscillations with rather complex, irregular waveforms. Note that the exact form of these is dependent on the time step used in the algorithm. At C, the differential resistance is still negative but has a higher magnitude so λ now has an imaginary component leading to the formation of a steady limit cycle and the current and voltage oscillate almost sinusoidally. Finally, at point D the resistance is again positive, but large enough to produce exponentially damped transient oscillations. Note the difference between the two types of oscillatory behaviour at B and C: at B the total current J closely follows the sample

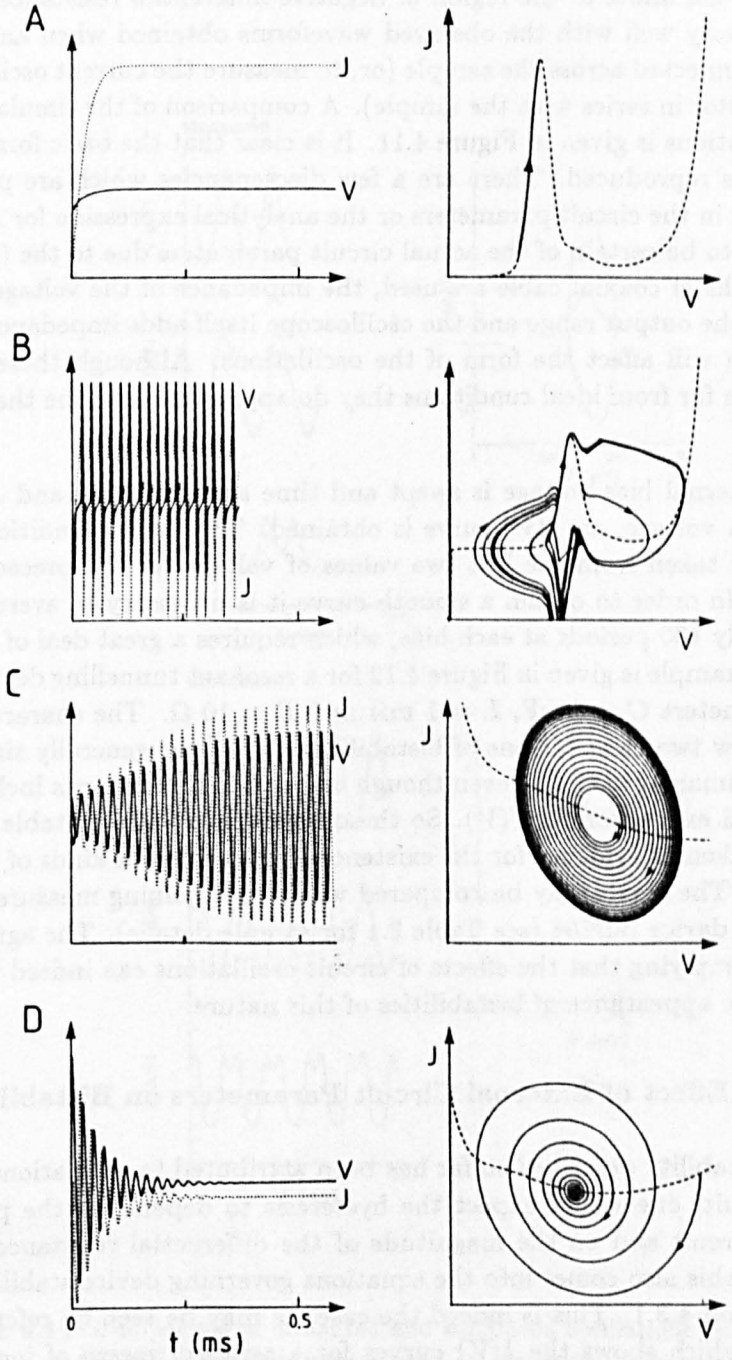

Figure 4.10: Simulated waveforms for a double barrier device at several points on the $I(V)$ curve of Figure 4.9.

current I for much of the time, only deviating in the rapid loops at the end points of the oscillation, whereas at point C the total current and the sample current are only equal at two points. In both cases, the total current can swing well beyond the limits of the region of negative differential resistance. These plots agree very well with the observed waveforms obtained when an oscilloscope was connected across the sample (or, to measure the current oscillations, across a resistor in series with the sample). A comparison of the simulated and actual oscillations is given in Figure 4.11. It is clear that the basic form of the oscillations is reproduced. There are a few discrepancies which are probably due to errors in the circuit parameters or the analytical expression for $I(V)$. It is very hard to be certain of the actual circuit parameters due to the fact that several lengths of coaxial cable are used, the impedance of the voltage source depends on the output range and the oscilloscope itself adds impedance to the circuit which will affect the form of the oscillations. Although these results were taken in far from ideal conditions they do approximate to the theoretical simulations.

If the external bias voltage is swept and time averages of V and J calculated at each voltage, an $I(V)$ curve is obtained. The initial conditions $V_{i=0}$ and $V_{i=1}$ are taken from the last two values of voltage for the preceding external bias. In order to obtain a smooth curve it is necessary to average over approximately 100 periods at each bias, which requires a great deal of computation. An example is given in Figure 4.12 for a resonant tunnelling device with circuit parameters $C = 1$ μF, $L = 1$ mH and $R = 10$ Ω. The characteristics obtained show two clear regions of bistability and appear generally similar to those of Goldman *et al.* [173], even though only one resonance was included in the analytical expression for $I(V)$. So the observation of two bistable regions can *not* be taken as evidence for the existence of two different kinds of state in the emitter. The result may be compared with the adjoining measured characteristics of device *NU104* (see Table 2.1 for sample details). The agreement is excellent, implying that the effects of circuit oscillations can indeed be used to explain the appearance of bistabilities of this nature.

4.3.3 The Effect of External Circuit Parameters on Bistability

Since the bistability described so far has been attributed to oscillations in the external circuit, one would expect the hysteresis to depend on the parameters of the circuit and on the magnitude of the differential resistance of the device, since this also comes into the equations governing device stability outlined in Section 4.3.1. This is indeed the case, as may be seen be referring to Figure 4.13 which shows the $I(V)$ curves for a series of mesas of increasing diameter (4 μm–10 μm) of sample *NU104*: (a) with no external capacitor and (b) with a 10 μF capacitor in parallel with the devices. For the set of curves without a parallel capacitance, the low current curves show bistability and the high current curve (large diameter mesa) does not. This is because the lower resistance in the larger sample leads to oscillations similar to those shown in Figure 4.10B rather than limit cycle formation which occurs for the higher resistance mesas. The width of the current plateau, *i.e.* the range over which the device oscillates, increases as the current increases as a consequence of the stability condition $1/|r| > R/LC$. When a parallel capacitor is added, all the

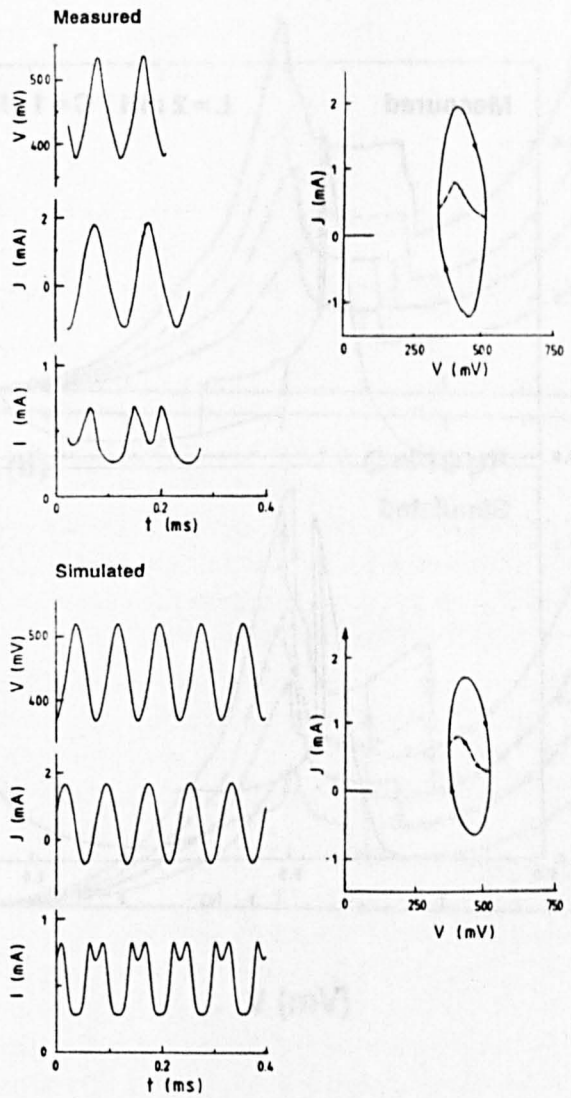

Figure 4.11: Comparison of measured and simulated oscillations for sample *NU104* at a bias of 470 mV. The parameters used to generate the simulated curves were $L = 1$ mH, $C = 1$ μF and $R = 20$ Ω.

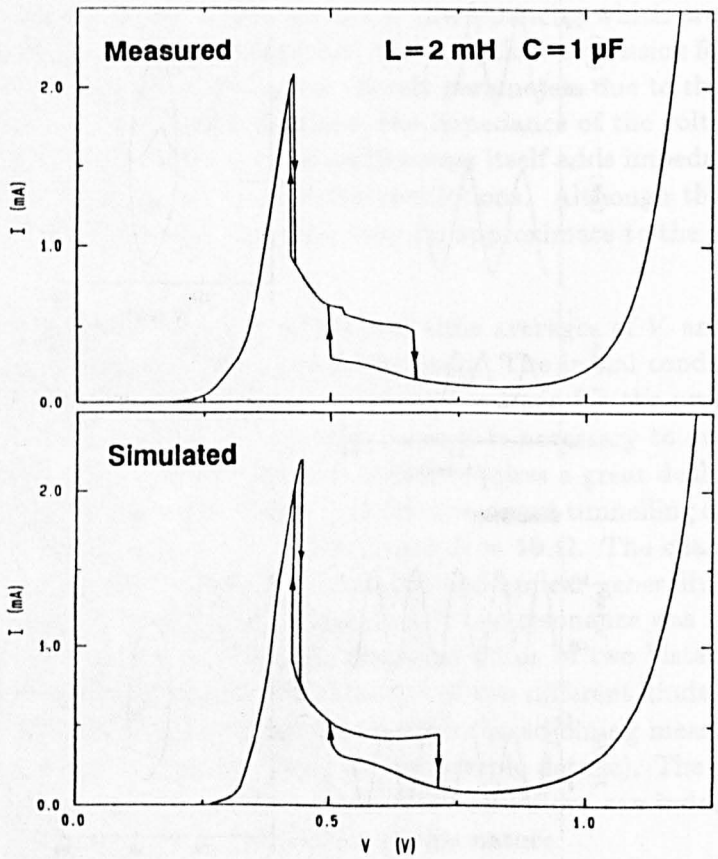

Figure 4.12: Simulated and measured characteristics of a 10 μm diameter mesa of sample *NU104* when the device is undergoing high-frequency oscillations, showing how the simulation is able to accurately reproduce *both* regions of bistable behaviour.

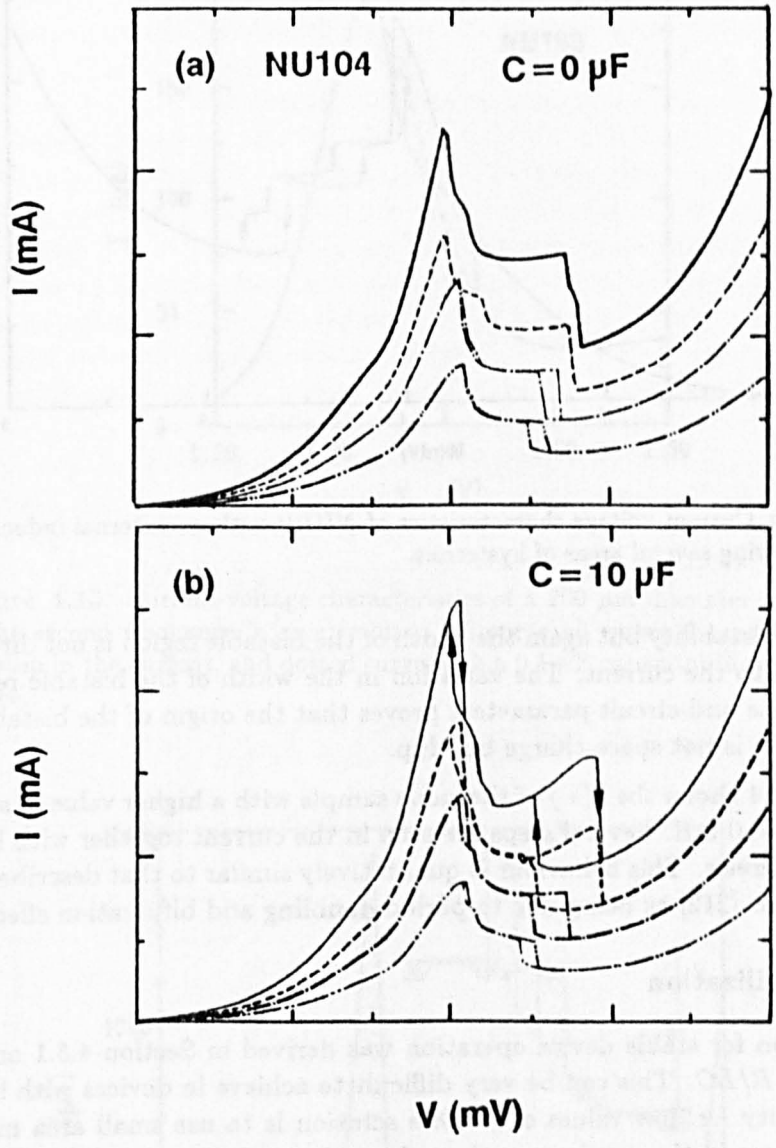

Figure 4.13: Current-voltage characteristics of *NU104* for a set of mesas of increasing size in the range 4 (bottom trace) to 10 μm (top trace), (a) with no external capacitance, (b) with a 1 μF capacitor in parallel with the devices.

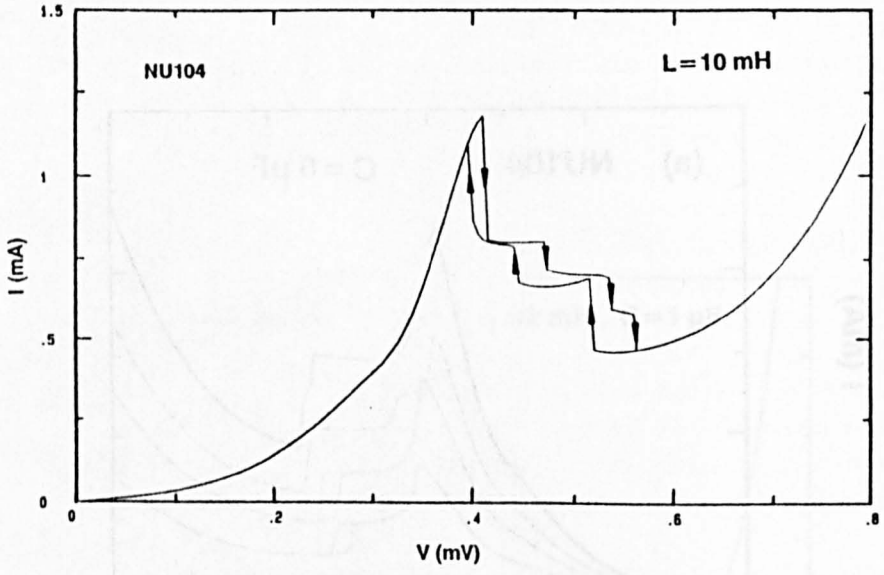

Figure 4.14: Current-voltage characteristics of *NU104* with an external inductance of 10 mH showing several areas of hysteresis.

mesas show bistability but again the width of the bistable region is not directly proportional to the current. The variation in the width of the bistable region with mesa size and circuit parameters proves that the origin of the bistability in this sample is not space charge buildup.

Figure 4.14 shows the $I(V)$ of the same sample with a higher value of series inductor, L =10 mH. Several steps are seen in the current together with large areas of hysteresis. This behaviour is qualitatively similar to that described by Hellman *et al.* [212] as being due to period doubling and bifurcation effects.

4.3.4 Stabilization

The condition for stable device operation was derived in Section 4.3.1 and is that $1/|r| < R/LC$. This can be very difficult to achieve in devices with large current density *i.e.* low values of r. One solution is to use small area mesas similar to those in the previous section where the peak currents are less than $\sim$ 1 mA. An alternative approach is to restrict the current by fabricating samples with thick barriers and therefore low tunnelling probability. A good example of this is sample *NU183* which has barriers of thickness 83 and 111 Å where the current at the first resonance in reverse bias is so low, < 1 μA, that the device is stable without the need for external capacitance — see the $I(V)$ characteristics given in Figure 3.37. Figure 4.15 shows the second resonance in reverse bias which has a higher current and undergoes oscillations (note the characteristic step shape after the peak). When a 0.1 μF capacitor is connected in parallel with the device, the oscillations are suppressed and a smooth $I(V)$ is obtained. Further results on stabilization with an external capacitor are given in Foster *et al.* [176].

A different approach to device stabilization was first applied to resonant tunnelling devices by Gavrilovic *et al.* [22] who used a parallel resistor instead of a capacitor. This simply makes the net resistance of the device and the ex-

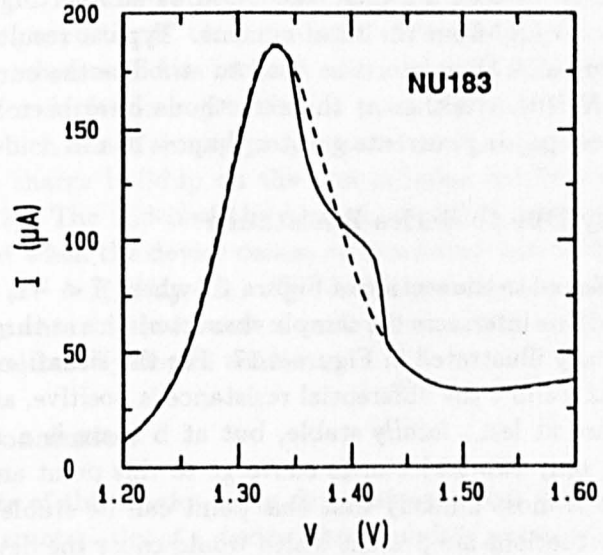

Figure 4.15: Current-voltage characteristics of a 200 μm diameter mesa of *NU183* at the second resonance in reverse bias: full curve no external capacitance — note the step in the current, and dotted curve with a 0.1 μF capacitor in parallel with the device.

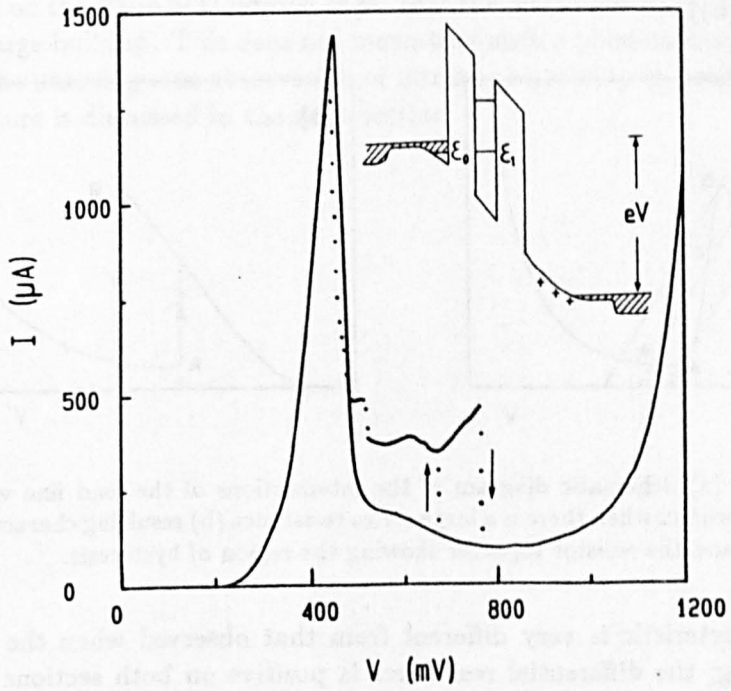

Figure 4.16: Current-voltage characteristics of *NU104* with (full line) and without (dotted line) a stabilising resistor in parallel with the device.

ternal resistor positive — even in the region of negative differential resistance *i.e.* $R_p + r > 0$ [182, 148], thereby preventing oscillation. The $I(V)$ characteristics of the device on its own are then calculated by subtracting the current through the resistor V/R_p from the total current. Typical results are shown in Figure 4.16 where a 20 Ω resistor was used to stabilize the current-voltage characteristics of *NU104*. Neither of these methods have been found to be successful for devices passing currents greater than ~ 10 mA.

4.3.5 Bistability Due to Series Resistance

We have not yet referred to the section of Figure 4.7 where $\beta < -1$, *i.e.* $R > |r|$. In this case the load line intersects the sample characteristics at three points a,b and c as schematically illustrated in Figure 4.17. For the situation depicted in the figure, at points a and c the differential resistance is positive, and therefore these two points are at least *locally* stable, but at b there is a *saddle point* in phase-space *i.e.* only two trajectories converge to this point and all others diverge from it. It is most unlikely that this point can be stable in any real situation where fluctuations are present which would cause the device to move away from this point. Hence the behaviour of the sample is governed by the conditions at the two other fixed points. If these are stable then the device remains at one or other of these points, depending on the direction of the bias sweep. If the bias is swept down through the resonance, the device follows the low-current portion of the curve until it reaches point A, where it switches to the high-current curve. Similarly, if the bias is swept in the opposite direction, the device follows the high-current curve before switching down at point B. Therefore there is hysteresis in the measured current-voltage characteristics (Figure 4.17(b)).

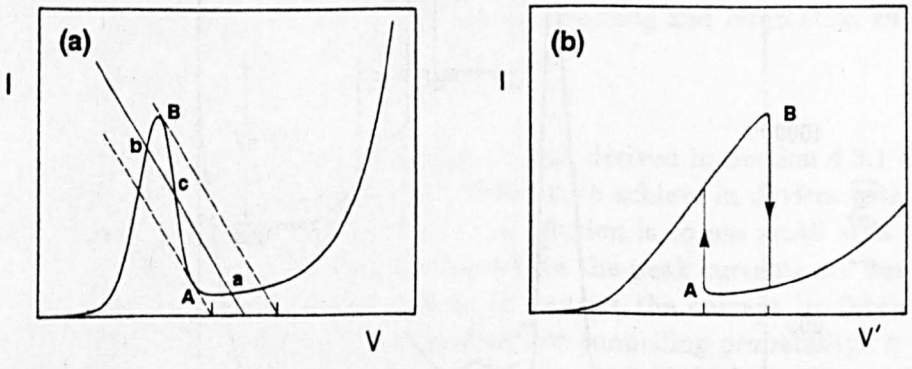

Figure 4.17: (a) Schematic diagram of the intersections of the load line with the device characteristics when there is a large series resistance (b) resulting characteristics for the device and the resistor together showing the region of hysteresis.

This characteristic is very different from that observed when the device was oscillating; the differential resistance is positive on both sections of the curve and there is no plateau in I. If one of the fixed points has negative differential resistance and undergoes oscillation, the device can switch between a stable state and a limit-cycle oscillation [212]. The bistable characteristics due to series resistance are rather similar to those expected for the intrinsic effect (compare Figures 4.17 and 4.3), which could lead to confusion. This

similarity is not surprising since both effects involve a voltage drop which is in series with that across the double barrier region and which increases with the current. The difference is that for the extrinsic effect this voltage drop is directly proportional to the current flow and takes place across a series resistance; whereas in the intrinsic case the voltage is mainly dropped across the collector depletion region and is governed by the electrostatic charge in the well which is not simply proportional to the current (due to the effect of increasing charge buildup on the transmission coefficients of the barriers — Section 4.2). The width of the bistable region is proportional to the drop in the current when the device comes off resonance and to the value of the series resistance $\Delta V \sim R_S/(I_p - I_v)$. The series-resistance-induced bistability can be avoided by ensuring low contact resistances and low currents *e.g.* with thick barriers and heavily-doped contacts.

4.3.6 Conclusion

The results of this section have demonstrated that bistability in the current-voltage characteristics of a device which exhibits negative differential resistance may be caused by extrinsic effects, such as high-frequency oscillations or large values of series resistance, which are properties of the measuring circuit rather than of the device itself. These effects can be satisfactorily modelled using a simple equivalent circuit model which reproduces both the time-averaged $I(V)$ curve and the form of the oscillations. Devices which show regions of bistability very similar to those assigned by Goldman *et al.* to the intrinsic effect [173] can be stabilized against oscillation by the addition of a capacitor or a resistor in parallel with the device. This procedure eliminates the bistable region, casting doubt on the claim of Goldman *et al.* that the bistability they observed was due to charge buildup. This does not mean that such a phenomenon does not exist and the unambiguous observation of intrinsic bistability in a suitably-designed structure is discussed in the next section.

4.4 Intrinsic Bistability in an Asymmetric Device

As we have seen in the preceding sections, there is a well-justified theoretical basis for bistability in the current-voltage characteristics of resonant tunnelling devices due to electrostatic feedback, however care must be taken to eliminate external causes of bistable behaviour, since devices showing hysteresis under some conditions may not do so with a different configuration of the external circuit. This section describes how these difficulties may be overcome and an unambiguously intrinsic effect observed.

4.4.1 Device Parameters

In order to observe a genuinely intrinsic bistability, it is necessary to maximize the conditions favouring the buildup of space charge and to prevent bistability due to extrinsic causes. The width of the bistable region was shown by Sheard and Toombs [99] to be governed by equation 4.5; $\Delta V = Q_m/C_2$ where Q_m is the maximum charge in the well (given in equation 4.2.1) and C_2 is the capacitance of the collector barrier and depletion region.

The following four steps can be taken into account when designing a sample to show the intrinsic effect:

1. Minimize the transmission coefficient of the collector barrier relative to that of the emitter barrier [179]. This enhances the charge buildup (see equation 4.2.1). There are two means of achieving this; making one barrier thicker than the other as reported by Alves *et al.* [180, 182] or one barrier higher (*i.e.* with a greater aluminium concentration) as reported by Zaslavsky *et al.* [181]. When the device is biased appropriately, electrons tunnel into the well through the thin(low) emitter barrier but are inhibited from tunnelling out to the collector by the low transmission coefficient of the thick(high) second barrier. This retains space charge in the well [179]. In the opposite sense of bias, the barrier asymmetry has the opposite effect and there is very little charge buildup (see the schematic band diagrams in Figure 4.18).

2. Decreasing the capacitance of the collector region $C_2 = \varepsilon_0\varepsilon_r/(\lambda_s + b_2 + w/2)$. Increasing the screening length in the collector contact by reducing the doping level will magnify the electrostatic feedback effect.

3. A large value of k_F in the emitter contact will lead to a larger charge concentration in the well since $Q_m = ek_F^2/2\pi\ T_e/(T_e+T_c)$ (equation 4.5). Therefore the doping in the emitter side should be high *i.e.* the doping, as well as the barrier thicknesses, should be asymmetric.

4. The barriers should be thick to reduce the resonant current densities so making it easier to stabilize the device against high frequency oscillation (Section 4.3.4) and to avoid hysteresis due to external series resistance (Section 4.3.5).

Device *NU183* consists of a 58 Å wide quantum well in between $(Al_{0.4}Ga_{0.6})As$ barriers, one 83 Å thick and one 111 Å thick. The detailed layer structure is

given in Table 2.1. The doping on either side of the double barrier structure is 10^{16} cm^{-3} for 500 Å. This doping level was chosen to maximize the voltage drop in the collector region (point 2 above) but was symmetrical and so did not take full advantage of point 3. A transfer matrix calculation of the energy levels in this device shows one level at an energy of 67 meV above the band edge and one at ~220 meV. The disadvantage of an asymmetry in barrier thickness, as opposed to an asymmetry in barrier height, is that the threshold voltage depends on bias direction — making comparison between the two directions less clear cut, however problems associated with thermal excitation of carriers over the lower barrier are avoided.

4.4.2 Effect of a Two-Dimensional Emitter State on Charge Buildup

One consequence of the low doping level in the emitter contact region is that when a bias is applied to the device a quasi-two-dimensional bound state is formed in the accumulation layer potential adjacent to the emitter barrier. As described in Section 1.5.5, this alters the condition for resonance. The two-dimensional nature of this state is verified by the dependence of the magnetoquantum oscillations in the tunnel current on the angle between the magnetic field direction and the normal to the barrier interfaces as described in Section 3.3. The device comes onto resonance when the energy of the quasi-bound state in the emitter essentially coincides with that of one of the states in the well. Here we neglect any anti-crossing effects [200] since a simple calculation shows that the level repulsion is much less than the energy width of the levels (several meV — see Section 3.2) given the relatively thick barriers in this sample. The tunnelling rate from the emitter to the well $F(V_e)$ is a sharply-peaked function of the voltage drop across the emitter barrier and accumulation region V_e. If the levels were truly bound, this would be a δ-function. Since tunnelling can occur, neither is strictly-speaking a bound state and they both have a finite energy width. Scattering processes also contribute to the broadening of the resonant peak as discussed in Section 1.5.3.

If space charge effects are neglected, the current peak is narrow, as shown schematically in Figure 4.18 (reverse bias). However, as the device is brought onto resonance, charge accumulates in the well. A small change in V_e corresponding to climbing up to the peak of $F(V_e)$ leads to a much greater change in the total bias ($\Delta V = \Delta V_e + \Delta Q_w/C_2$). The extra voltage is dropped almost entirely across the collector depletion region, due to the screening effect of the charge in the well. An electrostatic feedback mechanism similar to that for a three-dimensional emitter operates (see Section 4.2). In this case any adjustments in n_a are much smaller because the tunnelling rate is such a sharply-peaked function. V_e changes only slightly through the complete range of the resonance, so the sheet charge density in the 2D emitter state, $Q_e = en_a$, is also approximately constant as the charge builds up in the well (from Gauss's Law).

The maximum charge density in the well, $Q_w = en_w$, is the same as in the 3D case described in Section 4.2 and is given by equation 4.2.1. The charge density in the emitter is now directly related to the Fermi energy by

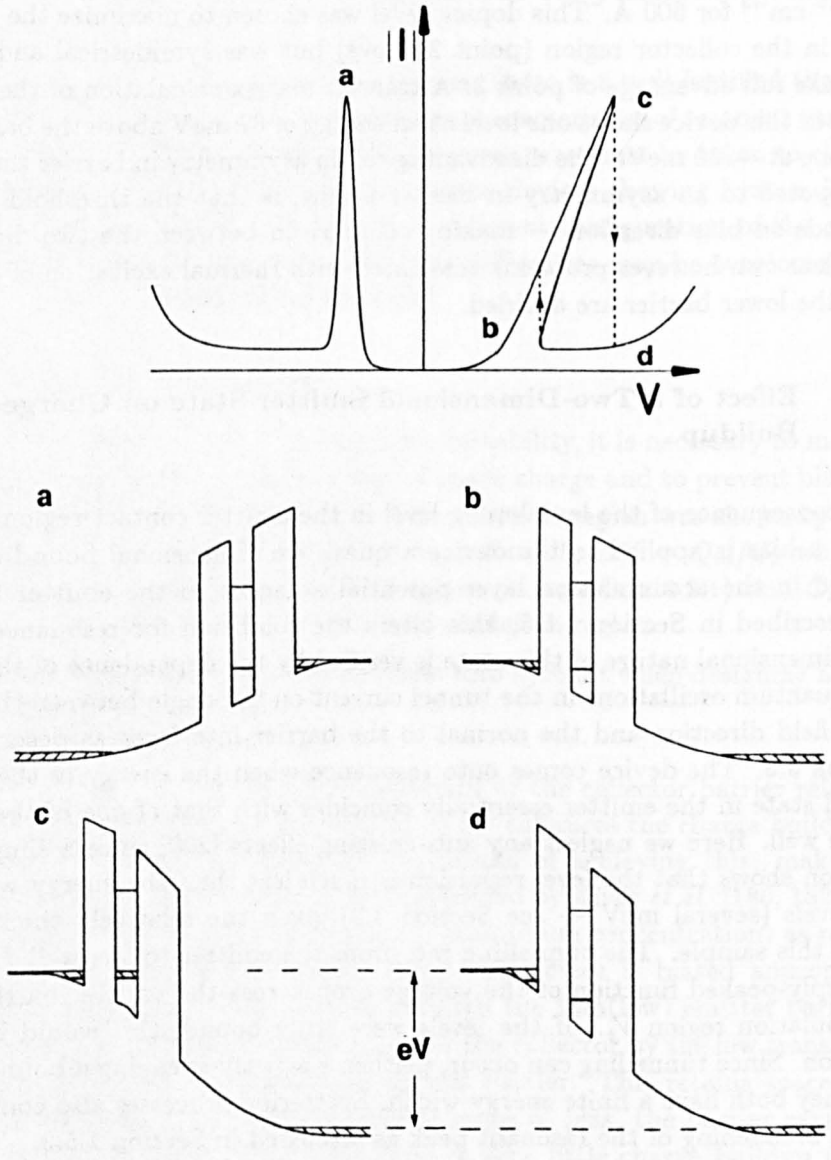

Figure 4.18: Schematic diagrams illustrating the effect of space charge buildup in an asymmetric double barrier structure with a two-dimensional emitter state. (a) When biased such that the thinner barrier is on the collector side of the well, the electrons easily escape from the well and there is no charge buildup. In this case the current is a sharply-peaked function of bias. (b) The device comes onto resonance when the bound states in the emitter and the well coincide; (c) if the collector barrier is thick, charge builds up in the well causing an additional voltage drop in the collector. (d) There is a state with the same applied bias with no charge in the well, therefore the device is bistable with the two charge distributions corresponding to different tunnel currents.

$n_w = k_F^2/2\pi$, so we can write

$$n_w = n_a \frac{\tau_c}{\tau_c + \tau_e} \tag{4.28}$$

where $n_{a,w}$ is the number density in the accumulation layer or well and $\tau_{c,e}$ is the dwell time of the electrons in the well for decay into collector or emitter states respectively. As in the three-dimensional case, the peak of the resonance is shifted by $\Delta V = Q_m/C_2$. Once the maximum charge density is attained, any further increase in bias forces n_a to increase, thereby increasing the voltage drop across the emitter barrier and taking the device off resonance. This causes the charge in the well to be ejected, that in the emitter accumulation layer to increase to compensate and leads to a large drop in the current as shown in Figure 4.18. Sweeping the voltage up and down reveals the hysteresis in the current-voltage characteristics. The effect should be more pronounced for a 2D emitter state because the resonance width without charge buildup is much smaller than when the emitter contact is heavily-doped.

It should be remembered that τ_e and τ_c in equation 4.28 are strongly dependent on the voltage drop across the barriers. Consequently, as charge builds up in the well τ_c varies, which in turn affects the amount of charge in the well — completing the feedback loop. Another possibly significant effect is the variation in the bound state energies with bias. The emitter bound state energy depends on the value of n_a since this determines the shape of the accumulation layer potential. Any adjustments in n_a therefore affect the resonance condition by changing both V_e and the bound state energy. The energy level in the well is affected by changes in the number density in two ways

- Stark effects: Changes in n_a or n_w alter the electric field in the well leading to a Stark shift of the energy level. The nonlinear distribution of charge within the well gives rise to a larger effect than the constant field due to the emitter charge (this contribution is zero to first order). A simple estimate of the energy shift is obtained from $< \psi|V(x)|\psi >$ where $V(x)$ is given by $\nabla^2 V = e|\psi^2|/\epsilon$ by taking the wavefunction to be $\psi = \sqrt{2/w}\cos(\pi x/w)$. This gives an energy change $\sim$ 3 meV for a charge concentration of $n_w = 2.2 \times 10^{11}$ cm^{-2}.

- Many-body effects: Electron interaction and correlation effects may be important at low temperatures and high concentrations of charge leading to a significant variation in the bound state energy as the well is charged. Coon and Bandara [198] have calculated that exchange effects are as much as one-half the straightforward electrostatic effects. Although this seems a surprisingly large effect, we have no way of measuring it.

Any changes in the energy level in the well as it fills with charge can be accommodated by small changes in the emitter charge keeping the two states aligned and so producing a further feedback mechanism. It was suggested by Ricco and Azbel [94] that, if the quasi-bound state in the well was very narrow, the electrostatic effect of space charge on the energy level would lead to oscillation *i.e.* a positive feedback mechanism. The finite width of the states leads instead to a negative feedback effect and no oscillations are observed.

Using the device parameters given above and a simple transfer matrix approach it is possible to calculate values of τ_c and τ_e. At zero applied bias these are $\tau_c \sim 0.8$ μs, $\tau_e \sim 25$ ns so one would expect the charge density in the well at the peak of the resonance to be approximately equal to that in the emitter (equation 4.5).

4.4.3 Current-Voltage Characteristics

The current-voltage characteristics $I(V)$ of a 200 μm diameter mesa of *NU183* at a temperature of 4 K are shown in Figure 4.19 [180, 182]. When the device is biased with the top contact positive, referred to as forward bias for this sample, the electrons tunnel into the well through the thinner barrier and out through the thicker barrier — leading to enhanced charge buildup. Both resonances in

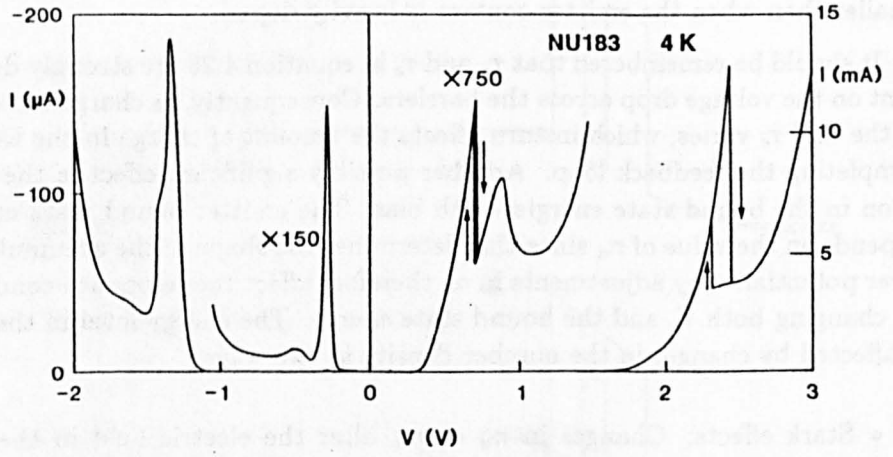

Figure 4.19: Current-voltage characteristics of a 200 μm diameter mesa of *NU183* at 4 K, clearly showing two regions of intrinsic bistability in forward bias.

this bias direction show clear regions of bistability. This bistability was found in all samples investigated regardless of mesa size and was reproducible to within very small fluctuations. In reverse bias, the electrons can easily tunnel out of the well, reducing charge buildup and no bistability is seen at either resonance. The difference in collector barrier thickness is also evident in the asymmetry in the widths of the resonances; in reverse bias the first resonance has a width of 50 mV compared to 400 mV for the corresponding resonance in forward bias. As mentioned in Section 4.3.4, the currents in reverse bias are low enough for the resonances to be easily stabilized. The peak-to-valley ratio at the first resonance in reverse bias is as high as 26:1 at 4 K, indicating the high-quality of the material and also that the large asymmetry in transmission coefficients does not destroy the resonant effect as some authors have suggested [94].

The device comes onto resonance at slightly lower biases in reverse bias than in forward bias: reverse $V_{th1} = -0.25$ V, $V_{th2} = -1.2$ V and forward $V_{th1} = 0.3$ V, $V_{th2} = 1.6$ V. This asymmetry reflects the fact that in forward bias a higher electric field is needed to produce the same voltage drop across the emitter barrier since this is the thin barrier in this bias direction. Therefore to

lower the well state to the same energy as the bound state in the accumulation layer requires a larger value of n_a and hence the applied bias must be greater. The asymmetry in the current values is the consequence of the charge buildup in the well increasing the transmission coefficient of the collector barrier and of the higher number density in the emitter at resonance.

The rough calculations presented in Section 3.2.2 indicated that the energy level in the well has an energy width of $\sim$ 4 meV, consistent with the narrow voltage width of the first resonance in reverse bias. The width of the resonance in forward bias from V_{th} to V_p, is an indication of the amount of charge buildup in the well. The voltage range from V_{th} to V_v, the point where the current switches up to the resonant state, relates to the energy width of the levels. It is surprising that such a wide resonance, implying a large buildup of charge, shows such a narrow region of bistability, $\sim$20 mV at 4 K. If the energy width of the state was the same as in reverse bias, one would expect the region of bistability to extend over almost the complete range of the resonance *i.e.* at least 300 mV. Broadening of the energy levels due to layer fluctuations *etc.* should be independent of the bias direction. There is no indication from the quality of the magneto-oscillations that the emitter state is any broader in forward bias. A possible explanation for the broadness of the energy levels in forward bias is that the buildup of charge in the well may bring in additional scattering mechanisms, for example electron-electron scattering, which broaden the energy levels. This will be discussed further in Section 4.6 in the context of the temperature dependence of the bistability width.

Subsidiary maxima beyond the main resonance can be seen for all the resonances. As described in Section 3.4 these are due to LO phonon-emission-assisted transitions. This feature is particularly pronounced for the first resonance in forward bias, this is associated with charge buildup in the well beyond the main resonance due to the LO phonon process.

The rapid increase in current at biases of 2.7 V and -1.9 V is caused by the onset of tunnelling through a single barrier, at these biases the top of the collector barrier is below the energy of the quasi-bound state in the emitter contact leading to a rapid increase in transmission coefficient.

4.4.4 Is the Bistability Intrinsic ?

Section 4.3 described the possible external causes of bistable behaviour. This section is intended to show how these can be ruled out as causes of the bistability observed in this sample. First, note that for both forward bias resonances dI/dV is positive on both branches of the $I(V)$ curve. For oscillation to occur it is necessary for the device to be biased at a point where the differential resistance is negative, this is not the case on either resonance and no oscillations in the current or voltage were observed in the complete range of forward bias. In addition, the shape of the resonances clearly differs from that typical of the oscillatory effect in that there is no plateau region between the peak and the valley, see Section 4.3.2. The nature of the current oscillations observed in an unstable device, and hence the bistability, depends critically on the parameters of the external measuring circuit and on the magnitude of the device resistance, see Section 4.10. Figure 4.20 shows the current-voltage characteristics in the region of the second forward bias resonance for (a) a 200 μm diameter device

with a 50 Ω resistor in parallel, (b) a 200 μm diameter device with a 0.2 μF capacitor in parallel and (c) a 100 μm diameter device with no capacitor or resistor. There is very little variation in the current-voltage characteristics in these three cases. This shows that the bistability is not affected by the external circuit parameters and *can not be due to high frequency current oscillations.*

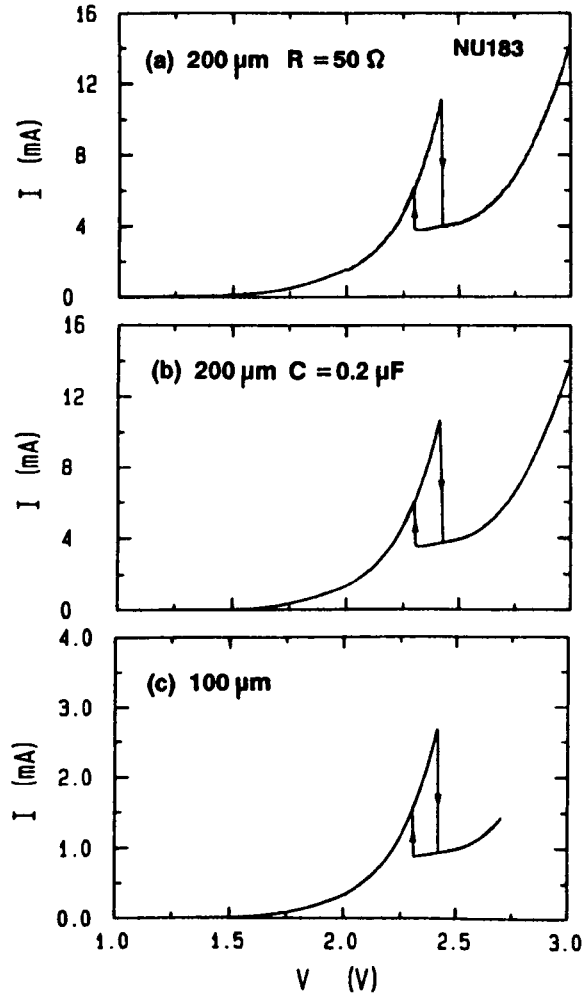

Figure 4.20: Current-voltage characteristics of *NU183* at the second resonance in forward bias (a) 200 μm diameter device with a 50 Ω resistor in parallel, (b) a 200 μm diameter device with a 0.2 μF capacitor in parallel and (c) a 100 μm diameter device with no capacitor or resistor. This demonstrates that the bistable region is not affected by the external circuit parameters

The curves do resemble rather more closely those where the bistability is caused by a high value of series resistance R_S (Section 4.3.5). The minimum value of R_S which could produce bistability is $R_m = \Delta V/\Delta I$ where ΔV is the width of the bistable region and ΔI is the change in current between the peak and the valley. For a mesa diameter of 200 μm, this is 6 kΩ for the first resonance and 15 Ω for the second resonance, therefore the resistor could not be ohmic. Also note that there is no bistability on the second resonance in reverse bias — even though the current at this point is higher than that at the peak of the first resonance in forward bias. If there were an ohmic resistor in series with the device, one would expect this resonance to show bistability as well. There remains the possibility of a highly non-ohmic resistance, such

as a Schottky barrier in the contact region. However, devices with identical doping profiles but thinner barriers have shown much lower resistance at similar voltages ($\sim 10\ \Omega$) so it is hard to see why such an effect should be confined to this one sample. Also, the lack of variability between a large number of devices processed in both Nottingham and Sheffield argues against some kind of processing difficulty. It is not possible to completely rule out an extrinsic effect solely on the basis of the $I(V)$ characteristics however, such a notional non-ohmic element would have to have an impedance that closely mimicked the behaviour of a buildup of charge in the well — so it is simpler to conclude that the observed behaviour *is* due to the electrostatic effects of a buildup of space charge. This is confirmed by the temperature and magnetic field dependence of the bistability described in Sections 4.6 and 4.7.

4.5 Capacitance Studies of Charge Buildup

Capacitance is directly related to the electrostatic charge stored within a device and therefore is a most suitable probe for the investigation of charge buildup. This section describes capacitance-voltage studies of charge buildup and intrinsic bistability in an asymmetric resonant tunnelling device and interprets measured characteristics in terms of a simple equivalent circuit taking into account the way in which the capacitance is measured.

4.5.1 Capacitance-Voltage Characteristics

Figure 4.21 shows a plot of the current, I, AC conductance, G and the differential capacitance, C, against applied voltage V, for a 200 μm diameter mesa of *NU183* at a temperature of 4 K. The AC measurements were taken with a Hewlett-Packard model 4275A LCR meter, with the bias voltage applied externally with a Keithley voltage source and the DC current was measured simultaneously, as described in Section 2.1. The measurement frequency was 1 MHz and the modulation voltage was 3 mV. The meter was in the mode in which the measured impedance is interpreted in terms of a resistor and capacitor in parallel. As detailed later in this section, this has a significant effect on the parameters obtained. The curve has been corrected for the series resistance of the LCR meter and the leakage current through the Keithley voltage source.

The main features of the forward-bias capacitance curve are the general fall-off from zero bias, the step up in the capacitance at $\sim$ 0.3 V (corresponding to the current threshold), and a step down in the capacitance at $\sim$ 0.73 V, the bias where the device switches to the off-resonant state. There is a clear region of bistability near the peak. From this curve it appears that there is an increase in capacitance associated with the resonant tunnelling process. Beyond the main resonance there is a peak in C at $\sim$ 0.95 V, corresponding to the LO phonon related peak in the current.

The capacitance in reverse bias is shown in Figure 4.22. There is a much smaller effect associated with the resonance in this bias direction, indicating that the capacitance is indeed sensitive to charge buildup. There is a small decrease in C as the current moves up the resonant peak then an increase when the device is biased into the negative differential resistivity region. It is not possible to make reliable measurements of the capacitance for the second resonance in either direction of bias because the impedance of the device becomes too low.

The variation of C and G with measurement frequency is shown in Figure 4.23 for frequencies between 100 kHz and 10 MHz. The most obvious change is that the peak in the region of negative differential resistance associated with the LO phonon feature becomes much stronger at low frequency and is eliminated at frequencies above 4 MHz. The small decrease in C just before this feature which is apparent at low frequencies also disappears at high frequency. For frequencies less than 0.4 MHz, the characteristics on resonance are essentially independent of frequency. At higher frequencies, there is a shift of the apparent threshold for resonance to higher bias, so that at 10 MHz the capacitance remains low up to a voltage of 0.57 V — a shift of 250 mV

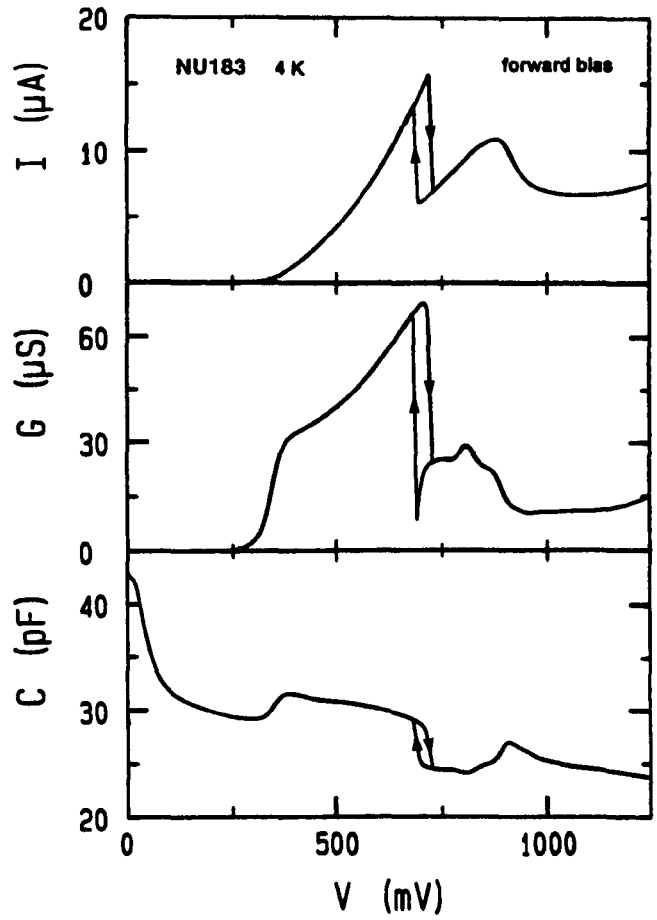

Figure 4.21: Voltage dependence of the DC current I, AC conductance G and the differential capacitance C in the region of the first resonance in forward bias for a 200 μm diameter mesa of *NU183*, measured at 1 MHz and 4 K.

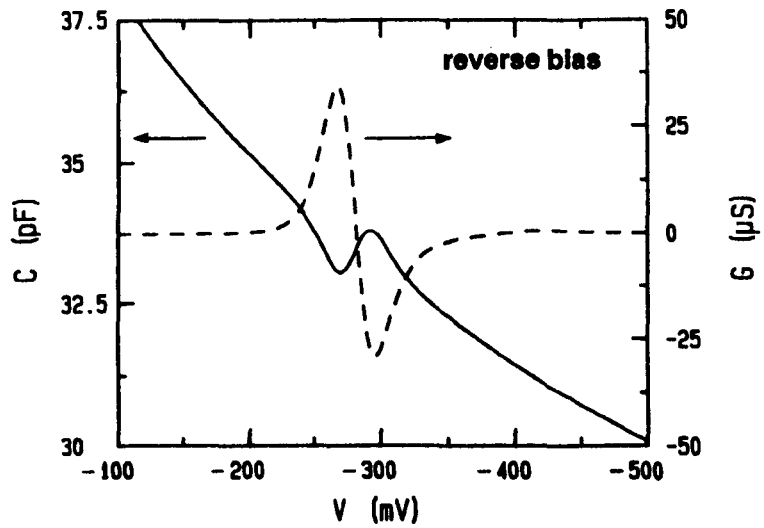

Figure 4.22: Plots of C (full line) and G (dashed line) for the first resonance in reverse bias, measured at 4 K and 1 MHz.

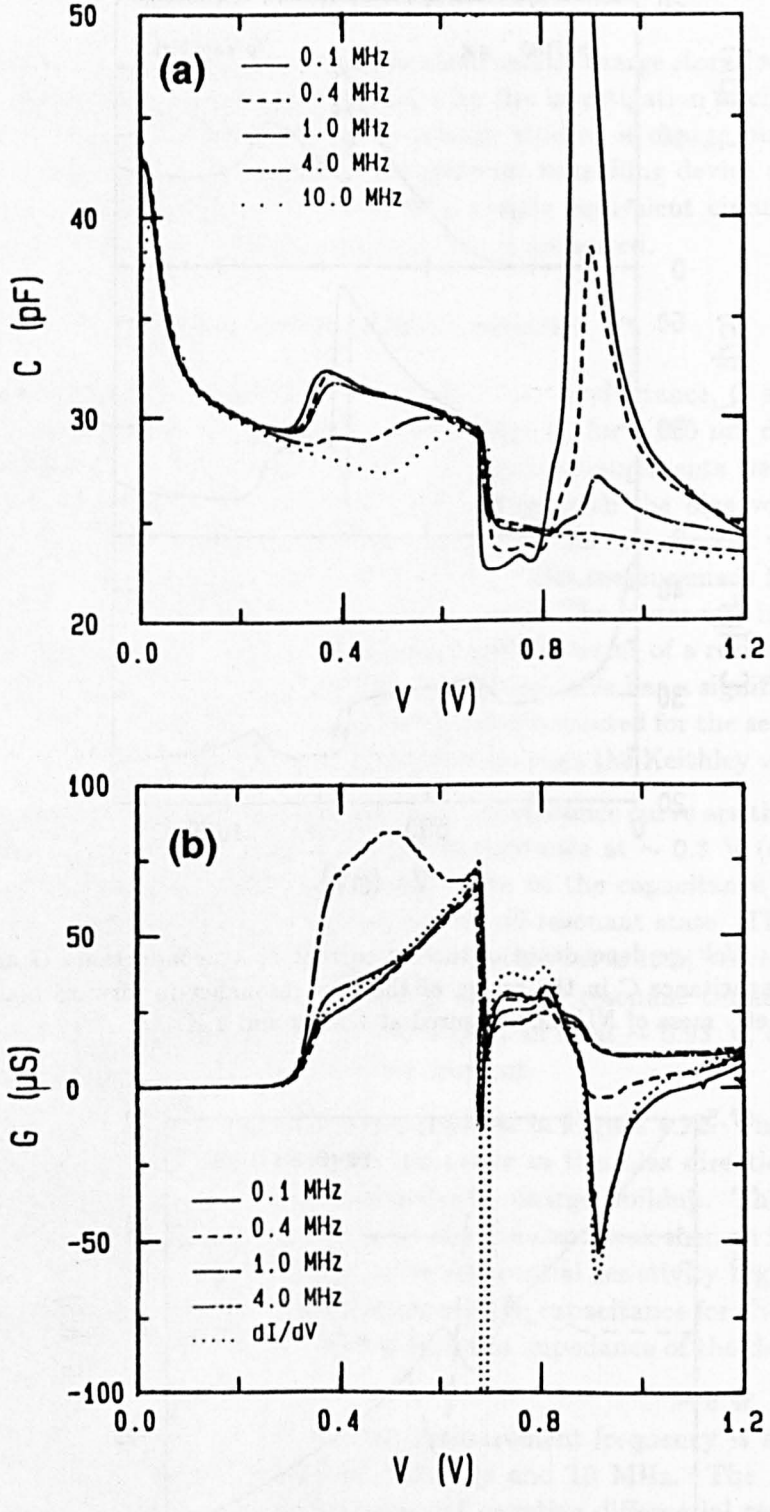

Figure 4.23: Variation of (a) differential capacitance and (b) AC conductance with measurement frequency between 40 kHz and 10 MHz. The high-frequency traces have been compensated for the impedance of the measuring leads.

compared to the low-frequency curves. The high-frequency curves have been corrected for the frequency-dependent impedance of the measuring cables (see Section 2.1). Without correction, the 10 MHz trace lies approximately 17 pF below the low-frequency data. At low frequencies, the conductance closely follows the DC value dI/dV but at high frequency there is significant divergence from this value.

4.5.2 A Simple Model

The simplest model to describe the device capacitance is that outlined in Section 3.2.3. The device is considered to be two parallel plate capacitors in series with sheets of charge in the emitter and collector representing the outer plates and the charge in the well forming the common central plate. In this device the two capacitances are unequal, as illustrated in Figure 4.24. The values are

$$C_1 = \frac{dQ_a}{dV_e} = \frac{\varepsilon_0 \varepsilon_r}{\gamma x_0 + b_1 + w/2} \tag{4.29}$$

$$C_2 = \frac{d(Q_a + Q_w)}{dV_c} = \frac{\varepsilon_0 \varepsilon_r}{\lambda_c + b_2 + w/2} \tag{4.30}$$

where Q_a, Q_w are the sheet charges in the emitter accumulation layer and the well respectively, V_e and V_c are the voltage drops across the two halves of the device and the barriers have widths of b_1 and b_2. x_0 is the stand-off distance of the accumulation layer 2DEG from the emitter barrier interface which is estimated from the Fang-Howard wavefunction and $\gamma \sim 0.6$ (Section 3.2). The equivalent length in the collector contact is the depletion length λ_c, this

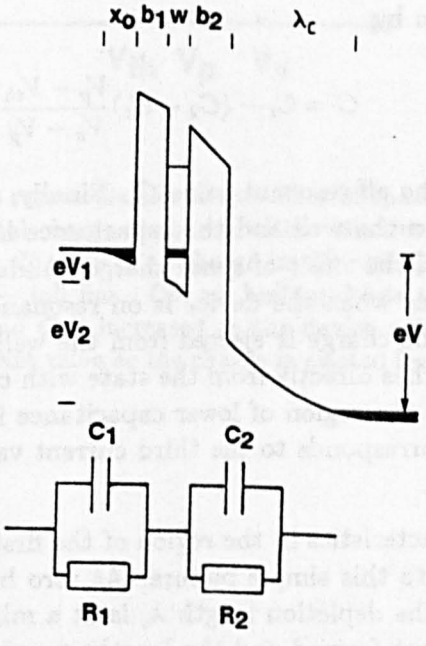

Figure 4.24: Schematic band diagram showing the charge distribution within an asymmetric double barrier device. The simple equivalent circuit is also shown.

is usually much longer than x_0 due to the low doping levels in the contact.

Both depend on the applied bias, particularly the depletion length, and this should be included in any model of the device. There is also the 'quantum capacitance', $C_Q = e^2\mathcal{D}(\epsilon_F)$, of the emitter accumulation layer which is in series with C_1. This is approximately 1.5 nF for a 200 μm diameter mesa. This is much larger than C_1 or C_2 and does not depend on bias and therefore in most of the following discussion this term will be neglected, however C_Q does make an important contribution to the magnetoquantum oscillations described in Section 4.7.2.

Off resonance, there is no space charge buildup in the well and, for constant values of λ_c and x_0, the device behaves as a perfect parallel plate capacitor, with the charge accumulated at the emitter plate proportional to the applied voltage, as shown in the schematic plot of Figure 4.25. The device has a capacitance of $(1/C_1 + 1/C_2)^{-1} = C_t$. When the threshold voltage V_{th} is reached, Q_a is held constant and Q_w increases. The increase in voltage appears entirely across the collector capacitor and therefore the measured capacitance is C_2. Since $C_2 > C_t$, this corresponds to the step up in Figure 4.21, *i.e.* to produce a given change in the applied bias more charge is needed in the well than the emitter since the electric field acts over a shorter distance. The quantum capacitance does not have much effect on the size of the step as long as we assume that the density of states of the quasi-bound level in the well is the same as that of the emitter state; off-resonance we have C_Q, C_1 and C_2 in series and on-resonance the quantum capacitance of the emitter is simply replaced by that of the well so we have C_Q in series with C_2.

At a bias of V_p, charge starts to be lost from the well as the bias is increased. If an increase in bias of ΔV causes Q_w to decrease by ΔQ then, to maintain the applied voltage, Q_a must increase by $\Delta Q\ C_t/C_2$. Therefore in the region between V_p and V_v (the bias at which there is no charge left in the well), $C = dQ/dV$ is given by

$$C = C_t - (C_2 - C_t)\frac{V_p - V_{th}}{V_v - V_p} \tag{4.31}$$

which is less than the off-resonant value C_t. Finally, at biases greater than V_v there is no charge in the well and the capacitance is again given by C_t. So, in this simple model the effect of space charge buildup is to produce a region of higher capacitance when the device is on resonance and a region of lower capacitance when the charge is ejected from the well. The device considered here (*NU183*), switches directly from the state with charge in the well to that with no charge, *i.e.* the region of lower capacitance is not accessed. The low capacitance state corresponds to the third current value in Figure 4.2, which is also not observed.

The actual characteristics in the region of the first forward bias resonance are broadly similar to this simple picture. At zero bias, the capacitance is a maximum because the depletion length λ_c is at a minimum. At low bias the emitter 2DEG has not formed and the lengths x_0 and λ_c should be replaced with a screening length, which is estimated to be $\sim$ 165 Å. This gives a capacitance of 51 pF, in reasonable agreement with the measured value of 46 pF. Since the doping level is so low, some of the electrons may be frozen out onto shallow donor states at 4 K, leading to an increase in the screening

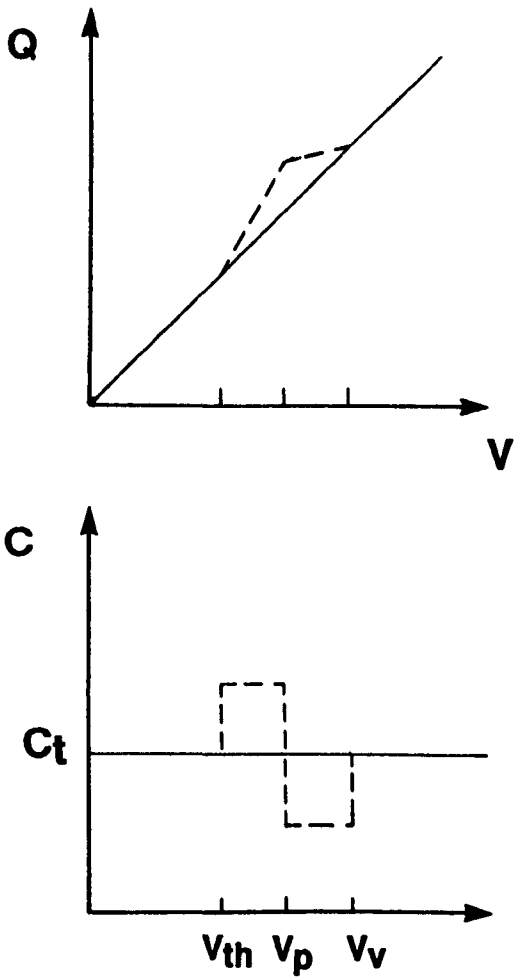

Figure 4.25: Schematic representation of the effect of space charge buildup in the quantum well on the total charge Q stored within the device and the differential capacitance $C = dQ/dV$. If there is no charge in the well Q increases linearly with bias and C is constant — full line. Charge buildup leads to a higher total stored charge at a given bias and C is increased as the device comes onto resonance and drops below the off-resonant value as the charge is ejected from the well.

length and a decrease in the capacitance. This only occurs for small biases since the electrons are easily ionized by a relatively low electric field. This is the origin of the small dip near zero bias. This becomes much more pronounced in the presence of a magnetic field as described in Section 4.7.4. The asymmetry in the capacitance between forward and reverse bias means that the depletion lengths are unequal and, therefore, that the doping levels are not the same on both sides of the double barrier structure. This is not unexpected, due to factors such as silicon diffusion in the growth direction. The capacitance is higher in reverse bias and therefore the depletion length is smaller when the collector is the top contact of the mesa, *i.e.* the doping level above the double barrier structure is higher than that below it. This doping asymmetry may also contribute to a shift in the position of maximum capacitance away from zero bias, of about 10 mV. This relatively small shift argues that there is little space charge in the barriers, in contrast to observations by Eaves *et al.* for single barrier samples where substantial concentrations of negative space charge were found in the (AlGa)As barrier regions [70].

Since the differential capacitance is defined as $C = dQ/dV$, the total charge accumulated within the device may be obtained from $Q = \int C\,dV$. This only holds if the measured parameter corresponds to the true device capacitance. Using this procedure it is possible to obtain values for the charge density in the emitter accumulation layer and in the well. Up to threshold charge is only building up in the emitter so can calculate $Q_a = \int_0^{V_{th}} C\,dV$ which gives a value of 2.2×10^{11} cm^{-2}. When the device is on resonance the charge buildup occurs only in the well so we then use $Q_w = \int_{V_{th}}^{V_p} CdV = 2 \times 10^{11}$ cm^{-2}. This value is in good agreement with that obtained from the magneto-transport measurements described in the next section. The agreement is not exact because the measured capacitance in this case is not quite the same as the true capacitance of the device due to the way in which the capacitance is measured. The amount of charge buildup is controlled by the relative values of the tunnelling rates through the emitter and collector barriers (see Section 4.6). The fact that Q_w and Q_a are so similar shows that the transmission rate through the collector barrier is very much less than that through the emitter barrier. A simple calculation using transfer matrix techniques gives a value of $Q_w/Q_a = T_e/(T_e + T_c) \simeq 0.96$ in agreement with this observation.

Using this simple picture it is clear that the step in the capacitance (up at threshold or down at peak) corresponds to changing the effective width of the capacitor by a width $\gamma x_0 + b_1 + w/2$. Therefore we can obtain values for x_0 from

$$\gamma x_0 = \varepsilon_0 \varepsilon_r \left(\frac{1}{C_t} - \frac{1}{C_2} \right) - b_1 - w/2 \tag{4.32}$$

Where C_t is taken to be the off resonant capacitance and C_2 is taken as the capacitance on resonance. This gives values of x_0 of 75 Å at threshold and 190 Å at the peak. These must be compared with expected values (calculated from the Fang-Howard variational wavefunction) of 130 Å and 117 Å. It is clear that there is significant disagreement here. The cause of this is the fact that we have not considered a realistic model of the device or the way in which the LCR meter obtains a value for C. These points will be discussed in the next section.

4.5.3 Equivalent Circuit

This simple model fails to account for the frequency dependence of the observed characteristics, for the structure in the capacitance in the region of the LO phonon-related current peak and the reverse bias resonance and for the actual size of the steps in capacitance at the current threshold and peak. Obviously the model of the device outlined so far is unrealistic since it does not allow a DC current to flow through the structure. C_1 and C_2 must be considered to be leaky capacitors *i.e.* the equivalent circuit should be modified to include resistors R_1 in parallel with C_1 and R_2 in parallel with C_2, see Figure 4.24. These resistors represent the impedance of the barriers for charging and discharging the well. When the device is off resonance, these will have very high resistance. The argument of the previous section is equivalent to the assumption that on resonance R_1 becomes small and effectively shorts out C_1.

In order to explain the features in the $C(V)$ curves more completely, we must also bear in mind the way the measured values of capacitance are obtained by the LCR meter (Section 2.1). The meter actually measures the total impedance $|Z|$ and the phase angle θ and then calculates values for R and C assuming that the device consists of only a *single* capacitor and a *single* resistor in parallel (or in series). This may not be an adequate description of the device in many circumstances. The equivalent circuit contains *two* resistor-capacitor pairs and therefore the measured values of C_M and $G_M = 1/R_M$ do not necessarily correspond to the actual device parameters C_1, C_2, R_1 and R_2. The impedance of the equivalent circuit is

$$Z = \frac{R_1}{1 + i\omega C_1 R_1} + \frac{R_2}{1 + i\omega C_2 R_2} = |Z|e^{i\theta} \tag{4.33}$$

The LCR meter interprets this as

$$\begin{aligned} R_M &= |Z|\sqrt{1 + \tan^2\theta} \\ &= \frac{(R_1 + R_2)^2 + \omega^2(C_1 + C_2)^2 R_1^2 R_2^2}{R_1 + R_2 + \omega^2 R_1 R_2 (C_1^2 R_1 + C_2^2 R_2)} \end{aligned} \tag{4.34}$$

$$\begin{aligned} C_M &= \frac{\sqrt{1 + \tan^2\theta}}{\omega |Z| \tan\theta} \\ &= \frac{(R_1+R_2)(C_1R_1+C_2R_2) - (C_1+C_2)R_1R_2(1-\omega^2 C_1 C_2 R_1 R_2)}{(R_1 + R_2)^2 + \omega^2(C_1 + C_2)^2 R_1^2 R_2^2} \end{aligned} \tag{4.35}$$

Where $\omega = 2\pi f$ is the angular frequency. The low-frequency impedance, as expected, is simply $R_1 + R_2$. Off resonance, R_1 and R_2 are high, and if $R_{1,2} \gg 1/\omega C_{1,2}$,

$$C_M = \frac{C_1 C_2}{C_1 + C_2} = C_t \tag{4.36}$$

On resonance, $R_{1,2} < 1/\omega C_{1,2}$ which means that the other terms in equation 4.6 cannot be neglected. If $R_1 \ll R_2$ then $C_M = C_2$. If this is not the case, $C_M < C_2$ for $R_1 > 0$ and $C_M > C_2$ for $R_1 < 0$. The reduction of C_M by the non-negligible resistance of the first barrier explains why the value of x_0 deduced from the capacitance step at threshold in the 1 MHz trace was too small. If we take a value for $R_1/R_2 \sim 20$ at the foot of the resonance, we obtain $C_M \sim 0.9\,C_2$, which would account for the value of x_0 obtained. Adjusting for

this shift gives $x_0 \simeq 140$ Å in much better agreement with the Fang-Howard result (130 Å). At the peak of the resonance R_1 is much smaller and $C_M \simeq C_2$. A higher value for C at the start of the resonance would also give a higher value of $Q_w = \int_{V_{th}}^{V_p} C\,dV$.

The threshold voltage for the step in C will occur approximately when $R_1 \sim 1/\omega C_1$. At low frequencies this coincides with the current threshold. However for $f > 0.4$ MHz there is a reduction in C and a shift in this threshold to higher bias (Figure 4.23). This is due to the reduction in the impedance of the capacitor. Taking $C_1 \sim 150$ pF (from the value of $x_0 = 140$ Å) and the threshold to be the point halfway up the step, we can deduce that $R_1 = 1150\ \Omega$ at 0.35 V, 285 Ω at 0.45 V and 115 Ω at 0.55 V from the 1 MHz, 4 MHz and 10 MHz traces respectively. These values are reasonable but unreliable due to the qualitative nature of the argument. In conjunction with the DC conductance these values give $R_2 \sim 65$ kΩ, 27 kΩ and 21 kΩ. A detailed consideration of the tunnelling process and the equivalent circuit is necessary to deduce theoretical values of R_1 and R_2 [113].

It is interesting to note from equation 4.32 that if $R_1 = -R_2/(1+\omega^2(C_1+C_2)^2R_2^2)$, the value of C_M will reach a peak value of

$$C_{\max} = C_2 - \frac{C_1}{1+\alpha} + \frac{C_1+C_2}{\alpha} + \frac{C_t}{1+\alpha} \tag{4.37}$$

where $\alpha = (\omega(C_1+C_2)R_2)^2$. This can be many times larger than C_2 at low frequencies. This now explains the origin of the structure in $C(V)$ for $f \leq 2$ MHz near the LO phonon peak and the first resonance on reverse bias. This peak is simply an artifact of the measuring system associated with the negative differential resistance of the device and is unrelated to any change in the true capacitance of the device. Note that the capacitance peak disappears at about the same frequency at which G no longer goes negative. Therefore in regions of negative differential resistance no information about the capacitance can be obtained from low-frequency measurements. A similar situation occurs in 'Hickmott' structures where oscillations in the capacitance have been observed (see Eaves *et al.* [215]) caused by a modulation in the resistance of the undepleted part of an n-(InGa)As layer. It is therefore possible to obtain marked structure in C_M due to structure in R_1 rather than in C_1 or C_2. Particular attention must be paid to this point when attempting to analyse magneto-capacitance data, see Section 4.7.4. The peak in C is in anti-phase with the conductance, which is important for identifying this anomalous effect. This is seen very clearly in Figure 4.26 which shows capacitance and conductance plots for sample *NU207* with a 1200 Å wide well (see Table 2.1 for details), as soon as the conductance starts to go negative there is a series a sharp well-defined peaks in C.

4.5.4 Summary

For a full explanation of high frequency behaviour, and a model for the values of the parameters in the equivalent circuit we must turn once more to the analysis of Sheard and Toombs [113]. At high frequencies the time delays associated with charging the well must be taken into account. As suggested by Brown *et al.* [195], this causes changes in the current to lag behind those in the

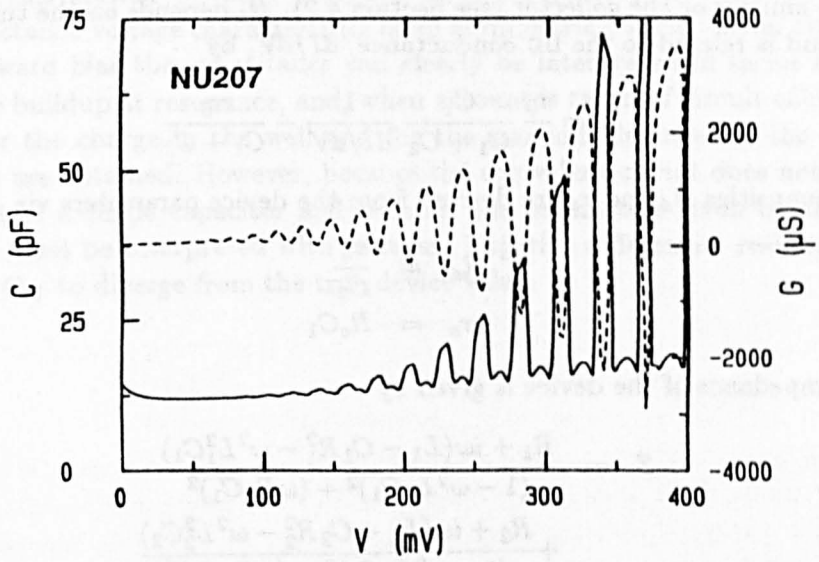

Figure 4.26: Differential capacitance (full curve) and conductance (dashed curve) for sample *NU207* (1200 Å well) at a frequency of 1 MHz, showing the anomalous structure in C when the conductance goes negative.

voltage. This may be modelled by including an inductance in the circuit $\sim \tau R$. When the device is biased in the region of negative resistance this inductance will also be *negative*. The equivalent circuit of a resonant tunnelling device derived from the theory of sequential tunnelling by Sheard and Toombs is given in Figure 4.27. It consists of two elements, each consisting of a resistor

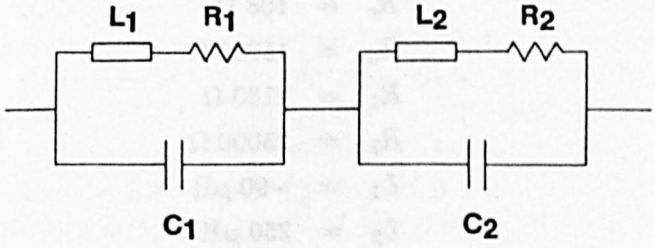

Figure 4.27: Equivalent circuit for a double barrier device as derived by Sheard and Toombs [113].

and inductor with a capacitor in parallel. The parameters are given by

$$R_1 = R_c\left(\frac{\tau_2/\tau_0 + \omega^2\tau_2^2}{1+\omega^2\tau_2^2}\right) \tag{4.38}$$

$$R_2 = R_d(1+\tau_c/\tau_0) \tag{4.39}$$

$$L_1 = -\frac{R_c\tau_2^2}{\tau_1(1+\omega^2\tau_2^2)} \tag{4.40}$$

$$L_2 = R_d\tau_c \tag{4.41}$$

with C_1 and C_2 given by equation 4.29. $1/\tau_0 = 1/\tau_1 + 1/\tau_2$ where $\tau_{1,2}$ is the time for an electron in a state in the well to decay into an unoccupied state

in the emitter or the collector (see Section 4.2). R_c depends on the tunnelling rate and is related to the DC conductance, dI/dV, by

$$R_c = \frac{\tau_0}{\tau_2}\frac{C_1}{C_1+C_2}\frac{1}{dI/dV} - \frac{\tau_0}{C_1+C_2} \tag{4.42}$$

The quantities R_d and τ_c are derived from the device parameters via

$$R_d = \frac{\tau_2}{C_2} \tag{4.43}$$

$$\tau_c = R_c C_1 \tag{4.44}$$

The impedance of the device is given by

$$\begin{aligned} Z = & \frac{R_1 + i\omega(L_1 - C_1R_1^2 - \omega^2 L_1^2 C_1)}{(1-\omega^2 L_1 C_1)^2 + (\omega R_1 C_1)^2} \\ & + \frac{R_2 + i\omega(L_2 - C_2R_2^2 - \omega^2 L_2^2 C_2)}{(1-\omega^2 L_2 C_2)^2 + (\omega R_2 C_2)^2} \end{aligned} \tag{4.45}$$

At low frequencies, this is identical to the circuit considered in the previous section. Values for this device at a bias of 0.5 V and $f = 1$ MHz are

$$\begin{aligned} C_1 &= 150 \text{ pF} \\ C_2 &= 33 \text{ pF} \\ dI/dV &= 37\ \mu\text{S} \\ \tau_1 &= 25 \text{ ns} \\ \tau_2 &= 0.5\ \mu\text{s} \\ \tau_c &= 16 \text{ ns} \\ R_c &= 108\ \Omega \\ R_d &= 15000\ \Omega \\ R_1 &= 2160\ \Omega \\ R_2 &= 25000\ \Omega \\ L_1 &= -90\ \mu\text{H} \\ L_2 &= 250\ \mu\text{H} \end{aligned}$$

The values for R_1 and R_2 obtained from the frequency dependence are reasonably close to those calculated here from estimates of the DC conductance and the dwell times. However the impedance due to L_1 and L_2 cannot be neglected; at 1 MHz, $\omega L_1 \sim 25\%$ of R_1 and $\omega L_2 \sim 5\%$ of R_2. Therefore the inductors could have a significant influence on the device characteristics. This is because the thick barriers in this sample lead to a long charging time and so the inductance becomes appreciable at relatively modest frequencies. In more typical devices the barriers are much thinner and therefore the inductance is only important at very high frequencies. Whether any effect of the inductors can be seen in the measured AC characteristics is unclear, however they are not expected to fundamentally alter the explanation offered so far. For example, the inclusion of inductors will not affect the periodicity of the magneto-oscillations since they are both proportional to R_c, which is controlled by the tunnelling probability through the emitter barrier. Therefore the inductance will vary with magnetic field in a similar way to the resistance.

In this section we have presented data for the capacitance-voltage and conductance-voltage characteristics of an asymmetric double barrier structure. In forward bias the capacitance can clearly be interpreted in terms of space charge buildup at resonance, and, when account is taken of circuit effects, values for the charge in the well and for the standoff distance for the emitter 2DEG are obtained. However, because the equivalent circuit does not simply consist of a single capacitor and resistor, the parameters given by the LCR meter must be interpreted with caution. Negative differential resistance can cause C_M to diverge from the true device value.

4.6 The Temperature Dependence of Intrinsic Bistability

This section describes the influence of increasing temperature on the $I(V)$ and $C(V)$ characteristics of an asymmetric double barrier structure (*NU183*) which shows intrinsic bistability at low temperatures. The loss of bistability at high temperatures [183] is related to a decrease in the charge buildup which is modelled by considering the thermal population of higher-energy subbands which have much larger transmission coefficients.

4.6.1 Results

The current-voltage characteristics of NU183 are shown in Figure 4.28 in the region of the first resonance in forward bias for a range of temperatures between 4 and 300 K. As the temperature is increased from 4 K, the bistability initially becomes more pronounced. At $T \sim 30$ K the voltage width ΔV of the bistable region is over three times greater than the 4 K value. Above this temperature there is a decrease in the voltage width, until the bistability disappears altogether at 150 K. At higher temperatures, the peak of the resonance starts to shift to lower bias and the off-resonant current increases. At room temperature, the resonance can no longer be seen directly in the current, but it is still identifiable in the derivative or in the differential capacitance. The LO phonon related peak at ~ 0.9 V is also attenuated with increasing temperature. At biases below the threshold voltage, there is an increase in the current, which is attributed to the thermally activated tunnelling process described in Section 3.5.2.

Similar features can be observed in the capacitance-voltage characteristics shown in Figure 4.29. As the temperature increases, the step in the capacitance at V_{th} becomes less sharp, and the capacitance on resonance decreases from its low temperature value. When the resonance broadens out at high temperatures, a region of negative differential resistance emerges, this causes a peak to develop in the capacitance, for the reasons discussed in the previous section. The variation in the width of the bistable region, ΔV, and the peak position V_p are shown in Figures 4.30 and 4.31. The reverse bias characteristics have been discussed in Section 3.5.2. The second resonance is shown in Figures 4.32 and 4.33. There is no increase in the width of the bistable region at low temperatures, just a monotonic decrease in ΔV with increasing T. The bistability is lost at a temperature ~ 200 K. The peak of the resonance moves rapidly to lower bias reaching 1.9 V at room temperature, where again the resonance is only observed in derivative plots.

4.6.2 Discussion

The increase in the width of the bistable region at the first resonance when the temperature is increased from 4 K to 30 K seems to indicate that the energy width of the resonance is decreasing at higher temperatures. As discussed in Section 1.5, any scattering process which changes the phase of the electron wavefunction contributes to a broadening of the resonance. If the width of the resonant state was the same in forward bias as in reverse bias (< 5 meV),

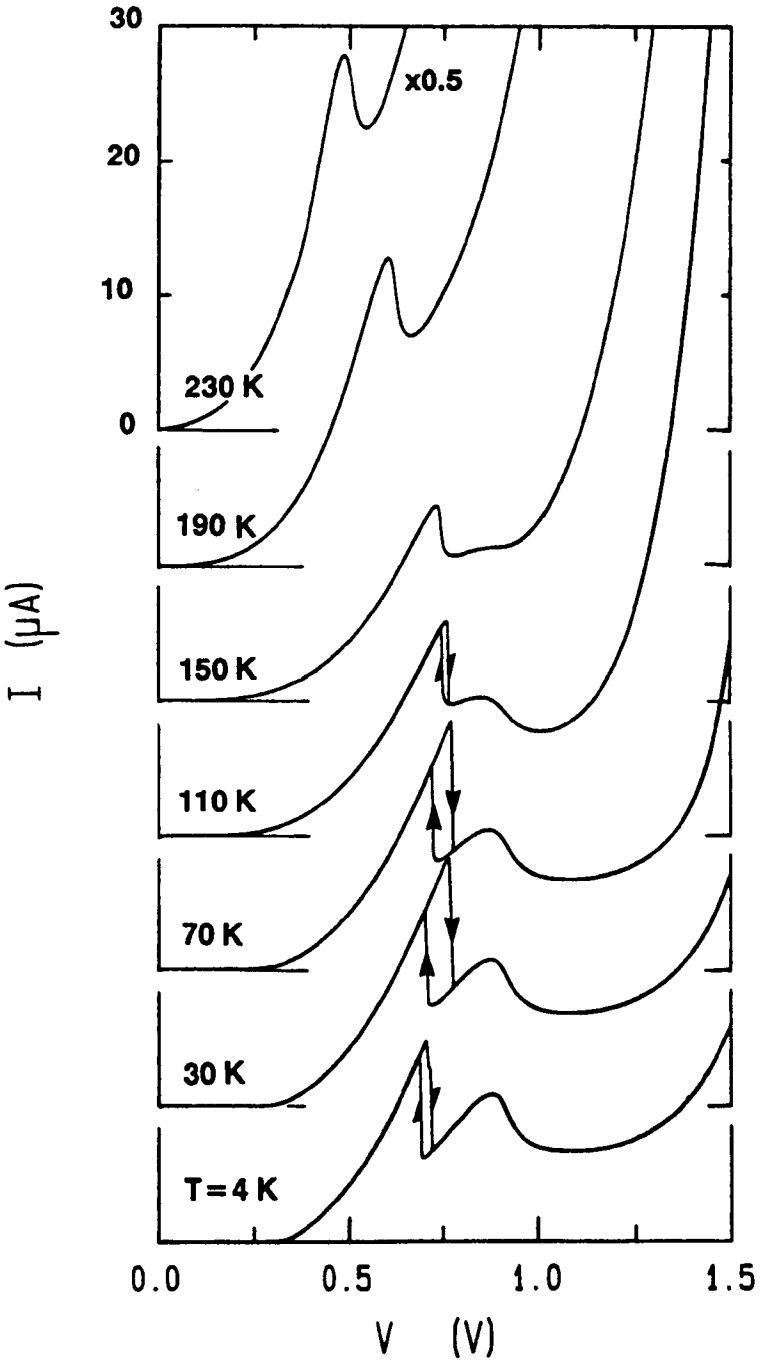

Figure 4.28: Temperature dependence of the current-voltage characteristics of *NU183* in the region of the first resonance in forward bias showing the quenching of the bistability and the shift in the peak position to lower bias as charge is lost from the well.

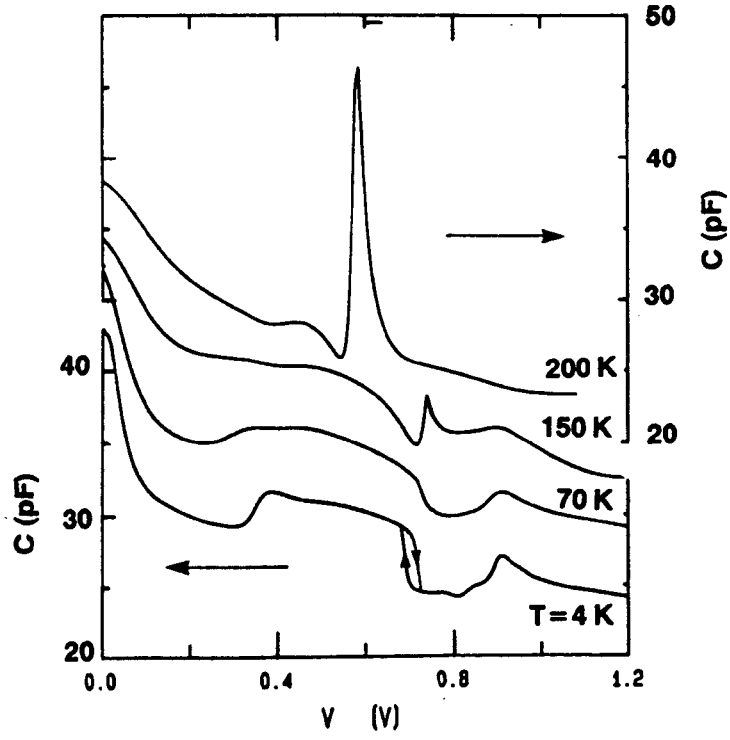

Figure 4.29: Temperature dependence of the differential capacitance of *NU183* in the region of the first resonance in forward bias.

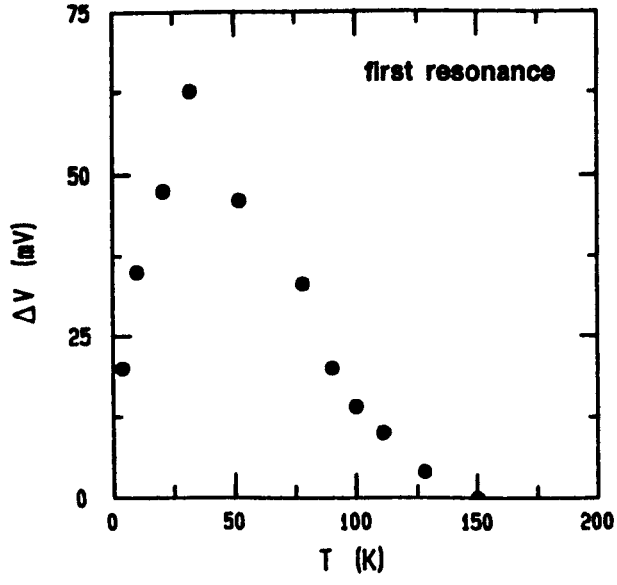

Figure 4.30: Plot of the width of the bistable region ΔV against temperature for the first resonance.

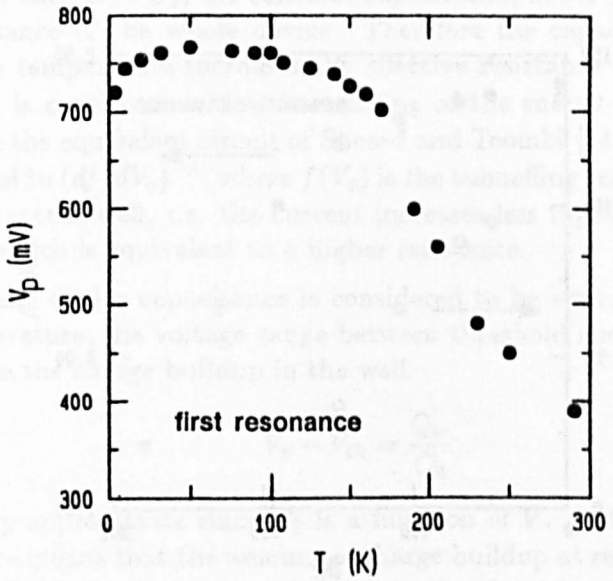

Figure 4.31: Plot of the voltage at the current peak V_p against temperature for the first resonance.

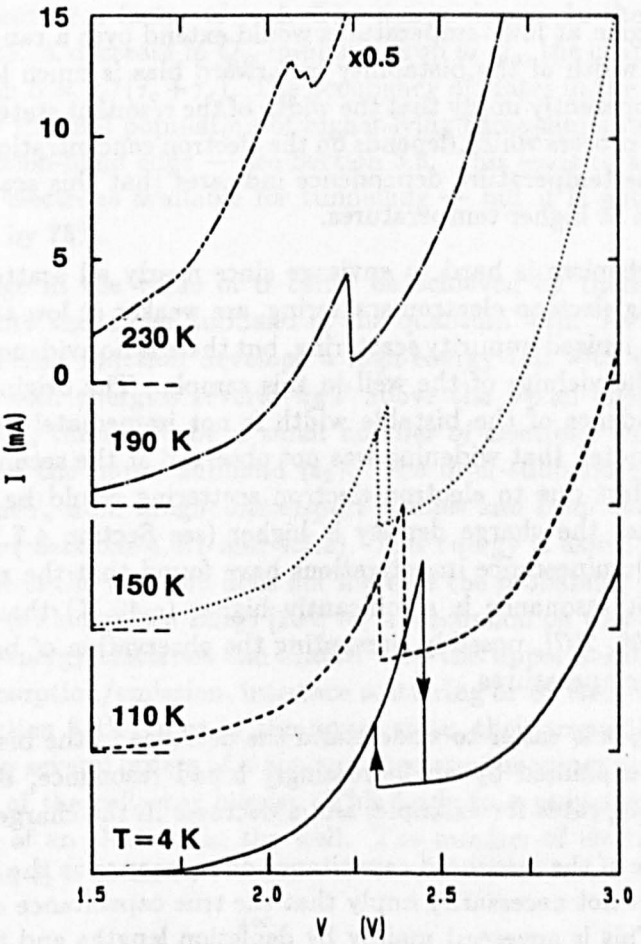

Figure 4.32: The current-voltage characteristics of *NU183* at the second resonance in forward bias plotted for several temperatures.

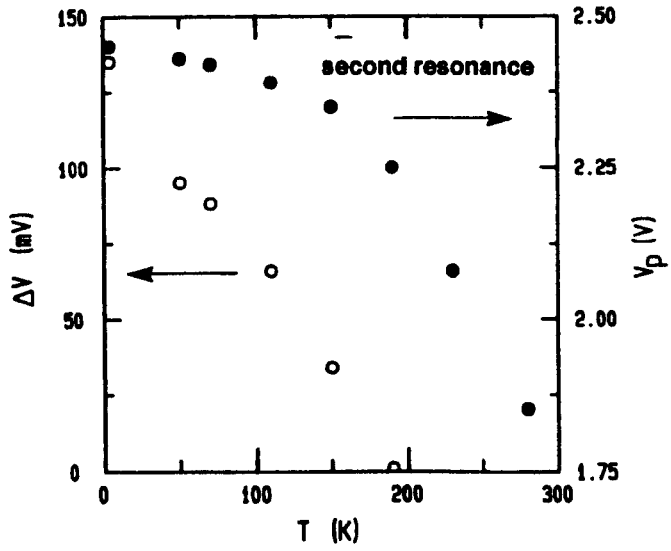

Figure 4.33: Plots of the bistable width and the peak voltage against temperature for the second resonance.

the bistable region at low temperatures would extend over a range of at least 300 mV. The width of the bistability in forward bias is much less than this which would apparently imply that the width of the resonant state is controlled by a scattering process which depends on the electron concentration in the well. In addition, the temperature dependence indicates that this scattering must be less effective at higher temperatures.

Such a mechanism is hard to envisage since nearly all scattering mechanisms, including electron-electron scattering, are weaker at low temperatures. An exception is ionized impurity scattering, but there is no evidence for charged impurities in the vicinity of the well in this sample. The origin of the temperature dependence of the bistable width is not immediately apparent. It should also be noted that widening was not observed at the second resonance, whereas any effect due to electron-electron scattering would be expected to be stronger since the charge density is higher (see Section 4.7.2); although magneto-photoluminescence investigations have found that the electron temperature at this resonance is significantly higher (~40 K) than the lattice temperature [206, 207], possibly preventing the observation of broadening at lower electron temperatures.

Above 30 K, it is easier to understand the decrease in the bistable width. This could be explained by an increasingly broad resonance, due to faster phonon scattering rates for example, and a decrease in the charge buildup.

The decrease of the measured capacitance on resonance as the temperature is increased does not necessarily imply that the true capacitance of the device has changed. This is governed mainly by depletion lengths and the stand-off distance of the emitter 2DEG from the interface (equation 4.29). Therefore it might be expected that the capacitance would depend only weakly on temperature. However, as has been described in Section 4.5.3 the value of capacitance given by the LCR meter depends on the resistance of the emitter barrier, R_1;

if this is low then $C \sim C_2$, the collector capacitance, but if this is high $C \sim C_t$, the capacitance of the whole device. Therefore the capacitance data imply that as the temperature increases the effective resistance of the first barrier rises. This is consistent with a broadening of the energy width of the resonance since the equivalent circuit of Sheard and Toombs [113] shows that R_1 is proportional to $(df/dV_e)^{-1}$, where $f(V_e)$ is the tunnelling rate from the emitter into the quantum well, *i.e.* the current increases less rapidly for a broadened resonance which is equivalent to a higher resistance.

If the true device capacitance is considered to be approximately constant with temperature, the voltage range between threshold and peak will be proportional to the charge buildup in the well

$$V_p - V_{th} = \frac{Q_w}{C_2} \tag{4.46}$$

This is only approximate since C_2 is a function of V. A decrease in V_p with temperature means that the amount of charge buildup at resonance is decreasing. The voltage threshold does not change significantly with temperature — although it is harder to identify at high temperatures due to the thermally activated resonant tunnelling current. The decrease in V_p does not become very rapid until $T > 150$ K. By room temperature the accumulated charge has decreased by a factor of ~ 4. The charge density in the well is given by equation 4.5. A decrease in Q_w implies a drop in Q_a, the charge in the emitter 2DEG, or in $\alpha = \tau_c/(\tau_c + \tau_e)$. The occupancy of states in the emitter 2DEG is reduced by thermal population of higher-lying three-dimensional states above the conduction-band edge — see Section 3.5. This leads to a reduction in the number of electrons available for tunnelling — but it is not large enough to reduce Q_w by 75%.

A change in the value of α could be achieved by thermal activation of electrons into the upper subband of the quantum well. As the temperature rises, the Fermi function develops a high-energy tail with electrons occupying states with energies several k_BT above the Fermi energy. When T is large enough, there will be a small number of electrons with energy higher than that of the upper subband (ϵ_2). The inter-subband energy separation is ~ 150 meV, from magnetotransport studies and from the transfer matrix calculation (Sections 4.4.1 and 4.7.2). This energy is associated with motion in the plane of the well and does not increase the probability of tunnelling out of the well (although see Luryi [105] for a discussion on this point). However, these high-energy electrons can scatter into the upper subband ϵ_2 either via phonon absorption/emission, interface scattering or by electron-electron interaction (Section 3.4). Once in the upper state, their tunnelling probability is enhanced by several orders of magnitude because the upper energy level is close to the top of the collector barrier. This leads to a reduction in the effective dwell time of an electron in the well. The number of electrons with energy greater than ϵ_2 is given by

$$n_2 = \int_{\epsilon_2}^{\infty} \frac{1}{1 + e^{(\epsilon-\mu)/k_BT}} \mathcal{D}(\epsilon)\, d\epsilon \tag{4.47}$$

where $\mathcal{D}(\epsilon)$ is the density of states and μ the chemical potential. If $(\epsilon - \mu) \gg k_BT$ the Fermi function can be approximated by $e^{-(\epsilon-\mu)/k_BT}$ and the chemical

potential is given by

$$\mu = k_B T \log\left(\frac{\pi\hbar^2 n_w}{m^* k_B T}\right) \tag{4.48}$$

This gives

$$n_2 = n_w \exp\left(-\frac{\epsilon_2 - \epsilon_1}{k_B T}\right) \tag{4.49}$$

The dwell time will now be given by

$$\tau_c^{-1} = n_1 \nu_1 T_2(\epsilon_1) + n_2 \nu_2 T_2(\epsilon_2) \tag{4.50}$$

where $T_2(\epsilon)$ is the energy-dependent tunnelling probability through the collector barrier and $\nu = 2w/\sqrt{2\epsilon/m^*}$ is the classical attempt rate. There is an equivalent expression for the emitter barrier. The above expression for τ is used rather than a simple average for the two subbands because it is directly related to the current flow out of the well and this determines the dwell time. The above expression was derived by assuming that *all* electrons with energy above ϵ_2 scatter into the upper subband. Since the escape rate from the upper subband is much higher than that for the lower one, this is reasonable. The bias across the device means that there is a bigger reduction in τ_c than in τ_e because ϵ_2 is much closer to the top of the collector barrier than to the top of the emitter barrier. This would lead to a reduction in α as required.

Another process which should be taken into consideration is the thermal population of states of even higher energies which can scatter into travelling wave states with energies above the top of the collector barrier. An electron which scatters into one of these states is likely to reach the collector contact. This process is also asymmetric in τ_c and τ_e due to the applied bias. Although the population of these states is very small, their tunnelling rate is so much higher (~ 1) that they will make a significant contribution to the reduction in τ_c. Figure 4.34 shows a plot of α against temperature, calculated using a transfer matrix method to give the transmission coefficients at ϵ_1 and ϵ_2. The above-barrier states were taken to have unity transmission and the populations were given by statistics similar to those outlined above. There is a rapid decrease in α for temperatures greater than 150 K. τ_c is calculated to decrease by several orders of magnitude when the temperature is raised to 300 K. By comparing this plot to Figure 4.31, it is clear that this mechanism provides a reasonable qualitative explanation. The reason for the threshold at 150 K is that the population of ϵ_2 is negligible at lower temperatures. Even at room temperature, less than 0.3% of electrons have sufficient energy to be able to scatter into the upper subband.

Although there is a large uncertainty in the parameters used, *e.g.* barrier heights and energy levels, and the explanation is only supposition, it does seem to provide a surprisingly good fit to the data. There will also be contributions from non-resonant processes such as LO or acoustic phonon absorption. The phonon population increases rapidly with T leading to a decrease in the dwell times and an increase in the tunnel current. Since there are more accessible states in the collector than in the emitter, this process may also lead to a reduction in α.

It might be expected that the bistability at the second resonance should disappear at a lower temperature than the first resonance because the energy level

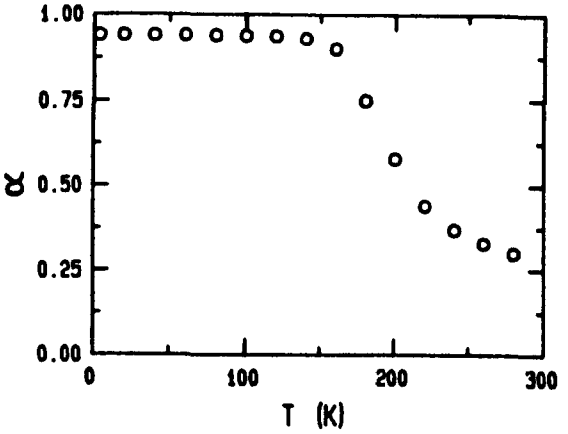

Figure 4.34: Plot of α against temperature calculated taking into account the thermal population of the upper subband in the well and the continuum states above the top of the barrier.

is nearer to the top of the barrier. However, as will be shown in Section 4.7.2, the charge in the well at this resonance is also resident in the lower subband due to intersubband scattering. Therefore the temperature dependence of the two resonances is generally similar.

4.7 Magnetic Fields Studies of Intrinsic Bistability

4.7.1 Introduction

This section details the use of high magnetic fields to investigate the phenomena of space charge buildup and intrinsic bistability in an asymmetric resonant tunnelling device (*NU183*). Firstly, the sheet charge density in the quantum well at resonance is determined by Fourier analysis of magnetoquantum oscillations in the current and the capacitance when a magnetic field is applied in a direction perpendicular to the plane of the barriers [182, 183, 185]. This direct measurement of charge buildup indicates that the peak sheet charge density in the well is equal to that in the 2DEG of the emitter contact. The observation of magnetoquantum oscillations means that there is a cold distribution of electrons with a Fermi level distinct from that in the emitter; this demonstrates that the electrons undergo energy relaxation whilst in the well and constitutes an unequivocal example of a sequential tunnelling process. The second section reports the effect of a magnetic field $\boldsymbol{B} \parallel \boldsymbol{J}$ on the current-voltage characteristics. A significant enhancement of the bistability is obtained together with a three-fold increase in the peak tunnelling current. This is explained by the increased degeneracy of the Landau levels in the quantum limit [187]. The third section describes magnetocapacitance measurements relating to magnetic freeze-out in the contacts, Landau level filling and off-resonant processes. Finally, in Section 4.7.5 the effect of a magnetic field applied in the plane of the barriers ($\boldsymbol{B} \perp \boldsymbol{J}$) is briefly discussed.

4.7.2 Charge Buildup and Energy Relaxation

Origin of the magnetoquantum oscillations

A full discussion of the processes which lead to oscillations in the current, capacitance and conductivity of a tunnelling structure in a magnetic field $\boldsymbol{B} \parallel \boldsymbol{J}$ has been given in Section 3.3. Briefly, the application of a magnetic field perpendicular to the plane of the barriers quantises the electron motion in the emitter 2DEG leading to the formation of Landau levels. The density of states in a high magnetic field consists of a series of sharp peaks of degeneracy $2eB/h$ separated by the cyclotron energy, $\hbar\omega_c$. Sweeping the magnetic field, whilst maintaining a constant bias across the device, causes these levels to pass through the Fermi level and depopulate. Unlike the Shubnikov-de Haas effect in metals or parallel transport in semiconductors, neither the Fermi energy nor the number density is constant in a tunnelling device. Self-consistent analysis has shown that renormalisation of the charge distribution occurs [132] leading to oscillatory behaviour in the bound state energy, the sheet charge density n_a and the stand-off distance of the 2DEG from the emitter barrier x_0. These three parameters determine the tunnelling probability and affect both the current and the capacitance. The oscillations are periodic in $1/B$ with a frequency of $B_f = hn_a/2e$, as for the more usual Shubnikov-de Haas oscillations (n_a is taken to be the value at zero-field).

This explanation will suffice when the device is biased off-resonance, how-

ever the presence of a resonance in the transmission coefficient adds several complications. Firstly, any alteration in n_a changes the voltage drop across the emitter barrier (from Gauss's Law) and therefore may break the resonance condition (in addition to changing the transmission coefficients of the barriers). Equally, a variation in the quasi-bound state energy of the 2DEG could take the device off-resonance. This would affect the charge density in the well n_w — again altering the transmission coefficients and the voltage distribution within the device. Therefore the problem should be treated in a self-consistent fashion including these feedback mechanisms. However, there has been no theoretical treatment of the case of resonant tunnelling from a 2DEG in a magnetic field to date.

Landau levels are also formed in the well and, if the charge distribution has a definite Fermi level (the condition for this is that $k_B T_e \ll \epsilon_F$), the passage of these levels through the Fermi level of the well also gives rise to magnetoquantum effects. The origins of such oscillations are less clear than for those associated with the 2DEG in the emitter. There is no requirement for the Fermi level in the well to be at a fixed voltage above the Fermi level in the collector contact, which is the case for the emitter 2DEG. Neither is the binding energy of the well state as strongly-dependent on the amount of charge held, although there are electrostatic and interaction contributions which do depend on the number density. However, any alteration in n_w as a Landau level is swept through the Fermi energy in the well changes the voltage distribution within the device and the transmission coefficients of the barriers. Since the total applied bias is held constant, a drop in n_w must be compensated by an increase in n_a *i.e.* the voltage drop across the emitter barrier is increased and that across the collector barrier is decreased. Again there is a feedback loop in operation which adjusts n_a and n_w in a self-consistent manner, modulating the tunnelling current. There is a contribution to the capacitance oscillations from the feedback of n_w on n_a changing the 2DEG stand-off distance, but the main effects will be on the depletion length in the collector contact, which determines the value of C_2 see Section 4.5, and on the density of states at the Fermi level – the 'quantum capacitance' described in Section 3.2.3. Whenever the Fermi level lies in the region of low density of states between Landau levels the capacitance drops as discussed in Section 3.3. In the absence of any theoretical treatments, it is less clear whether the current should be lower or higher at such points. I is independent of the density of states at the Fermi level as this does not affect the probability of tunnelling. It turns out that the current also drops at these magnetic fields as will be seen in the results presented later in this section. We assume that the periodicity of the magneto-oscillations is related to the sheet density via $B_f^w = hn_w/2e$ in the same way as for the emitter 2DEG. This only applies for a degenerate electron gas whose number density does not vary significantly as the field is swept. The applicability of these conditions will be examined below.

Reverse bias

We start with a summary of the results in reverse bias for *NU183* where no bistability is seen. This allows a comparison to be made with the forward bias results, where the effects of charge buildup are expected to be more important. A sequence of magneto-oscillation traces with $\boldsymbol{B} \parallel \boldsymbol{J}$ for several voltages is

shown in Figure 4.35 at a temperature of 4 K. Note the large number of oscillations apparent and the low fields at which Landau levels can be seen (< 0.7 T). This is an indication of high device quality.

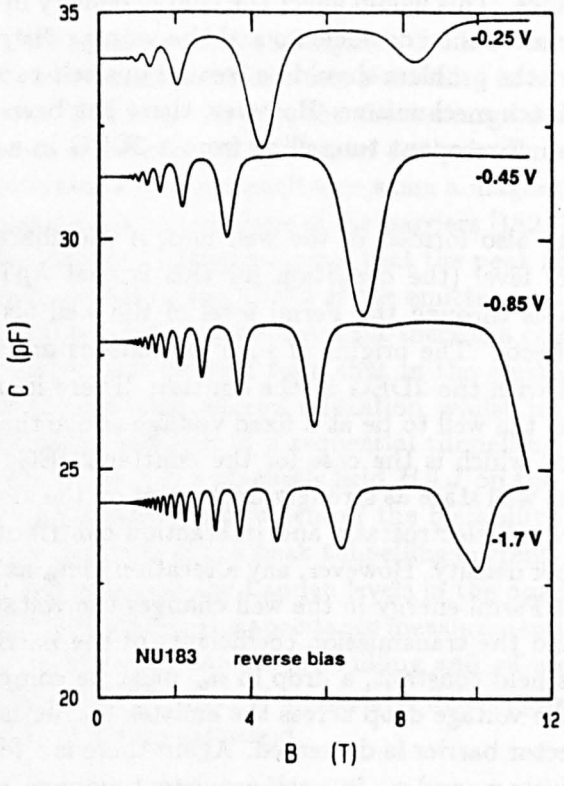

Figure 4.35: Magnetoquantum oscillations in the differential capacitance for sample *NU183* in reverse bias at 4 K in a magnetic field $\boldsymbol{B} \parallel \boldsymbol{J}$. The traces are for voltages of -0.25, -0.45, -0.85 and -1.7 V. The -1.7 V curve is displaced downwards by 2 pF.

The values of n_a derived from the periodicity of these traces are given in Figure 4.36. The charge density increases monotonically with bias and the device is behaving to all intents and purposes like a simple parallel plate capacitor. The curvature apparent in the n_a-V plot is due to the increase in the depletion length with bias which reduces the device capacitance $e\, dn_a/dV = C_t = \varepsilon_0\varepsilon_r/(\gamma x_0 + b_1 + w + b_2 + \lambda_c)$ (see Section 4.5). Simple modelling of the device using the Fang-Howard wavefunction for the 2DEG in the emitter, as described in Section 3.2, provides a good fit to the n_s values if the doping level in the collector contact is taken to be slightly less than the nominal doping (0.6×10^{16} cm^{-3} rather than 1×10^{16} cm^{-3}). The variation of n_a with bias is also consistent with the measured values of differential capacitance:— $C = \delta Q/\delta V = e\pi r^2\, dn_a/dV$ where r is the radius of the device For example, at a bias of -1 V the slope of n_a against V gives C =26 pF compared with a measured value of 27.2 pF (Figure 4.22).

For applied biases greater than -1.7 V, there is a modulation of the magnetoquantum oscillations at low field. This is because a second subband forms in the accumulation layer potential, adding an additional periodicity to the oscillations — see Section 3.3. This is clearly seen in Figure 4.37 which plots

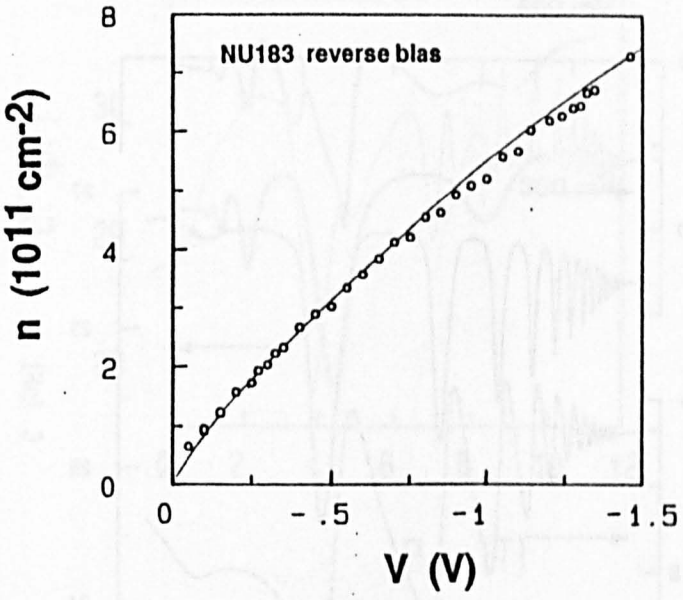

Figure 4.36: Electron sheet density, n_a, in the 2DEG of the emitter contact plotted against applied bias, deduced from magneto-oscillations in the tunnel current or differential capacitance as shown in Figure 4.35. The solid line is the sheet density calculated using the expressions in Section 3.2.

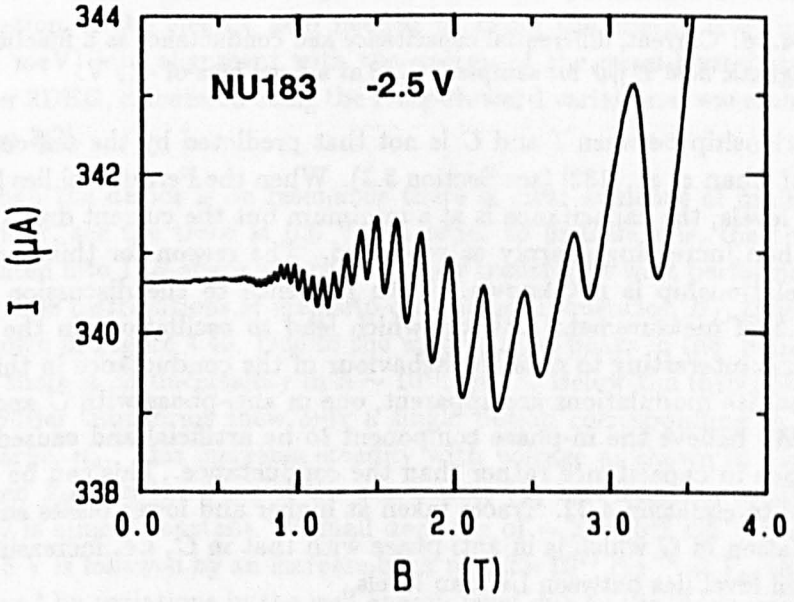

Figure 4.37: Current against magnetic field for *NU183* at T =4 K at a fixed applied bias of -2.5 V, showing the modulation of the magneto-oscillations caused by the presence of a second subband in the emitter accumulation layer.

the tunnel current as a function of magnetic field for an applied bias of -2.5 V.

Figure 4.38 shows $I(B)$, $C(B)$ and $G(B)$ for a fixed bias of -1.2 V. Note that

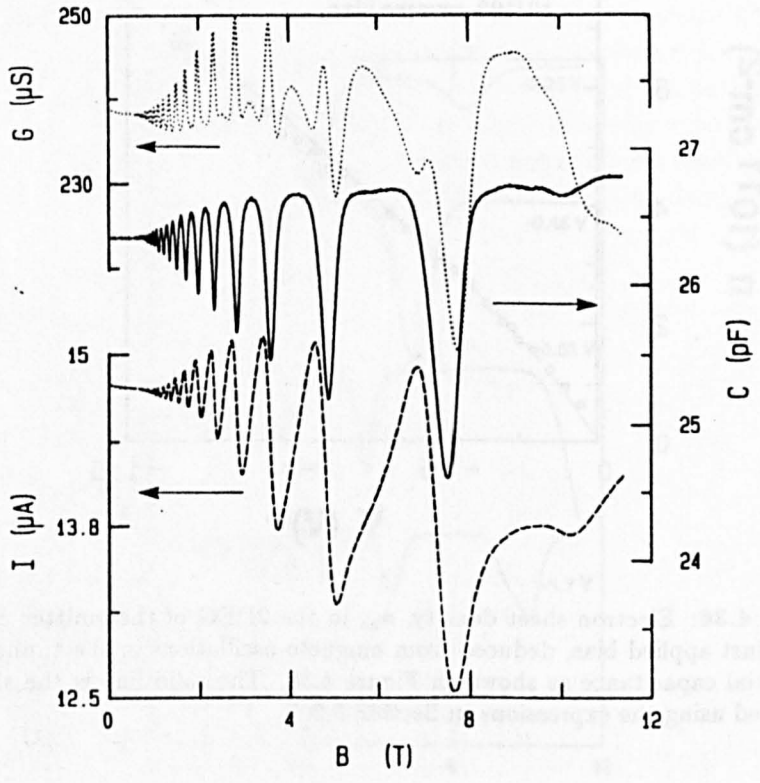

Figure 4.38: Current, differential capacitance and conductance as a function of applied magnetic field $\boldsymbol{B} \parallel \boldsymbol{J}$ for sample *NU183* at a fixed bias of -1.2 V.

the relationship between I and C is not that predicted by the self-consistent theory of Chan *et al.* [132] (see Section 3.3). When the Fermi level lies between Landau levels, the capacitance is at a minimum but the current drops sharply rather then increasing sharply as predicted. The reason for this anomalous phase relationship is not known. With reference to the discussion in Section 4.5.3 of measurement artifacts which lead to oscillations in the capacitance, it is interesting to note the behaviour of the conductance in this trace. Two separate modulations are apparent, one in anti-phase with C and one in phase. We believe the in-phase component to be artificial and caused by the oscillations in capacitance rather than the conductance. This can be seen by reference to equation 4.32. Traces taken at higher and lower biases show only an oscillation in G which is in anti-phase with that in C, *i.e.* increasing when the Fermi level lies between Landau levels.

Forward bias – first resonance

This resonance shows very strong effects due to charge buildup. Typical magnetocapacitance traces at voltages of 300 mV (near threshold) and 600 mV (near the resonant peak) are shown in Figure 4.39.

Below the threshold voltage V_{th} ~325 mV, the results are very similar to those in reverse bias with a single series of oscillations corresponding to Landau

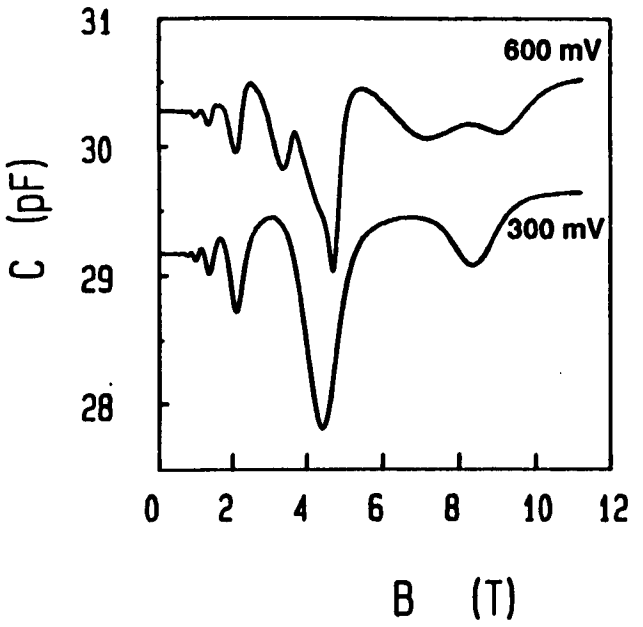

Figure 4.39: Magnetocapacitance traces for *NU183* at 4 K at forward biases of 300 and 600 mV.

levels passing through the Fermi energy of the emitter 2DEG. The values of n_a obtained are slightly less than those obtained in reverse bias. This again indicates that there is some asymmetry in the doping levels –see Section 4.5. The value of n_a at threshold, $n_a = 2.2 \times 10^{11}\text{cm}^{-2}$, is consistent with a simple calculation of the electric field needed to bring the energy level in the well ($\sim$ 68 meV) into alignment with the energy of the quasi-bound state of the emitter 2DEG, calculated using the Fang-Howard variational wavefunction (see Section 3.2).

When the device is on resonance there is clear evidence of multi-periodic behaviour, see the trace at 0.6 V. In order to analyse this, the traces were translated into $1/B$-space and then Fourier transforms were performed numerically. The distributions of magneto-oscillation frequencies, B_f, thus obtained are shown in Figure 4.40. Due to the width of the peaks in the Fourier transforms there is an uncertainty in $n \sim 10^{10}$ cm^{-2}. Below the threshold voltage, the Fourier transforms show only a single period corresponding to the emitter charge, n_a. This increases steadily with voltage as shown in Figure 4.41. Between V_{th} and the peak of the resonance, V_p, this magneto-oscillation frequency is almost constant. A small decrease of $\sim 2 \times 10^{10}$ cm^{-2} between V_{th} and 0.5 V is followed by an increase back to 2.2×10^{11} cm^{-2} at V_p, this may be explained by variations in the well energy level due to the electrostatic effects of increasing charge buildup.

Within this voltage range, a second magneto-oscillation frequency is observed. This appears as a weak peak at low B_f at $V \sim 0.4$ V. We attribute this peak to a thermalised, degenerate charge distribution in the quantum well [183, 185]. The frequency of this peak gives the sheet charge density in the quantum well. This increases throughout this voltage range and approaches

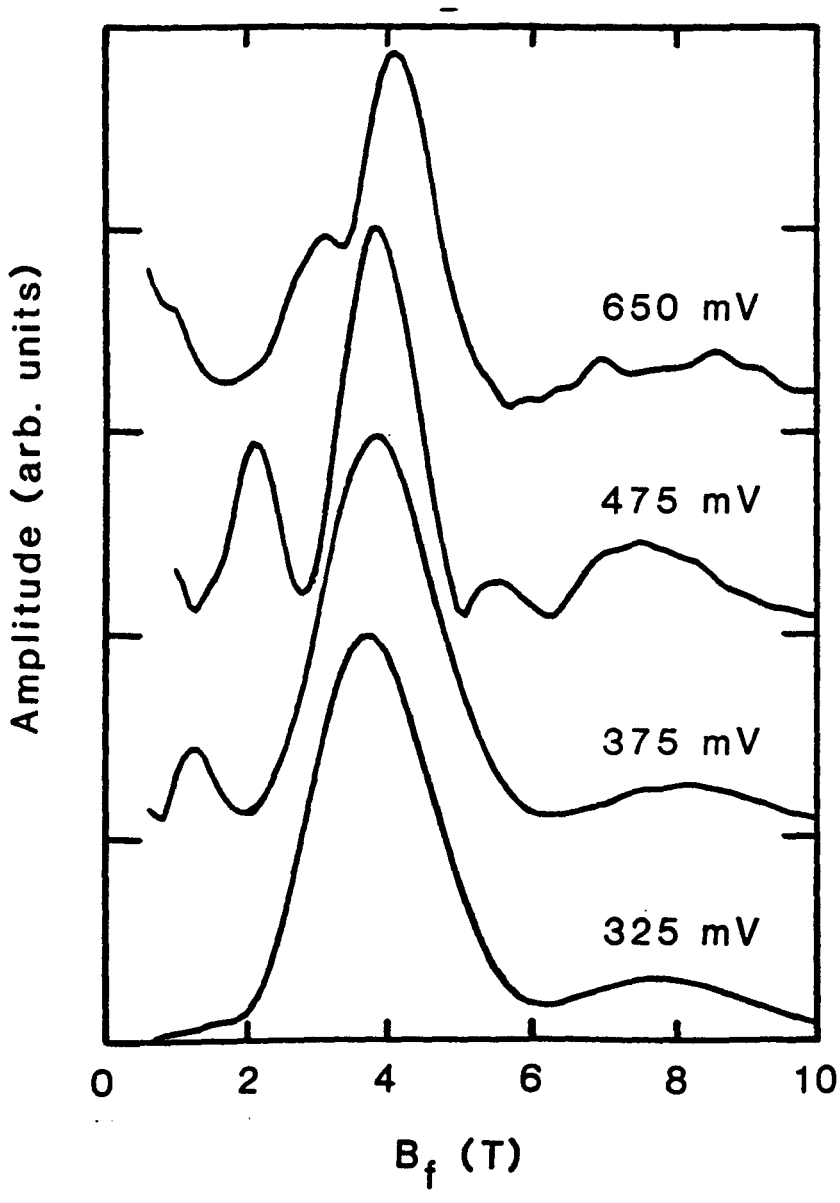

Figure 4.40: Spectrum of the magneto-oscillation frequencies B_f for *NU183* in reverse bias obtained by Fourier transforming the traces of $C(B)$ in 1/B space. The peak position B_f for each voltage gives the inverse period.

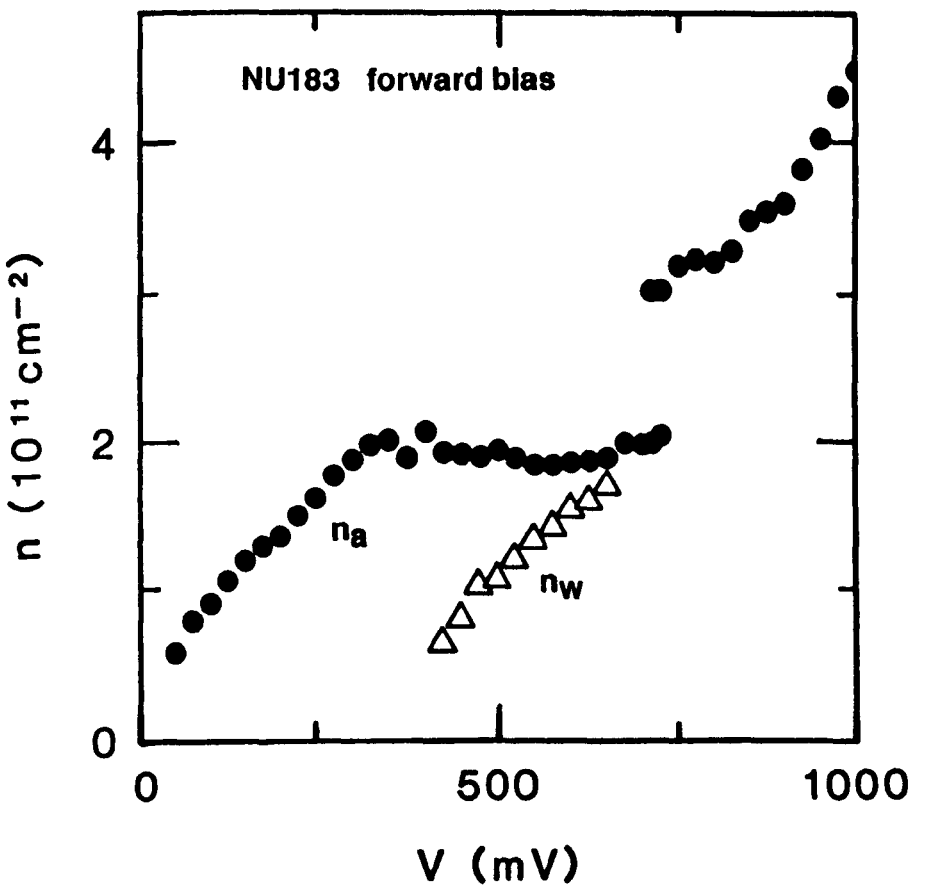

Figure 4.41: Areal charge density n vs. voltage for charge in the accumulation layer n_a (•) and in the well n_w (△). The electron densities are deduced from the peaks in the Fourier spectra of the magneto-oscillations.

n_a at $V = V_p$, as shown by the points marked Δ in Figure 4.41. The equality of n_w and n_a at the peak of the resonance is to be expected theoretically since the transition rate into the well is much greater than the decay rate out of the well through the collector barrier (Section 4.4.1). The dynamically-determined occupancy of states in the well [99] is then close to unity and the quasi-Fermi levels in the emitter and in the well are coincident. The maximum charge density in the well ($\sim 2.2 \times 10^{11}$ cm^{-2}) is much higher than that found in previous investigations of charge buildup. For example, the slight flattening off in the n_a curve shown in Figure 3.8 for a symmetric device (*NU104*) corresponds to a peak sheet density of less than 5×10^{10} cm^{-2} (Section 3.3). The space charge buildup in *NU183* has recently been supported by photoluminescence investigations by Hayes *et al.* [206].

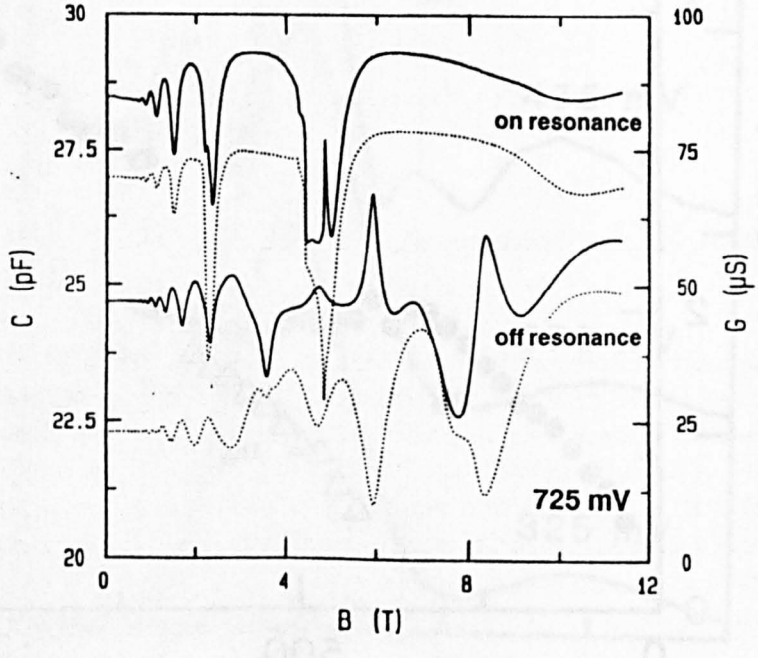

Figure 4.42: Capacitance (full curve) and conductance (dotted) for *NU183* at 0.725 V for both the on resonance (upper curves) and off resonance (lower curves) states. This clearly shows the different periodicities although the applied bias is the same and the different phase relationship between C and G in the two states.

When V increases above V_p, no more charge can be accommodated in the well since the Fermi level is already equal with that in the emitter contact. A transition occurs in which charge is ejected from the well with a consequent redistribution of potential and resonant tunnelling can no longer occur. This results in a step-wise increase in the accumulation layer density to $n_a \simeq 3 \times 10^{11}$ cm^{-2}. In the bistable region around resonance, magnetoquantum oscillations may be seen for both the on-resonance state (high current, high capacitance) and the off-resonance state (low current and capacitance). This is shown in Figure 4.42 for a frequency of 1 MHz. The difference in periodicity is apparent, as is the different phase relation between C and G. The difference in the charge density in the emitter for these two traces is further strong evidence for the bistability being intrinsic (see also Zaslavsky *et al.* [181]).

By comparing the traces in Figure 4.42, it can be seen that on resonance

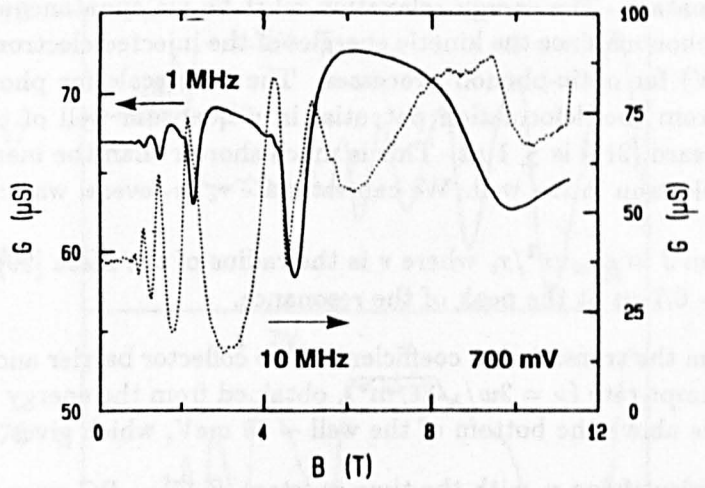

Figure 4.43: Conductance as a function of magnetic field at an applied bias of 700 mV for frequencies of 1 MHz (solid line, left-hand scale) and 10 MHz (dotted, right-hand scale).

the capacitance and conductance are in-phase whereas in the off-resonant state they are in anti-phase. This argues that there are separate physical mechanisms responsible for the two sets of oscillations, which supports the assignment of the oscillations on resonance to a modulation of the charge in the well and those off resonance to charge in the emitter. However, Figure 4.43 compares the conductance for a bias of 700 mV at frequencies of 1 MHz (solid curve, left-hand scale) and 10 MHz (dotted, right-hand scale). These are in anti-phase. This indicates that the physical mechanism responsible for the magnetoquantum oscillations and how this relates to the measured device parameters is not understood.

In the region just beyond the first resonance, n_s is still well below the values in reverse bias, see Figure 4.41. This discrepancy is caused by the presence of space charge in the well due to the LO phonon emission assisted tunnelling process described in Section 3.4. We estimate the charge density remaining in the well to be $\sim 5 \times 10^{10}$ cm^{-2}. For biases above 1 V, all the charge has been expelled from the well.

Energy Relaxation

The existence of a separate series of magneto-oscillations due to the charge distribution in the well requires that there is a well-defined quasi-Fermi level distinct from that in the emitter contact. These oscillations are observed down to magnetic fields as low as 1 T. This means that the electron temperature in the well is low ($k_B T_e \ll \hbar\omega_c$). Conservation of transverse momentum in the tunnelling process requires the Fermi levels in the well and the emitter to coincide. The theory of resonant tunnelling [99] shows that the states of transverse momentum within the well are only partially occupied, since the occupancy is determined dynamically by the balance between the transition rates into and out of the well. However, if the energy relaxation time is much less than the charge storage time in the well, the electron distribution will

cool to the lattice temperature and establish a Fermi level below that in the emitter contact. The energy relaxation must be via spontaneous emission of acoustic phonons since the kinetic energies of the injected electrons are too low ($\sim$ 7 meV) for optic-phonon processes. The time scale for phonon emission derived from the deformation potential in a quantum well of this width by F. W. Sheard [216] is $\leq$ 1 ns. This is much shorter than the mean dwell time τ_c of an electron in the well. We can estimate τ_c in several ways:

1. From $I = en_w\pi r^2/\tau_c$ where r is the radius of the mesa [99], which gives $\tau_c \sim 0.7$ μs at the peak of the resonance.

2. From the transmission coefficient of the collector barrier and the classical attempt rate ($\nu = 2w/\sqrt{2\epsilon/m^*}$), obtained from the energy of the bound state above the bottom of the well $\sim$ 68 meV, which gives $\tau_c \sim 0.2$ μs.

3. By identifying τ_c with the time constant $R_2C_2 \sim RC$ on resonance. The values shown in Figure 4.21 give $\tau_c \sim 0.4$ μs.

Although these three values do not agree, they are all much greater than the energy relaxation time. Therefore the tunnelling process in this sample is truly sequential. This is the first direct observation of a degenerate electron gas in the well of a resonant tunnelling device. Previous investigations, *e.g.* references [140] and [177], revealed no evidence of a series of oscillations due to an equilibrated Fermi level in the well. In such cases, it is likely that the dwell time is less than the energy relaxation rate so the electron distribution remains too hot to give rise to magnetoquantum oscillations. The extremely long dwell time in the well for this sample is due to the very thick collector barrier.

Note that although electron-electron scattering will be extremely rapid at these high sheet charge densities and is known to lead to a thermalised electron distribution on a time scale of less than 100 fs [217, 218], this distribution will be characterised by an electron temperature much higher than the lattice temperature and would not be degenerate. Electron-electron scattering can only redistribute energy amongst the electrons and does not contribute to the overall energy relaxation of the distribution.

Second resonance

A series of magneto-oscillations in the tunnel current at biases beyond the first resonance is shown in Figure 4.44. At $V = 1.5$ V, below the onset of the second resonance, two series of oscillations are clearly observed. At low magnetic fields there is the series due to the charge in the emitter contact n_a. This increases steadily in this range as shown in Figure 4.45, demonstrating that charge is once again accumulating in the emitter and not in the quantum well.

The high-frequency series of oscillations, which dominates the high-field data, is due to scattering-induced, $k_\perp$-nonconserving transitions into the upper Landau levels of the lower subband ϵ_1, as described in Section 3.4. This process modulates the charge density in the well and the tunnel current. In fact two series of these oscillations are observed with differing frequencies B_f, as shown by Figure 4.46 which plots d^2I/dB^2 against $1/B$ for a bias of 1.35 V. The higher frequency series corresponds to elastic transitions from the emitter to the well with a change in the Landau level index and the lower to transitions

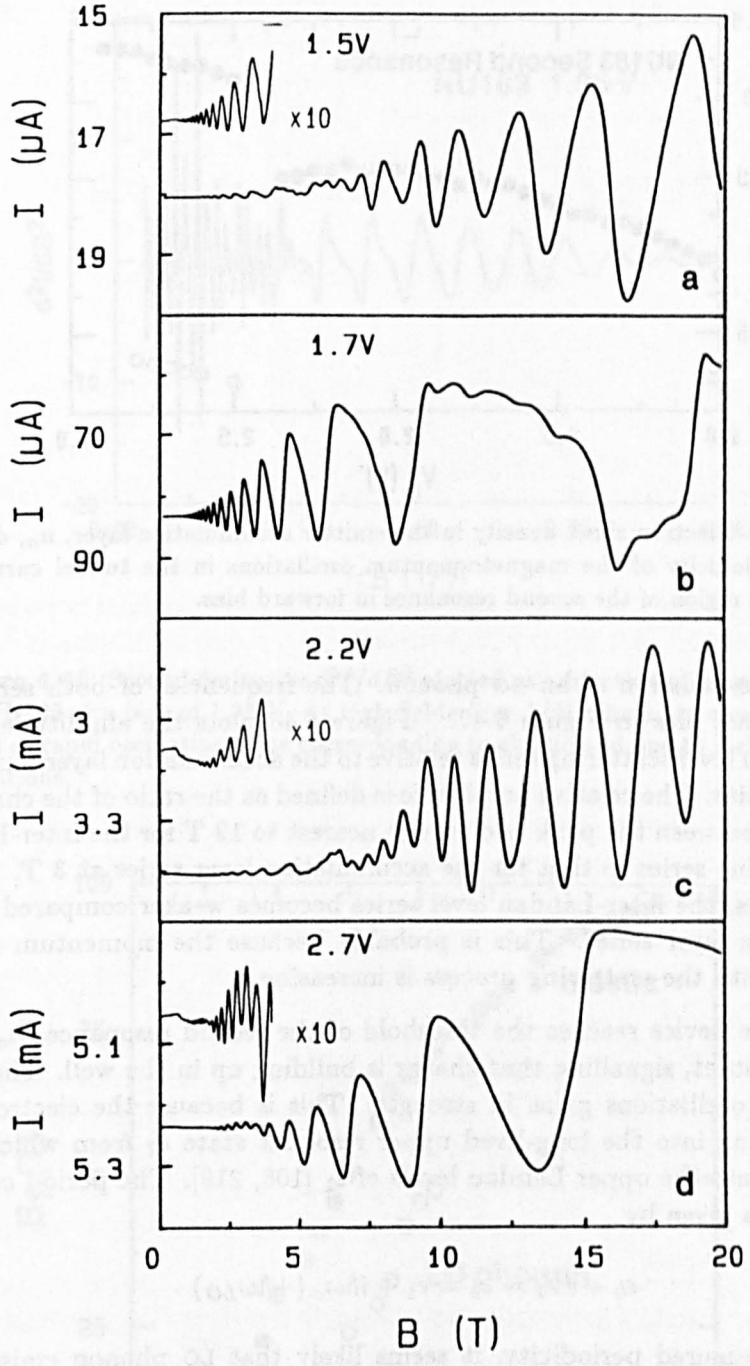

Figure 4.44: Magneto-oscillations in the tunnel current for *NU183* in the region of the second resonance at biases of (a) 1.5 V, (b) 1.7 V, (c) 2.2 V and (d) 2.7 V.

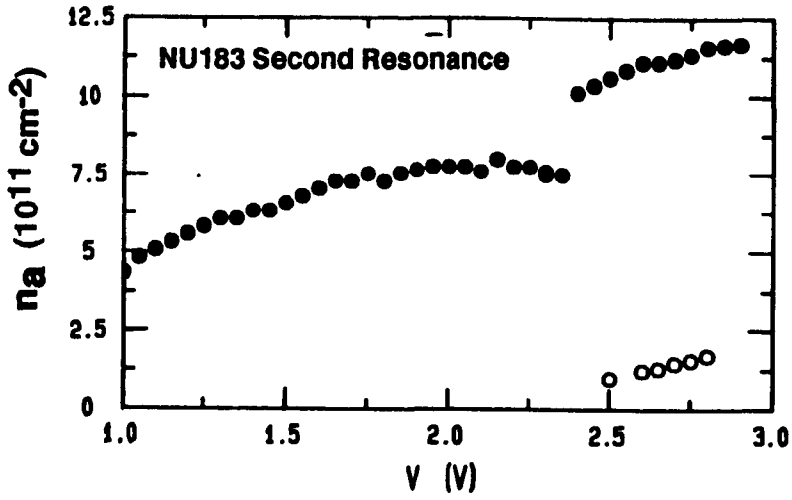

Figure 4.45: Electron sheet density in the emitter accumulation layer, n_a, deduced from the periodicity of the magnetoquantum oscillations in the tunnel current for *NU183* in the region of the second resonance in forward bias.

involving the emission of an LO phonon. The frequencies of both series are plotted against bias in Figure 4.47. Figure 4.48 plots the amplitude of the inter-Landau level scattering series relative to the accumulation layer series as a function of bias. The relative amplitude is defined as the ratio of the change in the current between the peak and trough nearest to 12 T for the inter-Landau level scattering series to that for the accumulation layer series at 3 T. As the bias increases, the inter-Landau level series becomes weaker compared to the accumulation layer series. This is probably because the momentum change associated with the scattering process is increasing.

When the device reaches the threshold of the second resonance, n_a again remains constant, signalling that charge is building up in the well. The high-B_f series of oscillations gains in strength. This is because the electrons are now tunnelling into the long-lived upper resonant state ϵ_2 from which they can scatter into the upper Landau levels of ϵ_1 [108, 219]. The period of these oscillations is given by

$$\epsilon_0 + eV_1 \sim \epsilon_2 = \epsilon_1 + i\hbar\omega_c \ (+\hbar\omega_{LO}) \tag{4.51}$$

From the measured periodicity, it seems likely that LO phonon emission is not actually involved in the intersubband transition. Instead, it could occur by electron-electron scattering which is faster. The fact that the high-B_f series strengthens considerably as the charge buildup in the well increases lends support to this hypothesis. The results of Eaves *et al.* [108] also show that the high-B_f series is only strong when there is substantial charge buildup. The rate of change in the period of these oscillations with bias shows a marked decrease at the threshold of the second resonance see Figure 4.47. This is because the energy level in the well is now staying approximately constant relative to the quasi-bound state of the 2DEG in the emitter contact.

When the device is biased at the second resonance we do not observe any magneto-oscillations from space charge in the quantum well. This means that

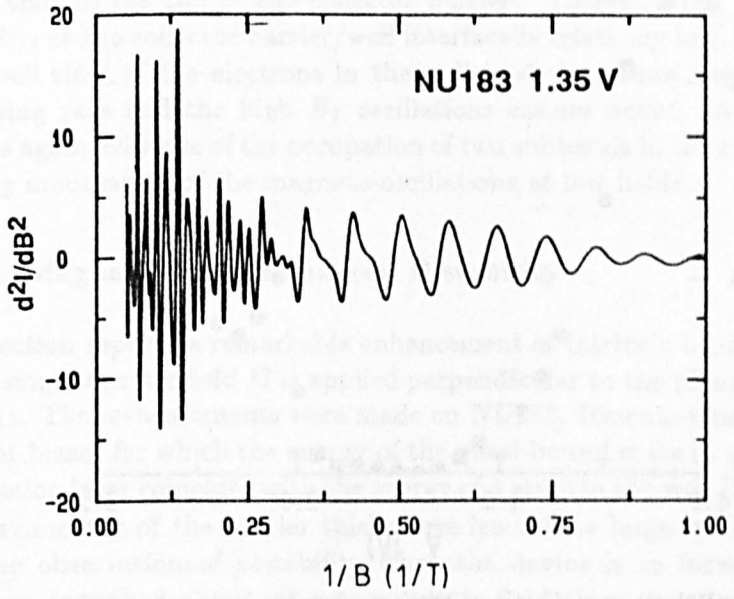

Figure 4.46: Second derivative d^2I/dB^2 plotted as a function of magnetic field $\boldsymbol{B} \parallel \boldsymbol{J}$ for *NU183* at a bias of 1.35 V. At high fields (low $1/B$) there are clearly two distinct series of rapid oscillations, one corresponding to elastic and one to inelastic scattering transitions.

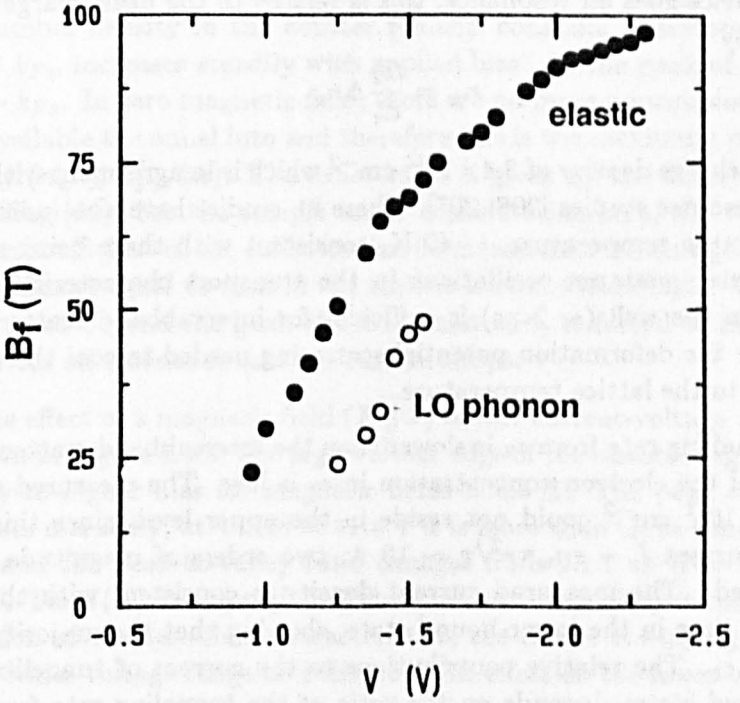

Figure 4.47: Periodicity of the high-frequency oscillations corresponding to inter-Landau level scattering transitions, • elastic and o inelastic series of oscillations.

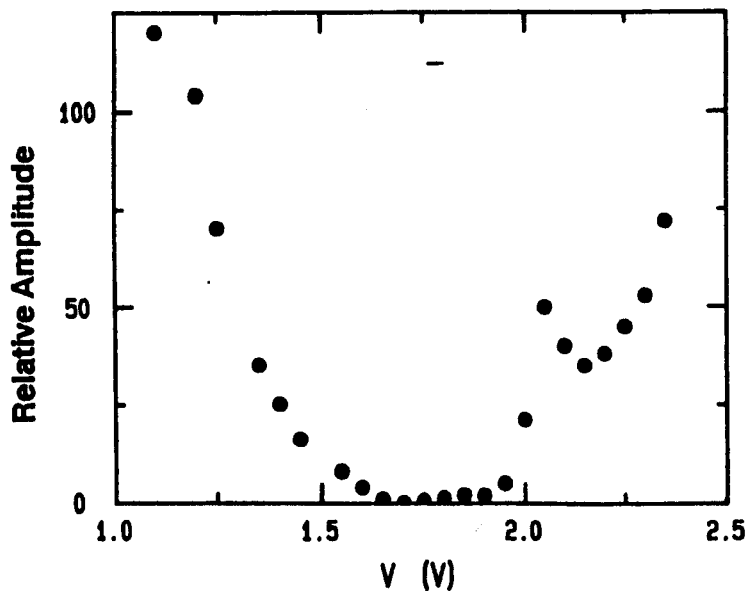

Figure 4.48: Relative amplitude of the inter-Landau level series and the oscillations due to the emitter 2DEG as a function of bias.

the electron temperature must be significantly above the lattice temperature, probably in excess of 50 K (at this temperature, most of the emitter series of oscillations have been lost). The charge density on resonance can still be estimated from the values of n_a [177, 182]. If we consider the step up in n_a when the device goes off resonance, this is related to the peak charge density in the well by

$$n_w = \frac{C_2}{C_t}\Delta n_a \tag{4.52}$$

This gives a charge density of 3.4×10^{11} cm^{-2} which is in agreement with recent photoluminescence studies [206, 207]. These PL studies have also indicated an elevated electron temperature, $\sim$ 40 K, consistent with there being no well-defined magnetoquantum oscillations in the transport characteristics. The dwell time in the well ($\sim$ 2 ps) is sufficient for intersubband scattering but too short for the deformation potential scattering needed to cool the electron distribution to the lattice temperature.

The tunnelling rate from ϵ_2 is slower than the intersubband scattering rate ($\leq$ 1 ps) and the electron concentration in ϵ_2 is low. The measured value of $n_w = 3.4 \times 10^{11}$ cm^{-2} could not reside in the upper level, since this would produce a current $I \sim en_w\pi r^2/\tau \sim 10$ A, two orders of magnitude greater than observed. The measured current density is consistent with the much longer dwell time in the lower bound state, showing that the majority of the charge is in ϵ_1. The relative contributions to the current of tunnelling from the two bound states depends on the ratio of the tunneling rate from ϵ_2 to the intersubband scattering rate, as well as the tunnelling rate from ϵ_1. These quantities are not known to any great accuracy, but a simple estimate from a transfer matrix method (taking a conduction band offset of 320 meV) shows that the majority of the current is due to electrons in ϵ_2.

At biases beyond the peak of the resonance, the high-B_f series is quenched,

because the electrons are injected into the well with energies very close to or above that of the top of the collector barrier. Therefore the probability of reflection at the collector barrier/well interface is relatively low. Consequently the dwell time of the electrons in the well is shorter than the intersubband scattering rate and the high B_f oscillations cannot occur. At these biases there is again evidence of the occupation of two subbands in the emitter contact causing modulation of the magneto-oscillations at low fields.

4.7.3 Magnetic-Field Enhanced Bistability

This section reports a remarkable enhancement of intrinsic bistability when a quantising magnetic field B is applied perpendicular to the plane of the tunnel barriers. The measurements were made on *NU183*. Resonant tunnelling takes place at biases for which the energy of the quasi-bound state in the emitter accumulation layer coincides with the energy of a state in the well (Section 4.4.2). The asymmetry of the barrier thicknesses leads to a large buildup of charge and the observation of bistability when the device is in forward bias. As has been described above, at zero-magnetic field electrons tunnnel from the two-dimensional emitter state into the quasi-bound state of the well with the conservation of transverse momentum. They then undergo energy relaxation to form a degenerate two-dimensional electron gas. This process is schematically shown in Figure 4.49 where the occupied emitter states are represented as a disc of states in k-space with transverse wavevector $k_\perp$ up to k_{Fa}, the Fermi wavevector in the emitter. Occupied states in the well also lie on a disc in k-space, but with a smaller radius, k_{Fw}. As charge buildup occurs, the number density in the emitter remains constant, therefore so does k_{Fa}, whilst k_{Fw} increases steadily with applied bias. At the peak of the resonance $k_{Fw} \sim k_{Fa}$. In zero magnetic field, there are no more unoccupied states in the well available to tunnel into and therefore this is the maximum possible charge density ($n_w \leq k_{Fa}^2/2\pi$). The exact value is given by the theory of sequential tunnelling [99]. For the sample under consideration here, the very low transmission coefficient of the collector barrier means that the charge density in the well is almost equal to that in the emitter accumulation layer. When the bias is increased beyond the peak of the resonance, n_a is forced to increase, taking the device off resonance and the current drops.

The effect of a magnetic field ($B \parallel J$) on the current-voltage characteristics is shown in Figure 4.50. The high-voltage edge of the bistable region, V_p, moves rapidly to higher bias for magnetic fields > 4.5 T. The peak current I_p also increases markedly; at a field of 11.4 T it is more than three times its low-field value and the peak-to-valley ratio changes from 2.1:1 at $B = 0$ to > 9:1 at 11.4 T. The $I(V)$ in the region of the enhanced bistability is simply a smooth extension of the zero-field characteristics; the device is staying on resonance over a wider voltage range and there is little effect on the lower-voltage section of the resonance. This would not be the case for a field-dependent series resistance (Section 4.3.5) which would merely move the peak to higher bias without changing the peak current value. Figure 4.51 plots the magnetic field dependence of V_p and of the low-voltage edge of the bistability, labelled V_v in Figure 4.50. For low magnetic fields, V_p is an oscillatory function of B, but for B > 4.5 T it increases almost linearly with field whilst V_v moves to a slightly

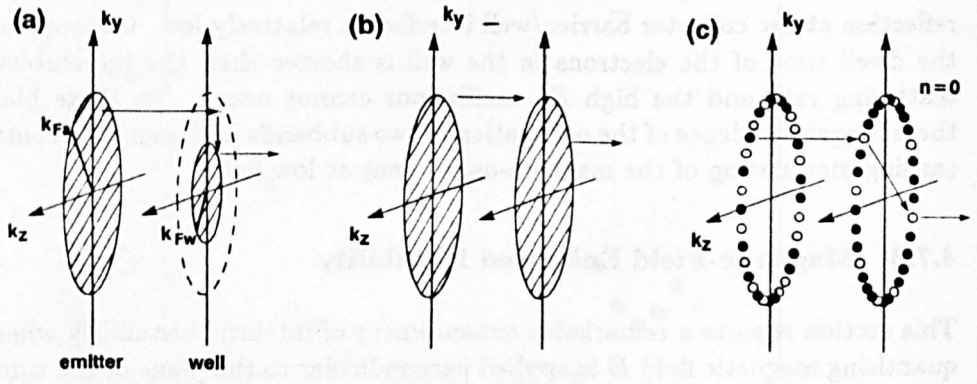

Figure 4.49: Schematic diagrams illustrating the tunnelling and thermalisation of electrons in a magnetic field. (a) At $B = 0$, electrons tunnel from the Fermi disc of states in the emitter of radius k_{Fa} into the well and then thermalise to form a disc of occupied states with a smaller radius, k_{Fw}. (b) At the peak of the resonance the Fermi wavevectors are equal and no more charge can be accommodated in the well. (c) In a high magnetic field the allowed energy levels lie on a circle. Due to rapid intra-Landau level scattering in the well it is possible for there to be a higher number of electrons in the well than in the emitter.

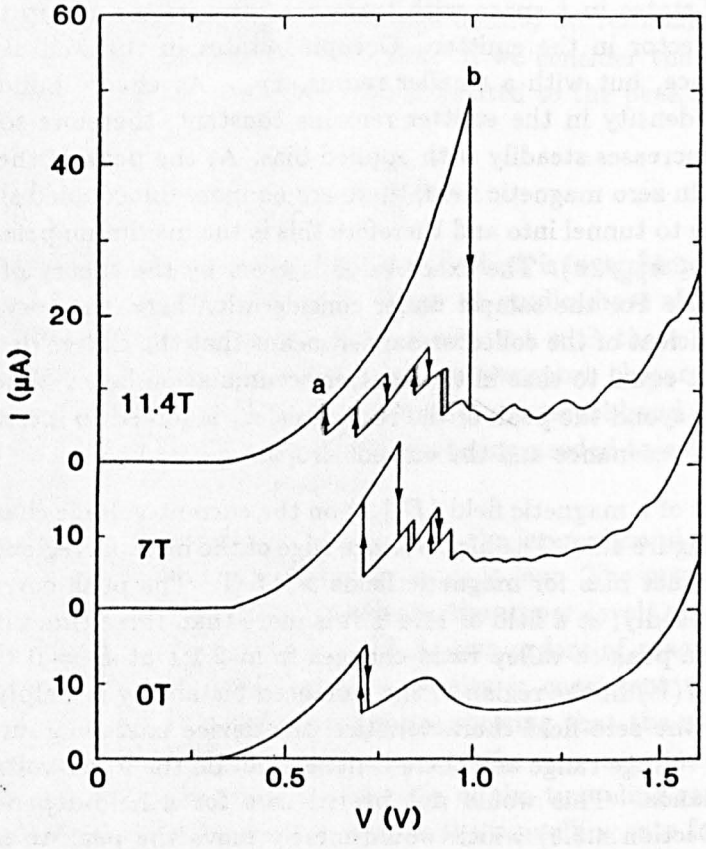

Figure 4.50: The effect of a magnetic field $B \| J$ on the $I(V)$ characteristics of *NU183* in the region of the first resonance in forward bias showing the magnetic field enhanced bistability.

lower bias at high fields. At the maximum available field (11.4 T) the bistable region extends over a voltage range greater than 300 mV compared with only $\sim$ 25 mV at zero field.

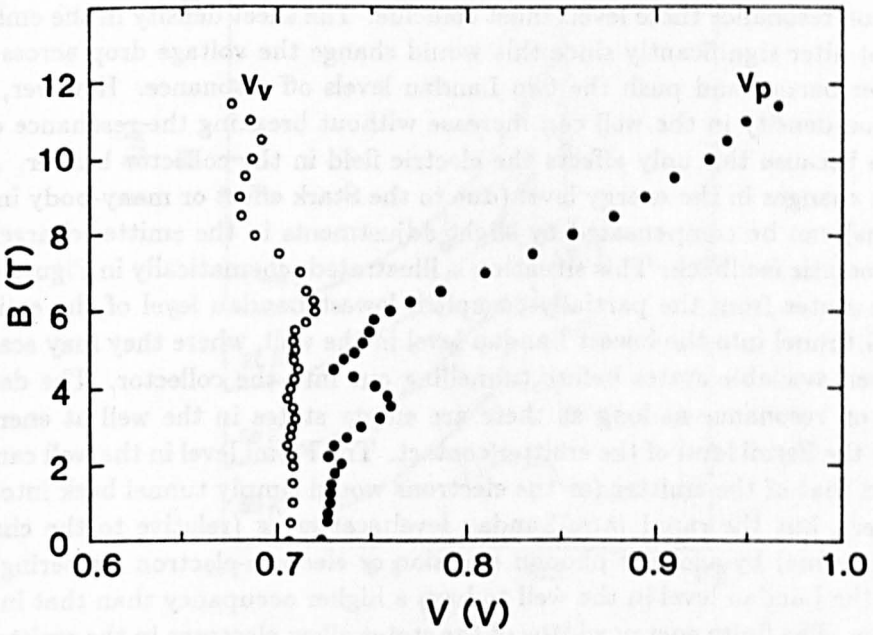

Figure 4.51: Variation of the voltages at the edges of the hysteresis loop, V_p and V_v, with magnetic field $\boldsymbol{B} \parallel \boldsymbol{J}$ at 4 K.

In a magnetic field, the $I(V)$ curve in the off-resonant portion of the bistability loop shows an additional series of peaks, some of which themselves show bistable regions whose voltage-width increase with magnetic field. The $I(V)$ curve is tristable in these regions. The replica structures are due to the LO phonon emission and elastic scattering processes described in Section 3.4. These inter-Landau level transitions lead to a significant buildup of space charge, which is enhanced by the magnetic field in the same way as the main resonant peak. Due to the presence of space charge in the quantum well, these structures do not follow the simple linear dependence with magnetic field observed previously (Section 3.4).

A quantising magnetic field $\boldsymbol{B} \parallel \boldsymbol{J}$ leads to the formation of discrete Landau levels in the emitter and the well with energies given by

$$\epsilon_n = \epsilon_i + (n + 1/2)\hbar\omega_c$$

where $n = 0, 1, 2\ldots$, $\omega_c = eB/m^*$ and ϵ_i is the bound state energy (Section 3.3). The states are completely quantised and the resonant tunnelling condition is satisfied when Landau levels of the same index n are aligned. This quantisation corresponds to fixed values of $k_\perp$, so all states now lie on a series of concentric circles rather than in a complete disc as shown in Figure 4.49. Each Landau level has a degeneracy of $2eB/h$ including spin. At magnetic fields below 4.5 T, the degeneracy of a single Landau level is insufficient to accommodate all the charge in the well at the peak of the resonance. In this

field range the charge buildup is little-changed and V_p and V_v remain close to their zero field values.

Above 4.5 T, the quantum limit is attained in both the emitter and the well and all the electrons are in a single Landau level. For the device to remain on resonance these levels must coincide. The sheet density in the emitter cannot alter significantly since this would change the voltage drop across the emitter barrier and push the two Landau levels off resonance. However, the electron density in the well can increase without breaking the resonance condition because this only affects the electric field in the collector barrier. Any minor changes in the energy level (due to the Stark effect or many-body interactions) can be compensated by slight adjustments in the emitter charge via electrostatic feedback. This situation is illustrated schematically in Figure 4.49 where states from the partially-occupied, lowest Landau level of the emitter 2DEG tunnel into the lowest Landau level in the well, where they may scatter between available states before tunnelling out into the collector. The device stays on resonance as long as there are empty states in the well at energies below the Fermi level of the emitter contact. The Fermi level in the well cannot exceed that of the emitter (or the electrons would simply tunnel back into the emitter), but the rapid *intra*-Landau level scattering (relative to the charge storage time) by acoustic phonon emission or electron-electron scattering enables the Landau level in the well to have a higher occupancy than that in the emitter. The finite energy widths of the states allow electrons in the emitter to tunnel into the well and then scatter into unoccupied states at slightly lower energy, producing a higher number density in the well. The high degeneracy of the Landau levels means that a small energy range can accommodate a large number of electrons. Therefore the device remains on resonance over a wider range of bias as the magnetic field increases.

The sheet charge density in the well can be obtained from integration of the differential capacitance (Section 4.5). This gives a peak sheet charge density of 3.7×10^{11} cm^{-2} at 11.4 T, considerably less than the Landau level degeneracy. The reason for the occupancy falling below unity is probably that the increasing space charge density in the well leads to a higher voltage drop across the collector barrier and hence to a more rapid tunnelling rate. The analysis of Sheard and Toombs [99] outlined in Section 4.2 is no longer directly applicable since $n_w > n_a$. Transfer matrix calculations involve considerable uncertainty but are not inconsistent with this supposition.

Some enhancement of the bistability is present at temperatures in excess of 80 K, as may be seen in Figure 4.52 and Figure 4.53 which show $I(V)$ curves at $B = 10$ T for temperatures up to 80 K and a plot of ΔV against temperature for a magnetic field of 10 T, respectively. As the temperature is increased, the dwell times of electrons in the well are reduced and so is the charge buildup (Section 4.6). At high temperatures, $k_B T \sim \hbar\omega_c$, the 2DEGs in the emitter and the well are no longer in the quantum limit and so no enhancement of bistability occurs.

These results could not be explained by extrinsic effects such as a series resistance or high-frequency circuit oscillations (Section 4.3). They provide further evidence for the intrinsic nature of the bistability. No field-dependence of the bistability in an asymmetric structure was observed by Zaslavsky *et al.*

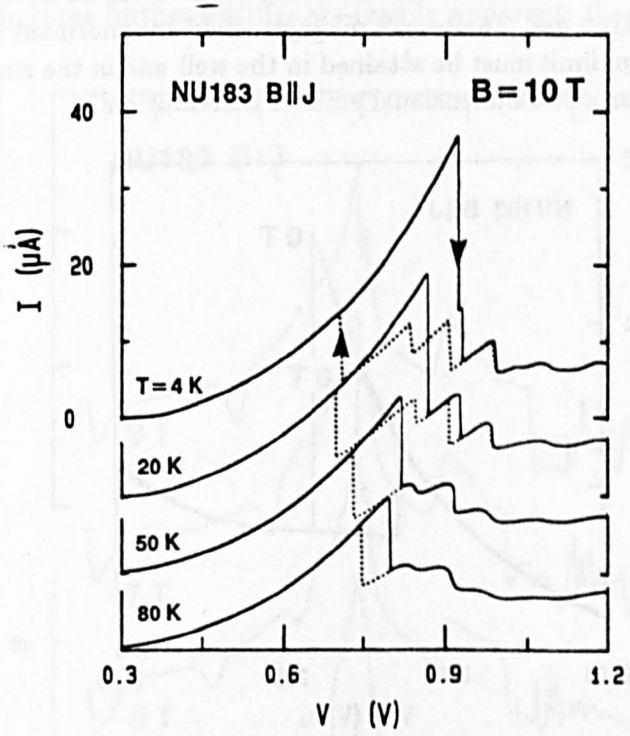

Figure 4.52: $I(V)$ curves for *NU183* at a magnetic field of 10 T showing the effect of increasing temperature on the magnetic-field-enhanced bistability.

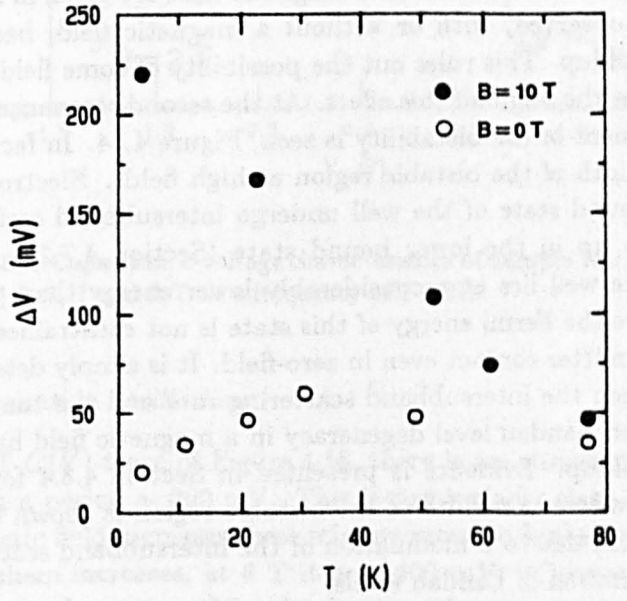

Figure 4.53: Width of the bistable region ΔV against temperature for zero field (o) and $B = 10$ T (•) showing the temperature dependence of the magnetic field induced enhancement of bistability

[181]. This may be due to the much higher doping levels in the contacts of their device (5×10^{17} cm^{-3}), so that tunnelling occurs from an essentially three-dimensional electron gas. To observe magnetic field enhancement as described here, the quantum limit must be attained in the well *and* in the emitter — this can only occur for a two-dimensional emitter distribution.

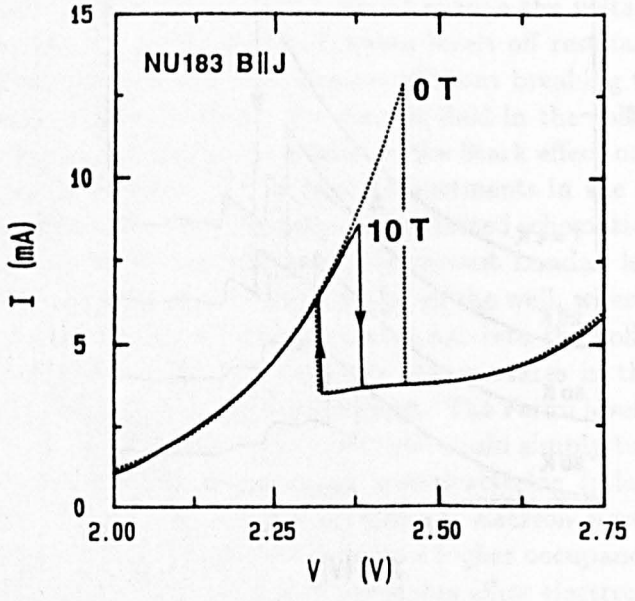

Figure 4.54: Current-voltage characteristics of the second resonance in forward bias for sample *NU183* in a magnetic field $\boldsymbol{B} \parallel \boldsymbol{J}$ of 11 T (full curve) and 0 T (dotted). In this case, the bistability is reduced by the application of a field.

The reverse-bias characteristics in a magnetic field are given in Section 3.4. No bistability is observed, with or without a magnetic field, because there is little charge buildup. This rules out the possibility of some field-dependent external resistor as the origin of this effect. At the second resonance in forward bias, no enhancement of the bistability is seen, Figure 4.54. In fact there is a decrease in the width of the bistable region at high fields. Electrons injected into the upper bound state of the well undergo intersubband scattering and the charge builds up in the lower bound state (Section 4.7.2). The lower bound state of the well lies at a considerably lower energy than the emitter state and therefore the Fermi energy of this state is not constrained to be less than that in the emitter contact even in zero-field. It is simply determined by the balance between the intersubband scattering rate and the tunnelling out rate. The increased Landau level degeneracy in a magnetic field has no effect on the charge buildup. Evidence is presented in Section 4.8.4 for a similar sample (*NU221*), where the width of the bistable region is shown to oscillate as a function of field due to a modulation of the intersubband scattering rate caused by the formation of Landau levels.

4.7.4 Magnetocapacitance

Figure 4.55 shows the capacitance-voltage characteristics for magnetic fields of 2, 3, 5, 7 and 9 T ($\boldsymbol{B} \parallel \boldsymbol{J}$) taken with the Hewlett-Packard LCR meter described in Section 2.1. The modulation used was 3 mV at a frequency of 1 MHz. The

traces are displaced for clarity. The enhancement of the bistability described in the above section is also seen in the capacitance traces as shown in Figure 4.56. In addition three further features are readily apparent; these will be described in turn.

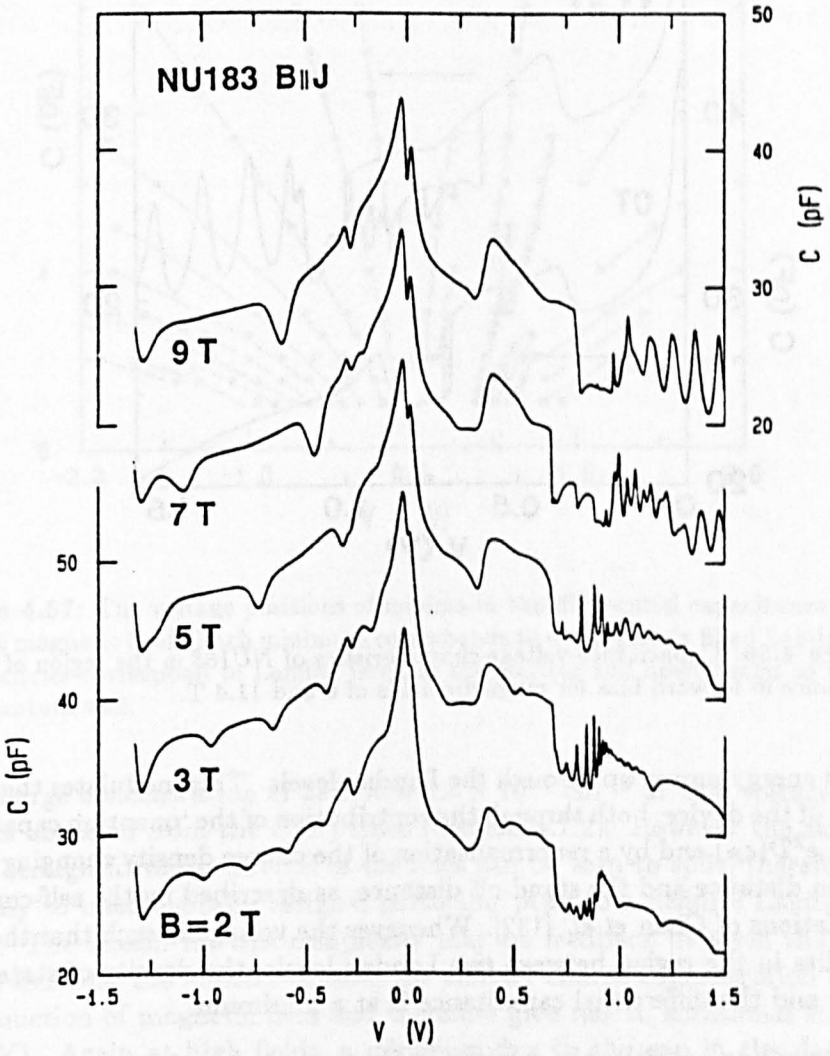

Figure 4.55: Capacitance-voltage characteristics of sample *NU183* in magnetic fields $B \parallel J$ of 2, 3, 5, 7 and 9 T at a frequency of 1 MHz.

Magnetoquantum oscillations

In the 2 T $C(V)$ trace of Figure 4.55, there is an almost periodic modulation in C with a period $\sim$ 200 mV. This is particularly clear in reverse bias. As the magnetic field increases these minima move to higher bias and the spacing between them increases, at 6 T it is $\sim$ 600 mV. They are obviously associated with the formation of Landau levels with energy spacing $\hbar\omega_c = \hbar eB/m^*$. The origin of the structure in $C(V)$ is exactly the same as for that in $C(B)$ described in Section 3.3. The application of a magnetic field quantises the density of states in the emitter 2DEG (and the well) into Landau levels each of which can accommodate $2eB/h$ electrons. Sweeping the bias voltage causes the number density in the accumulation layer n_a to increase and therefore the

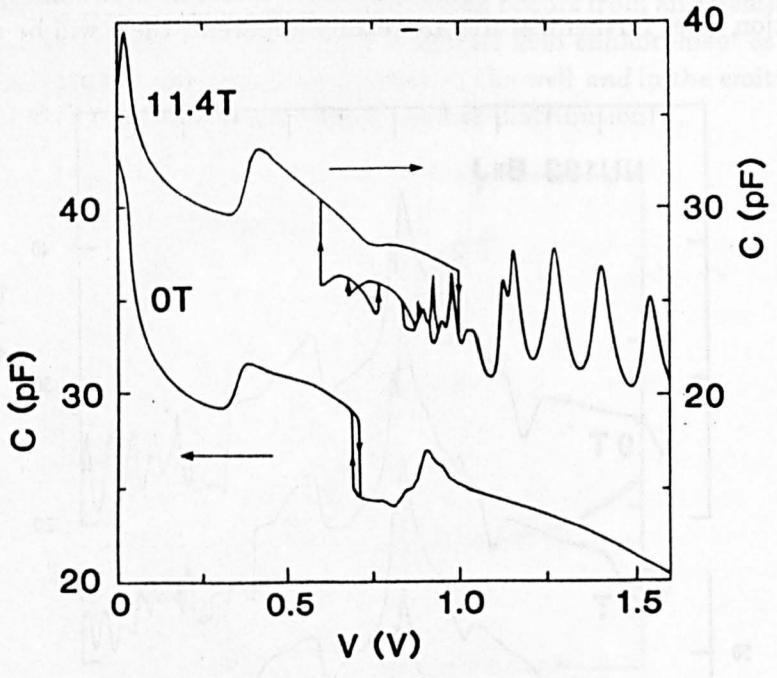

Figure 4.56: Capacitance-voltage characteristics of *NU183* in the region of the first resonance in forward bias for magnetic fields of 0 and 11.4 T.

Fermi energy moves up through the Landau levels. This modulates the capacitance of the device, both through the contribution of the 'quantum capacitance' $C_Q = e^2\mathcal{D}(\epsilon_F)$ and by a renormalisation of the charge density changing the depletion distance and the stand-off distance, as described by the self-consistent calculations of Chan *et al.* [132]. Whenever the voltage is such that the Fermi level lies in the region between two Landau levels, the density of states at ϵ_F is low and the differential capacitance is at a minimum.

The voltage positions of minima in C are plotted against magnetic field in Figure 4.57. The voltage spacing is determined by the voltage drop needed to completely fill another Landau level, *i.e.* to increase n_a by $2eB/h$ (neglecting spin splitting). For example, at $B = 6$ T there are adjacent minima at -0.4 V and at -0.92 V so $C = \Delta Q/\Delta V = 2e^2\pi r^2 B/h = 28$ pF which is in good agreement with the measured capacitance value (r is the radius of the mesa). The curvature in the $B-V$ plots is caused by the increasing depletion length in the collector contact producing a decrease in the capacitance. At fields above 4 T, a weaker minima becomes apparent at low biases, this corresponds to $n_a = eB/h$ *i.e.* to all the electrons being in the same spin direction. The fact that this feature is weaker than the inter-Landau level minima suggests that the spin levels are less well resolved than the Landau levels, consequently the density of states between them is higher and the quantum capacitance greater.

In the region of the first resonance in forward bias, where charge buildup is occurring, the structure in the capacitance is complex. Here it is due to filling complete Landau levels in the well and so constitutes an alternative method of determining the charge in the well, *e.g.* the minimum at 0.6 V, 3 T corresponds

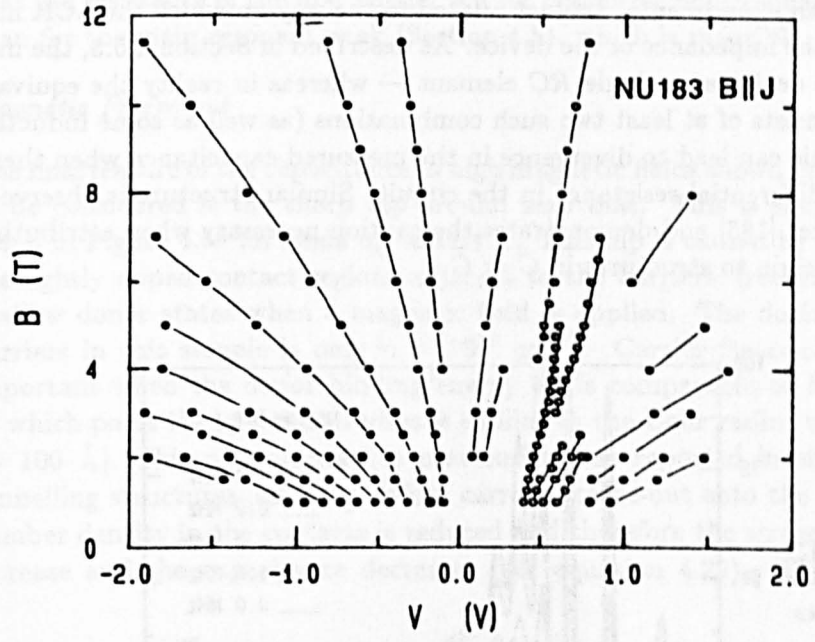

Figure 4.57: The voltage positions of minima in the differential capacitance plotted against magnetic field. Each minimum corresponds to a completely filled Landau level. Filled circles correspond to Landau levels in the emitter and open circles to those in the quantum well.

to a charge concentration of $2eB/h = 1.4 \times 10^{11}$ cm^{-2} at this voltage, equal to that obtained from the $C(B)$ trace (Section 4.7.2). However the structure is not straightforward. Several of the lines can be seen to split, therefore it is not easy to unequivocally assign a particular peak to a definite Landau level filling. The reason for this complexity may be feedback between the charge in the well and the emitter causing the emitter charge concentration to vary as a function of magnetic field and therefore give rise to additional structure in $C(V)$. Again at high fields, a minimum due to the gap in the density of states between the two spin states of the lowest Landau level is seen. At biases beyond the resonance, the emitter minima can again be identified, although they are partly masked by the additional features described below.

Non-resonant transitions

One of the most striking features of the $C(V)$ curves of Figure 4.55 is the sharply-peaked structure in the region of bias beyond the first resonance in forward bias. This appears to be associated with the $k_\perp$-nonconserving transitions described in Section 3.4. At first sight it is tempting to assign the structure to charge entering the well whenever the energy difference between the emitter bound state and the energy level in the well is equal to a multiple of $\hbar\omega_c$, particularly since the height of the peaks in the 1 MHz trace is approximately the same as the value of differential capacitance in the on-resonance state. However, Figure 4.58 shows this structure as a function of frequency at a field of 3 T, together with the corresponding plot of the AC conductance G. At low frequencies the height of the peaks is much increased, whereas for the

4 MHz trace there is very little structure. This shows that the structure in C is in fact an experimental artifact related to the way on which the LCR meter analyzes the impedance of the device. As described in Section 4.5.3, the meter treats the device as a single RC element — whereas in reality the equivalent circuit consists of at least two such combinations (as well as some inductance [113]). This can lead to divergence in the measured capacitance when there is negative differential resistance in the circuit. Similar structure is observed in $C(B)$ traces [183] and demonstrates the caution necessary when attributing a physical origin to structures in C or G.

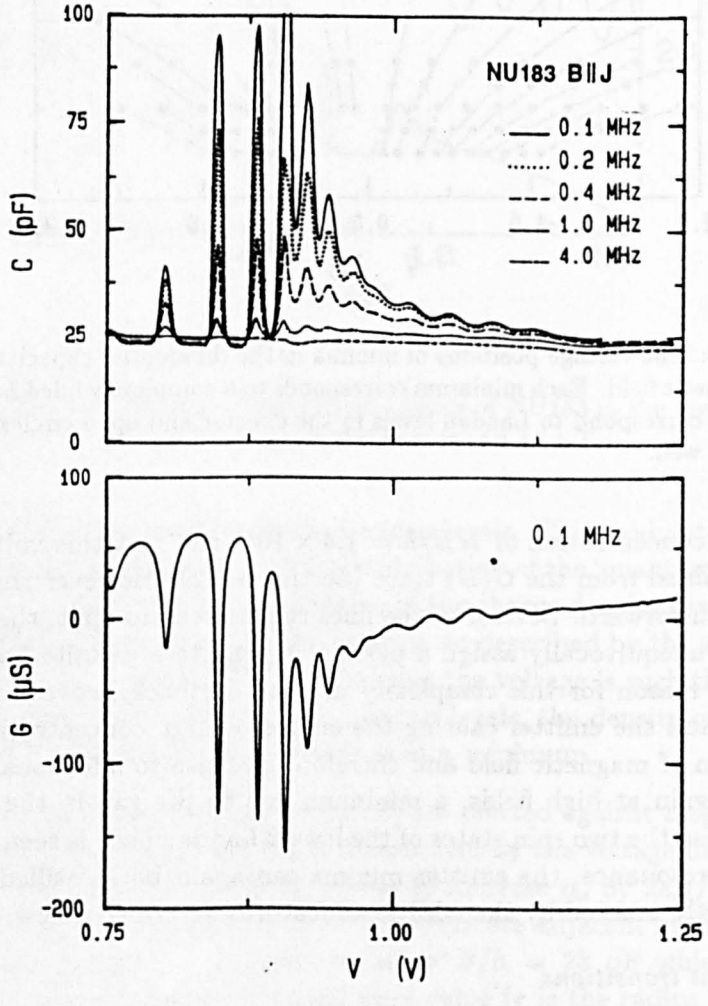

Figure 4.58: The differential capacitance and conductance for *NU183* in the bias region beyond the first resonance in a magnetic field of 3 T $B \parallel J$ as a function of the measuring frequency. This demonstrates that the structure in the capacitance is an artifact which merely reflects the negative differential conductance and is not related to the device capacitance

The much smaller structure in the capacitance on the low-current part of the hysteresis loop (Figure 4.56) may well be genuine since this is in phase with the conductance variation, rather than out of phase like the structure at higher biases, and there is no negative differential resistance in this region — even at low frequencies. If this is the case, the structure would indicate charge

buildup in the well at these biases, with the low value of capacitance implying that the resistance of the first barrier is a lot higher for non-resonant processes than for the main resonant peak (Section 4.5), which is plausible.

Magnetic Freeze-out

The final feature of the capacitance in high magnetic fields shown in Figure 4.55 to be considered is the sharp dip around zero bias. This is shown in more detail in Figure 4.59 for fields up to 11.4 T. This dip is caused by electrons in the lightly doped contact regions adjacent to the barriers 'freezing out' onto shallow donor states when a magnetic field is applied. The doping near the barriers in this sample is only $n = 10^{16}$ cm^{-3}. Carrier freeze-out becomes important when the donor binding energy ϵ_D is comparable to $\hbar\omega_c/2$ [123], at which point the cyclotron radius is similar to the Bohr radius of the donor ($\sim$ 100 Å). This phenomena has previously been reported in single-barrier tunnelling structures [69, 116]. When carriers freeze-out onto the donors, the number density in the contacts is reduced and therefore the screening lengths increase and the capacitance decreases (see equation 4.29). The observed

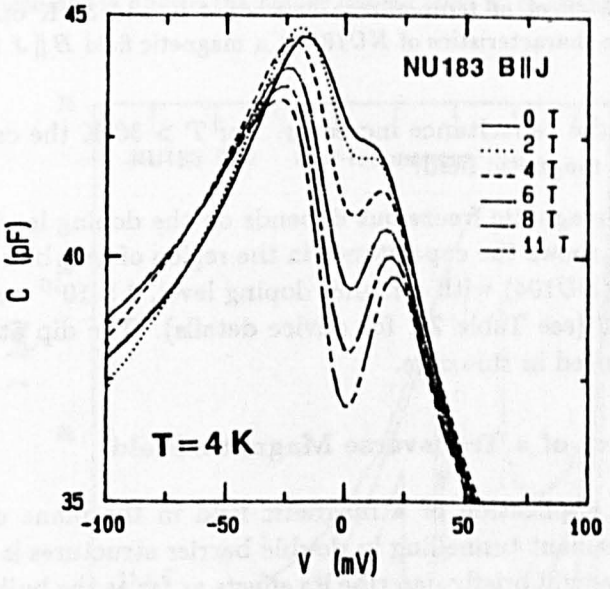

Figure 4.59: Differential capacitance of *NU183* near zero bias in magnetic fields $B \parallel J$ up to 11.4 T. The dip in C is caused by the magnetic freeze-out of electrons onto the donor ions.

drop in capacitance at zero bias from 42.5 pF at 0 Tesla to 37 pF at 11.4 T corresponds to an increase in the effective width of the parallel plate capacitor from 900 Å to 1100 Å.

When a bias is applied to the device, the electric field produced in the contact regions ionizes the donor states by field-emission and the capacitance returns to its zero magnetic field value. This occurs for voltages greater than $\sim$ 40 mV. Magnetic freeze-out is unimportant at the much higher voltages where the resonances occur. Figure 4.60 shows the effect of increasing the temperature. When the temperature is raised, the donors become ionized

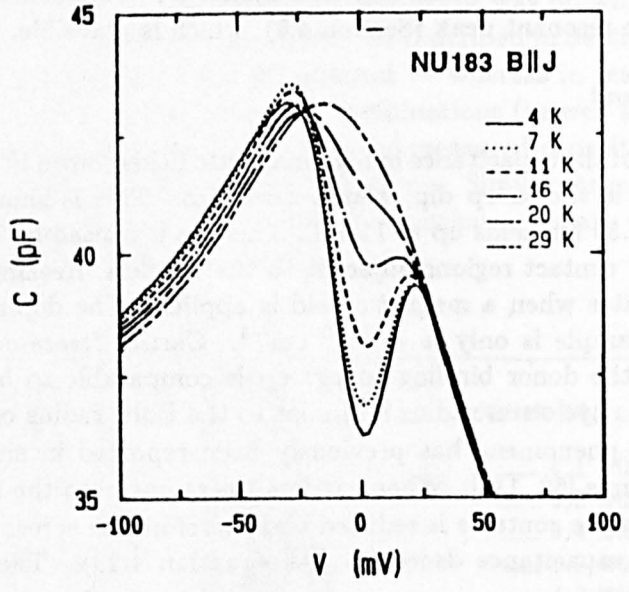

Figure 4.60: The effect of temperature between 4 K and 30 K on the low-bias capacitance-voltage characteristics of *NU183* at a magnetic field $B \parallel J$ of 11.4 T.

($k_BT \sim \epsilon_D$) and the capacitance increases. For $T > 30$ K the capacitance is unaffected by the magnetic field.

The extent of magnetic freeze-out depends on the doping level in the contacts. Figure 4.61 shows the capacitance in the region of zero bias for a double barrier structure (*NU104*) with a higher doping level, 2×10^{16} cm^{-3}, at fields of 0 T and 11.4 T (see Table 2.1 for device details). The dip at zero bias is much less pronounced in this case.

4.7.5 The Effect of a Transverse Magnetic Field

The effect of the application of a magnetic field in the plane of the barriers ($B \perp J$) on resonant tunnelling in double barrier structures is the topic of Chapter 5. Here we will briefly describe its effects as far as the buildup of space charge is concerned. The magnetic field changes the condition for resonance by introducing the vector potential **A** into the Hamiltonian. The tunnelling direction is x and the magnetic field is applied along z, and the vector potential is taken to be $\boldsymbol{A} = (0, Bx, 0)$. Conservation of transverse momentum, $m^*\boldsymbol{v}_\perp$, is now replaced by that of canonical momentum $\hbar\boldsymbol{k}_\perp = m^*\boldsymbol{v}_\perp - e\boldsymbol{A}$. This introduces a diamagnetic shift in the resonance position $\sim C_1/C_t \times e^2B^2\Delta x^2/2m^*$ where Δx is the distance between the emitter 2DEG and the centre of the well — see Section 5.3. Therefore both the threshold and the peak voltage move to higher bias with increasing field. Due to the inclusion of the vector potential, the resonance condition has a dependence on the value of k_y. This has the effect of spreading the resonance over a range of values of V_e (the voltage drop across the emitter barrier and accumulation layer), whereas at zero field there is only a single value of V_e for resonance. The transmission coefficients of the barriers are also affected, the vector potential effectively increases the barrier height [220].

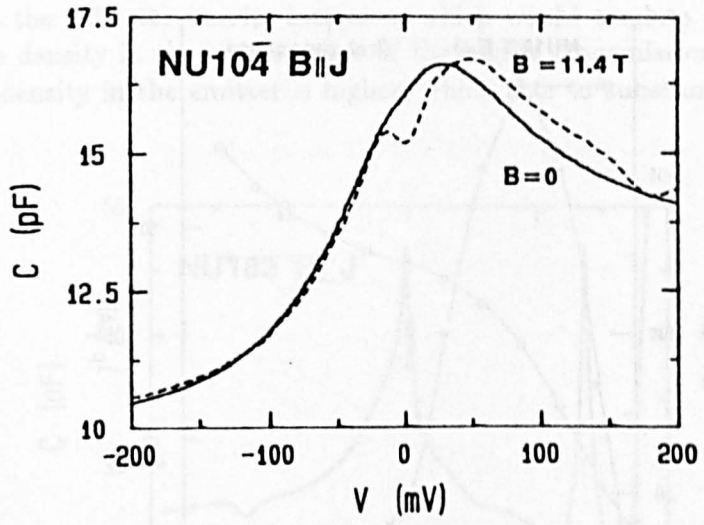

Figure 4.61: Capacitance-voltage characteristics of *NU104* at $B = 0$ T (solid line) and $B = 11.4$ T $B \| J$ (dashed line) at a temperature of 4 K. The reduced effect of magnetic freeze-out is due to the higher doping level in the contact.

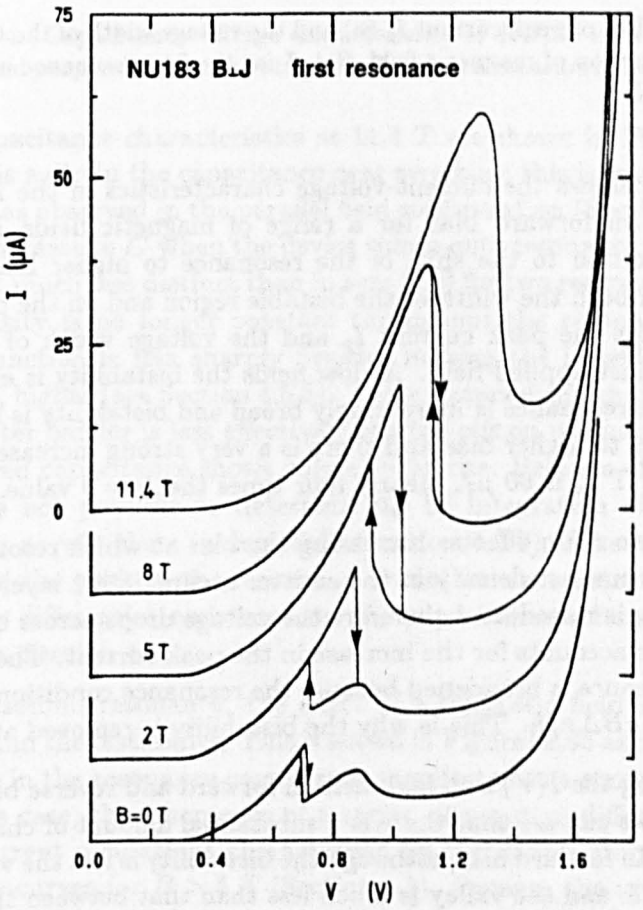

Figure 4.62: Current-voltage characteristics of *NU183* at the first resonance in forward bias at magnetic fields $B \perp J$ of 0, 2, 5, 8, and 11.4 T.

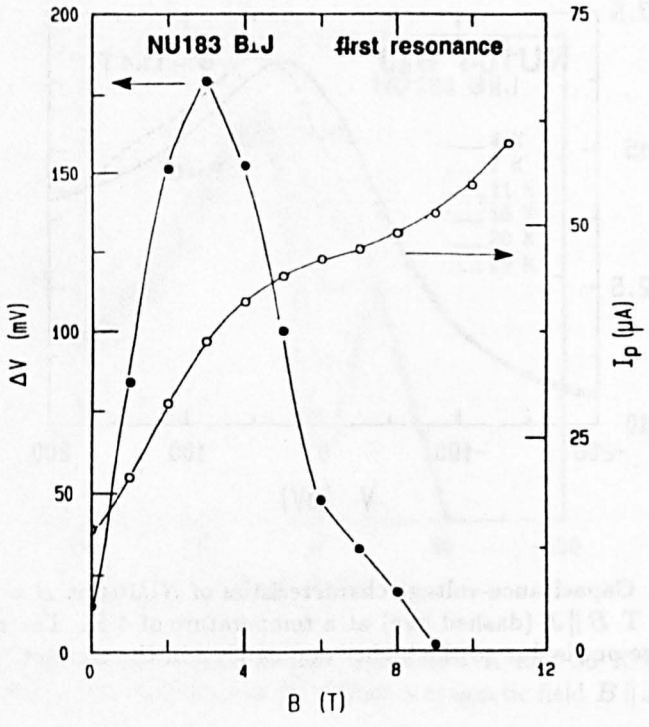

Figure 4.63: Plots of peak current I_p (o) and the voltage width of the bistable region ΔV (•), as a function of magnetic field $\boldsymbol{B} \perp \boldsymbol{J}$ for the first resonance in forward bias of sample *NU183*.

Figure 4.62 shows the current-voltage characteristics in the region of the first resonance in forward bias for a range of magnetic fields $\boldsymbol{B} \perp \boldsymbol{J}$ up to 11.4 T. In addition to the shift of the resonance to higher bias, there is a strong effect on both the width of the bistable region and on the peak current. Figure 4.63 plots the peak current I_p and the voltage width of the bistable region ΔV against applied field. At low fields the bistability is enhanced but for $B > 5$ T the resonance is increasingly broad and bistability is lost by 11 T. The peak moves to higher bias and there is a very strong increase in the peak current; at 11.4 T I_p is 60 μA, nearly four times the $B = 0$ value.

There are two main effects: increasing the bias at which resonance occurs means that the number density in the emitter accumulation layer at the peak of the resonance is raised, and therefore the voltage drops across both barriers are higher. This accounts for the increase in the peak current. The other effect is that the resonance is broadened because the resonance condition depends on k_y and on $k_0 = eB\Delta x/\hbar$. This is why the bistability is removed at high fields.

By comparing the $I(V)$'s at high field in forward and reverse biases (shown in Figure 5.6), we can see that there is a substantial amount of charge buildup even at 11.4 T. In forward bias, although the bistability is lost the voltage range between the peak and the valley is much less than that between the threshold and the peak whilst the opposite is true for the reverse bias resonance where there is no charge buildup. This implies that in forward bias the charge in the well on resonance is responsible for shifting the peak of the resonance to higher bias. This shift is estimated to be ~ 0.3 V which would require a charge density

very similar to that in zero field ($\sim 2 \times 10^{11}$ cm^{-2}). Although the voltage drop across the collector barrier increases, which would tend to produce a lower charge density in the well because of the higher transmission coefficient, the sheet density in the emitter is higher, which acts to substantially counteract this.

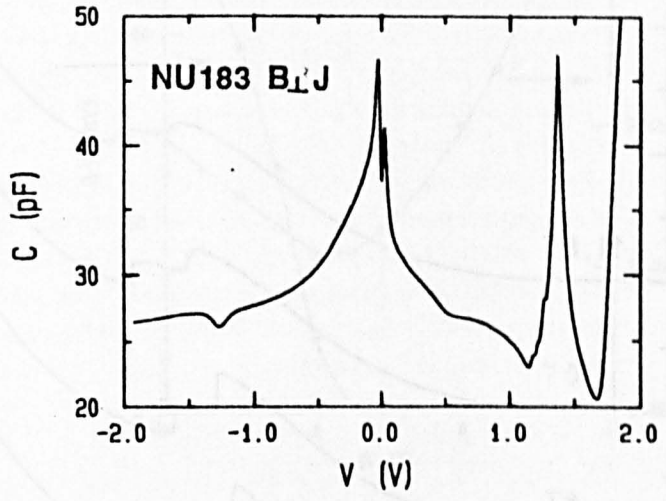

Figure 4.64: Capacitance-voltage characteristics of *NU183* in a magnetic field of 11.4 T applied perpendicular to the current $B \perp J$ at a measuring frequency of 1 MHz.

The capacitance characteristics at 11.4 T are shown in Figure 4.64. Note that there is a dip in the capacitance near zero bias; this is caused by magnetic freeze-out, as observed in the parallel field configuration (Section 4.7.4). There is still an increase in C when the device comes onto resonance at about 0.45 V. This step is much less distinct than in zero field for two reasons: (i) the emitter charge density is no longer constant throughout the resonance and (ii) the resonant function is less sharply peaked, making the impedance of the first barrier, R_1, higher (see Section 4.5.3). These factors mean that the capacitance of the emitter barrier is less effectively shorted out on resonance and therefore the measured capacitance shows only a slight rise. Because of the uncertainty in n_a, it is not possible to determine n_w by integration of the differential capacitance as was done in zero field (Section 4.5.2). The sharp spike in C just beyond the peak in the resonance is another demonstration of the effect of negative differential resistance on the capacitance-voltage characteristics discussed in Section 4.5.

At the second resonance, the effect of a magnetic field is to quench the resonance and the bistability. This is shown in Figures 4.65 and 4.66. Again the broadening in the resonance condition is manifested as a removal of bistability and, in this case, the emergence of a region of negative differential resistance leads to current oscillations characterised by the double-stepped structure in $I(V)$ in the curves for $B > 5$ T (Section 4.3). Because the upper bound state is so close to the top of the barrier, the increase in bias needed to achieve resonance in the presence of a perpendicular field rapidly reduces the dwell time in the well. This leads to a reduction in the charge stored in the well which tends to shift the peak to a lower bias, as observed in Figure 4.66 for

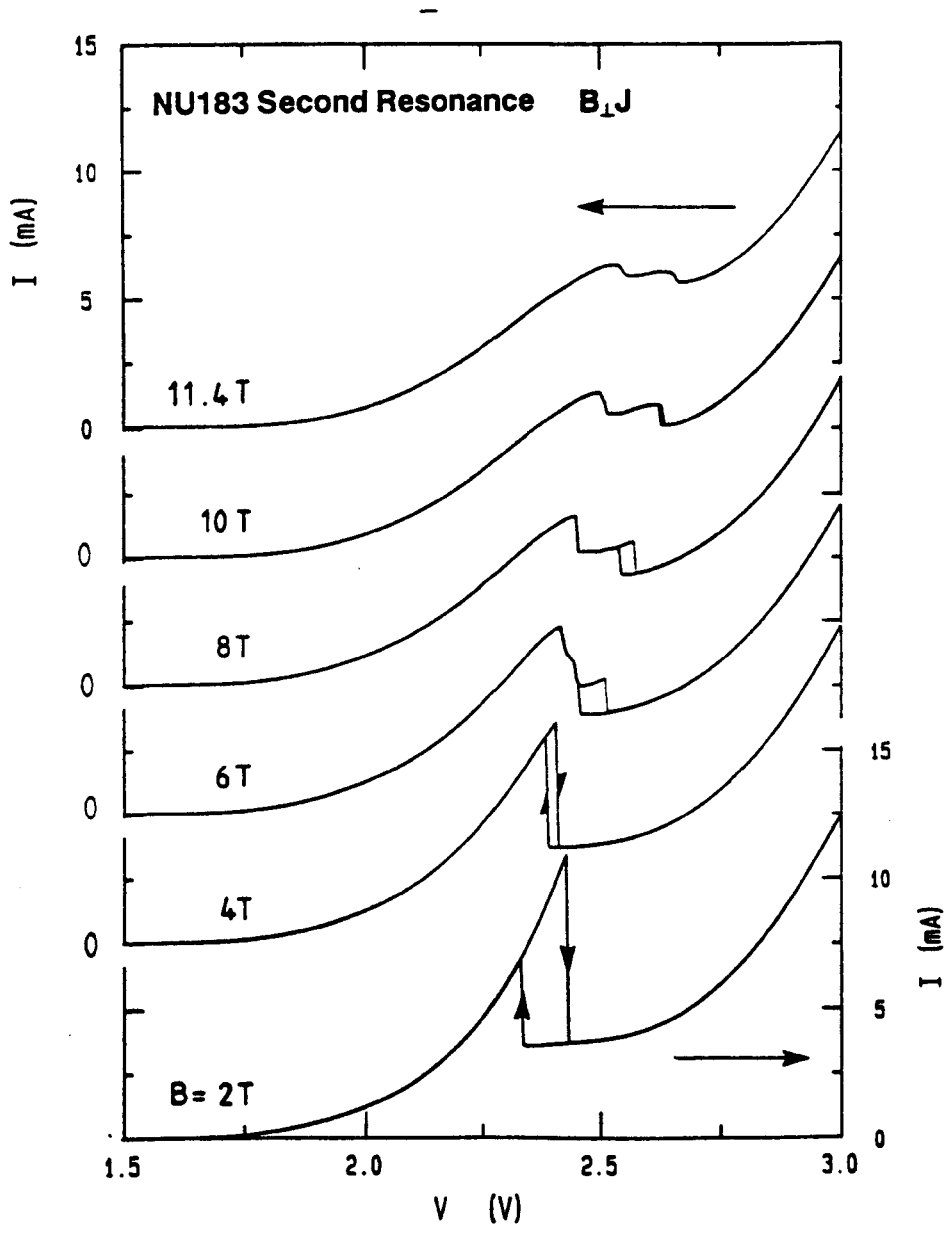

Figure 4.65: Current-voltage characteristics in a transverse magnetic field, $B \perp J$, for the second resonance in forward bias of sample *NU183*.

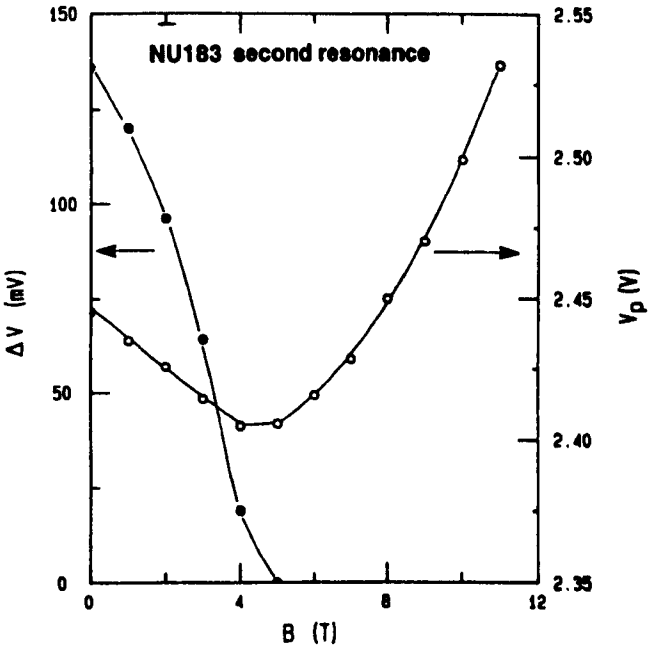

Figure 4.66: Plots of the width of the bistable region, ΔV (•), and the voltage at the peak of the resonance, V_p (o), against perpendicular magnetic field.

$B < 5$ T. At higher magnetic fields the bistability has been lost and there is little space charge in the quantum well. In this field range, the peak voltage moves to higher bias due to the diamagnetic shift in the resonance condition.

4.8 Inverted Bistability

4.8.1 Introduction

This section describes magnetotransport investigations of an intrinsic bistability effect in an asymmetric resonant tunnelling device in which, over a range of bias voltages, the off-resonant current exceeds the resonant current giving rise to a 'butterfly-shaped' hysteresis loop. This situation is the opposite of that described previously in this chapter for the conventional intrinsic bistability effect, therefore we term this an 'inverted' bistability. This new effect is caused by an enhancement of space charge buildup in a strongly asymmetric structure by intersubband scattering processes. The application of a quantising magnetic field $\boldsymbol{B} \parallel \boldsymbol{J}$ modulates the scattering rate leading to periodic oscillations in the width of the bistable region. Magnetotransport studies are also used to determine the space charge stored within the device. However these measurements are only able to give information as to the amount of charge stored and a careful analysis must be made to discover whether the number density obtained corresponds to a charge distribution in the accumulation layer of the emitter contact or in the quantum well. At low biases, the current density is very low and so capacitance measurements are used to investigate the device in the region of the first resonance. These results, together with current-voltage measurements in both parallel and perpendicular fields at higher bias, indicate that the first resonance presents very anomalous behaviour in which the charge density in the well is not limited by that in the emitter. For a wide range of applied bias, the charge in the emitter is constant whilst that in the well increases to a value several times greater. This behaviour is interpreted in terms of the extremely low transmission rate through the thick collector barrier and strong non-resonant scattering processes. These results show that the basic picture of space charge buildup presented over the course of this chapter does not completely describe the situation in all tunnelling devices.

4.8.2 Current-Voltage Characteristics

The active area of sample *NU221* consists of two $Al_{0.4}Ga_{0.6}As$ barriers of thicknesses 57 and 141 Å enclosing a quantum well of width 59 Å. The full parameters are given in Table 2.1. The doping profile in the contacts is identical to that for *NU183* — the asymmetric double barrier structure considered in the preceding sections.

The current-voltage characteristics of a 100 μm diameter mesa at 4 K are shown in Figure 4.67. Forward bias in this sample corresponds to electrons being injected into the well through the thinner barrier *i.e.* the top contact is biased positively with respect to the substrate. At high forward bias, a crossing in the current and a region of inverted bistability are observed [188, 189, 190]. At slightly lower bias ($\sim$ 2 V), structure is seen in the first derivative dI/dV, this will be discussed in Section 4.8.5. In reverse bias, a resonance is observed -0.75 V and weak features in the first derivative at -1.6 V and -2.5 V. The reverse bias resonance is relatively narrow, indicating that no buildup of space charge in the well occurs in this bias direction. The extremely low current densities are attributed to the low transmission coefficient of the 140 Å thick

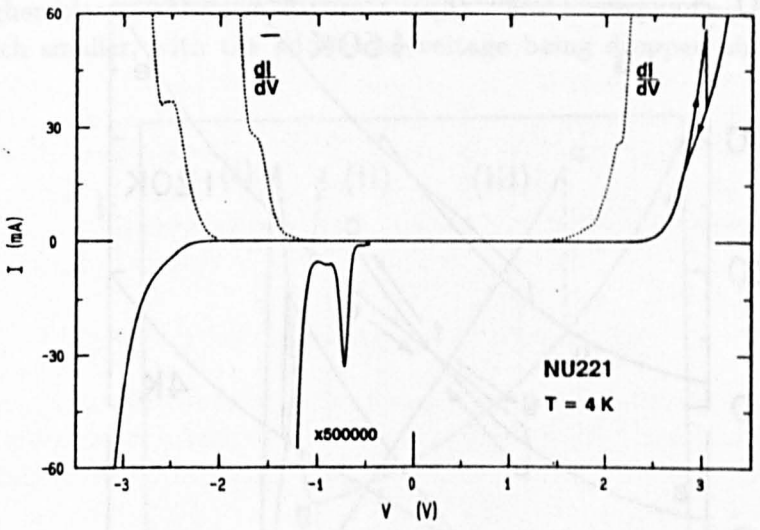

Figure 4.67: Current-voltage characteristics and first derivative, dI/dV, of a 100 μm diameter mesa of the strongly asymmetric double barrier structure *NU221* (barriers of width 57 Å and 141 Å) at 4 K.

barrier.

The resonance observed in reverse bias at -0.75 V is believed to correspond to tunnelling into the second subband of the quantum well because samples with similar well widths and doping profiles, but slightly different barrier thicknesses (83 Å - 111 Å *NU183* and 67 Å - 111 Å [221]), show a resonance in the region of 0.2–0.3 V in reverse bias. This resonance is not observed in this sample, presumably due to the low current density — in *NU183* the current increases by a factor of $\sim$ 200 between the first and second resonances, if this ratio were the same in this sample the first resonance would have a peak current of less than 0.3 nA.

The rapid increase in current in both bias directions at $\sim$ 3 V occurs when the bias is so large that the electrons are injected into the well with energies in excess of that of the top of the collector barrier and hence tunnel through only the emitter barrier — leading to a higher current density.

4.8.3 Inverted Bistability

The current-voltage characteristics in the region of the inverted bistability are shown in Figure 4.68(a) for a range of temperatures. As described previously, resonant tunnelling occurs when the bound state energy of the emitter 2DEG is aligned with that of a state in the quantum well. Because of the finite, but narrow, widths of these states, the tunnelling rate from the emitter to the well is a sharply-peaked function of the voltage drop across the accumulation layer, emitter barrier and first half of the well V_e. This picture will be slightly modified at the end of this section. In the absence of space charge buildup in the well, the observed variation of current with applied voltage would also be sharply-peaked, as is observed in reverse bias (Figure 4.68(b)) and shown schematically in Figure 4.69(i). Space charge in the well increases the electric

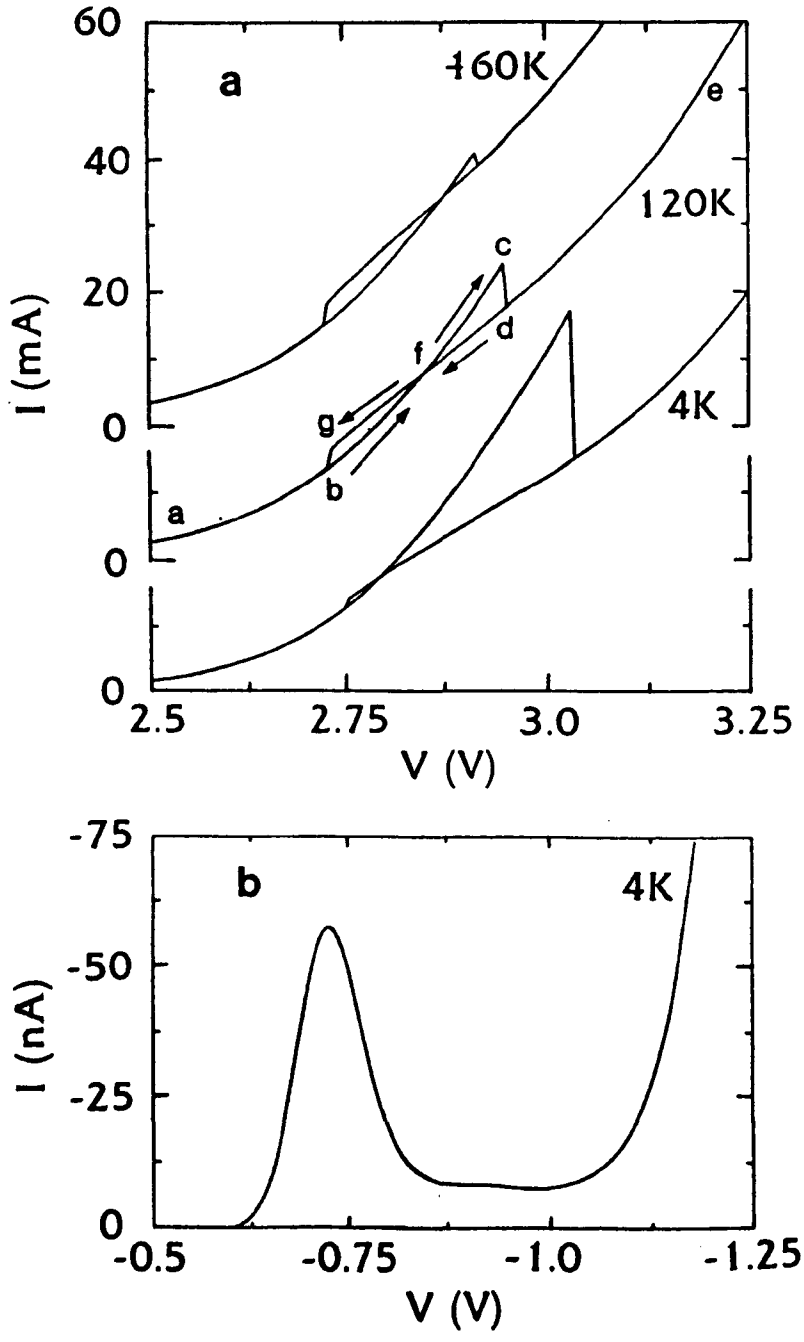

Figure 4.68: (a) Current-voltage characteristics of *NU221* in the region of inverted bistability for temperatures of 4 K, 120 K and 160 K. (b) Expanded plot of the current in the region of the first observed resonance in reverse bias.

field in the collector region and therefore the peak of the resonance is shifted to higher bias as shown in Figure 4.69(ii). The corresponding change in V_e is much smaller, with the additional voltage being dropped almost entirely

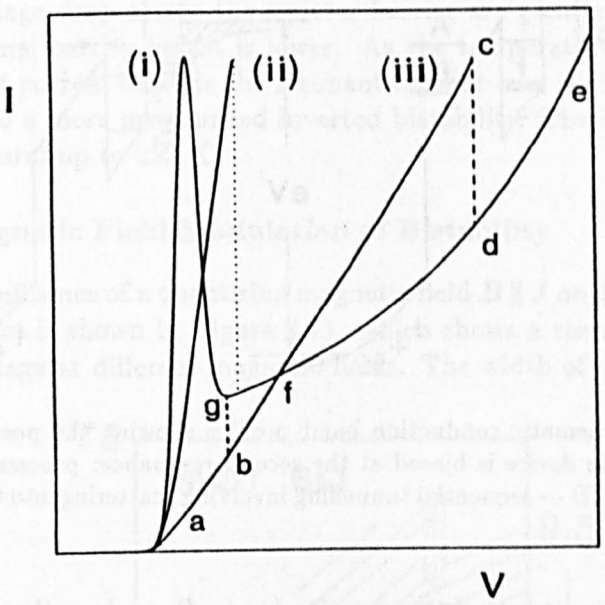

Figure 4.69: Schematic diagram illustrating the effect of space charge buildup on the current-voltage characteristics (i) no charge buildup (ii) intrinsic bistability due to charge buildup (iii) large buildup of charge leading to a region of inverted bistability where the off-resonant current exceeds the resonant current.

across the collector barrier and depletion layer. In the conventional intrinsic bistability effect described in Section 4.4, the resonant current always exceeds the off-resonant current. In this new device, the effect of space charge is even more pronounced, curve (iii), and causes the inverted bistability in which the off-resonant current in the range g to f exceeds the resonant value. This is the origin of the butterfly-shaped hysteresis loop.

Let us now consider the tunnelling processes shown in Figure 4.70. Electrons tunnelling into ϵ_2 reach the collector either by tunneling coherently through the second barrier (process A) or by a sequential process (B) involving scattering into the lower subband (ϵ_1) and subsequent tunnelling out into the collector. Due to the low probability of tunnelling out of the lower bound state, process B leads to a significant buildup of electronic space charge (n_w) in the quantum well. As will be discussed below, it is not immediately clear whether the electrons are actually resonantly tunnelling into ϵ_2 in this voltage range, or whether the $k_\perp$-nonconserving transitions from the emitter into the lower bound state are sufficiently strong to cause the space charge buildup. This question, however, has little bearing on the following discussion. The space charge in the well and in the emitter can be determined from the magnetoquantum oscillations in I and C when a magnetic field is applied $\boldsymbol{B} \parallel \boldsymbol{J}$ (Section 4.7.2). These will be described in Section 4.8.5. The charge in the well is found to reach a value $\sim 7 \times 10^{11}$ cm^{-2}, much greater than that in *NU183*.

As the voltage is increased beyond the peak of the resonance (point c in

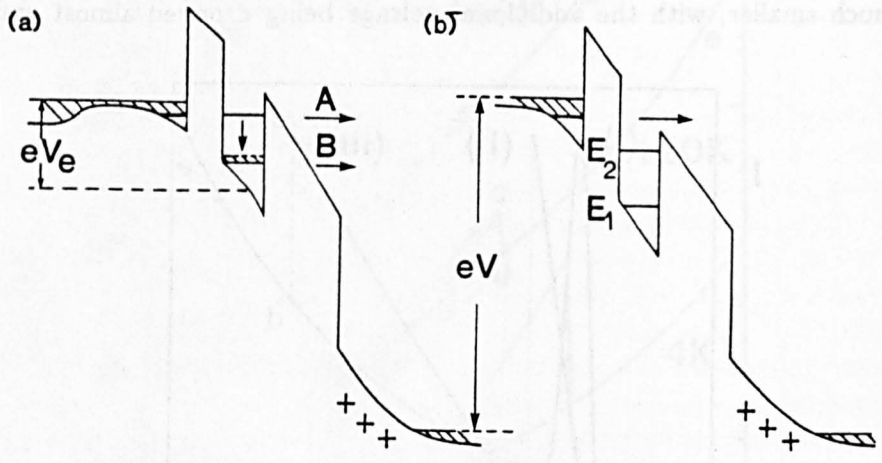

Figure 4.70: Schematic conduction band profiles showing the possible tunnelling processes when the device is biased at the second resonance: process A — coherent tunnelling, process B — sequential tunnelling involving scattering into the lower bound state of the well.

Figure 4.68), the current drops rapidly ($c \rightarrow d$) as does the electron sheet density in the well, n_w. This is compensated by an increase in the charge density in the emitter n_a which maintains the voltage drop across the device. At point d the device is in the low-current state in which the charge density in the well is low. It remains in this state when the voltage is increased up to and beyond point e or reduced back to point g. From the sheet charge density in the accumulation layer and in the well, we can use Gauss's law to determine the potential distribution across the device over a wide range of operating conditions as described in Section 3.2. Such an analysis shows that over the voltage range from e to g the electrons are injected into the well at energies well above the height of the collector barrier (for any reasonable choice of conduction band offset) as shown in Figure 4.69(b). Therefore they encounter only one tunnel barrier.

When the voltage is further reduced, the device makes the transition back to the high-current state ($g \rightarrow b$). In state b, n_w is significantly larger, and n_a significantly lower, than in state g, so that the top of the collector barrier is at a considerably higher potential energy, as can be seen by comparing the two conduction band profiles of Figure 4.70. Because of the increased height of the collector barrier in state b, the lifetime of electrons in the well is sufficiently long to allow them to scatter into ϵ_1, from where they tunnel into the collector with a low transmission rate. Scattering may be due to interface roughness, alloy fluctuations or phonon emission, see Section 3.4. Since the tunnelling rate is determined only by the kinetic energy associated with the tunnelling direction, and not that due to motion in the plane of the barriers, this scattering process greatly reduces the tunnelling probability of electrons in the well. As can be seen from Figure 4.70, the non-resonant current exceeds the resonant current because the electrons only have to tunnel through the emitter barrier, across which the voltage drop is higher than in the 'resonant' case.

This analysis is supported by the temperature dependence of the bista-

bility shown in Figure 4.68. The non-resonant current is more sensitive to temperature due to increased contributions from phonon-assisted processes and energetic electrons in the high-energy tail of the distribution function of the emitter. Off resonance, both the bound state energy in the emitter 2DEG and the voltage drop across the emitter barrier are greater, therefore the effective thermal barrier height is lower. As the temperature is increased, the non-resonant current exceeds the resonant current over a wider range of bias, giving rise to a more pronounced inverted bistability. The bistability persists to temperatures up to 250 K.

4.8.4 Magnetic Field Modulation of Bistability

The strong influence of a quantising magnetic field $\boldsymbol{B} \parallel \boldsymbol{J}$ on the current-voltage characteristics is shown in Figure 4.71, which shows a series of sweeps of increasing voltage at different magnetic fields. The width of the bistable region

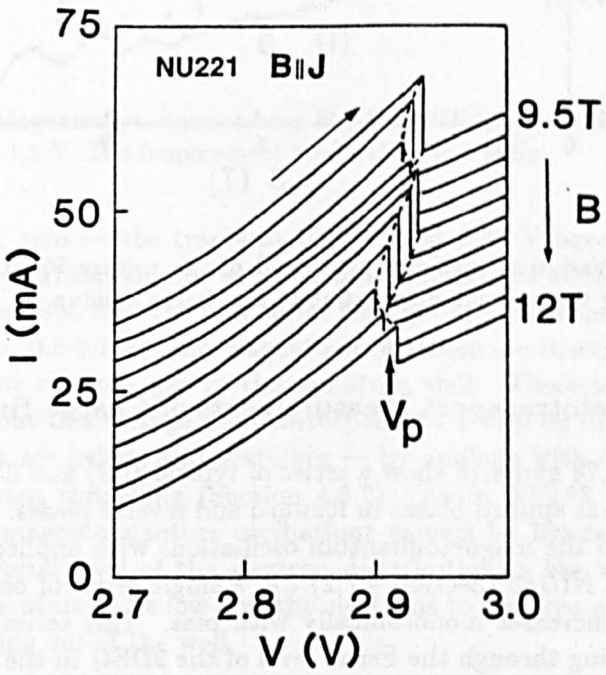

Figure 4.71: The effect of magnetic field $\boldsymbol{B} \parallel \boldsymbol{J}$ on the current-voltage characteristics (increasing V) of *NU221* at $T = 4$ K. The vertical axis corresponds to the tunnel current for the 12 T curve and the other curves are displaced for clarity.

decreases at low fields and then the voltage position at the peak of the resonance V_p oscillates, as shown in Figure 4.72 which plots V_p as a function of magnetic field. We attribute this to a modulation of the scattering rate into ϵ_1 due to the formation of Landau levels. The scattering rate is maximum when

$$\epsilon_0 + eV_1 - \epsilon_1 = j\hbar\omega_c = \hbar eB_f/m^*$$

where j is an integer, V_1 is the voltage droppped across the emitter barrier and the first half of the well ($= V_e - V_a$), $\hbar\omega_c$ is the cyclotron energy and B_f is the frequency of the magneto-oscillations. The modulation of the scattering rate by the magnetic field alters the charge buildup in ϵ_1. This affects the distribution of potential through the device and hence the voltage position of

the peak, as well as the tunnel current. The variation in V_p with field shown in Figure 4.72 is periodic in $1/B$ with a B_f-value $\sim$ 70 Tesla. This gives an energy difference of $\sim$ 125 meV which is approximately equal to that of the intersubband energy separation in a quantum well of this width under bias. The dependence of the peak position on magnetic field is good evidence for the charge buildup occurring in the lower subband rather than ϵ_2.

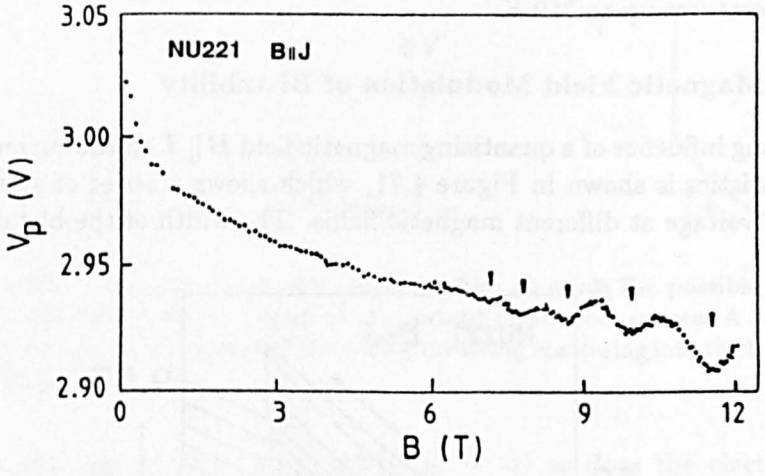

Figure 4.72: Variation with magnetic field of the voltage V_p at the peak of the current, showing the periodic modulation of the charge buildup.

4.8.5 Magnetotransport Measurements of Charge Buildup

Figures 4.73, 4.74 and 4.75 show a series of typical $I(B)$ and $C(B)$ traces for a range of constant applied biases in forward and reverse biases. In reverse bias the variation of the magnetoquantum oscillations with applied bias is similar to that seen in *NU183* (Section 4.7.2) *i.e.* a single series of oscillations whose frequency B_f increases monotonically with bias. This series is due to Landau levels passing through the Fermi level of the 2DEG in the emitter contact (section 3.3). At high biases (> -1.8 V) there is a modulation of the magnetoquantum oscillations at low magnetic fields due to the presence of a second subband in the emitter accumulation layer. The charge densities deduced from these oscillations (using $n_a = 2eB_f/h$ — Section 3.3) are plotted in Figure 4.76. The steady increase in n with bias indicates the lack of space charge buildup in the well in this direction of bias as expected from the device specifications and the $I(V)$ characteristics. The charge densities may be fitted fairly well by the simple model of Section 3.2 based on Gauss's law and the Fang-Howard variational wavefunction. This is shown as the solid line in Figure 4.76.

At low forward bias there is a single series of oscillations. The corresponding values of sheet charge density are plotted in Figure 4.77. Since the assignment of charge to the well or to the 2DEG in the emitter is uncertain at this stage, the number density is simply labelled n. The n values at low bias are very similar to those in reverse bias, therefore this series of oscillations is attributed to Landau-level effects in the accumulation layer of the contact. Once the bias reaches 0.3 V, this series is replaced by one of lower frequency whose B_f

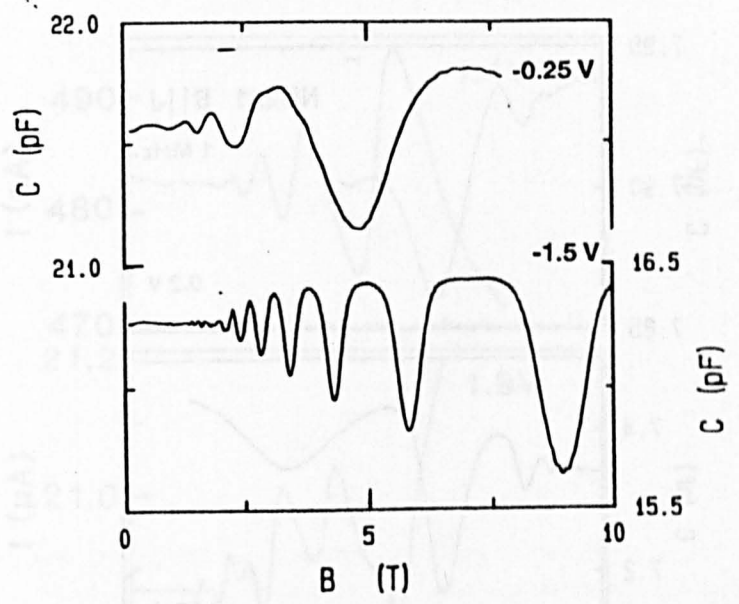

Figure 4.73: Magnetocapacitance traces $B \parallel J$ for *NU221* in reverse bias at voltages of -0.25 V and -1.5 V. The frequency of modulation is 1 MHz.

increases from zero — the traces at 0.25 V and 0.55 V have the almost the same frequency. This is similar to the situation in *NU183* at the first resonance (0.35-0.75 V) except that the new series totally dominates the $C(B)$ trace. In this bias range (0.3-0.7 V), the magneto-oscillations are therefore attributable to a degenerate electron gas in the quantum well. There is no measurable current here, but this voltage does correspond to a step up in the capacitance characteristics, see below, and therefore — by analogy with *NU183* — to the onset of resonant tunnelling (Section 4.5.2). As in *NU183*, the observation of a series of magnetoquantum oscillations caused by Landau levels passing through the Fermi level of the electron distribution in the well requires the electron temperature to be low and the electrons to undergo energy relaxation before tunnelling out of the well.

In *NU183* there was a step-like increase in n_a at ~ 0.75 V where the device went off resonance and the charge was ejected from the well. However in *NU221*, the series of oscillations attributed to the charge distribution in the well continues beyond 0.7 V with increasing B_f and no break in the curve is observed, even though n_w now exceeds the number density in the emitter. It was argued in Section 4.7.2 that once the charge in the well is equal to that in the emitter there are no more unoccupied states in the well available to tunnel into and hence any further increases in bias should take the device off-resonance. Possible explanations of why this should not apply in this particular sample are offered below. An alternative view is to assume that at biases beyond 0.7 V, the measured B_f corresponds to the charge density in the emitter accumulation layer rather than to the charge in the well. A comparison of the measured sheet charge density n with the amount of space charge calculated to be present from Gauss's law, as indicated by the dashed line in Figure 4.77, shows that there must be an additional amount of charge above that measured from the magnetoquantum oscillations in order to produce the

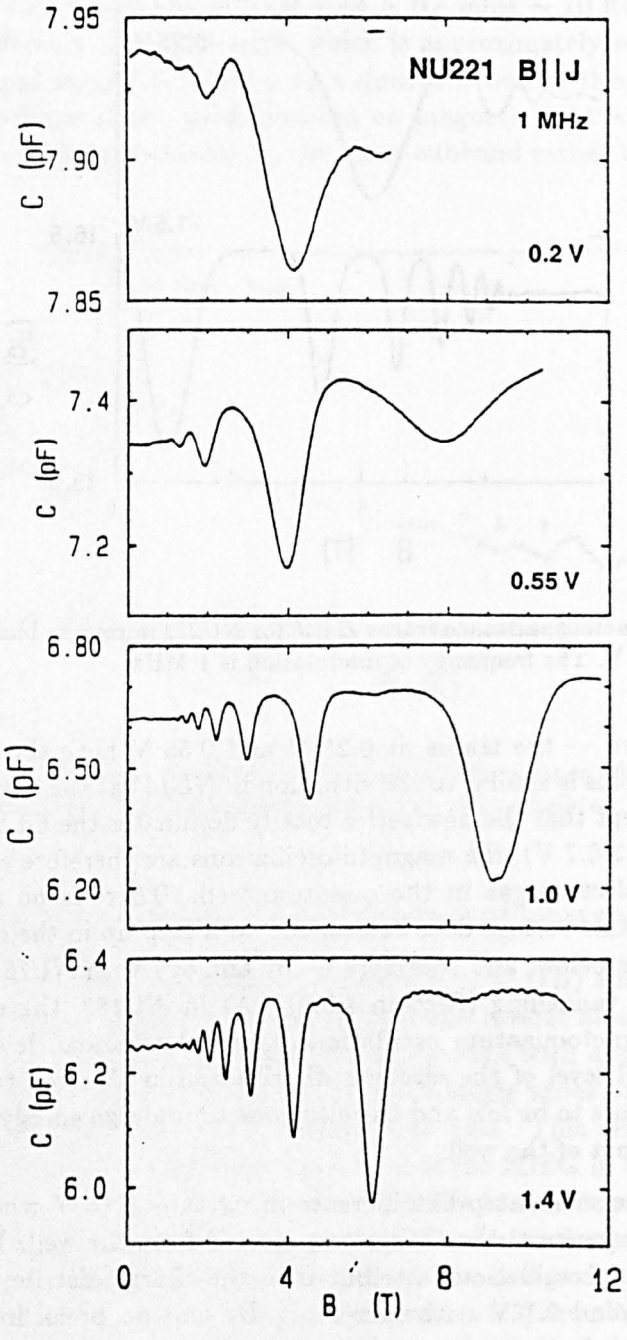

Figure 4.74: Magnetocapacitance in $\boldsymbol{B} \| \boldsymbol{J}$ for *NU221* at 4 K for biases of 0.2 V, 0.55 V, 1.0 V and 1.4 V.

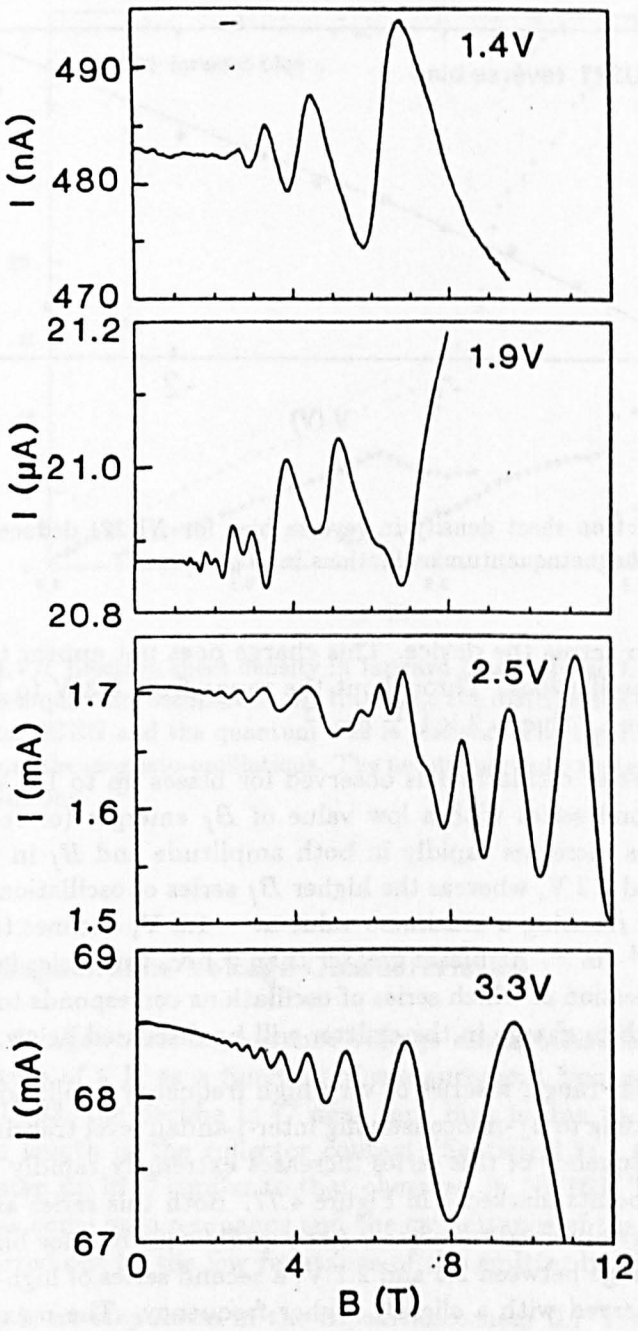

Figure 4.75: Tunnel current as a function of magnetic field for *NU221* at biases of 1.4 V, 1.9 V, 2.5 V and 3.3 V.

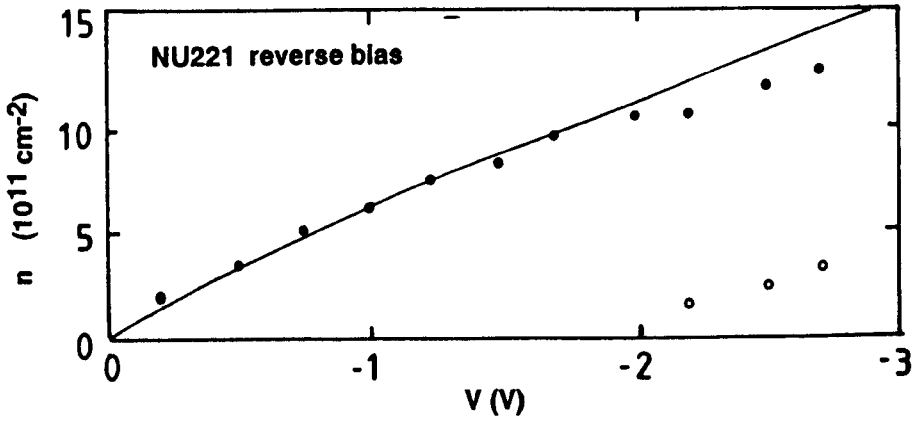

Figure 4.76: Electron sheet density in reverse bias for *NU221* deduced from the periodicity of the magnetoquantum oscillations in $\boldsymbol{B} \parallel \boldsymbol{J}$.

total voltage drop across the device. This charge does not appear to give rise to any magneto-oscillations. Throughout the range from 0.3 V to 1.6 V, this is required to have a value $\sim 2 \times 10^{11}$ cm^{-2}.

Only one series of oscillations is observed for biases up to 1.6 V. Beyond this point, a second series with a low value of B_f emerges (or re-emerges). This second series increases rapidly in both amplitude and B_f in the region between 1.8 V and 2.2 V, whereas the higher B_f series of oscillations becomes weaker and, after reaching a maximum value at $\sim$ 1.9 V, declines to a charge density $\sim 5 \times 10^{11}$ cm^{-2}. At biases greater than 2.1 V, this series is no longer observed. The question of which series of oscillations corresponds to charge in the well and which to charge in the emitter will be discussed below.

Also in this bias range, a series of very high frequency oscillations are observed, corresponding to $k_\perp$-nonconserving inter-Landau level transitions (Section 3.4). The frequency of this series increases extremely rapidly with bias, as shown by the points marked $\diamond$ in Figure 4.77. Both this series and that at lower frequency are observed to increase less rapidly with bias for biases above $\sim$ 2.2 V. In the range between 2.5 and 2.7 V, a second series of high-frequency oscillations is observed with a slightly higher frequency. The maximum frequency observed for these two high-B_f series is 75 Tesla, corresponding to an energy of 130 meV.

When the device goes off-resonance at $\sim$3 V, there is a step-like increase in the B_f of the lower frequency series of magneto-oscillations, similar to that which occurs in *NU183* at 0.75 V. This shows that charge has been ejected from the well and n_a has increased to compensate. It is not possible to obtain many points on the high- and low-current portions of the hysteresis loop because the width of the bistable region is much reduced by the application of a magnetic field (Figure 4.72). At biases beyond the peak of the resonance there are two occupied subbands in the emitter accumulation layer, although the magneto-oscillations from the upper level are very weak. This is possibly because the tunnelling rate from this subband is comparable with the energy relaxation

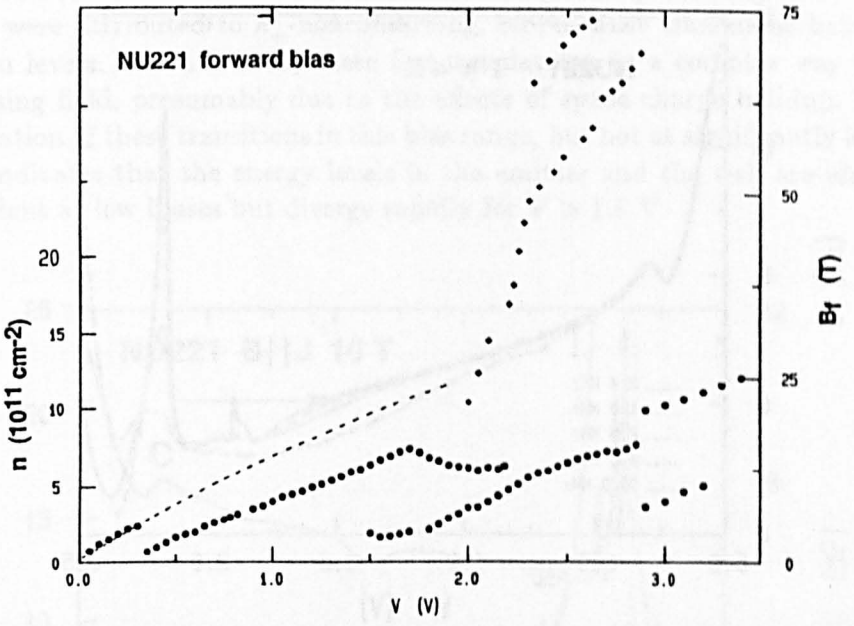

Figure 4.77: Electron sheet density in forward bias deduced from the periodicity of the magnetoquantum oscillations. At this stage the distribution of the charge between the emitter 2DEG and the quantum well is unclear. The right-hand scale shows the frequency of the magneto-oscillations. The points marked ◇ represent the inter-Landau level transitions.

time.

4.8.6 Capacitance-Voltage Characteristics

Figure 4.78 shows the capacitance voltage characteristics of the device at a temperature of 4 K as a function of measurement frequency up to 10 MHz. As in *NU183*, the decline in C near zero bias is due to the increase in the depletion length in the collector contact (Section 4.5). At 0.3 V there is a distinct step up in C similar to that observed in *NU183*. This shows that the device has come onto resonance and the capacitance of the emitter barrier has been shorted out by the low resistance of the emitter barrier [182, 183].

There is no step down in the capacitance near 0.7 V to indicate that the device goes off resonance which would have been expected on the basis of the results of *NU183* — see Section 4.5. The frequency dependence of the capacitance in this bias range is also anomalous. In *NU183* the capacitance near threshold decreases as the frequency increases because the impedance of the emitter barrier is no longer low enough to short out the capacitance of the emitter region (*i.e.* $R_1 \sim 1/\omega C_1$). However as the voltage is swept up to the resonant peak, the resistance of the barrier decreases and the capacitance at high frequencies approaches the low-frequency value. The results for the more asymmetric sample *NU221* show the opposite behaviour with respect to bias — the high frequency curves at threshold closely follow those at lower frequency, but for biases greater than 0.7 V there is a progressive decrease in C with increasing measurement frequency. This apparently indicates that the

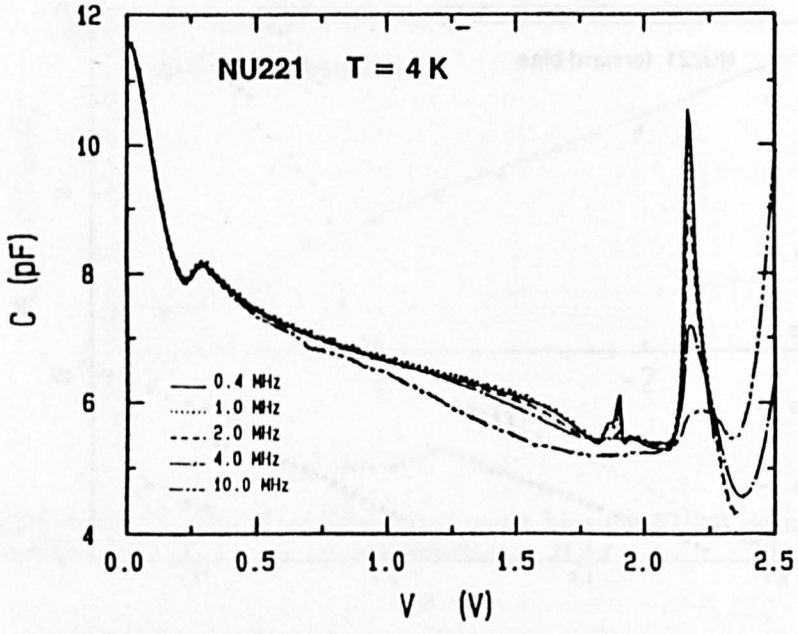

Figure 4.78: Capacitance-voltage characteristics of a 100 μm diameter mesa of *NU221* at 4 K at frequencies between 0.4 MHz and 10 MHz.

effective impedance of the emitter barrier is actually *higher* at biases above 0.7 V, although still low enough to short out the emitter capacitance at low frequencies.

At much higher bias $\sim$ 1.85 V, there is a fall in the capacitance followed by a peak. There is a larger peak in C at 2.15 V. This peak becomes stronger at low frequencies, this is indicative of a measurement artifact of the LCR meter and is caused by a variation in the conductance not in the true device capacitance (see Section 4.5.3). The conductance in this region is shown in Figure 4.67. The peaks in the capacitance coincide with troughs in the conductance, confirming that the origin of the capacitance features is the way in which the LCR meter analyses the device impedance. The presence of these features does imply that that there is some significant change in device parameters in this voltage range. The peaks in the capacitance occur at the bias voltages where the charge density measurements first show an increase in the rate of change with bias and then a flattening off.

4.8.7 Parallel Magnetic Field

The current-voltage (dashed line) and capacitance-voltage characteristics (full line) are shown in Figure 4.79 at a magnetic field of 10 Tesla, $\boldsymbol{B} \parallel \boldsymbol{J}$. A region of bistability around 1.8 V is clearly seen, and at higher bias there are a large number of step-like features in I which are highlighted in the conductance (dotted). An expanded plot of the region of bistability is shown in Figure 4.80. The bistability develops from the small feature in the conductance near 1.8 V observed at zero field (see Figure 4.67). In the capacitance trace there are several minima corresponding to a reduction in the quantum capacitance when the Fermi level lies between two Landau levels (see Sections 3.3 and 4.7.4).

At biases beyond the bistability, there is a set of sharply-peaked structures in C and G, reminiscent of those seen in the corresponding bias range of *NU183*. These were attributed to $k_\perp$-nonconserving, off-resonant transitions between Landau levels. As in *NU183*, these features develop in a complex way with increasing field, presumably due to the effects of space charge buildup. The observation of these transitions in this bias range, but not at significantly lower bias, indicates that the energy levels in the emitter and the well are almost coincident at low biases but diverge rapidly for $V > 1.8$ V.

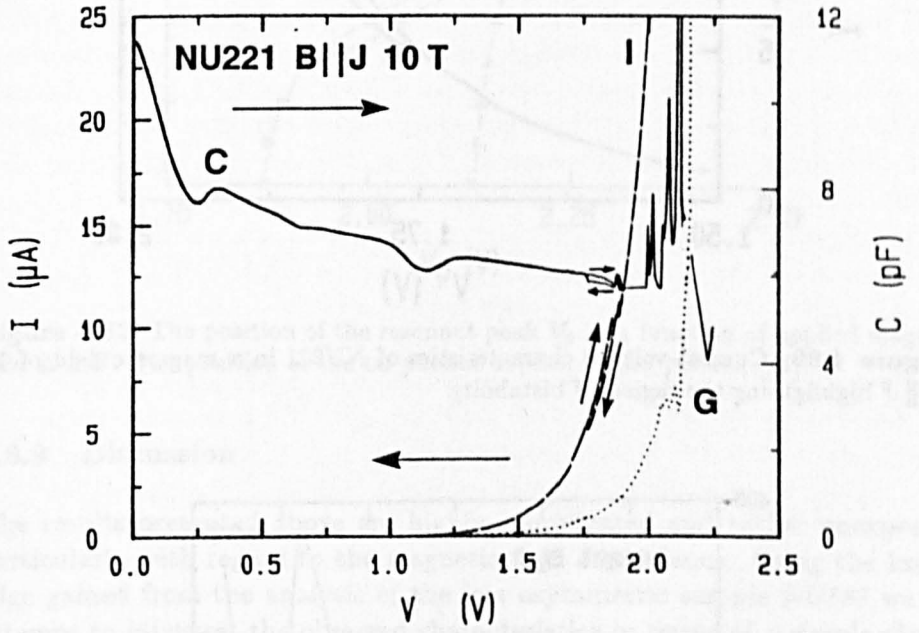

Figure 4.79: Current I (dashed line), conductance G (dotted) and differential capacitance C (full line) of *NU221* in a magnetic field of 10 T $\boldsymbol{B} \| \boldsymbol{J}$ for a measuring frequency of 1 MHz.

4.8.8 Transverse Magnetic Field

The effect of a magnetic field applied in the plane of the barriers is shown in Figure 4.81. Again, the curves strongly resemble those obtained in *NU183* (Section 4.7.5), with an increase in peak current together with a shift to higher bias voltages. The current at the 'peak' of the resonance (or the minimum in the conductance at low fields) increases by nearly two orders of magnitude by 12 T. It is remarkable that such a small feature in the conductance at zero field develops into a strong resonance with a region of bistability over 50 mV wide. The position of the resonant peak V_p is plotted in Figure 4.82. As the field increases, the peak-to-valley ratio reaches a maximum of 2.5:1 at 8 T before declining slightly at higher fields, this decline occurs as the 'resonance' moves to high bias where the background current is increasing rapidly. The traces at 4 and 6 Tesla clearly show a resonant peak with a subsidiary peak at higher voltage. By comparison with *NU183*, we attribute this replica peak to tunnelling assisted by the emission of an LO phonon (Section 3.4). At low field this feature extrapolates back to the dip in the conductance at 2.15 V.

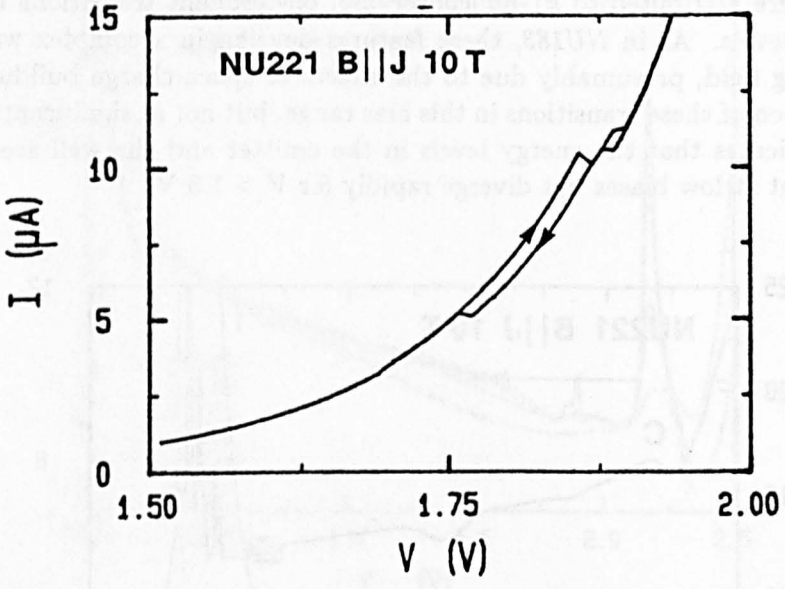

Figure 4.80: Current-voltage characteristics of *NU221* in a magnetic field of 10 T $B \parallel J$ highlighting the region of bistability.

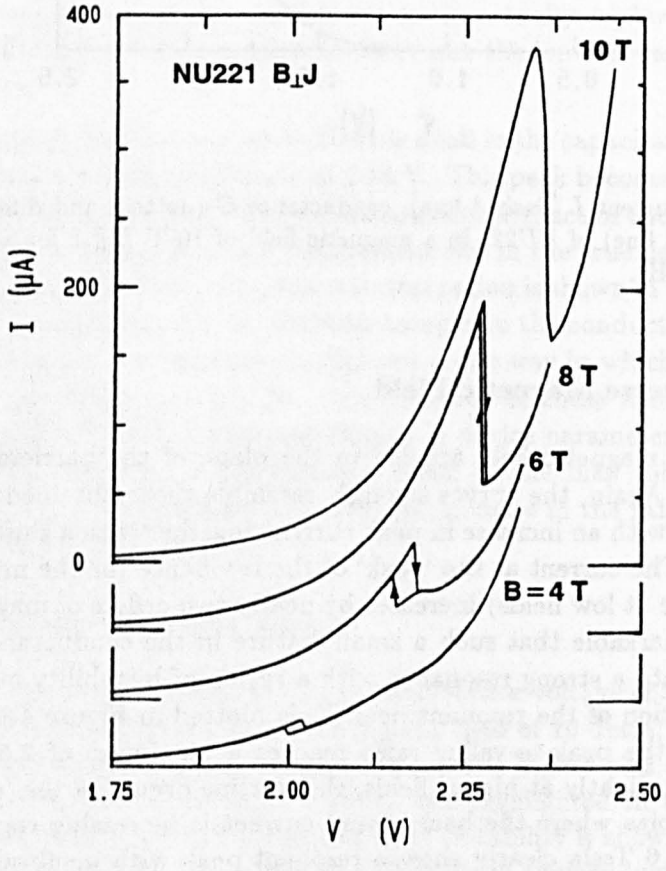

Figure 4.81: Current-voltage characteristics of *NU221* at 4 K in magnetic field $B \perp J$ of 4 T, 6 T, 8 T and 10 T, showing the development of the resonant peak.

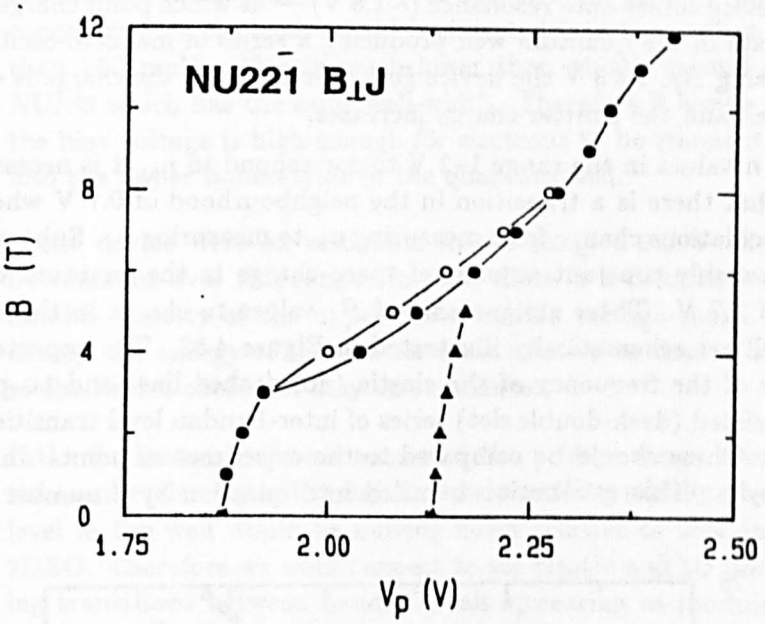

Figure 4.82: The position of the resonant peak V_p as a function of applied magnetic field $B \perp J$. The position of the LO phonon replica is also plotted ($\triangle$).

4.8.9 Discussion

The results presented above are highly complicated and rather unexpected, particularly with regard to the magnetic field dependence. Using the knowledge gained from the analysis of the less asymmetric sample *NU183* we will attempt to interpret the observed characteristics in terms of a simple picture of space charge buildup and scattering processes. Since the behaviour of this sample in a magnetic field over the range of bias from 1.5 to 2.5 V is so similar to that of *NU183* in the region of the first resonance, it is reasonable to conclude that the small feature in the capacitance and conductance observed in the zero-field characteristics does indeed correspond to a genuine resonance. However the magneto-oscillation frequencies in the bias range from 0.3 to 0.7 V and from 2 to 3 V also resemble those observed for *NU183*. This throws up a large number of problems of interpretation concerning the distribution of space charge within the device and the tunnelling mechanisms which appear to differ from those previously outlined for sample *NU183*. Two possible interpretations of the experimental results are discussed below. The first assigns the charge distributions by analogy with *NU183* and is shown to fail to explain the experimental data, and an alternative model is outlined which is based on scattering-assisted nonresonant transitions rather than on resonant tunnelling.

'Conventional' Interpretation

Intuitively, it would be tempting to view the values of sheet charge density, n, obtained in the region 1.5-3 V as being analogous to those obtained in *NU183* in the region 0-1.0 V, the 'conventional' intrinsic bistability (compare Figures 4.41 and 4.77). In this scenario, the series with higher B_f corresponds to the charge in the emitter, and the lower trace to the charge in the well [189]. The charge in the emitter initially increases and then reaches a maximum value

when the device comes onto resonance (~1.8 V) — at which point charge starts to accumulate in the quantum well producing a series of magneto-oscillations with increasing B_f. At 3 V the device goes off-resonance, the charge is ejected from the well and the emitter charge increases.

For the n values in the range 1–2 V to correspond to n_a, it is necessary to postulate that there is a transition in the neighbourhood of 0.7 V where the magneto-oscillations change from measuring n_w to measuring n_a. Subsequently there is a roughly constant amount of space charge in the quantum well up to a bias of 1.7 V. These assignments of B_f values to charge in the emitter and the well are schematically illustrated in Figure 4.83. The expected bias dependence of the frequency of the elastic (dot-dashed line) and LO phonon emission assisted (dash-double dot) series of inter-Landau level transitions are also shown. These should be compared to the experimental points which are indicated by ◇. This attribution is called into question by a number of the

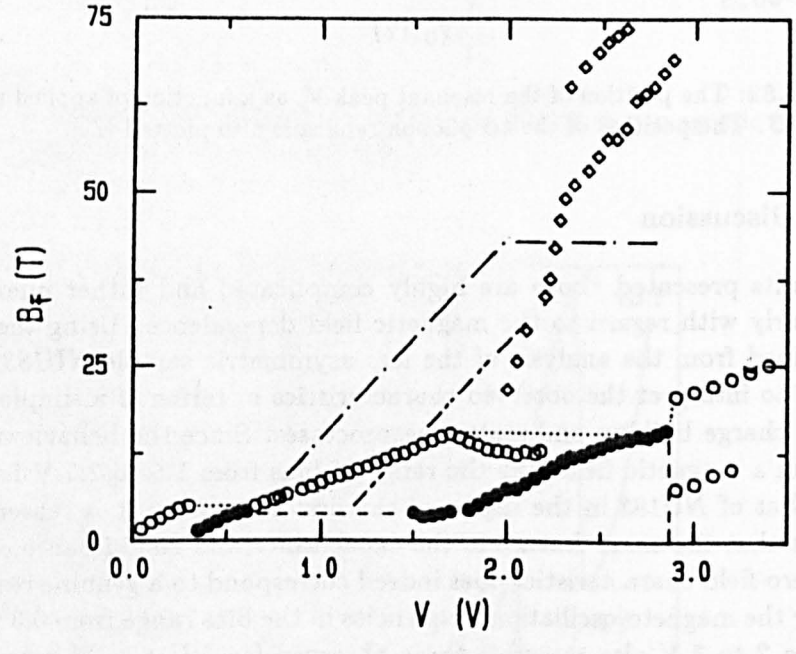

Figure 4.83: A possible assignment of the charge densities plotted in Figure 4.77 to the emitter (○) or to the quantum well (●). The proposed variation of n_a and n_w with bias are indicated by the dotted and dashed lines respectively. The dot/dashed line is the frequency of the elastic series of inter-Landau level transitions expected on the basis of this model, and the double-dot/dash line is that for the LO phonon series. The actual magneto-frequencies for these series are plotted as ◇.

observations described above:

1. There is no sign of any jump in B_f in the region of 0.7 V.
2. There is no step or other feature in the capacitance at this bias to indicate that any transition has occurred.
3. There is no change in the character of the $C(B)$ traces at this bias.
4. This interpretation offers no explanation of the frequency-dependence of the differential capacitance.

5. The charge density at V=1.7 V is only 6×10^{11} cm^{-2}. For this charge concentration, electrons would be injected into the well at energies less than 160 meV. This is much lower than at the second resonance in *NU183* which has the same well-width. Therefore it seems unlikely that the bias voltage is high enough for electrons to be resonantly tunnelling into the upper bound state of the quantum well.

6. If the device were on resonance in the range 2-2.2 V then n_a should be constant over this range. In fact, there is a definite decrease in the number density of the upper curve in this voltage range. This would change the energy of the emitter state relative to that of the well state so the device could not stay on resonance.

7. If the device were off-resonance over the voltage range above 0.7 V and the number density in the emitter was increasing rapidly, then the energy level in the well would be moving down relative to that in the emitter 2DEG. Therefore we would expect to see elastic and LO phonon scattering transitions between Landau levels appearing as modulations in the conductance and capacitance over this whole range of bias. They are only observed at biases greater than $\sim$ 1.6 V. Similarly, the high-frequency series of magnetoquantum oscillations in $I(B)$ would be expected to commence close to 0.7 V. The fact that they are not observed for biases less than 2 V indicates that the energy levels in the well and in the emitter are in fact relatively close together throughout this voltage range.

8. Again considering the high B_f series, if the device was on resonance and n_a remaining roughly constant for biases above 2 V, the difference between the energy levels in the well and the emitter would be approximately the same. Therefore the period of the high-B_f series would be unchanged. As can be seen, in reality it increases by a factor of three.

9. This model offers no explanation for the feature in the capacitance and conductance at 1.8 V in zero-field or for its development into a clear resonant peak with regions of bistability in a magnetic field both parallel and perpendicular to the current.

10. Similarly there is no explanation for the strong feature in the capacitance at 2.15 V which would appear to be a phonon replica of the 1.8 V feature.

Therefore this model of the device must be abandoned. The behaviour of this device is divergent from that of the conventional intrinsic bistability device *NU183* in several significant aspects.

'Alternative' Model

The alternative model reverses the original assignment of charge in the region between 0.7 V and 3 V so that at the bias region originally referred to as the 'second resonance' [189], it is the charge density in the *emitter* that is increasing and not that in the quantum well. The proposed attributions of well and emitter charges to the observed series of magneto-oscillations are given in Figure 4.84.

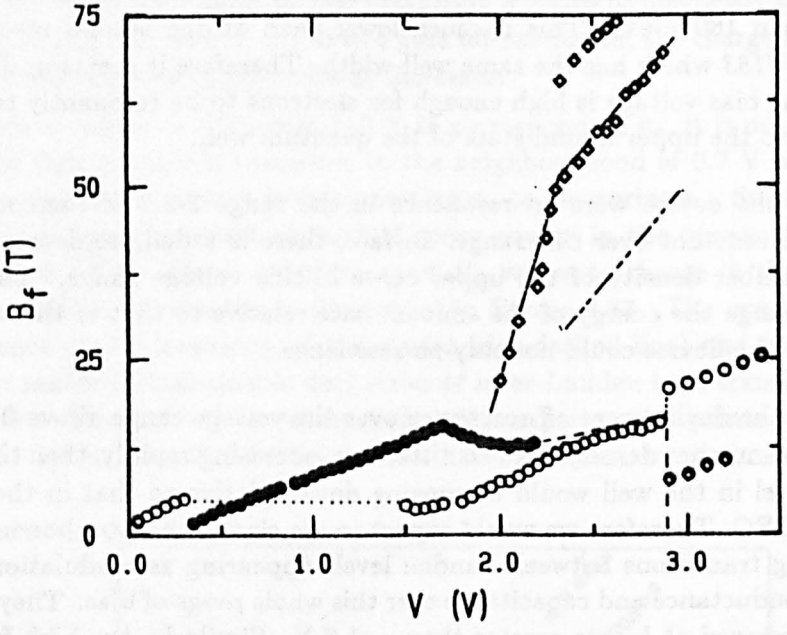

Figure 4.84: Revised model for the assignment of space charge to the emitter (o) and the well (•) and the frequencies of the elastic and LO phonon series (dash-dotted and dash-double-dotted lines).

The magneto-oscillations at low biases (<0.3 V) can only be associated with sheet charge density the 2DEG in the emitter n_a. The device comes onto resonance at a bias of 0.3 V when the energy level in the well coincides with that in the emitter accumulation layer. Charge density then builds up in the well and this gives rise to the observed magnetoquantum oscillations, as shown by the increasing B_f-values obtained, and the series due to the electron density in the emitter is no longer observed. As in *NU183*, n_a is constant in this bias range.

At a bias of 0.7 V, the two sheet charge densities are equal, however it is clear that the whole of the $B_f - V$ curve from 0.35 to 2.2 V corresponds to charge in the well, n_w, *i.e.* the well continues to accumulate charge even though it now has a Fermi energy greater than that in the emitter accumulation layer. The Fermi level in the well cannot be above that in the emitter, or else the current would flow in the opposite direction. Therefore, for biases above that at which the two number densities coincide ($\sim$ 0.7 V), the two quasi-bound states must be at different energies, as illustrated in Figure 4.85, *i.e. they are no longer truly on resonance.* For charge buildup to occur even though the two energy levels do not coincide, non-resonant transmission into the well (for example via $k_\perp$-nonconserving elastic transitions) must be much more rapid than tunnelling out of the well through the collector barrier. This is in fact quite plausible since the transmission coefficient of the collector barrier at low biases is seven orders of magnitude less than that of the emitter barrier. As long as non-resonant transitions into the well are allowed (basically if the energy level in the well is below the Fermi energy in the emitter) they can lead to charge buildup in the well due to the almost impenetrable nature of the collector barrier. The frequency dependence of the capacitance indicates

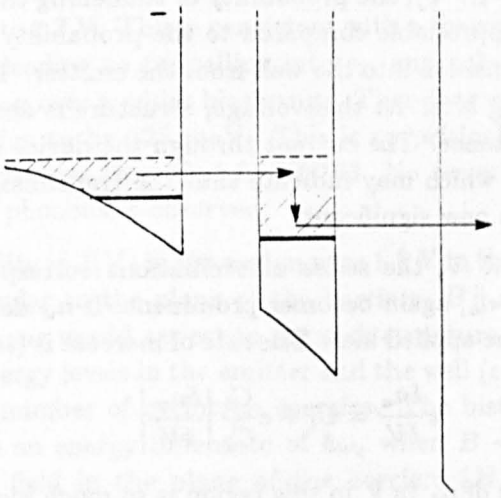

Figure 4.85: Schematic diagram showing the relative positions of the energy levels in the emitter and the quantum well at a bias where there is a higher charge density in the well than in the emitter.

that the impedance of the emitter barrier is greater for biases above 0.7 V, which would be consistent with it now being necessary for electrons to scatter in order to enter the well. So the basic picture is that the device *does* indeed go off 'resonance' at the bias expected — but that the impedance of the collector barrier is so high that this does not affect the amount of space charge in the well which continues to buildup due to scattering-assisted transitions.

In order to reconcile the measured n_w with the total voltage drop, it is necessary for the charge density in the emitter n_a to be roughly constant in this voltage range at $\sim 2.0 \times 10^{11}$ cm^{-2}. The energy difference between the two bound states is simply given by the difference in Fermi energies of the two charge distributions. This increases from 0 at 0.7 V to 16 meV at 1.7 V where n_w is almost three times n_a. This small energy difference ($< \hbar\omega_{LO}$) between the two states explains why there is no series of magneto-oscillations corresponding to LO phonon assisted tunnelling at low biases.

This explanation begs the question of what limits the increase in n_w. As in the case considered by Sheard and Toombs [99], the steady-state charge density in the well is given by the balance between the tunnelling rate into the well — due to scattering-assisted transitions — and that out of the well — which is governed by the transmission coefficient of the collector barrier. As charge density builds up in the well, the voltage drop across the collector barrier increases and therefore so does its transmission coefficient, although even at a bias of 1.7 V it is still nearly four orders of magnitude less than that of the emitter barrier. In addition, as n_w increases so does the energy difference between the emitter and the well states, although only at a relatively slow rate. This leads to some reduction in the transmission rate into the well since most scattering processes become weaker for larger momentum changes. This transmission rate is in any case much less than the simple coherent tunnelling probability for the emitter barrier, T_e, since some scattering mechanism must

be involved. We suggest that as n_w reaches $\sim 6 \times 10^{11}$ cm^{-2} (corresponding to an applied bias of ~1.7 V), the probability of tunnelling through the collector barrier becomes appreciable compared to the probability of undergoing a scattering-assisted transition into the well from the emitter. This causes n_w to decline with increasing bias. At this voltage, structure is observed in the capacitance and conductance. The current through the device increases rapidly at biases above 1.7 V which may indicate that the transmission rate through the collector barrier is now significant.

At biases above 1.7 V, the series of oscillations corresponding to space charge in the emitter, n_a, again becomes prominent. If n_w decreases, n_a must increase to maintain the applied bias. The rate of increase is (see equation 4.31)

$$e\frac{\delta n_a}{\delta V} = C_t + e\frac{C_t}{C_2}\left|\frac{\delta n_w}{\delta V}\right|$$

which is why the slope of n_a vs V in this region is so much higher than that of n_w vs V at lower biases (12×10^{11} cm^{-2}V^{-1} compared to 6×10^{11} cm^{-2}V^{-1}). Therefore in this bias region the energy level in the well is moving rapidly down relative to the emitter 2DEG. The rapid rise in the frequency of the high-B_f series is consistent with this; $\delta n_a/\delta V = 12 \times 10^{11} \Rightarrow \delta(\epsilon_0 + eV_1 - \epsilon_1)/\delta V \sim$ 200 meV/V $\Rightarrow \delta B_f/\delta V \sim 120$ T/V. This is close to the slope observed in this region.

Once the energy difference is such that there are unoccupied states in the well at energies more than $\hbar\omega_{LO} = 36$ meV below the emitter Fermi level, LO phonon assisted transitions into the well are possible. This occurs at a bias between 2.15 and 2.25 V — close to the bias where the second feature in the conductance and the large peak in the differential capacitance are observed. Once LO phonon processes can take place, there is an additional channel for transmission of charge into the well. Hence it is possible that the charge density in the well increases again, although this series of magnetoquantum oscillations is no longer observable — possibly because the electron distribution in the well is no longer cold enough.

Recent photoluminescence investigations of the device are consistent with an increase in sheet density in the well from 5.5 to 7×10^{11} cm^{-2} between 2.2 and 3.1 V [222]. These PL studies also suggest that for biases above ~ 2 V the charge distribution in the well is not completely cold.

An increase in n_w once LO phonon scattering can contribute to the charge buildup explains the much-reduced rate of increase of n_a and the frequency of the high-B_f series at biases greater than 2.2 V. In this bias range $\delta n_a/\delta V \sim$ 2.8×10^{11} cm^{-2}V^{-1} corresponding to $\delta B_f/\delta V \sim 40$ T/V. This value is again in close agreement with the measured value.

The second periodicity in the high-B_f oscillations which is observed in the region of 2.6 V does not correspond to the presence of elastic and LO phonon series of oscillations since the energy difference between the two series is less than the LO phonon energy. However, they may be explained by noticing that the difference in the B_f values of the two series is corresponds to an energy of ~ 20 meV which is close to the Fermi energy in the emitter contact at this bias. It is possible that the second energy level in the well passes below the emitter Fermi level at this voltage. This would lead to a series of magneto-oscillations

of periodicity $B_f = m^*(\epsilon_2 - \epsilon_1)/e\hbar$, as opposed to $B_f = m^*(\epsilon_0 + eV_1 - \epsilon_1)/e\hbar$. At high temperatures only a single periodicity, $B_f \sim 73$ T, is observed over the range from 1.7 to 2.7 V. This is consistent with a thermal spread of the energies in the emitter leading to tunnelling into ϵ_2, and subsequent scattering down into ϵ_1, occurring over a wider bias range. Therefore we take the intersubband energy separation to be 125 meV. This is surprisingly low for a well of this width, and rather less than that in *NU183*. No series of oscillations from the emission of LO phonons is observed.

The bistability in $I(V)$ in the region near 1.8 V in the presence of a magnetic field perpendicular to the plane of the barriers, $B \parallel J$, can be accounted for by noting that one would expect to see such structure whenever the difference between the energy levels in the emitter and the well $(\epsilon_0 + eV_1 - \epsilon_1)$ corresponds to an integral number of cyclotron energies. The bistability at 1.8 V simply corresponds to an energy difference of $\hbar\omega_c$ when $B \sim 10$ T. The behaviour in a magnetic field in the plane of the barriers $(B \perp J)$ suggests that the transmission coefficient of the collector barrier decreases in the presence of a magnetic field but the scattering rate into the well does not, leading to an increase in bias before the point is reached at which the transition rates into and out of the well become comparable and n_w starts to decrease.

We stress that the reversal of the assignments of the charge in the bias region between 2 and 3 volts does not affect in any way the argument for the origin of the inverted bistability at 3 V. When the device is biased on the 'resonant' part of the curve, incident electrons must still traverse two tunnel barriers whereas beyond the resonance the voltage distribution through the device is such that they only encounter the emitter barrier. The pronounced magneto-oscillation in the position of the resonant peak (Figure 4.72) is further evidence for the importance of scattering in the buildup of space charge at this point. It is not necessary for this argument for the second resonance proper ever to be reached, *i.e.* electrons may not actually tunnel via the upper bound state at any bias. However from the frequency of the inter-Landau level transitions it seems probable that tunnelling into the upper state does occur in the bias range above 2.9 V, although it is not possible to verify this. The switch-off point of the resonance (marked *c* in Figure 4.68) occurs when the tunnelling rate through the collector barrier exceeds the scattering rate in the well and it is no longer possible to maintain the charge buildup. At this point the charge is ejected from the well.

4.8.10 Summary

This section has described magnetotransport investigations of a device showing very different, and rather more complex, properties to those reported in the previous sections of this chapter. The charge buildup is much greater and appears to be mainly associated with non-resonant processes, charge is present in the well over a voltage range of nearly 3 V, and small features in the zero-field characteristics evolve into full-blown resonances in the presence of a magnetic field. The model presented above attempts to account for all the major features of the device behaviour by invoking strong elastic scattering and an impenetrable collector barrier. In this it is reasonably successful. However, there is no detailed theoretical basis for the proposed solution which

would require modelling of the effects of such high charge concentrations and accurate treatment of the scattering processes. Although the barrier widths have only been altered by ~20 Å from *NU183* the device behaviour is radically changed, it is a relief to note that had the samples been grown in the opposite sequence an explanation of the bistability effects would have been much harder to achieve.

4.9 Conclusions

This chapter has considered in some detail the various origins of bistable behaviour in the current-voltage characteristics of resonant tunnelling devices. We have shown that in order to observe the intrinsic effect caused by space charge buildup and electrostatic feedback it is first necessary to eliminate external causes of bistability. The presence of a negative differential resistance in a typical measuring circuit gives rise to high-frequency current oscillations which are successfully modelled using a simple equivalent circuit. The presence of these oscillations produces bistability in the current-voltage characteristics remarkably similar to that originally attributed to intrinsic causes. The device can be stabilized against such oscillations by a suitably chosen resistor or capacitor connected in parallel with the device.

A detailed study has been presented of an asymmetric double barrier device (*NU183*) where we have been able to rule out extrinsic circuit effects and believe that the observed behaviour is the first observation of a genuinely intrinsic bistability. The asymmetry in the barrier thicknesses increases the amount of space charge buildup in the quantum well — thus strengthening the bistable effect. We have also presented the first measurements of the capacitance-voltage characteristics of a double barrier device and related the measured parameters to the physics of space charge buildup using a simple equivalent circuit. It has been shown that high temperatures lead to a loss of charge from the well, due to thermal excitation of carriers, resulting in the loss of the bistability. High magnetic field investigations have been successfully used to directly determine the space charge density in the well and demonstrate that electrons undergo energy relaxation prior to tunnelling out of the well. Therefore the tunnelling process is truly sequential in this sample. The application of a magnetic field perpendicular to the plane of the barriers, leads to a remarkable increase in the voltage range of the bistable loop caused by the increased degeneracy of Landau levels in the quantum limit.

The wide variety of possible device behaviour is well illustrated by the characteristics shown in Figure 4.86 [172]. This device has a 217 Å wide quantum well (see sample *NU154* in Table 2.1) and shows seven resonances in its $I(V)$ characteristics (resonance 7 is not shown in the figure). At low bias, the current density is small and therefore so is the negative differential conductivity at the first resonance. This is stable even without a parallel capacitor. The second resonance has a considerably higher current and breaks into oscillation with small regions of extrinsic bistability. For the third, fourth and fifth resonances the increase in current from threshold to peak extends over a wide range of bias indicating that space charge buildup is occurring in the quantum well. For the fourth and fifth resonances this buildup is large enough to produce wide regions of intrinsic bistability. As for the upper resonance in *NU183*, the charge resides in the lowest energy level due to intersubband scattering. We estimate the charge density in the well to be $1\text{–}1.2\times10^{11}$ cm^{-2} at these resonances. This stresses the importance of scattering events in charge buildup processes. Magnetotransport traces of this device in this region of bias are shown in Section 3.4. For the final two resonances, the corresponding quantum well levels are virtual states with energies above the top of the

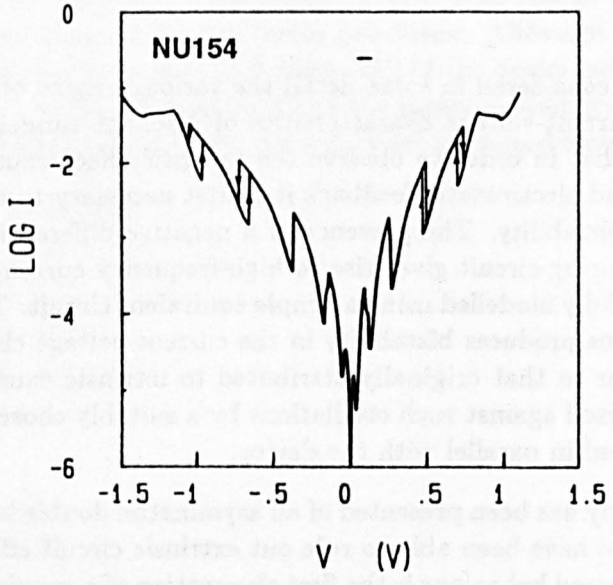

Figure 4.86: Logarithm of the current plotted against bias voltage for sample *NU154* (217 Å well) at 4 K. This sample shows several of the different types of behaviour: at resonance 1 the device is stable, at resonance 2 it undergoes high-frequency oscillation, resonances 3, 4 and 5 show bistability due to charge buildup and resonance 6 shows the effects of circuit oscillations.

collector barrier and therefore much less charge buildup occurs. Instead, the device breaks into high-frequency oscillations producing the step-like structure observed in the current.

Finally, we have investigated a completely new kind of bistable behaviour in a sample with one very thick barrier in which the off-resonant current exceeds the resonant one over a range of bias, producing a 'butterfly-shaped' hysteresis loop. The width of this loop is modulated by Landau level formation in high magnetic fields. A careful analysis of a wide range of data for this sample reveals that the mechanisms leading to space charge buildup are substantially different from those previously considered, resulting in highly complex behaviour.

These investigations have proved that the buildup of space charge in the quantum well of suitably-designed double barrier tunnelling structures does indeed lead to bistability in the current-voltage characteristics and that magnetic field and capacitance investigations can be used to reveal a wealth of complex and novel device behaviour.

CHAPTER 5

Resonant Tunnelling in a Transverse Magnetic Field

5.1 Introduction

Quasi-two-dimensional electrons in the presence of high magnetic fields have been the subject of numerous experimental and theoretical investigations over the last twenty-five years [63]. In the vast majority of these studies, the magnetic field is applied in a direction perpendicular to the plane of the 2DEG. In this configuration the effects of the electric and magnetic fields are separable and the energy associated with motion in the plane is quantised into Landau levels as described in Section 3.3. When the magnetic field is in the plane of the confining potential, there is strong mixing of the electrostatic and magnetic quantisation which leads to a more complex situation. There have been relatively few investigations in this configuration. The transverse magnetic field deflects the electron through the action of the Lorentz force producing circular motion with a radius of $\sqrt{2n+1}\, l_B$. If the resulting orbit can be contained within the width of the confining potential, bulk Landau levels are formed. If, however, the orbit intersects the barrier, the electron performs a 'skipping' motion along the interface.

Skipping orbits have been directly observed by means of the technique of electron focusing in a classical regime in metals [223, 224, 225] and in quantum ballistic transport in a the plane of a two-dimensional electron gas [158]. These skipping states are of fundamental interest from the point of view of the quantum mechanics of the problem and because of the importance of the formation of interfacial Landau levels, for example in the Quantum Hall Effect [226] and its quenching in narrow structures [227]. The first investigations of hybrid magnetoelectric quantisation involved the observation of oscillatory structure in the surface impedance of metals at microwave frequencies when a magnetic field was applied parallel to the surface [228, 229] which was interpreted by Prange and Nee [230] as being due to resonant transitions between surface states bound by the magnetic field. The first observation of interfacial Landau

levels in a tunnelling structure was made by Snell *et al.* [159, 231] in single barrier InP/(InGa)As heterostructures. Similar investigations have been made in Si MOSFETs [232] and in double barrier structures [147, 233, 160, 234, 235].

In this Chapter, we use resonant tunnelling in double barrier heterostructures to investigate the quantum mechanics of electron transport in crossed electric and magnetic fields. At zero magnetic field, the electrons are confined electrostatically in the quantum well formed between the (AlGa)As barriers or between the emitter barrier interface and the accumulation potential. Thus the electrons are in 'box-quantised' quasi-bound states. When a very high magnetic field is applied in the plane of the barriers (*i.e.* perpendicular to the direction of current flow bper), the confinement is purely magnetic and bulk Landau levels are formed. By monitoring the resonances in the current-voltage characteristics, we are able to demonstrate this transition from magnetic to electric quantisation.

Section 5.2 describes the effect of a transverse magnetic field on electron tunnelling within a Transfer Hamiltonian approach. The application of a magnetic field affects the energy levels in the well and in the emitter, the transmission coefficients of the barriers and the conservation conditions. Section 5.3 describes results for samples with relatively narrow wells in which the quantisation is dominated by the electrostatic confinement and the effect of the magnetic field on the energy levels described as a perturbation [119]. With increasing magnetic field, the resonances broaden considerably and move to higher bias [139, 24]. This is simply explained using a graphical interpretation of the conservation conditions [236]. The observed shift in the threshold and valley voltages is found to be in good agreement with the predictions of a model which takes into account the bias dependence of the Fermi energy in the emitter 2DEG and the voltage distribution within the device.

In samples with wider quantum wells (Section 5.4), the effect of the magnetic field on the energy levels in the well becomes significant and resonant tunnelling into two types of hybrid magnetoelectric states is observed: 'traversing' orbits where the electrons interact with both barriers, and 'skipping' orbits in which the electrons are localised at one barrier. In addition, we observe two series of magneto-oscillations in d^2I/dB^2 due to electrons tunnelling with different components of momentum parallel to the plane of the barriers. These two sets of oscillations simply correspond to the opening and closing of possible tunnelling channels. Tunnelling into bulk states is not observed due to the large value of transverse momentum required [237, 238]. In contrast to the recently reported results for single barrier structures [159, 231], these magneto-oscillations are not periodic in $1/B$. Due to the presence of a large electric field in the well the skipping orbits observed in the double barrier structures are fundamentally different from those reported by Snell *et al.* [159]. A model based on the WKB approximation is used to predict the voltage positions of the resonant peaks [231, 239] producing good qualitative agreement.

Rotation of the magnetic field in the (100) plane parallel to the barriers is investigated in Section 5.5. These measurements reveal an angular dependence of the magneto-oscillations due to the anisotropy of the Γ-conduction band at high electron energies [240, 241]. The magnitude of the observed shift in the resonance positions is used to estimate the anisotropy of the conduction

band and is found to be in reasonable agreement with theoretical expectations. These results show the potential of resonant tunnelling studies as a probe of the band structure at high energies.

When the magnetic field direction is rotated in a plane perpendicular to the barriers, a completely new set of resonant peaks arise, as reported in Section 5.6. In narrow well samples, the relaxation of Landau-level index conservation allows the observation of a series of peaks in $I(V)$ corresponding to inter-Landau-level transitions. Where there are many Landau levels within the width of the Fermi distribution in the emitter, *i.e.* the intersubband energy separation is low, a series of rapid oscillations is observed in the current-voltage characteristics.

5.2 Tunnelling in Crossed Electric and Magnetic Fields

This section briefly outlines the effects of a transverse magnetic field $\boldsymbol{B} \perp \boldsymbol{J}$ on electron tunnelling. The approach adopted uses the transfer Hamiltonian method and a detailed exposition of the theoretical analysis of the problem is given by Fromhold [242]. This theory is based on that developed by Chan *et al.* to describe tunnelling into interfacial Landau levels in single-barrier heterostructures [159, 231, 238, 243, 239]. A similar method has recently been used by Brey *et al.* [244]. It provides a good explanation of all the experimental results presented in this chapter.

In the transfer Hamiltonian formalism of Bardeen [245], the energy levels $\epsilon_{L,R}$ and eigenfunctions $\psi_{L,R}$ on either side of the barrier are obtained separately, and then the rate at which an electron initially occupying a state ψ_L localised at the emitter side of the barrier evolves into a final state ψ_R localised in the well is calculated. Since the two states are not orthogonal, transitions may occur between them — subject to the conservation of energy and components of momentum perpendicular to the tunnelling direction. Therefore it is natural to consider the effects of the magnetic field on the energy levels separately, and then on the transition rates between them. The changes in the energy of the quasi-bound states in the accumulation layer and the well, together with the appropriate conservation conditions, give the evolution of the resonant peak positions with magnetic field. The effect of B on the coupling between the initial and final states allows the tunnel current to be calculated [242].

5.2.1 Energy Levels

Electron motion in crossed fields

The classical equation of motion for an electron in crossed fields is

$$\dot{\boldsymbol{p}} = -e(\boldsymbol{E} + \boldsymbol{v} \times \boldsymbol{B}) \tag{5.1}$$

where $\boldsymbol{v}$ is the velocity of the electron, $\boldsymbol{E} = (-E, 0, 0)$ and $\boldsymbol{B} = (0, 0, B)$, *i.e.*

$$\begin{aligned} m^* \dot{v}_x &= eE - eBv_y \\ m^* \dot{v}_y &= eBv_x \\ m^* \dot{v}_z &= 0 \end{aligned}$$

Taking the initial conditions to be $\boldsymbol{v}_{t=0} = (0, 0, v_0)$, the solution is

$$v_x = \frac{E}{B} \sin \omega_c t$$

$$v_y = \frac{E}{B}(1 - \cos \omega_c t)$$

$$v_z = v_0$$

$$x = \frac{E}{\omega_c B}(1 - \cos\omega_c t)$$

$$y = \frac{E}{\omega_c B}(\omega_c t - \sin\omega_c t)$$

$$z = v_0 t$$

This corresponds to free motion along z, since there is no component of Lorentz force in this direction, with a cycloidal motion in the xy plane which is equivalent to circular motion with radius $E/\omega_c B$ superimposed on a uniform drift velocity $v_d = E/B$ parallel to y *i.e. perpendicular* to both E and B. This motion is schematically illustrated in Figure 5.1.

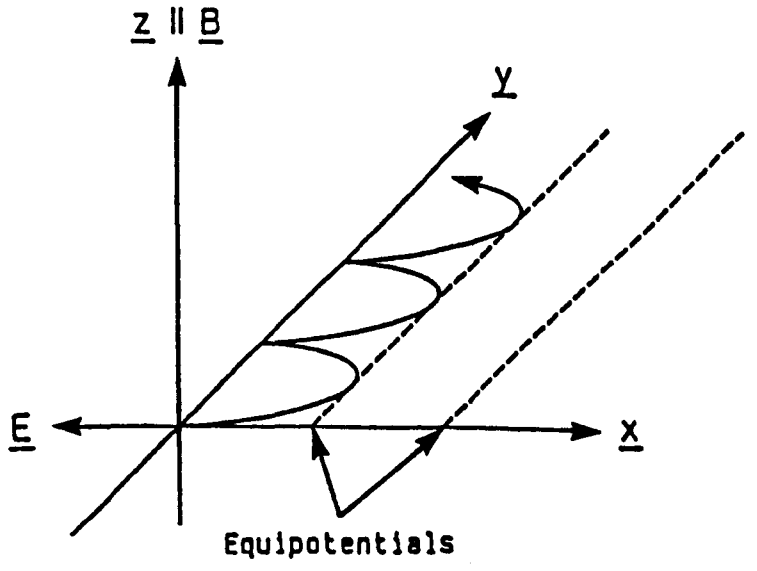

Figure 5.1: Motion of electrons in crossed electric and magnetic fields.

If v_x and v_y are initially non-zero, a more complex path results. Changing v_y is equivalent to shifting the origin of the circular motion, which is referred to as the orbit centre position. Note that the classical component of canonical momentum, $m^* v_y - eBx$, is a constant of the motion (zero in the case shown in Figure 5.1). There is no net motion in the direction of the applied electric field, hence electrons must scatter out of these orbits if they are to contribute to a current parallel to the electric field.

If there is a barrier at $x > 0$, the electron is reflected before completing an orbit. Assuming the reflection to be specular, the electron then performs a 'skipping' motion parallel to the interface, see Figure 5.2(a). Similarly, a barrier at $x < 2E/\omega_c B$ causes reflection at the other side of the orbit forming a 'traversing' orbit, shown in Figure 5.2(b). Again different values of v_y correspond to different orbit centre positions, with negative v_y giving an orbit center displaced towards the centre of the well and positive values have orbit

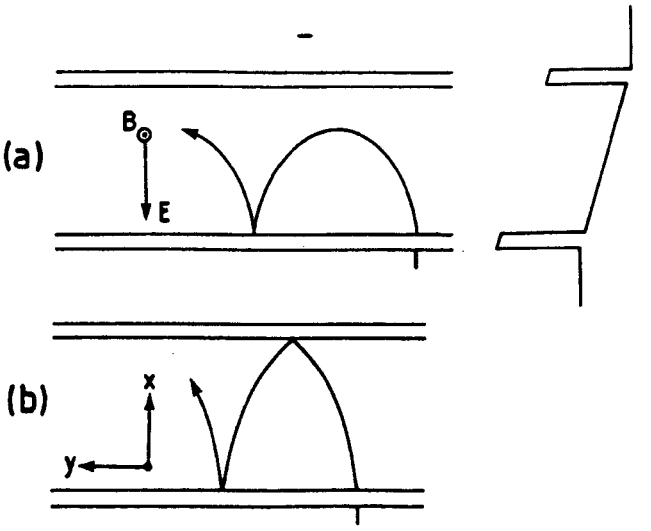

Figure 5.2: Schematic diagram of the electron motion in the xy plane for crossed electric and magnetic fields: (a) 'skipping' orbit (b) 'traversing' orbit (c) skipping orbits with opposite values of v_y.

centres inside the barrier ($x < 0$). If electrons with the same initial v_x but opposite v_y enter the well, the electron with $+v_y$ will perform an orbit more closely bound to the barrier, as shown in Figure 5.2(c). In a tunnelling device, electrons are injected into the well with a spread of v_y between $-v_F$ and v_F (the Fermi velocity), and a range of orbits are performed, which can include both skipping and traversing orbits for the same initial value of v_x. Classically all orbits are allowed, but in fact the motion is quantised with a limited number of orbit centres, as shown below.

Bulk Landau Levels

In a magnetic field, the canonical momentum is $\boldsymbol{p} = m^*\boldsymbol{v} + q\boldsymbol{A}$, where $\boldsymbol{A}$ is the magnetic vector potential, and the kinetic energy is given by $(\boldsymbol{p}+e\boldsymbol{A})^2/(2m^*)$. Again taking $\boldsymbol{E} = -(E,0,0), \boldsymbol{B} = (0,0,B)$ and choosing the gauge such that $\boldsymbol{A} = (0,Bx,0)$, the Hamiltonian for a free electron in crossed electric and magnetic fields is

$$\begin{aligned}\mathcal{H} &= \frac{(\boldsymbol{p}+e\boldsymbol{A})^2}{2m^*} + e\boldsymbol{E}.\boldsymbol{r} \\ &= \frac{p_x^2}{2m^*} + \frac{p_z^2}{2m^*} + \frac{p_y^2 + 2ep_yBx + e^2B^2x^2}{2m^*} - eEx \end{aligned} \tag{5.2}$$

The potential energy is only a function of x, so we may look for solutions of the form $\psi = \exp(ik_yy + ik_zz)\phi(x)$. Therefore $p_y = \hbar k_y$ and $p_z = \hbar k_z$ are conserved in the motion. We can then write the one-dimensional Schrödinger equation

$$\left(-\frac{\hbar^2}{2m^*}\frac{\partial^2}{\partial x^2} + \frac{m^*\omega_c^2}{2}(x-X_0)^2 - eEX_0 + \frac{m^*v_d^2}{2} + \frac{\hbar^2k_z^2}{2m^*}\right)\phi(x) = \epsilon\,\phi(x) \tag{5.3}$$

with the origin of the simple harmonic potential given by

$$- X_0 = \frac{m^* E}{eB^2} - \frac{\hbar k_y}{eB} \tag{5.4}$$

The application of a magnetic field adds a quadratic potential term which confines the electrons in the x direction. The kinetic energy due to the drift velocity along y is $m^* v_d^2/2 = m^* E^2/2B^2$ and $-eEX_0$ represents the potential energy at the orbit centre. $\phi_n(x)$ is the simple harmonic oscillator wavefunction given by the Hermite polynomials. The energy eigenvalues $\epsilon_n = \epsilon - \hbar^2 k_z^2/2m^*$, $n = 0, 1, 2, \ldots$, are

$$\epsilon_n = (n + 1/2)\hbar\omega_c + m^* v_d^2/2 - eEX_0(k_y) \tag{5.5}$$

5.2.2 The Effect of a Confining Potential

Zawadzki [246] has considered the energy levels within a quantum well with infinitely high potential barriers, and Merkt [247] examines the equivalent situation in a triangular potential well. The wavefunction must be zero at the barrier interfaces. The eigenfunctions are constructed from parabolic cylinder functions whose zeroes can be approximately calculated [247, 248] — these functions are closely related to the Hermite polynomials when n is an integer. Electrons whose orbit centres lie a long way from the interface have energies given by equation 5.5, but when the electron orbit intersects the barrier the electron is confined by the electrostatic potential and the energy is increased. These states are known as interfacial Landau levels. Figure 5.3 shows the energy levels at a potential step of infinite height with no applied electric field. When the orbit centre coincides with the barrier interface the electron is confined in one half of the simple harmonic oscillator potential and therefore the eigenfunctions are simply ϕ_n for odd values of n, with corresponding energies. The bending of the Landau levels near the interface implies the existence of states in the gap between the bulk eigenenergies, and the presence of an edge current. This is important in some theoretical treatments of the Quantum Hall Effect [249]. Since the higher Landau levels have larger cyclotron radii they are more strongly affected by the interface potential.

Figure 5.4 shows the energy of the lowest subband for a triangular potential plotted against orbit centre position X_0 for several values of the dimensionless parameter $k_D l_B = (m^* E/eB^2)/l_B = eEl_B/\hbar\omega_c$ (taken from Merkt [247]). For high values of $k_D l_B$, the quantisation is mostly electric and the dispersion relation tends to that of the unperturbed potential, $\epsilon = \hbar^2 k_y^2/2m^*$, whereas for low values the energy levels are those of interfacial Landau levels and the dispersion relation is no longer symmetric.

The triangular well is similar to the accumulation layer potential, however we will assume that the quantisation in this region of the device is dominated by the electrostatic confinement for the whole range of magnetic fields used and treat the magnetic field as a perturbation. The situation in the quantum well is rather more complex than that considered by either Merkt (where there is only one interface) or Zawadzki (where E=0). Although, in principle, the same methods could be used to derive the dispersion relation, we use perturbation theory for samples with well widths much less than the cyclotron radius (Section 5.3) and the semi-classical WKB approximation for wide quantum wells (Section 5.4).

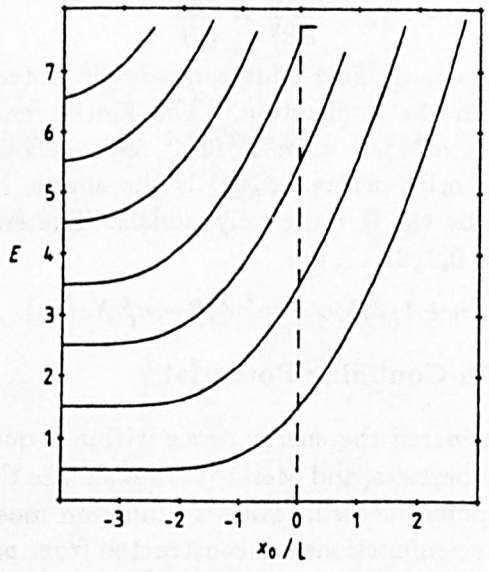

Figure 5.3: Energy levels at an infinite potential step as a function of orbit center position, from reference [250].

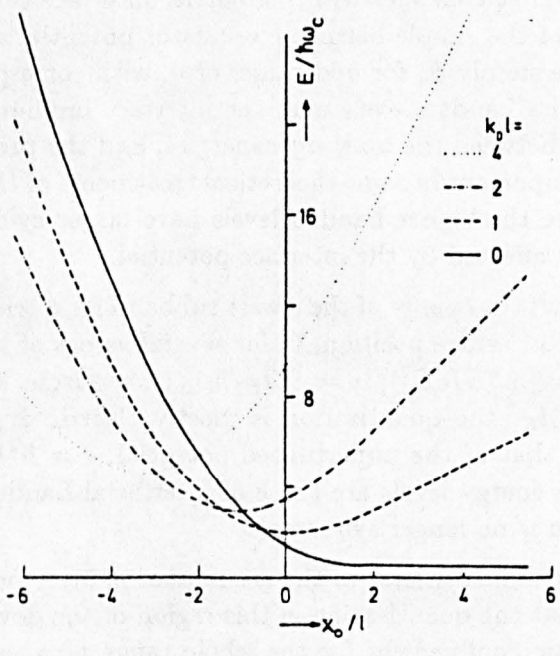

Figure 5.4: The energy of the lowest subband for a triangular potential plotted against orbit centre position for several values of the dimensionless parameter $k_D l_B = eEl_B/\hbar\omega_c$, showing the transition from electric to magnetic quantisation (taken from reference [247]).

Perturbation calculation

In the limit of low magnetic fields, or strong electrostatic confinement, we can consider the magnetic field to be a perturbation of the system, as proposed by Stern and Howard [119]. The Schrödinger equation 5.3 can be rewritten as

$$\left[\frac{p^2}{2m^*} + eV(x) + \frac{e^2B^2x^2}{2m^*} + \frac{e\hbar k_y Bx}{m^*}\right]\phi(x) = \epsilon\,\phi \tag{5.6}$$

where $eV(x)$ is the conduction band profile at zero magnetic field. The first two terms on the left correspond to the zero-field Hamiltonian which has eigenfunctions ϕ_0 and energies $\epsilon(0) = \epsilon_0 + \hbar^2(k_y^2 + k_z^2)/2m^*$. The last two terms give the first-order perturbation

$$\delta\epsilon = \epsilon - \epsilon(0) = \frac{e^2B^2}{2m^*}\langle x^2\rangle + \frac{\hbar eBk_y}{m^*}\langle x\rangle \tag{5.7}$$

The origin of coordinates in this section is taken to be at the centre of the well.

Quantum well For the lowest subband in the quantum well we neglect penetration of the wavefunction into the barrier and the applied electric field and take the wavefunction to be

$$\phi(x) = \sqrt{\frac{2}{w}}\cos\left(\frac{\pi x}{w}\right) \tag{5.8}$$

This gives $\langle x\rangle = 0$, $\langle x^2\rangle = w^2/12$. Therefore the energy of an electron in the well is

$$\epsilon_w = \epsilon_1 + \frac{\hbar^2(k_y^2 + k_z^2)}{2m^*} + \frac{e^2B^2w^2}{24m^*}. \tag{5.9}$$

For a quantum well of width 60 Å this gives a change in energy of 4 meV for a magnetic field of 10 Tesla, compared with an unperturbed energy level of ~ 70 meV.

Accumulation layer For the accumulation layer we use the variational wavefunction of Fang and Howard [71] described in Section 3.2, this also neglects penetration of the wavefunction into the barrier region. The expectation value of x is just $-(x_0 + b_1 + w/2)$, where $x_0 = 3/a$ is the stand-off distance of the 2DEG, and $\langle x^2\rangle = 3/a^2 + \langle x\rangle^2$. If we set $k_0 = -eB\langle x\rangle/\hbar = (x_0 + b_1 + w/2)/l_B^2$, the energy of an electron in the accumulation layer may be written as

$$\epsilon_a = \epsilon_0 + \frac{3m^*\omega_c^2}{2a^2} + eE(b + w/2) + \frac{\hbar^2k_z^2}{2m^*} + \frac{\hbar^2(k_y - k_0)^2}{2m^*} \tag{5.10}$$

Semi-classically, $\hbar k_0$ corresponds to the change in the y-component of the momentum due to the action of the Lorentz force as the electron tunnels from the emitter 2DEG to the centre of the quantum well. The energy change is again ~ 4 meV at a field of 10 Tesla for a number density of 2×10^{11} cm^{-2}.

Validity The perturbation approximation is valid where there is only a small change in the energy level. A reasonable criterion for the applicability of this approach is to consider the field at which a cyclotron orbit just fits within the width of the electrostatic potential well. For a quantum well in crossed electric and magnetic fields is $B^2 \sim 2Em^*/ew$. If the charge in the emitter is 2×10^{11} cm^{-2} and the well-width 60 Å, we can use the perturbation calculation for $B \leq 19$ Tesla. For the emitter accumulation layer, approximately described as a triangular potential of width x_0, the cyclotron orbit fits within the potential for $B^2 > 2m^*Ea/3e$ yielding a limit of $B < 13$ T for $n_a = 2 \times 10^{11}$ cm^{-2}.

5.2.3 Tunnel Current

Following the analysis of Sheard [243] for the single-barrier case, the current calculated using the transfer Hamiltonian method is given by

$$J = \frac{e}{L_y L_z} \sum_{k,q,n} f_k \frac{2\pi}{\hbar} |M_n(k_x, k_y)|^2 \, \delta_{k,q} \, \delta(\epsilon_a, \epsilon_{w,n}) \tag{5.11}$$

where the occupancy of states in the well and in the collector is neglected. The δ-functions ensure conservation of energy and canonical momentum. It is assumed that the transmission coefficient of the collector barrier is much greater than that of the emitter barrier due to the applied bias and so all electrons entering the well are taken to contribute to the current. At $T = 0$ K, occupied emitter states have kinetic energies up to the Fermi energy *i.e.*

$$(k_y - k_0)^2 < k_F^2 \tag{5.12}$$

The integral over k_z can be performed to give

$$J = \frac{2e}{\hbar\pi} \sum_n \int_{-k_F}^{+k_F} dk'_y \, (k_F^2 - k'^2_y)^{1/2} \, |M_n(k'_y)|^2 \, \delta(\epsilon_a, \epsilon_w) \tag{5.13}$$

where $k'_y = k_y - k_0$. Changing variable from k'_y to $\Delta\epsilon = \epsilon_a - \epsilon_w$, $\int dk'_y$ is replaced by $\int (d(\Delta\epsilon)/dk'_y)^{-1} d(\Delta\epsilon)$. The energy conservation condition is only satisfied by a discrete number of states and this integral becomes a summation over those values of k'_y which obey the conservation condition and are occupied, *i.e.* $|k'_y| < k_F$. This gives [243, 242]

$$J = \frac{2e}{\hbar\pi} \sum_{n,i} (k_F^2 - k_i^2)^{1/2} \, |M(k_i)|^2 \left(\left| \frac{\partial \epsilon_a}{\partial k'_y} - \frac{\partial \epsilon_w}{\partial k'_y} \right|_{k_y = k_i} \right)^{-1} \tag{5.14}$$

Where the set of k_i are the values k_y which satisfy the energy conservation condition and lie below the Fermi level of the emitter 2DEG. The conservation condition on energy and canonical momentum can be interpreted graphically by looking for intersections of the two dispersion relations in the $\epsilon - k_y$ plane. This is basically the same approach used by Davies *et al.* to describe tunnelling between superlattices in a transverse field [236]. Figure 5.5 illustrates this by plotting the dispersion relations for the emitter and collector states of the single barrier samples studied by Snell *et al.* [159]. In the emitter there is an approximately parabolic relation and in the collector the dispersion relation is similar to that shown in Figure 5.3. The intersections of the two curves

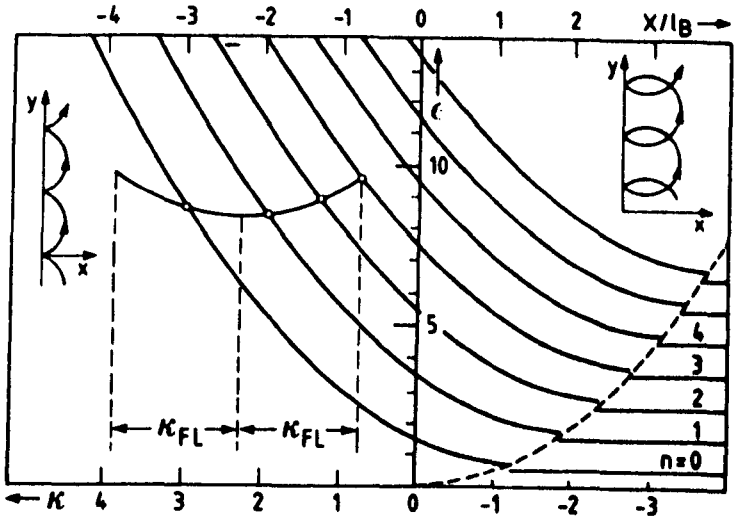

Figure 5.5: Dispersion relations for interfacial Landau states in a single barrier structure, from Snell *et al.* [159]. The energy is scaled in units of $\hbar\omega_c$ and $\kappa = k_y l_B$. The intersection points marked by open circles correspond to allowed channels for tunnelling.

are marked by the open circles and each corresponds to a possible channel for tunnelling. At a given voltage, the emitter curve intersects with more than one Landau level of the collector. The tunnel current is given by summing the contributions from all the possible channels. Sweeping the voltage or magnetic field changes the number of intersections thereby producing structure in the tunnel current and its derivatives [231, 242]. The main differences in samples with two tunnel barriers are that in the absence of the magnetic field the carriers are still confined due to the quantum well potential and there is a large electric field in the quantum well region. Both of these factors change the dispersion relations on the right-hand side of the tunnel barrier. At high fields, the dispersion relation for the wide well double barrier devices considered in Section 5.4 is similar to that shown in Figure 5.5, whereas in the sample with a narrow quantum well described in Section 5.3, there is only one intersection for each bias because the electrostatic confinement in the well increases the energy separation between the levels.

The tunnel current depends on the number of intersections, the number of electrons which can tunnel at each intersection, the gradients of the dispersion relations at the intersecting points and the matrix elements $|M(k_y)|^2$. Neglecting the variation of $|M|^2$ with k_y, the peak in the contribution for a given resonance occurs for $k_y' = 0$ since this corresponds to the largest number of available states in the emitter.

The matrix element for a double barrier structure at $B = 0$ is

$$|M|^2 = \hbar^2 \nu_a \nu_w T(\epsilon_0) \tag{5.15}$$

where $\nu_{a,w}$ is the semi-classical attempt rate for the emitter or the quantum well, as discussed in Chapter 1 — see reference [87] for a derivation of this

expression. An equivalent expression has been derived by T. M. Fromhold for non-zero magnetic field [242]. Here we will briefly summarise some of the qualitative trends which are relevant to the interpretation of the experimental data.

Conservation conditions: At zero magnetic field, all of the electrons in the emitter can tunnel resonantly at the bias at which the quasi-bound state energies are equal, but this is the only bias where resonance occurs. Therefore the current peak is narrow. The effect of the Lorentz force is to shift the energy distribution of emitter states in k-space by $k_0 = -eB\langle x\rangle/\hbar$. For a given energy level in the well, there is now only one value of k_y which satisfies the conservation conditions on the energy and canonical momentum at a particular applied bias. Therefore there is now a range of bias for which the two dispersion relations intersect but only a fraction of the electrons in the emitter are able to tunnel at a given bias voltage. This means that the resonance is much broader than in zero-field and the peak current is reduced [24].

Attempt rate: In zero magnetic field, the attempt rate is just given by the electron's velocity in the tunnelling direction divided by twice the width of the confining potential, $\nu = v_z/2w$. In a transverse field this no longer applies because the velocity varies around the orbit and (for skipping states) the width of the confining potential is field-dependent. The attempt rate must be obtained by integrating the velocity over the whole orbit. The Lorentz force reduces the kinetic energy associated with motion in the tunnelling direction so, for states which extend right across the quantum well (traversing states), the attempt rate is reduced. For skipping states, the magnetic field binds the electrons closer to the barrier, reducing the effective width of the confining potential and this compensates for the reduction in the velocity in the tunnelling direction. Therefore the effect of a magnetic field on the attempt rate reduces the contributions from traversing states at high fields and increases those of skipping states.

Dispersion relation: From a comparison of equations 5.9 and 5.10 we can see that the term in equation 5.14 ($\partial\epsilon_a/\partial k_y' - \partial\epsilon_w/\partial k_y'$), which originates from the density of states, increases with magnetic field, (in the perturbation calculation it is equal to $\hbar^2 k_0/m^*$). This term also contributes to a lowering of the current with increasing field.

Transmission coefficient: The tunnel current through a single barrier is found to decrease strongly in a transverse magnetic field [251, 220]. The Lorentz force deflects the electron path, reducing the kinetic energy of motion along the x-axis and increasing it along the y-axis. This reduction in the kinetic energy of the tunnelling electron is equivalent to an increase in the potential barrier height, given by the last two terms in equation 5.5, which is dependent on the value of k_y. Eaves, Stevens and Sheard [220] have used the WKB approximation to show that the total transmission coefficient through a potential barrier of height ϕ and width b for an incident kinetic kinetic energy in the x-direction

of ϵ_x is

$$T(\epsilon_0, B) = T_0 \exp\left(-\frac{\kappa b}{\phi}\left(-\frac{eEb}{2} + \frac{m^*\omega_c^2 b^2}{6}\right)\right) \tag{5.16}$$

where $\kappa^2 = 2m^*(\phi - \epsilon_x)/\hbar^2$. This expression is obtained by performing a Taylor expansion of the exponential term containing p_y and integrating over p_y up to the Fermi momentum [252]. This predicts that $\log(J/J_0) \propto -B^2$ in approximate agreement with experiment [251].

Since the expression for the current in a double barrier structure only involves evaluating T for the set of k_y values corresponding to the allowed transitions, this integrated expression is not directly applicable to resonant tunnelling. However the general point that the effective barrier height is increased by the magnetic field and that T is a function of k_y still applies. The calculations of Fromhold [239] show that the current due to a particular intersection varies quite slowly with k_y and hence it is not appropriate to consider only one value of k_y as was attempted by England *et al.* [253]. A detailed description of the model discussed above is given in reference [242]. There is reasonably good agreement with the experimental results for wide quantum wells presented in Section 5.4. It has not as yet been extended to cover the case of the narrow well samples of Section 5.3.

5.2.4 Other Models

Cury *et al.* [254, 255] have calculated the global transmission coefficient for a double barrier structure using a transfer matrix method involving dividing the structure into segments at constant potential and matching plane waves at each interface. The true eigenfunctions are parabolic cylinder functions [246] so this will yield only an approximate result. They find that the resonance position is diamagnetically shifted as expected. However they fail to integrate over the full range of occupied k_y states and therefore cannot correctly predict the variation of the sample current with field.

Ancillotto [256] has calculated the transmission coefficient by matching the wavefunction in the double barrier region to plane wave solutions in the contacts. He finds that the position of the resonance is shifted slightly to higher energy but that the peak transmission coefficient is unaffected. However the energy width of the resonant peak is reduced which is equivalent to an increase in the electron dwell time in the well and so the current decreases with field. Unfortunately the conservation of k_y is neglected in this work and so the resonance is not broadened and shifted to higher bias as is observed experimentally [24].

Helm *et al.* [234] have performed a self-consistent solution of the Poisson and Schrödinger equations for a double barrier structure in crossed fields. This has been extended to include an expression for the current flow by Peeters [257]. A resonant feature occurs when an anti-crossing of the energy levels on either side of the barrier goes below the Fermi energy since these states have a high amplitude on both sides of the barrier [244]. The anti-crossings obtained from the quantum-mechanical solution are equivalent to the intersections of the dispersion relations described above. In the limit of very thick barriers, where the transfer Hamiltonian method is applicable, the energy splitting caused

by level repulsion goes to zero and identical results are obtained from the two methods. Since the transfer Hamiltonian approach, together with the WKB approximation, gives essentially analytical solutions [231] which clearly illustrate the underlying physics, it is to be preferred.

5.3 The Effect of a Transverse Magnetic Field on the $I(V)$ Characteristics of a Resonant Tunnelling Device

The effect of a transverse magnetic field $\boldsymbol{B} \perp \boldsymbol{J}$ on the current-voltage characteristics of a double barrier device was first noted by Mendez *et al.* [139] and Levi *et al.* [161] who stated that the resonances were attenuated but supplied no explanation. This effect was also reported by Hayes *et al.* [170] who found that quantum interference effects in the collector arm of a hot electron transistor were quenched in a magnetic field. Leadbeater *et al.* [24] investigated resonant tunnelling devices with a three-dimensional electron gas in the emitter and found that the amplitude of the resonances decreased rapidly with field and that the resonances moved to higher bias. This was interpreted in terms of the effects of the Lorentz force using a simple graphical model to describe the conservation conditions which was also used by Davies *et al.* [236] to describe tunnelling between superlattices and is the basis of the explanation of the results presented here. More recently Ben Amor *et al.* [258] and Guéret *et al.* [155] have presented similar results. Investigations of tunnelling between two-dimensional electron states has also shown a broadening of the resonances and a decrease in the current [142, 259].

5.3.1 Current-Voltage Characteristics

The sample investigated in this section is *NU183* consisting of a 58 Å wide quantum well between barriers of thickness 83 Å and 111 Å. The growth details are given in Table 2.1 and the current-voltage characteristics have been described in Chapter 4. In this section we consider the bias direction in which electrons are injected into the well through the thicker barrier, which is defined as 'reverse' bias. Tunnelling occurs from a two-dimensional electron gas which forms in the accumulation layer of the emitter contact when a bias is applied to the device (Section 3.2). Figure 5.6 shows the current-voltage characteristics of a 200 μm diameter mesa of *NU183* at 4 K in magnetic fields $\boldsymbol{B} \perp \boldsymbol{J}$ between 0 and 11.5 Tesla. The main effects are summarised below:

- There is a very rapid decrease in the peak current with magnetic field; at 4 T the peak current is less than half the zero-field value. This trend is reversed at higher fields where there is a gradual increase. This contrasts with results reported for InP/(InGa)As tunnelling structures where the resonance was completely quenched [24] but agrees with the observations of Ben Amor *et al.* [258]. The variation of peak current with applied field is shown in Figure 5.7.

- The peak position moves to higher bias as the field increases, by 11 T, V_p has changed by more than 300 mV. The threshold and cut-off voltages also shift rapidly to higher voltages. Figure 5.8 plots the threshold, peak and cut-off voltages against magnetic field. The threshold and cut-off voltages were deduced by extrapolating the linear portions of the $I(V)$ characteristics to zero current.

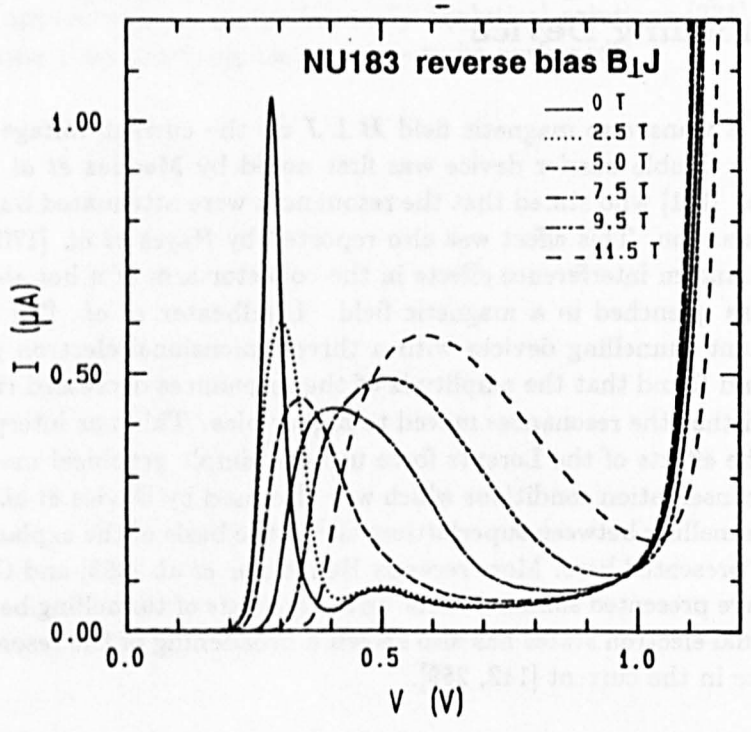

Figure 5.6: Current-voltage characteristics of a 200 μm diameter mesa of *NU183* at the first resonance in reverse bias at 4 K in magnetic fields $\boldsymbol{B} \perp \boldsymbol{J}$ up to 12 Tesla.

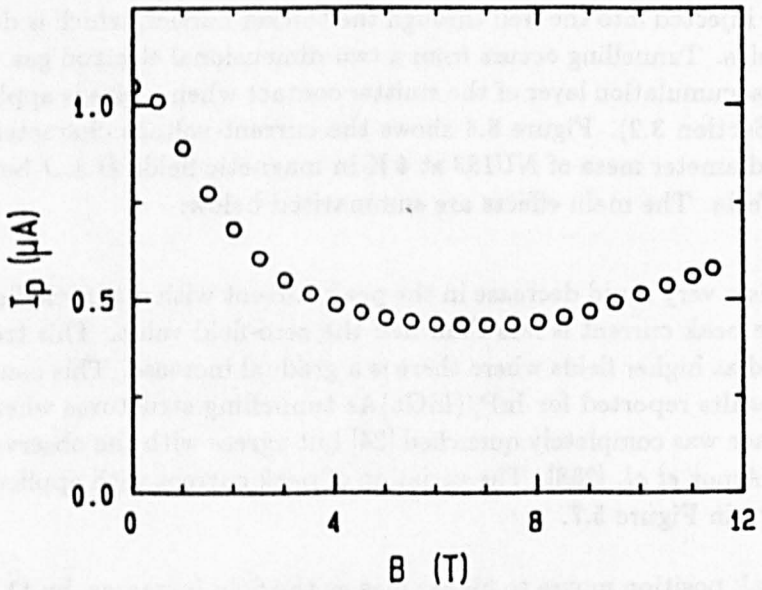

Figure 5.7: The peak current I_p for *NU183* plotted against magnetic field $\boldsymbol{B} \perp \boldsymbol{J}$.

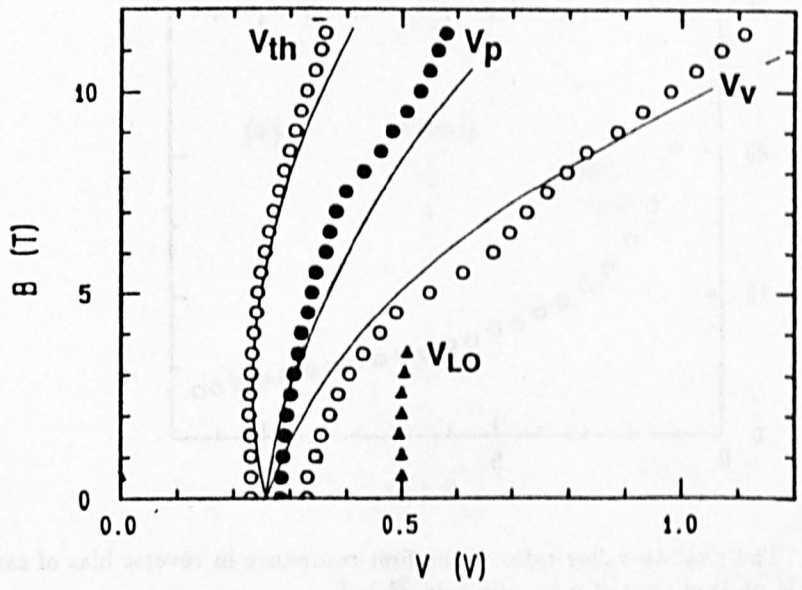

Figure 5.8: Plot of the threshold, peak and cut-off voltages for *NU183* against magnetic field $B \perp J$, showing the broadening of the resonance and the diamagnetic shift in the peak position. The solid lines show the calculated field-dependence of the voltages discussed in Section 5.3.2. The position of the LO phonon peak ($\triangle$) does not change with field since this transition does not conserve transverse momentum.

- The resonance becomes very much broader. At $B = 0$, the resonance is extremely sharp and has a full-width half-maximum of less than 100 mV. This sharp resonance is characteristic of resonant tunnelling from a two-dimensional state [142, 259, 182]. At 11 T the resonance is more than 400 mV wide.

- The peak-to-valley current ratio falls dramatically with field, from ~26:1 at zero field to 1.8:1 at 11 T, as shown in Figure 5.9.

- At $B = 0$, the resonant peak is almost symmetrical and the line-shape resembles the expected Lorentzian (see Chapter 1). However, at higher fields the peak in the current is markedly closer to the threshold voltage than to the cut-off — see Figure 5.8.

- The LO phonon replica peak at $V \sim 500$ mV (see Section 3.4) does not shift with magnetic field and disappears for $B > 5$ T. The position of the LO phonon peak is also plotted in Figure 5.8, marked $\triangle$.

5.3.2 Interpretation and Discussion

Resonance position

Resonant tunnelling can only occur when there is an occupied state in the two-dimensional electron gas of the emitter contact with the same values of total energy ϵ and components of canonical momentum k_y and k_z as an unoccupied state in the quantum well. Since both the accumulation layer potential and the quantum well are relatively narrow in this sample, the quantisation is

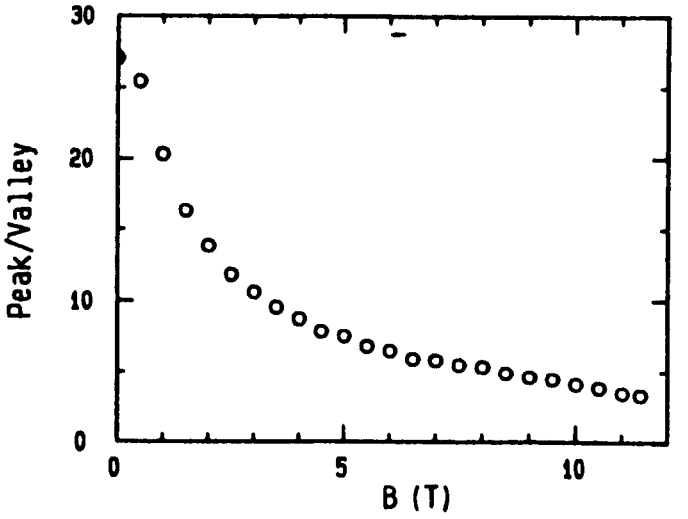

Figure 5.9: The peak-to-valley ratio of the first resonance in reverse bias of sample *NU183* at 4 K plotted against magnetic field $\boldsymbol{B} \perp \boldsymbol{J}$.

dominated by the electrostatic potential and we can describe the effect of a transverse field on the energy levels using the perturbation approach described in Section 5.2. The results of this calculation, where the origin is taken at the centre of the well, are (see equations 5.9 and 5.10)

$$\epsilon_a = \epsilon_0 + eE(b_1 + w/2) + \frac{3m^*\omega_c^2}{2a^2} + \frac{\hbar^2 k_z^2}{2m^*} + \frac{\hbar^2(k_y - k_0)^2}{2m^*}$$

$$\epsilon_w = \epsilon_1 + \frac{m^*\omega_c^2 w^2}{24} + \frac{\hbar^2 k_z^2}{2m^*} + \frac{\hbar^2 k_y^2}{2m^*}$$

where ϵ_1 is the bound state energy in the well, ϵ_0 is the energy of the bound state in the accumulation layer, E is the applied electric field, a the variational parameter of the Fang-Howard wavefunction (see Section 3.2) and $k_0 = eB(3/a + b_1 + w/2)/\hbar$ which corresponds to the change in the wavevector due to the action of the Lorentz force on the tunnelling electron. Resonant tunnelling occurs for $\epsilon_a = \epsilon_w$. If we assume that the effective mass is the same in the emitter and the well, the kinetic energies for motion in the z-direction are equal and so the conservation condition may be written as

$$\epsilon_0 + eE(b_1 + w/2) + \Delta\epsilon + \frac{\hbar^2(k_y - k_0)^2}{2m^*} = \epsilon_1 + \frac{\hbar^2 k_y^2}{2m^*} \qquad (5.17)$$

where $\Delta\epsilon$ is the difference in the diamagnetic energy shifts, $m^*\omega_c^2(3/a^2 - w^2/12)/2$, which is small. At low temperatures, only states in the emitter with $|k_y - k_0| < k_F$ are occupied, therefore filled states can be represented in $\epsilon - k_y$ space as a section of a parabola centred at $k_y = k_0$, between the points $k_0 - k_F$ and $k_0 + k_F$. The well states lie on a parabola centred at $k_y = 0$. The conservation conditions can be interpreted graphically by looking for intersections of these two curves, as illustrated in Figure 5.10. At $B = 0$, $k_0 = 0$ so the two parabolas are centred about the same axis. At zero bias the emitter

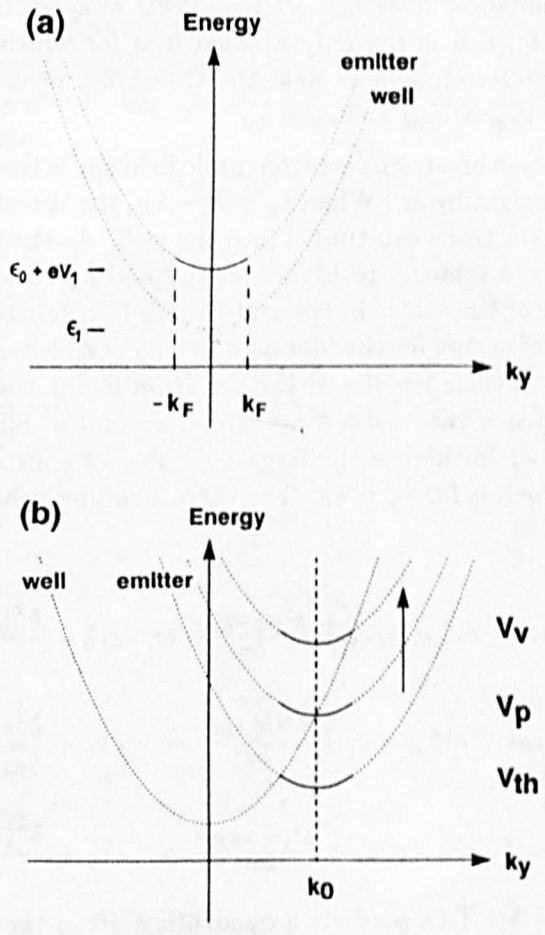

Figure 5.10: Schematic diagram illustrating the conservation conditions which govern resonant tunnelling in a transverse magnetic field. The occupied states in the emitter are represented by the portion of a parabola between $k_0 - k_F$ and $k_0 + k_F$. Resonant tunnelling occurs for biases where this curve intersects the parabola representing the electron states in the quantum well. (a) $B = 0$: The parabolas have a common axis and only coincide for one value of bias, (b) $B > 0$: The origin of the emitter parabola is displaced by $k_0 = eB(x_0 + b_1 + w/2)/h$ and the two parabolas intersect for a range of bias voltages between V_{th} where $k_y = k_0 - k_F$ and V_v where $k_y = k_0 + k_F$. This produces a much broader resonance.

curve is below the energy level in the well and resonant tunnelling cannot occur. As the bias is swept, the emitter curve moves up relative to the well state and when the voltage drop across the emitter region and the first half of the quantum well is $eV_{e,th} = \epsilon_1 + \epsilon_F$ (or equivalently $\epsilon_0 + eV_1 = \epsilon_1$), the device comes onto resonance. If we neglect the effects of space charge buildup in the well (Chapter 4), this is the only applied bias for which resonant tunnelling can occur, so at zero magnetic field the threshold, peak and cut-off voltages are coincident, $V_{e,p} = V_{e,th} = V_{e,v} = V_0$.

The application of a transverse magnetic field shifts the centre of the emitter parabola to the right by k_0. When $k_y = k_0 - k_F$, the threshold of the resonance is reached and electrons can tunnel into the well. As the bias is increased, the point of intersection moves to higher energy and k_y. There is a range of bias for which some of the states in the emitter are in resonance with states in the well. The cut-off occurs for the bias at which $k_y = k_0 + k_F$. If we neglect charge buildup in the quantum well and the variation in the transmission coefficient with k_y (which is a reasonable approximation at low biases [260]), the peak current occurs when there is the largest number of emitter states available to tunnel from which is for $k_y = k_0$. The corresponding voltage drops across the emitter are

$$\textit{Threshold} \quad eV_{e,th} = \epsilon_1' + \frac{\hbar^2(k_0 - k_F)^2}{2m^*} = eV_0 + \frac{\hbar^2(k_0^2 - 2k_0k_F)}{2m^*} \tag{5.18}$$

$$\textit{Peak} \quad eV_{e,p} = \epsilon_1' + \frac{\hbar^2(k_0^2 + k_f^2)}{2m^*} = eV_0 + \frac{\hbar^2 k_0^2}{2m^*} \tag{5.19}$$

$$\textit{Cut-off} \quad eV_{e,v} = \epsilon_1' + \frac{\hbar^2(k_0 + k_F)^2}{2m^*} = eV_0 + \frac{\hbar^2(k_0^2 + 2k_0k_F)}{2m^*} \tag{5.20}$$

where $\epsilon_1' = \epsilon_1 - \Delta\epsilon$. This predicts a quadratic shift in the peak position and a linear increase in the width of the resonance. However, the Fermi energy of the emitter 2DEG is a function of the applied bias since it depends on the number density in the emitter n_a, $\epsilon_F = \hbar^2\pi n_a/m^*$. This can be obtained from the periodicity of the oscillations in the tunnel current or differential capacitance when the magnetic field is applied perpendicular to the interfaces ($\boldsymbol{B} \parallel \boldsymbol{J}$) as described in Section 3.2. The results for this sample are given in Section 4.7.2. In addition, the voltage drop across the emitter region is not linearly related to the total applied bias. The distribution of the potential within the device varies due to the depletion of the collector contact; V_e can be approximately related to the total applied bias V by

$$V = V_e\left(1 + \frac{x_0 + b_1 + w/2}{w/2 + b_2 + \lambda_c}\right) \tag{5.21}$$

where λ_c is the (voltage-dependent) depletion length in the collector — see Section 3.2. Since λ_c increases with bias whereas x_0 decreases, the proportion of the applied bias dropped across the emitter decreases as the voltage increases, so changing the dependence of V_p on B. Both of these factors tend to make the peak move more rapidly to higher bias than expected from equation 5.18. In particular, the increase in k_F with bias leads to the resonance being asymmetric about the peak since the Fermi wavevector at cut-off is greater than that at

threshold. Using the model outlined in Section 3.2 together with the magneto-transport results for $\boldsymbol{B} \parallel \boldsymbol{J}$ of Section 4.7.2 and taking the bound state energy in the well to be 68 meV, we can predict the variation in the resonance voltage with field. This is shown as the solid curves in Figure 5.8. The agreement is generally good, however this was achieved by reducing the stand-off distance of the 2DEG in the emitter by 30%. It is to be expected that penetration of the wavefunction into the barrier will account for part of this, the rest of the discrepancy may be due to the effect of the magnetic field on the dispersion relation in the emitter.

Current

The decrease in the peak current at low fields can be explained by the broadening of the resonance, although the peak current decreases to about half the zero-field value at 4 T, the total area under the $I(V)$ curve is little changed *i.e.* the magnetic field has merely spread the same total amount of resonant current over a wider range of bias. This does not hold for fields greater than about 5 Tesla where the area under the curve and the peak current are clearly increasing. As the bias at resonance increases the electron sheet density in the emitter accumulation layer increases and so does the voltage drop across the barriers. Both of these factors increase the tunnel current; there is a larger number of electrons available to tunnel and the transmission coefficients of the barriers are increasing. The higher voltage drop across the barrier must be weighed against the extra barrier height due to the magnetic vector potential. In this sample it appears that the increasing electric field has a more significant effect. The valley current is mostly unaffected by the magnetic field, but the shift of the resonance to higher bias means that there is some increase in the valley current at high fields. The peak-to-valley ratio drops as a consequence.

LO *phonon peak*

The replica peak at $V \sim 500$ mV is due to the emission of LO phonons by the tunnelling electrons and therefore this process does not conserve k_y. Hence the conservation conditions described above for the resonant process do not affect the voltage at which LO phonon emission can occur. The condition for emission of phonons remains that the energy difference between the Fermi energy in the emitter and the energy level in the well must be at least $\hbar\omega_{LO} = 36$ meV and the bias at the peak of the LO phonon replica corresponds to the energy level in the well being 36 meV below that in the emitter — irrespective of the applied magnetic field. This is also true for the other $k_\perp$-nonconserving contributions to the valley current (Section 3.4).

Charge buildup

If there is a buildup of space charge in the quantum well at resonance, the voltage drops within the sample is not described by equation 5.21. The amount of space charge buildup depends on the ratios of the transmission coefficients of the two barriers and this may change with bias and magnetic field. The number density in the emitter affects the charge buildup in the well which in turn affects the transmission coefficients of the barriers. Hence the effect of a transverse magnetic field on a resonance where there is significant charge buildup is much harder to analyse. The results presented in Sections 4.7.5 and 4.8 show that

while the first resonance is strongly enhanced by a transverse magnetic field, the resonance with the upper bound state of the well is quenched.

Three-dimensional emitter state

The equivalent expressions for the threshold and cut-off voltages when there is a three-dimensional electron gas in the emitter have been given by Leadbeater *et al.* [24]

$$\textit{Threshold} \quad eV_{e,th}^{3D}(B) = eV_{e,th}^{3D}(0) + \frac{\hbar^2(k_0 - k_F)^2}{2m^*}\theta(k_0 - k_F) \tag{5.22}$$

$$\textit{Cut-off} \quad eV_{e,v}^{3D}(B) = eV_{e,v}^{3D}(0) + \frac{\hbar^2(k_0^2 + 2k_0k_F)}{2m^*} \tag{5.23}$$

Again the voltage drop across the emitter must be related to the total bias, but in this case k_F is not a function of V. These expressions neglect the effects of the magnetic field on the contact regions [220]. This is justified if there is a lot of scattering in the contacts which broaden out the Landau levels.

Tejedor *et al.* [261] consider the quantisation in the contacts and obtain complex structure in the transmission coefficient due to the intersections of the interfacial Landau levels on either side of the double barrier structure. This was not observed experimentally in double barrier structures [24]. They attribute this to sequential tunnelling involving scattering in the well, but broadening of the states in the contacts due to the much stronger scattering in the doped regions is also a possible explanation — although note that the interfacial Landau levels observed by Snell *et al.* [159] were formed in a heavily-doped region.

The peak position for resonant tunnelling from a 3D emitter is hard to determine for several reasons: the expression for the current must be integrated over k_x as well as k_y, the intersection of the two dispersion relations does not correspond to a line in k-space but to a surface and the attempt rate in the emitter is less well-defined in a magnetic field. Note that at zero-field for a perfectly narrow resonant state, the peak coincides with the cut-off voltage but that for $B > 0$ this is not so, therefore Guéret *et al.* [155] are incorrect to apply equation 5.22 to the variation of the peak voltage. They also neglect the difference between the voltage drop across the emitter and the total applied bias which more than accounts for the discrepancy they observe between the length deduced from the variation of the peak position and the width of the emitter barrier.

Wide well samples

Figure 5.11 plots the second derivative of the current against voltage in magnetic fields $\boldsymbol{B} \perp \boldsymbol{J}$ of 7 and 17 T for sample *NU154* which has a 217 Å wide quantum well. The positions of peaks in the current are plotted in Figure 5.12. At the third, fourth and fifth resonances, there is a substantial amount of space charge in the well at zero field, which builds up due to intersubband scattering processes as discussed in Section 4.9. These resonances shift rapidly to lower bias with increasing magnetic field, whereas the sixth and seventh resonances hardly move at low fields. This is because space charge is being lost from the

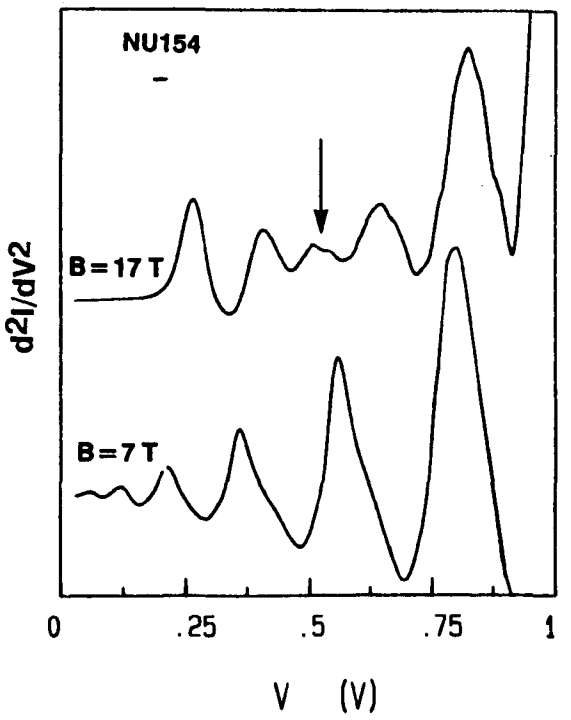

Figure 5.11: Plot of d^2I/dV^2 for *NU154* at magnetic fields $B \perp J$ of 7 and 17 Tesla.

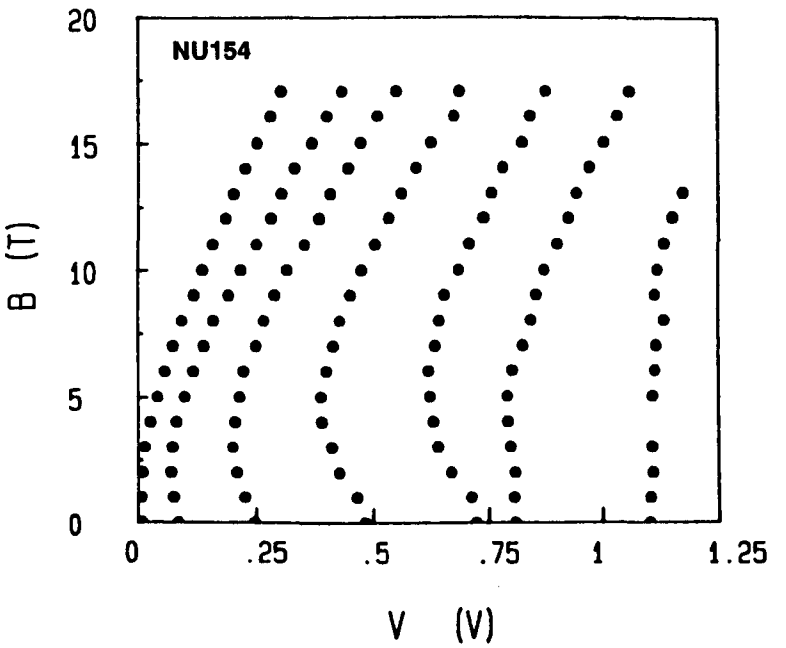

Figure 5.12: The position of current peaks for sample *NU154* (217 Å well) as a function of magnetic field $B \perp J$.

well The behaviour of these resonances is similar to that shown by the second resonance in forward bias of sample *NU183* which was described in Section 4.7. It is not clear why a transverse field should reduce charge buildup and quench the resonance for the upper bound states of the well but appear to enhance it for the lowest level — see Section 4.7.5.

Of more significance is the variation in the position of the lowest lying resonances; these occur at significantly lower bias than predicted by the perturbation estimate. This means that we are no longer able to describe the states in the well using this approach because the radius of the electron orbit is comparable to the width of the well for $B > 6$ T, at $V \sim 200$mV. This is shown in the second derivative plot for 17 T where there appears to be a minimum in the amplitude of the resonances at a voltage of 500 mV. Therefore we must consider tunnelling into hybrid magnetoelectric energy levels.

5.4 Resonant Tunnelling Studies of Hybrid Magnetoelectric Quantisation

In this section we investigate resonant tunnelling in crossed electric and magnetic fields for double barrier structures with well widths considerably greater than those described in the previous section. This allows the electron orbit to fit within the width of the quantum well at high fields and we are able to observe the transition from electric to magnetic quantisation in double barrier resonant tunnelling structures for the first time [147, 233, 160]. A schematic diagram illustrating the electron orbits in a wide quantum well in crossed fields is shown in Figure 5.13.

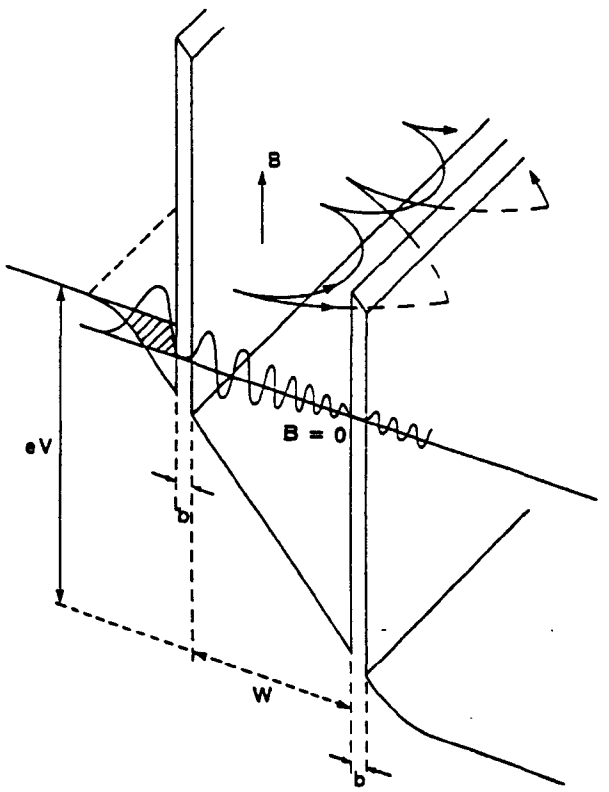

Figure 5.13: Schematic illustration of a double barrier structure in crossed electric and magnetic fields.

The samples studied are *NU167* with a 600 Å wide quantum well, *NU207* with a 1200 Å wide well and *NU288* with an 1800 Å wide well. All three samples have barriers of thickness 56 Å and the doping levels in the contacts are nominally identical — see Table 2.1. The current-voltage characteristics for these samples at zero magnetic field have been discussed in Section 3.6. The very wide quantum wells mean that as many as 70 resonances can be observed in the zero-field conductance, most of which correspond to virtual states at energies above the top of the collector barrier [233, 165, 172]. The $I(V)$ characteristics make the samples ideal for studying the effect of a confining potential (the quantum well) on the electron eigenstates in crossed electric and magnetic fields, $-\boldsymbol{E} \parallel \boldsymbol{x}$, $\boldsymbol{B} \parallel \boldsymbol{z}$.

5.4.1 Current-voltage Characteristics in a Transverse Field

Plots of d^2I/dV^2 against V for device *NU167* are shown in Figure 5.14 for several magnetic fields $\boldsymbol{B} \perp \boldsymbol{J}$. The temperature is 4.2 K and the mesa has a diameter of 100 μm. Note that the plots are not to scale.

The magnetic field reduces the tunnel current and attenuates the resonances, as was the case for the narrow well samples of the previous section. At high fields, a new series of resonances emerge at low bias whose amplitude decreases with increasing bias, these are labelled a_- in Figure 5.14. These resonances correspond to tunnelling into 'skipping' states bound at the emitter barrier/well interface. The higher-bias resonances (labelled b_+ and b_-) are due to 'traversing' states where the electron wavefunction extends right across the well, as described in Section 5.2. The structure in d^2I/dV^2 apparent in the $B = 0$ curve is due to the current breaking into high-frequency oscillations in the region of negative differential resistivity (NDR) (Section 4.3). This is removed by very low magnetic fields $B \leq 1$ T since the broadening of the resonances leads to a loss of NDR. At low fields and high biases, the structure in d^2I/dV^2 is dominated by the features labelled b_+ which correspond to a decrease in the number of tunnelling channels, and at low biases and higher fields structure due an increase in tunnelling channels is dominant (labelled b_- for traversing states or a_- for skipping). The reasons for this change over are complex and depend on the detailed matrix elements for the different transitions as described in reference [242].

The cross-over between tunnelling into skipping (type a) and traversing (type b) orbits is marked by an arrow in the plot for $B = 7$ T in Figure 5.14. This transition occurs when the electron orbit just grazes the collector barrier. If we assume that the electrons tunnelling from the emitter emerge into the well with a kinetic energy which is small compared to the potential drop across the well then the electron motion approximates to that of a free electron starting from rest at the emitter barrier/well interface, *i.e.* it undergoes cycloidal motion with a radius of $r = m^*E/eB^2$ as described in Section 5.2. Therefore, grazing incidence occurs for $w = 2r = 2m^*E/eB^2$. In these samples, the number density in the accumulation layer, and hence the electric field in the well, is roughly linearly related to the applied bias, as shown in Figure 5.15. Therefore we would expect the critical voltage for the transition between skipping and traversing states to vary quadratically with magnetic field. This is verified by the plot in Figure 5.16.

Figure 5.17 plots the positions of the resonances (minima in d^2I/dV^2) for the cycloidal skipping states against $B^{3/2}$ for a wide range of voltage and magnetic field. The almost linear relationship can be understood in terms of the energies of the cycloidal orbits discussed above; when quantised, the energy of the circular motion $m^*\omega_c^2 r^2/2$ takes allowed values $(n + \varphi)\hbar\omega_c$, where φ is a phase factor (equal to 3/4 in the WKB approximation). The quantisation condition can be expressed as

$$\frac{m^{*2}E^2}{2e\hbar B^3} = n + \varphi \tag{5.24}$$

This shows that for a given applied bias (constant E) the resonances are periodic in $1/B^3$. This is in contrast to the results obtained for skipping states in

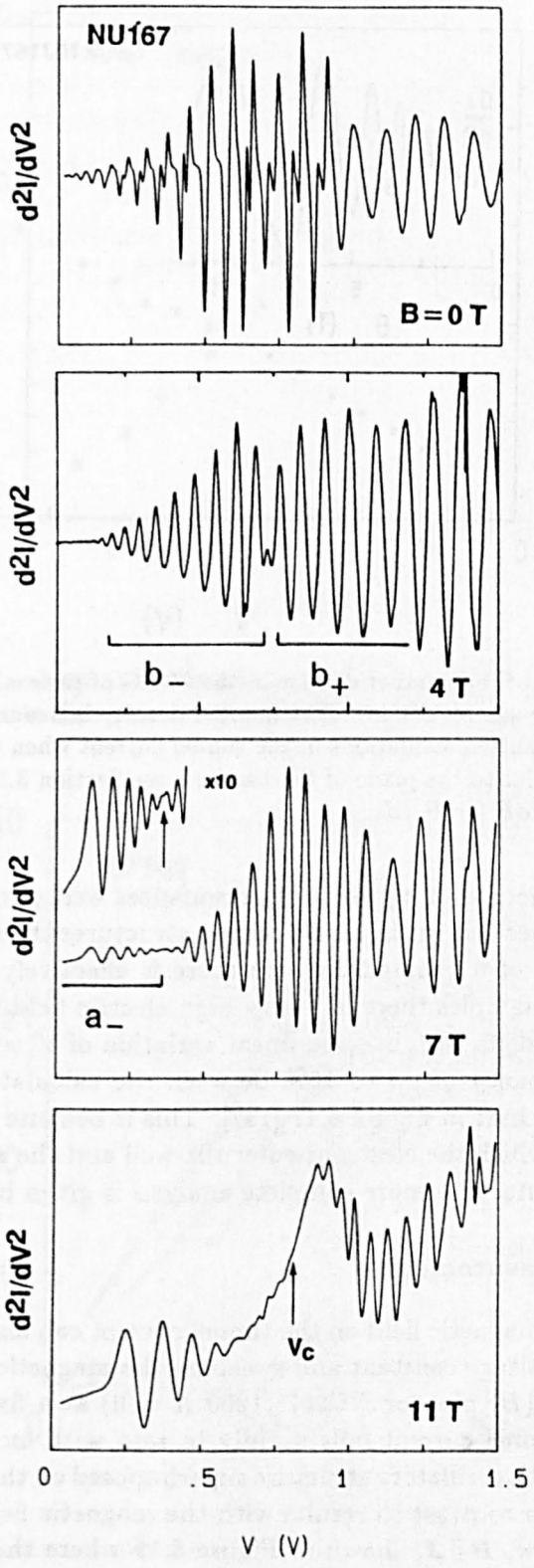

Figure 5.14: Plots of d^2I/dV^2 versus V for device *NU167* (600 Å well) at 4 K for various magnetic fields ($\boldsymbol{B} \perp \boldsymbol{J}$): B = 0 T, 4 T, 7 T and 11 T. For $B > 2$ T, a series of oscillations due to tunnelling into magnetically quantised interface states can be observed. The crossover between tunnelling into skipping and traversing orbits is indicated by an arrow.

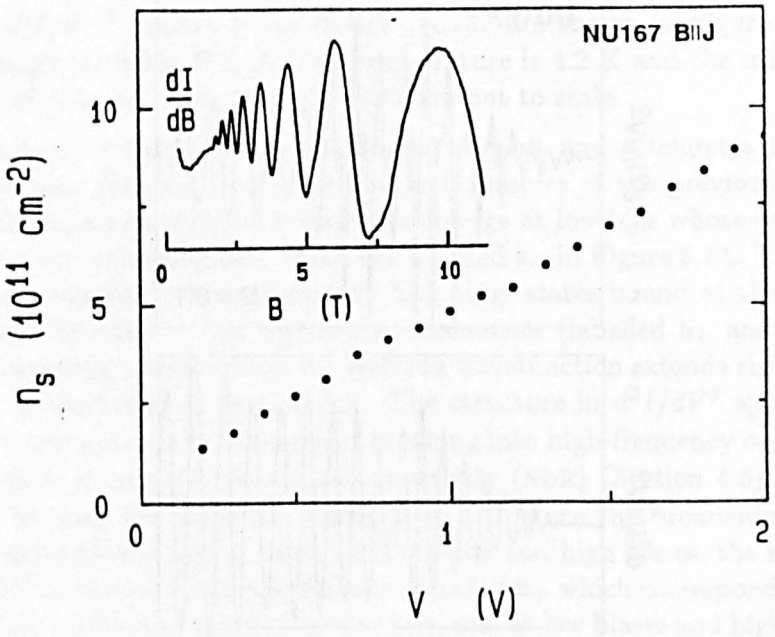

Figure 5.15: Plot of the number density in the 2DEG of the emitter contact against the applied bias for sample *NU167*. The number density is deduced from the periodicity of magnetoquantum oscillations in the tunnel current when the magnetic field is applied perpendicular to the plane of the barriers, see Section 3.3. The inset shows a typical trace of dI/dB for $\boldsymbol{B} \parallel \boldsymbol{J}$.

single-barrier structures [159] where the resonances were periodic in $1/B$. This difference arises because in the single barrier structures the skipping states develop in a region of n^+ material where there is effectively zero electric field whereas in these samples there is a very high electric field in the well. Equation 5.24 also predicts the observed linear variation of V with $B^{3/2}$. However there is a discrepancy of up to 15% between the calculated slopes and the slopes of the fan chart in Figure 5.17 [147]. This is because we have neglected the energy with which the electrons enter the well and the spread of k_y-values in the emitter contact. A more complete analysis is given below.

5.4.2 $I(B)$ Measurements

The effect of the magnetic field on the tunnel current can also be seen by holding the applied voltage constant and sweeping the magnetic field. Figure 5.18 shows a typical $I(B)$ plot for *NU207* (1200 Å well) at a fixed bias voltage of 600 mV. The tunnel current falls rapidly to zero with increasing transverse magnetic field, with oscillatory structure superimposed on this decreasing background. This is in contrast to results with the magnetic field applied parallel to the current flow, $\boldsymbol{B} \parallel \boldsymbol{J}$, shown in Figure 5.19 where there is only a small reduction in the tunnel current. This result can be understood classically since there is no Lorentz force component associated with the motion in the tunnel direction in the $\boldsymbol{B} \parallel \boldsymbol{J}$ configuration whereas for $\boldsymbol{B} \perp \boldsymbol{J}$ the electronic motion in the well is greatly modified. The oscillatory structure of $I(B)$ is revealed more clearly in the plots of the second derivative, d^2I/dB^2, which are also shown in Figures 5.18 and 5.19. As was described in Section 3.3, in a parallel field

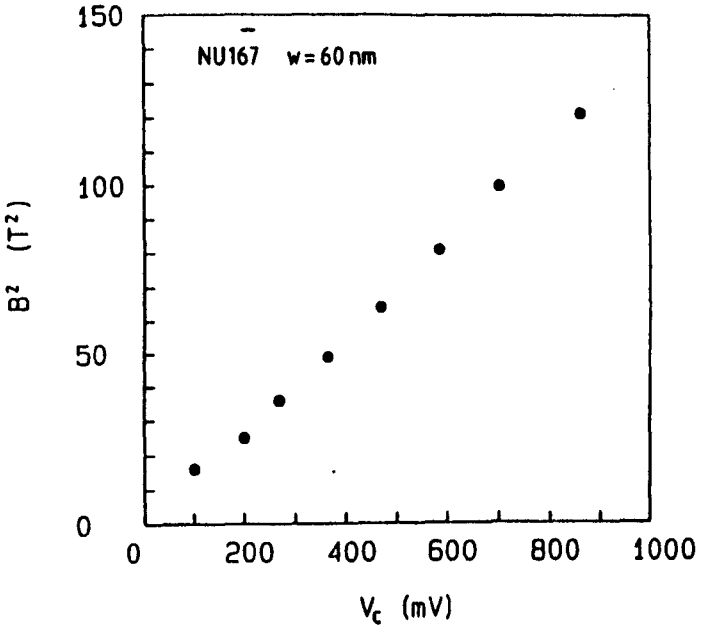

Figure 5.16: The voltage at which the transition from skipping to traversing orbits occurs plotted against the square of the applied transverse magnetic field for *NU167*.

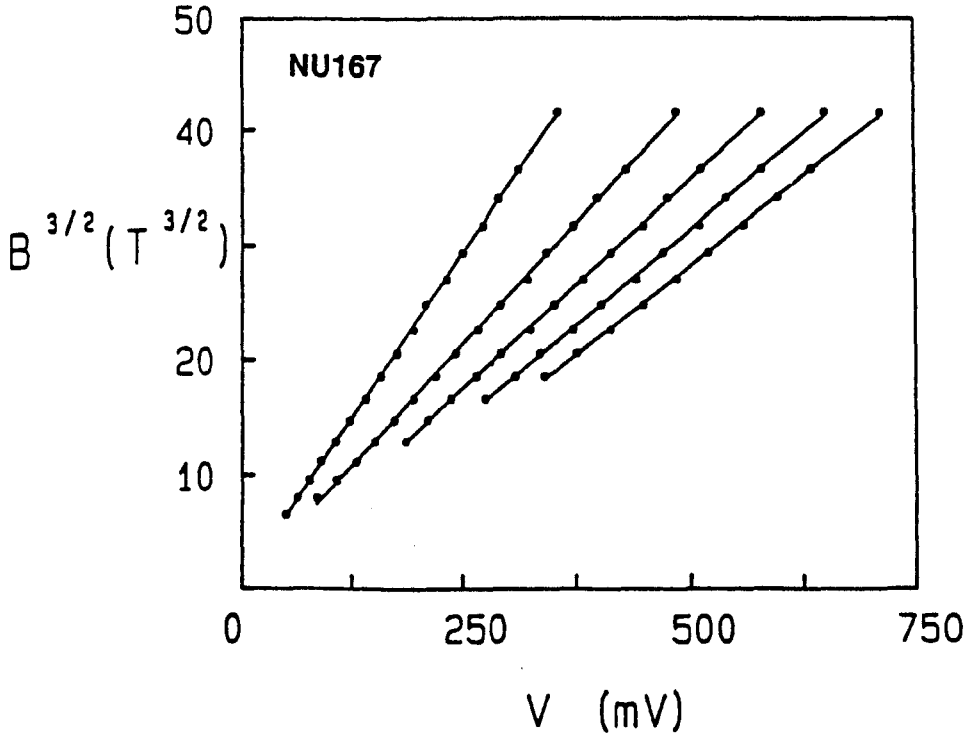

Figure 5.17: The voltage positions of the resonances for the skipping states plotted as a function of $B^{3/2}$ showing the approximately linear dependence discussed in the text.

there is a single series of oscillations which is periodic in $1/B$ and is related to Landau levels in the emitter 2DEG passing through the Fermi level. The structure in $\boldsymbol{B} \perp \boldsymbol{J}$ is more complex with three distinct series of oscillations labelled b_+, b_- and a_-. The labels a and b refer to the skipping and traversing states respectively, the subscripts will be explained below. None of the series is periodic in $1/B$, which would be the case if they were associated with Landau level effects in the bulk regions of the emitter contact as has been suggested by Schulz *et al.* [262]. The series due to tunnelling into skipping states (series a) is roughly periodic in $1/B^3$ as expected from equation 5.24.

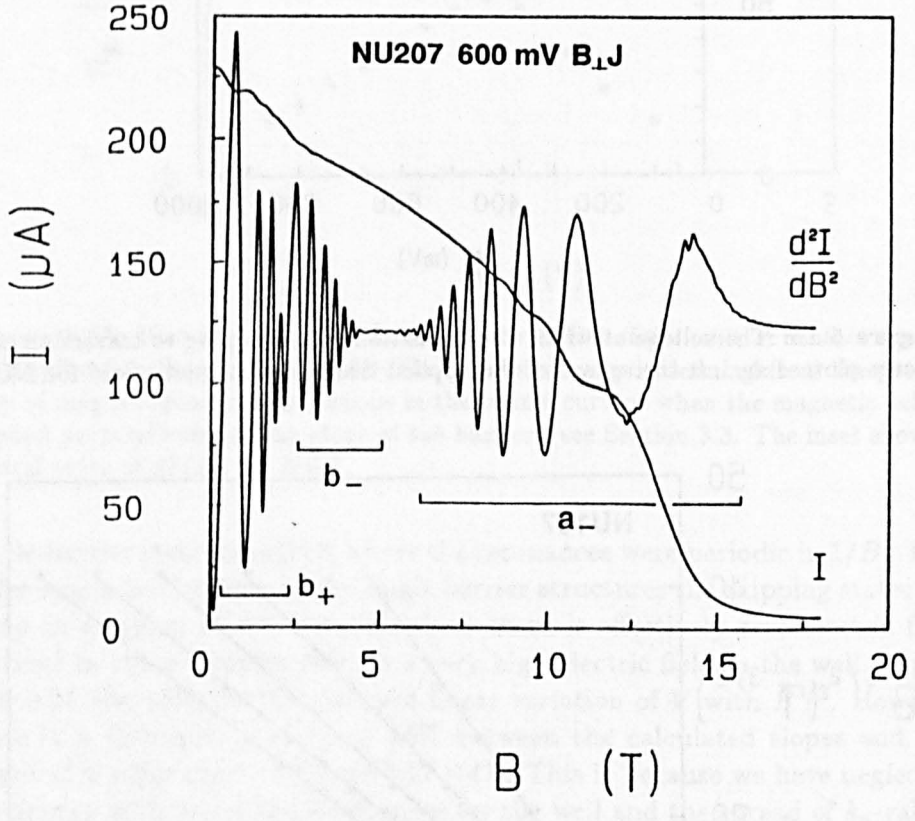

Figure 5.18: Plots of $I(B)$ and d^2I/dB^2 at $V = 600$ mV, $T = 4$ K for a 100 μm diameter mesa of *NU207* (1200 Å well) in $\boldsymbol{B} \perp \boldsymbol{J}$ showing the oscillatory structure due to tunnelling into magnetoelectric states and the quenching of the tunnel current.

In the previous section, the resonance for a narrow well sample was found to be broadened by a magnetic field due to the effect of a magnetic field on the conservation conditions. This is also the case in these wide well samples, however the spacing between the levels is much smaller and therefore the observed tunnel current is the sum of many different resonances which overlap; each resonance corresponding to an intersection of the dispersion relations of the emitter and the well as discussed in Section 5.2. Structure in the current occurs whenever the number of resonant channels for tunnelling changes. Therefore we naturally get two sets of oscillatory structure in the second derivative for each level in the quantum well, one at the magnetic field where the state comes on to resonance (these are denoted by the subscript +) and one

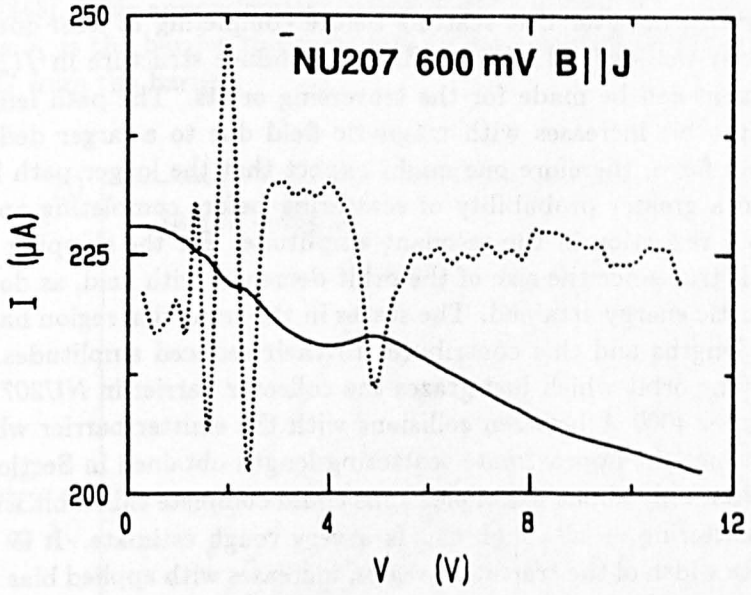

Figure 5.19: Plots of $I(B)$ and d^2I/dB^2 at $V = 600$ mV for *NU207* in $\boldsymbol{B} \| \boldsymbol{J}$. The oscillatory structure here is due to Landau levels in the 2DEG of the emitter contact passing through the Fermi level.

where it comes off resonance, denoted by $-$. Note that this refers to sweeping B, in a voltage sweep the threshold of a resonance corresponds to b_- and the cut-off to b_+.

Amplitude of the resonances

The b_+ series dominates at low fields but is rapidly attenuated as the magnetic field increases and no oscillations assigned to this series are observed above 10 Tesla. Similarly we see no structure which we can attribute to a_+-type resonances, *i.e.* an increase in the number of tunnelling channels due to a skipping orbit state coming into resonance with the emitter 2DEG, although there is strong structure due to these states coming off-resonance, *i.e.* the a_- series. This is attributable to the low matrix element for these transitions [238, 242].

The transition from traversing to skipping states, *i.e.* between b_- and a_-, is accompanied by a strong reduction in the amplitude of the oscillatory structure in d^2I/dB^2, see the region between 5 and 7 Tesla in Figure 5.18. This is predicted by the theory of Fromhold *et al.* [239, 242] from a consideration of the matrix elements derived from the transfer Hamiltonian approach. The argument in its simplest form is that for the traversing orbits the attempt rate decreases with field due to the action of the Lorentz force so leading to a reduction in the transmission rate, whereas the skipping orbits are more tightly bound to the barrier as the magnetic field rises and so their matrix elements increase with field. This produces the characteristic minimum in the amplitude of the resonances in the transition region. A more detailed description of the physics determining the relative coupling strengths is given in reference [242].

A further contribution to the variation in amplitude is the role of scatter-

ing. Clearly an electron in a skipping orbit must scatter to contribute to the measured current, however if it scatters before completing *at least* one orbit the state is not well-defined and so will not produce structure in $I(B)$. A similar argument can be made for the traversing orbits. The path length of the traversing orbit increases with magnetic field due to a larger deflection by the Lorentz force, therefore one might expect that the longer path length would lead to a greater probability of scattering before completing an orbit and hence to a reduction in the resonant amplitude. For the skipping orbits the opposite is true since the size of the orbit decreases with field, as does the maximum kinetic energy attained. The states in the transition region have the longest path lengths and this contributes to their reduced amplitudes. The classical skipping orbit which just grazes the collector barrier in *NU207* has a path length of $\sim$ 4000 Å between collisions with the emitter barrier which is nearly three times the approximate scattering length obtained in Section 3.6. This implies that only about 5% of electrons could complete this orbit without undergoing scattering — although this is a very rough estimate. It is worth noting that the width of the transition region increases with applied bias which may indicate that the scattering rate increases at high energies.

Quenching of the current

The quenching of the current at high magnetic fields is equivalent to an increase in the resistance of the device of more than three orders of magnitude. The magnetic field at which the current goes to zero depends on the applied bias. Figure 5.20 shows the tunnel current in a magnetic field divided by its zero-field value, $I(B)/I(0)$, plotted against magnetic field for sample *NU207* at biases of 100, 200, 400 and 800 mV. The magnetic field needed to quench the current increases from $\sim$ 6 T at 100 mV to $\sim$ 18 T at 800 mV. At this field the

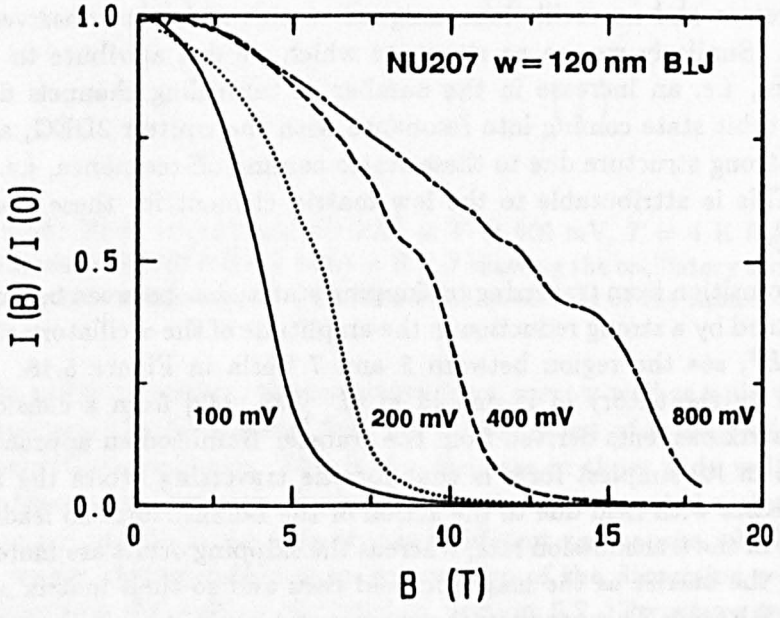

Figure 5.20: $I(B)/I(0)$ plotted against B for *NU207* at 100, 200, 400 and 800 mV showing the increase in the magnetic field needed to quench the current.

Lorentz force on a tunnelling electron is sufficient to deflect it back into the

emitter before it reaches the well and therefore it cannot couple to states in the well [243]. This approximately corresponds to a field $B = \sqrt{2m^*E/e(b_1 + x_0)}$ where b_1 is the barrier thickness and x_0 the stand-off distance of the emitter 2DEG from the barrier.

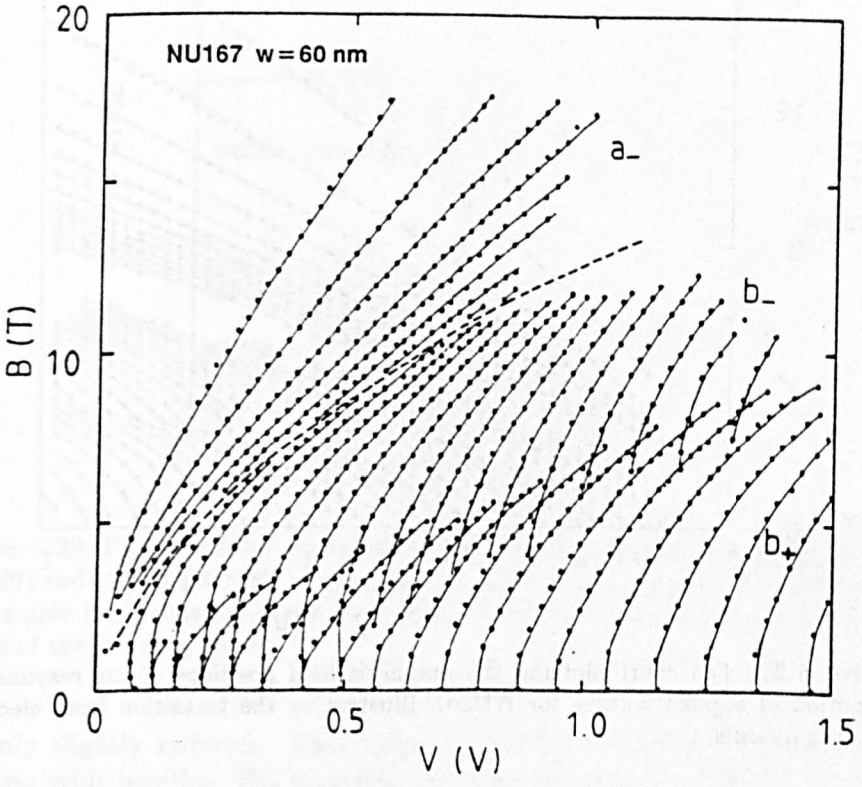

Figure 5.21: Fan chart plotting the magnetic field positions of the resonances (taken to be minima in the second derivative) as a function of applied voltage for sample *NU167* in $\boldsymbol{B} \perp \boldsymbol{J}$. Note that both sets of b oscillations (traversing states) extrapolate back to the positions of the zero-field box-quantised states.

Fan charts

Figures 5.21 and 5.22 are fan charts plotting the variation of the magnetic field positions of the resonances (taken to be minima in the second derivative) as a function of applied voltage for *NU167* and *NU207*. The evolution of the three sets of resonances can be clearly seen. At zero field, the resonance between a perfect 2DEG in the emitter and a quantum well state is a δ-function. At low fields, each 'box-quantised' state of the well splits into two features in the second derivative, one marking the start (b_+) and one the end ($b-$) of the resonance. As the field increases, the voltages at resonance rise and the resonances weaken. Note that the turn-off voltages b_+ increase more rapidly with magnetic field than do the threshold voltages showing the broadening noted for the narrow well sample.

At high fields, the cyclotron orbit can fit within the width of the well and the traversing orbits become skipping states bound at the emitter barrier interface, this transition is shown by the dashed line between the b_- and a_- states. Note that this is really a gradual transition due to the finite penetration

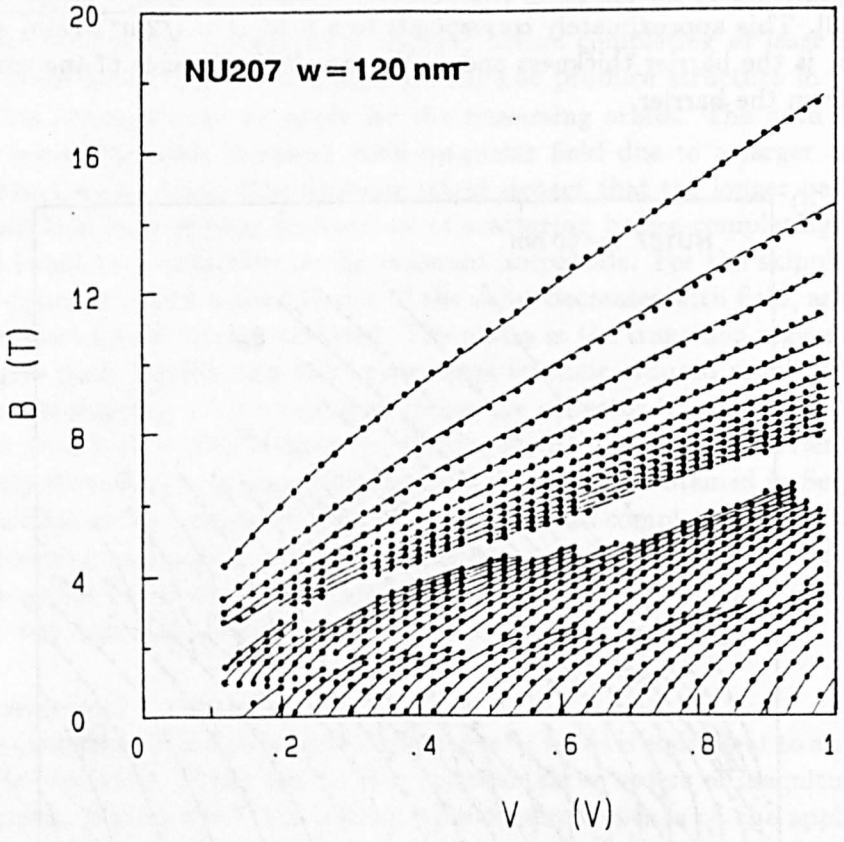

Figure 5.22: Fan chart plotting the magnetic field positions of the resonances as a function of applied voltage for *NU207*, illustrating the transition from electric to magnetic quantisation.

of the wavefunction into the barriers. We stress that there is a one-to-one correspondence between the 'box-quantised' states at zero magnetic field and the magnetically-quantised interface states at high fields.

Interfacial nature of the high-field states

The interfacial nature of the high-field orbits can be illustrated by comparing the magneto-oscillations for the three samples of different well widths at the same applied electric field. Because of the difference in the widths of the quantum well, this does not correspond to the same applied bias for each sample. The voltages at which the electric fields are equal can be ascertained from the magnetoquantum oscillations in $\boldsymbol{B} \parallel \boldsymbol{J}$ which directly measure the electron sheet density in the accumulation layer 2DEG. Figure 5.23 plots $I(B)$ traces for wells of width 600 Å (*NU167*), 1200 Å (*NU207*) and 1800 Å (*NU288*) in a magnetic field $\boldsymbol{B} \perp \boldsymbol{J}$ at an applied electric field of 3×10^6 Vm^{-1}. The positions of the resonances at high magnetic fields coincide almost exactly, proving that the states are only associated with the emitter barrier interface.

5.4.3 Temperature Dependence

Figure 5.24 shows d^2I/dV^2 for *NU167* in a magnetic field of 6 Tesla, $\boldsymbol{B} \perp \boldsymbol{J}$, for temperatures of 4 and 22 K. The low bias skipping orbit oscillations are completely quenched, whereas the amplitudes of the traversing orbit resonances

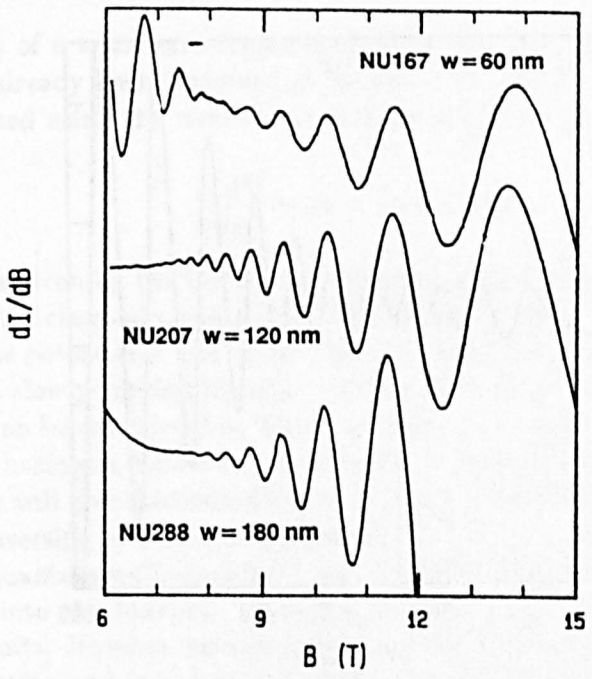

Figure 5.23: Plots of dI/dB for samples with wells of width 600 Å (*NU167*), 1200 Å (*NU207*) and 1800 Å (*NU288*) at an applied electric field of 3×10^6 Vm^{-1} and $\boldsymbol{B} \perp \boldsymbol{J}$. The sample independence of the high field resonances demonstrates the interfacial nature of the skipping states.

are only slightly reduced. This rather surprising result is explained by the differing orbit lengths. The skipping orbits have longer path lengths between collisions with the emitter barrier than the traversing states and therefore they are more sensitive to an increase in the scattering rate with temperature.

A related effect is shown in Figure 5.25 which plots d^2I/dV^2 against V at $B = 2$ Tesla for *NU167* at temperatures of 20 K and 90 K. At low bias the 20 K trace (dotted) is dominated by the b_- series since these have higher matrix elements. As the bias increases, the b_+ series emerges as a set of peaks at slightly lower bias than the b_- series. There is a region between 400 and 650 mV where both are seen, and then the b_- peaks die away. When the temperature is raised to 90 K (full curve), only the b_+ series of oscillations remains. This again can be related to the longer path length of the b_- orbit.

5.4.4 Modelling of the Resonance Positions

The fan charts in Figures 5.21 and 5.22 can be modelled fairly successfully using the methods outlined in Section 5.2. We use the approach described in reference [231] and consider the effects of the magnetic field on the energy levels in the well, ϵ_w, and the accumulation layer, ϵ_a, separately and then consider the transitions allowed by the selection rules. Note that throughout this section we take the origin to be at the right-hand interface of the emitter barrier, $\boldsymbol{B} = (0, 0, B)$, $\boldsymbol{E} = (-E, 0, 0)$ and $\boldsymbol{A} = (0, Bx, 0)$.

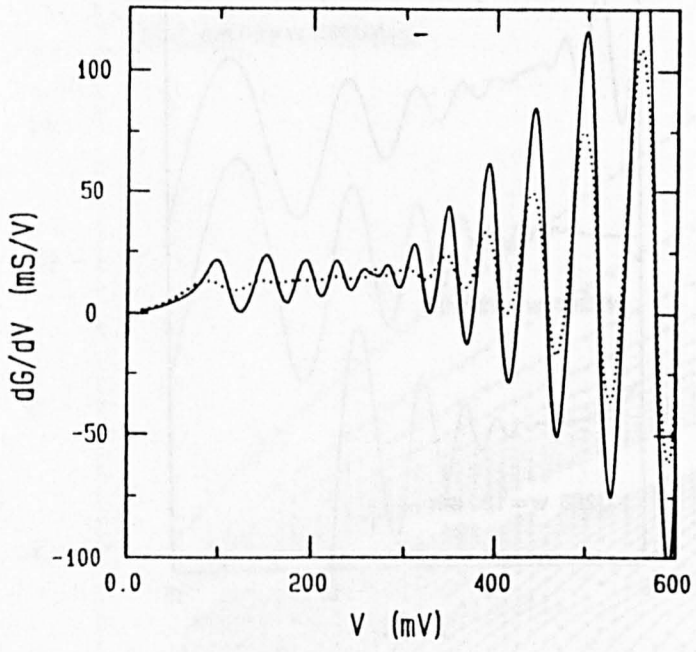

Figure 5.24: d^2I/dV^2 for *NU167* (600 Å well) in a magnetic field of 6 Tesla $\boldsymbol{B} \perp \boldsymbol{J}$ for temperatures of 4 K (full curve) and 22 K (dotted curve). This shows the greater sensitivity of the skipping states to increased temperature.

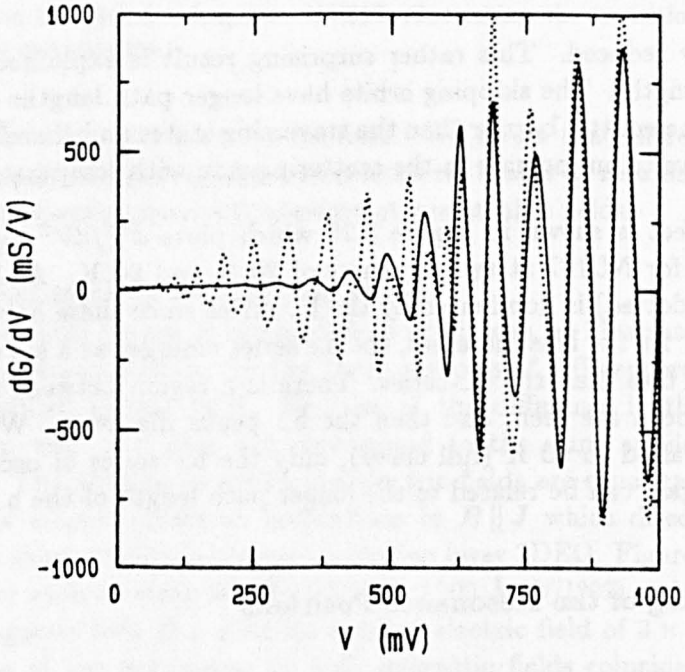

Figure 5.25: d^2I/dV^2 for *NU167* in a magnetic field of 2 Tesla, $\boldsymbol{B} \perp \boldsymbol{J}$, for temperatures of 20 K (dotted curve) and 90 K (full curve).

Energy levels in the quantum well

The effects of a transverse-magnetic field on the energy levels of a quantum well have already been discussed in Section 5.2, here we show how these may be calculated using the semi-classical WKB approximation. Allowed energies satisfy

$$\int_{x_0}^{x_1} p_x \, dx = (n + \varphi)\pi\hbar \tag{5.25}$$

where p_x is given by the local kinetic energy $p_x^2/2m^*$, φ is a phase factor and x_0, x_1 are the classical turning points of the motion. The value of φ depends on whether the potential at the turning point is 'hard' ($\rightarrow \infty$) in which case $\varphi = 1$ or 'soft' (a slowly-varying function), which gives $\varphi = 0.5$. The quantum well potential can be considered as 'hard', at least in the limit of high barriers, and the simple harmonic oscillator potential due to the magnetic vector potential is 'soft'. This will give discontinuities in the energy levels when the orbit changes from a traversing one to a skipping state. This is unphysical, and, in any case, the quantum well potential is not truly hard since the wavefunction can penetrate into the barriers. In reality there is a smooth transition between the two limits. However we will take $\varphi = 1$ for traversing states, $\varphi = 0.75$ for skipping states and $\varphi = 0.5$ for bulk Landau levels. The non-parabolicity of the band structure means that the effective mass is a function of energy, and therefore of position. This is neglected in the treatment given below, as are any effects due to spin-splitting.

The Schrödinger equation for the energy levels in the quantum well, equation 5.3, may be rewritten as

$$\frac{p_x^2}{2m^*} + U_x - eEX_0 + \frac{m^* v_d^2}{2} + \frac{m^*\omega_c^2(x - X_0)^2}{2} + \frac{\hbar^2 k_z^2}{2m^*} = \epsilon_n(k_y) + \frac{\hbar^2 k_z^2}{2m^*} \tag{5.26}$$

where $\epsilon_n(k_y) = \epsilon_w - \hbar^2 k_z^2/2m^*$ and U_x is the confining quantum well potential ($U_x = 0$ for $0 < x < w$ and $U_x = \infty$ otherwise). The WKB integral is

$$\int_{x_1}^{x_2} (2m^*(\epsilon_n(k_y) + eEX_0 - m^* v_d^2/2 - m^*\omega_c^2(x - X_0)^2/2))^{1/2} dx$$

$$= (n + \varphi)\hbar\pi \tag{5.27}$$

which may be evaluated to give

$$\epsilon_n(k_y) = \frac{(n + \varphi)\pi}{\alpha}\hbar\omega_c + \frac{m^* v_d^2}{2} - eEX_0 \tag{5.28}$$

where α is

$$\left[\sin^{-1} u + u(1 - u^2)^{1/2}\right]_{u_1}^{u_2} \tag{5.29}$$

and

$$\begin{aligned} u_i^2 &= \frac{m^*\omega_c^2/2}{\epsilon_n + eEX_0 - m^* v_d^2/2}(x_i - X_0)^2 \\ &= \beta^2(x_i - X_0)^2 \end{aligned} \tag{5.30}$$

Bulk levels: For bulk Landau levels $\varphi = 0.5$ and the classical turning points are at $x = X_0 \pm 1/\beta$ which corresponds to $u = \pm 1$, giving $\alpha = \pi$ and

$$\epsilon_n(k_y) = (n + 0.5)\hbar\omega_c + m^* v_d^2/2 - eEX_0$$

in agreement with equation 5.5. These energy levels are in region d of the $\epsilon - k_y$ diagram plotted in Figure 5.26.

Emitter skipping orbits: If $X_0 - 1/\beta < 0$ the orbit impinges on the emitter barrier and a skipping orbit is formed with $u_1 = -\beta X_0$ and $u_2 = 1$. Since $u_1 > -1$, $\alpha < \pi$ and hence the energy of this orbit is higher than the bulk level. These states correspond to region a in Figure 5.26.

Traversing states: For $X_0 - 1/\beta < 0$ and $X_0 + 1/\beta > w$ the turning points are determined by the barrier potential and the electron interacts with both barriers. $u_1 = -\beta X_0 > -1$, $u_2 = \beta(w - X_0) < 1$ so α is further reduced and the energy level is increased. These states are in region b.

Collector barrier skipping orbits: Finally the case where $X_0 - 1/\beta > 0$ but $X_0 + 1/\beta > w$ corresponds to states localised at the collector barrier which do not interact with the emitter barrier, these are shown in region c.

Accumulation layer

The energy of the bound state of the emitter 2DEG is given by the perturbation calculation of Section 5.2 as long as the electrostatic confinement energy is very much greater than the magnetic confinement.

$$\epsilon_a = \epsilon_0 + \frac{3m^*\omega_c^2}{2a^2} + eEb + \frac{\hbar^2(k_y - k_0)^2}{2m^*} + \frac{\hbar^2 k_z^2}{2m^*} \tag{5.31}$$

with $k_0 = eB(b + x_0)/\hbar$ where x_0 is the mean stand-off distance of the 2DEG from the emitter barrier interface ($x_0 = 3/a$). At low temperatures, only states with $|k_y - k_0| < k_F$ are occupied so the available states for tunnelling can be represented by the parabola centred at $k_y = k_0$ in Figure 5.26.

Resonance condition

The allowed transitions are given by the intersections of the dispersion curves in Figure 5.26 (Section 5.2). These correspond to the discrete set of k_y values satisfying $\epsilon_a(k_y, k_z) = \epsilon_w(k_y, k_z)$ and each intersection represents a finite number of electrons in the emitter which contribute to the current. Sweeping either voltage or magnetic field causes the parabola of emitter states to move relative to the the well dispersion curves (whose energies are also changing) and therefore the number of intersections — and hence the current — changes. This leads to two sets of oscillations, one associated with each extremity of the parabola, *i.e.* '+' oscillations for $k_y - k_0 = +k_F$ and '−' oscillations for $k_y - k_0 = -k_F$. When the extremities of the parabola move into different regions of the $\epsilon - k_y$ plane, the intersections correspond to resonances with different types of states (skipping or traversing) and have a distinct voltage and field dependence.

As an example, let us consider sweeping the magnetic field as in Figure 5.18. At low magnetic field, the parabola of occupied emitter states lies near the

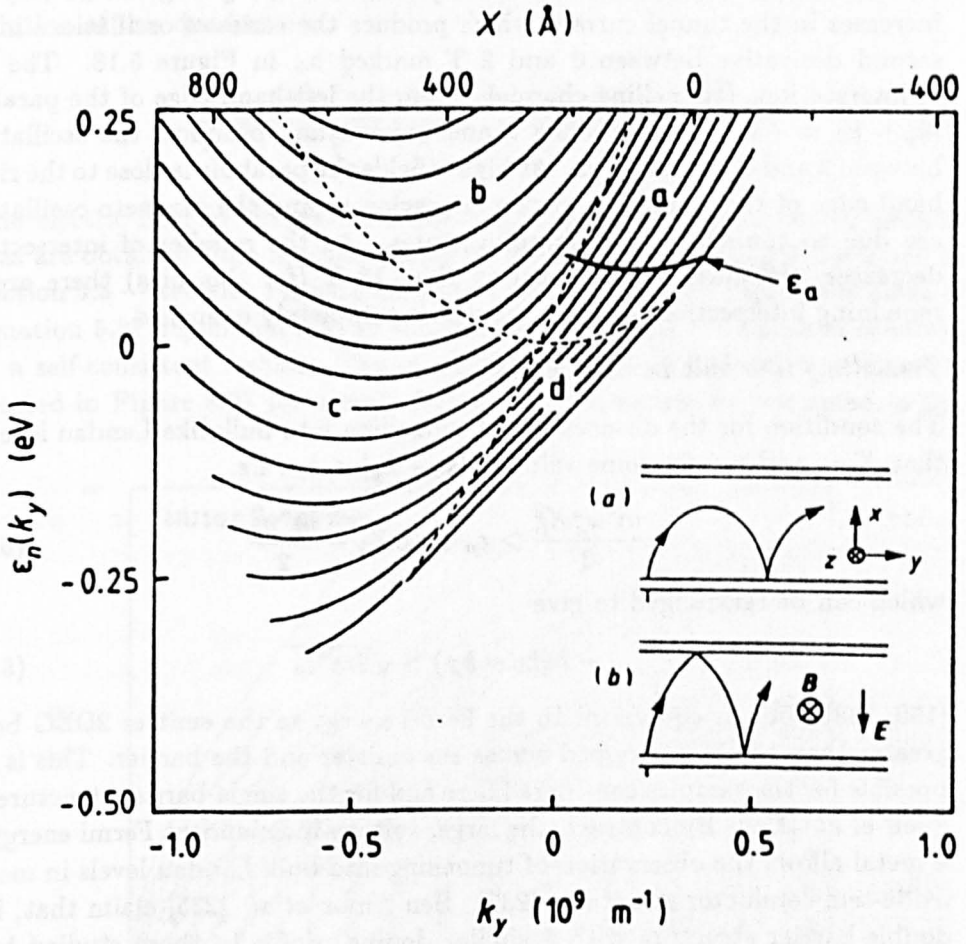

Figure 5.26: Plot of the energy eigenvalues $\epsilon_n(k_y)$ of the hybrid magnetoelectric states in the 600 Å well of device *NU167* for V=1 V and B=10 T $\boldsymbol{B} \perp \boldsymbol{J}$. The energies were calculated using the WKB approximation. The parabola marked ϵ_a corresponds to the energies of the occupied states in the emitter accumulation layer. Allowed tunnelling transitions correspond to the intersections of the two dispersion relations. The inset shows the semiclassical orbits corresponding to (a) skipping and (b) traversing states.

centre of region b and electrons tunnel into traversing states. Increasing the field causes the emitter parabola to shift towards higher energy and higher k_y (due to the increase in k_0) and the energies of states in the well rise because of the increased confining effect of the magnetic field. Intersections enter the parabola at the right-hand edge (at $k_y - k_0 = +k_F$) giving rise to step-like increases in the tunnel current which produce the series of oscillations in the second derivative between 0 and 2 T marked b_+ in Figure 5.18. The loss of intersections (tunnelling channels) from the left-hand edge of the parabola ($k_y - k_0 = -k_F$) decreases the tunnel current and produces the oscillations between 2 and 5 T marked b_-. At higher fields the parabola is close to the right-hand edge of the dispersion curves (in region a) and the magneto-oscillations are due to tunnelling into skipping states. As the number of intersections decreases, the current falls until at $B \sim 18$ T (for this bias) there are no remaining intersections and the current is completely quenched.

Tunnelling into bulk Landau levels

The condition for the observation of tunnelling into bulk-like Landau levels is that $X_0 - 1/\beta > 0$ for some value of $|k_0 - k_y| < k_F$, *i.e.*

$$\frac{m^*\omega_c^2 X_0^2}{2} > \epsilon_n + eEX_0 - \frac{m^* v_d^2}{2} \tag{5.32}$$

which can be rearranged to give

$$-\hbar(k_0 - k_F) > \sqrt{2m^*\epsilon_n} \tag{5.33}$$

[159, 238]. This is equivalent to the Fermi energy in the emitter 2DEG being greater than the bias dropped across the emitter and the barrier. This is impossible for the samples considered here and for the single-barrier structures of Snell *et al.* [159]. By contrast, the large, voltage-independent Fermi energy in a metal allows the observation of tunnelling into bulk Landau levels in metal-oxide-semiconductor structures [237]. Ben Amor *et al.* [235] claim that, in a double-barrier structure with a similar doping profile to those studied here, there is a transition to tunnelling into bulk-like orbits at the magnetic field where the last trough in d^2I/dB^2 occurs. This claim arises from a misunderstanding of the nature of the tunnelling process, and in particular a failure to consider the conservation conditions on ϵ and k_y. The last resonance in the second derivative corresponds to the loss of all possible tunnelling channels and the reason there is no more resonant structure in d^2I/dB^2 is that there is no more resonant current.

Fan charts

Quantitative predictions for the positions of extrema in the derivative of the tunnel current can be made by setting $\epsilon_a(k_0 \pm k_F)$ equal to $\epsilon_w(k_y = \pm k_F)$. Using equations 5.28 and 5.31 this gives

$$\epsilon_0 + \frac{3m^*\omega_c}{2a^2} + eEb + \frac{\hbar^2 k_F^2}{2m^*} = \frac{(n+\varphi^{\pm})\pi\hbar\omega_c}{\alpha^{\pm}} + \frac{m^* v_d^2}{2} - eEX_0^{\pm} \tag{5.34}$$

where the superscripts refer to $k_y = \pm k_F$. The left-hand side is simply equal to the total voltage drop across the emitter and the barrier, $= eE(b + x_0)$ and

$$X_0^{\pm} = \frac{m^* E}{eB^2} - \frac{\hbar k_0}{eB} \mp \frac{\hbar k_F}{eB} \tag{5.35}$$

Remembering that $k_0 = eB(b + x_0)/\hbar$ and $v_d = E/B$ we can rearrange equation 5.34 to give

$$E^2 = \frac{2(n+\varphi^{\pm})\pi\hbar eB^3}{\alpha^{\pm}m^{*2}} \pm \frac{2\hbar k_F B}{m^*}E \tag{5.36}$$

Which agrees with the simple result derived in equation 5.24 for $k_F = 0$. The solution of this quadratic is

$$\frac{E}{B} = \frac{\hbar k_F}{m^*}\left(\pm 1 + \left[1 + \frac{\pi(n+\varphi^{\pm})}{\alpha^{\pm}}\frac{\hbar\omega_c}{\epsilon_F}\right]^{\frac{1}{2}}\right) \tag{5.37}$$

The electric field in the well and the Fermi energy as a function of applied bias are obtained from magnetotransport measurements in $\boldsymbol{B} \parallel \boldsymbol{J}$ discussed in Section 3.3 — see also Figure 5.15. Since both the left and right-hand sides of equation 5.37 depend on bias as well as magnetic field, the equation is solved in a self-consistent fashion. The resulting fan chart of resonance positions is plotted in Figure 5.27 for sample *NU167*. This should be compared to the

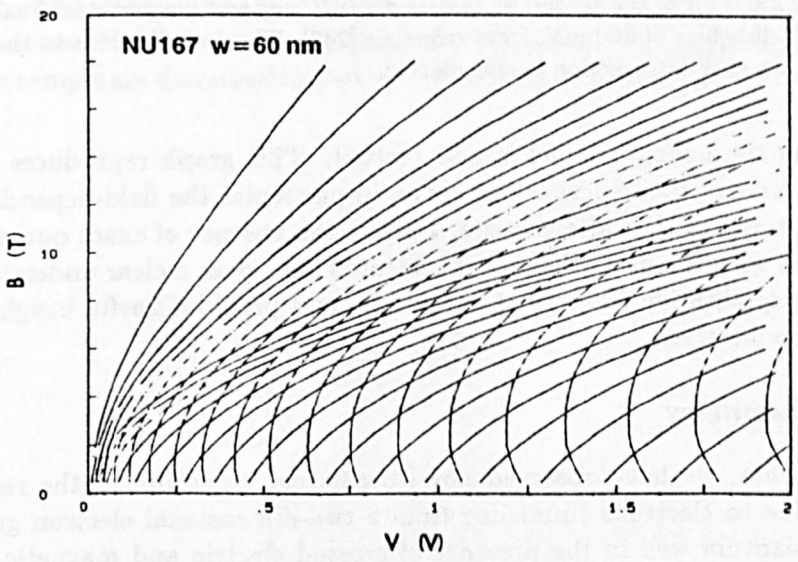

Figure 5.27: Fan chart showing the calculated resonance positions (from equation 5.37) in $B - V$ space for sample *NU167*.

experimental data in Figure 5.21. There is good qualitative agreement in that the broadening of the resonances is clearly seen, the resonant features move to higher bias with increasing field and the transition from traversing to skipping states is obtained. However detailed agreement is lacking in both the positions of the zero magnetic field resonances and in the slopes of the lines. This is primarily due to the finite height of the potential barriers, a possible buildup of space charge in the quantum well and the neglect of non-parabolicity in the band structure, which is important because the electrons reach kinetic energies of several hundred meV when traversing the well — see Section 3.6.

Figure 5.28 shows the second derivative of the tunnel current for *NU207* at a bias of 600 mV, as calculated from the transfer Hamiltonian method by T. M. Fromhold [239, 242]. The contribution to the tunnel current from each

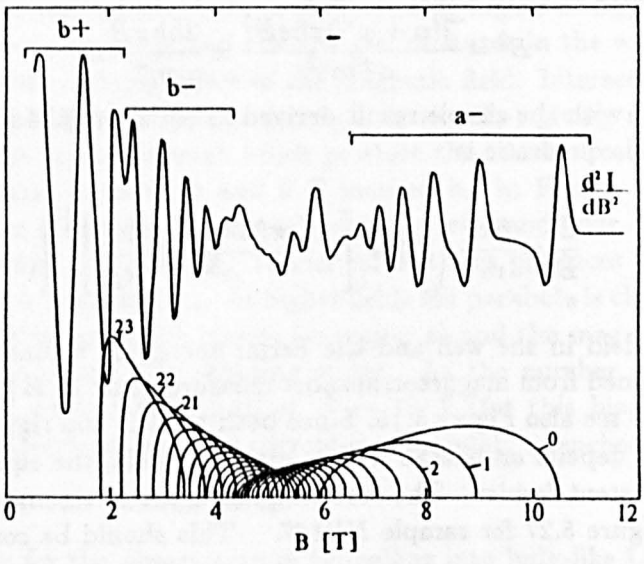

Figure 5.28: Plot of the second derivative d^2I/dB^2 against magnetic field calculated for *NU207* at a bias of 600 mV, from reference [242]. The contribution to the tunnel current from each intersection is also plotted.

individual tunnelling channel is also plotted. This graph reproduces all the main features of the experimental curve, in particular the field-dependence of the amplitudes of the various series. Despite the absence of exact quantitative agreement with the data, the model presented here gives a clear understanding of all the qualitative features of the results and provides useful insights into the physics involved.

5.4.5 Summary

In conclusion, we have observed novel oscillatory structure in the resonant current due to electrons tunnelling from a two-dimensional electron gas into a wide quantum well in the presence of crossed electric and magnetic fields. This is attributed to the interfacial Landau level structure in the quantum well. At high magnetic fields the tunnel current is completely quenched due to the action of the Lorentz force. The resonances illustrate the development of hybrid magnetoelectric quantisation. The classical skipping trajectory which just grazes the collector barrier has a path length of $\sim$ 4000 Å between intersections with the emitter barrier. The observation of magneto-oscillations due to electrons tunnelling into this orbit requires that a significant number of electrons have a ballistic path length of at least this length. A model based on the transfer Hamiltonian approach together with the WKB approximation provides a clear explanation of the experimental data.

5.5 Hot Electron Magneto-Spectroscopy: A Probe Of Conduction Band Anisotropy

Having established in the previous section that when a magnetic field is applied in the plane of the quantum well, electrons tunnel into hybrid magnetoelectric states which interact with one or both barriers, we demonstrate how these resonances can be used to provide a novel method of investigating the high-energy band structure of the quantum well material [240, 241]. By rotating the magnetic field in the plane of the quantum well, we observe a clear angular dependence of the magneto-oscillations due to the anisotropy of the Γ-conduction band at high energies. A model based on the WKB approximation similar to that outlined in Section 5.4.4 is used to show that the observed angular variation gives a reasonable value of anisotropy compared to theoretical models of the band structure [263].

5.5.1 Experimental Results

The sample considered in this section is *NU207* consisting of a 1200 Åwide well between two 56 Å barriers — see Table 2.1. The current-voltage characteristics of this sample are described in Section 3.6. Figure 5.29 schematically illustrates

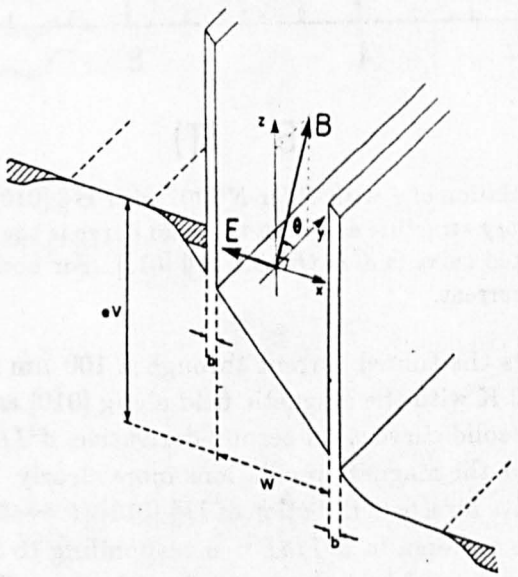

Figure 5.29: Schematic diagram showing the field configuration for measurement of the anisotropy in the magneto-oscillations.

the configuration of the electric and magnetic fields relative to the quantum well for the measurement of the anisotropic magneto-oscillations in transverse field.

The sample was grown on a ⟨100⟩-oriented GaAs substrate. For the measurements reported in this section, we take the electric field to be in the [$\bar{1}$00]-direction and the magnetic field direction is rotated between [010] and [001] in the (100) plane — so the magnetic field is always perpendicular to the growth direction and to the direction of current flow *i.e.* $\boldsymbol{B} \perp \boldsymbol{J}$. The measurements

were taken by mounting the sample on a rotatable table whose orientation is controlled by means of a micrometer (see Section 2.1). As will become apparent in the following section, it is important that the sample should be mounted with the growth direction perpendicular to the magnetic field, this was achieved to within $\sim 5°$. The accuracy in measuring the angle is probably no better than $\pm 2°$. All angles were set by rotating the table in the same direction to avoid backlash. The angle of the field θ is taken from [010] *i.e.* $\boldsymbol{B} \parallel [010] \Rightarrow \theta = 0°$, $\boldsymbol{B} \parallel [011] \Rightarrow \theta = 45°$ and $\boldsymbol{B} \parallel [001] \Rightarrow \theta = 90°$.

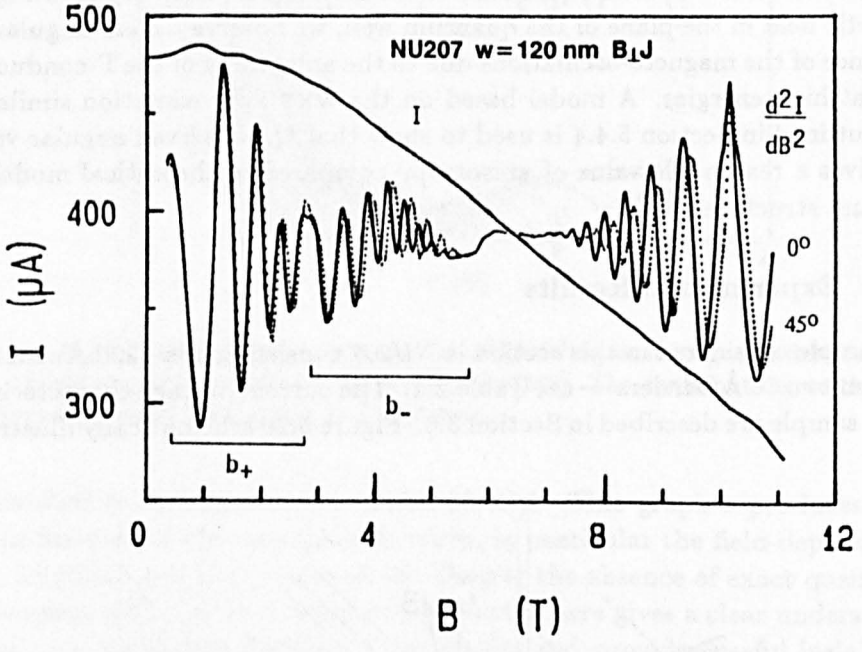

Figure 5.30: The variation of I with B for *NU207* with $\boldsymbol{B} \parallel [010]$, $V = 800$ mV and $T = 4$ K. The oscillatory structure shown in the solid curve is the corresponding plot of d^2I/dB^2. The dotted curve is d^2I/dB^2 for $\boldsymbol{B} \parallel [011]$. For both orientations $\boldsymbol{B}$ is perpendicular to the current.

Figure 5.30 shows the tunnel current through a 100 μm diameter mesa of sample *NU207* at 4.2 K with the magnetic field along [010] and a fixed applied bias of 800 mV. The solid curve is the second derivative, d^2I/dB^2, for this field direction which shows the magneto-oscillations more clearly. The dotted curve is the second derivative for a field direction of $\boldsymbol{B} \parallel [011]$ ($\theta = 45°$). The magnetic field positions of the extrema in d^2I/dB^2 corresponding to all three series of oscillations move to higher field relative to the $\theta = 0°$ curve. This is particularly noticeable in the region between 4 and 9 Tesla where the resonances change over from traversing to skipping states, whereas at low fields there is very little change in the resonance positions. Note that the shift, ΔB, in the position of a trough in d^2I/dB^2 is not a monotonically increasing function of magnetic field. An expanded plot of the first derivative in the high-field region, $B > 6$ T, is shown in Figure 5.31 with a constant applied bias of 600 mV and various values of θ. For angles greater than 45°, the resonances move back towards their $\theta = 0°$ positions. This plot highlights the decrease in ΔB at the highest fields.

Figure 5.32, plots magnetic field position at a trough in d^2I/dB^2, against θ for an applied bias of 900 mV. Again note that both low and high-field traces show less anisotropy than those near the transition between skipping

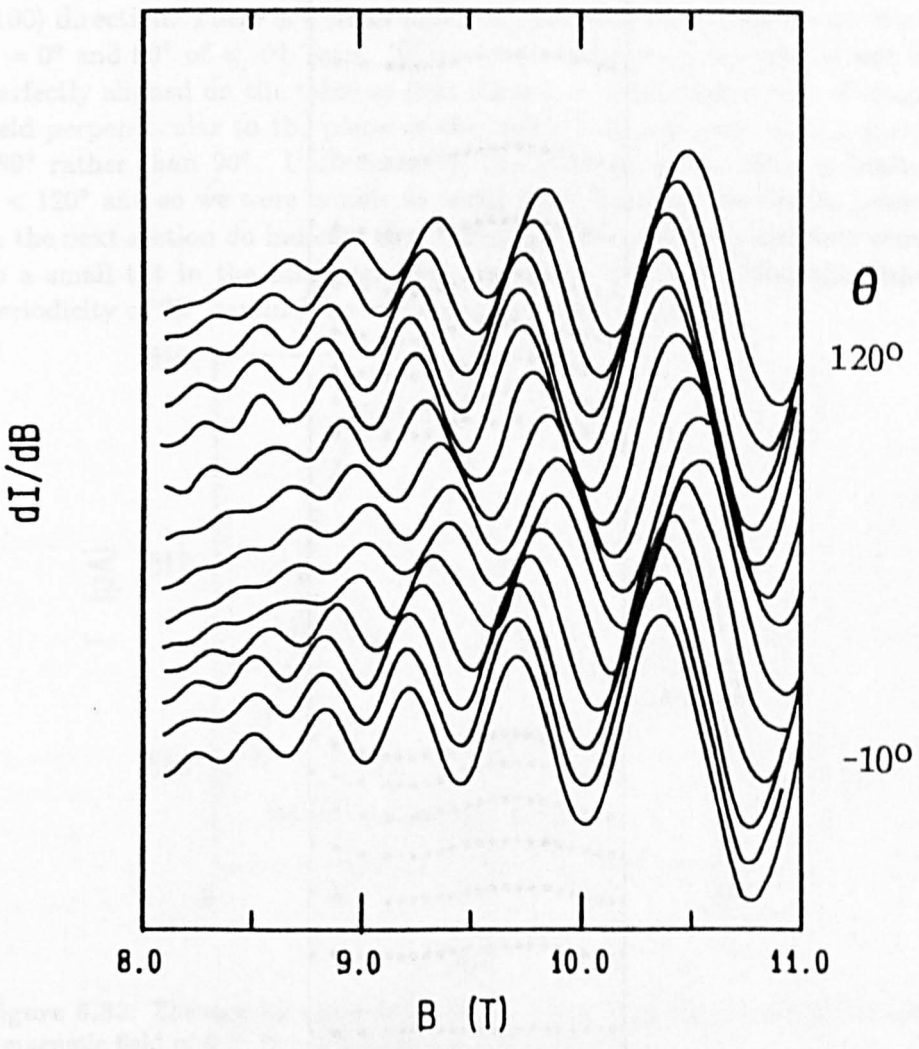

Figure 5.31: Plot of the first derivative dI/dB at angles θ at intervals of 10° between $-10°$ and 120° for *NU207* at an applied bias of 600 mV.

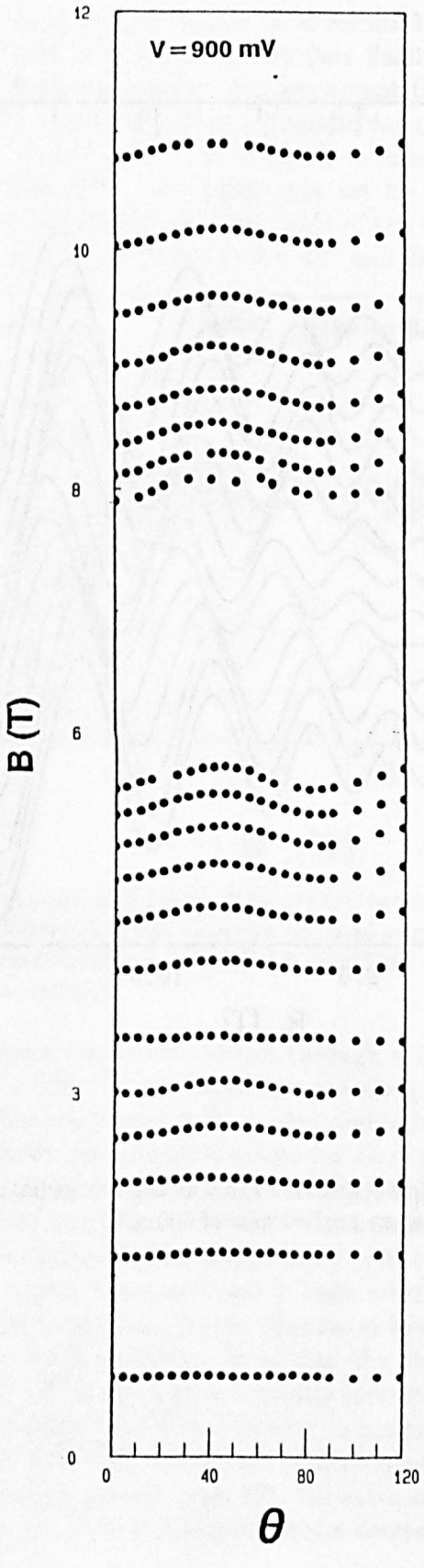

Figure 5.32: The magnetic field positions of minima in d^2I/dB^2 plotted against θ for an applied bias of 900 mV, showing the periodic variation in the resonance positions.

and traversing states. This figure clearly demonstrates that the resonance position is a periodic function of angle, with $B \parallel [001]$ being equivalent to $B \parallel [010]$. This corresponds to the cubic symmetry of the crystal about a $\langle 100 \rangle$ direction. There is a small difference between the resonance positions at $\theta = 0°$ and 90° of $< .02$ Tesla. This is probably due to the crystal not being perfectly aligned on the table so that there is a small component of magnetic field perpendicular to the plane of the well which will vary with a period of 180° rather than 90°. Unfortunately, the rotation of the table is limited to $\theta < 120°$ and so we were unable to verify this. However the results presented in the next section do indicate that the magneto-oscillations are very sensitive to a small tilt in the magnetic filed direction. We stress that the observed periodicity of 90° cannnot be explained by misalignment.

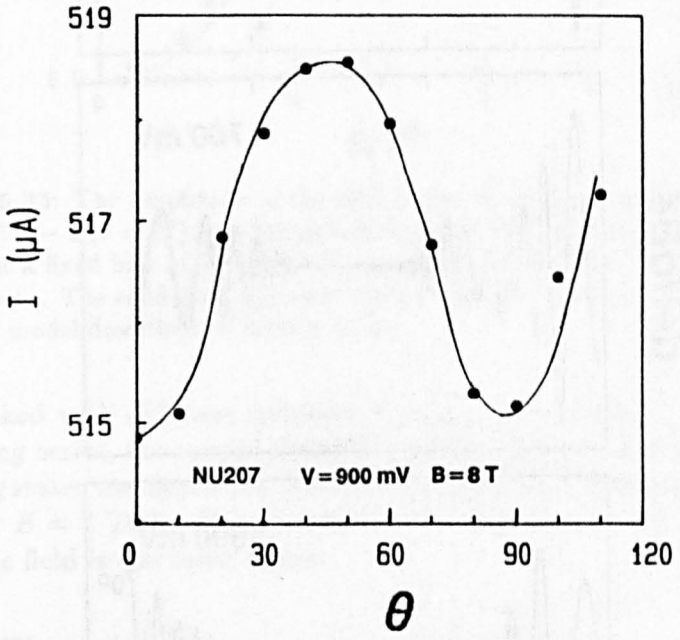

Figure 5.33: The angular dependence of the tunnel current at a bias of 900 mV and a magnetic field of 8 T $B \perp J$ for sample *NU207* at 4 K.

The tunnel current itself also shows an angular dependence which is given in Figure 5.33 which shows the variation in I with θ for a constant applied voltage (900 mV) and a constant magnetic field (8 Tesla). The cubic symmetry is again seen. The variation in the current is only about 1% at this bias. If instead we measure near the point where the current is quenched we obtain a modulation of I by a factor of 10.

Figure 5.34 shows the second derivative in high magnetic fields for $\theta = 0°$ and 45° at biases of 400, 700 and 1000 mV. At 400 mV there is very little shift in the resonance positions with angle but there is clearly much more anisotropy at high biases where the electrons are reaching much higher kinetic energies. Since the resonances shift far more rapidly with field than they do with angle (a typical resonance shifts by $\sim$ 500mV between $B = 0$ and $B = 12$, but only 50 mV from $\theta = 0°$ to 45°) it is difficult to unambiguously compare the magnitude of the shift for different voltages.

Figure 5.35 plots the maximum shift in the resonance position Δ against magnetic field for a fixed applied bias of 900 mV. The three kinds of resonances

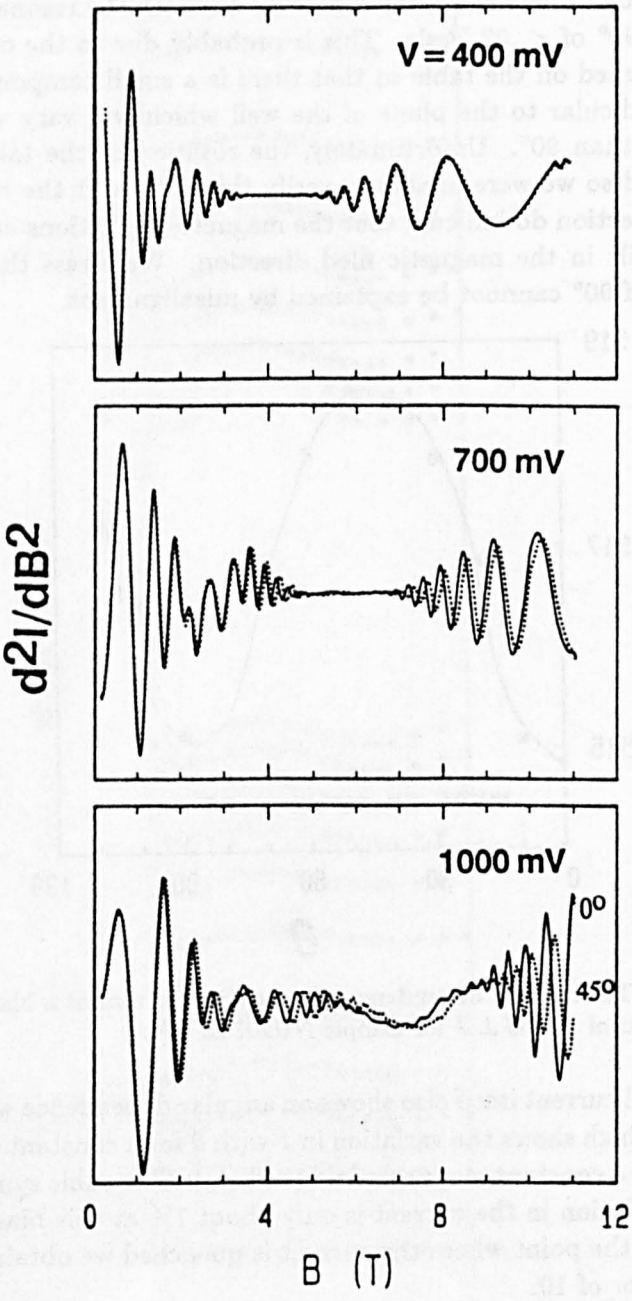

Figure 5.34: d^2I/dB^2 versus B for $\theta = 0°$ (full lines) and $\theta = 45°$ (dotted lines) for *NU207* at biases of 400 mV, 700 mV and 1000 mV.

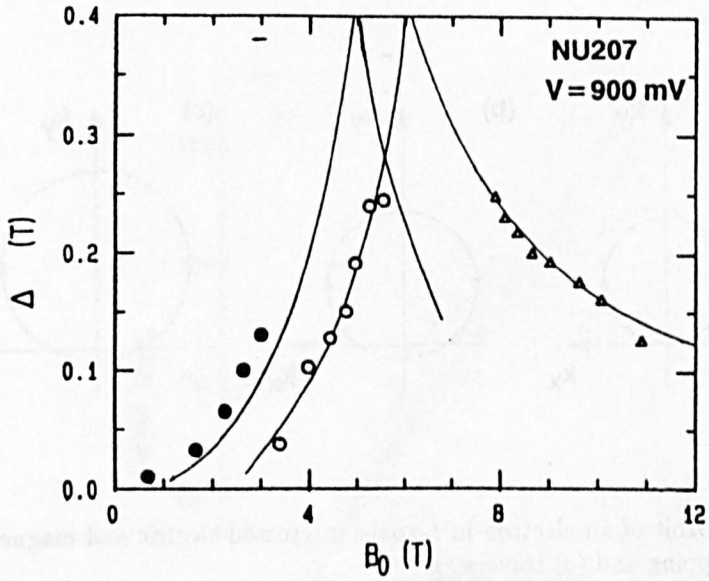

Figure 5.35: The amplitude of the shift in the resonance position with angle, $\Delta = B(\theta = 45°) - B(\theta = 0°)$, plotted as a function of applied magnetic field, $\boldsymbol{B} \perp \boldsymbol{J}$, for *NU207* at a fixed bias of 900 mV. The resonances are marked thus: • = b_+, ○ = b_- and △ = a_-. The solid lines represent the calculated variation of amplitude obtained from the model described in Section 5.5.3.

are marked with different symbols: • = b_+, ○ = b_- and △ = a_-. For both traversing series, the amplitude of the anisotropy increases with field but for skipping states the amplitude decreases at high field. There is a peak of $\Delta \sim 0.2$ Tesla at $B = 7$ Tesla. The variation of the anisotropy with bias and applied magnetic field is discussed below.

5.5.2 Discussion

For a parabolic, isotropic band structure, the cyclotron orbit in k-space in crossed electric and magnetic fields, which is cycloidal in real space, forms a circle in the plane perpendicular to $\boldsymbol{B}$. This can be seen by replacing $\dot{\boldsymbol{p}}$ in equation 5.1 by $\hbar\dot{\boldsymbol{k}}$ and solving the equation of motion. The radius of the orbit is $m^*E/\hbar B$ and the circle is offset from the origin by $m^*E/\hbar B$ along the k_y axis. This offset corresponds to the uniform drift velocity of $v_d = E/B$ in the y-direction. The effect of confining barriers on this orbit is simply to reverse k_x at each collision with a barrier and so only part of the cyclotron circle is traced out, this is schematically illustrated in Figure 5.36. For a material with an isotropic band structure, rotating the magnetic field would merely change the plane of the orbit without changing its shape, *i.e.* a 360° rotation would trace out a perfect toroid. However, if there is any anisotropy the shape of the orbit depends on the plane via the influence of m^*. This will also affect the quantisation of the orbit, which is most simply brought in using the WKB condition $\int k_x\, dx = (n + \varphi)\pi$, and hence the positions of the resonances.

Although the Γ-conduction band minimum of GaAs is usually considered to be isotropic — as it has been to date in this thesis — this is only valid at low energies, as can be seen from Figure 5.37. At very high energies there

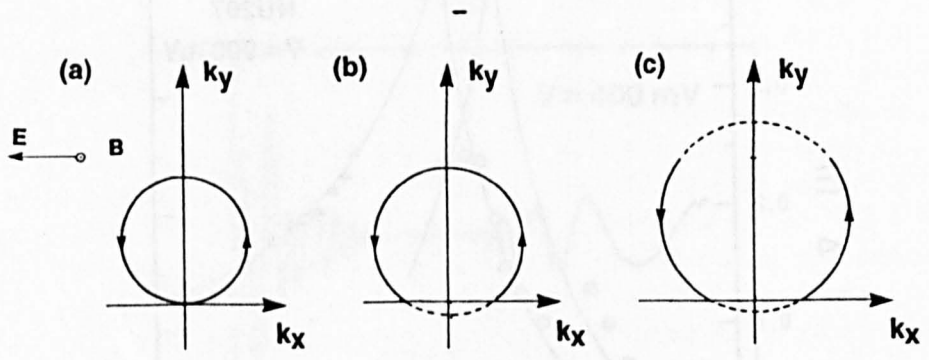

Figure 5.36: Orbit of an electron in k-space in crossed electric and magnetic fields (a) bulk (b) skipping and (c) traversing.

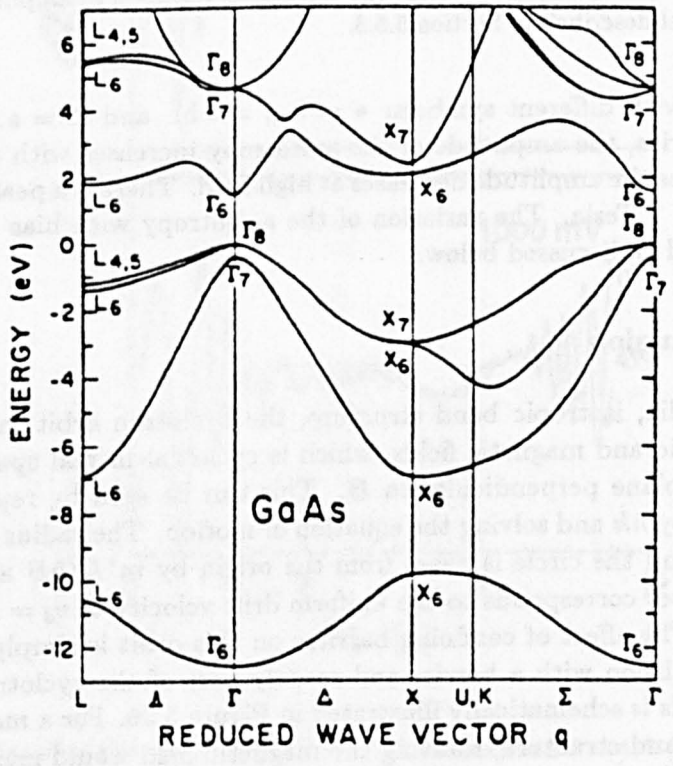

Figure 5.37: Conduction band of GaAs showing the anisotropy, taken from Chelikowsky and Cohen [264].

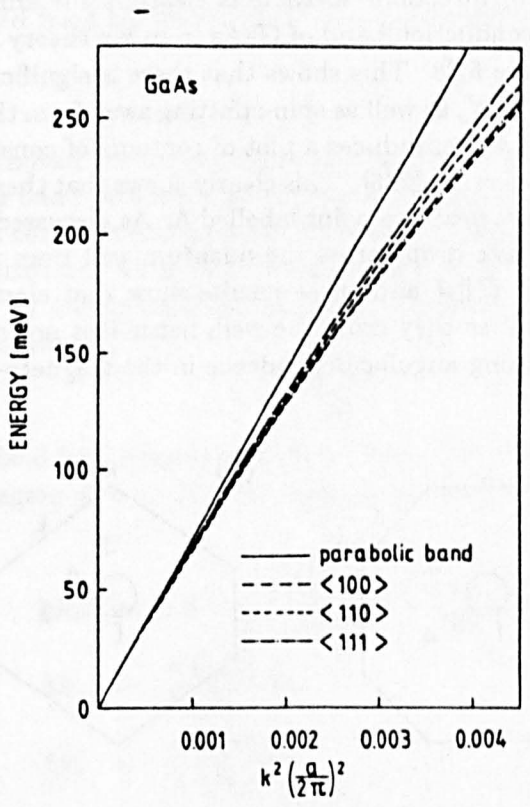

Figure 5.38: Conduction band of GaAs in the vicinity of the Γ minimum as calculated by Rössler [263] from $k.p$ theory.

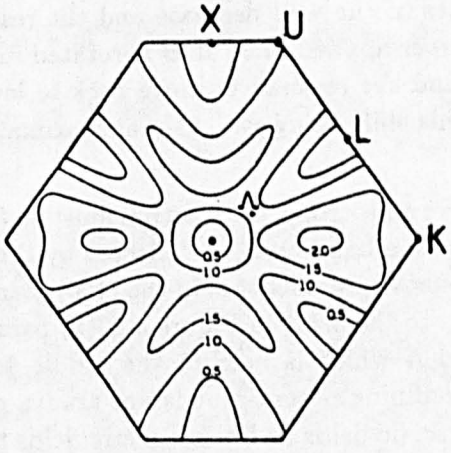

Figure 5.39: A plot of contours of constant energy in the (011) plane, taken from Hess [265].

is a maximum in the band structure at $\sim$ 1 eV in the $\langle 111 \rangle$ directions and $\sim$ 2 eV in the $\langle 100 \rangle$ directions so there is clearly some anisotropy. A recent calculation of the conduction band of GaAs from $k.p$ theory by Rössler [263] is reproduced in Figure 5.38. This shows that there is significant anisotropy for energies above 200 meV, as well as spin-splitting away from the main symmetry directions. Figure 5.39 reproduces a plot of contours of constant energy in the $\{011\}$ plane from reference [265]. This clearly shows that there is a saddle point in the band structure near the point labelled Λ. As discussed in Section 3.6 we can obtain the voltage drop across the quantum well from magnetotransport measurements with $\boldsymbol{B} \parallel \boldsymbol{J}$ and these results show that electrons gain kinetic energy of up to 1 eV as they cross the well, hence it is not surprising that we are able to see a strong angular dependence in the magneto-oscillations.

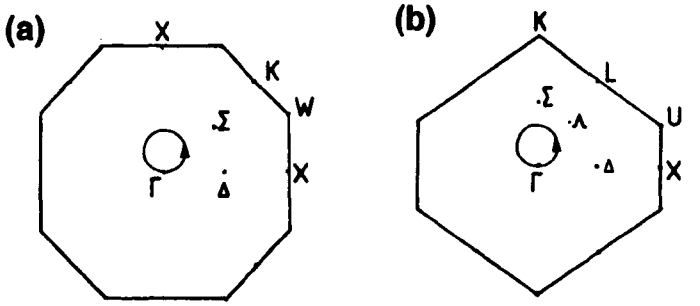

Figure 5.40: Electron orbit in k-space for $\boldsymbol{E} \parallel [\bar{1}00]$ and (a) $\boldsymbol{B} \parallel [010]$ ($\theta = 0°$) and (b) $\boldsymbol{B} \parallel [011]$ ($\theta = 45°$).

Figure 5.40 shows schematically an electron orbit (a) in the (010) plane and (b) in the (011) plane. The energy level depends on the effective mass 'averaged' over the orbit. This is greater for the (011) plane and so as the magnetic field direction is rotated from $\boldsymbol{B} \parallel [010]$ to $\boldsymbol{B} \parallel [011]$ ($\theta = 45°$) the energies of the states in the well decrease and the resonances shift to higher magnetic field, or lower applied bias. If $\boldsymbol{B}$ is rotated further, the orbit returns to an $\{001\}$ plane and the resonances move back to lower fields. A model for the magnitude of this shift using the WKB approximation is presented in the next section.

In order to observe anisotropy, the electron must be (a) accelerated to a high energy in the conduction band and (b) deflected by the magnetic field so that it has a large component of momentum in the (100) plane *i.e.* perpendicular to $\boldsymbol{E}$. This corresponds to the orbit in Figure 5.40(b) passing as close as possible to the point marked Λ which is near to the saddle point in the conduction band. Due to the confining potential it is not always possible to achieve this since at very high electric fields or low magnetic fields the electron is reflected at the interface before it has obtained significant momentum in the (100) plane whilst at very high magnetic fields or low electric fields the electron is localised near the emitter barrier in a skipping state and does not gain much kinetic energy from the electric field. This qualitatively explains the trends apparent in Figure 5.35. For the traversing orbits of both series (b_+ and b_-), the energy gained from the electric field is constant but increasing B increases the deflection of the orbit and so the anisotropy increases with field. For the skip-

ping orbits the electron path is unaffected by the collector barrier but as the magnetic field rises, the orbit is more tightly bound to the emitter barrier so the energy gained from the electric field drops and there is less anisotropy.

5.5.3 Model

The relations derived in Section 5.4.4 are no longer appropriate since they assume that the band structure is isotropic and parabolic and hence that the effective mass is constant and may be taken outside the WKB integral. In order to model the anisotropy we must include the variation of m^* around the orbit. We can do this by noting that the electron velocity in equation 5.1 is related to the band structure by

$$v = \frac{1}{\hbar}\frac{\partial \epsilon(k)}{\partial k} \tag{5.38}$$

The magnetic field has components $B_x = B\sin\theta$ and $B_y = B\cos\theta$ and the electric field is again $E = (-E, 0, 0)$. Therefore the equation of motion can be written as

$$\begin{aligned}
\hbar\dot{k}_x &= eE - \frac{e}{\hbar}\left(\frac{\partial \epsilon(k)}{\partial k_x}B_z - \frac{\partial \epsilon(k)}{\partial k_z}B_y\right) \\
\hbar\dot{k}_y &= \frac{e}{\hbar}\frac{\partial \epsilon(k)}{\partial k_x}B_z \\
\hbar\dot{k}_z &= \frac{e}{\hbar}\frac{\partial \epsilon(k)}{\partial k_x}B_y
\end{aligned} \tag{5.39}$$

This equation not only gives the electron orbit in k-space but allows us to evaluate the WKB integral along this path. The values of $\partial\epsilon/\partial k_i$ at each point can be obtained from the analytical approximation to the band structure given by Rössler [263]

$$\begin{aligned}
\epsilon &= \frac{\hbar k^2}{2m_0^*} + (\alpha_0 + \alpha_1 k)k^4 + (\beta_0 + \beta_1 k)(k_y^2k_z^2 + k_z^2k_x^2 + k_x^2k_y^2) \\
&\quad \pm(\gamma_0 + \gamma_1 k)[k^2(k_y^2k_z^2 + k_z^2k_x^2 + k_x^2k_y^2) - 9k_x^2k_y^2k_z^2]^{1/2}
\end{aligned} \tag{5.40}$$

where $m^* = .0665m_e$, $\alpha_0 = -2132 \times 10^{-32}$ cm^4, $\alpha_1 = 9030 \times 10^{-40}$ cm^5, $\beta_0 = -2493 \times 10^{-32}$ cm^4, $\beta_1 = 12594 \times 10^{-40}$ cm^5, $\gamma_0 = 30 \times 10^{-24}$ cm^3 and $\gamma_1 = -154 \times 10^{-32}$ cm^4.

We neglect the effects of the spin-splitting even though this is as significant as the anisotropy itself — see Figure 5.38. We also make the assumption that the application of a magnetic field does not significantly affect the band structure, which may also be unjustified. Starting from the initial condition $k(t = 0)$ given by the voltage drop across the emitter region and the deflection due to the Lorentz force as the electron traverses the barrier, we can calculate $k(t + \delta t) = k(t) + \dot{k}\delta t$ and $r(t + \delta t) = r(t) + v(t)\delta t$ and hence obtain $\int k_x\,dx$ around the orbit. The upper limit of this integration is $x = w$ or $k_x = 0$ depending on whether the orbit is traversing or skipping. We then vary B until the integral has a value of $(n + \varphi)\hbar\pi$. This must be repeated for each value of n and for $\theta = 0°$ and $45°$ to obtain the shift in the resonance position Δ as a function of magnetic field. Having achieved this, the procedure must then be repeated to find the value for β in best agreement with the experimental

results. This somewhat cumbersome procedure is improved by including higher order terms in the algorithm for $k(t)$ which allows a longer time interval — although too great an interval produces uncertainty in the turning point.

The results of these calculations for a fixed bias of 900 mV are shown in Figure 5.35 together with the experimental results. The fit is reasonably good, particularly in reproducing the peak in Δ at around 7 Tesla where the changeover from skipping to traversing orbits occurs. The peak for the + orbits is displaced to lower magnetic field since these orbits have a greater momentum in the (100) plane, for a given bias and magnetic field. There is some disagreement, particularly at the low and high-field regions; this could partly be explained by the considerable uncertainty in the experimentally-determined peak shift. The value of β_0 which gives the best fit to the data is 3×10^{-32} cm^4 which is about 20% larger than that given by Rössler. This is reasonable agreement in view of the fact that we are very near to the limits of the $k.p$ expansion he uses (approximately 500 mV) and we have neglected the spin-splitting terms in equation 5.40. This method gives a potentially useful method of investigating the high-energy form of the band structure which is not well-characterised experimentally, however further work is needed to improve the quality of the theoretical modelling.

5.5.4 Conclusion

The anisotropy of the conduction band of GaAs has recently been investigated by means of cyclotron resonance [266]. In such experiments, the electron describes an orbit of constant energy so that the angular dependence of the cyclotron resonance peak position gives a direct measure of the anisotropy at the cyclotron energy. In the experiments reported here the energy of the skipping (or traversing) orbit varies over a wide range as the electron gains energy from the voltage dropped across the quantum well. Therefore the angular dependence of each resonance corresponds to a (weighted) average of the anisotropy over the energy range of the orbit. Hence this is not such a direct method of obtaining the band structure parameters but the maximum energies reached ($\sim$ 1 eV) are far in excess of those attained in cyclotron resonance.

It is interesting to consider what would happen if the electron orbit could be made to pass through the minimum in $\epsilon(k)$ near the point marked Λ — see Figure 5.37. This would presumably lead to the formation of an open orbit which would have interesting consequences for the resistance of the device. However, for a well-width of 1200 Å this requires an electric field of at least 1.4×10^7 V/m at a magnetic field of 5 Tesla. This value of electric field is only reached at $\sim$ 2 V where the resonances are very weak and it is not possible to observe this effect in this sample. An alternative would be to grow the sample in a different orientation of substrate, for example a {111}-plane, however this presents problems in terms of the growth process.

5.6 Resonant Tunnelling in a Tilted Magnetic Field

So far we have only considered the configurations with the magnetic field parallel or perpendicular to the electric field since these are the simplest to analyse. A magnetic field parallel to the tunnel current, $\boldsymbol{B} \parallel \boldsymbol{J}$, quantises the energy of the electron motion in the plane of the well leading to the formation of regularly-spaced Landau levels. The passage of these levels through the Fermi energy of either the emitter or the well leads to periodic magneto-oscillations in the tunnel current or differential capacitance of the device, as described in Section 3.3. A magnetic field in this direction has little effect on the form of the current-voltage characteristics. By contrast, a transverse magnetic field, $\boldsymbol{B} \perp \boldsymbol{J}$, rapidly broadens the resonance and reduces the current (Section 5.3) and, in wide wells, tunnelling into interfacial Landau levels is observed (Section 5.4).

This section briefly examines the intermediate case when the magnetic field is at an angle ϕ to the electric field. For samples with narrow quantum wells we find that the effects can be described by considering the effects of the parallel and perpendicular components of field separately. There is a series of equally-spaced peaks in the current-voltage characteristics corresponding to transitions from the emitter 2DEG into the well with a change in Landau level index. These are allowed in tilted field but not in parallel field due to the change in the selection rules caused by the magnetic vector potential. In wide quantum well samples we observe a rapid oscillation in the tunnel current with a period much less than those seen in either parallel or perpendicular field alone. This again is attributed to the relaxation of the conservation conditions.

A two-dimensional electron gas in a tilted magnetic field was first considered by Stern and Howard [119] who treated the transverse component as a perturbation, see Section 5.2. Fang and Stiles found that the periodicity of the Shubnikov-de Haas oscillations in a silicon MOSFET was solely determined by the component of magnetic field perpendicular to the surface of the 2DEG [137]. There have been several experimental investigations in this configuration, initially performed on electrons at the surface of liquid helium [267]. It has proved particularly useful in cyclotron resonance because transitions which do not conserve Landau level index, and which are not normally allowed, are observed. This has been termed 'combined intersubband-cyclotron resonance' and was first investigated by Beinvogl and Koch [268], see also Maan *et al.* [269] and Craseman *et al.* [270]. The theory of this effect has been studied by Ando [271] and Bhattacharya [272]. Here we present the first study of resonant tunnelling in a tilted field.

The theoretical treatment of a tilted field is complicated because the Hamiltonian is no longer separable and in most cases is not easily solved, an exception being a parabolic quantum well which has been considered by Maan [273]. We take the angle between the tunnel direction, x, and the magnetic field to be ϕ and put $\boldsymbol{B} = (B_{\parallel}, 0, B_{\perp}) = (B\cos\phi, 0, B\sin\phi)$ and $\boldsymbol{A} = (0, xB_{\perp} - zB_{\parallel}, 0)$, as sketched in Figure 5.41. The Hamiltonian is

$$\mathcal{H} = \frac{p_x^2}{2m^*} + eV(x) + \frac{p_z^2}{2m^*} + \frac{p_y^2 + 2ep_y(xB_{\perp} - zB_{\parallel}) + e^2(xB_{\perp} - zB_{\parallel})^2}{2m^*} \quad (5.41)$$

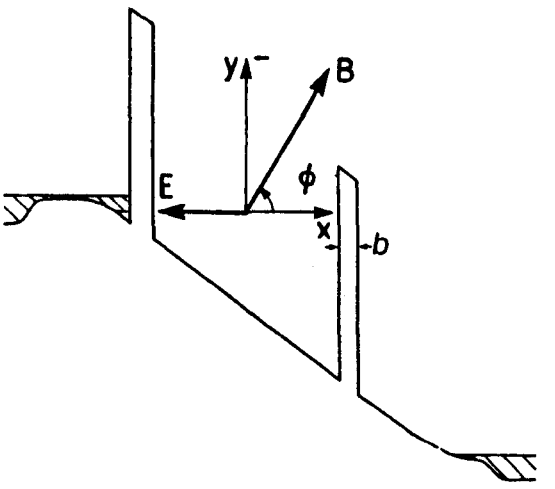

Figure 5.41: Schematic diagram showing the tilted field configuration.

where $V(x)$ is the conduction band profile. The potential does not depend on y so we can write the wavefunction as $\psi(x,z)\exp(ik_y y)$. If we make the substitution

$$z' = z - \frac{\hbar k_y}{eB_{||}} \tag{5.42}$$

which is only valid for $B_{||} \neq 0$, the Schrödinger equation can be written as

$$\left(\frac{p_x^2 + p_z^2}{2m^*} + eV(x) + \frac{e^2(xB_\perp - z'B_{||})^2}{2m^*}\right) e^{ik_y y}\psi(x,z) = \epsilon\, e^{ik_y y}\psi(x,z) \tag{5.43}$$

As pointed out by Maan [273], this does not depend explicitly on k_y and consequently all eigenvalues with different k_y are degenerate with a degeneracy per Landau level of $eB_{||}/h$, which is why the Shubnikov-de Haas oscillations in parallel transport are only dependent on the component of field perpendicular to the interface [71]. In a tunnelling structure, where a self-consistent analysis is necessary to explain the magnetoquantum oscillations in $\boldsymbol{B} \parallel \boldsymbol{J}$ [132, 131], it is not clear that this is true — but the results of Section 3.3 indicate that it holds at least approximately. Writing equation 5.43 as

$$\left(\frac{p_x^2 + 2e\hbar k_y x B_\perp + e^2x^2B_\perp^2}{2m^*} + eV(x) + \frac{p_z^2}{2m^*} + \frac{e^2B_{||}^2z'^2}{2m^*} - \frac{e^2xzB_{||}B_\perp}{2m^*}\right)\psi = \epsilon\psi \tag{5.44}$$

it is clear that the first two terms are the same as in the transverse field problem (equation 5.2) and the next two are associated with the parallel field (equation 3.41) but the final term on the left-hand side involves a mixing of the two magnetic field directions. For small transverse components of field and narrow confining potentials, the transverse field component can be treated as a perturbation (Section 5.2.1) which would approximately give energies of

$$\epsilon = \epsilon_0 + \frac{e^2B_\perp^2\langle x^2\rangle}{2m^*} + \frac{e\hbar k_y B_\perp\langle x\rangle}{m^*} + (n+1/2)\hbar eB_{||}/m^* - \left\langle\frac{e^2xzB_\perp B_{||}}{2m^*}\right\rangle \tag{5.45}$$

If the last term is small, we can treat the effects of the two components of field separately, the transverse component introducing a diamagnetic shift of the energy level (treated as a perturbation) and the parallel component producing Landau levels. This approximation is reasonable in narrow quantum wells where the biggest term is the electrostatic confinement. In wide well samples it is no longer possible to treat the transverse field as a perturbation and a complete solution would have to be attempted, no reports of this exist in the literature.

5.6.1 Inter-Landau-level Transitions in Narrow Wells

The sample described here is *NU183* with a well-width of 60 Å and barriers of 83 Å and 111 Å whose $I(V)$ characteristics in a transverse field were discussed in Section 5.3.

The current-voltage characteristics of *NU183* at the first resonance in reverse bias are shown in Figure 5.42 for a magnetic field of 11.4 T as a function of orientation. For a parallel field ($\phi = 0°$), the trace is dominated by the main resonant peak with much weaker structure in the valley current caused by the LO phonon emission assisted tunnelling process discussed in Section 3.4. This is emphasized in the plot of the second derivative (dotted line). In a transverse field ($\phi = 90°$), the peak is broadened and shifted to higher bias as described in Section 5.3, and there is no structure in the current. However for intermediate values of ϕ, the peak is split into many smaller peaks.

Figure 5.43 shows the $I(V)$ characteristics for a constant component of parallel magnetic field $B_{\|} = 9$ Tesla and a transverse field $B_{\perp}$ increasing from 0 to 7 Tesla. For $B_{\perp} = 0$ there is one main resonant peak with a peak-to-valley ratio of ~28:1 and a series of small replica peaks in the valley current associated with elastic and inelastic scattering processes. As the transverse component of the magnetic field increases, the amplitude of the main peak is reduced and a series of roughly equally spaced peaks emerge; note that the spacing of these peaks does not change with increasing $B_{\perp}$. The overall 'envelope' of the structure closely follows the transverse field results shown in Section 5.3 — with a broadening and a shift to higher bias — but there is strong additional structure superimposed. At the maximum available field ($B_{\|} = 9$ T, $B_{\perp} = 7$ T), the current at the first peak has decreased by a factor of six and as many as eight other peaks are visible.

Some understanding of this structure can again be obtained by considering the graphical interpretation of the conservation conditions as described in Section 5.3, although in this case we need to consider k_z as well as k_y. Figure 5.44 shows the allowed tunnelling transitions for the different field configurations. At zero magnetic field (Figure 5.44(a)), the emitter states consist of a paraboloid in k-space which is occupied for $k_{\perp} < k_F$. Applying a bias voltage moves this paraboloid of states up in energy relative to the energy of the states in the well (also represented by a paraboloid). When the two *surfaces* coincide resonant tunnelling occurs — this happens for a *single* value of bias.

Adding a magnetic field parallel to the current quantises the motion in the plane of the well but does not change the bound state energy. The quantisation

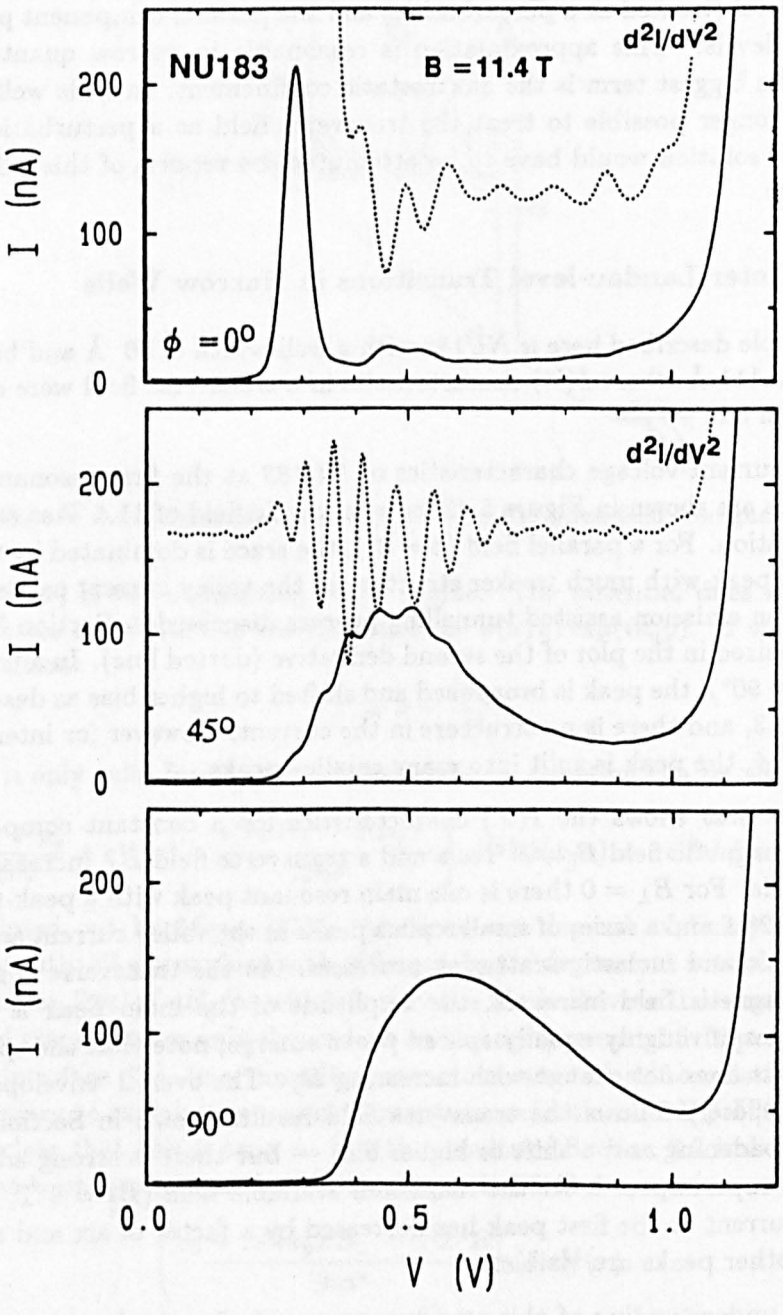

Figure 5.42: $I(V)$ characteristics of *NU183* in reverse bias for a magnetic field of 11.4 T. (a) $\phi = 0°$ (b) $\phi = 45°$ and (c) $\phi = 90°$. For the 0° and 45° curves the second derivative is also shown (dotted curves).

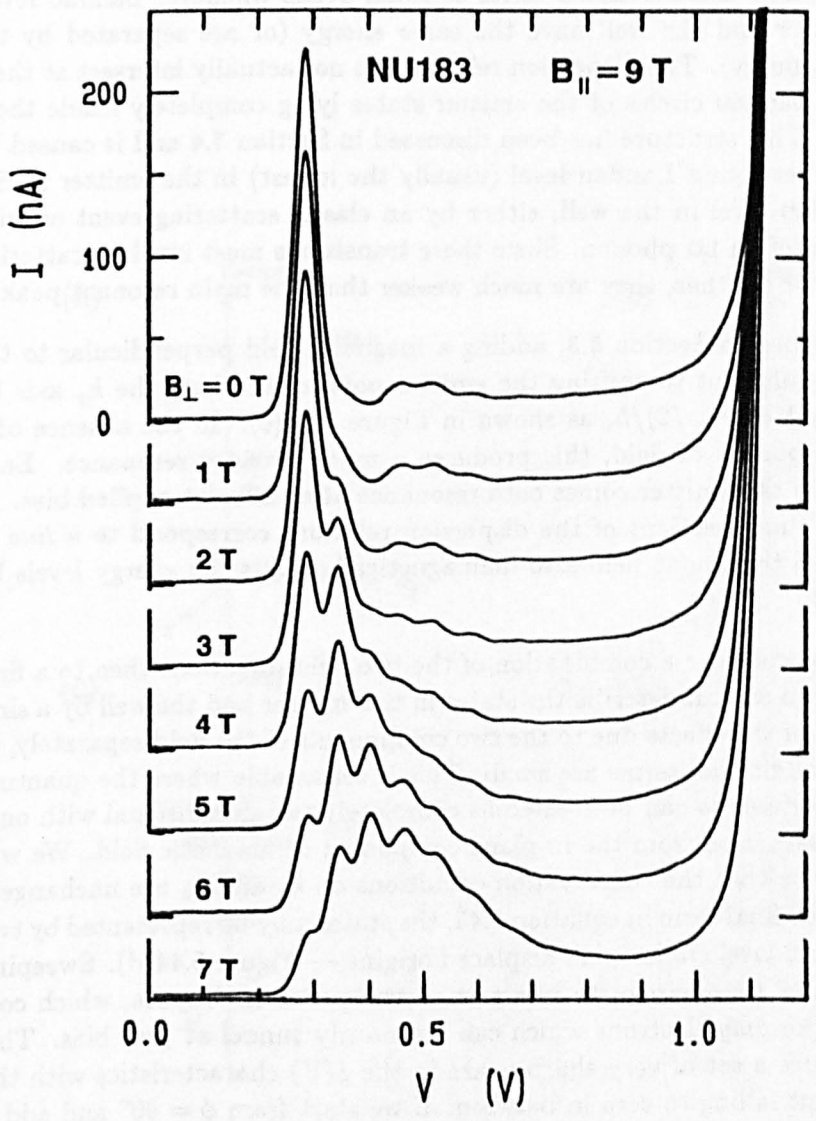

Figure 5.43: Current-voltage characteristics of a 100 μm diameter mesa of *NU183* at the first resonance in reverse bias at a temperature of 4 K. The magnetic field component parallel to the tunnel current is $B_{\|} = 9$ T, the transverse component, $B_{\perp}$ increases from 0 (top) to 7 T (bottom), showing the emergence of inter-Landau level transitions.

can be represented as producing a series of concentric circles with equally-spaced energies corresponding to the Landau levels — Figure 5.44(b). These all coincide when the applied bias is the same as at the zero-field resonance. At higher biases there is also a series of small peaks whenever Landau levels in the emitter and the well have the same energy (or are separated by the LO phonon energy). The dispersion relations do not actually intersect at these points, the Landau circles of the emitter states lying completely inside those of the well. This structure has been discussed in Section 3.4 and is caused by transitions between a Landau level (usually the lowest) in the emitter 2DEG and a Landau level in the well, either by an elastic scattering event or with the emission of an LO phonon. Since these transitions must involve scattering of one kind or another, they are much weaker than the main resonant peak.

As described in Section 5.3, adding a magnetic field perpendicular to the current is equivalent to shifting the emitter paraboloid along the k_y axis by $k_0 = eB(x_0 + b_1 + w/2)/\hbar$, as shown in Figure 5.44(c). In the absence of a parallel component of field, this produces a much broader resonance. Each value of k_y in the emitter comes onto resonance at a different applied bias. In this case the intersections of the dispersion relations correspond to a *line* in k-space. The transverse field also diamagnetically shifts the energy levels by $m^*\omega_c^2\langle x^2\rangle/2$.

If we now consider a combination of the two field directions then to a first approximation we can describe the states in the emitter and the well by a simple addition of the effects due to the two components of the field separately, as long as the additional terms are small. This is reasonable where the quantum well is narrow and so can be treated as completely two-dimensional with only a small perturbation from the in-plane component of magnetic field. We will further assume that the conservation conditions on k_y and k_z are unchanged. Neglecting the final term in equation 5.45, the states may be represented by two sets of Landau level circles with displaced origins — Figure 5.44(d). Sweeping the bias causes these circles to intersect at two *points* in k-space, which correspond to the *only* electrons which can resonantly tunnel at that bias. This should produce a set of very sharp peaks in the $I(V)$ characteristics with the tunnel current falling to zero in between. If we start from $\phi = 90°$ and add a parallel component of magnetic field, the quantisation due to the parallel field means that electrons only tunnel at some of the applied biases which were on resonance for a transverse field alone, producing structure in the current-voltage characteristics. The spacing of the peaks increases with the parallel field component.

Conversely, the addition of a transverse component to a large parallel field means that the inter-Landau level transitions which previously required the electron to scatter are now allowed with no need for scattering and therefore they are strengthened, *i.e.* the transverse field breaks the conservation condition on the Landau level index. When the shift in the origin k_0 is greater than the diameter of the k-space circle corresponding to the lowest Landau level the 'resonant' peak (*i.e.* that which is at the same bias as the zero-field resonance) is completely quenched. The spacing of the peaks should, however, be determined solely by the parallel component of field in this approximate treatment. In reality, the structure in the current is fairly smooth rather than

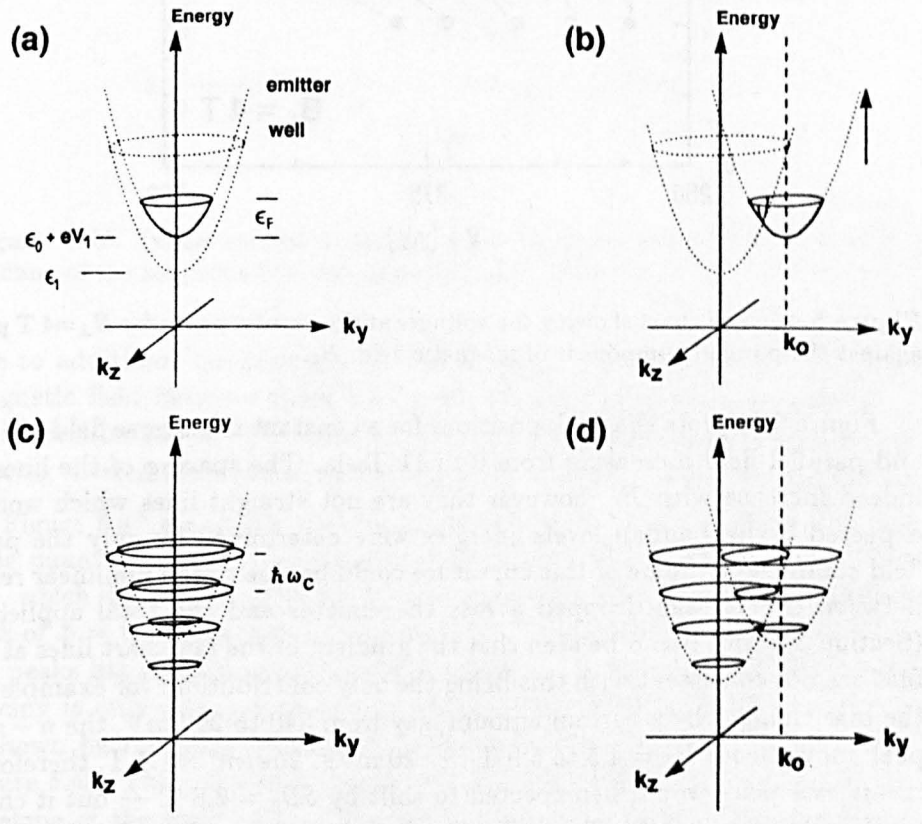

Figure 5.44: Schematic illustration of the resonance condition in the different field configurations, (a) zero field $B_{\|} = B_{\perp} = 0$ (b) parallel field $\phi = 0°$, $B_{\|} > 0$, $B_{\perp} = 0$ (c) transverse field $\phi = 90°$, $B_{\|} = 0$, $B_{\perp} > 0$ (d) tilted field $0° < \phi < 90°$, $B_{\|} > 0$, $B_{\perp} > 0$.

consisting of a series of δ-functions which, as usual, is due to the broadening of the energy levels by scattering processes.

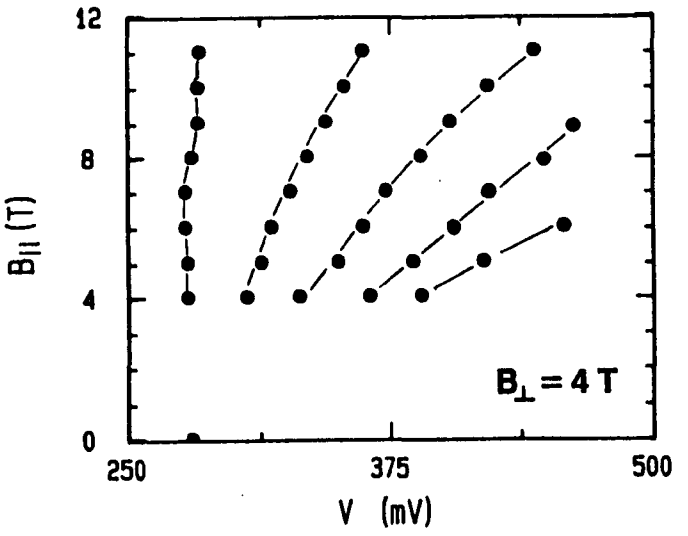

Figure 5.45: Fan chart showing the voltages at the current peaks for $B_\perp$=4 T plotted against the parallel component of magnetic field, $B_{||}$.

Figure 5.45 plots the peak positions for a constant transverse field of 4 Tesla and parallel field increasing from 0 to 11 Tesla. The spacing of the lines does indeed increase with $B_{||}$, however they are not straight lines which would be expected if the Landau levels energies were determined by only the parallel field component. Some of this curvature could be due to the nonlinear relation between the voltage dropped across the emitter and the total applied bias (Section 3.2) but it can be seen that the gradient of the fan-chart lines at given bias are not consistent with this being the only contribution: for example when the bias changes by a certain amount, say from 340 to 360 mV, the $n - n' = 2$ peak moves from $B_{||} = 4.5$ to 5.9 T *i.e.* 20 mV$\equiv 2\hbar e/m^* \times 1.4$ T, therefore the $n - n' = 1$ peak would be expected to shift by $\delta B_{||} = 2.8$ T — but it changes position by only 2.0 T. This indicates that the energy of the Landau levels is affected by the transverse component of the magnetic field however this is a relatively small shift and it is quite a good approximation to take the two field directions as being separable.

5.6.2 Novel Oscillatory Structure in the $I(V)$ Characteristics in a Tilted Magnetic Fields

For samples with wide quantum wells, we have already noted in Section 5.4.2 that there is a pronounced difference in the effects of parallel and transverse fields on the $I(V)$ characteristics; $B_{||}$ causes only a small reduction in I whereas $B_\perp$ completely quenches the current at high fields. Figure 5.46 shows the tunnel current as a function of ϕ for *NU207* (1200 Å well). This angular dependence can be used to calibrate the rotation probe.

A parallel field does not affect the positions of the resonant peaks in the current (see Section 3.6) and in a transverse field, hybrid magnetoelectric states evolve which have an energy spacing greater than that of the zero-field states

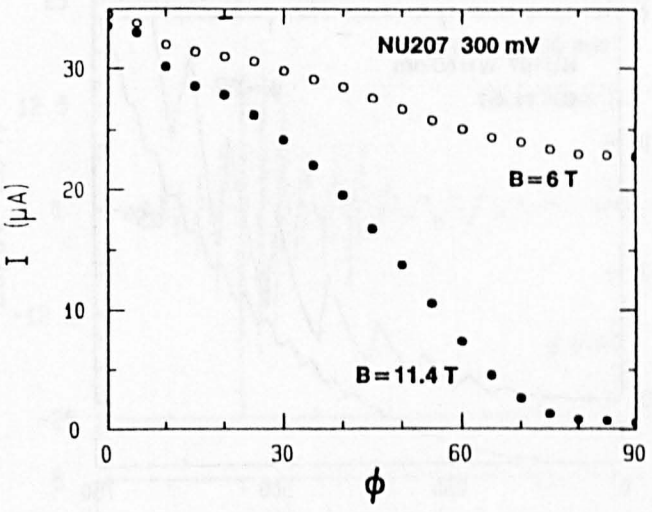

Figure 5.46: Tunnel current at for a 100 μm diameter mesa of *NU207* at 4 K as a function of the magnetic field direction for a bias of 300 mV.

due to additional confinement by the magnetic vector potential. Tilting the magnetic field between these two configurations produces a completely new set of oscillations in $I(V)$ with remarkably complex structure and a voltage spacing several times less than that in either parallel or transverse field alone.

Figure 5.47 shows the $I(V)$ characteristics of *NU167*, which has a 600 Å wide quantum well, in a magnetic field of 11.4 T for angles of $\phi = 0°$ and 25°, which shows a set of resonances with a voltage spacing approximately half that of $\phi = 0°$ and a reduced amplitude. At higher angles the frequency of the peaks has approximately doubled again, so at an angle of 55° the voltage spacing is only one quarter of the electrostatic resonances of $\phi = 0°$. This is shown by the plots of the second derivative for 0°, 25°, and 55° given in Figure 5.48. There is also a strong voltage and orientation dependence of the envelope of the oscillations. The resonances at higher bias are less affected, with the frequency roughly staying constant but the amplitude reduced by two orders of magnitude. The change in the periodicity of the oscillations is not simply related to the parallel component of magnetic field which is 11.4 T for $\phi = 0°$, 10.3 T for 25°, where the voltage spacing has halved, and 6.5 T at $\phi = 55°$, where the spacing has again decreased by a factor of two.

Similar structure is observed in a sample with a 1200 Å well, *NU207*, although the amplitude is reduced and so it is necessary to remove the monotonically increasing background current in order to reveal the oscillatory structure. This is achieved by subtracting a fourth order polynomial from the $I(V)$ characteristics, as shown in Figure 5.49 for $B = 11.4$ T, $\phi = 30°$. The amplitude of the oscillations is about 1% of the background current. Again the voltage spacing of these peaks is much less than for $\phi = 0°$, approximately 13 mV compared to 40 mV in this bias range in at $\phi = 0°$.

Figure 5.50 shows a series a dG/dV traces for sample *NU207* in a magnetic field of 11.4 Tesla as the field direction is rotated from $\boldsymbol{B} \parallel \boldsymbol{J}$ to $\boldsymbol{B} \perp \boldsymbol{J}$. The

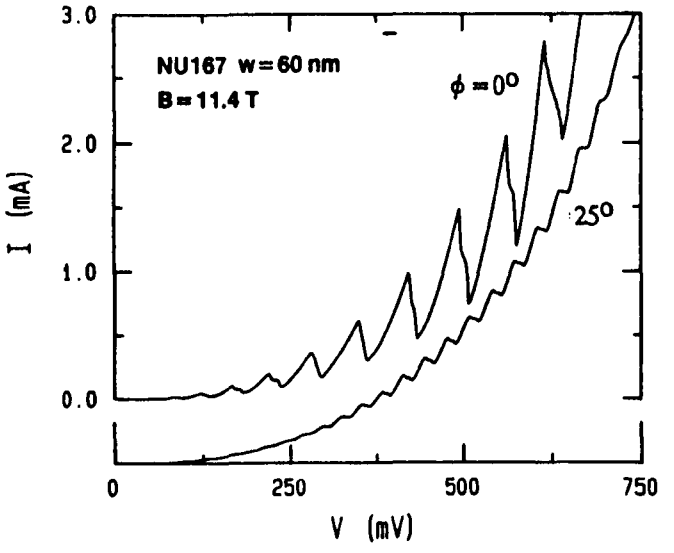

Figure 5.47: Current-voltage characteristics of *NU167* (600 Å well) in a magnetic field of 11.4 T for angles of $\phi = 0°$ and 25°, at a temperature of 4 K.

structure is extremely sensitive to the value of ϕ with changes of as little of 1° producing quite different traces.

As the transverse field is increased, the resonances are, at first, rapidly quenched — the amplitude of the oscillations at 10° is roughly twenty times lower than that at 0°. The resonances at high bias are particularly strongly affected. In the trace taken at 15°, the resonances appear to split in the voltage range around 500 mV, whilst the amplitude is still decreasing. This region of rapid oscillation spreads over a wider range of bias as the angle increases — as shown by the 20° trace, where a beating pattern in the low bias structure is also apparent. By $\phi = 25°$, the frequency of the resonances between 150 and 500 mV is between two and three times that at $\phi = 0°$. In the region of bias around 600 mV a slightly different frequency of oscillation emerges. This grows in strength as the angle is increased further. In the 30° trace this series of oscillations dominates and has a sharply-peaked envelope. In the bias region below 400 mV there is a complex beating pattern set up between the two sets of oscillations. We stress that this structure reproduces accurately and is also present for $\theta = -30°$. The oscillatory structure has a maximum amplitude at about 32° where it is about 10% of the amplitude of $\phi = 0°$. Beyond this point the envelope continues to develop in an interesting way with a particularly sharp cut off seen in the 40° trace. Also note that the peak amplitude is gradually moving to lower bias. The trace taken for $\phi = 45°$ shows a small periodic modulation in the envelope and at 50° the frequency of the oscillations has increased by a factor of approximately 5/4. At higher angles the oscillations are too weak to be observed even in the second derivative. At angles above 70°, a series of very slow oscillations is seen which move to lower bias with increasing angle and can be identified as the interfacial Landau levels discussed earlier in this chapter.

This extremely rich structure is at first sight baffling since it is hard to

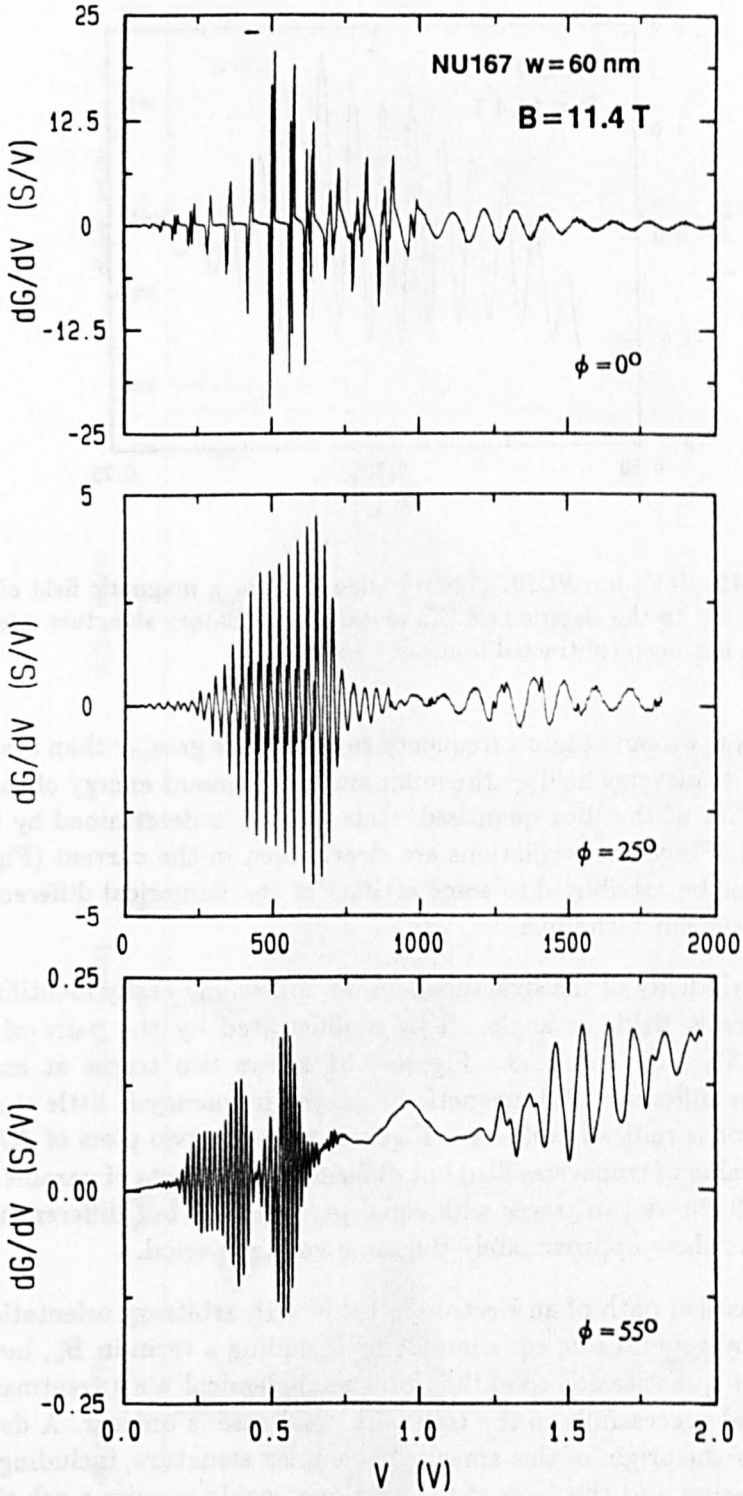

Figure 5.48: Plots of the derivative of the conductance against voltage for *NU167* at angles of $\phi = 0°$, 25° and 55°. The frequency of the low bias oscillations is approximately double in each trace.

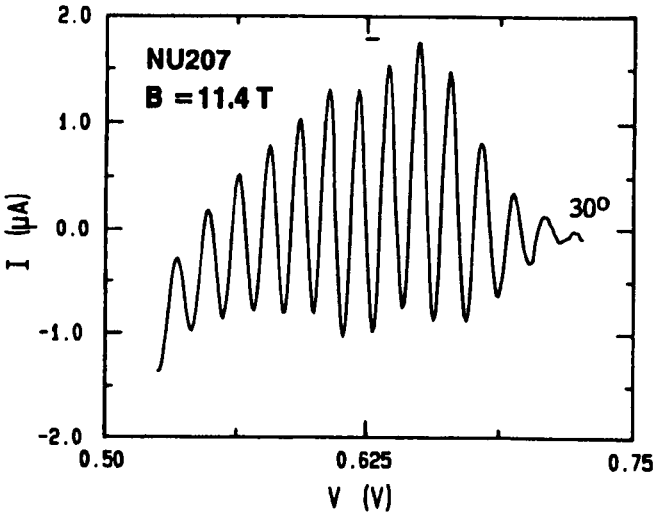

Figure 5.49: $I(V)$ for *NU207* (1200 Å wide well) in a magnetic field of 11.4 T at an angle of 30° to the electric field. To reveal the oscillatory structure a fourth order polynomial has been subtracted from the current.

envisage how we can obtain a frequency several times greater than that in either parallel or transverse field — the minimum confinement energy of the electron states is that of the 'box-quantised' states which is determined by the width of the well. Since the oscillations are clearly seen in the current (Figure 5.47) they cannot be attributed to some artifact of the numerical differentiation or the measurement technique.

The periodicity of the structure does not follow any easily identifiable trend with magnetic field, or angle. This is illustrated by the pairs of traces in Figures 5.51, 5.52 and 5.53. Figure 5.51 shows two traces at an angle of $\phi = 30°$ for different total magnetic fields, the frequency is little changed but the envelope is radically different. Figure 5.52 shows two plots of dG/dV with the same value of transverse field but differing components of parallel field, and Figure 5.53 shows two traces with equal parallel field but different transverse field. These show approximately the same voltage period.

The classical path of an electron in fields with arbitrary orientation is simply given by generalising equation 5.1 by including a term in B_x, however the appropriate quantisation condition for a semi-classical WKB treatment similar to that used successfully in the transverse field case is unclear. A detailed description of the origin of this amazingly complex structure, including both the voltage spacing and the form of the envelope, would require a solution of the Schrödinger equation for an arbitrary field direction as well as a clear understanding of the conservation conditions. However it is suggestive to note that there are several competing frequencies at approximately half-integral multiples of the peak spacing in $\phi = 0°$. Persisting with the assumption that at least to some extent we can treat the two components of field separately, the application of a perpendicular component of field allows transitions between the emitter and the well which do not conserve Landau-level number but do not involve scattering processes. In an ideal system these would consist of a

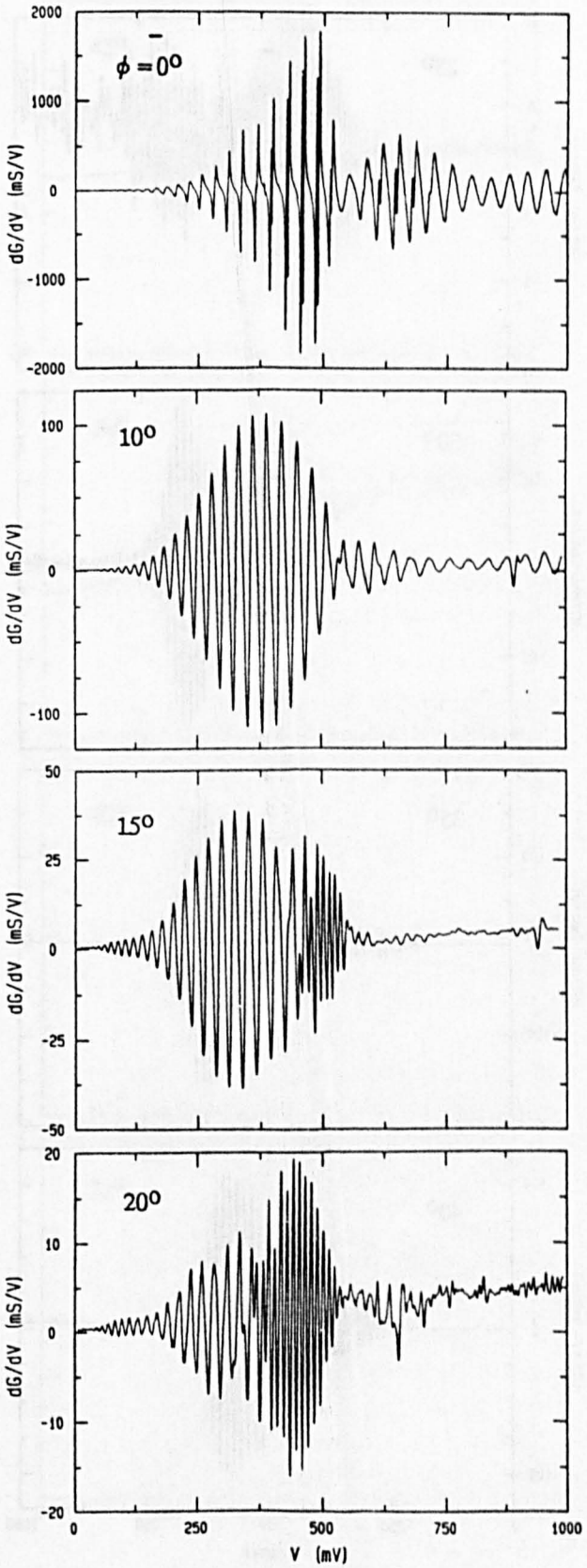
$\phi = 0^o$
10^o
15^o
20^o
dG/dV (mS/V)
V (mV)
2000
1000
0
-1000
-2000
100
-100
50
25
-25
-50
20
10
-10
-20
0
250
500
750
1000

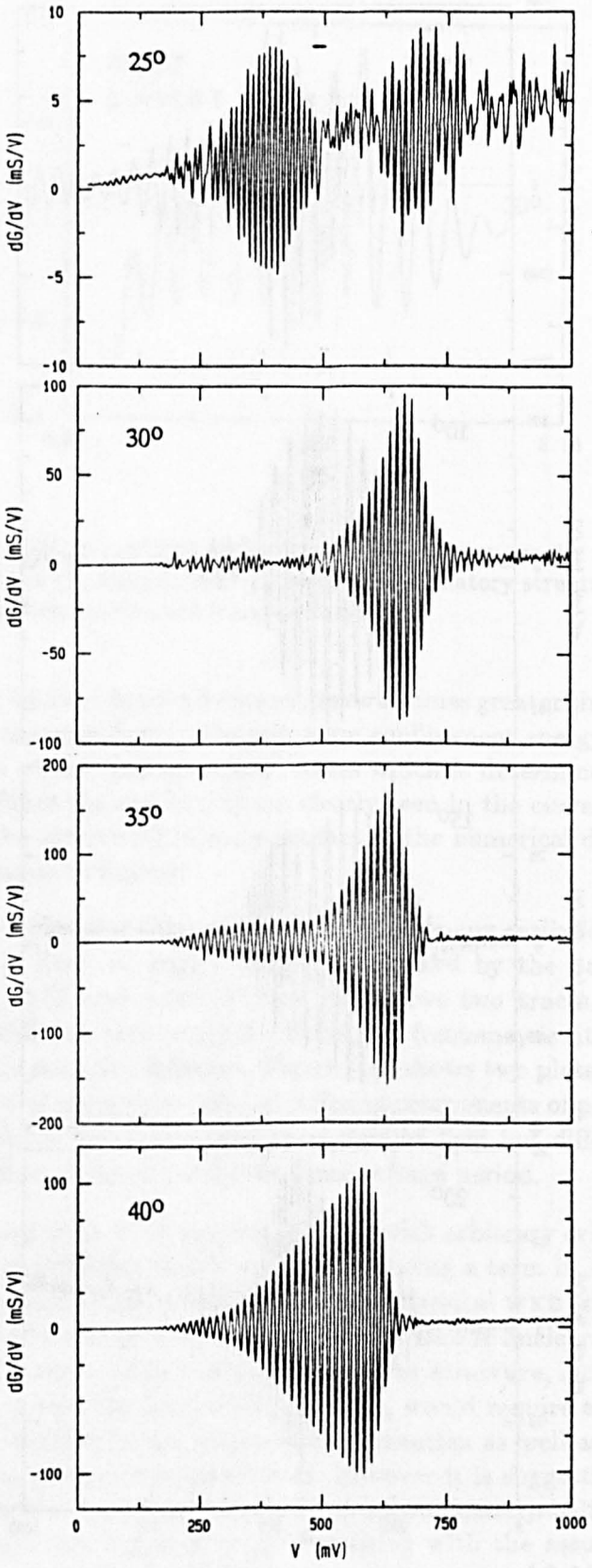
25°
30°
35°
40°
dG/dV (mS/V)
V (mV)
10
5
0
-5
-10
100
50
-50
-100
200
-200
250
500
750
1000

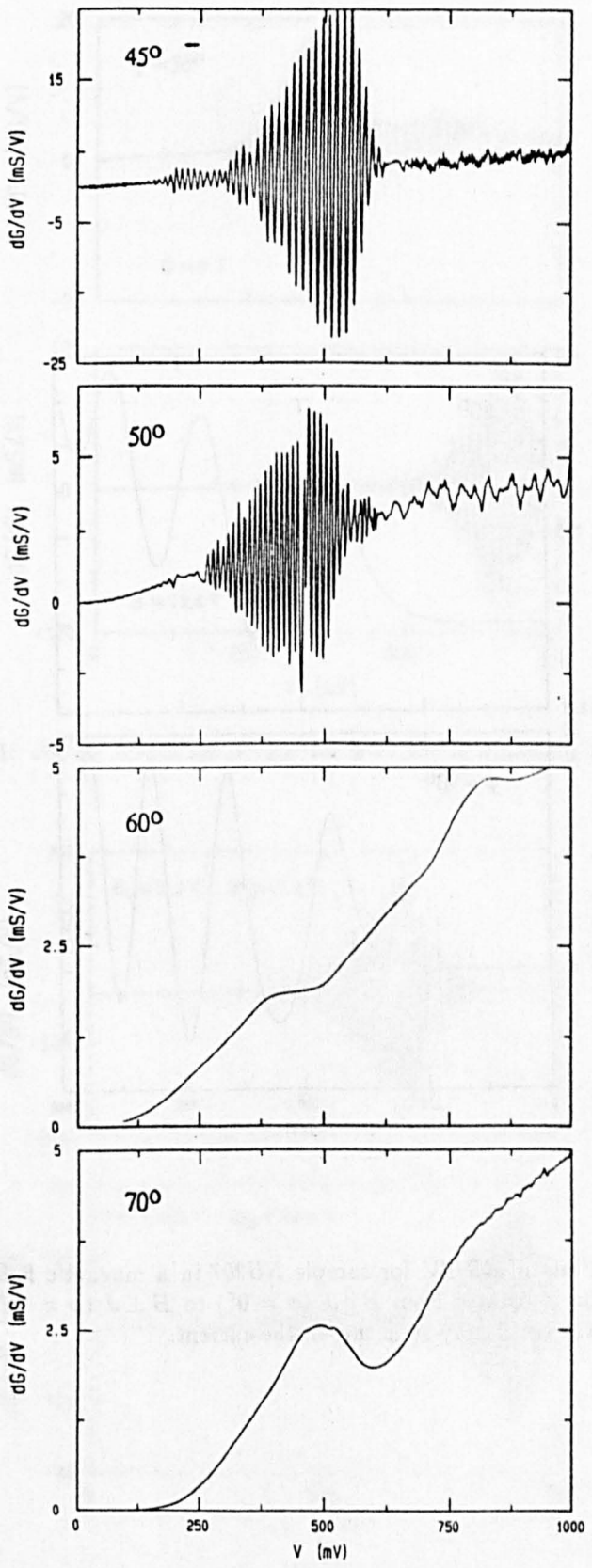
45°
50°
60°
70°
dG/dV (mS/V)
15
-5
-25
5
0
-5
2.5
0
250
500
750
1000
V (mV)

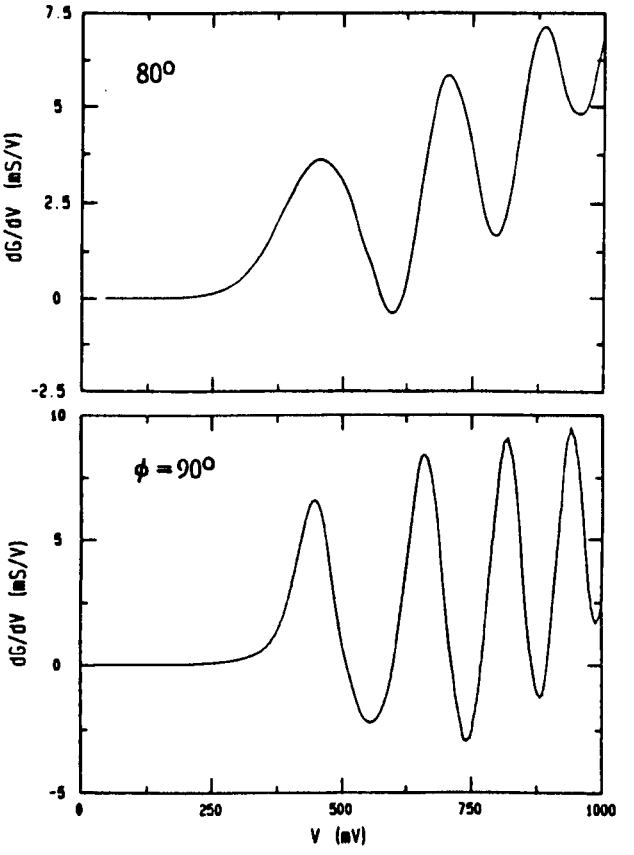

Figure 5.50: Plots of dG/dV for sample *NU207* in a magnetic field of 11.4 T as the field direction is rotated from $\boldsymbol{B} \parallel \boldsymbol{J}$ ($\phi = 0°$) to $\boldsymbol{B} \perp \boldsymbol{J}$ ($\phi = 90°$) showing the development of the oscillatory structure in the current.

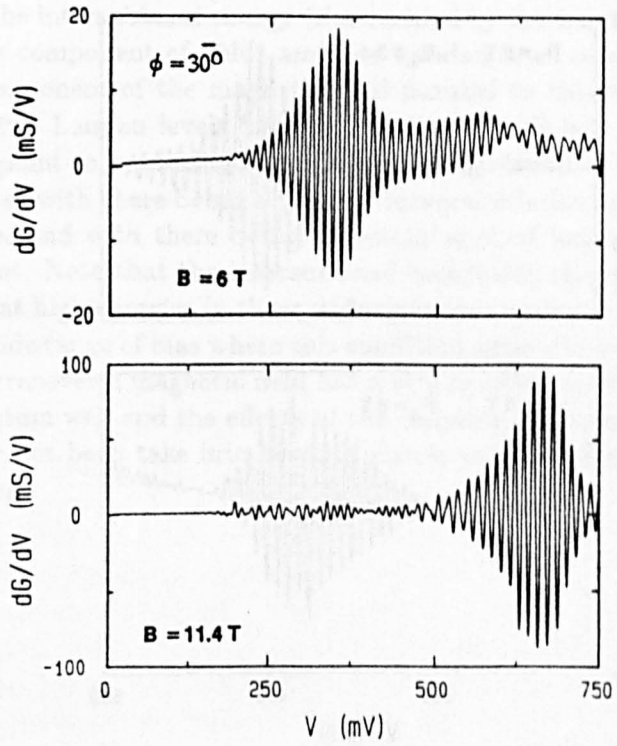

Figure 5.51: dG/dV traces for *NU207* for $\phi = 30°$ at magnetic fields of 6 and 11.4 Tesla.

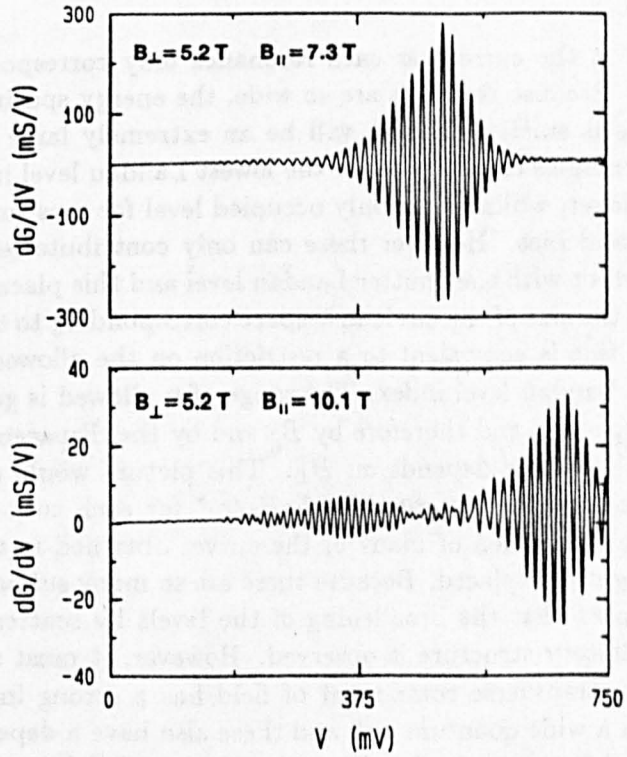

Figure 5.52: dG/dV traces with the same transverse field (5.2 T) but different parallel components, the periodicity is little changed.

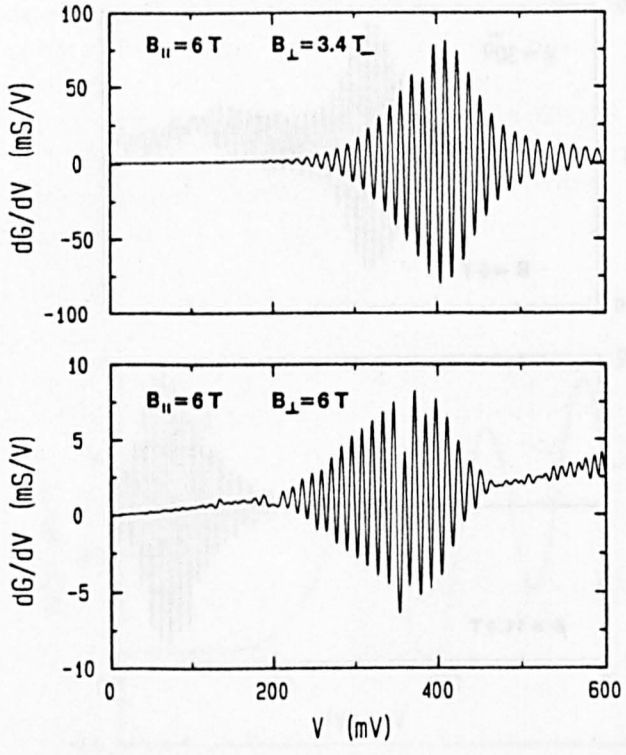

Figure 5.53: dG/dV traces with the same parallel component of B, but different transverse field, showing that although the transverse field has almost doubled the voltage period changes by less than 20%.

set of δ-functions in the current as each resonance only corresponds to two points in k-space. Because the wells are so wide, the energy spacing between adjacent subbands is small and there will be an extremely large number of Landau levels at energies close to that of the lowest Landau level in the emitter accumulation layer, which is the only occupied level for most of the range of magnetic field and bias. However these can only contribute resonantly if they actually intersect with the emitter Landau level and this places an upper and lower limit on the size of the circle in k-space corresponding to the Landau levels in the well, this is equivalent to a restriction on the allowed values of Δn, the change in Landau level index. The range of n allowed is governed by the Landau level spacing, and therefore by $B_{||}$ and by the dispacement of the emitter states, k_0 — which depends on $B_\perp$. This picture would apparently predict a sequence of peaks separated by $\hbar e B_{||}/m^*$ for each subband in the well, very like a superposition of many of the curves obtained in the narrow well sample but slightly displaced. Because there are so many subbands in the well one might expect that the broadening of the levels by scattering would mean that no oscillatory structure is observed. However, it must also be remembered that the transverse component of field has a strong influence on the energy levels in a wide quantum well and these also have a dependence on the orbit center position given by k_y. Since the transverse field term and the cross-term in $B_x B_z$ are no longer small compared to the electrostatic terms in equation 5.45, they can no longer be treated as perturbations, *i.e.* the finite width of the quantum well means that it is no longer adequate to treat it as a perfect two-dimensional system.

A possible interpretation of the experimental data is that if the relation between the intersubband energy (determined by the barrier potential and the transverse component of field) and the Landau level separation (determined by the component of the magnetic field parallel to the current) is a ratio of integers, two Landau levels from different subbands will be on resonance at the same point so producing particularly strong structure in the current. This would agree with there being a roughly integral relation between the different frequencies and with there being a certain applied bias where the structure is strongest. Note that the intersubband separation changes relatively slowly with bias at high energies in these wide quantum wells so there could be a reasonably wide range of bias where this condition approximately holds. However, since the transverse magnetic field has a strong effect on the energy levels in a wide quantum well and the effects of the coupling between the two field directions have not been take into account this is only put forward as a tentative explanation.

5.7 Conclusion

In this Chapter we have shown that a transverse magnetic field produces a range of new and interesting insights into the resonant tunnelling process. In a narrow well sample, the resonance between a two-dimensional state in the emitter and a state in the well is dramatically broadened and the peak-to-valley ratio decreases by an order of magnitude for a field of 10 Tesla. This can be clearly explained with the aid of a simple graphical interpretation of the conservation conditions. Very good agreement is obtained for the position and width of the resonant peak when the distribution of voltage within the device is taken into account.

We have also described the first observation of tunnelling into hybrid magnetoelectric states in double barrier structures in samples where the wide quantum wells allow the whole range between electrostatic 'box-quantisation' and magnetically confined skipping states to be explored. A calculation of the resonance positions using the semi-classical WKB approximation provides reasonable agreement with the data. At high magnetic fields, the current is quenched due to the electron being deflected back into the emitter by the action of the Lorentz force. The extremely high quality of the samples investigated allow us to observe many more resonances and much clearer quantisation effects than in other more recent investigations.

By rotating the direction of the magnetic field in the plane of the quantum well we have demonstrated the potential for a new probe of the high-energy band structure. The angular dependence of the magnetoquantum oscillations clearly reveals the cubic anisotropy of the Γ-conduction band at high energies. Again the WKB approximation is found to be most useful in modelling this effect and a reasonable value for the anisotropy is obtained. Tunnelling at high electron energies could provide much useful information about both the non-parabolicity and the anisotropy of the conduction band.

We have also presented the first investigation of the effects of a magnetic field which is tilted with respect to the direction of current flow. The magnetic field component parallel to the current quantises the electron energy into Landau levels and the perpendicular component breaks the conservation condition on the Landau level index, therefore we are able to observe strong peaks due to inter-Landau level transitions which are normally only possible via scattering processes. In samples with very wide quantum wells, remarkable complex structure is seen in the current-voltage characteristics possibly due to coupling between the Landau level separation and the intersubband energy.

References

[1] L. Esaki and R. L. Tsu, *IBM J. Res. Dev.* **14**, 16 (1970).

[2] M. J. Kelly and C. J. Weisbuch (Eds.), *Physics and Fabrication of Sub-Micron Structures*, Springer-Verlag (1986).

[3] *IEEE J. Quantum Electronics* **QE-22**, No. 9 (1986).

[4] L. V. Iogansen, *Sov. Phys. JETP* **18**, 146 (1964). *ibid.* **20**, 180 (1965).

[5] L. Esaki, in *Electronic Properties of Multilayers and Low-Dimensional Semiconductors*, J. M. Chamberlain, L. Eaves and J. C. Portal (Eds.), Plenum Press (1989).

[6] L. D. Landau and I. M. Lifshitz, *Quantum Mechanics*, 3rd Edition, Pergamon (1977).

[7] D. Bohm, *Quantum Theory*, Prentice-Hall (1951).

[8] R. F. Kazarinov and R. A. Suris, *Sov. Phys. Semicond.* **5**, 707 (1971).

[9] R. L. Tsu and L. Esaki, *Appl. Phys. Lett.* **22**, 562 (1973).

[10] S. Luryi, *Appl. Phys. Lett.* **47**, 490 (1986).

[11] L. L. Chang, L. Esaki and R. L. Tsu, *Appl. Phys. Lett.* **24**, (1974).

[12] T. C. L. G. Sollner, W. D. Goodhue, P. E. Tannenwald, C. D. Parker and D. D. Peck, *Appl. Phys. Lett.* **43**, 588 (1983).

[13] T. C. L. G. Sollner, P. E. Tannenwald, C. D. Parker and W. D. Goodhue, *Appl. Phys. Lett.* **45**, 1319 (1984).

[14] T. C. L. G. Sollner, H. Q. Le, C. A. Correa and W. D. Goodhue *Appl. Phys. Lett.* **47**, 36 (1985).

[15] T. J. Shewchuk, P. C. Chapin, P. D. Coleman, W. Kopp, R. Fischer and H. Morkoç, *Appl. Phys. Lett.* **46**, 508 (1985).

[16] M. Tsuchiya, H. Sakaki and J. Yoshino, *Jap. J. Appl. Phys.* **24**, L466 (1985).

[17] W. D. Goodhue, T. C. L. G. Sollner, H. Q. Le, E. R. Brown and B. A. Vojak, *Appl. Phys. Lett.* **49**, 1086 (1986).

[18] C. I. Huang, M. J. Paulus, C. A Bozada, S. C. Dudley, K. R. Evans, C. E. Stutz, R. L. Jones and M. E. Cheney, *Appl. Phys. Lett.* **51**, 121 (1987).

[19] O. H. Hughes, M. Henini, E. S. Alves, L. Eaves, M. L. Leadbeater, T. J. Foster, A. Celeste and J. C. Portal, *J. Vac. Sci. Technol. B* **6**, 1161 (1988).

[20] T. Inata, S. Muto, Y. Nakata, S. Sasa, T. Fujii and S. Hiyamizu, *Jap. J. Appl. Phys.* **26**, L1332 (1987).

[21] T. P. E. Broekaert, W. Lee and C. G. Fonstad, *Appl. Phys. Lett.* **53**, 1545 (1988).

[22] P. Gavrilovic, J. M. Brown, R. W. Kaliski, N. Y. Holonyak Jnr., K. Hess, M. J. Ludowise, W. T. Dietze and C. R. Lewis, *Sol. State Comm.* **52**, 237 (1984).

[23] T. H. H. Vuong, D. C. Tsui and W. T. Tsang, *Appl. Phys. Lett.* **50**, 212 (1987).

[24] M. L. Leadbeater, L. Eaves, P. E. Simmonds, P. A. Claxton, G. Hill and M. A. Pate, *Solid-State Electron.* **31**, 707 (1988).

[25] A. W. Higgs, L. L. Taylor, N. Apsley, S. J. Bass and H. J. Hutchison, *Electron. Lett.* **24**, 322 (1988).

[26] E. E. Mendez, W. I. Wang, B. Ricco and L. Esaki, *Appl. Phys. Lett.* **47**, 415 (1985).

[27] L. F. Luo, R. Beresford and W. I. Wang, *Appl. Phys. Lett.* **53**, 2320 (1988).

[28] M. A. Reed, R. J. Koestner and M. W. Goodwin, *Appl. Phys. Lett.* **49**, 1293 (1986).

[29] H. C. Liu, D. Landheer, M. Buchanan and D. C. Houghton, *Appl. Phys. Lett.* **52**, 1809 (1988).

[30] S. S. Rhee, J. S. Park, R. P. G. Karunasir, Q. Ye and K. L. Wang, *Appl. Phys. Lett.* **53**, 204 (1988).

[31] S. Miyazaki, Y. Ihara and M. Hirose, *Phys. Rev. Lett.* **59**, 125 (1987).

[32] N. Tabatabaie, T. Sands, J. P. Harbison, H. L. Gilchrist and V. G. Keramidas, *Appl. Phys. Lett.* **53**, 2528 (19888).

[33] T. C. L. G. Sollner, E. R. Brown, W. D. Goodhue and H. Q. Le, *Appl. Phys. Lett.* **50**, 332 (1987).

[34] E. R. Brown, T. C. L. G. Sollner, W. D. Goodhue, C. D. Parker and C. L. Chen, *Appl. Phys. Lett.* **55**, 1777 (1989).

[35] J. F. Whitaker, G. A. Mourou, T. C. L. G. Sollner and W. D. Goodhue, *Appl. Phys. Lett.* **53**, 385 (1988).

[36] T. C. L. G. Sollner, E. R. Brown, W. D. Goodhue and C. A. Correa *J. Appl. Phys.* **64**, 4248 (1988).

[37] T. C. L. G. Sollner, E. R. Brown, C. D. Parker and W. D. Goodhue, in *Electronic Properties of Multilayers and Low Dimensional Semiconductor Structures*, J. M. Chamberlain, L. Eaves and J. C. Portal (Eds.), Plenum Press (1989).

[38] N. Yokoyama, K. Imamura, S. Muto, S. Hiyamizu and H. Nishi, *Jap. J. Appl. Phys.* **24**, L853 (1985).

[39] T. Futatsugi, Y. Yamaguchi, K. Imamura, S. Muto, N. Yokoyama and A. Shibatomi, *Jap. J. Appl. Phys.* **26**, L131 (1987).

[40] K. K. Woodward, T. C. McGill, H. F. Chung and R. D. Burnham, *Appl. Phys. Lett.* **51**, 1542 (1987).

[41] S. Sen, F. Capasso, F. Beltram and A. Cho, *IEEE Trans. Electron. Dev.* **ED-34**, 1768 (1987).

[42] A. R. Bonnefoi, D. H. Chow and T. C. McGill, *Appl. Phys. Lett.* **47**, 888 (1985).

[43] M. A. Reed, W. R. Frensley, R. J. Matyi, J. N. Randall and A. C. Seabaugh, *Appl. Phys. Lett.* **54**, 1034 (1989).

[44] F. Capasso, K. Mohammed and A. Y. Cho, *IEEE J. Quantum Electronics* **QE-22**, 1853 (1986).

[45] S. Luryi, *Appl. Phys. Lett.* **52**, 501 (1988).

[46] S. Luryi in *Heterojunctions: Band Discontinuities and Device Applications*, F. Capasso and G. Magaritondo (Eds.), Elsevier (1987).

[47] J. S. Blakemore, *J. Appl. Phys.* **53**, R123 (1982).

[48] S. Adachi, *J. Appl. Phys.* **58**, R1 (1985).

[49] *Landoldt-Börnstein Vol. 17a, Semiconductors*, O. Madelung (Ed.), Springer-Verlag, New York (1982).

[50] H. C. Casey and M. B. Panish, *Heterostructure Lasers*, Academic Press, New York (1978).

[51] T. J. Foster, M. L. Leadbeater, D. K. Maude, E. S. Alves, L. Eaves, M. Henini, O. H. Hughes, A. Celeste, J. C. Portal, D. Lancefield and A. R. Adams, *Solid-State Electron.* **32**, 1731 (1989).

[52] J. H. Lee, L. Y. Juravel, J. C. Woolley and A. J. SpringThorpe, *Phys. Rev. B* **21**, 659 (1980).

[53] E. M. Conwell, *High Field Transport in Semiconductors*, Academic Press, New York (1967).

[54] B. K. Ridley, *Quantum Processes in Semiconductors*, Second Edition, Oxford University Press (1988).

[55] R. Ferreira and G. Bastard, *Phys. Rev. B* **40**, 1074 (1989).

[56] A. S. Barker Jr. and A. J. Sievers, *Rev. Mod. Phys.* **47**, S1 (1975).

[57] O. K. Kim and W. G. Spitzer, *J. Appl. Phys.* **50**, 4362 (1979).

[58] K. J. Nash, M. S. Skolnick and S. J. Bass, *Semicond. Sci. Technol.* **2**, 329 (1989).

[59] A. S. Barker, J. L. Merz and A. C. Gossard, *Phys. Rev. B* **17**, 3183 (1978).

[60] R. L. Anderson, *IBM J. Res. Dev.* **4**, 283 (1960).

[61] H. Kroemer *Surf. Sci.* **174**, 299 (1986).

[62] H. L. Störmer, R. Dingle, A. C. Gossard, W. Wiegmann and M. D. Sturge, *Sol. State Comm.* **29**, 705 (1979).

[63] T. Ando, A. B. Fowler and F. Stern, *Rev. Mod. Phys* , (1982).

[64] L. Pfeiffer, K. W. West, H. L. Stormer and K. W. Baldwin. *Appl. Phys. Lett.* **55**, 1888 (1989).

[65] D. C. Tsui, H. L. Störmer and A. C. Gossard, *Phys. Rev. Lett.* **48**, 1559 (1982).

[66] B. J. van Wees, H. van Houten, C. W. J. Beenakker, J. G. Williamson, L. P. Kouwenhoven, D. van der Marel and C. T. Foxon, *Phys. Rev. Lett.* **60**, 848 (1988).

[67] D. A. Wharam, T. J. Thornton, R. Newbury, M. Pepper, H. Ahmed, J. E. Frost, D. G. Hasko, D. C. Peacock, D. A. Ritchie and G. A. C. Jones, *J. Phys. C* **21**, L209 (1988).

[68] D. Weiss, K. von Klitzing, K. Ploog and G. Weimann, in *High Magnetic Fields in Semiconductor Physics II*, G. Landwehr (Ed.), Springer-Verlag, Berlin (1989).

[69] T. W. Hickmott, *Phys. Rev. B* **32**, 6531 (1985).

[70] L. Eaves, B. R. Snell, D. K. Maude, P. S. S. Guimarães, D. C. Taylor, F. W. Sheard, G. A. Toombs, J. C. Portal, L. Dmowski, P. A. Claxton, G. Hill, M. A. Pate and S. J. Bass, *Proc. 18th Int. Conf. Physics of Semiconductors, Stockholm*, World Scientific Press, Singapore (1986).

[71] F. F. Fang and W. E. Howard, *Phys. Rev. Lett.* **16**, 797 (1966).

[72] J. R. Oppenheimer, *Physical Review* **41**, 66 (1928).

[73] G. Gamow, *Z. Physik* **51**, 204 (1928).

[74] See the articles by L. Esaki, I. Giaever and B. Josephson, in *Rev. Mod. Phys.* **46**, (1974).

[75] C. B. Duke, *Tunneling in Solids*, Academic Press, New York (1969).

[76] M. Büttiker and R. Landauer, *Phys. Rev. Lett.* **49**, 1739 (1982).

[77] S. Collins, D. Lowe and J. R. Barker, *J. Phys. C* **20**, 6213 (1987).

[78] C. R. Leavens and G. C. Aers, *Phys. Rev. B* **39**, 1202 (1989).

[79] A. P. Jauho and M. Jonson, *J. Phys: Condensed Matter* **1**, 9027 (1989).

[80] E. H. Hauge, J. P. Falck and T. A. Fieldly, *Phys. Rev. B* **36**, 4203 (1987).

[81] L A. Schiff, *Quantum Mechanics*, McGraw-Hill, New York (1968).

[82] R. Lassnig, *Sol. State Comm.* **61**, 577 (1987).

[83] D. Y. K. Ko and J. C. Inkson, *Phys. Rev. B* **38**, 12416 (1988).

[84] P. Guéret, E. Marclay and H. Meier, *Appl. Phys. Lett.* **53**, 1617 (1988).

[85] M. C. Payne, *J. Phys. C* **19**, 1145 (1986).

[86] T. Weil and B. Vinter, *Appl. Phys. Lett.* **51**, 1281 (1987).

[87] G. A. Toombs and F. W. Sheard, in *Electronic Properties of Multilayers and Low-Dimensional Semiconductor Structures*, J. M. Chamberlain, L. Eaves and J. C. Portal, (Eds.), Plenum, London (1989).

[88] D. S. Pan and C. C. Meng, *J. Appl. Phys.* **61**, 2082 (1987).

[89] B. Jogai and K. L. Wang, *Appl. Phys. Lett.* **48**, 1003 (1986).

[90] T. B. Bahder, C. A. Morrison and J. D. Bruno, *Appl. Phys. Lett.* **51**, 1089 (1987).

[91] D. D. Coon and H. C. Liu. *Appl. Phys. Lett.* **51**, 1089 (1987).

[92] E. R. Brown, W. D. Goodhue and T. C. L. G. Sollner, *J. Appl. Phys.* **64**, 1519 (1988).

[93] K. F. Brennan and C. J. Summers, *J. Appl. Phys.* **61**, 614 (1986).

[94] B. Ricco and M. Ya Azbel, *Phys. Rev. B* **29**, 1970 (1984).

[95] P. J. Price, *Superlatt. Microstruct.* **2**, 593 (1986).

[96] M. Büttiker, *IBM J. Res. Dev.* **32**, 63 (1985).

[97] P. J. Price, *Phys. Rev. B* **38**, 1994 (1988).

[98] F. Chevoir and B. Vinter, *Appl. Phys. Lett.* **55**, 1859 (1989).

[99] F. W. Sheard and G. A. Toombs, *Appl. Phys. Lett.* **54**, 1228 (1988).

[100] M. C. Payne, *J. Phys. C* **21**, L579 (1988).

[101] T. B. Bahder, J. D. Bruno, R. G. Hay and C. A. Morrison, *Phys. Rev. B* **37**, 6256 (1988).

[102] M. Jonson and A. Grincwajg, *Appl. Phys. Lett.* **51**, 1729 (1987).

[103] A. D. Stone and P. A. Lee, *Phys. Rev. Lett.* **54**, 1196 (1988).

[104] R. Gupta and B. K. Ridley, *J. Appl. Phys.* **64**, 3089 (1988).

[105] S. Luryi, *Superlatt. Microstruct.* **5**, 375 (1989).

[106] A. J. Leggett, in *Nanostructure Physics and Fabrication*, M. A. Reed and W. P. Kirk (Eds.), Academic Press, Boston (1989).

[107] G. Bergmann, *Physics Reports* **107**, 1 (1984).

[108] L. Eaves, G. A. Toombs, F. W. Sheard, C. A. Payling, M. L. Leadbeater, E. S. Alves, T. J. Foster, P. E. Simmonds, M. Henini and O. H. Hughes, *Appl. Phys. Lett.* **52**, 212 (1988).

[109] P. J. Price, *Phys. Rev. B* **36**, 1314 (1987).

[110] W. R. Frensley, in *Nanostructure Physics and Fabrication*, M. A. Reed and W. P. Kirk (Eds.), Academic Press, Boston (1989).

[111] R. Lassnig and W. Boxleitner, *Sol. State Comm.* **64**, 979 (1987).

[112] J. C. Picoche, P. Rub and H. J. Schneider-Muntau, *J. Mag. Magn. Mat.* **11**, 308 (1979).

[113] F. W. Sheard and G. A. Toombs, *Solid-State Electron.* **32**, 1443 (1989).

[114] A. C. Gossard, *IEEE J. Quantum Electronics* **QE-22**, 1649 (1986).

[115] E. E. Mendez, in *Physics and Applications of Quantum Wells and Superlattices*, E. E. Mendez and K. von Klitzing (Eds.), *NATO ASI Series B Physics* **170**, Plenum, New York (1987).

[116] D. K. Maude *Ph.D Thesis*, University of Nottingham (1988).

[117] G. A. Baraff and J. A. Appelbaum, *Phys. Rev. B* **5**, 475 (1972).

[118] Y. Rajakarunanayake and T. C. McGill, *J. Vac. Sci. Technol. B* **5**, 1288 (1987).

[119] F. Stern and W. E. Howard, *Physical Review* **163**, 816 (1967).

[120] G. Bastard, *Appl. Phys. Lett.* **43**, 591 (1983).

[121] D. Weiss, K. von Klitzing and V. Mosser, in *Two-Dimensional Systems: Physics and New Devices*, G. Bauer, F. Kuchar and H. Heinrich (Eds.), Springer-Verlag, Berlin (1986).

[122] T. P. Smith, B. B. Goldberg, P. J. Stiles and M. Heiblum, *Phys. Rev. B* **32**, 2696 (1985).

[123] K. Seeger, *Semiconductor Physics*, Springer, New York (1982).

[124] N. W. Ashcroft and N. D. Mermin, *Solid State Physics*, Holt, Rinehart and Winston, New York (1976).

[125] K. von Klitzing, G. Dorda and M. Pepper, *Phys. Rev. Lett.* **45**, 494 (1980).

[126] F. F. Fang, T. P. Smith III and S. L. Wright, *Surf. Sci.* **196**, 310 (1988).

[127] E. Gornik, R. Lassnig, G. Strasser, H. L. Störmer, A. C. Gossard and W. Wiegmann, *Phys. Rev. Lett.* **54**, 1820 (1985).

[128] J. P. Eisenstein, H. L. Störmer, V. Narayanamurti, A. Y. Cho, A C. Gossard and C. W. Tu, *Phys. Rev. Lett.* **55**, 875 (1985).

[129] D. Weiss, V. Mosser, V. Gudmundsson, R. R. Gerhardts and K. von Klitzing, *Sol. State Comm.* **62**, 89 (1987).

[130] T. P. Smith III, W. I. Wang and P. J. Stiles, *Phys. Rev. B* **34**, 2995 (1986).

[131] E. Böckenhoff, K. von Klitzing and K. Ploog, *Phys. Rev. B* **31**, 10120 (1988).

[132] K. S. Chan, F. W. Sheard and G. A. Toombs, *unpublished*, (1987).

[133] M. Kaplit and J. N. Zimel, *Phys. Rev. Lett.* **21**, 212 (1968).

[134] C. A. Payling, E. S. Alves, L. Eaves, T. J. Foster, M. Henini, O. H. Hughes, P. E. Simmonds, J. C. Portal, G. Hill and M. A. Pate, *J. Physique* **C-5**, 289 (1987).

[135] C. A. Payling, *Ph. D. Thesis*, University of Nottingham (1989).

[136] D. R. Leadley, R. J. Nicholas, J. J. Harris and C. T. Foxon, *Semicond. Sci. Technol.* **4**, 885 (1989).

[137] F. F. Fang and P. J. Stiles, *Physical Review* **174**, 823 (1968).

[138] M. A. Reed and J. W. Lee, *Appl. Phys. Lett.* **50**, 845 (1987).

[139] E. E. Mendez, L. Esaki and W. I. Wang, *Phys. Rev. B* **33**, 2893 (1986).

[140] V. J. Goldman, D. C. Tsui and J. E. Cunningham, *Phys. Rev. B* **35**, 9387 (1987).

[141] G. A. Toombs, E. S. Alves, L. Eaves, T. J. Foster, M. Henini, O. H. Hughes, M. L. Leadbeater, C. A. Payling, F. W. Sheard, P. A. Claxton, G. Hill, M. A. Pate and J. C. Portal, *Proc. 14th Int. Symp. GaAs and Related Compounds. IOP Conference Series* **91**, 581 (1988).

[142] H. Bando, T. Nakagawa, H. Tokumoto, K. Ohta and K. Kajimura, *Proc. 18th Int. Conf. Low Temperature Physics, Kyoto. Jap. J. Appl. Phys.* **26**, Supplement 26-3, DO14 (1987).

[143] V. J. Goldman, D. C. Tsui and J. E. Cunningham, *Phys. Rev. B* **36**, 7635 (1987).

[144] W. Pötz and Z. Q. Li, *Solid-State Electron.* **32**, 1353 (1989).

[145] N. S. Wingreen, K. W. Jacobsen and J. W. Wilkins, *Phys. Rev. Lett.* **61**, 1396 (1988).

[146] W. Cai, T. F. Zheng, P. Hu, B. Yudanin and M. Lax, *Phys. Rev. Lett.* **63**, 418 (1989).

[147] L. Eaves, E. S. Alves, T. J. Foster, M. Henini, O. H. Hughes, M. L. Leadbeater, F. W. Sheard, G. A. Toombs, K. S. Chan, A. Celeste, J. C. Portal, G. Hill and M. A. Pate, in *Physics and Technology of Submicron Structures*, H. Heinrich, G. Bauer and F. Kuchar (Eds.), Springer-Verlag, Berlin (1988).

[148] M. L. Leadbeater, E. S. Alves, L. Eaves, M. Henini, O. H. Hughes, A. Celeste, J. C. Portal, G. Hill and M. A. Pate, *Phys. Rev. B* **39**, 3438 (1989).

[149] M. L. Leadbeater, E. S. Alves, L. Eaves, M. Henini, O. H. Hughes, A. Celeste, J. C. Portal, G. Hill and M. A. Pate, *Superlatt. Microstruct.* **6**, 63 (1989).

[150] E. Wolak, K. L. Lear, P. M. Pitner, E. S. Hellman, B. G. Park, T. Weil, J. S. Harris, Jr. and D. Thomas, *Appl. Phys. Lett.* **53**, 201 (1988).

[151] J. Söderstrom, T. G. Andersson and Z. G. Chen, *Proc. 19th Int. Conf. Physics of Semiconductors, Warsaw*, (1988).

[152] A. Celeste, L. A. Cury, J. C. Portal, M. Allovon, D. K. Maude, L. Eaves, M. Davies, M. Heath and M. Maldonado, *Solid-State Electron.* **32**, 1191 (1989).

[153] S. M. Sze, *Physics of Semiconductor Devices*, 2nd Edition, John Wiley, New York (1982).

[154] F. W. Sheard, *Private Communication*, (1987).

[155] P. A. Guéret, C. Rossel, E. Marclay and H. Meier, *J. Appl. Phys.* **66**, 278 (1989).

[156] M. A. Reed, J. W. Lee and H-L. Tsai, *Appl. Phys. Lett.* **49**, 158 (1986).

[157] T. J. Foster, *Ph. D. Thesis*, University of Nottingham (1990).

[158] H. van Houten, B. J. van Wees, C. W. J. Beenakker, J. G. Williamson and C. T. Foxon, *Europhysics Lett*, **5**, 721 (1988).

[159] B. R. Snell, K. S. Chan, F. W. Sheard, L. Eaves, G. A. Toombs, D. K. Maude, J. C. Portal, S. J. Bass, P. Claxton, G. Hill and M. A. Pate, *Phys. Rev. Lett.* **59**, 2806 (1987).

[160] M. L. Leadbeater, E. S. Alves, L. Eaves, M. Henini, O. H. Hughes, A. Celeste, J. C. Portal, G. Hill and M. A. Pate, *J. Phys: Condensed Matter* **1**, 4865 (1989).

[161] A. F. J. Levi, R. J. Spāh and J. H. English, *Phys. Rev. Lett.* **36**, 9402 (1987).

[162] S. Sen, F. Capasso, A. C. Gossard, R. A Spah, A. L. Hutchinson and S. N. G. Chu, *Appl. Phys. Lett.* **51**, 1428 (1987).

[163] S. Y. Chou and J. S. Harris, Jr., *Appl. Phys. Lett.* **52**, 1422 (1988).

[164] R. C. Potter and A. A. Lakhani, *Appl. Phys. Lett.* **52**, 1349 (1988).

[165] M. Henini, M. L. Leadbeater, E. S. Alves, L. Eaves and O. H. Hughes, *J. Phys: Condensed Matter* **1**, 3025 (1989).

[166] E. Böckenhoff, K. von Klitzing and K. Ploog, *Proc. 18th Int. Conf. Physics of Semiconductors, Warsaw*, (1988).

[167] T. W. Hickmott, P. M. Solomon, F. F. Fang, F. Stern, R. Fischer and H. Morkoç, *Phys. Rev. Lett.* **52**, 2053 (1984).

[168] L. Eaves, D. K. Maude, F. W. Sheard and G. A. Toombs, in *High Magnetic Fields in Semiconductors*, G. Landwehr (Ed.), Springer-Verlag, Berlin (1986).

[169] M. Heiblum, M. V. Fischetti, W. P. Dumke, D. J. Frank, I. M. Anderson, C. M. Knoedler and L. Osterling, *Phys. Rev. Lett.* **58**, 816 (1987).

[170] J. R. Hayes, P. England and J. P. Harbison, *Appl. Phys. Lett.* **52**, 1578 (1988).

[171] P. C. Becker, H. L. Fragnito, C. H. Brito-Cruz, J. Shah, R. L. Fork, J. E. Cunningham, J. E. Henry and C. V. Shank, *Appl. Phys. Lett.* **53**, 2089 (1988).

[172] E. S. Alves, M. L. Leadbeater, L. Eaves, M. Henini and O. H. Hughes, *Solid-State Electron.* **32**, 1627 (1989).

[173] V. J. Goldman, D. C. Tsui and J. E. Cunningham, *Phys. Rev. Lett.* **58**, 1257 (1987).

[174] T. C. L. G. Sollner, *Phys. Rev. Lett.* **59**, 1622 (1987).

[175] V. J. Goldman, D. C. Tsui and J. E. Cunningham, *Phys. Rev. Lett.* **59**, 1623 (1987).

[176] T. J. Foster, M. L. Leadbeater, L. Eaves, M. Henini, O. H. Hughes, C. A. Payling, F. W. Sheard, P. E. Simmonds and G. A. Toombs, *Phys. Rev. B* **39**, 6205 (1989).

[177] C. A. Payling, E. S. Alves, L. Eaves, T. J. Foster, M. Henini, O. H. Hughes, P. E. Simmonds, F. W. Sheard, G. A. Toombs and J. C. Portal, *Surf. Sci.* **196**, 404 (1987).

[178] J. F. Young, B. M. Wood, G. C. Aers, R. L. S. Devine, H. C. Liu, D. Landheer, M. Buchanan, A. J. SpringThorpe and P. Mandeville. *Phys. Rev. Lett.* **60**, 2085 (1988).

[179] V. J. Goldman, D. C. Tsui and J. E. Cunningham, *Solid-State Electron.* **31**, 731 (1988).

[180] E. S. Alves, L. Eaves, M. Henini, O. H. Hughes, M. L. Leadbeater, F. W. Sheard and G. A. Toombs, *Electron. Lett.* **24**, 1190 (1988). See also *Proc. Int. Conf. Electronic Materials, Tokyo, June 1988*, Published by the Materials Research Society (1989).

[181] A. Zaslavsky, V. J. Goldman, D. C. Tsui and J. E. Cunningham, *Appl. Phys. Lett.* **50**, 1281 (1988).

[182] M. L. Leadbeater, E. S. Alves, L. Eaves, M. Henini, O. H. Hughes, F. W. Sheard and G. A. Toombs, *Semicond. Sci. Technol.* **3**, 1060 (1988).

[183] M. L. Leadbeater, E. S. Alves, L. Eaves, M. Henini, O. H. Hughes, F. W. Sheard, G. A. Toombs, G. Hill and M. A. Pate, *Superlatt. Microstruct.* **6**, 59 (1989).

[184] M. L. Leadbeater, E. S. Alves, L. Eaves, M. Henini, O. H. Hughes, F. W. Sheard and G. A. Toombs, in *Nanostructure Physics and Fabrication*, M. A. Reed and W. P. Kirk (Eds.), Academic Press, Boston (1989).

[185] M. L. Leadbeater, E. S. Alves, F. W. Sheard, L. Eaves, M. Henini, O. H. Hughes and G. A. Toombs, *J. Phys: Condensed Matter* **1**, 10605 (1989).

[186] L. Eaves, M. L. Leadbeater, D. G. Hayes, E. S. Alves,F. W. Sheard, G. A. Toombs, P. E. Simmonds, M. S. Skolnick, M. Henini and O. H. Hughes, *Solid-State Electron.* **32**, 1101 (1989).

[187] M. L. Leadbeater and L. Eaves, *to be published* (1990).

[188] M. L. Leadbeater, L. Eaves, M. Henini and O. H. Hughes, *Appl. Phys. Lett.*, to be published (1990).

[189] M. L. Leadbeater, L. Eaves, M. Henini, O. H. Hughes, G. Hill and M. A. Pate. *Solid-State Electron.* **32**, 1467 (1989).

[190] M. L. Leadbeater, L. Eaves, M. Henini and O. H. Hughes, *Proc. 16th Int. Symp. GaAs and Related Compounds, Karuizawa, Japan, 1989. IOP Conf. Series*, to be published (1990).

[191] M. Cahay, M. McLennon, S. Datta and M. S. Lundstrom, *Appl. Phys. Lett.* **50**, 612 (1987).

[192] H. Ohnishi, T. Inata, S. Muto, N. Yokoyama and A. Shibatomi, *Appl. Phys. Lett.* **49**, 1248 (1986).

[193] B. Jogai, K. L. Wang and K. W. Brown, *J. Appl. Phys.* **59**, 2969 (1986).

[194] M. C. Payne, *Semicond. Sci. Technol.* **2**, 797 (1987).

[195] E. R. Brown, C. D. Parker and T. C. L. G. Sollner, *Appl. Phys. Lett.* **54**, 934 (1989).

[196] H. L. Berkowitz and R. A. Lux, *J. Vac. Sci. Technol. B* **53**, 967 (1987).

[197] P. J. Price, *Phys. Rev. B* **38**, 10652 (1988).

[198] D. D. Coon and K. M. S. V. Bandara, *Appl. Phys. Lett.* **53**, 1865 (1988).

[199] D. D. Coon, K. M. S. V. Bandara and H. Zhao, *Appl. Phys. Lett.* **54**, 2115 (1989).

[200] D. Thomas, F. Chevoir, P. Bois and E. Barbier, *Superlatt. Microstruct.* **5**, 219 (1989).

[201] S. Ben Amor, K. P. Martin, J. J. L. Rascol, R. J. Higgins, R. C. Potter, A. A. Lakhani and H. Hier, *Appl. Phys. Lett.* **54**, 1908 (1989).

[202] C. A. Payling, C. R. H. White, L. Eaves, E. S. Alves, M. L. Leadbeater, J. C. Portal, P. D. Hodson, D. J. Robbins, R. H. Wallis, J. I. Davies and A. C. Marshall, *Superlatt. Microstruct.* **6**, 193 (1989).

[203] J. F. Young, B. M. Wood, G. C. Aers, R. L. S. Devine, H. C. Liu, D. Landheer, M. Buchanan, A. J. SpringThorpe and P. Mandeville, *Superlatt. Microstruct.* **5**, 411 (1989).

[204] W. R. Frensley, M. A. Reed and J. H. Luscombe, *Phys. Rev. Lett.* **62**, 1207 (1989).

[205] J. F. Young, B. M. Wood, G. C. Aers, R. L. S. Devine, H. C. Liu, D. Landheer, M. Buchanan, A. J. SpringThorpe and P. Mandeville, *Phys. Rev. Lett.* **62**, 1208 (1989).

[206] D. G. Hayes, M. S. Skolnick, P. E. Simmonds, L. Eaves, D. P. Halliday, M. L. Leadbeater, M. Henini and O. H. Hughes, *Proc. 4th Int. Conf. Modulated Semiconductor Structures, Ann Arbor, U.S.A.*, to be published in *Surf. Sci.* (1989).

[207] M. S. Skolnick, D. G. Hayes, P. E. Simmonds, A. W. Higgs, G. W. Smith, H. J. Hutchinson, L. Eaves, M. Henini, O. H. Hughes, M. L. Leadbeater and D. P. Halliday, *Phys. Rev. B*, to be published (1990).

[208] T. J. Shewchuk, J. M. Gering, P. C. Chapin, P. D. Coleman, W. Kopp, C. K. Peng and H. Morkoç, *Appl. Phys. Lett.* **47**, 986 (1985).

[209] J. F. Young, B. M. Wood, H. C. Liu, M. Buchanan, D. Landheer, A. J. SpringThorpe and P. Mandeville, *Appl. Phys. Lett.* **52**, 1398 (1988).; *ibid* **53**, 719 (1988).

[210] H. C. Liu, *J. Appl. Phys.* **64**, 4792 (1988).

[211] H. C. Liu, *Appl. Phys. Lett.* **53**, 485 (1988).

[212] E. S. Hellman, K. L. Lear and J. S. Harris, *J. Appl. Phys.* **64**, 2798 (1988).

[213] J. M. Gering, D. A. Crim, D. G. Morgan, P. D. Coleman, W. Kopp and H. Morkoç, *J. Appl. Phys.* **61**, 271 (1987).

[214] The computer program is based on an algorithm supplied by Dr. G. A. Toombs.

[215] L. Eaves, F. W. Sheard and G. A. Toombs, *Physica Scripta* **T19**, 179 (1987).

[216] F. W. Sheard, *Proc. Int. Conf. Phonon Physics, Heidelberg*, to be published (1989).

[217] W. H. Knox, D. S. Chemla and G. Livescu, *Solid-State Electron.* **31**, 425 (1988).

[218] B. Deveaud, J. Shah, T. C. Damen, A. C. Gossard and P. Lugli, *Solid-State Electron.* **31**, 435 (1988).

[219] O. H. Hughes, M. Henini, E. S. Alves, L. Eaves, M. L. Leadbeater, F. W. Sheard, G. A. Toombs, G. Hill, M. A. Pate, J. C. Portal and A. Celeste, *J. Cryst. Growth* **95**, 352 (1989).

[220] L. Eaves, F. W. Sheard and K. W. H. Stevens, in *Physics and Fabrication of Microstructures and Microdevices*, M. J. Kelly and C. Weisbuch (Eds.), Springer-Verlag (1986).

[221] E. S. Alves, *Private Communication* (1989).

[222] C. R. H. White, *Unpublished results*, (1990)

[223] Y. V. Sharvin, *Sov. Phys. JETP* **21**, 655 (1965).

[224] V. S. Tsoi, *JETP Lett.* **19**, 70 (1974).

[225] P. A. M. Benistant, G. F. A. van der Walle, H. van Kempen and P. Wyder, *Phys. Rev. B* **33**, 690 (1986).

[226] A. H. MacDonald and P. Středa, *Phys. Rev. B* **29**, 1616 (1984).

[227] C. W. J. Beenakker and H. van Houten, *Phys. Rev. Lett.* **60**, 2406 (1988).

[228] M. S. Khaikin, *Sov. Phys. JETP* **12**, 152 (1961).

[229] J K. Koch and C. C. Kuo, *Phys. Rev.* **143**, 470 (1965).

[230] R. E. Prange and T-W Nee, *Phys. Rev.* **168**, 779 (1968).

[231] K. S. Chan, L. Eaves, D. K. Maude, F. W. Sheard, B. R. Snell, G. A. Toombs, E. S. Alves, J. C. Portal and S. J. Bass, *Solid-State Electron.* **31**, 711 (1988).

[232] U. Kunze, *Surf. Sci.* **196**, 374 (1988).

[233] E. S. Alves, M. L. Leadbeater, L. Eaves, M. Henini, O. H. Hughes, A. Celeste, J. C. Portal, G. Hill and M. A. Pate, *Superlatt. Microstruct.* **5**, 527 (1989).

[234] M. Helm, F. M. Peeters, P. England, J. R. Hayes and E. Colas, *Phys. Rev. B* **39**, 3427 (1989).

[235] S. Ben Amor, K. P. Martin, J. J. L. Rascol, R. J. Higgins, R. C. Potter, A. A. Lakhani and H. Hier, *Proc. 4th Int. Conf. Modulated Semiconductor Structures, Ann Arbor, U.S.A.*, to be published in *Surf. Sci.* (1989).

[236] R. A. Davies, D. J. Newson, T. G. Powell, M. J. Kelly and H. W. Myron, *Semicond. Sci. Technol.* **2**, 61 (1987).

[237] D. C. Tsui, *Phys. Rev. B* **12**, 5739 (1975).

[238] F. W. Sheard, K. S. Chan, G. A. Toombs, L. Eaves and J. C. Portal, *Proc. 14th Int. Symp. GaAs and Related Compounds, Crete, 1987*, published in *IOP conference series* **91**, 387 (1988).

[239] T. M. Fromhold, F. W. Sheard and G. A. Toombs, *Proc. 4th Int. Conf. Modulated Semiconductor Structures, Ann Arbor, U.S.A.*, to be published in *Surf. Sci.* (1989).

[240] O. H. Hughes, M. Henini, E. S. Alves, M. L. Leadbeater, L. Eaves, M. Davies and M. Heath, *J. Vac. Sci. Technol. B* **7**, 1041 (1989).

[241] M. Henini, M. L. Leadbeater, E. S. Alves, L. Eaves, O. H. Hughes, G. Hill and M. A. Pate, *Proc. 4th Int. Conf. Modulated Semiconductor Structures, Ann Arbor, U.S.A.*, to be published in *Surf. Sci.* (1989).

[242] T. M. Fromhold, *Ph. D. Thesis*, University of Nottingham (1990).

[243] F. W. Sheard, *Unpublished notes*, (1987).

[244] L. Brey, G. Platero and C. Tejedor, *Phys. Rev. B* **38**, 9649 (1988).

[245] J. L. Bardeen, *Phys. Rev. Lett.* **6**, 57 (1961).

[246] W. Zawadzki, *Semicond. Sci. Technol.* **2**, 550 (1987).

[247] U. Merkt, *Phys. Rev. B* **32**, 6699 (1985).

[248] P. Dean, *Proc. Cambridge Philos. Soc.* **62**, 277 (1966).

[249] B. I. Halperin, *Phys. Rev. B* **25**, 2185 (1982).

[250] E. A. Johnson, A. MacKinnon and C. J. Goebel, *J. Phys. C* **20**, L521 (1987).

[251] L. Eaves, D. C. Taylor, J. C. Portal and L. Dmowski, in *Two-Dimensional Systems: Physics and New Devices*, G. Bauer, F. Kuchar and H. Heinrich (Eds.), Springer-Verlag, Berlin (1986).

[252] D. C. Taylor, *Ph. D. Thesis*, University of Nottingham (1987).

[253] P. England, J. R. Hayes, M. Helm, J. P. Harbison, L. T. Florez and S. J. Allen, Jr., *Appl. Phys. Lett.* **54**, 1469 (1989).

[254] L. A. Cury, A. Celeste and J. C. Portal, *Phys. Rev. B* **38**, 13482 (1988).

[255] L. A. Cury, A. Celeste and J. C. Portal, *Solid-State Electron.* **32**, 1689 (1989).

[256] F. Ancillotto, *J. Phys. C* **21**, 4657 (1988).

[257] F. M. Peeters, M. Helm, P. England, E. Colas, J. P. Harbison and L. T. Florez, *Solid-State Electron.* **32**, 1309 (1989).

[258] S. Ben Amor, K. P. Martin, J. J. L. Rascol, R. J. Higgins, A. Torabi, H. M. Harris and C. J. Summers, *Appl. Phys. Lett.* **53**, 2540 (1988).

[259] J. Smoliner, W. Demmerle, G. Berthold, E. Gornik, G. Weimann and W. Schlapp, *Phys. Rev. Lett.* **63**, 2116 (1989).

[260] T. M. Fromhold, *Private communication*, (1989).

[261] G. Platero, P. A. Schulz, L. Brey and C. Tejedor, *Proc. 4th Int. Conf. Modulated Semiconductor Structures, Ann Arbor, U.S.A.*, to be published in *Surf. Sci.* (1989).

[262] P. A. Schulz and C. Tejedor, *Phys. Rev. B* **39**, 11187 (1989).

[263] U. Rössler, *Sol. State Comm.* **49**, 943 (1984).

[264] J. R. Chelikowsky and M. L. Cohen, *Phys. Rev. B* **14**, 556 (1976).

[265] K. Hess, *Adv. Electron. Electron Phys.* **59**, 239 (1982).

[266] M. A. Hopkins, R. J. Nicholas, P. Pfeffer, W. Zawadski, D. Gauthier, J. C. Portal and M. A. DiForte-Poisson, *Semicond. Sci. Technol.* **2**, 568 (1987).

[267] C. L. Zipfel, T. R. Brown and C. C. Grimes, *Surf. Sci.* **58**, 283 (1976).

[268] W. Beinvogl and J. F. Koch, *Phys. Rev. Lett.* **40**, 1736 (1978).

[269] J. C. Maan, C. Uihlein, L. L. Chang and L. Esaki, *Sol. State Comm.* **44**, 653 (1982).

[270] J. H. Craseman and U. Merkt, *Sol. State Comm.* **47**, 917 (1983).

[271] T. Ando, *Phys. Rev. B* **19**, 2106 (1979).

[272] S. K. Bhattacharya, *Phys. Rev. B* **25**, 3756 (1982).

[273] J. C. Maan, in *Two-Dimensional Systems, Heterostructures and Superlattices*, G. Bauer, F. Kuchar and H. Heinrich (Eds.), Springer-Verlag, Berlin (1984).